Tesis doctoral

Microstructural tailoring of nanocomposite electrodes for solid oxide fuel cells

Javier Zamudio García

Programa de doctorado

Química y Tecnologías Químicas: Materiales y Nanotecnología

Directores

Enrique Ramírez Losilla

David Marrero López

Departamento de Química Inorgánica, Cristalografía y Mineralogía

Facultad de Ciencias

Universidad de Málaga

2023

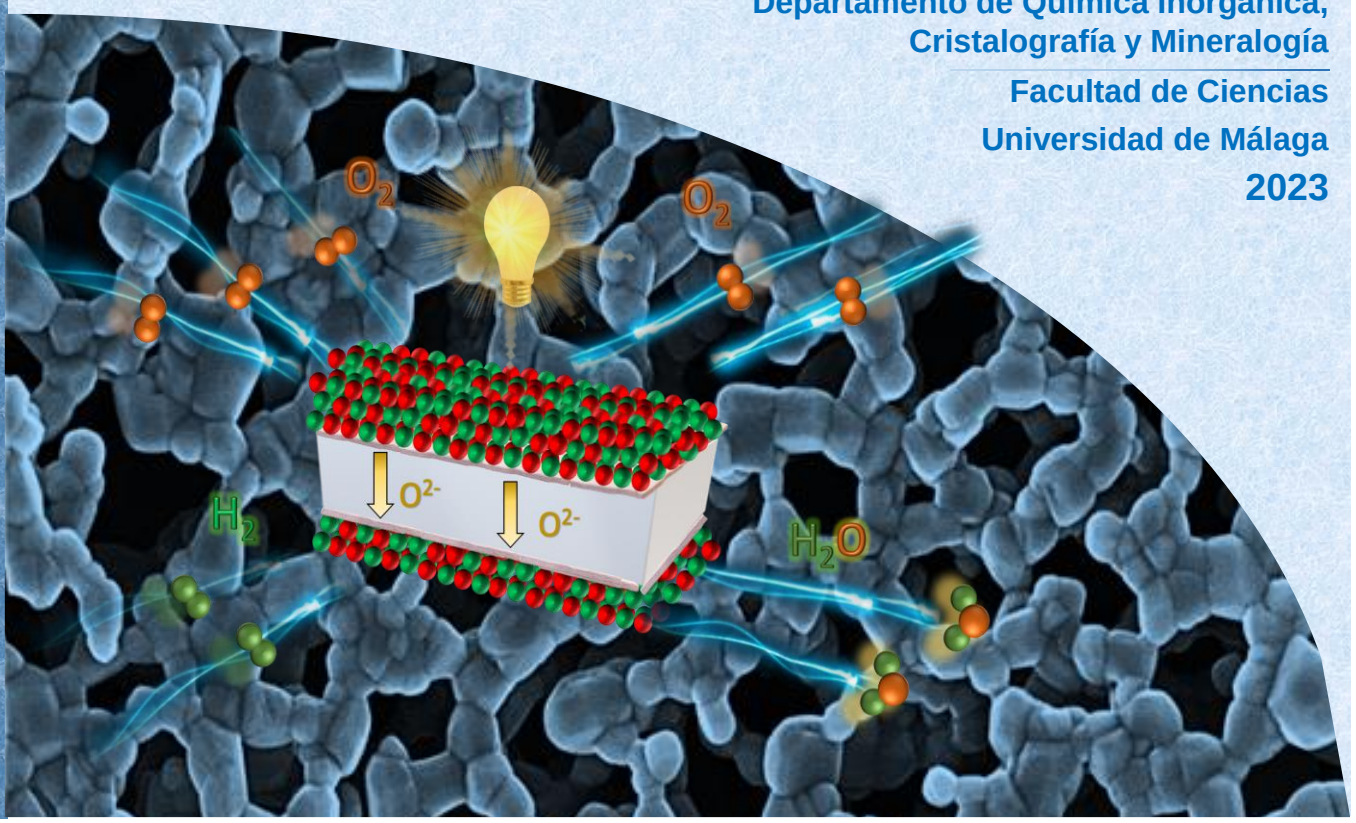

AUTOR: Javier Zamudio García

https://orcid.org/0000-0001-6717-6762

EDITA: Publicaciones y Divulgación Científica. Universidad de Málaga

Esta obra está bajo una licencia de Creative Commons Reconocimiento-NoComercial-SinObraDerivada 4.0 Internacional:
https://creativecommons.org/licenses/by-nc-nd/4.0/legalcode
Cualquier parte de esta obra se puede reproducir sin autorización
pero con el reconocimiento y atribución de los autores.
No se puede hacer uso comercial de la obra y no se puede alterar, transformar o hacer obras derivadas.

Esta Tesis Doctoral está depositada en el Repositorio Institucional de la Universidad de Málaga (RIUMA): riuma.uma.es

UNIVERSIDAD DE MÁLAGA

Tesis doctoral

Microstructural tailoring of nanocomposite electrodes for solid oxide fuel cells

Javier Zamudio García

Directores

Dr. Enrique Ramírez Losilla
Dr. David Marrero López

Programa de doctorado: Química y tecnologías químicas.
Materiales y nanotecnología
Departamento de Química Inorgánica, Cristalografía y Mineralogía
Facultad de Ciencias
Universidad de Málaga
2023

UNIVERSIDAD DE MÁLAGA

DECLARACIÓN DE AUTORÍA Y ORIGINALIDAD DE LA TESIS PRESENTADA PARA OBTENER EL TÍTULO DE DOCTOR

D./Dña JAVIER ZAMUDIO GARCÍA
Estudiante del programa de doctorado QUÍMICA Y TECNOLOGÍAS QUÍMICAS. MATERIALES Y NANOTECNOLOGÍA de la Universidad de Málaga, autor/a de la tesis, presentada para la obtención del título de doctor por la Universidad de Málaga, titulada: MICROSTRUCTURAL TAILORING OF NANOCOMPOSITE ELECTRODES FOR SOLID OXIDE FUEL CELLS.

Realizada bajo la tutorización de ENRIQUE RAMÍREZ LOSILLA y dirección de ENRIQUE RAMÍREZ LOSILLA Y DAVID MARRERO LÓPEZ.

DECLARO QUE:

La tesis presentada es una obra original que no infringe los derechos de propiedad intelectual ni los derechos de propiedad industrial u otros, conforme al ordenamiento jurídico vigente (Real Decreto Legislativo 1/1996, de 12 de abril, por el que se aprueba el texto refundido de la Ley de Propiedad Intelectual, regularizando, aclarando y armonizando las disposiciones legales vigentes sobre la materia), modificado por la Ley 2/2019, de 1 de marzo.
Igualmente asumo, ante a la Universidad de Málaga y ante cualquier otra instancia, la responsabilidad que pudiera derivarse en caso de plagio de contenidos en la tesis presentada, conforme al ordenamiento jurídico vigente.

En Málaga, a 10 de ABRIL de 2023

Fdo.: JAVIER ZAMUDIO GARCÍA Doctorando/a	Fdo.: ENRIQUE RAMÍREZ LOSILLA Tutor/a
Fdo.: ENRIQUE RAMÍREZ LOSILLA Director/es de tesis	DAVID MARRERO LÓPEZ

Edificio Pabellón de Gobierno. Campus El Ejido. 29071
Tel.: 952 13 10 28 / 952 13 14 61 / 952 13 71 10
E-mail: doctorado@uma.es

Edificio Pabellón de Gobierno. Campus El Ejido. 29071
Tel.: 952 13 10 28 / 952 13 14 61 / 952 13 71 10
E-mail: doctorado@uma.es

Dr. Enrique Ramírez Losilla, Catedrático de Química Inorgánica (Departamento de Química Inorgánica, Cristalografía y Mineralogía) y **Dr. David Marrero López**, Profesor Titular (Departamento de Física Aplicada I), ambos pertenecientes a la Facultad de Ciencias de la Universidad de Málaga,

CERTIFICAN:

Que la presente memoria titulada "Microstructural tailoring of nanocomposite electrodes for solid oxide fuel cells", ha sido realizada bajo nuestra dirección en el Departamento de Química Inorgánica, Cristalografía y Mineralogía de la Facultad de Ciencias de la Universidad de Málaga por el graduado en Química D. **Javier Zamudio García**. Este trabajo reúne, a nuestro juicio, contenido científico suficiente y las condiciones necesarias para optar al grado de Doctor con mención Internacional. Las publicaciones en coautoría que avalan la presente tesis doctoral no han sido utilizadas en ninguna tesis doctoral con anterioridad.

Málaga, a 10 de Abril de 2023

Fdo: Dr. Enrique Ramírez Losilla

Fdo: Dr. David Marrero López

UNIVERSIDAD DE MÁLAGA

Agradecimientos

Al fin ha llegado ese momento que tanto he estado esperando y por el que he trabajado cada día, la defensa de mi tesis doctoral. Tras cuatro años desarrollando este proyecto y después de muchas dificultades, esta etapa llega a su fin y me gustaría dedicar unas palabras de agradecimiento a todas las personas que me han acompañado en este arduo camino.

En primer lugar, quiero expresar mi más sincera gratitud a mis dos directores de tesis, sin los que esto no hubiera sido posible. Al Dr. Enrique Ramírez Losilla por confiar en mí desde el principio, enseñarme como ser un verdadero investigador y ayudarme a ser una persona más ordenada. Gracias por tener siempre los mejores consejos para mí y darme esta oportunidad. Al Dr. David Marrero López, por todo lo que he aprendido de ti y estar continuamente al pie del cañón cuando más lo he necesitado. Te agradezco enormemente todo el apoyo, el tiempo empleado y la capacidad de manejar de manera ejemplar situaciones en las merecía una buena reprimenda.

Igualmente, quiero agradecer a todos los profesores del departamento de Química Inorgánica, Cristalografía y Mineralogía por la calurosa acogida y por todo lo que he aprendido de ellos en estos años. Al Dr. Pedro J. Maireles Torres por su gran valor como director del departamento, al Dr. Aurelio Cabeza Díaz por estar siempre ahí cuando se le necesita para resolver cualquier duda, al Dr. Pascual Olivera Pastor por todo lo que he aprendido de nuestras conversaciones sobre cualquier tema científico y a las Dras. Mª Ángeles Gómez de la Torre y Josefa M. Mérida Robles por contagiarme sus ganas y motivación durante las prácticas de laboratorio.

También me gustaría agradecer a los Dres. Vincenzo Esposito, Nini Pryds y Francesco Chiabrera por darme la oportunidad hacer dos estancias de investigación en la Universidad Técnica de Dinamarca (DTU) y recibirme con los brazos abiertos. Gracias a Stefano, Subha, Stella, Blanka y Julie, esos 7 meses que pasé en Copenhague fueron inolvidables y llenos de buenos momentos que no olvidaré.

UNIVERSIDAD DE MÁLAGA

Al Dr. José M. Porras Vázquez por toda la ayuda que me ha brindado estos años y por los buenos ratos y anécdotas graciosas durante los congresos. A la Dra. Lucía dos Santos Gómez por contagiarme sus ganas y pasión por la investigación desde el primer momento y por estar siempre dispuesta a ayudarme.

Del mismo modo, me gustaría agradecer a todos mis compañeros de trabajo por el apoyo, los buenos momentos vividos y las cervezas que nos hemos tomado juntos. A mi consejo de sabios, Adrián, Abraham, Toni y Fernando, que me han apoyado y me han sacado una sonrisa en la etapa final de la tesis cuando más lo necesitaba. A Álvaro y Alejandro por llenar de alegría el departamento y por su humor negro. A don Benjamín por su energía y pasión por la ciencia. A Mari, Cinthya y Gabi por aguantar todas las barbaridades que hemos dicho en la sala de becarios. A Inés por su kit de rellenar capilares. A Rocío e Isa, por hacerme ver que no solo yo tengo mala suerte. A Juanjo por los buenos momentos y por el viaje a Nápoles, a Leire por toda la ayuda prestada y sus ganas de aprender. A Marco y Herculys, por su comprensión y subirme el ánimo con conversaciones sin ningún sentido. A todos los postdocs, muchas gracias por haberme ayudado cuando lo he necesitado.

A los técnicos de laboratorio, Antonio y David, por sus consejos a la hora de reparar los equipos y estar siempre disponibles para ayudarme en lo que fuese necesario. Al nuevo técnico, Jesús, por su paciencia y empeño en que todo esté impoluto.

A mis amigos de toda la vida, Fernan, Juanan, Berni, Iván y Jesús, por esos pequeños momentos del día a día que te animan cuando más lo necesitas y estar ahí siempre. A todas las personas que me acompañaron durante la carrera, en especial a Ana, Irene y Alicia, agradezco enormemente todo el cariño recibido durante estos años.

A mis padres y mi hermano por todo el apoyo y confianza que han depositado siempre en mí. Gracias por ser un pilar fundamental y acompañarme en todo este largo camino. Aprovecharé al máximo todas esas oportunidades que por desgracia la vida no os dio a vosotros y conseguiré aquello por lo que lucho desde el primer día que entré en la Universidad.

UNIVERSIDAD DE MÁLAGA

Por último, quiero agradecer al Ministerio de Educación por la beca de profesorado universitario para el desarrollo de esta tesis doctoral (FPU17/02621) y las ayudas para las dos estancias en el DTU (EST19/00115, EST21/00398).

Espero que la próxima etapa sea tan buena como esta y que la vida me siga juntando con personas tan extraordinarias como vosotros. Puede que quizás no sea la persona con más suerte, pero he insistido y luchado sin descanso para conseguir todo lo que tengo ahora mismo. Por lo que he vivido y está por venir.

Learn from yesterday, live for today, hope for tomorrow

UNIVERSIDAD DE MÁLAGA

UNIVERSIDAD
DE MÁLAGA

Index

UNIVERSIDAD DE MÁLAGA

UNIVERSIDAD DE MÁLAGA

UNIVERSIDAD DE MÁLAGA

UNIVERSIDAD DE MÁLAGA

UNIVERSIDAD DE MÁLAGA

UNIVERSIDAD
DE MÁLAGA

Abbreviations

AFC	Alkaline Fuel Cell	**LSCF$_{0.2}$**	$La_{0.6}Sr_{0.4}Co_{0.8}Fe_{0.2}O_{3-\delta}$
AFM	Atomic Force Microscopy	**LSCM**	$La_{0.75}Sr_{0.25}Cr_{0.5}Mn_{0.5}O_{3-\delta}$
A.L.	Active Layer	**LSF**	$La_{0.8}Sr_{0.2}FeO_{3-\delta}$
B	Bulk	**LSFT$_{0.2}$**	$(La_{0.8}Sr_{0.2})_{0.95}Fe_{0.8}Ti_{0.2}O_{3-\delta}$
BE	Backscattered Electrons	**LSFT$_{0.4}$**	$(La_{0.8}Sr_{0.2})_{0.95}Fe_{0.6}Ti_{0.4}O_{3-\delta}$
B.E.	Binding Energy	**LSGM**	$La_{0.9}Sr_{0.1}Ga_{0.8}Mg_{0.2}O_{2.85}$
BSCF	$Ba_{0.5}Sr_{0.5}Co_{0.8}Fe_{0.2}O_{3-\delta}$	**LSM**	$La_{0.8}Sr_{0.2}MnO_{3-\delta}$
BYO	$Bi_{1.5}Y_{0.5}O_3$	**MCFC**	Molten Carbonate Fuel Cell
BZCYYb	$BaZr_{0.1}Ce_{0.7}Y_{0.1}Yb_{0.1}O_{3-\delta}$	**MIEC**	Mixed ionic-electronic conductors
CE	Counter Electrode	**MPD**	Maximum Power Density
CGO	$Ce_{0.9}Gd_{0.1}O_{1.95}$	**OCV**	Open Circuit Voltage
CPE	Constant Phase Element	**ORR**	Oxygen Reduction Reaction
CPO	$Ce_{0.8}Pr_{0.2}O_{1.90}$	**PAFC**	Phosphoric Acid Fuel Cell
DC	Direct Current	**PBC**	$PrBaCo_2O_{5+\delta}$
DFT	Density Functional Theory	**PC-SOFC**	Proton conducting SOFC
DRT	Distribution of Relaxation Times	**PEMFC**	Proton Exchange Membrane FC
DTU	Technical University of Denmark	**PLD**	Pulsed Laser Deposition
DWSB	$Dy_{0.08}W_{0.04}Bi_{0.88}O_{1.56}$	**PMMA**	poly(methyl-methacrylate)
ECR	Electrochem. Conductivity Relaxation	**pO_2**	Oxygen Partial Pressure
EDTA	Ethylendiaminetetraacetic acid	**Q**	Constant Phase Element
EDS	Energy Dispersive X-ray Spectros.	**Q-SSOFC**	Quasi symmetrical SOFC
EIS	Electrochemical Impedance Spectros.	**RC**	Rocking Curve
ESB	$Er_{0.4}Bi_{1.6}O_3$	**RE**	Reference Electrode
ESD	Electrostatic Spray Deposition	**RP**	Ruddlesden-Popper
FE	Field Emission	**R_p**	Polarization Resistance
FIB	Focused Ion Beam	**RSM**	Reciprocal Space Mapping
FD	Freeze-drying	**RSOFC**	Reversible SOFC
FC	Fuel Cell	**SAED**	Selected Area Electron Diff.
FCE	Fuel Cell Energy	**SDC**	$Ce_{0.8}Sm_{0.2}O_{1.9}$
GB	Grain Boundary	**SE**	Secondary Electrons
HAADF	High Angle Annular Dark Field	**SEM**	Scanning Electron Microscopy
HOR	Hydrogen oxidation reaction	**SFM**	$Sr_2Fe_{1.5}Mo_{0.5}O_{6-\delta}$
HER	Hydrogen evolution reaction	**SOEC**	Solid Oxide Electrolysis Cell
HT-SOFC	High temperature SOFC	**SOFC**	Solid Oxide Fuel Cell
ICSD	Inorganic Crystal Structure Database	**SPTO**	$(Sr_{0.7}Pr_{0.3})_{0.95}TiO_{3-\delta}$
K.E.	Kinetic Energy	**SPTNO**	$(Sr_{0.9}Pr_{0.1})_{0.9}Ti_{0.9}Ni_{0.1}O_{3-\delta}$
LC	$La_{0.98}CrO_{3-\delta}$	**SSZ**	10 mol.% Sc_2O_3-ZrO_2
LCM	$La_{0.98}Cr_{0.75}Mn_{0.25}O_{3-\delta}$	**SSOFC**	Symmetrical SOFC
LCF	$La_{0.98}Cr_{0.75}Fe_{0.25}O_{3-\delta}$	**SSC**	$Sm_{0.5}Sr_{0.5}CoO_{3-\delta}$
LCO	$La_2Ce_2O_7$	**STO**	$SrTiO_3$
LSAT	$(LaAlO_3)_{0.3}(Sr_2TaAlO_6)_{0.7}$	**STEM**	Scanning TEM
LSC	$La_{0.6}Sr_{0.4}CoO_{3-\delta}$	**TEC**	Thermal Expansion Coefficient
LSCF	$La_{0.6}Sr_{0.4}Co_{0.2}Fe_{0.8}O_{3-\delta}$	**TEM**	Transmission Electron Micros.

UNIVERSIDAD DE MÁLAGA

Abbreviations

TPB	Triple Phase Boundary
VAN	Vertically Aligned Nanostructures
WE	Working Electrode
XPS	X-ray Photoelectron Spectroscopy
XRD	X-Ray Diffraction
YSZ	$Zr_{0.84}Y_{0.16}O_{1.92}$

UNIVERSIDAD DE MÁLAGA

Summary

UNIVERSIDAD
DE MÁLAGA

UNIVERSIDAD
DE MÁLAGA

Summary

(3000 words)

The high demand for electrical energy induced by the rapid population growth has arisen the necessity to develop sustainable and environmentally friendly energy sources. Nowadays, the global production of energy is still highly dependent on fossil fuels, which produce harmful carbon emissions. Additionally, the wholesale price of gas in 2022 was around four times higher than at the start of 2021. Now more than ever, it is indispensable to gradually move from fossil fuels to renewable energy sources [1]; however, the electrical production from these sources is discontinuous and intermittent, and consequently, alternative methods for electrical energy production and storage are needed.

In this context, fuel cells are one of the most promising technologies to obtain electrical energy from a wide variety of fuels with good efficiencies and lower emission of pollutants. In particular, Solid Oxide Fuel Cells (SOFCs) have attracted great attention in recent years due to their fuel flexibility, good tolerance to impurities in the

UNIVERSIDAD DE MÁLAGA

fuel and higher efficiencies [2]. In addition, they can operate in reverse mode (electrolysis) to produce hydrogen from water and electrical energy from renewable energy sources. In comparison to conventional batteries, fuel cells have several advantages, such as higher energy density, longer duration and more flexibility. However, the high operating temperatures of SOFCs (600-800 ºC) needed to achieve a good electrode performance and a sufficient ionic conductivity for the electrolyte, negatively affect the long-term stability of these devices. For this reason, decreasing the operating temperature is one of the main goals for the wide implementation of SOFCs [3]. Most of the investigations in this field in the last few years have been focused on the development of new materials or improvement of the cell performance via microstructural engineering of the cell components.

The anode-supported SOFCs are the most common configuration in these electrochemical devices, in which a thin film electrolyte of several microns is supported onto a thick porous anode to minimize the ohmic losses of the cell. In this cell configuration, the anode material is a Ni-cermet due to its high electronic conductivity and remarkable electrochemical activity for hydrogen oxidation, but suffers from several degradation issues, such as Ni agglomeration, sulphur poisoning or carbon deposition when fuelled directly with hydrocarbons [4].

Over the past years, researchers have investigated new electrode materials and cell configurations to partially solve these issues. One of the most promising SOFC configurations consists in the implementation of the same electrode material as both cathode and anode, commonly known as Symmetrical Solid Oxide Fuel Cells (SSOFCs). This configuration has several advantages when compared to traditional anode-supported cells, including fewer fabrication steps, better thermo-mechanical stability and chemical compatibility with the other cell components [5]. More importantly, the cell degradation induced by sulphur poisoning or carbon deposition can by partially solved by gas switching in the anode and cathode. In addition, the possibility of this cell configuration to operate in reversible mode (RSOFC) for CO_2 and steam electrolysis is highly attractive due to its multifunctionality and versatility for local needs, leading to energy storage and also decreasing CO_2 emissions [6]. Redox stable symmetrical electrodes with single perovskite-type structure, such as $La(Cr,Mn)O_{3-\delta}$, $(La,Sr)FeO_{3-\delta}$ and $(La,Sr)TiO_{3-\delta}$ or layered perovskites, such as

UNIVERSIDAD DE MÁLAGA

$PrBaMn_2O_{5+\delta}$ or $Sr_2Fe_{1.5}Mo_{0.5}O_{6-\delta}$, have been investigated, improving their electrochemical properties by appropriate doping strategies in A- and B-site.

It is well known that the crystal structure and composition of the electrodes play a key role in the electrochemical performance; nevertheless, the microstructural optimization of the electrodes has demonstrated to be crucial to boost the electrochemical properties at low operating temperatures in both oxidizing and reducing conditions. In general, electrodes with low porosity and relatively large grain size are obtained from conventional preparation methods during multiple synthesis steps and at high sintering temperatures. Such calcination processes lower the active sites for the electrochemical reactions and thus the electrode performance. Different deposition methods have been investigated to prepare the electrodes directly onto the electrolyte surface at low temperatures, such as spray-pyrolysis, pulsed laser deposition (PLD) or magnetron sputtering. Among them, spray-pyrolysis has demonstrated to be a simple, cost-effective and versatile technique to obtain homogenous thin films with different microstructural architectures over large areas at reduced temperatures (Figure 1) [7,8].

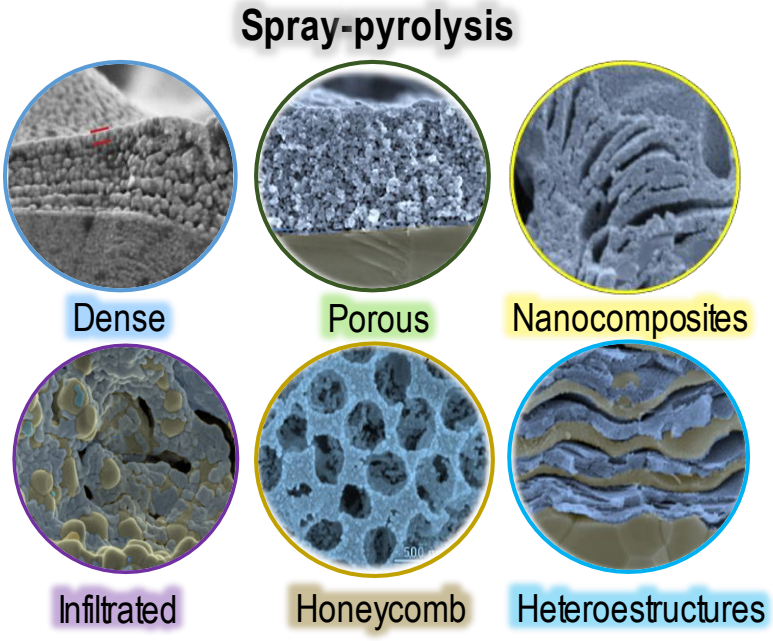

Figure 1. Different electrode microstructures obtained by spray-pyrolysis [7].

UNIVERSIDAD DE MÁLAGA

In order to enhance the electrochemical properties of traditional electrodes, different microstructural strategies have been explored. Figure 2 shows all the microstructural architectures investigated in this Thesis: (a) traditional electrodes with poor ionic conductivity and limited TPB at the electrode/electrolyte interface; (b) composite electrode formed by the mixture of an ionic and an electronic conductor; (c) electrodes with mixed ionic-electronic conductivity (MIEC); (d) nanostructured electrodes with low particle size; (e) nanocomposite electrodes assembled directly onto the electrolyte; (f) infiltration of the electrode into a porous electrolyte backbone; (g) exsolution of metal nanoparticles, such as Ni, on the electrode surface; (h) active layers at the electrode/electrolyte interface and (i) Vertically Aligned Nanostructures (VANs) deposited by PLD to act as an active layer.

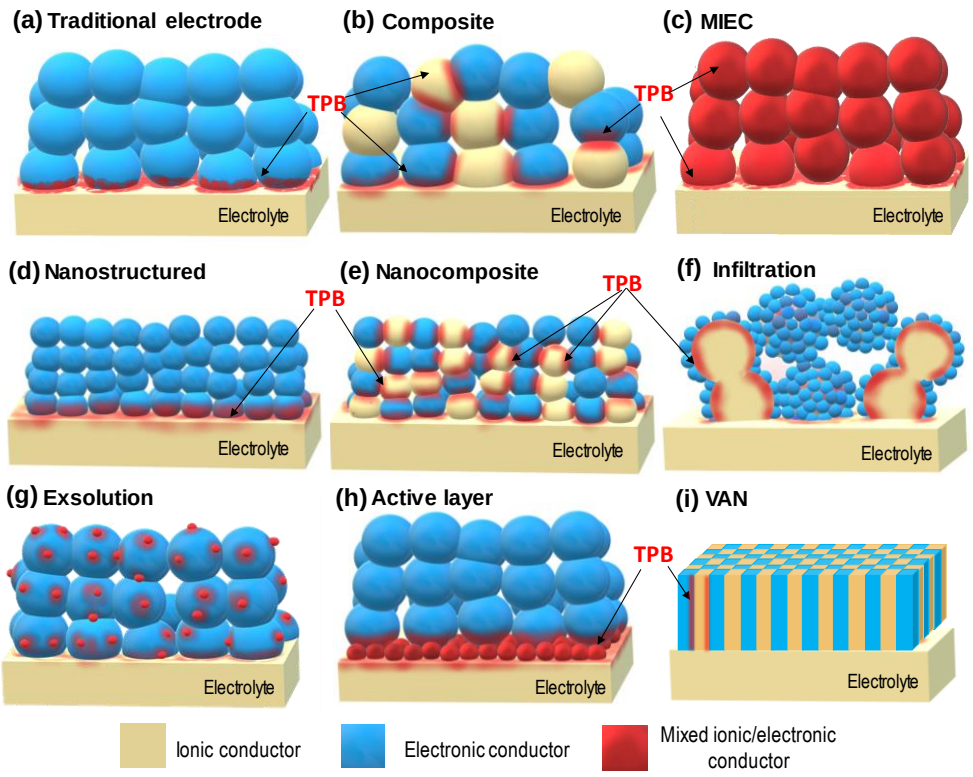

Figure 2. Illustration of different microstructural strategies employed to enhance the electrochemical performance of SOFC electrodes: (a) traditional electrode, (b) composite electrode, (c) MIEC, (d) nanostructured electrode (e) nanocomposite electrode (f) infiltrated electrode, (g) electrode with exsolved metal nanoparticles, (h) electrode with an active layer and (i) VAN.

UNIVERSIDAD DE MÁLAGA

In recent years, the implementation of nanocomposite electrodes has demonstrated improved electrochemical properties and better thermal stability when compared to single-phase nanostructured electrodes [9,10]. In particular, the nanoscale contact between two different phases in a nanocomposite electrode hinders the grain growth due to cation diffusion limitations at the grain boundary, avoiding the typical performance degradation observed in nanostructured electrodes over time due to uncontrolled grain growth. Moreover, the intimate mixture between an ionic and an electronic conductor extends the triple-phase-boundary (TPB) sites where electrochemical reactions take place.

In this work, different nanostructured and nanocomposite electrode layers based on the combination of perovskite-type electrodes, *i.e.* $LaCrO_3$, $SrTiO_3$ or $LaFeO_3$ and the ionic conductor $Ce_{0.9}Gd_{0.1}O_{1.95}$ (CGO) with fluorite-type structure have been prepared and tested for their implementation in SSOFCs. The electrode layers were prepared directly onto $Zr_{0.84}Y_{0.16}O_{1.92}$ (YSZ) or $La_{0.9}Sr_{0.1}Ga_{0.8}Mg_{0.2}O_{2.85}$ (LSGM) electrolytes by spray-pyrolysis. Additionally, pulsed laser deposition (PLD) was employed for the preparation of active layers [11,12]. For comparison purposes, the same electrode compositions were prepared as powders from freeze-dried precursors and then deposited onto the electrolyte by screen-printing method.

The structural characterization of the electrodes was performed by XRD. Additionally, rocking curve and reciprocal space maps were carried out for the thin films deposited by PLD. The microstructure was studied by SEM, TEM, HAADF-STEM and AFM. The chemical composition was analysed by EDS and XPS. A complete electrochemical characterization was carried out by electrochemical impedance spectroscopy (EIS) and the four-probe Van der Pauw method. The total conductivity and polarization resistance of the electrodes were analyzed in different atmospheres (air, 5% H_2-Ar and H_2) at different temperatures and as a function of the oxygen partial pressure (pO_2). The best electrode candidates were tested under real operation conditions in a fuel cell.

During the development of this Thesis, new electrochemical cells for 3-probe electrode configuration were implemented in our lab for anodic and cathodic polarization measurements, as well as conductivity experiments at different oxygen

UNIVERSIDAD DE MÁLAGA

partial pressures. Distribution of relaxation times (DRT) was employed as an alternative method to classical equivalent circuits to analyse the electrode contributions of the impedance spectra.

The main results obtained during this PhD Thesis are discussed in two different sections: (i) nanocomposite electrode materials for SSOFCs prepared by spray-pyrolysis deposition (Chapters 4-6) and (ii) nanocomposite active layers deposited by spray-pyrolysis (Chapter 7) and VANs deposited by PLD (Chapters 8-9). The most relevant results of each section are briefly summarized below.

(i) In the first section of the Thesis, composite electrode materials with advanced electrode architectures were prepared by spray-pyrolysis deposition for their potential application in SSOFCs (Table 1). Since, $LaCrO_3$-based materials were the first candidates for symmetrical electrodes, several doping strategies in the A-site with Ca and Sr and in the B-site with different transition metals (Mn, Fe, Ti and Cu) were tested to obtain nanostructured layers via spray-pyrolysis deposition (Chapter 4). Firstly, we investigated the incorporation of alkaline-earth cations into $LaCrO_3$ layers; however, secondary phases of $(Sr,Ca)CrO_{4-\delta}$ were found at temperatures lower than 1200 ºC. Such high calcination temperatures lead to electrode layers with relatively large grain size and reduced porosity, and consequently, poor electrochemical performance with polarization resistance values of 1.95 Ω cm^2 at 700 ºC in air.

For this reason, a B-site doping strategy was investigated in $La_{0.98}Cr_{0.75}M_{0.25}O_{3-\delta}$ (M= Mn, Fe, Cu and Ti). These electrodes were deposited by spray-pyrolysis onto a porous CGO backbone to obtain a composite electrode formed by CGO particles coated with the $LaCrO_3$-based electrode catalyst. The best electrochemical properties in both air and H_2 atmospheres for $La_{0.98}Cr_{0.75}Mn_{0.25}O_{3-\delta}$ (LCM), *i.e.* 0.35 and 0.53 Ω cm^2, respectively, at 700 ºC. Alternatively, LCM-CGO nanocomposite electrodes with different LCM content (0-60 wt.%) were prepared by spray-pyrolysis at low temperatures directly on the electrolyte surface from a single aqueous precursor solution.

UNIVERSIDAD DE MÁLAGA

Table 1. Composition, fabrication method and electrochemical properties representative electrode materials investigated in Chapters 4-6. The synthetic methodology and microstructural strategy employed for the synthesis of powders and layers are indicated as follows: Freeze-dried powders (FD), composite by powder mixture (PM), composite by co-synthesis obtained by freeze-drying (Cosyn). Layers deposited directly on the electrolyte by spray-pyrolysis (SP), infiltration by spray-pyrolysis into a porous backbone (SP-Inf), nanocomposite by spray-pyrolysis deposition (SP-NC). R_p values are given at 700 ºC for the electrodes deposited onto YSZ electrolytes. A# indicates the article. Non published data are indicated as NP.

	Composition	Preparation method	R_p^{Air/H_2} (Ω cm^2)	Power Density $^{800\ ºC}$ (mW cm^{-2})	Ref
Chapter 4	$La_{0.98}CrO_{3-\delta}$	SP-Inf	0.91/-	-	A1
	$La_{0.98}Cr_{0.75}Cu_{0.25}O_{3-\delta}$	SP-Inf	0.70/-	-	A1
	$La_{0.98}Cr_{0.75}Fe_{0.25}O_{3-\delta}$	SP-Inf	0.52/0.91	-	A1
	$La_{0.98}Cr_{0.75}Mn_{0.25}O_{3-\delta}$	SP-Inf	0.35/0.53	470	A1
	$La_{0.98}Cr_{0.75}Mn_{0.25}O_{3-\delta}$	SP	5.1/3.8	-	A1
	50 wt.%$La_{0.98}Cr_{0.75}Mn_{0.25}O_{3-\delta}$-CGO	FD-PM	5.6	-	A2
	50 wt.%$La_{0.98}Cr_{0.75}Mn_{0.25}O_{3-\delta}$-CGO	SP-NC	0.80/0.18	570	A2
Chapter 5	$(Sr_{0.7}Pr_{0.3})_{0.95}TiO_{3\pm\delta}$	FD	4.81/-	-	A3
	50 wt.%$(Sr_{0.7}Pr_{0.3})_{0.95}TiO_{3\pm\delta}$-CGO	FD-PM	2.45/-	-	A3
	50 wt.%$(Sr_{0.7}Pr_{0.3})_{0.95}TiO_{3\pm\delta}$-CGO	FD-Cosyn	1.60/2.37	125	A3
	50 wt.%$(Sr_{0.7}Pr_{0.3})_{0.95}TiO_{3\pm\delta}$-CGO	SP-NC	0.50/0.46	354	A3
	40 wt.%$(Sr_{0.7}Pr_{0.3})_{0.95}TiO_{3\pm\delta}$-CGO	SP-NC	0.50/1.17	-	A3
	60 wt.% $(Sr_{0.7}Pr_{0.3})_{0.95}TiO_{3\pm\delta}$-CGO	SP-NC	0.59/0.88	-	A3
Chapter 6	$(La_{0.8}Sr_{0.2})_{0.95}Fe_{0.8}Ti_{0.2}O_{3-\delta}$	SP-Inf	0.23/0.41	-	A4,NP
	50 wt.%$(La_{0.8}Sr_{0.2})_{0.95}Fe_{0.8}Ti_{0.2}O_{3-\delta}$-CGO	FD-PM	1.19/-	309	A4,NP
	50 wt.%$(La_{0.8}Sr_{0.2})_{0.95}Fe_{0.8}Ti_{0.2}O_{3-\delta}$-CGO	SP-NC	0.30/0.58	-	NP
	$(La_{0.8}Sr_{0.2})_{0.95}(Fe_{0.8}Ti_{0.2})_{0.9}Ni_{0.1}O_{3-\delta}$	SP-Inf	0.34/0.11	496	NP
	50$(La_{0.8}Sr_{0.2})_{0.95}(Fe_{0.8}Ti_{0.2})_{0.9}Ni_{0.1}O_{3-\delta}$-CGO	FD-PM	-/0.72	617	NP
	$(La_{0.8}Sr_{0.2})_{0.95}Fe_{0.6}Ti_{0.4}O_{3-\delta}$	SP-Inf	0.67/0.20	-	NP
	50 wt.%$(La_{0.8}Sr_{0.2})_{0.95}Fe_{0.6}Ti_{0.4}O_{3-\delta}$-CGO	FD-PM	8.84/-	-	NP

UNIVERSIDAD DE MÁLAGA

The nanocomposite electrodes, consisting of a mixture of perovskite and fluorite-type phases, were formed at only 800 ºC and more interestingly, they exhibited a particle size of only 30 nm diameter, in comparison to 122 nm for 100 wt. % LCM, due to the intimate mixture of LSM and CGO phases at the nanoscale level, suppressing the cation diffusion and thus the grain growth during the co-sintering process. The results were compared with those obtained for screen-printed electrodes by mixing LCM and CGO powders.

The best polarization resistance (R_p) values were obtained for the nanocomposite electrode with composition 50 wt.% LCM-CGO, 0.80 and 0.18 Ω cm^2 in air and H_2, respectively, at 700 ºC. Furthermore, a remarkable maximum power density of 570 mW cm^{-2} at 800 ºC was achieved for a 300 µm LSGM-supported SSOFC. The R_p of the nanocomposite electrodes were almost one order of magnitude lower than the same composition deposited by screen-printing (5.6 Ω cm^2 at 700 ºC in air) due to the higher sintering temperature needed (1100 ºC) to achieve adequate adhesion to the electrolyte. Such high sintering temperature induces a significant grain growth and the reduction of the TPB length.

$SrTiO_3$-based electrodes were also investigated due to their good redox stability, as well as carbon and sulphur tolerance. In order to enhance the electrochemical properties for ORR, a Pr-doping strategy was employed to increase the electrical conductivity in air due to the variable oxidation states of Pr^{4+}/Pr^{3+}. Nanocomposite electrodes with nominal composition $(Sr_{0.7}Pr_{0.3})_{0.95}TiO_{3\pm\delta}$-$Ce_{0.9}Gd_{0.1}O_{1.95}$ (40-60 wt.% SPTO) were directly assembled on the electrolyte surface by spray-deposition and their properties were compared with the analogous screen-printed electrodes (Chapter 5).

The lower preparation temperature of the nanocomposite electrodes not only inhibits the grain growth (~20 nm at 800 ºC) but also hinders the formation of layered ordered extended defects, which have demonstrated to be detrimental to the conducting properties of $SrTiO_3$-based materials. More interestingly, the electrodes obtained by co-synthesis were stable at temperatures as high as 1300 ºC without the presence of secondary phases. R_p values of 0.50 and 0.46 Ω cm^2 in air and H_2, respectively, at 700 ºC were obtained for 50 wt.% SPTO-CGO nanocomposite, values

UNIVERSIDAD DE MÁLAGA

that were almost an order of magnitude lower than those obtained for the same composition prepared by screen-printing (Table 1).

Finally, (La,Sr)$FeO_{3-\delta}$ based perovskite materials were investigated due to their excellent performance reported as cathode materials (Chapter 6). In order to improve the redox stability for potential application as both air and fuel electrodes, Ti-doped compositions were prepared $(La_{0.8}Sr_{0.2})_{0.95}Fe_{1-x}Ti_xO_{3-\delta}$-$Ce_{0.9}Gd_{0.1}O_{1.95}$ ($LSFT_x$; x=0.2 and 0.4). Different electrode architectures were tested, including traditional screen-printed powder electrodes of (a) mechanically mixed powders of $LSFT_x$ and CGO; (b) co-synthesis powders from freeze-dried precursors and nanocomposite layers directly prepared on (c) the electrolyte and (d) CGO scaffolds. Among them, the electrodes prepared by infiltration, using spray-pyrolysis, rendered the best performance as a consequence of the highly enhanced TPB length and higher electrode porosity. In the case of $(La_{0.8}Sr_{0.2})_{0.95}Fe_{0.8}Ti_{0.2}O_{3-\delta}$ infiltrated electrode, R_p values of 0.23 and 0.41 Ω cm^2 were obtained in air and H_2, respectively, at 700 ºC. The $(La_{0.8}Sr_{0.2})_{0.95}Fe_{0.6}Ti_{0.4}O_{3-\delta}$ composition showed R_p values of 0.67 and 0.20 Ω cm^2 in air and H_2, respectively, at the same temperature. Higher Ti-content induced lower conductivity values and poorer electrochemical properties in air but better performance in reducing conditions due to the partial reduction of Ti^{4+} to Ti^{3+}.

In addition, Ni-doped $LSFT_{0.2}$ electrodes were prepared to promote the Ni metal exsolution on the electrode surface under a reducing atmosphere, thus improving the HOR activity. Ni nanoparticles of 15 nm diameter were observed for $(La_{0.8}Sr_{0.2})_{0.95}(Fe_{0.8}Ti_{0.2})_{0.9}Ni_{0.1}O_{3-\delta}$ after reduction, lowering the polarization resistance values to 0.11 Ω cm^2 at 700 ºC in H_2 with a remarkable and stable maximum power density of 617 mW cm^{-2} at 800 ºC.

(ii) In the second section of the Thesis, the electrode/electrolyte interface was tailored in order to minimize the electrode contribution related to the oxide-ion transport from the TPB to the electrolyte (Chapter 7). Preliminary results revealed a great influence of the ionic conductivity of the electrolyte on the electrochemical properties of nanostructured $La_{0.6}Sr_{0.4}Co_{0.2}Fe_{0.8}O_{3-\delta}$ (LSCF) cathodes. The R_p values of LSCF deposited onto YSZ, CGO, LSGM and $Bi_{1.5}Y_{0.5}O_3$ (BYO) decreased as the ionic conductivity increases, *i.e.* 0.21, 0.11, 0.09 and 0.058 Ω cm^2 at 700 ºC,

UNIVERSIDAD DE MÁLAGA

respectively. These results showed that the limited ionic conductivity of the electrolyte is a bottleneck for the electrode efficiency (Table 2).

Table 2. Composition, fabrication method and electrochemical properties of the different electrode materials investigated in Chapters 7-8. The synthetic methodology and microstructural strategy employed for the synthesis of powders and layers are indicated as follows: Commercial powders (Com), layers deposited directly on the electrolyte by spray-pyrolysis (SP) and layers obtained by pulsed laser deposition in form of single compound (PLD) or vertically aligned nanocomposite (VAN). R_p values are given at 700 ºC for the electrodes deposited onto YSZ electrolytes, when another electrolyte is employed, it is indicated in parenthesis. A# indicates the article. Non-published data are indicated as NP.

	Composition	Preparation method	R_p^{Air/H_2} (Ω cm^2)	Power Density $^{800\ ºC}$ (mW cm^{-2})	Ref
Chapter 7	$La_{0.6}Sr_{0.4}Co_{0.2}Fe_{0.8}O_{3-\delta}$ (YSZ)	SP	0.21/-	-	A6
	$La_{0.6}Sr_{0.4}Co_{0.2}Fe_{0.8}O_{3-\delta}$ (CGO)	SP	0.11/-	-	A6
	$La_{0.6}Sr_{0.4}Co_{0.2}Fe_{0.8}O_{3-\delta}$ (LSGM)	SP	0.09/-	-	A6
	$La_{0.6}Sr_{0.4}Co_{0.2}Fe_{0.8}O_{3-\delta}$ (BYO)	SP	0.06/-	-	A6
	$La_{0.8}Sr_{0.2}MnO_{3-\delta}$	Com	1.71/-	790	A7
	$La_{0.8}Sr_{0.2}MnO_{3-\delta}$*	SP	0.95/-	-	A7
	50 wt.% $La_{0.8}Sr_{0.2}MnO_{3-\delta}$-CGO*	SP	0.62/-	1200	A7
	50 wt.% $La_{0.8}Sr_{0.2}MnO_{3-\delta}$-$Pr_6O_{11}$*	SP	0.46/-	-	A7
	50 wt.% $La_{0.8}Sr_{0.2}MnO_{3-\delta}$-BYO*	SP	0.29/-	-	A7
Chap. 8	$(La_{0.8}Sr_{0.2})_{0.95}Fe_{0.8}Ti_{0.2}O_{3-\delta}$#	PLD	6.2/225.4	-	NP
	50 wt.% $(La_{0.8}Sr_{0.2})_{0.95}Fe_{0.8}Ti_{0.2}O_{3-\delta}$-CGO#	VAN	1.1/75.9	-	NP

* Composition of the active layer using $La_{0.8}Sr_{0.2}MnO_{3-\delta}$ as cathode.
# R_p values are given at 650 ºC.

Nanocomposite active layers were studied to boost the electrochemical performance of the traditional $La_{0.8}Sr_{0.2}MnO_{3-\delta}$ (LSM) air electrode. The nanocomposite functional layers were prepared by spray-pyrolysis by combining LSM with different oxide-ion conductors, such as CGO, BYO and Pr_6O_{11}.

UNIVERSIDAD DE MÁLAGA

Among the different active layers, LSM-CGO functional layer displayed improved microstructural characteristics, including lower particle size and better adherence to the electrolyte without cracks or delamination after several thermal cycles. The incorporation of a LSM-CGO functional layer decreased the polarization resistance of LSM from 1.71 to 0.46 Ω cm^2 at 700 ºC. The analysis of the impedance spectra by equivalent circuits and distribution of relaxation times (DRT) revealed a faster oxide-ion transport at the electrode/electrolyte interface. More surprisingly, the active layer also decreased the electrochemical processes that take place on the electrode surface, indicating that the introduction of the nanostructured active layers extended the surface active paths to the electrolyte surface. In addition, LSM-CGO nanocomposite layer provides both electronic and ionic conducting paths, increasing the TPB sites at the electrolyte interface. A Ni-YSZ/YSZ/LSM-CGO/LSM anode-supported cell with a LSM-CGO active layer showed a power density of 1.20 W cm^{-2} at 800 ºC, outperforming the values obtained for the same cell without an active layer (0.79 W cm^{-2} at 800 ºC).

Finally, active layers with advanced electrode architectures, deposited by pulsed laser deposition (PLD), were tested in both oxidizing and reducing atmospheres. These layers were prepared during two external research stays at the Technical University of Denmark (DTU) under the supervision of Profs. Nini Pryds and Vincenzo Esposito. The microstructural and electrical measurements were performed at the University of Málaga.

Vertically Aligned Nanostructures (VAN) thin films based on $(La_{0.8}Sr_{0.2})_{0.98}Fe_{0.8}Ti_{0.2}O_{3-\delta}$-$Ce_{0.9}Gd_{0.1}O_{1.95}$ ($LSFT_{0.2}$-CGO) were grown epitaxially by PLD onto different single crystals, STO and YSZ (001), for their implementation as a functional layer (Chapter 8). VANs were formed by the spontaneous ordering of two immiscible phases on the substrates, enabling both in-plane and vertical strain with numerous interfaces to tailor the electrochemical properties. Epitaxial $LSFT_{0.2}$-CGO VAN films showed a dense long-range ordered columnar microstructure with a column width of about 5 nm perpendicular to the STO (001) substrate.

The conductivity of the $LSFT_{0.2}$-CGO VAN was considerably higher than that observed for the polycrystalline $LSFT_{0.2}$-CGO pellets in Chapter 6 (*i.e.* 0.0017 and

UNIVERSIDAD DE MÁLAGA

0.06 S cm^{-1}, in air and 5% H_2-Ar, respectively). Additionally, the $LSFT_{0.2}$-CGO VAN showed a R_p value of 1.1 Ω cm^2 at 650 ºC in air, greatly outperforming that observed for the epitaxial $LSFT_{0.2}$ at the same temperature, 6.2 Ω cm^2. In a H_2 atmosphere, the R_p values of the $LSFT_{0.2}$-CGO VAN were also significantly lower when compared to epitaxial $LSFT_{0.2}$, 75.9 and 225.4 Ω cm^2, respectively, at 650 ºC. These results revealed the great influence of vertical strain engineering on the electrochemical properties.

In order to boost the performance in reducing conditions and explore the Ni exsolution process for the first time in a VAN film, $(Sr_{0.9}Pr_{0.1})_{0.9}Ti_{0.9}Ni_{0.1}O_{3-\delta}$-$Ce_{0.9}Gd_{0.1}O_{1.95}$ (SPTNO-CGO) were prepared by PLD (Chapter 9). The samples were reduced at 650 ºC in 5% H_2-Ar to study the exsolution process in both single and VAN films. In reducing conditions, the numerous vertical interfaces in the SPTNO-CGO VAN film provided a good diffusion path for NiO to the surface, followed by a reduction to Ni-metal: $Ni^{2+} + 2e^- \rightarrow Ni^0$. The particle size, shape and population density of the exsolved Ni nanoparticles were different for the epitaxial SPTNO and VAN films. In particular, the SPTNO-CGO VAN film exhibited smaller particle size and higher population density, which is desirable for different high-temperature energy applications. The shape of the Ni nanoparticles was also different for the single SPTNO and SPTNO-CGO VAN films. Spherical nanoparticles were observed in the SPTNO film while square-shaped nanoparticles were found in the case of the SPTNO-CGO VAN. These results suggested that the VAN microstructure promotes the formation of highly oriented Ni nanoparticles.

Reducing treatments at different times provided information about the Ni migration and nucleation process. Ni-nanoparticles with an average grain size of ∼17 nm and a high population density (∼100 particles μm^{-2}) were obtained at 650 ºC for 1 minute, while for longer times (1 to 6 h) the Ni particles grew with an irregular shape and they were surrounded by a secondary phase, presumably nickel oxide, which is migrating across the surface. This hypothesis was confirmed by the absence of this phase at longer calcination times (650 ºC for 12 h) and the higher particle size, suggesting that the growing process has concluded. At this temperature, coalescence and Ostwald ripening are the most feasible mechanisms due to the nanoparticles are

UNIVERSIDAD DE MÁLAGA

close to each other. Interestingly the Ni nanoparticles were stable under several oxidation/reduction redox cycles.

The presence of vertical nanocolumns with good electronic (SPTNO) and ionic (CGO) conductivity together with higher Ni nanoparticle density on the films promoted faster kinetics for fuel oxidation in the VAN sample with k_{chem} values of $1.27 \cdot 10^{-6}$ cm s^{-1} at 650 ºC which was better to that observed for epitaxial SPTNO measured in the same conditions, $7.53 \cdot 10^{-7}$ cm s^{-1}.

UNIVERSIDAD DE MÁLAGA

UNIVERSIDAD
DE MÁLAGA

Resumen

(3000 palabras)

La gran demanda de energía eléctrica debida al rápido crecimiento demográfico ha hecho surgir la necesidad de desarrollar fuentes de energía sostenibles y respetuosas con el medio ambiente. En la actualidad, la producción mundial de energía sigue dependiendo en gran medida de los combustibles fósiles, que producen emisiones nocivas de óxidos de carbono. Además, el precio del gas en 2022 era unas cuatro veces superior al de principios de 2021. Por tanto, ahora más que nunca, es necesario realizar progresivamente una transición energética desde un sistema basado en combustibles fósiles a fuentes de energía renovables [1]. Sin embargo, la producción eléctrica a partir de estas fuentes es discontinua e intermitente, por lo que se necesitan métodos alternativos de producción y almacenamiento de energía eléctrica.

En este contexto, las pilas de combustible son una de las alternativas más prometedoras para obtener energía eléctrica a partir de una amplia variedad de

UNIVERSIDAD DE MÁLAGA

combustibles, obteniendo buenas eficiencias y una menor emisión de contaminantes. En particular, las pilas de combustible de óxido sólido (SOFC) han atraído gran atención en los últimos años debido a su flexibilidad para utilizar diferentes combustibles, su buena tolerancia a impurezas en el combustible y sus mayores eficiencias respecto a los métodos tradicionales [2]. Además, pueden funcionar en modo inverso (electrólisis) para producir hidrógeno a partir de agua y de electricidad obtenida de fuentes renovables. Además, las pilas de combustible presentan una mayor densidad energética, mayor duración y más flexibilidad. Sin embargo, las altas temperaturas de funcionamiento de las SOFCs (600-800 ºC), necesarias para lograr un buen rendimiento del electrodo y una buena conductividad iónica del electrolito, afectan negativamente a la estabilidad a largo plazo de estos dispositivos. Por esta razón, una disminución de su temperatura de funcionamiento es uno de los principales objetivos para la implementación a gran escala de las SOFCs [3]. En los últimos años, la mayoría de las investigaciones en este campo se han centrado en el desarrollo de nuevos materiales o en la mejora del rendimiento mediante el control microestructural de sus componentes.

Las SOFC soportadas sobre el ánodo es la configuración tradicional en estos dispositivos electroquímicos, en los que un electrolito muy delgado de varias micras de espesor es soportado sobre un ánodo poroso para minimizar las pérdidas óhmicas de la celda. En esta configuración, el material del ánodo es un Ni-cermet debido a su alta conductividad electrónica y su buena actividad electroquímica para la oxidación del hidrógeno, pero presenta problemas de degradación debidos a la aglomeración del Ni, el envenenamiento por azufre o la deposición de carbono cuando se utilizan hidrocarburos como combustible [4].

En los últimos años, los investigadores han estudiado nuevos materiales de electrodo y otras configuraciones de celda para resolver parcialmente estos problemas. Una de las configuraciones más prometedoras consiste en utilizar el mismo material de electrodo como cátodo y como ánodo, lo que se conoce como pilas de combustible de óxido sólido simétricas (SSOFC). Esta configuración presenta varias ventajas en comparación con las pilas tradicionales soportadas por ánodo, entre las que se incluyen un menor número de pasos de fabricación, mejor estabilidad termomecánica y buena compatibilidad química con los demás componentes de la

UNIVERSIDAD DE MÁLAGA

pila [5]. Entre ellas, una de las ventajas más importantes es que la degradación de la pila inducida por el envenenamiento por azufre o la deposición de carbono puede resolverse parcialmente intercambiando los gases en el ánodo y el cátodo. Además, la posibilidad funcionar en modo reversible (RSOFC) para la electrólisis de CO_2 y vapor es muy atractiva debido a su multifuncionalidad y versatilidad para las necesidades locales, permitiendo el almacenamiento de energía y también disminuyendo las emisiones de CO_2 [6]. Se han investigado diferentes electrodos simétricos estables en atmosferas oxidantes y reductoras con estructura tipo perovskita simple, $La(Cr,Mn)O_{3-\delta}$, $(La,Sr)FeO_{3-\delta}$ y $(La,Sr)TiO_{3-\delta}$ o perovskita doble, como $PrBaMn_2O_{5+\delta}$ y $Sr_2Fe_{1.5}Mo_{0.5}O_{6-\delta}$, mejorando sus propiedades electroquímicas mediante estrategias de dopaje adecuadas en las posiciones A y B.

Es bien conocido que la estructura cristalina y la composición de los electrodos desempeñan un papel fundamental en las propiedades electroquímicas. Sin embargo, la optimización microestructural de los electrodos también ha demostrado ser crucial para potenciar las propiedades electroquímicas a bajas temperaturas de funcionamiento para los materiales de cátodo y de ánodo. En general, métodos de preparación convencionales en múltiples etapas de síntesis y a altas temperaturas de sinterización dan lugar a electrodos con baja porosidad y con tamaño de grano relativamente grande. Los múltiples procesos de calcinación reducen los sitios activos para las reacciones electroquímicas y, por tanto, el rendimiento del electrodo. Se han investigado diferentes métodos de deposición para preparar los electrodos directamente sobre la superficie del electrolito a bajas temperaturas, por ejemplo, spray pirólisis, deposición por láser pulsado (PLD) o el *magnetron sputtering*. Entre ellos, spray pirólisis ha demostrado ser una técnica sencilla, económica y versátil para obtener capas delgadas y homogéneas con diferentes microestructuras sobre grandes áreas a temperaturas bajas (Figura 1) [7,8].

UNIVERSIDAD DE MÁLAGA

Figura 1. Diferentes microestructuras de los electrodos preparados por spray pirólisis [7].

Con el objetivo de mejorar las propiedades electroquímicas de los electrodos tradicionales, se han explorado diferentes estrategias microestructurales. La Figura 2 muestra todas las microestructuras investigadas en esta Tesis: (a) electrodos tradicionales con baja conductividad iónica y TPB limitada en la interfase electrodo/electrolito; (b) electrodo composite formado por la mezcla de un conductor iónico y uno electrónico; (c) electrodos con conductividad mixta iónica-electrónica (MIEC); (d) electrodos nanoestructurados con menor tamaño de partícula; (e) electrodos nanocompuestos depositados directamente sobre el electrolito; (f) infiltración del electrodo en una capa porosa de electrolito; (g) exsolución de nanopartículas metálicas, como Ni, en la superficie del electrodo; (h) capas activas en la interfaz electrodo/electrolito y (i) *Vertically Aligned Nanostructures* (VANs) depositadas por PLD para actuar como capa activa.

UNIVERSIDAD DE MÁLAGA

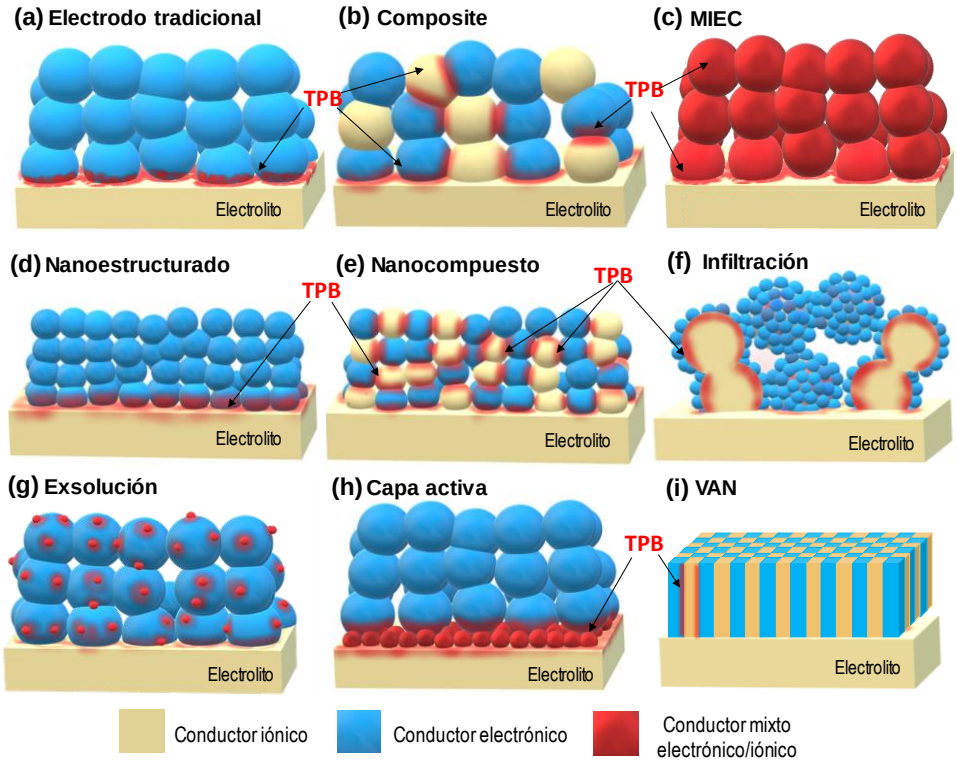

Figura 2. Ilustración de las diferentes estrategias microestructurales empleadas para mejorar la eficiencia de los electrodos para SOFC: (a) electrodo tradicional, (b) electrodo composite, (c) MIEC, (d) electrodo nanoestructurado (e) electrodo nanocompuestos (f) electrodo infiltrado, (g) electrodo con nanopartículas metálicas, (h) electrodo con una capa activa e (i) VAN.

En los últimos años, la implementación de electrodos nanocompuestos ha demostrado mejores propiedades electroquímicas y una mayor estabilidad térmica en comparación con los electrodos nanoestructurados monofásicos [9,10]. En particular, el contacto a nivel nanométrico entre dos fases diferentes limita el crecimiento del grano por difusión de cationes a través del límite de grano, evitando la pérdida de rendimiento observada en los electrodos nanoestructurados como consecuencia de un crecimiento incontrolado del grano. Además, una mezcla íntima entre un conductor iónico y uno electrónico aumenta los sitios activos donde tienen lugar las reacciones electroquímicas.

UNIVERSIDAD DE MÁLAGA

En este trabajo se han preparado diferentes electrodos nanocompuestos para SOFCs basados en la combinación de materiales tipo perovskita, $LaCrO_3$, $SrTiO_3$ y $LaFeO_3$ y el conductor iónico $Ce_{0.9}Gd_{0.1}O_{1.95}$ (CGO) con estructura tipo fluorita. Las capas de electrodos se prepararon directamente mediante spray pirólisis sobre electrolitos de $Zr_{0.84}Y_{0.16}O_{1.92}$ (YSZ) y $La_{0.9}Sr_{0.1}Ga_{0.8}Mg_{0.2}O_{2.85}$ (LSGM). Además, se empleó la técnica de deposición de láser pulsado (PLD) para la preparación de capas activas [11,12]. Los mismos electrodos se prepararon en forma de polvo mediante el método del precursor liofilizado y luego se depositaron sobre el electrolito por el método de serigrafía para compararlos con los electrodos directamente depositado sobre el electrolito.

La caracterización estructural de los electrodos se realizó mediante XRD. Además, se realizaron análisis de *rocking curve* and *reciprocal space maps* para las láminas delgadas depositadas por PLD. La microestructura se estudió mediante SEM, TEM, HAADF-STEM y AFM. La composición química se analizó mediante EDS y XPS. Se llevó a cabo una exhaustiva caracterización electroquímica mediante espectroscopia de impedancia y la conductividad en cuatro puntas por el método de Van der Pauw. La conductividad total y la resistencia de polarización de los electrodos se analizaron a diferentes temperaturas, atmósferas (aire, 5% H_2-Ar y H_2) y en función de la presión parcial de oxígeno (pO_2). Los mejores electrodos se probaron en condiciones reales de funcionamiento en una pila de combustible.

Durante el desarrollo de esta Tesis, se implementaron en nuestro laboratorio nuevas celdas electroquímicas para las medidas de impedancia por 3 electrodos bajo polarización anódica y catódica, así como celdas para medidas de conductividad a diferentes presiones parciales de oxígeno. Además, se empleó el método de distribución de tiempos de relajación (DRT) como alternativa al método de circuitos equivalentes para analizar las diferentes contribuciones en los espectros de impedancia.

Los principales resultados obtenidos durante esta Tesis Doctoral se discuten en dos secciones diferentes: (i) materiales nanocomposites de electrodos para SSOFCs preparados por spray pirólisis (Capítulos 4-6) y (ii) capas activas nanocomposites depositadas por spray pirólisis (Capítulo 7) y VANs depositadas por

UNIVERSIDAD DE MÁLAGA

PLD (Capítulos 8-9). A continuación, se resumen brevemente los resultados más relevantes de cada sección.

(i) En la primera sección de la Tesis, se prepararon electrodos composites con microestructuras optimizadas mediante spray pirólisis para su potencial aplicación en SSOFCs (Tabla 1). Dado que los materiales basados en $LaCrO_3$ fueron los primeros candidatos para electrodos simétricos, se probaron varias estrategias de dopaje en la posición A con Ca y Sr, y en la posición B con diferentes metales de transición (Mn, Fe, Ti y Cu) para obtener electrodos nanoestructurados mediante deposición por spray pirólisis (Capítulo 4). En primer lugar, se investigó la incorporación de cationes alcalinotérreos en $LaCrO_3$. Sin embargo, se formaron fases secundarias de $(Sr,Ca)CrO_{4-\delta}$ a temperaturas inferiores a 1200 ºC. Estas temperaturas de calcinación tan elevadas producen un excesivo crecimiento de grano, disminuyendo la porosidad de las capas y, en consecuencia, la resistencia de polarización aumenta hasta 1.95 Ω cm^2 a 700 ºC en aire.

Por este motivo, se investigaron dopados en la posición B en $La_{0.98}Cr_{0.75}M_{0.25}O_{3-\delta}$ (M= Mn, Fe, Cu y Ti). Estos electrodos se depositaron mediante spray pirólisis sobre una capa porosa de CGO para obtener un electrodo compuesto formado por partículas de CGO recubiertas con el electrodo de $LaCrO_3$, mejorándose las propiedades electroquímicas tanto en aire como en H_2 para $La_{0.98}Cr_{0.75}Mn_{0.25}O_{3-\delta}$ (LCM), por ejemplo, 0.35 y 0.53 Ω cm^2, respectivamente, a 700 ºC. Alternativamente, se prepararon electrodos nanocompuestos de LCM-CGO mediante spray pirólisis a bajas temperaturas directamente sobre el electrolito a partir de una única solución acuosa con diferente contenido en LCM (0-60 % en peso)

UNIVERSIDAD DE MÁLAGA

Tabla 1. Composición, método de fabricación y propiedades electroquímicas de los materiales de electrodo más representativos investigados en los Capítulos 4-6. La metodología de síntesis y la estrategia microestructural empleados para la síntesis de los materiales en forma de polvos y capas se indican a continuación: Materiales liofilizados (FD), electrodo compuesto a partir de mezcla de polvos cerámicos (PM), electrodo compuesto obtenido por cosíntesis (Cosyn). Capas depositadas directamente sobre el electrolito por spray pirólisis (SP), electrodos infiltrados por spray-pirólisis sobre una capa porosa (SP-Inf), nanocomposite mediante spray pirólisis (SP-NC). Los valores R_p se dan a 700 ºC para los electrodos depositados sobre electrolitos de YSZ. A# indica el artículo. Los datos no publicados se indican como NP.

	Composición	Método de preparación	R_p^{Aire/H_2} (Ω cm^2)	Potencia^{800ºC} (mW cm^{-2})	Ref
Capítulo 4	$La_{0.98}CrO_{3-\delta}$	SP-Inf	0.91/-	-	A1
	$La_{0.98}Cr_{0.75}Cu_{0.25}O_{3-\delta}$	SP-Inf	0.70/-	-	A1
	$La_{0.98}Cr_{0.75}Fe_{0.25}O_{3-\delta}$	SP-Inf	0.52/0.91	-	A1
	$La_{0.98}Cr_{0.75}Mn_{0.25}O_{3-\delta}$	SP-Inf	0.35/0.53	470	A1
	$La_{0.98}Cr_{0.75}Mn_{0.25}O_{3-\delta}$	SP	5.1/3.8	-	A1
	50 wt.%$La_{0.98}Cr_{0.75}Mn_{0.25}O_{3-\delta}$-CGO	FD-PM	5.6	-	A2
	50 wt.%$La_{0.98}Cr_{0.75}Mn_{0.25}O_{3-\delta}$-CGO	SP-NC	0.80/0.18	570	A2
Capítulo 5	$(Sr_{0.7}Pr_{0.3})_{0.95}TiO_{3\pm\delta}$	FD	4.81/-	-	A3
	50 wt.%$(Sr_{0.7}Pr_{0.3})_{0.95}TiO_{3\pm\delta}$-CGO	FD-PM	2.45/-	-	A3
	50 wt.%$(Sr_{0.7}Pr_{0.3})_{0.95}TiO_{3\pm\delta}$-CGO	FD-Cosyn	1.60/2.37	125	A3
	50 wt.%$(Sr_{0.7}Pr_{0.3})_{0.95}TiO_{3\pm\delta}$-CGO	SP-NC	0.50/0.46	354	A3
	40 wt.%$(Sr_{0.7}Pr_{0.3})_{0.95}TiO_{3\pm\delta}$-CGO	SP-NC	0.50/1.17	-	A3
	60 wt.% $(Sr_{0.7}Pr_{0.3})_{0.95}TiO_{3\pm\delta}$-CGO	SP-NC	0.59/0.88	-	A3
Capítulo 6	$(La_{0.8}Sr_{0.2})_{0.95}Fe_{0.8}Ti_{0.2}O_{3-\delta}$	SP-Inf	0.23/0.41	-	A4,NP
	50 wt.%$(La_{0.8}Sr_{0.2})_{0.95}Fe_{0.8}Ti_{0.2}O_{3-\delta}$-CGO	FD-PM	1.19/-	309	A4,NP
	50 wt.%$(La_{0.8}Sr_{0.2})_{0.95}Fe_{0.8}Ti_{0.2}O_{3-\delta}$-CGO	SP-NC	0.30/0.58	-	NP
	$(La_{0.8}Sr_{0.2})_{0.95}(Fe_{0.8}Ti_{0.2})_{0.9}Ni_{0.1}O_{3-\delta}$	SP-Inf	0.34/0.11	496	NP
	50$(La_{0.8}Sr_{0.2})_{0.95}(Fe_{0.8}Ti_{0.2})_{0.9}Ni_{0.1}O_{3-\delta}$-CGO	FD-PM	-/0.72	617	NP
	$(La_{0.8}Sr_{0.2})_{0.95}Fe_{0.6}Ti_{0.4}O_{3-\delta}$	SP-Inf	0.67/0.20	-	NP
	50 wt.%$(La_{0.8}Sr_{0.2})_{0.95}Fe_{0.6}Ti_{0.4}O_{3-\delta}$-CGO	FD-PM	8.84/-	-	NP

UNIVERSIDAD DE MÁLAGA

Los electrodos nanocompuestos, formados por una mezcla de fases de tipo perovskita y fluorita, se obtuvieron a sólo 800 ºC y, mostraron un tamaño de partícula de sólo 30 nm de diámetro, en comparación a los 122 nm del LCM puro. Esto es debido a una mezcla íntima del LSM y CGO a escala nanométrica, que suprime la difusión de cationes y, por tanto, el crecimiento de grano durante el proceso de cosinterización. Los resultados se compararon con los electrodos obtenidos por serigrafía a partir de una mezcla en polvo de LCM y CGO.

Los mejores valores de resistencia a la polarización (R_p) se obtuvieron para el electrodo nanocomposite de composición LCM-CGO con 50 % en peso, 0.80 y 0.18 Ω cm^2 en aire y H_2, respectivamente, a 700 ºC y una potencia de 570 mW cm^{-2} a 800 ºC en una SSOFC de 300 µm soportada sobre LSGM. La R_p de los electrodos nanocompuestos fue casi un orden de magnitud inferior a la de la misma composición depositada por serigrafía (5.6 Ω cm^2 a 700 ºC en aire) debido a la mayor temperatura de sinterización necesaria (1100 ºC) para lograr una adecuada adhesión al electrolito. Esta elevada temperatura de sinterización induce un importante crecimiento de grano y la reducción de los sitios activos (TPB).

También se investigaron electrodos basados en $SrTiO_3$ debido a su buena estabilidad en condiciones reductoras, así como a su buena tolerancia a la contaminación por carbono y al azufre. Con el fin de mejorar las propiedades electroquímicas para ORR, se empleó Pr como dopante para aumentar la conductividad electrónica en aire debido a los estados de oxidación variables del Pr^{4+}/Pr^{3+}. Los electrodos nanocomposites de composición nominal $(Sr_{0.7}Pr_{0.3})_{0.95}TiO_3$-$Ce_{0.9}Gd_{0.1}O_{1.95}$ (40-60 % en peso de SPTO) se depositaron directamente sobre la superficie del electrolito mediante spray pirólisis y sus propiedades se compararon con las de los electrodos obtenidos por serigrafía (Capítulo 5).

La menor temperatura de preparación de los electrodos nanocompuestos inhibió el crecimiento de grano (20 nm a 800 ºC) y dificultó la formación de defectos ordenados, que han demostrado ser perjudiciales para las propiedades conductoras de los materiales basados en $SrTiO_3$. Además, los electrodos obtenidos por cosíntesis son estables a temperaturas de 1300 ºC, sin la presencia de fases secundarias. Se obtuvieron valores de R_p de 0.50 y 0.46 Ω cm^2 en aire e H_2,

UNIVERSIDAD DE MÁLAGA

respectivamente, a 700 ºC para el electrodo nanocomposite SPTO-CGO al 50 % en peso, valores que fueron casi un orden de magnitud inferiores a los obtenidos para la misma composición preparada por serigrafía (Tabla 1).

Por último, se investigaron materiales tipo perovskita basados en (La,Sr)$FeO_{3-\delta}$ debido a su excelente rendimiento como materiales de cátodo (Capítulo 6). Con el objetivo de mejorar la estabilidad para su posible aplicación en condiciones oxidantes y reductoras, se prepararon composiciones dopadas con Ti $(La_{0.8}Sr_{0.2})_{0.95}Fe_{1-x}Ti_xO_3$-$Ce_{0.9}Gd_{0.1}O_{1.95}$ ($LSFT_x$; x=0.2 y 0.4). Se investigaron diferentes microestructuras para los electrodos, incluyendo electrodos tradicionales en forma de polvos y depositados por serigrafía a partir de (a) polvos mezclados mecánicamente de $LSFT_x$ y CGO; (b) polvos obtenidos por cosíntesis mediante el método del precursor liofilizado y capas nanocomposites preparadas directamente sobre (c) el electrolito y (d) capas porosas de CGO. Entre ellos, los electrodos preparados por infiltración mediante spray pirólisis presentaron el mejor rendimiento, como consecuencia del aumento de los sitios activos y la mayor porosidad. En el caso del electrodo infiltrado de $(La_{0.8}Sr_{0.2})_{0.95}Fe_{0.8}Ti_{0.2}O_{3-\delta}$, se obtuvieron valores de R_p de 0.23 y 0.41 Ω cm^2 en aire e H_2, respectivamente, a 700 ºC. La composición $(La_{0.8}Sr_{0.2})_{0.95}Fe_{0.6}Ti_{0.4}O_{3-\delta}$ mostró valores de R_p de 0.67 y 0.20 Ω cm^2 en aire e H_2, respectivamente, a la misma temperatura. Un mayor contenido en Ti disminuyó los valores de conductividad y las propiedades electroquímicas en aire, pero mejoró sus propiedades en condiciones reductoras debido a la reducción parcial de Ti^{4+} a Ti^{3+}.

Además, se prepararon también electrodos de composición $LSFT_{0.2}$ dopados con Ni para promover la exsolución del Ni metálico en la superficie del electrodo en atmósfera reductora, mejorando así la actividad para HOR. Se observaron nanopartículas de Ni de 15 nm de diámetro en $(La_{0.8}Sr_{0.2})_{0.95}(Fe_{0.8}Ti_{0.2})_{0.9}Ni_{0.1}O_{3-\delta}$ tras la reducción, disminuyendo los valores de R_p a 0.11 Ω cm^2 a 700 ºC en H_2, así como una potencia máxima de 617 mW cm^{-2} a 800 ºC estable con el tiempo.

(ii) En la segunda sección de la Tesis, se modificó la interfaz electrodo/electrolito para minimizar la contribución del electrodo relacionada con el transporte de iones de óxido desde la TPB al electrolito (Capítulo 7). Resultados preliminares revelaron una gran influencia de la conductividad iónica del electrolito en

UNIVERSIDAD DE MÁLAGA

las propiedades electroquímicas de los cátodos nanoestructurados de $La_{0.6}Sr_{0.4}Co_{0.2}Fe_{0.8}O_{3-\delta}$ (LSCF). Los valores de R_p del LSCF depositado sobre YSZ, CGO, LSGM y $Bi_{1.5}Y_{0.5}O_3$ (BYO) disminuyen a medida que la conductividad del electrolito aumenta, con valores de 0.21, 0.11, 0.09 y 0.058 Ω cm^2 a 700 ºC, respectivamente. Estos resultados sugieren que la limitada conductividad iónica del electrolito es un cuello de botella para el rendimiento del electrodo (Tabla 2).

Tabla 2. Composición, método de preparación y propiedades electroquímicas de los diferentes materiales de electrodo investigados en los Capítulos 7-8. La metodología de síntesis y la estrategia microestructural empleadas para la síntesis de materiales en forma de polvos y capas se indican a continuación: Materiales en polvo comerciales (Com), capas depositadas directamente sobre el electrolito por spray pirólisis (SP) y capas de compuestos monofásicos obtenidos mediante deposición de laser pulsado (PLD) o *Vertically Aligned Nanostructures* (VAN). Los valores de R_p se dan a 700 ºC para los electrodos depositados sobre electrolitos de YSZ; cuando se emplea otro electrolito, se indica entre paréntesis. A# indica el artículo. Los datos no publicados se indican como NP.

	Composición	Método de preparación	R_p^{Aire/H_2} (Ω cm^2)	Potencia $^{800\ ºC}$ (mW cm^{-2})	Ref
Capítulo 7	$La_{0.6}Sr_{0.4}Co_{0.2}Fe_{0.8}O_{3-\delta}$ (YSZ)	SP	0.21/-	-	A6
	$La_{0.6}Sr_{0.4}Co_{0.2}Fe_{0.8}O_{3-\delta}$ (CGO)	SP	0.11/-	-	A6
	$La_{0.6}Sr_{0.4}Co_{0.2}Fe_{0.8}O_{3-\delta}$ (LSGM)	SP	0.09/-	-	A6
	$La_{0.6}Sr_{0.4}Co_{0.2}Fe_{0.8}O_{3-\delta}$ (BYO)	SP	0.06/-	-	A6
	$La_{0.8}Sr_{0.2}MnO_{3-\delta}$	Com	1.71/-	790	A7
	$La_{0.8}Sr_{0.2}MnO_{3-\delta}$*	SP	0.95/-	-	A7
	50 wt.% $La_{0.8}Sr_{0.2}MnO_{3-\delta}$-CGO*	SP	0.62/-	1200	A7
	50 wt.% $La_{0.8}Sr_{0.2}MnO_{3-\delta}$-$Pr_6O_{11}$*	SP	0.46/-	-	A7
	50 wt.% $La_{0.8}Sr_{0.2}MnO_{3-\delta}$-BYO*	SP	0.29/-	-	A7
Cap. 8	$(La_{0.8}Sr_{0.2})_{0.95}Fe_{0.8}Ti_{0.2}O_{3-\delta}$#	PLD	6.2/225.4	-	NP
	50 wt.% $(La_{0.8}Sr_{0.2})_{0.95}Fe_{0.8}Ti_{0.2}O_{3-\delta}$-CGO#	VAN	1.1/75.9	-	NP

* Composición de la capa activa empleada, utilizando siempre $La_{0.8}Sr_{0.2}MnO_{3-\delta}$ como cátodo.
# Valores de R_p dados a 650 ºC.

Se estudiaron capas activas nanocomposites para potenciar las propiedades electroquímicas del electrodo de cátodo tradicional $La_{0.8}Sr_{0.2}MnO_{3-\delta}$ (LSM). Las capas

UNIVERSIDAD DE MÁLAGA

funcionales nanocomposites se prepararon mediante spray pirólisis combinando LSM con diferentes conductores de ion óxido, como CGO, BYO y Pr_6O_{11}.

Entre las diferentes capas activas estudiadas, la capa de LSM-CGO mostró las mejores propiedades, incluyendo un menor tamaño de partícula y una mejor adherencia al electrolito sin grietas ni delaminaciones tras varios ciclos térmicos. Además, la incorporación de la capa activa de LSM-CGO disminuyó la resistencia a la polarización del LSM de 1.71 a 0.46 Ω cm^2 a 700 ºC. El análisis de los espectros de impedancia, mediante circuitos equivalentes y distribución de tiempos de relajación (DRT), reveló un mejor transporte de iones óxido en la interfase electrodo/electrolito. Sorprendente, la capa activa también disminuyó los procesos electroquímicos que tienen lugar en la superficie del electrodo, debido a un mejor transporte iónico y electrónico hacia el electrolito. Además, la capa LSM-CGO proporciona conducción tanto electrónica como iónica, aumentando la TPB en la interfaz del electrolito. Una pila de Ni-YSZ/YSZ/LSM-CGO/LSM soportada sobre el ánodo con capa activa de LSM-CGO alcanzó una potencia de 1.20 W cm^{-2} a 800 ºC, superando los valores obtenidos para la misma pila sin capa activa (0.79 W cm^{-2} a 800 ºC).

Por último, se analizaron capas activas con microstructuras de electrodo avanzadas, depositadas mediante deposición de láser pulsado (PLD), tanto en atmósferas oxidantes como reductoras. Estas capas se prepararon durante dos estancias de investigación en la Universidad Técnica de Dinamarca (DTU) bajo la supervisión de los profesores Nini Pryds y Vincenzo Esposito. Las medidas microestructurales y eléctricas se realizaron en la Universidad de Málaga.

Se depositaron por PLD capas heteroepitaxiales con estructura *Vertically Aligned Nanostructures* (VAN) basadas en $(La_{0.8}Sr_{0.2})_{0.98}Fe_{0.8}Ti_{0.2}O_{3-\delta}$-$Ce_{0.9}Gd_{0.1}O_{1.95}$ ($LSFT_{0.2}$-CGO) sobre diferentes monocristales, STO y YSZ (001), para su implementación como capa funcional (Capítulo 8). Los VANs se formaron por la ordenación espontánea de dos fases inmiscibles sobre los sustratos, obteniéndose materiales compuestos de numerosas interfaces que modifican las propiedades electroquímicas. Las capas epitaxiales de $LSFT_{0.2}$-CGO VAN mostraron una

UNIVERSIDAD DE MÁLAGA

microestructura columnar ordenada densa con una anchura de columna de unos 5 nm perpendicular al sustrato STO (001).

La conductividad del $LSFT_{0.2}$-CGO VAN fue considerablemente superior a la observada para el material policristalino de $LSFT_{0.2}$-CGO en el capítulo 6 (0.0017 y 0.06 S cm^{-1}, en aire y 5% H_2-Ar, respectivamente). Además, el $LSFT_{0.2}$-CGO VAN mostró un valor de R_p de 1.1 Ω cm^2 a 650 ºC en aire, superando el observado para el $LSFT_{0.2}$ epitaxial a la misma temperatura, 6.2 Ω cm^2. En atmósfera de H_2, los valores de R_p del $LSFT_{0.2}$-CGO VAN también fueron significativamente inferiores en comparación con el $LSFT_{0.2}$ epitaxial, 75.9 y 225.4 Ω cm^2, respectivamente, a 650 ºC. Estos resultados revelaron la gran influencia de la mejora microestructural en las propiedades electroquímicas.

Con el objetivo de potenciar el rendimiento en condiciones reductoras y estudiar el proceso de exsolución del Ni en un VAN por primera vez, se prepararon capas de $(Sr_{0.9}Pr_{0.1})_{0.9}Ti_{0.9}Ni_{0.1}O_{3-\delta}$-$Ce_{0.9}Gd_{0.1}O_{1.95}$ (SPTNO-CGO) mediante PLD (Capítulo 9). Las muestras se redujeron a 650 ºC en 5% H_2-Ar para estudiar el proceso de exsolución en las capas epitaxiales y el VAN. En condiciones reductoras, las numerosas interfaces verticales en el SPTNO-CGO VAN proporcionaron un buen camino de difusión para el NiO hacia la superficie, seguido de una reducción a Ni metálico: $Ni^{2+} + 2e^- \rightarrow Ni^0$. El tamaño, la forma y la densidad de población de las nanopartículas de Ni fue diferente en las películas epitaxiales de SPTNO y el SPTNO-CGO VAN. En particular, el SPTNO-CGO VAN mostró un menor tamaño de partícula y una mayor densidad de población, lo cual es deseable para diferentes aplicaciones energéticas a alta temperatura. La forma de las nanopartículas de Ni también fue diferente en las películas SPTNO y SPTNO-CGO VAN. En la capa de SPTNO se observaron nanopartículas esféricas, mientras que en el caso del SPTNO-CGO VAN se encontraron nanopartículas de forma cuadrada. Estos resultados sugieren que la peculiar microestructura del VAN provoca la formación de nanopartículas de Ni orientadas.

Los tratamientos térmicos a diferentes tiempos en atmósfera reductora proporcionaron información sobre el proceso de migración y nucleación del Ni. Se obtuvieron nanopartículas de Ni con un tamaño de grano medio de ∼17 nm y una

UNIVERSIDAD DE MÁLAGA

alta densidad de población (~100 partículas μm^{-2}) a 650 ºC durante 1 minuto, mientras que para tiempos más largos (de 1 a 6 h) las partículas de Ni crecieron con una forma irregular y estaban rodeadas por una fase secundaria, presumiblemente debida óxido de níquel, que está migrando a través de la superficie. Esta hipótesis se confirmó por la ausencia de esta fase a tiempos de calcinación más largos (650 ºC durante 12 h) y el mayor tamaño de las partículas, lo que sugiere que el proceso de crecimiento ha concluido. A esta temperatura, la coalescencia y el *Ostwald ripening* son los mecanismos de crecimiento más factibles debido a que las nanopartículas están próximas entre sí. Curiosamente, las nanopartículas de Ni fueron estables después de varios ciclos de oxidación/reducción.

La presencia de nanocolumnas verticales con buena conductividad electrónica (SPTNO) e iónica (CGO) junto con una mayor densidad de nanopartículas de Ni en las capas induce una cinética más rápida para la oxidación del combustible en el SPTNO-CGO VAN con un valor de k_{chem} de $1.27 \cdot 10^{-6}$ cm s^{-1} a 650 ºC, mejor que el observado para SPTNO epitaxial, $7.53 \cdot 10^{-7}$ cm s^{-1}, medido en las mismas condiciones.

References/Referencias

1. Qadir, S.A.; Al-Motairi, H.; Tahir, F.; Al-Fagih, L. Incentives and Strategies for Financing the Renewable Energy Transition: A Review. *Energy Reports* **2021**, *7*, 3590–3606, doi:10.1016/j.egyr.2021.06.041.
2. Mahato, N.; Banerjee, A.; Gupta, A.; Omar, S.; Balani, K. Progress in Material Selection for Solid Oxide Fuel Cell Technology: A Review. *Prog. Mater. Sci.* **2015**, *72*, 141–337, doi:10.1016/j.pmatsci.2015.01.001.
3. Connor, P.A.; Yue, X.; Savaniu, C.D.; Price, R.; Triantafyllou, G.; Cassidy, M.; Kerherve, G.; Payne, D.J.; Maher, R.C.; Cohen, L.F. Tailoring SOFC Electrode Microstructures for Improved Performance. *Adv. Energy Mater.* **2018**, *8*, 1–20, doi:10.1002/aenm.201800120.
4. Shaikh, S.P.S.; Muchtar, A.; Somalu, M.R. A Review on the Selection of Anode Materials for Solid-Oxide Fuel Cells. *Renew. Sustain. Energy Rev.* 2015, *51*, 1–8. doi 10.1016/j.rser.2015.05.069
5. Ruiz-Morales, J.C.; Marrero-López, D.; Canales-Vázquez, J.; Irvine, J.T.S. Symmetric and Reversible Solid Oxide Fuel Cells. *RSC Adv.* **2011**, *1*, 1403–1414, doi:10.1039/c1ra00284h.
6. Gómez, S.Y.; Hotza, D. Current Developments in Reversible Solid Oxide Fuel Cells. *Renew. Sustain. Energy Rev.* **2016**, *61*, 155–174, doi:10.1016/j.rser.2016.03.005.
7. dos Santos-Gómez, L.; Zamudio-García, J.; Porras-Vázquez, J.M.; Losilla, E.R.; Marrero-López, D. Recent Progress in Nanostructured Electrodes for Solid Oxide Fuel Cells Deposited by Spray Pyrolysis. *J. Power Sources* **2021**, *507*, 230277 doi:10.1016/j.jpowsour.2021.230277.

UNIVERSIDAD DE MÁLAGA

8. Leng, J.; Wang, Z.; Wang, J.; Wu, H.H.; Yan, G.; Li, X.; Guo, H.; Liu, Y.; Zhang, Q.; Guo, Z. Advances in Nanostructures Fabricated: Via Spray Pyrolysis and Their Applications in Energy Storage and Conversion. *Chem. Soc. Rev.* **2019**, *48*, 3015–3072, doi:10.1039/c8cs00904j.
9. Shimada, H.; Yamaguchi, T.; Kishimoto, H.; Sumi, H.; Yamaguchi, Y.; Nomura, K.; Fujishiro, Y. Nanocomposite Electrodes for High Current Density over 3 A cm^{-2} in Solid Oxide Electrolysis Cells. *Nat. Commun.* **2019**, *10*, 1–10, doi:10.1038/s41467-019-13426-5.
10. dos Santos-Gómez, L.; Zamudio-García, J.; Porras-Vázquez, J.M.; Losilla, E.R.; Marrero-López, D. Highly Efficient $La_{0.8}Sr_{0.2}MnO_{3-\delta}$-$Ce_{0.9}Gd_{0.1}O_{1.95}$ Nanocomposite Cathodes for Solid Oxide Fuel Cells. *Ceram. Int.* **2018**, *44*, 4961–4966, doi:10.1016/j.ceramint.2017.12.089.
11. Xu, M.; Yu, J.; Song, Y.; Ran, R.; Wang, W.; Shao, Z. Advances in Ceramic Thin Films Fabricated by Pulsed Laser Deposition for Intermediate-Temperature Solid Oxide Fuel Cells. *Energy and Fuels* **2020**, *34*, 10568–10582, doi:10.1021/acs.energyfuels.0c02338.
12. Baiutti, F.; Chiabrera, F.; Acosta, M.; Diercks, D.; Parfitt, D.; Santiso, J.; Wang, X.; Cavallaro, A.; Morata, A.; Wang, H.; Chroneos, A.; MacManus-Driscoll, J.; Tarancon, A. A High-Entropy Manganite in an Ordered Nanocomposite for Long-Term Application in Solid Oxide Cells. *Nat. Commun.* **2021**, *12*, 1–11, doi:10.1038/s41467-021-22916-4.

UNIVERSIDAD DE MÁLAGA

UNIVERSIDAD
DE MÁLAGA

Chapter 1

UNIVERSIDAD
DE MÁLAGA

UNIVERSIDAD
DE MÁLAGA

Introduction

The overuse of fossil fuels as an energy source during the last decade has caused a drastic increase of greenhouse gases concentration: CO_2, CH_4 and N_2O, with the consequent acceleration of global warming. Public concern over the impact of the temperature increase and the highly limited fossil-fuel supplies have induced a widespread interest in the implementation of new renewable energy resources. In the last years, the price of fossil fuels, such as coal and natural gas, has dramatically increased also inducing the skyrocketing price of electricity, which is currently at its maximum, negatively affecting industries, companies and consumers. For these reasons, it is crucial to develop a cost-effective infrastructure based on obtaining energy from renewable sources.

In the last decade, great advances in energy conversion and storage devices have been achieved, including solar cells, batteries, supercapacitors and fuel cells, not only obtaining higher efficiency but also lowering production costs [1]. Fuel cells are electrochemical devices for the efficient conversion of chemical energy into electricity, which can operate in reverse mode (electrolyser) to produce H_2 and other

UNIVERSIDAD DE MÁLAGA

fuels from electrical energy of renewable sources. Fuel cells have attracted research attention because they exhibit high energy conversion efficiency with low pollutant emissions and they are becoming a cost-competitive alternative due to the advances in the development of new materials for cell construction. Among the different fuel cells, Solid Oxide Fuel Cells (SOFCs) are one of the most promising because they can produce electricity from a wide variety of fuels, including H_2, hydrocarbons or natural gas [2]. SOFCs could play a key role in the initiatives to reverse the negative impact of the actual fossil-fuel energy system on the climate change, as described in the *Horizon 2020*, with promising projects like *FlexiFuel-SOFC* or *QSOFC* [3]. Great efforts to increase cell durability, robustness and reduce production costs have been carried out by numerous companies around the world [4].

In USA, *FuelCell Energy* (FCE), *LG* or *Bloom Energy* are pioneers in the development of SOFC power systems, *i.e.* FCE successfully built and tested in Pittsburgh a 50-kWe SOFC power device, which was integrated into the electrical grid with a 55% electrical efficiency and only a degradation rate of 0.9% for 1000 h [5]. Excellent results were also obtained in Japan by *Mitsubishi* or *Kyocera*, which reported a good electrical efficiency of 47% in a cell-stack operating at 700-750 ºC with very high overall energy efficiency (90%) [6]. *SOLIDpower* in China has also tested a 1.5 kW power stack continuously running for two years with a 59.6% electric efficiency [4]. Stimulated by all these excellent results, new projects about improving the durability of SOFC and also lowering production costs are under-way. The most promising SOFC cell-stacks prototypes are shown in Figure 1.1.

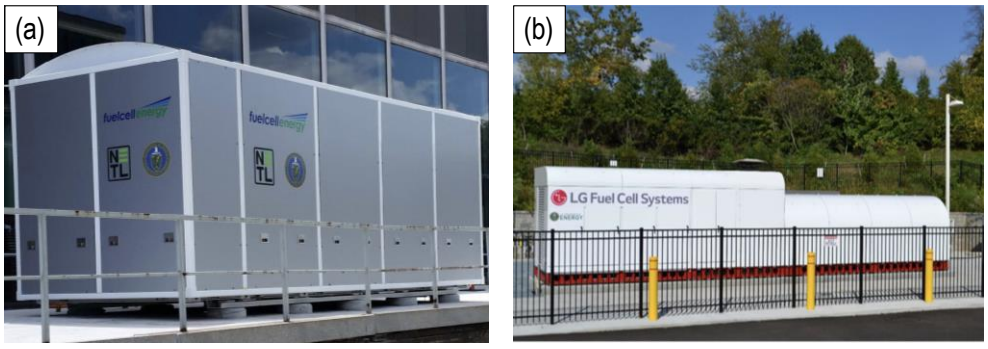

Figure 1.1. (a) FCE NG SOFC 50-kWe power system operating in Pittsburgh, USA and (b) LG Fuel Cell Systems SOFC prototype at Stark State College, Ohio, USA [4].

UNIVERSIDAD DE MÁLAGA

However, the relatively expensive technology, the high operating temperatures (700-900 ºC) and the coke deposition in the fuel electrode when hydrocarbons fuels are used, still hinder their wide implementation. In order to overcome these issues, the researchers have extensively worked on the development of alternative materials and fabrication techniques to improve the cell performance and lower the operating temperature.

1.1. Fuel cell technology

A typical fuel cell consists of different main components (cathode, anode and electrolyte). Electrical energy can be obtained by the continuous supply of a fuel (*i.e.* hydrogen or hydrocarbons) and an oxidant (O_2) to the anode and cathode, respectively. The chemical into electrical energy conversion is carried out in only one step, reaching 80% efficiency. In contrast, the electrical energy production from fuel combustion takes place in different steps, in which the chemical energy is firstly transformed into thermal energy, followed by mechanical energy and finally electricity, hindering the possibility to reach high efficiencies, mainly due to the thermal to mechanical transformation (Carnot cycle limitation).

The main advantages of fuel cells as energy conversion devices are:

- High efficiency when compared to other energy sources.
- Low greenhouse gas emissions.
- Improved environmental quality.
- Fuel flexibility.
- High reliability.
- No noise pollution.

The different types of fuel cells are proton exchange membrane fuel cells (PEMFC), alkaline fuel cells (AFC), phosphoric acid fuel cells (PAFC), molten carbonate fuel cells (MCFC) and solid oxide fuel cells (SOFC). Each fuel cell is suitable for certain applications, like stationary power generation or small portable devices [7]. Table 1.1 describes the main features of the different types of fuel cells.

UNIVERSIDAD DE MÁLAGA

Table 1.1. Features of the different types of fuel cells depending on the electrolyte employed and the operating temperature.

	Proton exchange membrane (PEMFC)	Alcaline (AFC)	Phosphoric acid (PAFC)	Molten carbonate (MCFC)	Solid oxide (SOFC)
Electrolyte	Nafion	KOH solution	H_3PO_4	Li_2CO_3- K_2CO_3	Oxide-ion conductors
Oxidant	Air, O_2	Air, O_2	Air, O_2	Air, CO_2, O_2	Air, O_2
Fuel	H_2/CO/CH_3OH	H_2	H_2/CO_2	H_2/CO	H_2/C_nH_{2n+2}
T (ºC)	50-100	90-100	150-200	600-1000	600-1000
Efficiency (%)	~50	~50	40-80	60-80	65-85
Disadvantages	-High cost of Pt -High fuel purity is required	-High cost -High sensibility to fuel impurities	-Corrosive electrolyte -Big size devices	-High corrosion at high T -Short service life devices	-High operating temperature

Nowadays, PEMFC and SOFC are the most investigated fuel cells for energy conversion. However, the low operation temperature (<90 ºC) of PEMFCs devices makes necessary an appropriate water management to simultaneously prevent dehydration of the membrane, such as Nafion®, and flooding of the electrodes [8]. Other drawbacks are the use of expensive noble metals, Pt (cathode) and IrO_2 (anode) for electrode fabrication, as well as the necessity of employing high purity H_2 or the electrode poisoning by CO and S traces in the fuel feed [9]. On the other hand, the high operating temperatures (600-800 ºC) of SOFCs induce some advantages, such as higher efficiency, better tolerance to impurities in the fuel feed and noble metals are not required. However, such high temperatures limit the materials that can be employed for cell construction and their lifetime.

1.2. Solid oxide fuel cells (SOFCs)

Traditionally, all SOFC components are ceramic materials with ionic or mixed ionic-electronic conductivity, depending on their role in the SOFC device. Figure 1.2a shows the working operation of a SOFC with an oxide-ion conductor electrolyte. The fuel (H_2) is oxidized in the anode to produce protons and electrons. The electrons move through an external circuit generating an electrical current and participate in the

UNIVERSIDAD DE MÁLAGA

reduction of the oxygen in the cathode generating oxide-ions (O^{2-}). Finally, the oxide ions migrate to the anode through the electrolyte and then react with the protons to produce H_2O in the anode side [2].

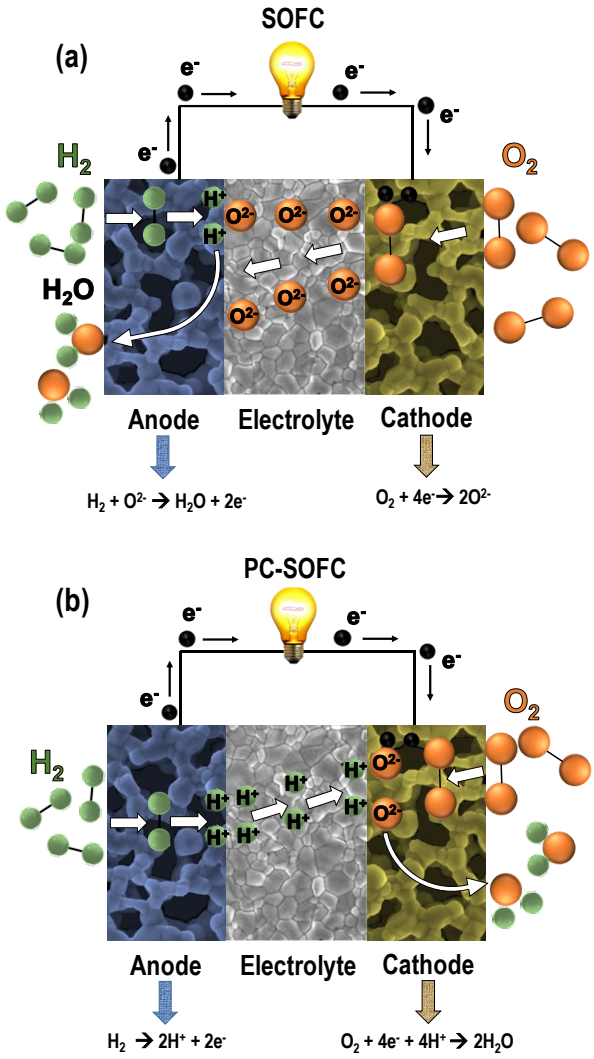

Figure 1.2. Schematic diagram of (a) solid oxide fuel cell (SOFC) with an oxide-ion conducting electrolyte and (b) solid oxide fuel cell with a proton-conducting electrolyte (PC-SOFC) when operating with H_2 as fuel.

In the last years, solid oxide fuel cells based on proton-conducting electrolytes (PC-SOFC) have demonstrated improved electrochemical performance at intermediate temperatures, which is explained by the greater mobility and lower

UNIVERSIDAD DE MÁLAGA

activation energy of protons (H^+) when compared to oxide-ions (O^{2-}) [10]. In this cell configuration, the protons migrate through the electrolyte to generate H_2O in the cathode side, thus avoiding the dilution of the fuel gas (Figure 1.2b).

SOFC technology has attracted great attention in recent years compared to the low-temperature fuel cells due to their numerous advantages, such as fuel flexibility, versatility or affordability (Figure 1.3). Additionally, the possibility of developing cell stacks from watt-sized devices to MW systems for both stationary applications and portable transportation make them very attractive for commercialization [11].

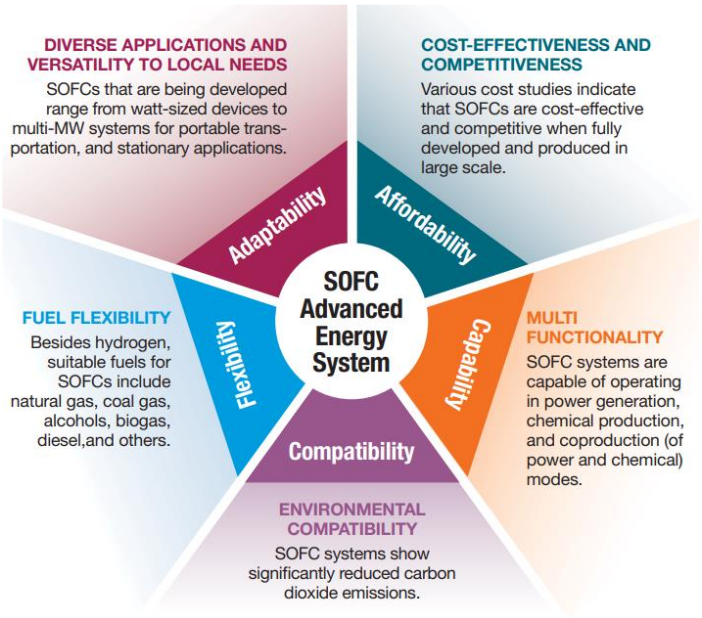

Figure 1.3. Advantages of a SOFC-based energy system. Reprinted with permission, Springer [11].

As commented previously, the high operating temperatures negatively affect the long-term stability of the cell, limiting the materials that can be used for cell components. For this reason, there are some issues that need to be considered to avoid performance degradation:

UNIVERSIDAD DE MÁLAGA

- Ferritic high-temperature stainless steels (Crofer 22 APU or SUS430) are proposed as alternative interconnector materials to the traditional $LaCrO_3$ in order to decrease the construction cost. However, one of the main issues is the Cr evaporation in the cathode side at high temperatures, resulting in the formation of $(Mn,Cr)_3O_4$ and $SrCrO_4$ secondary phases on the electrode surface [12,13].

- Sealing materials based on glass, used to avoid the contact between the fuel and oxidant feeds, can react with the electrolyte at high temperatures, generating insulating siliceous phases at the grain boundaries, highly decreasing the ionic conductivity [14].

- Deactivation of the anode due to the sulphur poisoning and carbon deposition, which block the active sites for electrocatalytic reactions, reducing the performance of the cell [15]. Even low concentrations of H_2S in the fuel can provoke the adsorption of S on the anode surface (Figure 1.4a), becoming necessary to explore alternative anode materials to Ni-cermets [16].

- Heating/cooling treatments and reversing the oxidant/fuel atmosphere can induce cracks or delamination of the cell layers (Figure 1.4b), hindering the long-term operation of the cells [17].

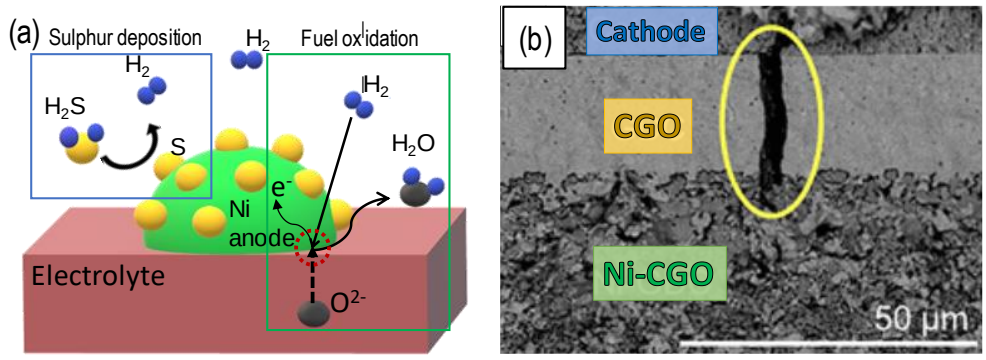

Figure 1.4. (a) Proposed mechanism for sulphur poisoning in a Ni-cermet anode and (b) electrolyte fracture after redox cycling. Reprinted with permission, American Chemical Society [17].

UNIVERSIDAD DE MÁLAGA

Nowadays, lowering the operating temperature to the intermediate temperature range (500-800 ºC) is the main challenge for the wide commercialization of SOFC. In the next sections, the state-of-the-art electrolyte and electrode materials for SOFCs are briefly commented.

1.2.1. Electrolyte materials

The main function of the electrolyte is to separate the cathode and anode sides, as well as provide an ionic conduction path between both materials [2,18]. One of the most important requirements is that the electrolyte has to be dense to avoid the contact between both fuel and oxidant gases. The typical electrolytes for SOFC applications are metal oxides in which the ionic transport occurs via oxide ion or proton migration. The main requirements for a SOFC electrolyte are:

(i) High ionic conductivity to reduce the ohmic losses, typically a minimum conductivity of 0.1 S cm^{-1} is required at working temperature.
(ii) Negligible electronic conductivity (σ_e) with electronic transport number ($t= \sigma_{el}/\sigma_{total}$) lower than 10^{-3} to avoid the electronic conduction through the electrolyte and the consequent short-circuit of the cell.
(iii) Good thermal stability at high temperatures in a wide range of oxygen partial pressures between 1 and 10^{-25} atm.
(iv) Chemical compatibility with the electrode materials to avoid the formation of reaction products at the electrode/electrolyte interface, which would result in a performance loss.
(v) Similar thermal expansion coefficient between the electrolyte and electrodes to avoid the formation of cracks or layer delamination during the thermal cycles.

1.2.1.1. ZrO_2-based electrolytes

One of the most studied electrolytes is doped-ZrO_2 with a fluorite-type structure. This material exhibits three different polymorphs depending on the temperature and doping level. The undoped compound crystallizes with a *monoclinic*

UNIVERSIDAD DE MÁLAGA

structure between room temperature and 1170 ºC, *tetragonal* from 1170 to 2370 ºC, and finally *cubic* above this temperature [2]. However, the cubic phase is stabilized at room temperature by aliovalent doping, *i.e.* Y^{3+} or Sc^{3+} (Figure 1.5). The composition with better stability at high temperatures is 8 mol.% Y_2O_3-doped ZrO_2 ($Zr_{0.84}Y_{0.16}O_{1.92}$, YSZ, yttria-stabilized zirconia), reaching 0.1 S cm^{-1} at 1000 ºC but rather low conductivity values at intermediate temperatures ($6 \cdot 10^{-3}$ S cm^{-1} at 650 ºC) [19].

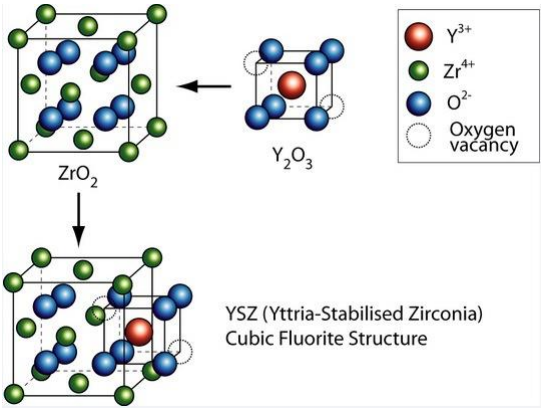

Figure 1.5. Formation of oxygen vacancies in ZrO_2 with a fluorite-type structure by Y-doping.

The highest ionic conductivity values were reported for Sc-doping, $(Sc_2O_3)_{0.1}$-$(ZrO_2)_{0.9}$ (SSZ, scandia-stabilized zirconia) (0.1 S cm^{-1} at 750 ºC [20]); nevertheless, the high price of Scandium hinders its implementation for commercial applications. It is worth mentioning that Y- and Sc-doping produce a lower lattice distortion in ZrO_2 and improved ionic conductivity when compared to other trivalent dopants [19]. One of the main disadvantages of ZrO_2-based electrolytes is their low chemical compatibility with highly efficient cathodes based on cobalt-iron perovskites, such as $La_{0.6}Sr_{0.4}Co_{0.2}Fe_{0.8}O_{3-\delta}$ (LSCF) or $Ba_{0.5}Sr_{0.5}Co_{0.8}Fe_{0.2}O_{3-\delta}$ (BSCF) [21,22]. Secondary phases with very low ionic conductivity are formed at the electrode/electrolyte interface, such as $SrZrO_3$ and $La_2Zr_2O_7$, drastically lowering the electrochemical performance under long-term operation [23]. For this reason, protective layers such as doped-CeO_2 thin films are required to minimize the SrO diffusion at the interface.

UNIVERSIDAD DE MÁLAGA

1.2.1.2. CeO_2-based electrolytes

$Ce_{1-x}Ln_xO_{2-x/2}$ (Ln=Sm^{3+} or Gd^{3+}, x = 0.1-0.2) have been proposed as an alternative to ZrO_2-based electrolytes [24]. The ionic conductivity of doped-CeO_2 is significantly higher than that of YSZ. The best ionic conductivity is reported for Sm^{3+} and Gd^{3+} doping, *i.e.* 0.01 S cm^{-1} at 500 ºC for $Ce_{0.9}Gd_{0.1}O_{1.95}$ (CGO) [25], making them suitable for intermediate temperature applications. In addition, CGO exhibits good physical and chemical compatibility with perovskite-type cathode materials.

The main limitation of CeO_2-based electrolytes is the partial reduction of Ce^{4+} (0.97 Å) to Ce^{3+} (1.14 Å) under reducing conditions (fuel atmosphere), increasing the electronic conductivity and thus lowering the thermomechanical stability due to the lattice expansion induced by the larger size of Ce^{3+}. This drawback restricts their use to temperatures lower than 700 ºC [24]. On the other hand, highly doped-CeO_2, such as $Ce_{0.5}La_{0.5}O_{1.75}$ ($La_2Ce_2O_7$), have been also investigated due to their high proton-conductivity at low temperatures (< 400 ºC) [26].

1.2.1.3. $LaGaO_3$-based and other electrolytes

Doped lanthanum gallates with perovskite structure, $La_{1-x}Sr_xGa_{1-y}Mg_yO_{3-\delta}$ (LSGM; x = 0.1-0.2, y = 0.15-0.2), have demonstrated to be one of the most promising electrolyte materials due to their high ionic conductivity and negligible electronic conductivity in both oxidizing and reducing atmospheres [27,28]. In addition, they exhibit high chemical compatibility with the most commonly used electrodes in SOFCs. For this reason, LSGM is widely used in electrolyte-supported SOFCs. However, the high cost of Gallium, the formation of secondary phases during the synthesis process, *i.e.* $LaSrGa_3O_7$ and $LaSrGaO_4$, and the chemical reactivity with nickel-based anodes have limited their application in commercial devices [29]. Alternatively, anode-supported $La_{0.2}Sr_{0.8}TiO_{3-\delta}$ cells with LSGM thin-film electrolyte and LSCF-CGO cathode have been also reported, rendering competitive maximum power density values of 1.12 W cm^{-2} at 650 ºC [30].

Oxide-ion conductors with different crystal structures have been also proposed for SOFCs, *i.e.* $La_2Mo_2O_9$, $La_{9.33}(SiO_4)_6O_2$ and doped-Bi_2O_3 [2,31,32].

UNIVERSIDAD DE MÁLAGA

Compositions like $Bi_{1.6}Er_{0.4}O_3$ (ESB), $Bi_{1.5}Y_{0.5}O_3$ (BYO) and $Dy_{0.08}W_{0.04}Bi_{0.88}O_{1.56}$ (DWSB) present ionic conductivity values more than one order of magnitude higher than those reported for YSZ [33,34]. However, these materials are not redox stable and the volatilization of Bi_2O_3 at high temperatures limits their application [35]. The conductivity values of the most employed oxide-ion conductor electrolytes for SOFCs are compared in Figure 1.6.

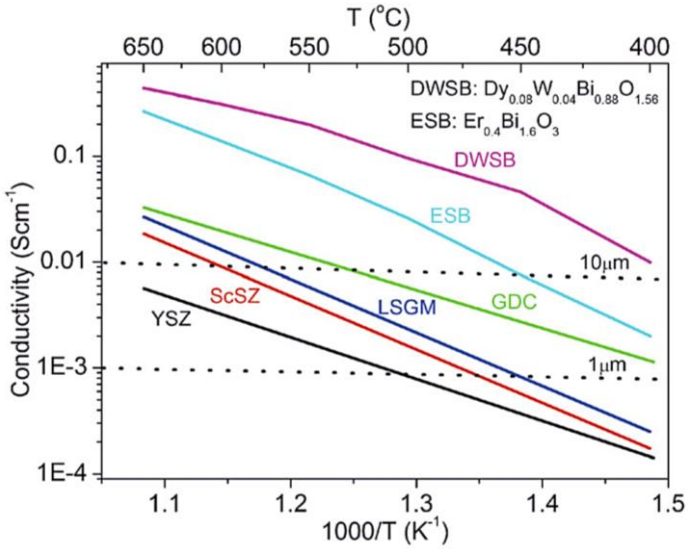

Figure 1.6. Conductivity values of the most employed electrolytes in SOFCs. Dashed lines indicate the conductivity/electrolyte thickness requirement to ensure good cell performance. Reprinted with permission, Royal Society of Chemistry [36].

1.2.1.4. Proton-conducting electrolytes

Recently, proton-conducting electrolyte materials (PC-SOFC) have attracted great attention due to their better conductivity at intermediate temperatures. Most of the research has been centered on doped-$BaCeO_3$ and $BaZrO_3$ perovskite materials [10,37]. Despite the fact that $BaCeO_3$ electrolytes exhibit high proton conductivity, they are not stable under H_2O and CO_2 atmospheres. On the contrary, doped-$BaZrO_3$ exhibit improved resistance to carbonation but sintering temperatures close to 1700 ºC are needed to achieve densification [37]. For this reason, $BaCe_{1-x}Zr_xO_3$ solid solutions or alternative compositions have been explored [10,38]. One of the most employed electrolytes for PC-SOFCs is $BaZr_{0.1}Ce_{0.7}Y_{0.1}Yb_{0.1}O_{3-\delta}$ (BZCYYb) proposed

UNIVERSIDAD DE MÁLAGA

by Yang *et al.* with ionic conductivity values of $6 \cdot 10^{-2}$ S cm^{-1} at 700 ºC in wet air, as well as excellent resistance to sulphur poisoning and coking [39,40]. The conductivity values of the most employed oxide-conductor and proton-conductor electrolytes for SOFCs are displayed in Table 1.2.

Table 1.2. Ionic conductivity of the most studied electrolyte in SOFCs. Conductivity values are given at 750 and 600 ºC. Temperature is included when data are not available.

	Electrolyte	Conductivity (S cm^{-1})		Ref
		750 ºC	600 ºC	
Oxide-ion conductors	$Zr_{0.84}Y_{0.16}O_{1.92}$ (YSZ)	$1.6 \cdot 10^{-2}$	$2 \cdot 10^{-3}$	[39]
	$(ZrO_2)_{0.9}$-$(Sc_2O_3)_{0.1}$ (SSZ)	$1 \cdot 10^{-1}$	$2 \cdot 10^{-2}$	[20]
	$Ce_{0.9}Gd_{0.1}O_{1.95}$ (CGO)	$6 \cdot 10^{-2}$	$2 \cdot 10^{-2}$	[39]
	$La_{0.9}Sr_{0.1}Ga_{0.8}Mg_{0.2}O_{2.85}$ (LSGM)	$5 \cdot 10^{-2}$	$1.2 \cdot 10^{-2}$	[41]
	$La_2Mo_2O_9$	$8 \cdot 10^{-2}$	$1.3 \cdot 10^{-2}$	[31]
	$La_{9.33}(SiO_4)_6O_2$	$1.3 \cdot 10^{-3}$ 700 ºC	$6 \cdot 10^{-4}$	[42]
	$Er_{0.4}Bi_{1.6}O_3$	$3.5 \cdot 10^{-1}$ 700 ºC	$1.8 \cdot 10^{-1}$	[33]
	$Dy_{0.08}W_{0.04}Bi_{0.88}O_{1.56}$	$5.7 \cdot 10^{-1}$ 700 ºC	$3 \cdot 10^{-1}$	[34]
Proton-conductors	$BaZr_{0.8}Y_{0.2}O_{3-\delta}$	-	$2.0 \cdot 10^{-2}$	[40]
	$BaCe_{0.9}Y_{0.1}O_{3-\delta}$	$1.8 \cdot 10^{-2}$	$1.8 \cdot 10^{-2}$	[43]
	$BaCe_{0.7}Zr_{0.1}Y_{0.2}O_{3-\delta}$	$5 \cdot 10^{-2}$	$1.7 \cdot 10^{-2}$	[39]
	$BaCe_{0.7}Zr_{0.1}Y_{0.1}Yb_{0.1}O_{3-\delta}$	$8 \cdot 10^{-2}$	$3 \cdot 10^{-2}$	[39]
	$La_2Ce_2O_7$	$1 \cdot 10^{-2}$	$3 \cdot 10^{-3}$	[44]

1.2.2. Cathode materials

The main function of the cathode is to provide active sites for the oxygen reduction reaction (ORR; $O_2+4e^- \rightarrow 2O^{2-}$). In order to achieve good electrochemical performance, the cathode materials should have: (i) high ionic-electronic conductivity; (ii) high porosity and surface area to allow the gas diffusion to the active sites; (iii) good chemical compatibility with the electrolyte; (iv) similar thermal expansion coefficient (TEC) to the electrolyte to avoid delamination between the cell components and (v) long-term stability in oxidizing conditions at high temperature. In particular, mixed ionic-electronic conductors (MIECs) with high ionic and electronic conductivity

UNIVERSIDAD DE MÁLAGA

are desirable for intermediate temperature applications. Most of the cathode materials in SOFCs are compounds with single perovskite-type structure (ABO_3), double perovskite ($AA'B_2O_6$) and Ruddlesden-Popper structure ($A_{n+1}B_nO_{3n+1}$) (Figure 1.7).

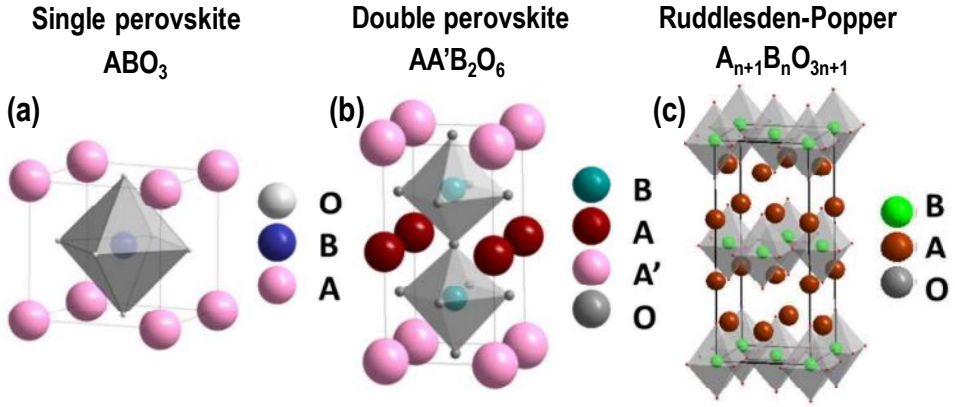

Figure 1.7. Crystal structures of the most common perovskite cathode materials for SOFCs: (a) Single perovskite, (b) Double perovskite and (c) Ruddlesden-Popper.

1.2.2.1. Single perovskites

Single perovskites (ABO_3) are by far the most employed cathode materials for SOFCs. Typically, in a cubic perovskite structure, the A-cation (12-fold coordination) is larger than the B-cation (6-fold coordination) and O corresponds to oxygen atoms (Figure 1.7a).

$La_{0.6}Sr_{0.4}MnO_{3-\delta}$ (LSM) is the state-of-the-art cathode material due to its excellent electronic conductivity (~235 S cm^{-1} at 900 ºC) and low reactivity with YSZ electrolyte [45], but its ionic conductivity is rather low ($4 \cdot 10^{-8}$ S cm^{-1} at 900 ºC) [46]. Despite the fact that the conductivity of LSM increases with Sr-content, secondary phases of $SrZrO_3$ are observed in contact with the YSZ electrolyte. In order to solve this issue, A-site deficient LSM was prepared to avoid the segregation of Sr-based compounds [47]. Since the ionic conductivity of LSM is relatively low, composite electrodes are usually prepared by mixing LSM with an ionic conductor, such as YSZ or CGO, greatly improving the electrochemical performance [48].

One of the best alternatives to the traditional LSM cathodes are doped lanthanum cobaltites. $La_{0.6}Sr_{0.4}CoO_{3-\delta}$ (LSC) exhibits electronic conductivity values

UNIVERSIDAD DE MÁLAGA

higher than 1600 S cm^{-1} and high values of ionic conductivity (0.4 S cm^{-1}) at 800º C [49]. However, the thermal expansion coefficient (TEC) of LSC is relatively high, above $25 \cdot 10^{-6}$ K^{-1}, and therefore mechanically incompatible with most of the electrolytes [49,50]. The TEC is lowered by incorporating Fe in the B-site, $La_{0.6}Sr_{0.4}Co_{1-y}Fe_yO_{3-\delta}$ ($0 \leq y \leq 0.8$), in which $La_{0.6}Sr_{0.4}Co_{0.2}Fe_{0.8}O_{3-\delta}$ (LSCF) is the most common composition due to the moderate TEC ($15 \cdot 10^{-6}$ K^{-1}), high electronic conductivity (320 S cm^{-1} at 700 ºC) [22], as well as good ionic conductivity (>10^{-2} S cm^{-1}) [51]. Very low polarization resistance is observed for LSCF cathodes, 0.3 Ω cm^2 at 700 ºC [52], values that were further reduced to 0.026 Ω cm^2 at the same temperature when LSCF-CGO was employed as a composite cathode [53]. However, it has to be noted that Sr-based compounds are segregated on the electrode surface during long-term operation, under cathodic polarization and at high temperatures, lowering the electrode performance and the oxygen reduction kinetics [54]. This process is partially reverted in anodic polarization, since the oxygen vacancy concentration at the electrode surface is considerably reduced, thus inhibiting the segregation of secondary phases due to the stronger attractive force between the oxygen vacancies and the Sr^{2+} in the lattice [55].

In order to overcome this issue, several approaches have been proposed. For instance, coating the electrode surface with a thin layer of ZrO_2 [56] or CGO infiltration [57], showing the LSCF-CGO infiltrated cathode a very low degradation rate when compared with the unprotected LSCF. A-site deficiency has also shown to be crucial to partially suppress the segregation of Sr-based compounds in LSCF, but partial degradation is usually observed during long-term operation [58].

Excellent electrochemical properties were also observed for $Ba_{0.5}Sr_{0.5}Co_{0.8}Fe_{0.2}O_{3-\delta}$ (BSCF), achieving polarization resistance values (R_p) as low as 0.6 Ω cm^2 at 500 ºC [21], but a phase transformation from cubic to hexagonal structure was observed during long-term operation [59]. Recently, $BaCo_{0.4}Fe_{0.4}Zr_{0.1}Y_{0.1}O_{3-\delta}$ (BCFZY) with mixed oxide-ion, proton and electronic conductivity was also proposed for both SOFCs and PC-SOFCs, showing R_p values as low as 0.1 Ω cm^2 at 600 ºC [60]. The R_p and conductivity values of the most employed cathodes for SOFC is displayed are Table 1.3.

UNIVERSIDAD DE MÁLAGA

Table 1.3. Electrochemical properties of the most employed cathode materials for SOFCs with single or layered perovskite-type structure. R_p and conductivity values are given at 700 ºC. Temperature is included when data are not available at 700 ºC.

	Electrode	R_p Air (Ω cm^2)	Conductivity (S cm^{-1})	Ref
Single Perovskites	$La_{0.8}Sr_{0.2}MnO_{3-\delta}$	3.1	190	[45,61]
	$La_{0.6}Sr_{0.4}CoO_{3-\delta}$	0.17	1800	[50,62]
	$La_{0.6}Sr_{0.4}Co_{0.2}Fe_{0.8}O_{3-\delta}$	0.30	320	[22,53]
	$Ba_{0.5}Sr_{0.5}Co_{0.8}Fe_{0.2}O_{3-\delta}$	0.01	10	[21]
	$BaCo_{0.4}Fe_{0.4}Zr_{0.1}Y_{0.1}O_{3-\delta}$	0.1	1.4 $^{600\ ºC}$	[60]
Layered Perovskites	$PrBaCo_2O_{5+\delta}$	0.04	1000	[63]
	$PrBa_{0.5}Sr_{0.5}Co_2O_{5+\delta}$	0.19	800	[64]
	$Sr_2Fe_{1.5}Mo_{0.5}O_{6-\delta}$	0.65 $^{650\ ºC}$	100	[65]
	$La_2NiO_{4+\delta}$	1.2	25	[66]
	$Pr_{1.2}Sr_{0.8}NiO_{4+\delta}$	0.5	130	[67]
	$La_2CuO_{4+\delta}$	0.4	5	[66,68]

1.2.2.2. Double perovskites

Double perovskites with the general formula $AA'BB'O_{6-\delta}$ are formed when two different cations, or the same one with different oxidation states, occupy the same crystallographic position (Figure 1.7b). This structure can accommodate high oxygen non-stoichiometry compared to single perovskites [63].

Different electrode materials derived from $NdBaCo_2O_{5+\delta}$, $PrBaCo_2O_{5+\delta}$ and $GdBaCo_2O_{5+\delta}$ have been investigated due to their high mixed ionic-electronic conductivity [63]. Co-free compositions were also explored, such as $NdBaFe_{1.9}Mn_{0.1}O_{5+\delta}$ or $NdBaFe_{1.9}Nb_{0.1}O_{5+\delta}$ with conductivity values higher than 100 S cm^{-1} at 500 ºC [69,70]. It has to be mentioned that promising results were also achieved for $Sr_2Fe_{1.5}Mo_{0.5}O_{6-\delta}$ as both air and fuel electrodes [65].

UNIVERSIDAD DE MÁLAGA

1.2.2.3. Ruddlesden-Popper

Ruddlesden-Popper (RP) phases with the following general formula: $A_{n+1}B_nO_{3n+1}$ are composed of ABO_3 perovskite layers and *n* AO layers with rock salt structure along the c-axis (Figure 1.7c). The most promising materials are those derived from $Ln_2NiO_{4+\delta}$ and $Ln_2CuO_{4+\delta}$, where *Ln* is a lanthanide cation.

RP phases show lower electronic conductivity when compared to cobalt-based perovskites (Table 1.3) [66]. However, relatively high surface exchange coefficients ($k=7.57\cdot10^{-6}$ cm s^{-1}) and oxygen diffusion kinetics ($D=4.15\cdot10^{-7}$ cm^2 s^{-1}) were reported for $Pr_2NiO_{4+\delta}$ at 900 ºC [71]. Yang *et al.* studied $Pr_{2-x}Sr_xNiO_{4+\delta}$ (x= 0.3, 0.5 and 0.8), achieving the best R_p values for $Pr_{1.2}Sr_{0.8}NiO_{4+\delta}$, 0.11 Ω cm^2 at 800 ºC [67]. The $Nd_2NiO_{4+\delta}$ composition was also explored showing a remarkable maximum power density (MPD) of 1.26 W cm^{-2} at 800 ºC in an anode-supported cell [72]. $La_2CuO_{4+\delta}$ infiltrated into a porous CGO backbone by spray-pyrolysis also rendered a very low R_p of 0.14 Ω cm^2 at 600 °C [68].

1.2.3. Anode materials

The traditional anode materials are usually composite materials that combine a ceramic ionic conductor with a metal (cermet) to provide both ionic and electronic conductivities for the hydrogen oxidation reaction (HOR). The most employed composite is the Ni-YSZ cermet (typically 60 wt.% NiO and 40 wt.% YSZ) due to its excellent electrochemical activity for hydrogen oxidation [73], as well as its relatively low cost when compared to noble metals. However, Ni particles tend to form aggregates at high operating temperatures, lowering the porosity and reducing the triple-phase-boundary (TPB), therefore, decreasing cell performance after long-term operation (Figure 1.8) [74].

Another drawback of the Ni-YSZ anodes is the tendency of Ni-metal to suffer from sulphur poisoning and carbon deposition. In particular, the carbon formation in Ni-based cermets is the main problem for hydrocarbon oxidation in SOFCs, being necessary the use of external reformers to obtain the hydrogen or the implementation of alternative anode materials [74]. Alternatively, Cu/Co-based cermets have shown

UNIVERSIDAD DE MÁLAGA

improved carbon tolerance [76], but lower catalytic activity for fuel oxidation compared to Ni-based anodes.

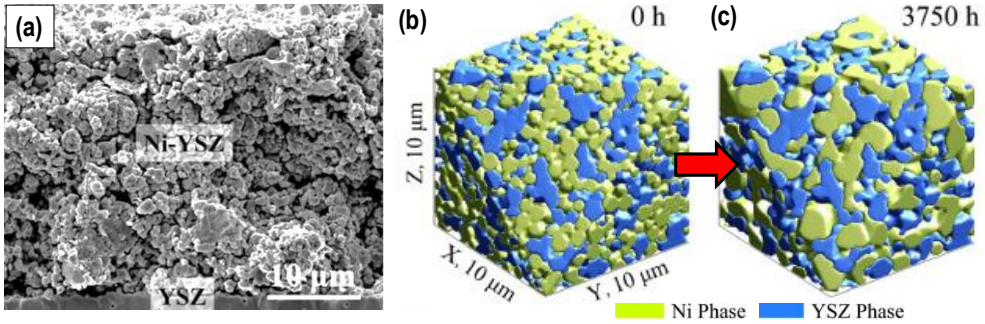

Figure 1.8. (a) SEM image of the Ni-YSZ anode and (b,c) 3D reconstruction of the morphological evolution of the Ni-YSZ anode during long-term operation. Reprinted with permission, Elsevier [75].

In order to overcome these issues, new anode materials based on redox stable perovskites have been proposed, including lanthanum strontium chromites (*i.e.* $La_{0.75}Sr_{0.25}Cr_{0.5}Mn_{0.5}O_{3-\delta}$), lanthanum strontium ferrites (*i.e.* $La_{0.8}Sr_{0.2}Fe_{0.8}M_{0.2}O_{3-\delta}$, where M is a transition metal) or strontium titanates derived from $SrTiO_3$, which have shown excellent results working as anodes with a wide variety of fuels, such as H_2, CH_4, C_2H_6 or syngas [77,78]. Most of these electrode compositions have also been tested as air electrodes in a new cell configuration that is known as Symmetrical Solid Oxide Fuel Cells (SSOFC). Due to the relevance of this cell configuration in this PhD Thesis, the advantages and properties of these electrodes will be further commented in detail in the next section.

1.3. Symmetrical solid oxide fuel cells (SSOFCs)

During the fabrication of a single SOFC, several steps are needed to assemble all the cell layers due to the different compositions of the anode and cathode. In the last few years, the researchers have deeply investigated alternative electrode compositions to work as both cathode and anode in a SSOFC. The advantages of this configuration not only rely on the lower fabrication costs, since the anode and cathode with the same composition are deposited and sintered in a single step on the electrolyte, but also the thermo-mechanical stability and chemical

UNIVERSIDAD DE MÁLAGA

compatibility between the cell components are improved because only one type of interface is presented [77,78].

SSOFCs are reversible to operate in fuel cell and electrolyser mode, depending on the electrical energy consumption and demand (Figure 1.9) [79]. Moreover, one of the most promising advantages of this cell configuration is the possibility to reverse the gas atmosphere from fuel to oxidant gases and vice versa to prevent sulphur poisoning or carbon deposition [16].

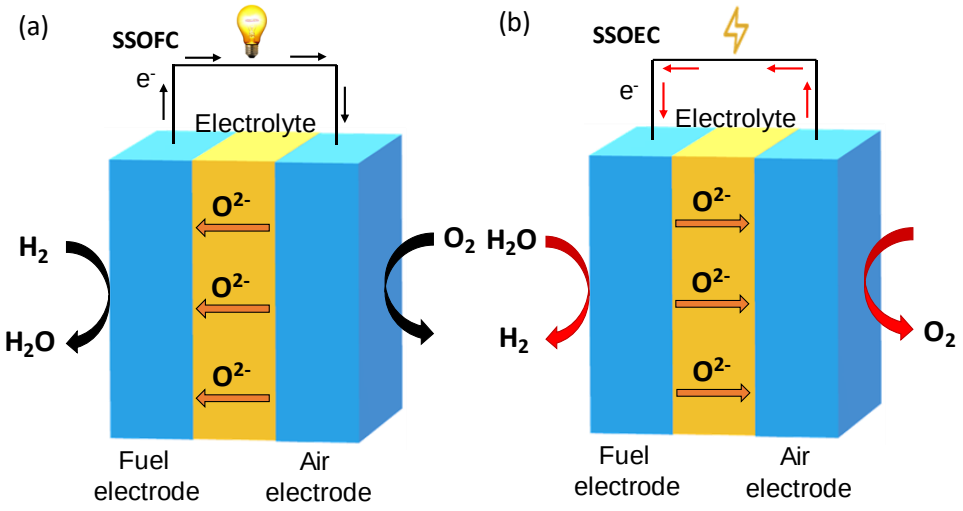

Figure 1.9. Illustration of a symmetrical solid oxide cell with identical electrodes in (a) fuel cell mode and (b) electrolysis mode.

The SSOFC configuration was proposed for the first time by Ruiz-Morales *et al.* and Bastidas *et al.* in 2006, implementing $La_{0.75}Sr_{0.25}Cr_{0.5}Mn_{0.5}O_{3-\delta}$ (LSCM) as a symmetrical electrode [80,81]. The best results were found for the LSCM-YSZ composite, rendering a YSZ-supported cell a maximum power density of 546 and 347 mW cm^{-2} at 950 ºC, in H_2 and CH_4, respectively [81]. From this point onwards, several strategies have been explored to implement the traditional cathode materials in SSOFCs, which typically show low redox stability under reducing conditions. Most of the research in the last years has been focused on incorporating transition metals with higher redox stability in the B-site of (La,Sr)(Fe,Co,M)O_3 perovskites (*i.e.* M= Sc^{3+}, Ti^{4+}, Zr^{4+}, Nb^{5+}, Mo^{6+}, W^{6+}), leading to an improvement of the electrochemical

UNIVERSIDAD DE MÁLAGA

properties and lowering the thermal expansion coefficients (TEC) in both oxidizing and reducing conditions [82].

One of the main drawbacks of this configuration is the difficulty of achieving good electrocatalytic activity simultaneously in both oxidizing and reducing conditions [83]. Most of the best SSOFC electrodes are derived from air electrodes, which typically show high performance in air conditions. However, the electrocatalytic activity in reducing conditions is rather modest, becoming necessary to implement alternative doping strategies, such as incorporating noble metals, *i.e.* Ni, Ru or Pd, that can be exsolved in reducing conditions on the electrode surface as metal nanoparticles with improved properties for hydrogen and hydrocarbon oxidation [77,78].

On the other hand, tailoring the electrode microstructure has shown to be crucial to enhance the electrochemical performance. Not only single perovskite-based electrodes, such as $La(Cr,Mn)O_{3-\delta}$, $(La,Sr)FeO_{3-\delta}$ or $(La,Sr)TiO_{3-\delta}$, have been deeply explored, but also layered perovskites with good phase stability, $Sr_2Fe_{1.5}Mo_{0.5}O_{6-\delta}$ or $PrBaMn_2O_{5+\delta}$. The most important compositions are discussed below.

It is worth mentioning that non-redox stable electrodes, such as LSCF [84], $La_2NiO_{4+\delta}$ [85] or $PrBaFe_2O_{5+\delta}$ [86] have also been tested in SSOFCs. These materials suffer a severe phase transformation in reducing conditions into different components, including large amounts of metal particles, which considerably improve the electrochemical properties. This electrode configuration is known in the literature as quasi-symmetrical electrodes (Q-SOFCs) due to the different composition of the fuel and air electrodes. Despite the improved performance of quasi-symmetrical electrodes, the significant microstructural changes during redox cycles could detrimentally affect the electrode stability. Additionally, the reversibility of these electrodes needs to be further investigated because in some cases, the original phase is not recovered after the reoxidation process in air.

1.3.1. $La(Cr,Mn)O_3$-based electrodes

Traditionally, $La(Cr,Mn)O_3$-based materials were employed as interconnectors and fuel electrodes due to their high redox stability at elevated

UNIVERSIDAD DE MÁLAGA

temperatures [87]. After the pioneer work of Ruiz-Morales *et al.* for $La_{0.75}Sr_{0.25}Cr_{0.5}Mn_{0.5}O_{3-\delta}$ (LSCM) as symmetrical electrode [81], numerous researchers have tried to improve the performance of LSCM by different doping strategies in A- and B-site of the perovskite as well as by microstructural optimization.

Rath *et al.* studied different transition metal dopants in $La_{0.7}Ca_{0.3}Cr_{0.8}M_{0.2}O_{3-\delta}$ (M= Fe, Mn, Co, Ti and Ni), improving the electrocatalytic activity in the following order: Ti < Co < Fe ≈ Ni < Mn with R_p values in H_2 ranging from 0.36 to 0.12 Ω cm^2 at 800 ºC [88]. Zhang *et al.* tested $La_{0.7}A_{0.3}Cr_{0.5}Mn_{0.5}O_{3-\delta}$ (A=Ca, Sr and Ba), not showing significant differences in terms of conductivity (~27 S cm^{-1} at 800 ºC for all samples) or R_p values (~0.5 Ω cm^2 at 900 ºC) in air [89].

Ce-doped samples were also studied due to the high activity of cerium for hydrocarbon oxidation. The electrochemical activity of $La_{0.75-x}Ce_xCr_{0.5}Mn_{0.5}O_{3-\delta}$ (x=0-0.375) for H_2 oxidation increased with the Ce-content [90]; however, the resistance to sulphur poisoning decreased for highly doped samples (x>0.15).

Recently, a Bi-doped $La_{0.65}Bi_{0.1}Sr_{0.25}Cr_{0.5}Fe_{0.5}O_{3-\delta}$-$Ce_{0.9}Sm_{0.1}O_{1.95}$ composite electrode was investigated [91]. A LSGM-supported cell delivered MPDs of 280 and 260 mW cm^{-2} using H_2 and syngas as fuels, respectively (Figure 1.10). Ni-doping in $La_{0.75}Sr_{0.25}Cr_{0.5}Mn_{0.3}Ni_{0.2}O_{3-\delta}$ was also explored in order to promote Ni metal nanoparticle exsolution on the electrode surface. However, high R_p values were obtained in air and H_2, 1.6 and 1.1 Ω cm^2 at 800 ºC, respectively [92].

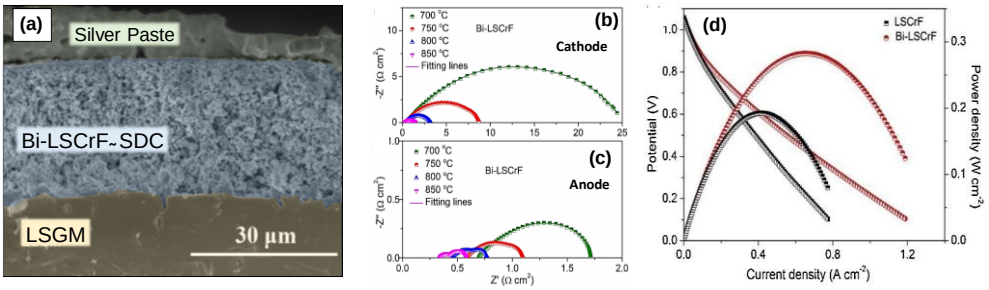

Figure 1.10. (a) Cross-sectional SEM image of $La_{0.65}Bi_{0.1}Sr_{0.25}Cr_{0.5}Fe_{0.5}O_{3-\delta}$-$Ce_{0.9}Sm_{0.1}O_{1.95}$ composite electrode on LSGM electrolyte. Impedance spectra in (b) air and (c) H_2 at different temperatures and (d) I-V-P curves of the LSGM-supported cell of the pristine electrode (LSCrF) and the Bi-doped sample (Bi-LSCrF). Reprinted with permission, Elsevier [91].

UNIVERSIDAD DE MÁLAGA

1.3.2. (La,Sr)FeO_3-based electrodes

(La,Sr)FeO_3-based (LSF) air electrodes have demonstrated high efficiency in air conditions but they typically show very low redox stability as fuel electrodes due to severe decomposition or phase transformation in reducing conditions [18,93]. In order to overcome this issue, numerous doping strategies have been implemented by incorporating less reducible cations, *i.e.* Ti^{4+}, Zr^{4+}, Nb^{5+}, Mo^{6+} and W^{6+} in the B-site of the perovskite.

In this context, Fernández-Ropero *et al.* tested $SrFe_{0.75}M_{0.25}O_{3-\delta}$ symmetrical electrodes (M= Cr^{3+}, Ti^{4+}, Zr^{4+}, V^{5+}, Nb^{5+}, Mo^{6+} and W^{6+}) [94]. The Ti-doped sample showed the lowest R_p values in air at 700 ºC (0.25 Ω cm^2), while the lowest values in 5% H_2-Ar were obtained for Zr-doped samples (0.3 Ω cm^2), significantly lower to that observed for the Ti-doped sample (1.5 Ω cm^2) [94]. Later, dos Santos-Gómez *et al.* studied the $Sr_{0.98}Fe_{1-x}Ti_xO_{3-\delta}$ (x= 0, 0.2, 0.4 and 0.8) series by spray-pyrolysis deposition into a porous CGO backbone [95]. The $Sr_{0.98}Fe_{0.8}Ti_{0.2}O_{3-\delta}$-CGO composition rendered R_p values of 0.1 and 0.4 Ω cm^2 at 700 ºC in air and wet 5% H_2-Ar, respectively. These R_p values were considerably lower than those observed for the analogous screen-printed powder electrodes, 0.55 and 1.4 Ω cm^2 in air and wet 5% H_2-Ar, respectively, at the same temperature. Additionally, a remarkable MPD of 700 mW cm^{-2} at 800 ºC was obtained for the electrodes prepared by spray-pyrolysis onto a 300 µm thick LSGM-supported cell. These findings further confirm the necessity of tailoring the electrode microstructure to achieve high electrochemical performance in both oxidizing and reducing conditions. The $SrFe_{0.8}W_{0.2}O_{3\pm\delta}$ composition was also explored by Cao *et al.* showing remarkable R_p values of 0.084 and 0.20 Ω cm^2 in air and H_2, respectively, at 800 ºC with a high MPD of 931 mW cm^{-2} at 850 ºC for a LSGM-supported cell [96].

Outstanding results were also observed for Mo-doped $La_{0.5}Sr_{0.5}Fe_{0.9}Mo_{0.1}O_{3\pm\delta}$ with R_p values as low as 0.08 and 0.09 Ω cm^2 at 850 ºC in air and H_2, respectively [97]. Alternative Ga or Sc-doping strategies were also explored, $La_{0.7}Sr_{0.3}Fe_{0.7}Ga_{0.3}O_{3-\delta}$ and $La_{0.6}Sr_{0.4}Fe_{0.9}Sc_{0.1}O_{3-\delta}$ [98,99]. One of the most promising results was recently obtained in 2021 by Hou *et al.* for the $La_{0.3}Sr_{0.7}Fe_{0.9}Ti_{0.1}O_{3-\delta}$ symmetrical electrode [100]. Low polarization resistance values were observed in both

UNIVERSIDAD DE MÁLAGA

air and H_2 conditions, 0.022 and 0.15 Ω cm^2, respectively, at 800 ºC, as well as high MPD and current density of 847 mW cm^{-2} and -1.9 A cm^{-2} in SOFC and SOEC modes, respectively. Ni and Ru were also incorporated into $LaFeO_3$-based electrodes to achieve nanoparticle exsolution in a reducing atmosphere. $Sr_{0.8}Ce_{0.2}Fe_{0.95}Ru_{0.05}O_{3-\delta}$ showed in-situ exsolution of SrO, CeO_2 and Ru-nanoparticles, which were responsible for the great MPD achieved for a LSGM-supported cell, 846 and 330 mW cm^{-2} at 800 ºC for H_2 and C_3H_8, respectively [101] (Figure 1.11).

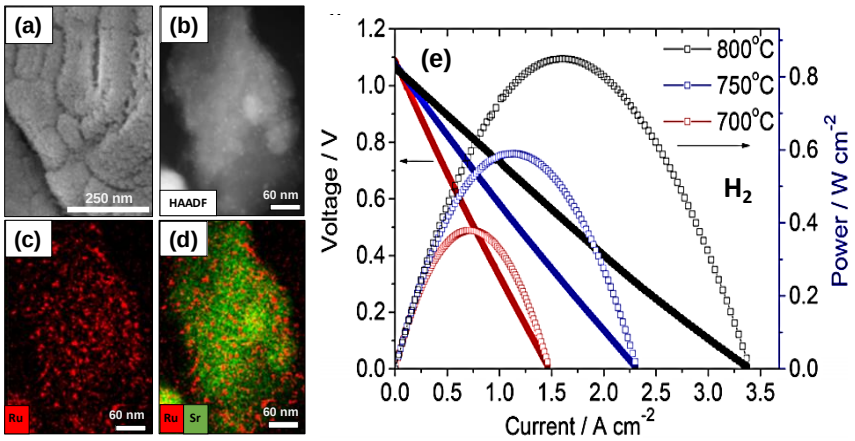

Figure 1.11. (a) SEM image, (b) HAADF-STEM image and (c,d) EDS mapping of the surface of $Sr_{0.8}Ce_{0.2}Fe_{0.95}Ru_{0.05}O_{3-\delta}$ in H_2 at 800 ºC. Ru nanoparticles are observed after reduction. (e) I-V-P curves at different temperatures in H_2 atmosphere of the symmetrical electrode onto a LSGM-supported cell. Reprinted with permission, American Chemical Society [101].

Tian *et al.* also reported Ni-Fe exsolved nanoparticles in a $La_{0.6}Ca_{0.4}Fe_{0.8}Ni_{0.2}O_{3-\delta}$-CGO composite, showing rather low R_p values in air and H_2, 0.24 and 0.13 Ω cm^2, respectively, at 800 ºC [102].

1.3.3. (La,Sr)TiO_3-based electrodes

Titanates have been considered highly promising fuel electrodes due to their great stability under reducing conditions and their high resistance to sulphur poisoning [103]. Typically, titanate-based electrodes show high electronic conductivity in reducing atmospheres due to the partial reduction of Ti^{4+} to Ti^{3+}; however, they are electrically insulating materials in air conditions, hindering their implementation as air electrode. For this reason, a partial substitution in A- and B-sites are necessary. For

UNIVERSIDAD DE MÁLAGA

instance, Pr-doping significantly enhances the electrical conductivity with values of 0.4 S cm^{-1} in air and 150 S cm^{-1} in 10% H_2-Ar for $Sr_{0.9}Pr_{0.1}TiO_{3\pm\delta}$ at 800 ºC [104].

A pioneer work from Canales-Vázquez *et al.* on $La_{1/3}Sr_{2/3}Ti_{1-x}Fe_xO_{3+\delta}$ (x=1/8-0.5) electrodes demonstrated a considerable increase of the electronic conductivity in air with increasing Fe-content, meanwhile similar conductivity values were observed in reducing conditions, regardless of the Fe content [105]. Martínez-Coronado *et al.* investigated the $La_{0.5}Sr_{0.5}Co_{0.5}Ti_{0.5}O_{3-\delta}$ electrode for its implementation in SSOFCs, achieving conductivity values of 25 and 0.05 S cm^{-1} at 800 ºC in air and 5% H_2-Ar, respectively [106].

1.3.4. $Sr_2Fe_{1.5}Mo_{0.5}O_{6-\delta}$ and $PrBa(Fe,Mn)_2O_{5+\delta}$

Layered perovskites have attracted great attention due to their improved conducting properties in both air and H_2 atmospheres. One of the most promising layered perovskites is $Sr_2Fe_{1.5}Mo_{0.5}O_{6-\delta}$ (SFM), which shows high electrical conductivity in both air and H_2, 550 and 310 S cm^{-1}, respectively [65].

Several doping strategies have also been explored to enhance the electrochemical properties of the pristine SFM. Yang *et al.* partially substituted Fe by Co in $Sr_2Fe_{1.3}Co_{0.2}Mo_{0.5}O_{6-\delta}$-CGO, showing R_p values of 0.036 and 0.047 Ω cm^2 in air and H_2, respectively, at 850 ºC, as well as a MPD of 986 mW cm^{-2} at the same temperature [107]. The formation of Ni-Fe nanoparticles was observed in $Sr_{1.95}Fe_{1.4}Ni_{0.1}Mo_{0.5}O_{6-\delta}$ after reduction but the R_p values were similar to that of undoped SFM in other works [108].

$PrBaFe_2O_{5+\delta}$ and $PrBaFe_{1.6}Ni_{0.4}O_{5+\delta}$ compositions have also demonstrated good redox stability up to 800 ºC [109]. The exsolution of Ni-Fe nanoparticle in the Ni-doped composition rendered R_p values as low as 0.034 Ω cm^2 at 650 ºC in H_2. However, $PrBaMn_2O_{5+\delta}$ has shown the most promising results in terms of redox stability and tolerance to sulphur poisoning and coke resistance [110]. The R_p values were 0.25 and 0.46 Ω cm^2 in air and H_2, respectively, at 800 ºC, values that were further decreased after Pr_6O_{11} infiltration, *i.e.* 0.016 and 0.20 Ω cm^2, in air and H_2,

UNIVERSIDAD DE MÁLAGA

respectively, at 800 ºC. Table 1.4 shows the polarization resistance values in oxidizing and reducing conditions and the power densities of the most relevant SSOFCs.

Table 1.4. Electrochemical properties of the most important symmetrical electrodes reported in the literature [111]. R_p and power density values are given at 800 ºC. Temperature is included when data are not available at 800 ºC.

	Electrode	R_p Air (Ω cm^2)	R_p H_2 (Ω cm^2)	Power Density (mW cm^{-2})	Ref
Single perovskites	$La_{0.75}Sr_{0.25}Cr_{0.5}Mn_{0.5}O_{3-\delta}$	0.35 900º C	0.30 900 ºC	300 900 ºC (YSZ)	[80]
	$La_{0.75}Sr_{0.25}Cr_{0.5}Mn_{0.5}O_{3-\delta}$-YSZ	0.27 900 ºC	0.34 900 ºC	546 950 ºC (YSZ)	[81]
	$La_{0.7}Ca_{0.3}Cr_{0.8}Mn_{0.2}O_{3-\delta}$	-	0.12	230 (LSGM)	[88]
	$La_{0.65}Bi_{0.1}Sr_{0.25}Cr_{0.5}Mn_{0.5}O_{3-\delta}$-SDC	2.90	0.32	280 (LSGM)	[91]
	$La_{0.75}Sr_{0.25}Cr_{0.5}Mn_{0.3}Ni_{0.2}O_{3-\delta}$	1.6	1.1	-	[92]
	$SrFe_{0.75}Zr_{0.25}O_{3-\delta}$	0.1 700 ºC	0.3 700 ºC	-	[94]
	$Sr_{0.98}Fe_{0.8}Ti_{0.2}O_{3-\delta}$ -CGO	0.1	0.07	700 (LSGM)	[95]
	$SrFe_{0.8}W_{0.2}O_{3-\delta}$	0.08	0.20	931 950 ºC (LSGM)	[96]
	$La_{0.5}Sr_{0.5}Fe_{0.9}Mo_{0.1}O_{3-\delta}$	0.08 850 ºC	0.09 850 ºC	640 850 ºC (LSGM)	[97]
	$La_{0.5}Sr_{0.5}Fe_{0.9}W_{0.1}O_{3-\delta}$	0.08	0.16	617 (LSGM)	[112]
	$La_{0.7}Sr_{0.3}Fe_{0.7}Ga_{0.3}O_{3-\delta}$	-	-	489 (LSGM)	[98]
	$La_{0.6}Sr_{0.4}Fe_{0.9}Sc_{0.1}O_{3-\delta}$	0.015	0.29	560 (LSGM)	[99]
	$La_{0.3}Sr_{0.7}Fe_{0.9}Ti_{0.1}O_{3-\delta}$	0.022	0.15	847 (LSGM)	[100]
	$La_{0.6}Ca_{0.4}Fe_{0.8}Ni_{0.2}O_{3-\delta}$-CGO	0.24	0.13	300 (LSGM)	[102]
	$Sr_{0.8}Ce_{0.2}Fe_{0.95}Ru_{0.05}O_{3-\delta}$	-	-	846 (LSGM)	[101]
	$La_{0.5}Sr_{0.5}Co_{0.5}Ti_{0.5}O_{3-\delta}$	-	-	110 (LSGM)	[106]
	$Sr_2Fe_{1.5}Mo_{0.5}O_{6-\delta}$	0.24	0.27	650 850 ºC (LSGM)	[65]
Layered perovskites	$Sr_2Fe_{1.3}Co_{0.2}Mo_{0.5}O_{6-\delta}$-CGO	0.036 850 ºC	0.046 850 ºC	986 950 ºC (LSGM)	[107]
	$Sr_{1.95}Fe_{1.4}Ni_{0.1}Mo_{0.5}O_{6-\delta}$	0.08	0.11	500 (LSGM)	[108]
	$PrBaFe_2O_{5+\delta}$	1.45 650 ºC	0.075 650 ºC	70 650 ºC (SDC)	[109]
	$PrBaFe_{1.6}Ni_{0.4}O_{5+\delta}$	3.89 650 ºC	0.034 650 ºC	120 650 ºC (SDC)	[109]
	$PrBaMn_2O_{5+\delta}$	0.25	0.46	245 (LSGM)	[110]
	$La_{0.6}Sr_{1.4}MnO_{4\pm\delta}$	0.87	2.07	59 (LSGM)	[113]

After a short overview of the recent advances in symmetrical electrodes for solid oxide fuel cells, we can conclude that not only new doping strategies are needed

UNIVERSIDAD DE MÁLAGA

to improve the electrode performance, but also alternative fabrication methods to optimize the electrode microstructure.

The traditional screen-printing deposition, followed by sintering at high temperatures to ensure adequate adhesion between the cell components, is still widely used. However, alternative deposition methods, such as spray-pyrolysis, could be further explored to obtain nanostructured electrodes at low temperature with advanced architectures and improved electrochemical properties.

1.4. Strategies to improve the electrode performance

The electrode materials for SOFCs have been traditionally obtained by solid-state reaction synthesis, followed by a screen-printing deposition at high sintering temperatures [2]. However, the electrodes obtained from this method show relatively high grain size and low porosity due to the high sintering temperatures needed to ensure a good adhesion to the electrolyte. The rather low specific surface area of the electrodes deposited by this method limits the active sites for electrochemical reactions, lowering the electrochemical performance. In comparison, electrode materials with larger surface area show considerably better electrochemical properties due to the extended triple phase boundary (TPB) length.

Different strategies have been proposed to enhance the electrochemical performance by microstructural optimization: (a) the incorporation of a second phase with good ionic conductivity (such as doped-CeO_2 or Bi_2O_3) to increase the TPB length [46]; (b) the implementation of mixed ionic-electronic conductor (MIEC) electrodes to extend the TPB to the whole electrode surface [2]; (c) the infiltration of an active electrode into a porous electrolyte backbone [114]; (d) the preparation of nanostructured electrodes at reduced temperature; (e) the preparation of nanocomposite layers by advanced chemical and physical deposition techniques [115]; (f) the incorporation of active or barrier layers to improve the oxide-ion transport at the cathode/electrolyte interface [116] or (g) the exsolution of metal nanoparticles, such as Ni, Ru or Pd, to improve the efficiency for the fuel oxidation in the anode [117]. A schematic representation of these microstructural strategies can be found in the

UNIVERSIDAD DE MÁLAGA

summary (Figure 2). In this section, the most promising techniques mentioned above to enhance the electrode efficiency are discussed in detail.

1.4.1. Composite electrodes

One of the first strategies to enhance the electrode efficiency is the preparation of composite electrodes, which are usually formed by mixing an electronic conductor with an oxide-ion conductor. This electrode configuration enlarges the TPB length, highly improving the electrochemical performance, even for highly efficient electrode materials. *i.e.* 1.20 Ω cm^2 for LSCF and 0.27 Ω cm^2 for LSCF-CGO (40:60 wt.%) at 600 ºC [118].

The composite electrodes not only exhibit better electrochemical properties but also lower the thermal expansion coefficients (TECs). It has to be noted that cell delamination, attributed to the TEC mismatch, is one of the most serious problems for cell degradation during thermal cycles [82]. For this reason, it is recommendable to prepare electrode materials with similar TEC values to those of the most common electrolytes, such as YSZ, CGO and LSGM, $10 \cdot 10^{-6}$, $12.5 \cdot 10^{-6}$ and $10.4 \cdot 10^{-6}$ K^{-1}, respectively [119].

The preparation of composite powders in one step by co-synthesis has been successfully used to obtain different electrodes, such as LSM-ESB, $Sm_{0.5}Sr_{0.5}CoO_{3-\delta}$-$Ce_{0.9}Sm_{0.1}O_{1.95}$ (SSC-SDC), LSCF-CGO or BSCF-CGO [115,120–122]. One of the main advantages of nanocomposite electrodes is the inhibition of the grain growth due to the nanoscale contact between two different materials. The intimate mixture between two phases with different electrical properties induces a higher concentration of active sites for electrochemical reactions. These nanocomposite electrodes rendered remarkable results when compared to the traditional composite electrodes obtained by physically mixing powders. For instance, BSCF-CGO nanocomposite cathode rendered a MPD of 2 W cm^{-2} at 550 ºC in H_2, with almost negligible degradation for 300 h under a current density of 1 A cm^{-2} [120].

However, these materials have to be screen-printed onto the electrolyte and then calcined at relatively high temperatures (T ≥ 1000 ºC) to achieve adequate

UNIVERSIDAD DE MÁLAGA

adhesion to the electrolyte. Such thermal treatment induces a large grain growth, lowering the electrocatalytic performance [123,124].

1.4.2. Nanocomposite electrodes by spray-pyrolysis

The grain growth could be limited by directly depositing the nanocomposite electrodes onto the electrolyte surface. On this way, spray-pyrolysis deposition has demonstrated to be a highly versatile and low-cost technique to obtain nanostructured electrodes at intermediate temperatures [125]. The first attempt to synthesize a nanocomposite electrode by spray-pyrolysis deposition was made in 2005 by Princivalle *et al.,* successfully obtaining LSM-YSZ nanocomposite films from a single precursor solution [126]. Later on, LSM-CGO nanocomposite cathodes were prepared by dos Santos-Gómez *et al* [127]. The LSM-CGO nanocomposite exhibited a grain size of only 15 nm compared to 50 nm for the blank LSM cathode. More interestingly, a Ni-YSZ/YSZ/LSM-CGO single cell with the nanocomposite cathode showed an MPD of 1.4 W cm^{-2} at 800 ºC compared to 0.8 W cm^{2} for the analogous cell with the screen-printed cathode (Figure 1.12) [127].

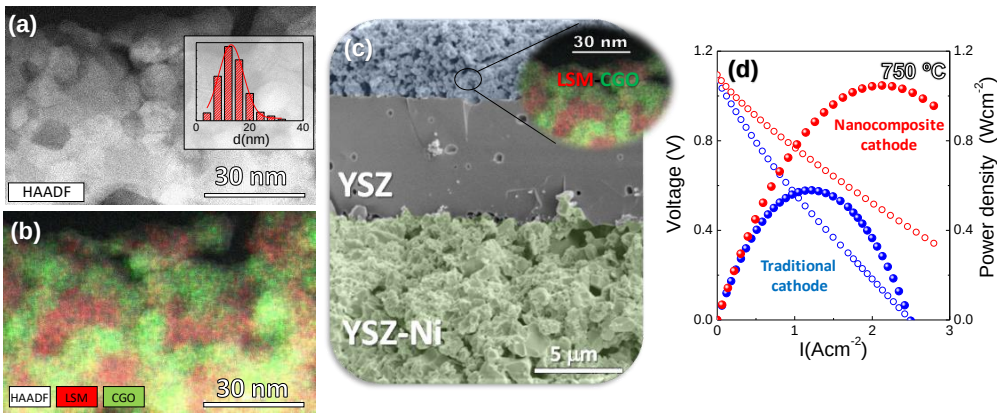

Figure 1.12. (a) HAADF-STEM image and (b) EDS analysis of LSM-CGO nanocomposite deposited by spray-pyrolysis. (c) SEM image of the Ni-YSZ/YSZ/LSM-CGO single cell and (d) I-V-P curves at 750 ºC. Reprinted with permission, Elsevier [127].

Sar *et al.* prepared LSCF-CGO by electrostatic spray deposition with coral and columnar microstructures, depending on the deposition temperature [128]. In

UNIVERSIDAD DE MÁLAGA

another work, dos Santos-Gómez *et al.* studied the LSCF-CGO nanocomposite by spray-pyrolysis with different LSCF contents. The R_p values decreased from 0.29 Ω cm^2 for the pristine LSCF to 0.16 Ω cm^2 for the 50 wt. % LSCF-CGO nanocomposite at 600 ºC [129].

Despite the fact that excellent results have been observed for nanocomposite cathodes, there are not related studies about their application as anode materials or symmetrical electrodes (SSOFC).

1.4.3. Infiltration method

The infiltration method is a highly promising strategy to improve the electrode performance. It consists in the impregnation of a cation precursor solution into a porous backbone to obtain a partial or complete coating of an electrode with good electrocatalytic activity [114,130]. After the infiltration process, a thermal treatment is used to decompose the precursors, obtaining discrete particles (Figure 1.13a) or a continuous film on the backbone surface (Figure 1.13b).

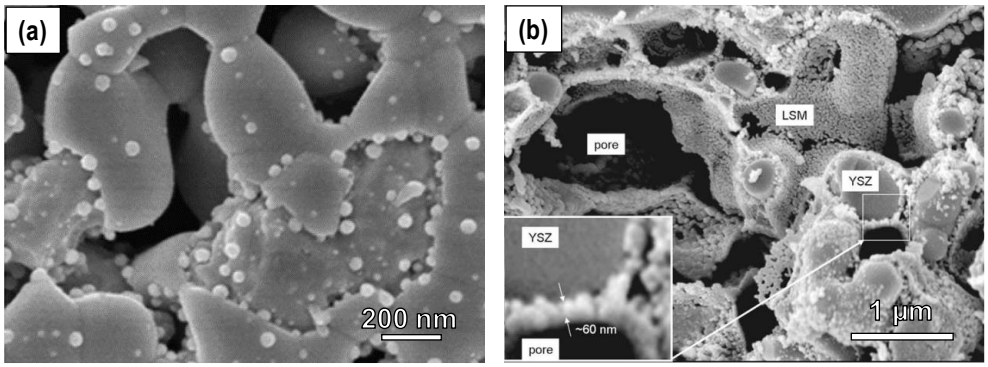

Figure 1.13. (a) SEM image of LSCM-YSZ composite impregnated with Pd. Reprinted with permission, Elsevier [131]. (b) SEM image of a YSZ backbone infiltrated with LSM. Reprinted with permission, Electrochemical Society [132].

Typically, a MIEC is infiltrated into an electrolyte backbone in several infiltration steps to ensure percolation and good electronic conductivity, maintaining the inner porous structure of the backbone. This method leads to new functional materials with advanced microstructure at a lower preparation temperature than

UNIVERSIDAD DE MÁLAGA

conventional screen-printing deposition, as well as relatively high stability over time, *i.e.* LSM-SSZ prepared by infiltration showed almost negligible degradation at 650 ºC under 150 mA cm^{-2} for 500 h [133].

Despite the fact that excellent results have been achieved for infiltrated electrodes, some drawbacks still hinder their industrial implementation. One of the main problems is the reproducibility and homogeneity of the infiltrated electrodes, because this process is carried out manually. Furthermore, multiple infiltration/calcination steps are necessary to obtain a good amount of infiltrated material, becoming a time-consuming process. In order to solve this problem, high concentrated solutions are used. In addition, complexing agents, such as ethylenediaminetetraacetic acid (EDTA) or citric acid, are required to stabilize the cation solution. In this context, several studies revealed that a high concentration of complexing agent could provoke delamination in the electrolyte backbone due to severe decomposition during the thermal treatments [134].

1.4.3.1. Infiltration method by spray-pyrolysis

Spray-pyrolysis deposition method has been recently used to prepare highly efficient nanostructured electrodes in only one deposition step with high reproducibility over large areas. In this way, spray-pyrolysis is one of the best alternatives to the classical infiltration method, in which a diluted precursor solution is sprayed into a porous backbone layer [125].

The first attempts to use spray-pyrolysis as an alternative method to the classical infiltration were made by dos Santos-Gómez *et al.* in 2015 [61]. An LSM cathode was infiltrated into different porous backbones of YSZ, CGO and BYO, which were previously deposited onto YSZ electrolytes. The microstructural study revealed a double-layer electrode, composed of a backbone homogenously coated by LSM particles and a ~ 500 nm top layer of LSM, which acted as a current collector. The LSM content infiltrated into the electrolyte backbone and the thickness of the top layer were tailored by changing the deposition conditions, *i.e.* deposition temperature and time. All infiltrated electrodes showed low R_p values when compared to those observed for the screen-printed LSM cathode (1.4 Ω cm^2 at 650 ºC), achieving the

UNIVERSIDAD DE MÁLAGA

best results for the LSM-BYO configuration, 0.06 Ω cm^2 at the same temperature [61]. This alternative preparation method was also used with different single perovskite-type electrodes, such as $La_{0.6}Sr_{0.4}Co_{1-x}Fe_xO_{3-\delta}$ (x= 0, 0.2, 0.8 and 1) and $BaCo_{0.4}Fe_{0.4}Zr_{0.1}Y_{0.1}O_{3-\delta}$ [135,136].

One of the best results was obtained for $PrBaCo_2O_{5+\delta}$ (PBC) deposited onto a CGO backbone (Figure 1.14a,b), showing R_p values as low as 0.027 Ω cm^2 at 600 ºC, one order of magnitude lower than those observed for the screen-printed electrode, 0.22 Ω cm^2 [137]. Interestingly, the spray-pyrolysis electrodes showed a lower degradation rate of 2 μΩ cm^{-2} h^{-1} compared to the screen-printed electrodes (65 μΩ cm^{-2} h^{-1}), which was attributed to the lower preparation temperature and lower chemical reactivity between the cell components (Figure 1.14c). A Ni-CGO/CGO/PBC-CGO anode-supported cell rendered a stable MPD of 0.95 W cm^{-2} at 600 ºC (Figure 1.14d).

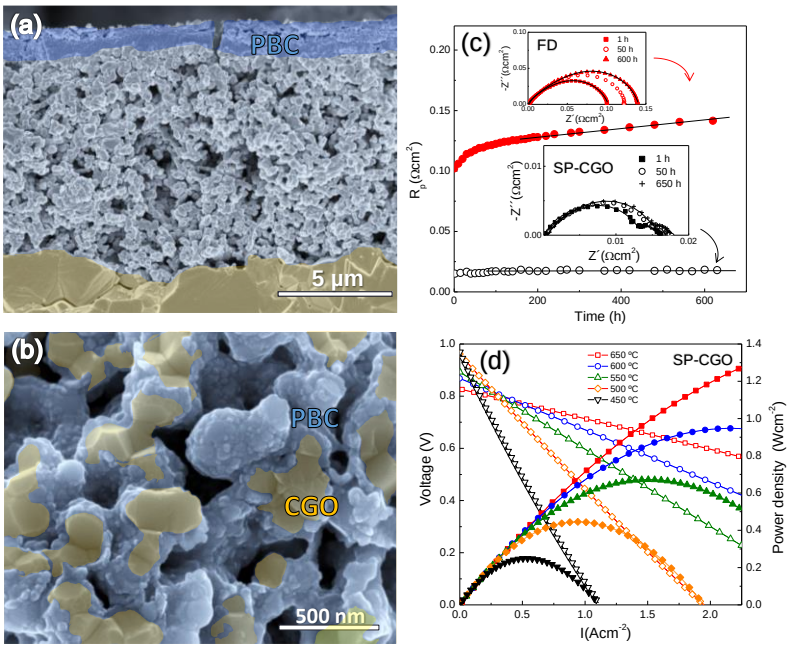

Figure 1.14. (a,b) SEM images of PBC electrode deposited by spray-pyrolysis onto a CGO backbone at different magnifications. (c) Variation of the R_p over time for the PBC-CGO deposited by screen printing (FD) and spray-pyrolysis (SP-CGO) and (d) I-V-P curves of the spray-pyrolysis electrodes at different temperatures. Reprinted with permission. Royal Society of Chemistry [137].

UNIVERSIDAD DE MÁLAGA

A similar approach was also proposed by infiltrating a protective CGO coating into the LSCF cathode to avoid the segregation of Sr-based compounds during long-term operation [57]. The coated electrodes not only showed a lower degradation rate over time but also better electrochemical activity due to the extension of the TPB sites. The MPD of the anode-supported cell with the coated electrode, 500 mW cm^{-2}, was slightly higher than that observed for the unprotected cathode, 390 mW cm^{-2} at 600 ºC.

1.4.4. Active layers

The incorporation of active and barrier layers at the electrode/electrolyte interface has demonstrated to lower the activation energy of the oxide-ion transport at this region, greatly boosting the electrochemical properties of several air electrodes [116,138]. In order to obtain these layers, different methods have been employed, such as screen-printing, spin coating, spray-pyrolysis, sputtering or pulsed laser deposition [125,139–142].

Traditionally, barrier layers such as SDC or CGO have been deposited by the screen-printing method to avoid the reaction between YSZ electrolyte and Co-based electrodes [143]. The main disadvantage of the screen-printed method is the relatively high porosity and high sintering temperature required (~1200 ºC) to ensure a good adhesion to the electrolyte. Furthermore, recent studies observed SrO diffusion from the LSCF phase through porous CGO barrier layers, inducing the formation of $SrZrO_3$ at the electrode/electrolyte interface [144,145].

Wachsman *et al.* revealed that Bi_2O_3-based functional layers, such as $Bi_{1.6}Er_{0.4}O_3$ (ESB) or $Bi_{1.5}Y_{0.5}O_3$ (BYO), highly enhanced the electrochemical performance of SOFC cathodes due to their higher oxide-ion conductivity when compared to doped-CeO_2 or YSZ electrolytes [146]. However, these layers were obtained by screen-printing or dip-coating and then calcined at high sintering temperatures, leading to partial evaporation of Bismuth [147]. For this reason, alternative deposition methods at lower fabrication temperatures are needed to obtain protective and functional layers. Among all the deposition methods described above, spray-pyrolysis and pulsed laser deposition have rendered the most promising results.

UNIVERSIDAD DE MÁLAGA

1.4.4.1. Active layers deposited by spray-pyrolysis

Spray-pyrolysis has been used to obtain protective CeO_2-based layers to avoid the reaction between LSCF and YSZ [148,149]. For instance, Molin *et al.* prepared dense CGO layers with different thicknesses (300, 700 and 1500 nm) to test the influence of the thickness and porosity in the cell degradation [148]. The NiO-YSZ/YSZ/CGO/LSCF cell with a 700 nm thick CGO film rendered the best performance, ~1 W cm^{-2} at 750 °C, as well as the lowest ohmic and polarization resistances and stability over time. The authors observed that porous CGO barrier layers or dense layers with low thicknesses (300 nm) do not prevent cation interdiffusion between the cell layers, whereas higher ohmic resistance was induced with thicker barrier layers (1500 nm). dos Santos-Gómez *et al.* also prepared by spray-pyrolysis dense CGO layers between the porous LSCF cathode and YSZ. The authors concluded that a low sintering temperature is the key to avoid the formation of $SrZrO_3$ at the LSCF/YSZ interface [149].

Additionally, Zapata-Ramírez *et al.* tested CGO, $Ce_{0.8}Pr_{0.2}O_{1.9}$ (CPO) and $SrFe_{0.9}Mo_{0.1}O_{3-\delta}$ active layers to improve the electrochemical properties of a $SrFe_{0.9}Mo_{0.1}O_{3-\delta}$-CGO cathode. Among them, the CPO active layer rendered the best results, decreasing the R_p values in air from 0.67 to 0.2 Ω cm^2 at 650 ºC. In this case, the mixed ionic-electronic conductivity of the CPO interlayer extended the surface paths for ORR [150]. Sharma *et al.* prepared Ln_2NiO_4 (Ln= La, Pr) porous functional layers, lowering the R_p values from 3.33 to 0.08 Ω cm^2 at 600 ºC for the electrodes without and with active layer, respectively [151]. Later on, the same authors proposed a Pr_6O_{11} porous functional layer topped with LSCF, which rendered one of the lowest R_p values reported to date, 0.02 Ω cm^2 at 600 ºC [152].

Recently, Kamecki *et al.* studied different active layers, LSC, SSC, LSCF and Pr_6O_{11} to enhance the electrochemical properties of LSCF cathode [153]. The best results were found for the LSC active layer with a R_p of 0.107 Ω cm^2 at 600 ºC compared to 0.5 Ω cm^2 without an active layer. A Ni-CGO anode supported cell with and without LSC functional layer reached MPD values of 1.22 and 0.74 W cm^{-2} at 600 ºC, respectively (Figure 1.15) [153].

UNIVERSIDAD DE MÁLAGA

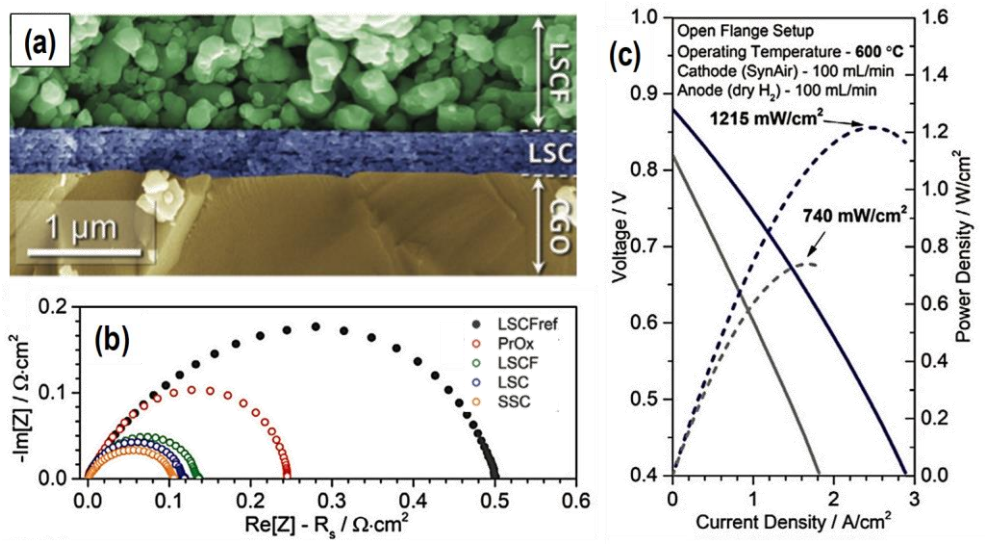

Figure 1.15. (a) Cross-sectional SEM image of LSC active layer deposited by spray-pyrolysis onto CGO, (b) impedance spectra of the different cell configurations at 600 ºC in air and (c) I-V-P curves of the Ni-CGO supported cell without and with LSC active layer. Reprinted with permission, Willey [153].

Most of the research has been focused on active layers composed of a single material, which can show a considerable increase of the grain size during long-term operation at high temperatures. In this sense, nanocomposite active layers are expected to exhibit improved properties due to the inhibition of the grain growth during the sintering process of the electrodes at high temperatures.

1.4.4.2. Active layers deposited by pulsed laser deposition

Pulsed laser deposition (PLD) has recently received considerable attention to obtain active layers for SOFCs due to its better control of the film quality, thickness, morphology and stoichiometry. The most common cathode materials, such as LSM, LSC, LSCF and BSCF have been successfully obtained by PLD as dense layers [142]. Numerous studies have confirmed the great benefits of implementing an active layer deposited by PLD. For instance, Su *et al.* incorporated a LSC layer between the CGO electrolyte and the screen-printed LSC, showing this configuration higher MPD than the cell without active layer, 0.27 and 0.16 W cm^{-2} at 650 ºC, respectively [154]. Similar results were observed for a SSC active layer [155]. Haile *et. col.* incorporated a 100

UNIVERSIDAD DE MÁLAGA

nm $PrBa_{0.5}Sr_{0.5}Co_{1.5}Fe_{0.5}O_{5+\delta}$ layer between a $BaZr_{0.4}Ce_{0.4}Y_{0.1}Yb_{0.1}O_3$ electrolyte and the screen-printed electrode, considerably reducing the ohmic losses of the cell due to the improved electrolyte-electrode contact, resulting in a performance increase of ~30% in both fuel cell and electrolysis modes [156,157]. Additionally, ceria-based buffer layers deposited by PLD have been successfully implemented to avoid the typical reaction between Co-based electrodes and YSZ electrolytes [158].

Recently, a new strategy based on Vertically Aligned Nanostructures (VAN) obtained by PLD has been proposed, in which two immiscible phases are simultaneously grown on a given substrate, obtaining a columnar microstructure with large vertical interfaces [15,159]. The unique nanostructure ordering of a VAN has demonstrated to promote excellent results in the field of magnetic materials, ferroelectrics, ionic conductors and fuel cells [160–162]. In a VAN structure, the spontaneous growth of nanocolumns of two different materials is influenced by the in-plane strain, the substrate orientation and the vertical interfacial strain due to the simultaneous growth of the nanodomains, leading to an out-of-plane coherence [159]. MacManus-Driscoll *et col.* highly boosted the ionic conductivity of Sm-doped CeO_2 by one order of magnitude in an SDC-STO VAN with vertical interfaces when compared to plain SDC films (Figure 1.16). The nanopillar structure with vertical strain induced a fast ion conduction through the interface and the SDC nanocolumns of 10 nm width, findings that were confirmed by Scanning Probe Microscopy (SPM) mappings [161].

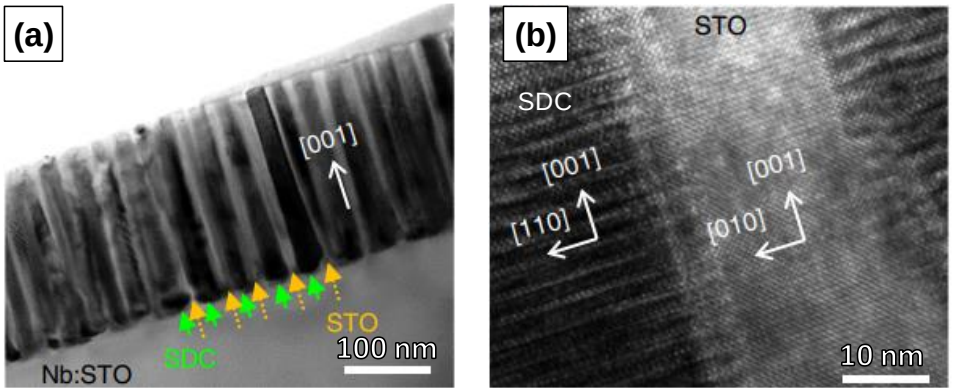

Figure 1.16. (a) Cross-sectional HRTEM image of the SDC-STO VAN film with a nanocheckerboard structure and (b) HRTEM image showing the SDC-STO vertical interfaces and the epitaxial growth. Reprinted with permission, Springer Nature [161].

UNIVERSIDAD DE MÁLAGA

Different VANs have been tested for their implementation in SOFC, such as LSM-SDC [163], LSC-CGO [164], PBC-CGO [165] and LSC-$(La_{0.5}Sr_{0.5})_2CoO_4$ [166]. All of them reported enhanced electrochemical properties when compared to the cells without active layers. For instance, in 2021, Develos-Bagarinao *et al.* implemented a LSCF-CGO VAN active layer between a porous LSC cathode and a YSZ/CGO electrolyte in an anode-supported cell [167] (Figure 1.17). The polarization resistance of the cell with a LSCF-CGO active layer decreased by ~ 50% when compared to the cell with LSCF active layer, 0.036 and 0.07 Ω cm^2 at 600 ºC, respectively.

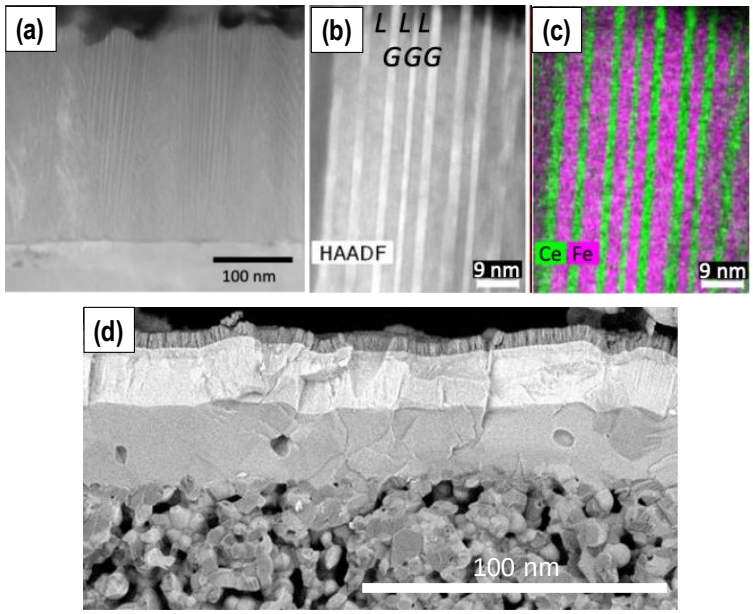

Figure 1.17. (a,b) HAADF-STEM image of LSCF-CGO nanocomposite active layer at different magnifications, (c) EDS analysis and (d) SEM image of the Ni-YSZ/YSZ/CGO/LSFC-CGO/LSC single cell. Reprinted with permission, Springer Nature [167].

Recently, a redox stable $La_{0.75}Sr_{0.25}Cr_{0.5}Mn_{0.5}O_{3-\delta}$-$Ce_{0.8}Sm_{0.2}O_{1.9}$ (LSCM-SDC) VAN active layer was reported by Sirvent *et al.*, working simultaneously in both oxidizing and reducing atmospheres. The R_p values of the VAN active layer were 27.8 and 14.7 Ω cm^2 at 750 ºC in air and H_2, respectively, outperforming the R_p of the single LSCM, 264 and 40 Ω cm^2 in air and H_2 at the same temperature [168].

UNIVERSIDAD DE MÁLAGA

These promising results confirmed the influence of implementing nanocomposite active layers at the electrode/electrolyte interface for air and fuel electrodes.

1.4.4.3. Ni exsolution in thin films deposited by PLD

One of the most promising approaches to enhance the performance of fuel electrodes is the incorporation of active metals into the crystal structure of the perovskite, *i.e.* Ni, Ru or Pd, which are exsolved into metal nanoparticles on the electrode surface after a reduction treatment [117,169]. Among them, Ni incorporation has demonstrated excellent results in hydrogen and hydrocarbon fuelled SOFC due to its lower cost compared to other noble metals. In recent years, numerous studies on highly efficient SOFC electrodes containing Ni exsolved nanoparticles have been reported in the literature, in which the nature of the Ni exsolution process in thin films deposited by PLD has attracted great attention [117,169–171].

In a recent report, the influence of the surface orientation of the substrate in the exsolution of Ni-nanoparticles was investigated by depositing $La_{0.2}Sr_{0.7}Ti_{0.9}Ni_{0.1}O_{3-\delta}$ films onto STO substrates with (001), (110) and (111) orientations [172]. The authors observed that the interfacial energies play a critical role in the morphology and nucleation of the Ni-exsolved nanoparticles, showing (001) and (111) oriented samples larger particle size and lower particle density when compared to (110)-facet.

In another study, the influence of the in-plain strain on the exsolution of Ni-nanoparticles in $La_{0.2}Sr_{0.7}Ti_{0.9}Ni_{0.1}O_{3-\delta}$ was explored by depositing the film onto different substrates: $(LaAlO_3)_{0.3}(Sr_2TaAlO_6)_{0.7}$ (LSAT) (001), STO (001), $DyScO_3$ (DSO) (001) and $GdScO_3$ (GSO) (110), with a lattice misfit strain (*f*) for the pristine films of −1.5, −0.5, +0.4, and +1.2%, respectively [173] (Figure 1.18). The results revealed that the compressive strained films (negative *f* values) generated a considerably larger number of exsolved Ni nanoparticles when compared to the tensile strained films (positive *f* values), obtaining an average Ni-nanoparticle size as low as 5 nm for the films deposited onto LSAT substrate.

UNIVERSIDAD DE MÁLAGA

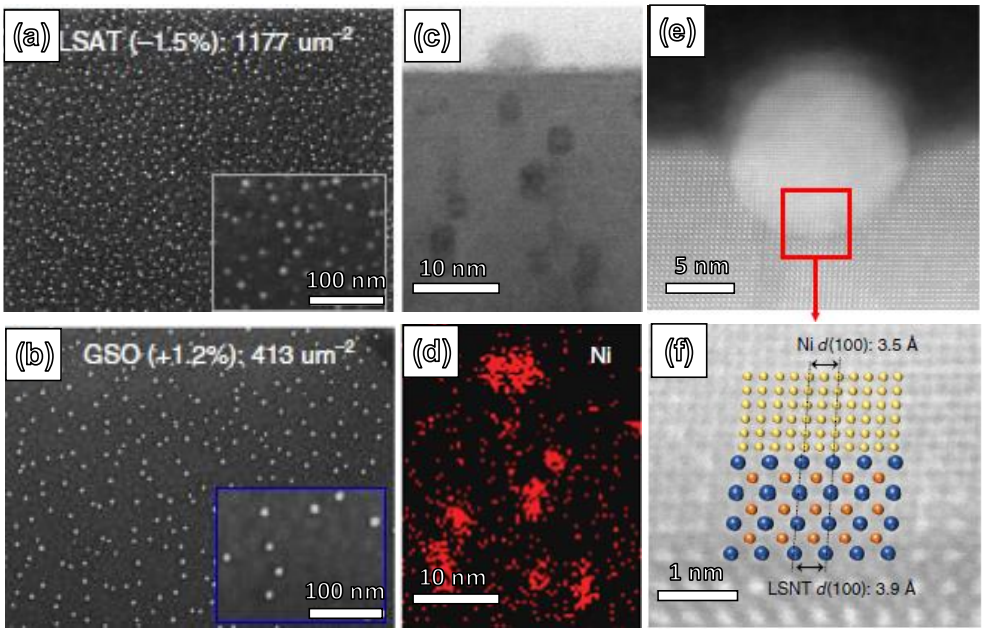

Figure 1.18. (a,b) SEM image of $La_{0.2}Sr_{0.7}Ti_{0.9}Ni_{0.1}O_{3-\delta}$ deposited by PLD onto LSAT and GSO (001) and reduced at 550 ºC for 80 h in pure H_2. (c) HAADF-STEM image and (d) EDS mapping of the reduced film on LSAT. (e,f) Bright-field STEM images at different magnifications of a Ni exsolved nanoparticle. Reprinted with permission, Springer Nature [173].

However, the exsolution of metal nanoparticles has only been studied in epitaxial films of single compounds. Since VANs have rendered excellent results for multiple energy applications, the study of the Ni exsolution process for the first time in films with columnar microstructure is very promising and challenging.

References

1. Qadir, S.A.; Al-Motairi, H.; Tahir, F.; Al-Fagih, L. Incentives and Strategies for Financing the Renewable Energy Transition: A Review. *Energy Reports* **2021**, *7*, 3590–3606, doi:10.1016/j.egyr.2021.06.041.
2. Mahato, N.; Banerjee, A.; Gupta, A.; Omar, S.; Balani, K. Progress in Material Selection for Solid Oxide Fuel Cell Technology: A Review. *Prog. Mater. Sci.* **2015**, *72*, 141–337, doi:10.1016/j.pmatsci.2015.01.001.
3. Https://Cinea.Ec.Europa.Eu/Programmes/Horizon-Europe/Energy-Use-Horizon-Europe/Horizon-2020-Energy-Efficiency_en.
4. Williams, M.C.; Vora, S.D.; Jesionowski, G. Worldwide Status of Solid Oxide Fuel Cell Technology. *ECS Trans.* **2020**, *96*, 1–10, doi:10.1149/09601.0001ecst.

UNIVERSIDAD DE MÁLAGA

5. Vora, S.D.; Lundberg, W.L.; Pierre, J.F. Overview of U.S. Department of Energy Office of Fossil Energy's Solid Oxide Fuel Cell Program. *ECS Meet. Abstr.* **2017**, *MA2017-03*, 1–1, doi:10.1149/ma2017-03/1/1.
6. Https://Www.Nedo.Go.Jp/English/News/AA5en_100255.Html.
7. Mekhilef, S.; Saidur, R.; Safari, A. Comparative Study of Different Fuel Cell Technologies. *Renew. Sustain. Energy Rev.* **2012**, *16*, 981–989, doi:10.1016/j.rser.2011.09.020.
8. Peighambardoust, S.J.; Rowshanzamir, S.; Amjadi, M. *Review of the Proton Exchange Membranes for Fuel Cell Applications*; Elsevier Ltd, **2010**; Vol. 35; ISBN 2177491223.
9. Chandan, A.; Hattenberger, M.; El-Kharouf, A.; Du, S.; Dhir, A.; Self, V.; Pollet, B.G.; Ingram, A.; Bujalski, W. High Temperature (HT) Polymer Electrolyte Membrane Fuel Cells (PEMFC)-A Review. *J. Power Sources* **2013**, *231*, 264–278, doi:10.1016/j.jpowsour.2012.11.126.
10. Zvonareva, I.; Fu, X.Z.; Medvedev, D.; Shao, Z. Electrochemistry and Energy Conversion Features of Protonic Ceramic Cells with Mixed Ionic-Electronic Electrolytes. *Energy Environ. Sci.* **2022**, *15*, 439–465, doi:10.1039/d1ee03109k.
11. Minh, N.Q.; Meng, Y.S. Future Energy, Fuel Cells, and Solid-Oxide Fuel-Cell Technology. *MRS Bulletin* **2019**, *44*, 682–683. doi: 10.1557/mrs.2019.209
12. Zhou, L.; Mason, J.H.; Li, W.; Liu, X. Comprehensive Review of Chromium Deposition and Poisoning of Solid Oxide Fuel Cells (SOFCs) Cathode Materials. *Renew. Sustain. Energy Rev.* **2020**, *134*, 110320, doi:10.1016/j.rser.2020.110320.
13. Wu, J.; Liu, X. Recent Development of SOFC Metallic Interconnect. *J. Mater. Sci. Technol.* **2010**, *26*, 293–305, doi:10.1016/S1005-0302(10)60049-7.
14. Lankin, M.; Du, Y.; Finnerty, C. A Review of the Implications of Silica in Solid Oxide Fuel Cells. *J. Fuel Cell Sci. Technol.* **2011**, *8*, 1–7, doi:10.1115/1.4003980.
15. Wang, X.; Wang, T.; Borovilas, J.; He, X.; Du, S.; Yang, Y. Vertically-Aligned Nanostructures for Electrochemical Energy Storage. *Nano Res.* **2019**, *12*, 2002–2017, doi:10.1007/s12274-019-2392-x.
16. Wang, F.; Kishimoto, H.; Ishiyama, T.; Develos-Bagarinao, K.; Yamaji, K.; Horita, T.; Yokokawa, H. A Review of Sulfur Poisoning of Solid Oxide Fuel Cell Cathode Materials for Solid Oxide Fuel Cells. *J. Power Sources* **2020**, *478*, 228763. doi 10.1016/j.jpowsour.2020.228763.
17. Hussain, A.M.; Huang, Y.L.; Pan, K.J.; Robinson, I.A.; Wang, X.; Wachsman, E.D. A Redox-Robust Ceramic Anode-Supported Low-Temperature Solid Oxide Fuel Cell. *ACS Appl. Mater. Interfaces* **2020**, *12*, 18526–18532, doi:10.1021/acsami.0c01611.
18. Hussain, S.; Yangping, L. Review of Solid Oxide Fuel Cell Materials: Cathode, Anode, and Electrolyte. *Energy Transitions* **2020**, *4*, 113–126, doi:10.1007/s41825-020-00029-8.
19. Minh, N.Q. Ceramics Fuels Cells. *J. Am. Ceram. Soc.* **1995**, *76*, 563–588. doi**:**10.1111/j.1151-2916.1993.tb03645.x
20. Lee, D.; Lee, I.; Jeon, Y.; Song, R. Characterization of Scandia Stabilized Zirconia Prepared by Glycine Nitrate Process and Its Performance as the Electrolyte for IT-SOFC. *Solid State Ionics* **2005**, *176*, 1021–1025, doi:10.1016/j.ssi.2005.01.004.
21. Shao, Z.; Haile, S.M. A High-Performance Cathode for the next Generation of Solid-Oxide Fuel Cells. *Nature* **2003**, *3*, 170-173, doi:10.1038/nature02863.
22. Tai, L.W.; Nasrallah, M.M.; Anderson, H.U.; Sparlin, D.M.; Sehlin, S.R. Structure and Electrical Properties of $La_{1-X}Sr_xCo_{1-Y}Fe_yO_3$. Part 2. The System $La_{1-X}Sr_xCo_{0.2}Fe_{0.8}O_3$. *Solid State Ionics* **1995**, *76*, 273–283, doi:10.1016/0167-2738(94)00245-N.

UNIVERSIDAD DE MÁLAGA

23. Esquirol, A.; Brandon, N.P.; Kilner, J.A.; Mogensen, M. Electrochemical Characterization of $La_{0.6}Sr_{0.4}Co_{0.2}Fe_{0.8}O_3$ Cathodes for Intermediate-Temperature SOFCs. *J. Electrochem. Soc.* **2004**, *151*, A1847, doi:10.1149/1.1799391.
24. Jaiswal, N.; Tanwar, K.; Suman, R.; Kumar, D.; Uppadhya, S.; Parkash, O. A Brief Review on Ceria Based Solid Electrolytes for Solid Oxide Fuel Cells. *J. Alloys Compd.* **2019**, *781*, 984–1005, doi:10.1016/j.jallcom.2018.12.015.
25. Steele, B.C.H. Appraisal of $Ce_{1-Y}Gd_yO_{2-y/2}$ Electrolytes for IT-SOFC Operation at 500 °C. *Solid State Ionics* **2000**, *129*, 95–110, doi:10.1016/S0167-2738(99)00319-7.
26. Zhu, Z.; Liu, B.; Shen, J.; Lou, Y.; Ji, Y. $La_2Ce_2O_7$: A Promising Proton Ceramic Conductor in Hydrogen Economy. *J. Alloys Compd.* **2016**, *659*, 232–239, doi:10.1016/j.jallcom.2015.11.041.
27. Huang, K.; Tichy, R.; Goodenough, J.B. Superior Perovskite Oxide-Ion Conductor. *J. Am. Ceram. Soc.* **1998**, *85*, 2581–2585. doi: 10.1111/j.1151-2916.1998.tb02662.x
28. Pelosato, R.; Cristiani, C.; Dotelli, G.; Latorrata, S.; Ruffo, R.; Zampori, L. Co-Precipitation in Aqueous Medium of $La_{0.8}Sr_{0.2}Ga_{0.8}Mg_{0.2}O_{3-\delta}$ via Inorganic Precursors. *J. Power Sources* **2010**, *195*, 8116–8123, doi:10.1016/j.jpowsour.2010.07.046.
29. Marrero-López, D.; Ruiz-Morales, J.C.; Peña-Martínez, J.; Martín-Sedeño, M.C.; Ramos-Barrado, J.R. Influence of Phase Segregation on the Bulk and Grain Boundary Conductivity of LSGM Electrolytes. *Solid State Ionics* **2011**, *186*, 44–52, doi:10.1016/j.ssi.2011.01.015.
30. Gao, Z.; Miller, E.C.; Barnett, S.A. A High Power Density Intermediate-Temperature Solid Oxide Fuel Cell with Thin $(La_{0.9}Sr_{0.1})_{0.98}(Ga_{0.8}Mg_{0.2})O_{3-\delta}$ Electrolyte and Nano-Scale Anode. *Adv. Funct. Mater.* **2014**, *24*, 5703–5709, doi:10.1002/adfm.201400295.
31. Marrero-López, D.; Ruiz-Morales, J.C.; Núñez, P.; Abrantes, J.C.C.; Frade, J.R. Synthesis and Characterization of $La_2Mo_2O_9$ Obtained from Freeze-Dried Precursors. *J. Solid State Chem.* **2004**, *177*, 2378–2386, doi:10.1016/j.jssc.2004.03.020.
32. Fergus, J.W. Electrolytes for Solid Oxide Fuel Cells. *J. Power Sources* **2006**, *162*, 30–40, doi:10.1016/j.jpowsour.2006.06.062.
33. Jiang, N.; Wachsman, E.D. Structural Stability and Conductivity of Phase-Stabilized Cubic Bismuth Oxides. *J. Am. Ceram. Soc.* **1999**, *82*, 3057–3064, doi:10.1111/j.1151-2916.1999.tb02202.x.
34. Jung, D.W.; Duncan, K.L.; Wachsman, E.D. Effect of Total Dopant Concentration and Dopant Ratio on Conductivity of $(DyO_{1.5})_x$-$(WO_3)_y$-$(BiO_{1.5})_{1-x-Y}$. *Acta Mater.* **2010**, *58*, 355–363, doi:10.1016/j.actamat.2009.08.072.
35. Yaremchenko, A.A.; Kharton, V. V.; Naumovich, E.N.; Tonoyan, A.A. Stability of δ-Bi_2O_3-Based Solid Electrolytes. *Mater. Res. Bull.* **2000**, *35*, 515–520, doi:10.1016/S0025-5408(00)00237-3.
36. Gao, Z.; Mogni, L. V.; Miller, E.C.; Railsback, J.G.; Barnett, S.A. A Perspective on Low-Temperature Solid Oxide Fuel Cells. *Energy Environ. Sci.* **2016**, *9*, 1602–1644, doi:10.1039/c5ee03858h.
37. Rashid, N.L.R.M.; Samat, A.A.; Jais, A.A.; Somalu, M.R.; Muchtar, A.; Baharuddin, N.A.; Wan Isahak, W.N.R. Review on Zirconate-Cerate-Based Electrolytes for Proton-Conducting Solid Oxide Fuel Cell. *Ceram. Int.* **2019**, *45*, 6605–6615, doi:10.1016/j.ceramint.2019.01.045.
38. Singh, K.; Kannan, R.; Thangadurai, V. Perspective of Perovskite-Type Oxides for Proton Conducting Solid Oxide Fuel Cells. *Solid State Ionics* **2019**, *339*, 114951, doi:10.1016/j.ssi.2019.04.014.

UNIVERSIDAD DE MÁLAGA

39. Yang, L.; Wang, S.; Blinn, K.; Liu, M.; Liu, Z.; Cheng, Z.; Liu, M. Enhanced Sulfur and Coking Tolerance of a Mixed Ion Conductor for SOFCs: BCZYYb. *Science* **2009**, *326*, 126–129. doi: 10.1126/science.1174811

40. Fabbri, E.; Bi, L.; Pergolesi, D.; Traversa, E. Towards the next Generation of Solid Oxide Fuel Cells Operating below 600 °c with Chemically Stable Proton-Conducting Electrolytes. *Adv. Mater.* **2012**, *24*, 195–208, doi:10.1002/adma.201103102.

41. Pelosato, R.; Cristiani, C.; Dotelli, G.; Latorrata, S.; Ruffo, R.; Zampori, L. Co-Precipitation in Aqueous Medium of $La_{0.8}Sr_{0.2}Ga_{0.8}Mg_{0.2}O_{3-\delta}$ via Inorganic Precursors. *J. Power Sources* **2010**, *195*, 8116–8123, doi:10.1016/j.jpowsour.2010.07.046.

42. Porras-Vázquez, J.M.; Losilla, E.R.; León-Reina, L.; Marrero-López, D.; Aranda, M.A.G. Microstructure and Oxide Ion Conductivity in a Dense $La_{9.33}(SiO_4)_6O_2$ Oxy-Apatite. *J. Am. Ceram. Soc.* **2009**, *92*, 1062–1068, doi:10.1111/j.1551-2916.2009.03032.x.

43. Caldes, M.T.; Kravchyk, K. V; Benamira, M.; Besnard, N.; Gunes, V.; Bohnke, O.; Joubert, O. Metallic Nanoparticles and Proton Conductivity: Improving Proton Conductivity of $BaCe_{0.9}Y_{0.1}O_{3-\delta}$ Using a Catalytic Approach. *Chem Mater.* **2012**, 24, 4641-4646. doi: 10.1021/cm301685x.

44. Zamudio-García, J.; Porras-Vázquez, J.M.; Canales-Vázquez, J.; Cabeza, A.; Losilla, E.R.; Marrero-López, D. Relationship between the Structure and Transport Properties in the $Ce_{1-x}La_xO_{2-x/2}$ System. *Inorg. Chem.* **2019**, *58*, 9368–9377, doi:10.1021/acs.inorgchem.9b01104.

45. Paydar, S.; Shariat, M.H.; Javadpour, S. Investigation on Electrical Conductivity of LSM/YSZ8, LSM/$Ce_{0.84}Y_{0.16}O_{0.96}$ and LSM/$Ce_{0.42}Zr_{0.4}2Y_{0.16}O_{0.96}$ Composite Cathodes of SOFCs. *Int. J. Hydrogen Energy* **2016**, *41*, 23145–23155, doi:10.1016/j.ijhydene.2016.10.092.

46. Ji, Y.; Kilner, J.A.; Carolan, M.F. Electrical Properties and Oxygen Diffusion in Yttria-Stabilised Zirconia (YSZ)-$La_{0.8}Sr_{0.2}MnO_{3\pm\delta}$ (LSM) Composites. *Solid State Ionics* **2005**, *176*, 937–943, doi:10.1016/j.ssi.2004.11.019.

47. Chen, G.; Gao, Y.; Luo, Y.; Guo, R. Effect of A Site Deficiency of LSM Cathode on the Electrochemical Performance of SOFCs with Stabilized Zirconia Electrolyte. *Ceram. Int.* **2017**, *43*, 1304–1309, doi:10.1016/j.ceramint.2016.10.082.

48. Jiang, S.P. *Development of Lanthanum Strontium Manganite Perovskite Cathode Materials of Solid Oxide Fuel Cells: A Review*; 2008; Vol. 43; ISBN 1085300829666.

49. Irshad, M.; Siraj, K.; Raza, R.; Ali, A.; Tiwari, P.; Zhu, B.; Rafique, A.; Ali, A.; Ullah, M.K.; Usman, A. A Brief Description of High Temperature Solid Oxide Fuel Cell's Operation, Materials, Design, Fabrication Technologies and Performance. *Appl. Sci.* **2016**, *6*, doi:10.3390/app6030075.

50. Tao, Y.; Shao, J.; Wang, J.; Wang, W.G. Synthesis and Properties of $La_{0.6}Sr_{0.4}CoO_{3-\delta}$ Nanopowder. *J. Power Sources* **2008**, *185*, 609–614, doi:10.1016/j.jpowsour.2008.09.021.

51. Teraoka, Y.; Zhang, H.M.; Okamoto, K.; Yamazoe, N. Mixed Ionic-Electronic Conductivity of $La_{1-X}Sr_xCo_{1-Y}Fe_yO_{3-\delta}$ Perovskite-Type Oxides. *Mater. Res. Bull.* **1988**, *23*, 51–58, doi:10.1016/0025-5408(88)90224-3.

52. Ralph, J.M.; Schoeler, A.C.; Krumpelt, M. Materials for Lower Temperature Solid Oxide Fuel Cells. *J. Mater. Sci.* **2001**, *36*, 1161–1172, doi:10.1023/A:1004881825710.

53. Wang, W.G.; Mogensen, M. High-Performance Lanthanum-Ferrite-Based Cathode for SOFC. *Solid State Ionics* **2005**, *176*, 457–462, doi:10.1016/j.ssi.2004.09.007.

54. Baumann, F.S.; Fleig, J.; Konuma, M.; Starke, U.; Habermeier, H.-U.; Maier, J. Strong Performance Improvement of $La_{0.6}Sr_{0.4}Co_{0.8}Fe_{0.2}O_{3-\delta}$ SOFC Cathodes by Electrochemical Activation. *J. Electrochem. Soc.* **2005**, *152*, A2074, doi:10.1149/1.2034529.

UNIVERSIDAD DE MÁLAGA

55. Chen, K.; Jiang, S.P. Surface Segregation in Solid Oxide Cell Oxygen Electrodes: Phenomena, Mitigation Strategies and Electrochemical Properties. *Electrochem. Energy Rev.* **2020**, *3*, 730–765, doi:10.1007/s41918-020-00078-z.

56. Gong, Y.; Patel, R.L.; Liang, X.; Palacio, D.; Song, X.; Goodenough, J.B.; Huang, K. Atomic Layer Deposition Functionalized Composite SOFC Cathode $La_{0.6}Sr_{0.4}Fe_{0.8}Co_{0.2}O_{3-\delta}$-$Gd_{0.2}Ce_{0.8}O_{1.9}$: Enhanced Long-Term Stability. *Chem. Mater.* **2013**, *25*, 4224–4231, doi:10.1021/cm402879r.

57. dos Santos-Gómez, L.; Porras-Vázquez, J.M.; Losilla, E.R.; Martín, F.; Ramos-Barrado, J.R.; Marrero-López, D. Stability and Performance of $La_{0.6}Sr_{0.4}Co_{0.2}Fe_{0.8}O_{3-\delta}$ Nanostructured Cathodes with $Ce_{0.8}Gd_{0.2}O_{1.9}$ Surface Coating. *J. Power Sources* **2017**, *347*, 178–185, doi:10.1016/j.jpowsour.2017.02.045.

58. Koo, B.; Kim, K.; Kim, J.K.; Kwon, H.; Han, J.W.; Jung, W.C. Sr Segregation in Perovskite Oxides: Why It Happens and How It Exists. *Joule* **2018**, *2*, 1476–1499, doi:10.1016/j.joule.2018.07.016.

59. Le, M.V.; Tsai, D.S.; Nguyen, T.A. BSCF/GDC as a Refined Cathode to the Single-Chamber Solid Oxide Fuel Cell Based on a LAMOX Electrolyte. *Ceram. Int.* **2018**, *44*, 1726–1730, doi:10.1016/j.ceramint.2017.10.103.

60. Duan, C.; Tong, J.; Shang, M.; Nikodemski, S.; Sanders, M.; Ricote, S.; Almansoori, A.; O'Hayre, R. Readily Processed Protonic Ceramic Fuel Cells with High Performance at Low Temperatures. *Science* **2015**, *349*, 1321–1326, doi:10.1126/science.aab3987.

61. Dos Santos-Gómez, L.; Losilla, E.R.; Martín, F.; Ramos-Barrado, J.R.; Marrero-López, D. Novel Microstructural Strategies to Enhance the Electrochemical Performance of $La_{0.8}Sr_{0.2}MnO_{3-\delta}$ Cathodes. *ACS Appl. Mater. Interfaces* **2015**, *7*, 7197–7205, doi:10.1021/acsami.5b00255.

62. Tai, L.; Nasrallah, M.; Anderson, H.; Sparlin, D.; Sehlin, S. Structure and Electrical Properties of $La_{1-x}Sr_xCo_{1-y}Fe_yO_3$. Part 1 . The System $La_{0.8}Sr_{0.2}Co_{1-y}Fe_yO_3$. *Solid State Ionics* **1995**, *76*. doi: 10.1016/0167-2738(94)00244-M

63. Afroze, S.; Karim, A.H.; Cheok, Q.; Eriksson, S.; Azad, A.K. Latest Development of Double Perovskite Electrode Materials for Solid Oxide Fuel Cells: A Review. *Front. Energy* **2019**, *13*, 770–797, doi:10.1007/s11708-019-0651-x.

64. Lü, S.; Long, G.; Meng, X.; Ji, Y.; Lü, B.; Zhao, H. $PrBa_{0.5}Sr_{0.5}Co_2O_{5+x}$ as Cathode Material Based on LSGM and GDC Electrolyte for Intermediate-Temperature Solid Oxide Fuel Cells. *Int. J. Hydrogen Energy* **2012**, *37*, 5914–5919, doi:10.1016/j.ijhydene.2011.12.134.

65. Liu, Q.; Dong, X.; Xiao, G.; Zhao, F.; Chen, F. A Novel Electrode Material for Symmetrical SOFCs. *Adv. Mater.* **2010**, *22*, 5478–5482, doi:10.1002/adma.201001044.

66. Ding, P.; Li, W.; Zhao, H.; Wu, C.; Zhao, L.; Dong, B.; Wang, S. Review on Ruddlesden-Popper Perovskites as Cathode for Solid Oxide Fuel Cells. *JPhys Mater.* **2021**, *4*, doi:10.1088/2515-7639/abe392.

67. Yang, J.; Cheng, J.; Jiang, Q.; Wang, Y.; Wang, R.; Gao, J. Preparation and Electrochemical Properties of Strontium Doped Pr_2NiO_4 Cathode Materials for Intermediate-Temperature Solid Oxide Fuel Cells. *Int. J. Hydrogen Energy* **2012**, *37*, 1746–1751, doi:10.1016/j.ijhydene.2011.09.146.

68. dos Santos-Gómez, L.; Porras-Vázquez, J.M.; Hurtado, J.; Losilla, E.R.; Marrero-López, D. Stability and Electrochemical Performance of Nanostructured $La_2CuO_{4+\delta}$ Cathodes. *J. Alloys Compd.* **2019**, *788*, 565–572, doi:10.1016/j.jallcom.2019.02.237.

69. Mao, X.; Yu, T.; Ma, G. Performance of Cobalt-Free Double-Perovskite $NdBaFe_{2-x}Mn_xO_{5+\delta}$

UNIVERSIDAD DE MÁLAGA

Cathode Materials for Proton-Conducting IT-SOFC. *J. Alloys Compd.* **2015**, *637*, 286–290, doi:10.1016/j.jallcom.2015.02.001.

70. Mao, X.; Wang, W.; Ma, G. A Novel Cobalt-Free Double-Perovskite $NdBaFe_{1.9}Nb_{0.1}O_{5+\delta}$ Cathode Material for Proton-Conducting IT-SOFC. *Ceram. Int.* **2015**, *41*, 10276–10280, doi:10.1016/j.ceramint.2015.03.326.
71. Boehm, E.; Bassat, J.M.; Dordor, P.; Mauvy, F.; Grenier, J.C.; Stevens, P. Oxygen Diffusion and Transport Properties in Non-Stoichiometric $Ln_{2-x}NiO_{4+\delta}$ Oxides. *Solid State Ionics* **2005**, *176*, 2717–2725, doi:10.1016/j.ssi.2005.06.033.
72. Chen, T.; Zhou, Y.; Yuan, C.; Liu, M.; Meng, X.; Zhan, Z.; Xia, C.; Wang, S. Impregnated $Nd_2NiO_{4+\delta}$-Scandia Stabilized Zirconia Composite Cathode for Intermediate-Temperature Solid Oxide Fuel Cells. *J. Power Sources* **2014**, *269*, 812–817, doi:10.1016/j.jpowsour.2014.07.073.
73. Shu, L.; Sunarso, J.; Hashim, S.S.; Mao, J.; Zhou, W.; Liang, F. Advanced Perovskite Anodes for Solid Oxide Fuel Cells: A Review. *Int. J. Hydrogen Energy* **2019**, *44*, 31275–31304, doi:10.1016/j.ijhydene.2019.09.220.
74. Jiang, S.P.; Chan, S.H. A Review of Anode Materials Development in Solid Oxide Fuel Cells. *J. Mater. Sci.* **2004**, *39*, 4405–4439, doi:10.1023/b:jmsc.0000034135.52164.6b.
75. Wang, Y.; Wu, C.; Du, Q.; Ni, M.; Jiao, K.; Zu, B. Morphology and Performance Evolution of Anode Microstructure in Solid Oxide Fuel Cell: A Model-Based Quantitative Analysis. *Appl. Energy Combust. Sci.* **2021**, *5*, 100016, doi:10.1016/j.jaecs.2020.100016.
76. Sarruf, B.J.M.; Hong, J.E.; Steinberger-Wilckens, R.; de Miranda, P.E.V. Ceria-Co-Cu-Based SOFC Anode for Direct Utilisation of Methane or Ethanol as Fuels. *Int. J. Hydrogen Energy* **2020**, *45*, 5297–5308, doi:10.1016/j.ijhydene.2019.04.075.
77. Ruiz-Morales, J.C.; Marrero-López, D.; Canales-Vázquez, J.; Irvine, J.T.S. Symmetric and Reversible Solid Oxide Fuel Cells. *RSC Adv.* **2011**, *1*, 1403–1414, doi:10.1039/c1ra00284h.
78. Su, C.; Wang, W.; Liu, M.; Tadé, M.O.; Shao, Z. Progress and Prospects in Symmetrical Solid Oxide Fuel Cells with Two Identical Electrodes. *Adv. Energy Mater.* **2015**, *5*, 1–19, doi:10.1002/aenm.201500188.
79. Gómez, S.Y.; Hotza, D. Current Developments in Reversible Solid Oxide Fuel Cells. *Renew. Sustain. Energy Rev.* **2016**, *61*, 155–174, doi:10.1016/j.rser.2016.03.005.
80. Bastidas, D.M.; Tao, S.; Irvine, J.T.S. A Symmetrical Solid Oxide Fuel Cell Demonstrating Redox Stable Perovskite Electrodes. *J. Mater. Chem.* **2006**, *16*, 1603–1605, doi:10.1039/b600532b.
81. Ruiz-Morales, J.C.; Canales-Vázquez, J.; Peña-Martínez, J.; López, D.M.; Núñez, P. On the Simultaneous Use of $La_{0.75}Sr_{0.25}Cr_{0.5}Mn_{0.5}O_{3-\delta}$ as Both Anode and Cathode Material with Improved Microstructure in Solid Oxide Fuel Cells. *Electrochim. Acta* **2006**, *52*, 278–284, doi:10.1016/j.electacta.2006.05.006.
82. Nikonov, A.; Kuterbekov, K.; Bekmyrza, Kz.; Pavzderin, N. A Brief Review of Conductivity and Thermal Expansion of Perovskite-Related Oxides for SOFC Cathode. *Eurasian J. Phys. Funct. Mater.* **2018**, 274–292, doi:10.29317/ejpfm.2018020309.
83. Shaikh, S.P.S.; Muchtar, A.; Somalu, M.R. A Review on the Selection of Anode Materials for Solid-Oxide Fuel Cells. *Renew. Sustain. Energy Rev.* **2015**, *51*, 1–8. 10.1016/j.rser.2015.05.069
84. Zhu, L.; Wei, B.; Zhang, Y.; Lü, Z.; Wang, Z.; Huang, X.; Cao, Z.; Jiang, W.; Li, Y. Investigation on a Novel Composite Solid Oxide Fuel Cell Anode with $La_{0.6}Sr_{0.4}Co_{0.2}Fe_{0.8}O_{3-\delta}$ Derived Phases. *Electrochim. Acta* **2015**, *160*, 89–93, doi:10.1016/j.electacta.2015.02.024.

UNIVERSIDAD DE MÁLAGA

85. Zheng, Y.; Guo, T.; Wu, Y.; Yang, Y.; Zhang, S.; Ou, X.; Ling, Y. Ni–La_2O_3 Cermet Hydrogen Electrode Originating from the in-Situ Decomposition of the $La_2NiO_{4+\delta}$ Oxide for Quasi-Symmetrical Solid Oxide Fuel Cells. *Int. J. Hydrogen Energy* **2020**, *45*, 27764–27771, doi:10.1016/j.ijhydene.2020.07.151.

86. Lu, C.; Niu, B.; Yi, W.; Ji, Y.; Xu, B. Efficient Symmetrical Electrodes of $PrBaFe_{2-x}Co_xO_{5+\delta}$ (x=0, 0.2,0.4) for Solid Oxide Fuel Cells and Solid Oxide Electrolysis Cells. *Electrochim. Acta* **2020**, *358*, 136916, doi:10.1016/j.electacta.2020.136916.

87. Fergus, J.W. Metallic Interconnects for Solid Oxide Fuel Cells. *Mater. Sci. Eng. A* **2005**, *397*, 271–283, doi:10.1016/j.msea.2005.02.047.

88. Rath, M.K.; Lee, K.T. Investigation of Aliovalent Transition Metal Doped $La_{0.7}Ca_{0.3}Cr_{0.8}X_{0.2}O_{3-\delta}$ (x=Ti, Mn, Fe, Co, and Ni) as Electrode Materials for Symmetric Solid Oxide Fuel Cells. *Ceram. Int.* **2015**, *41*, 10878–10890, doi:10.1016/j.ceramint.2015.05.029.

89. Zhang, L.; Chen, X.; Jiang, S.P.; He, H.Q.; Xiang, Y. Characterization of Doped $La_{0.7}A_{0.3}Cr_{0.5}Mn_{0.5}O_{3-\delta}$ (A = Ca, Sr, Ba) Electrodes for Solid Oxide Fuel Cells. *Solid State Ionics* **2009**, *180*, 1076–1082, doi:10.1016/j.ssi.2009.05.010.

90. Lay, E.; Benamira, M.; Pirovano, C.; Gauthier, G.; Dessemond, L. Effect of Ce-Doping on the Electrical and Electrocatalytical Behavior of La/Sr Chromo-Manganite Perovskite as New SOFC Anode. *Fuel Cells* **2012**, *12*, 265–274, doi:10.1002/fuce.201100070.

91. Wan, Y.; Xing, Y.; Xu, Z.; Xue, S.; Zhang, S.; Xia, C. A-Site Bismuth Doping, a New Strategy to Improve the Electrocatalytic Performances of Lanthanum Chromate Anodes for Solid Oxide Fuel Cells. *Appl. Catal. B Environ.* **2020**, *269*, 118809, doi:10.1016/j.apcatb.2020.118809.

92. Delahaye, T.; Jardiel, T.; Joubert, O.; Laucournet, R.; Gauthier, G.; Caldes, M.T. Electrochemical Properties of Novel SOFC Dual Electrode $La_{0.75}Sr_{0.25}Cr_{0.5}Mn_{0.3}Ni_{0.2}O_{3-\delta}$. *Solid State Ionics* **2011**, *184*, 39–41, doi:10.1016/j.ssi.2010.10.015.

93. Sun, C.; Hui, R.; Roller, J. Cathode Materials for Solid Oxide Fuel Cells: A Review. *J. Solid State Electrochem.* **2010**, *14*, 1125–1144, doi:10.1007/s10008-009-0932-0.

94. Fernández-Ropero, A.J.; Porras-Vázquez, J.M.; Cabeza, A.; Slater, P.R.; Marrero-López, D.; Losilla, E.R. High Valence Transition Metal Doped Strontium Ferrites for Electrode Materials in Symmetrical SOFCs. *J. Power Sources* **2014**, *249*, 405–413, doi:10.1016/j.jpowsour.2013.10.118.

95. Dos Santos-Gómez, L.; Porras-Vázquez, J.M.; Losilla, E.R.; Marrero-López, D. Ti-Doped $SrFeO_3$ Nanostructured Electrodes for Symmetric Solid Oxide Fuel Cells. *RSC Adv.* **2015**, *5*, 107889–107895, doi:10.1039/c5ra23771h.

96. Cao, Y.; Zhu, Z.; Zhao, Y.; Zhao, W.; Wei, Z.; Liu, T. Development of Tungsten Stabilized $SrFe_{0.8}W_{0.2}O_{3-\delta}$ Material as Novel Symmetrical Electrode for Solid Oxide Fuel Cells. *J. Power Sources* **2020**, *455*, 227951, doi:10.1016/j.jpowsour.2020.227951.

97. Bian, L.; Liu, C.; Li, S.; Peng, J.; Li, X.; Guan, L.; Liu, Y.; Peng, J.H.; An, S.; Song, X. Highly Stable $La_{0.5}Sr_{0.5}Fe_{0.9}Mo_{0.1}O_{3-\delta}$ Electrode for Reversible Symmetric Solid Oxide Cells. *Int. J. Hydrogen Energy* **2020**, *45*, 19813–19822, doi:10.1016/j.ijhydene.2020.05.117.

98. Yang, Z.; Chen, Y.; Jin, C.; Xiao, G.; Han, M.; Chen, F. $La_{0.7}Sr_{0.3}Fe_{0.7}Ga_{0.3}O_{3-\delta}$ as Electrode Material for a Symmetrical Solid Oxide Fuel Cell. *RSC Adv.* **2015**, *5*, 2702–2705, doi:10.1039/c4ra11358f.

99. Liu, X.; Han, D.; Zhou, Y.; Meng, X.; Wu, H.; Li, J.; Zeng, F.; Zhan, Z. Sc-Substituted $La_{0.6}Sr_{0.4}FeO_{3-\delta}$ Mixed Conducting Oxides as Promising Electrodes for Symmetrical Solid Oxide Fuel Cells. *J. Power Sources* **2014**, *246*, 457–463, doi:10.1016/j.jpowsour.2013.07.111.

100. Hou, Y.; Wang, L.; Bian, L.; Wang, Y.; Chou, K.C. Excellent Electrochemical Performance of

UNIVERSIDAD DE MÁLAGA

$La_{0.3}Sr_{0.7}Fe_{0.9}Ti_{0.1}O_{3-\delta}$ as a Symmetric Electrode for Solid Oxide Cells. *ACS Appl. Mater. Interfaces* **2021**, *13*, 22381–22390, doi:10.1021/acsami.1c02856.

101. Li, B.; He, S.; Li, J.; Yue, X.; Irvine, J.T.S.; Xie, D.; Ni, J.; Ni, C. A Ce/Ru Codoped $SrFeO_{3-\delta}$ Perovskite for a Coke-Resistant Anode of a Symmetrical Solid Oxide Fuel Cell. *ACS Catal.* **2020**, *10*, 14398–14409, doi:10.1021/acscatal.0c03554.
102. Tian, Y.; Liu, Y.; Jia, L.; Naden, A.; Chen, J.; Chi, B.; Pu, J.; Irvine, J.T.S.; Li, J. A Novel Electrode with Multifunction and Regeneration for Highly Efficient and Stable Symmetrical Solid Oxide Cell. *J. Power Sources* **2020**, *475*, 228620, doi:10.1016/j.jpowsour.2020.228620.
103. Alvarado Flores, J.J.; Ávalos Rodríguez, M.L.; Andrade Espinosa, G.; Alcaraz Vera, J.V. Advances in the Development of Titanates for Anodes in SOFC. *Int. J. Hydrogen Energy* **2019**, *4*, 12529–12542, doi:10.1016/j.ijhydene.2018.05.171.
104. Yaremchenko, A.A.; Macías, J.; Kovalevsky, A. V.; Arias-Serrano, B.I.; Frade, J.R. Electrical Conductivity and Thermal Expansion of Ln-Substituted $SrTiO_3$ for Solid Oxide Cell Electrodes and Interconnects: The Effect of Rare-Earth Cation Size. *J. Power Sources* **2020**, *474*, 228531, doi:10.1016/j.jpowsour.2020.228531.
105. Canales-Vázquez, J.; Ruiz-Morales, J.C.; Marrero-López, D.; Peña-Martínez, J.; Núñez, P.; Gómez-Romero, P. Fe-Substituted (La,Sr)TiO_3 as Potential Electrodes for Symmetrical Fuel Cells (SFCs). *J. Power Sources* **2007**, *171*, 552–557, doi:10.1016/j.jpowsour.2007.05.094.
106. Martínez-Coronado, R.; Aguadero, A.; Pérez-Coll, D.; Troncoso, L.; Alonso, J.A.; Fernández-Díaz, M.T. Characterization of $La_{0.5}Sr_{0.5}Co_{0.5}Ti_{0.5}O_{3-\delta}$ as Symmetrical Electrode Material for Intermediate-Temperature Solid-Oxide Fuel Cells. *Int. J. Hydrogen Energy* **2012**, *37*, 18310–18318, doi:10.1016/j.ijhydene.2012.09.033.
107. Yang, Y.; Li, S.; Yang, Z.; Chen, Y.; Zhang, P.; Wang, Y.; Chen, F.; Peng, S. One Step Synthesis of $Sr_2Fe_{1.3}Co_{0.2}Mo_{0.5}O_{6-\delta}$-$Gd_{0.1}Ce_{0.9}O_{2-\delta}$ for Symmetrical Solid Oxide Fuel Cells . *J. Electrochem. Soc.* **2020**, *167*, 084503, doi:10.1149/1945-7111/ab8927.
108. Xu, Z.; Hu, X.; Wan, Y.; Xue, S.; Zhang, S.; Zhang, L.; Zhang, B.; Xia, C. Electrochemical Performance and Anode Reaction Process for Ca Doped $Sr_2Fe_{1.5}Mo_{0.5}O_{6-\delta}$ as Electrodes for Symmetrical Solid Oxide Fuel Cells. *Electrochim. Acta* **2020**, *341*, doi:10.1016/j.electacta.2020.136067.
109. Chen, Y.; Cheng, Z.; Yang, Y.; Gu, Q.; Tian, D.; Lu, X.; Yu, W.; Lin, B. Novel Quasi-Symmetric Solid Oxide Fuel Cells with Enhanced Electrochemical Performance. *J. Power Sources* **2016**, *310*, 109–117, doi:10.1016/j.jpowsour.2016.02.013.
110. Gu, Y.; Zhang, Y.; Zheng, Y.; Chen, H.; Ge, L.; Guo, L. $PrBaMn_2O_{5+\delta}$ with Praseodymium Oxide Nano-Catalyst as Electrode for Symmetrical Solid Oxide Fuel Cells. *Appl. Catal. B Environ.* **2019**, *257*, 117868, doi:10.1016/j.apcatb.2019.117868.
111. Zamudio-García, J.; Caizán-Juanarena, L.; Porras-Vázquez, J.M.; Losilla, E.R.; Marrero-López, D. A Review on Recent Advances and Trends in Symmetrical Electrodes for Solid Oxide Cells. *J. Power Sources* **2022**, *520*, 230852. doi:10.1016/j.jpowsour.2021.230852.
112. Wang, S.; Wei, B.; Lü, Z. Electrochemical Performance and Distribution of Relaxation Times Analysis of Tungsten Stabilized $La_{0.5}Sr_{0.5}Fe_{0.9}W_{0.1}O_{3-\delta}$ Electrode for Symmetric Solid Oxide Fuel Cells. *Int. J. Hydrogen Energy* **2021**, *46*, 30101–30111, doi:10.1016/j.ijhydene.2021.06.140.
113. Zhou, J.; Chen, G.; Wu, K.; Cheng, Y. The Performance of $La_{0.6}Sr_{1.4}MnO_4$ Layered Perovskite Electrode Material for Intermediate Temperature Symmetrical Solid Oxide Fuel Cells. *J. Power Sources* **2014**, *270*, 418–425, doi:10.1016/j.jpowsour.2014.06.163.
114. Vohs, J.M.; Gorte, R.J. High-Performance SOFC Cathodes Prepared by Infiltration. *Adv.*

UNIVERSIDAD DE MÁLAGA

Mater. **2009**, *21*, 943–956, doi:10.1002/adma.200802428.

115. Shimada, H.; Yamaguchi, T.; Kishimoto, H.; Sumi, H.; Yamaguchi, Y.; Nomura, K.; Fujishiro, Y. Nanocomposite Electrodes for High Current Density over 3 A cm^{-2} in Solid Oxide Electrolysis Cells. *Nat. Commun.* **2019**, *10*, 1–10, doi:10.1038/s41467-019-13426-5.
116. Khan, M.Z.; Song, R.H.; Mehran, M.T.; Lee, S.B.; Lim, T.H. Controlling Cation Migration and Inter-Diffusion across Cathode/Interlayer/Electrolyte Interfaces of Solid Oxide Fuel Cells: A Review. *Ceram. Int.* **2021**, *47*, 5839–5869, doi:10.1016/j.ceramint.2020.11.002.
117. Sun, X.; Chen, H.; Yin, Y.; Curnan, M.T.; Han, J.W.; Chen, Y.; Ma, Z. Progress of Exsolved Metal Nanoparticles on Oxides as High Performance (Electro)Catalysts for the Conversion of Small Molecules. *Small* **2021**, *17*, 2005383, doi:10.1002/smll.202005383.
118. Leng, Y.; Chan, S.H.; Liu, Q. Development of LSCF-GDC Composite Cathodes for Low-Temperature Solid Oxide Fuel Cells with Thin Film GDC Electrolyte. *Int. J. Hydrogen Energy* **2008**, *33*, 3808–3817, doi:10.1016/j.ijhydene.2008.04.034.
119. Tsipis, E. V.; Kharton, V. V. Electrode Materials and Reaction Mechanisms in Solid Oxide Fuel Cells: A Brief Review : I Electrochemical Behavior vs. Materials Science Aspects. *J. Solid State Electrochem.* **2008**, *12*, 1367–1391, doi:10.1007/s10008-008-0611-6.
120. Lee, J.G.; Park, J.H.; Shul, Y.G. Tailoring Gadolinium-Doped Ceria-Based Solid Oxide Fuel Cells to Achieve 2 W cm^{-2} at 550 °C. *Nat. Commun.* **2014**, *5*, doi:10.1038/ncomms5045.
121. Lee, K.T.; Lidie, A.A.; Yoon, H.S.; Wachsman, E.D. Rational Design of Lower-Temperature Solid Oxide Fuel Cell Cathodes via Nanotailoring of Co-Assembled Composite Structures. *Angew. Chemie - Int. Ed.* **2014**, *53*, 13463–13467, doi:10.1002/anie.201408210.
122. Kumar, S.A.; Kuppusami, P.; Vengatesh, P. Auto-Combustion Synthesis and Electrochemical Studies of $La_{0.6}Sr_{0.4}Co_{0.2}Fe_{0.8}O_{3-\delta}$–$Ce_{0.8}Sm_{0.1}Gd_{0.1}O_{1.90}$ Nanocomposite Cathode for Intermediate Temperature Solid Oxide Fuel Cells. *Ceram. Int.* **2018**, *44*, 21188–21196, doi:10.1016/j.ceramint.2018.08.164.
123. Zakaria, Z.; Awang Mat, Z.; Abu Hassan, S.H.; Boon Kar, Y. A Review of Solid Oxide Fuel Cell Component Fabrication Methods toward Lowering Temperature. *Int. J. Energy Res.* **2020**, *44*, 594–611, doi:10.1002/er.4907.
124. Connor, P.A.; Yue, X.; Savaniu, C.D.; Price, R.; Triantafyllou, G.; Cassidy, M.; Kerherve, G.; Payne, D.J.; Maher, R.C.; Cohen, L.F. Irvine, J.T.S. Tailoring SOFC Electrode Microstructures for Improved Performance. *Adv. Energy Mater.* **2018**, *8*, 1–20, doi:10.1002/aenm.201800120.
125. dos Santos-Gómez, L.; Zamudio-García, J.; Porras-Vázquez, J.M.; Losilla, E.R.; Marrero-López, D. Recent Progress in Nanostructured Electrodes for Solid Oxide Fuel Cells Deposited by Spray Pyrolysis. *J. Power Sources* **2021**, *507*, doi:10.1016/j.jpowsour.2021.230277.
126. Princivalle, A.; Perednis, D.; Neagu, R.; Djurado, E. Porosity Control of LSM/YSZ Cathode Coating Deposited by Electrospraying. *Chem. Mater.* **2005**, *17*, 1220–1227, doi:10.1021/cm048503h.
127. dos Santos-Gómez, L.; Zamudio-García, J.; Porras-Vázquez, J.M.; Losilla, E.R.; Marrero-López, D. Highly Efficient $La_{0.8}Sr_{0.2}MnO_{3-\delta}$-$Ce_{0.9}Gd_{0.1}O_{1.95}$ Nanocomposite Cathodes for Solid Oxide Fuel Cells. *Ceram. Int.* **2018**, *44*, 4961–4966, doi:10.1016/j.ceramint.2017.12.089.
128. Sar, J.; Celikbilek, O.; Villanova, J.; Dessemond, L.; Martin, C.L.; Djurado, E. Three Dimensional Analysis of $Ce_{0.9}Gd_{0.1}O_{1.95}$-$La_{0.6}Sr_{0.4}Co_{0.2}Fe_{0.8}O_{3-\delta}$ Oxygen Electrode for Solid Oxide Cells. *J. Eur. Ceram. Soc.* **2015**, *35*, 4497–4505, doi:10.1016/j.jeurceramsoc.2015.08.019.
129. dos Santos-Gómez, L.; Porras-Vázquez, J.M.; Losilla, E.R.; Martín, F.; Ramos-Barrado, J.R.; Marrero-López, D. LSCF-CGO Nanocomposite Cathodes Deposited in a Single Step by

UNIVERSIDAD DE MÁLAGA

Spray-Pyrolysis. *J. Eur. Ceram. Soc.* **2018**, *38*, 1647–1653, doi:10.1016/j.jeurceramsoc.2017.10.010.

130. Ding, D.; Li, X.; Lai, S.Y.; Gerdes, K.; Liu, M. Enhancing SOFC Cathode Performance by Surface Modification through Infiltration. *Energy Environ. Sci.* **2014**, *7*, 552–575, doi:10.1039/c3ee42926a.
131. Jiang, S.P.; Ye, Y.; He, T.; Ho, S.B. Nanostructured Palladium-$La_{0.75}Sr_{0.25}Cr_{0.5}Mn_{0.5}O_3/Y_2O_3$-$ZrO_2$ Composite Anodes for Direct Methane and Ethanol Solid Oxide Fuel Cells. *J. Power Sources* **2008**, *185*, 179–182, doi:10.1016/j.jpowsour.2008.06.099.
132. Sholklapper, T.Z.; Lu, C.; Jacobson, C.P.; Visco, S.J.; De Jonghe, L.C. LSM-Infiltrated Solid Oxide Fuel Cell Cathodes. *Electrochem. Solid-State Lett.* **2006**, *9*, 376–378, doi:10.1149/1.2206011.
133. Sholklapper, T.Z.; Radmilovic, V.; Jacobson, C.P.; Visco, S.J.; De Jonghe, L.C. Synthesis and Stability of a Nanoparticle-Infiltrated Solid Oxide Fuel Cell Electrode. *Electrochem. Solid-State Lett.* **2007**, *10*, 74–77, doi:10.1149/1.2434203.
134. Jiang, S.P. Nanoscale and Nano-Structured Electrodes of Solid Oxide Fuel Cells by Infiltration: Advances and Challenges. *Int. J. Hydrogen Energy* **2012**, *37*, 449–470, doi:10.1016/j.ijhydene.2011.09.067.
135. Dos Santos-Gómez, L.; Porras-Vázquez, J.M.; Martín, F.; Ramos-Barrado, J.R.; Losilla, E.R.; Marrero-López, D. An Easy and Innovative Method Based on Spray-Pyrolysis Deposition to Obtain High Efficiency Cathodes for Solid Oxide Fuel Cells. *J. Power Sources* **2016**, *319*, 48–55, doi:10.1016/j.jpowsour.2016.04.034.
136. Santos-Gómez, L. Dos; Zamudio-García, J.; Porras-Vázquez, J.M.; Losilla, E.R.; Marrero-López, D. Nanostructured $BaCo_{0.4}Fe_{0.4}Zr_{0.1}Y_{0.1}O_{3-\delta}$ Cathodes with Different Microstructural Architectures. *Nanomaterials* **2020**, *10*, doi:10.3390/nano10061055.
137. Santos-Gómez, L. Dos; Porras-Vázquez, J.M.; Losilla, E.R.; Marrero-López, D. Improving the Efficiency of Layered Perovskite Cathodes by Microstructural Optimization. *J. Mater. Chem. A* **2017**, *5*, 7896–7904, doi:10.1039/c6ta10946b.
138. Shri Prakash, B.; Pavitra, R.; Senthil Kumar, S.; Aruna, S.T. Electrolyte Bi-Layering Strategy to Improve the Performance of an Intermediate Temperature Solid Oxide Fuel Cell: A Review. *J. Power Sources* **2018**, *381*, 136–155, doi:10.1016/j.jpowsour.2018.02.003.
139. Somalu, M.R.; Muchtar, A.; Daud, W.R.W.; Brandon, N.P. Screen-Printing Inks for the Fabrication of Solid Oxide Fuel Cell Films: A Review. *Renew. Sustain. Energy Rev.* **2017**, *75*, 426–439, doi:10.1016/j.rser.2016.11.008.
140. Sahu, N.; Parija, B.; Panigrahi, S. Fundamental Understanding and Modeling of Spin Coating Process: A Review. *Indian J. Phys.* **2009**, *83*, 493–502, doi:10.1007/s12648-009-0009-z.
141. Kelly, P.J.; Arnell, R.D. Magnetron Sputtering: A Review of Recent Developments and Applications. *Vacuum* **2000**, *56*, 159–172, doi:10.1016/S0042-207X(99)00189-X.
142. Xu, M.; Yu, J.; Song, Y.; Ran, R.; Wang, W.; Shao, Z. Advances in Ceramic Thin Films Fabricated by Pulsed Laser Deposition for Intermediate-Temperature Solid Oxide Fuel Cells. *Energy and Fuels* **2020**, *34*, 10568–10582, doi:10.1021/acs.energyfuels.0c02338.
143. Morales, M.; Roa, J.J.; Tartaj, J.; Segarra, M. Performance and Short-Term Stability of Single-Chamber Solid Oxide Fuel Cells Based on $La_{0.9}Sr_{0.1}Ga_{0.8}Mg_{0.2}O_{3-\delta}$ Electrolyte. *J. Power Sources* **2012**, *216*, 417–424, doi:10.1016/j.jpowsour.2012.05.076.
144. Wang, F.; Brito, M.E.; Yamaji, K.; Cho, D.H.; Nishi, M.; Kishimoto, H.; Horita, T.; Yokokawa, H. Effect of Polarization on Sr and Zr Diffusion Behavior in LSCF/GDC/YSZ System. *Solid State Ionics* **2014**, *262*, 454–459, doi:10.1016/j.ssi.2014.04.002.

UNIVERSIDAD DE MÁLAGA

145. Adijanto, L.; Küngas, R.; Bidrawn, F.; Gorte, R.J.; Vohs, J.M. Stability and Performance of Infiltrated $La_{0.8}Sr_{0.2}Co_xFe_{1-x}O_3$ Electrodes with and without $Sm_{0.2}Ce_{0.8}O_{1.9}$ Interlayers. *J. Power Sources* **2011**, *196*, 5797–5802, doi:10.1016/j.jpowsour.2011.03.022.

146. Wachsman, E.D.; Jayaweera, P.; Jiang, N.; Lowe, D.M.; Pound, B.G. Stable High Conductivity Ceria/Bismuth Oxide Bilayered Electrolytes. *J. Electrochem. Soc.* **1997**, *144*, 233–236, doi:10.1149/1.1837390.

147. Hou, J.; Bi, L.; Qian, J.; Zhu, Z.; Zhang, J.; Liu, W. High Performance Ceria-Bismuth Bilayer Electrolyte Low Temperature Solid Oxide Fuel Cells (LT-SOFCs) Fabricated by Combining Co-Pressing with Drop-Coating. *J. Mater. Chem. A* **2015**, *3*, 10219–10224, doi:10.1039/c4ta06864e.

148. Molin, S.; Karczewski, J.; Kamecki, B.; Mroziński, A.; Wang, S.F.; Jasiński, P. Processing of $Ce_{0.8}Gd_{0.2}O_{2-\delta}$ Barrier Layers for Solid Oxide Cells: The Effect of Preparation Method and Thickness on the Interdiffusion and Electrochemical Performance. *J. Eur. Ceram. Soc.* **2020**, *40*, 5626–5633, doi:10.1016/j.jeurceramsoc.2020.06.006.

149. dos Santos-Gómez, L.; Hurtado, J.; Porras-Vázquez, J.M.; Losilla, E.R.; Marrero-López, D. Durability and Performance of CGO Barriers and LSCF Cathode Deposited by Spray-Pyrolysis. *J. Eur. Ceram. Soc.* **2018**, *38*, 3518–3526, doi:10.1016/j.jeurceramsoc.2018.03.024.

150. Zapata-Ramírez, V.; Dos Santos-Gómez, L.; Mather, G.C.; Marrero-López, D.; Pérez-Coll, D. Enhanced Intermediate-Temperature Electrochemical Performance of Air Electrodes for Solid Oxide Cells with Spray-Pyrolyzed Active Layers. *ACS Appl. Mater. Interfaces* **2020**, *12*, 10571–10578, doi:10.1021/acsami.9b22966.

151. Sharma, R.K.; Burriel, M.; Dessemond, L.; Bassat, J.M.; Djurado, E. Design of Interfaces in Efficient $Ln_2NiO_{4+\delta}$ (Ln = La, Pr) Cathodes for SOFC Applications. *J. Mater. Chem. A* **2016**, *4*, 12451–12462, doi:10.1039/c6ta04845e.

152. Sharma, R.K.; Djurado, E. An Efficient Hierarchical Nanostructured Pr_6O_{11} Electrode for Solid Oxide Fuel Cells. *J. Mater. Chem. A* **2018**, *6*, 10787–10802, doi:10.1039/c8ta00190a.

153. Kamecki, B.; Karczewski, J.; Jasiński, P.; Molin, S. Improvement of Oxygen Electrode Performance of Intermediate Temperature Solid Oxide Cells by Spray Pyrolysis Deposited Active Layers. *Adv. Mater. Interfaces* **2021**, *8*, 1–11, doi:10.1002/admi.202002227.

154. Su, Q.; Yoon, D.; Kim, Y.N.; Gong, W.; Chen, A.; Cho, S.; Manthiram, A.; Jacobson, A.J.; Wang, H. Effects of Interlayer Thickness on the Electrochemical and Mechanical Properties of Bi-Layer Cathodes for Solid Oxide Fuel Cells. *J. Power Sources* **2012**, *218*, 261–267, doi:10.1016/j.jpowsour.2012.06.094.

155. Ju, Y.-W.; Inagaki, T.; Ida, S.; Ishihara, T. $Sm(Sr)CoO_3$ Cone Cathode on $LaGaO_3$ Thin Film Electrolyte for IT-SOFC with High Power Density. *J. Electrochem. Soc.* **2011**, *158*, B825, doi:10.1149/1.3592427.

156. Choi, S.; Kucharczyk, C.J.; Liang, Y.; Zhang, X.; Takeuchi, I.; Ji, H. Il; Haile, S.M. Exceptional Power Density and Stability at Intermediate Temperatures in Protonic Ceramic Fuel Cells. *Nat. Energy* **2018**, *3*, 202–210, doi:10.1038/s41560-017-0085-9.

157. Choi, S.; Davenport, T.C.; Haile, S.M. Protonic Ceramic Electrochemical Cells for Hydrogen Production and Electricity Generation: Exceptional Reversibility, Stability, and Demonstrated Faradaic Efficiency. *Energy Environ. Sci.* **2019**, *12*, 206–215, doi:10.1039/c8ee02865f.

158. Qian, J.; Hou, J.; Tao, Z.; Liu, W. Fabrication of $(Sm,Ce)O_{2-\delta}$ Interlayer for Yttria-Stabilized Zirconia-Based Intermediate Temperature Solid Oxide Fuel Cells. *J. Alloys Compd.* **2015**, *631*, 255–260, doi:10.1016/j.jallcom.2015.01.124.

UNIVERSIDAD DE MÁLAGA

159. Sun, X.; MacManus-Driscoll, J.L.; Wang, H. Spontaneous Ordering of Oxide-Oxide Epitaxial Vertically Aligned Nanocomposite Thin Films. *Annu. Rev. Mater. Res.* **2020**, *50*, 229–253, doi:10.1146/annurev-matsci-091719-112806.

160. Wang, Z.; Li, Y.; Viswan, R.; Hu, B.; Harris, V.G.; Li, J.; Viehland, D. Engineered Magnetic Shape Anisotropy in $BiFeO_3$-$CoFe_2O_4$ Self-Assembled Thin Films. *ACS Nano* **2013**, *7*, 3447–3456, doi:10.1021/nn4003506.

161. Yang, S.M.; Lee, S.; Jian, J.; Zhang, W.; Lu, P.; Jia, Q.; Wang, H.; Won Noh, T.; Kalinin, S. V.; MacManus-Driscoll, J.L. Strongly Enhanced Oxygen Ion Transport through Samarium-Doped CeO_2 Nanopillars in Nanocomposite Films. *Nat. Commun.* **2015**, *6*, 1–8, doi:10.1038/ncomms9588.

162. Harrington, S.A.; Zhai, J.; Denev, S.; Gopalan, V.; Wang, H.; Bi, Z.; Redfern, S.A.T.; Baek, S.H.; Bark, C.W.; Eom, C.B.; et al. Thick Lead-Free Ferroelectric Films with High Curie Temperatures through Nanocomposite-Induced Strain. *Nat. Nanotechnol.* **2011**, *6*, 491–495, doi:10.1038/nnano.2011.98.

163. Baiutti, F.; Chiabrera, F.; Acosta, M.; Diercks, D.; Parfitt, D.; Santiso, J.; Wang, X.; Cavallaro, A.; Morata, A.; Wang, H.; Tarancon, A. A High-Entropy Manganite in an Ordered Nanocomposite for Long-Term Application in Solid Oxide Cells. *Nat. Commun.* **2021**, *12*, 1–11, doi:10.1038/s41467-021-22916-4.

164. Yoon, J.; Cho, S.; Kim, J.H.; Lee, J.; Bi, Z.; Serquis, A.; Zhang, X.; Manthiram, A.; Wang, H. Vertically Aligned Nanocomposite Thin Films as a Cathode/Electrolyte Interface Layer for Thin-Film Solid Oxide Fuel Cells. *Adv. Funct. Mater.* **2009**, *19*, 3868–3873, doi:10.1002/adfm.200901338.

165. Cho, S.; Kim, Y.N.; Lee, J.; Manthiram, A.; Wang, H. Microstructure and Electrochemical Properties of $PrBaCo_2O_{5+\delta}$/$Ce_{0.9}Gd_{0.1}O_{1.95}$ Vertically Aligned Nanocomposite Thin Film as Interlayer for Thin Film Solid Oxide Fuel Cells. *Electrochim. Acta* **2012**, *62*, 147–152, doi:10.1016/j.electacta.2011.12.008.

166. Ma, W.; Kim, J.J.; Tsvetkov, N.; Daio, T.; Kuru, Y.; Cai, Z.; Chen, Y.; Sasaki, K.; Tuller, H.L.; Yildiz, B. Vertically Aligned Nanocomposite $La_{0.8}Sr_{0.2}CoO_3$/$(La_{0.5}Sr_{0.5})_2CoO_4$ Cathodes-Electronic Structure, Surface Chemistry and Oxygen Reduction Kinetics. *J. Mater. Chem. A* **2015**, *3*, 207–219, doi:10.1039/c4ta04993d.

167. Develos-Bagarinao, K.; Ishiyama, T.; Kishimoto, H.; Shimada, H.; Yamaji, K. Nanoengineering of Cathode Layers for Solid Oxide Fuel Cells to Achieve Superior Power Densities. *Nat. Commun.* **2021**, *12*, 1–12, doi:10.1038/s41467-021-24255-w.

168. Sirvent, J. de D.; Carmona, A.; Rapenne, L.; Chiabrera, F.; Morata, A.; Burriel, M.; Baiutti, F.; Tarancón, A. Nanostructured $La_{0.75}Sr_{0.25}Cr_{0.5}Mn_{0.5}O_3$-$Ce_{0.8}Sm_{0.2}O_2$ Heterointerfaces as All-Ceramic Functional Layers for Solid Oxide Fuel Cell Applications. *ACS Appl. Mater. Interfaces* **2022**, *14*, 42178–42187, doi:10.1021/acsami.2c14044.

169. Kwon, O.; Joo, S.; Choi, S.; Sengodan, S.; Kim, G. Review on Exsolution and Its Driving Forces in Perovskites. *JPhys Energy* **2020**, *2*, 032001, doi:10.1088/2515-7655/ab8c1f.

170. Kousi, K.; Tang, C.; Metcalfe, I.S.; Neagu, D. Emergence and Future of Exsolved Materials. *Small* **2021**, *17*, 2006479, doi:10.1002/smll.202006479.

171. Yang, Y.; Li, J.; Sun, Y. The Metal/Oxide Heterointerface Delivered by Solid-Based Exsolution Strategy: A Review. *Chem. Eng. J.* **2022**, *440*, 135868, doi:10.1016/j.cej.2022.135868.

172. Kim, K.J.; Han, H.; Defferriere, T.; Yoon, D.; Na, S.; Kim, S.J.; Dayaghi, A.M.; Son, J.; Oh, T.S.; Jang, H.M.; et al. Facet-Dependent in Situ Growth of Nanoparticles in Epitaxial Thin Films: The Role of Interfacial Energy. *J. Am. Chem. Soc.* **2019**, *141*, 7509–7517,

UNIVERSIDAD DE MÁLAGA

doi:10.1021/jacs.9b02283.

173. Han, H.; Park, J.; Nam, S.Y.; Kim, K.J.; Choi, G.M.; Parkin, S.S.P.; Jang, H.M.; Irvine, J.T.S. Lattice Strain-Enhanced Exsolution of Nanoparticles in Thin Films. *Nat. Commun.* **2019**, *10*, 1–8, doi:10.1038/s41467-019-09395-4.

UNIVERSIDAD DE MÁLAGA

UNIVERSIDAD
DE MÁLAGA

Chapter 2

UNIVERSIDAD
DE MÁLAGA

UNIVERSIDAD
DE MÁLAGA

Objectives

The main aim of this PhD Thesis is the preparation and characterization of novel nanocomposite layers with different electrode architectures for their implementation in symmetrical SOFCs. In order to achieve this goal, spray-pyrolysis deposition is proposed as a low-cost, versatile and scalable method to obtain electrode layers with different morphologies directly onto the electrolyte surface at low temperatures. In addition, pulsed laser deposition is also employed to obtain Vertically Aligned Nanostructured (VANs) layers. The most relevant specific objectives are summarized below:

- Preparation of novel nanocomposite layers with different microstructural architectures by using the spray-pyrolysis deposition method.

- Preparation of VANs and epitaxial films by pulsed laser deposition for potential application as active layers in both oxidizing and reducing atmospheres.

UNIVERSIDAD DE MÁLAGA

- Study the structure, microstructure and thermal stability of the nanocomposite layers in both oxidizing and reducing conditions for their potential application in Symmetrical Solid Oxide Fuel Cells.

- Evaluate the relationship between the structure, microstructure and composition of the nanocomposite layers and their electrochemical properties.

- Compare the properties and efficiency of the nanocomposite layers with those obtained by traditional screen-printing deposition.

- Test the performance and long-term stability of the nanocomposite layers in real SOFC conditions.

UNIVERSIDAD DE MÁLAGA

Chapter 3

UNIVERSIDAD
DE MÁLAGA

UNIVERSIDAD
DE MÁLAGA

Experimental methods

This chapter describes the synthesis and preparation of the materials in form of powders and layers, as well as the experimental techniques employed for their characterization.

3.1. Freeze-drying precursor method

The polycrystalline powders were prepared by the freeze-drying precursor method (FD). This synthesis method has been widely employed in materials science to obtain ultrafine powders [1]. In SOFC field, this is typically used to synthesize both electrolyte and electrode materials from a homogeneous aqueous solution, which is dehydrated by vacuum sublimation in a freeze-dryer. Figure 3.1 shows a P-T diagram of an aqueous solution.

UNIVERSIDAD DE MÁLAGA

This method usually leads to nanostructured materials with reduced particle size at lower sintering temperatures and shorter times when compared to the traditional solid-state reaction method. The resulting polycrystalline powders show improved properties due to the lower particle size and larger surface area.

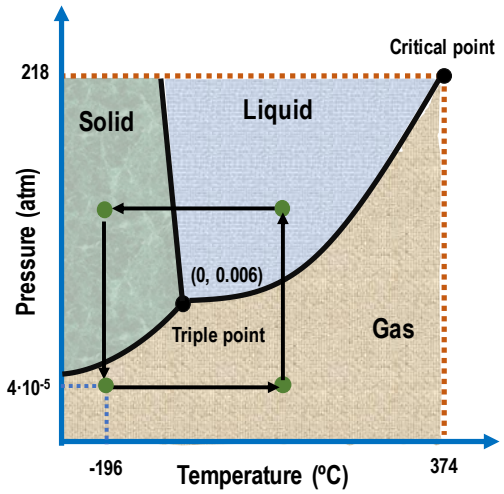

Figure 3.1. P-T diagram showing the freeze-drying process of an aqueous solution.

The freeze-drying process can be divided into different steps (Figure 3.2):

(i) Firstly, a diluted aqueous solution was prepared from the different metal salts in stoichiometric amounts with a total cation concentration of 0.1 mol L^{-1}. The salts employed in this work were mostly nitrates because of their high solubility in water. These were previously studied by thermogravimetric analysis to determine the correct water content. Additionally, ethylenediaminetetraacetic acid (EDTA) was added as complexing agent in a 1:1 ligand:metal molar ratio to avoid the cation precipitation during the preparation process. The pH of all solutions was fixed between 6 and 8, obtaining transparent solutions (Figure 3.2a).

(ii) Once the precursor solution is obtained, it is dropwise added into liquid nitrogen in a big beaker under constant stirring to avoid drop coarsening (Figure 3.2b). The fast frozen ensures the cation homogeneity of the starting solution during the cooling process.

UNIVERSIDAD DE MÁLAGA

(iii) The frozen drops were transferred to a round flask, connected to the Freeze-drier (Scanvac Coolsafe) and dehydrated by vacuum sublimation for 2 days (Figure 3.2c,d). The temperature and pressure of the condenser were -110 ºC and 0.05 mbar, respectively.

(iv) The dried precursors were immediately heated at 300 ºC for 1 h in a furnace to prevent rehydration. During this process, the organic matter was partially decomposed, considerably increasing the volume of the precursor powders (Figure 3.2e). Finally, the precursor is calcined at ~800 ºC to achieve crystallization and completely remove carbonaceous species (Figure 3.2f).

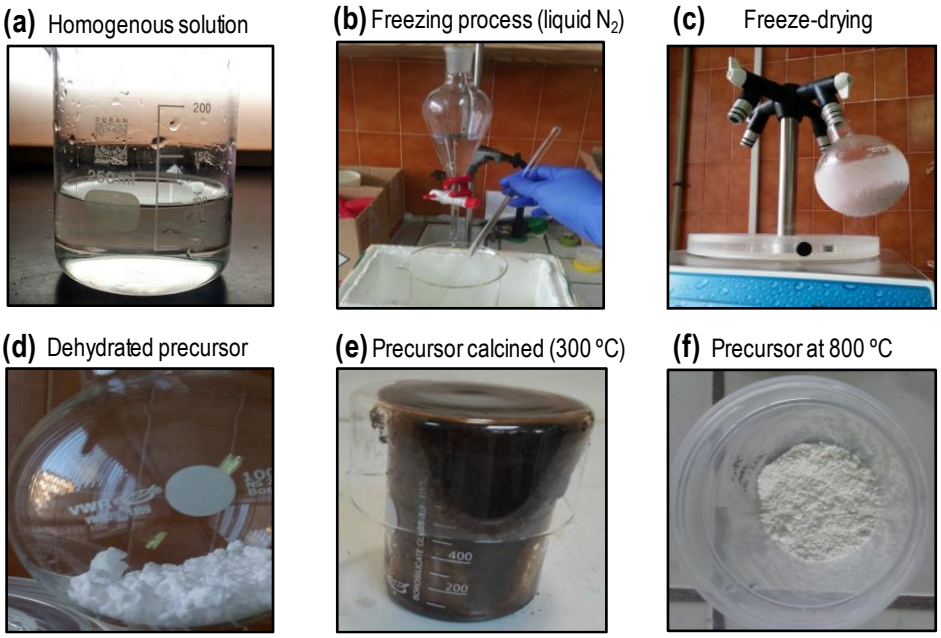

Figure 3.2. Different steps employed to obtain precursor powders by the freeze-drying method.

3.2. Preparation of electrolyte pellets

Commercial powders of $Zr_{0.84}Y_{0.16}O_{1.92}$ (YSZ, Tosoh), $Ce_{0.9}Gd_{0.1}O_{1.95}$ (CGO, Rhodia) and $La_{0.9}Sr_{0.1}Ga_{0.8}Mg_{0.2}O_{2.85}$ (LSGM, Kceracell) were used for the electrolyte preparation. The powders were pressed uniaxially into pellets of 10 and 1 mm of

UNIVERSIDAD DE MÁLAGA

diameter and thickness, respectively, and then sintered at 1400 ºC for 4 h to achieve relative densities above 95 %.

For the preparation of infiltrated electrodes into a porous backbone, porous CGO layers were previously deposited onto dense YSZ pellets by screen-printing a slurry of 50 wt.% CGO powders and Decoflux™ binder (Zschimmer and Schwarz). The porous CGO backbone was sintered at 1100 ºC for 1 h to ensure sufficient adhesion with the electrolyte.

3.3. Spray-pyrolysis deposition

Spray-pyrolysis is a versatile technique to prepare layers with different compositions, such as metal oxides and composite materials, with a wide variety of morphologies on different substrates [2]. In comparison to other deposition techniques, such as spin-coating, pulsed laser deposition (PLD) or magnetron-sputtering, spray-pyrolysis has demonstrated to be an efficient and economical approach, showing several advantages: (i) automatable, scalable over large areas and highly reproducible; (ii) simple preparation of layers in just one deposition step, lowering fabrication costs and time and (iii) high vacuum is not necessary to achieve high-quality films [2–5].

The spray-pyrolysis process is relatively simple. Firstly, a precursor solution was prepared and then sprayed onto a heated substrate (Figure 3.3). The substrate was placed on an aluminium block, which has inside four thermal resistances to homogeneously heat the substrates. The temperature was measured with a K-type thermocouple and controlled by a Eurotherm 3208 PID. The flow rate of the precursor solution (20 mL h^{-1}) was controlled by a syringe pump (Micrux NE-300). In order to achieve high reproducibility and homogeneity over large areas, the aluminium block was continuously moved under the spray nozzle by an electric motor.

The precursor solution was atomized by Venturi effect in a spray nozzle using compressed air. The resulting fine drops impacted on the heated substrate surface, evaporating the solvent and thermally decomposing the precursors, obtaining a layer.

UNIVERSIDAD DE MÁLAGA

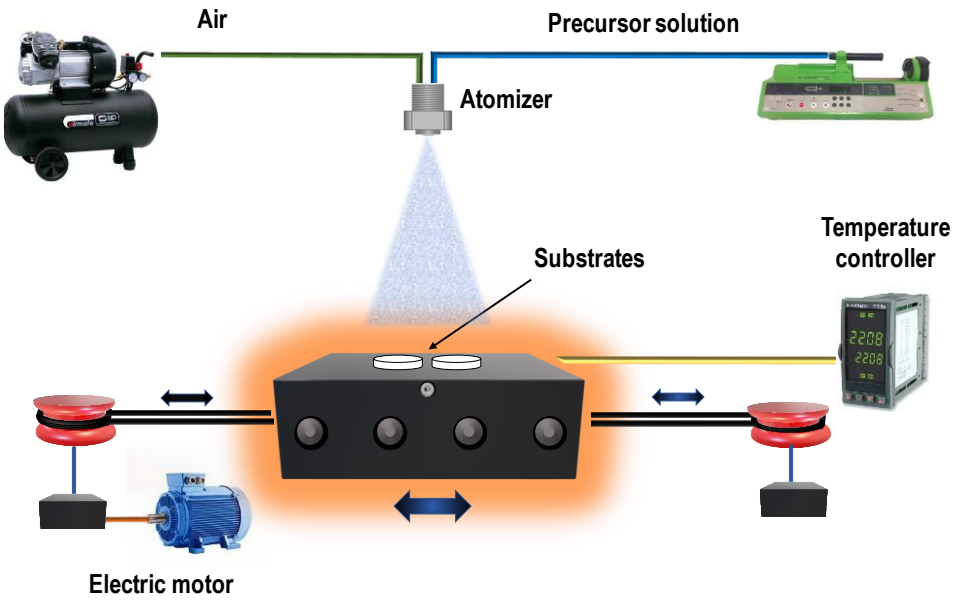

Figure 3.3. Illustration of the spray-pyrolysis system employed to obtain thin films on a substrate.

In general, the morphology and thickness of the layer can be easily tailored by controlling the deposition conditions, such as the precursor solution (salts employed, concentration, complexing agents or solvents), the nature of the atomization process (ultrasonic, pneumatic or electrostatic), the substrate (chemical composition, deposition temperature, nebulizer-substrate distance). The most relevant parameters to control the film morphology are summarized in the next paragraphs:

- **Precursor solution composition**. The composition of the precursor solution is one of the most important parameters to optimize the layer morphology, *i.e.* metal salts, solvent, cation concentration, additives, solution viscosity and surface tension because they will affect the size of the atomized droplets:

– *Metal salt*: Although any metal salt can be potentially employed for preparing a precursor solution, the solubility and decomposition temperature are two very important factors that will determine the morphology of the film [6]. Inorganic

UNIVERSIDAD DE MÁLAGA

metal salts like nitrates, chlorides, carbonates, oxalates and acetates can be used. However, the decomposition temperature of the nitrate salts is usually lower, avoiding the presence of undesired residues such as Cl from chloride salts.

– *Complexing agents*: In order to avoid the cation precipitation in the precursor solution and favour the phase formation, complexing agents like ethylenediaminetetraacetic acid (EDTA) or citric acid have been successfully employed in our research group for the synthesis of the different electrode layers. In addition, they have demonstrated to play a key role in the phase formation of different air electrodes, such as $SrFe_{0.8}Ti_{0.2}O_{3-\delta}$ or $PrBaCo_2O_{5+\delta}$ [7,8].

– *Solvent*: The choice of the right solvent is very important due to each one has a particular viscosity, vapour pressure, surface tension and solubility properties for the salts. All these will affect the droplet formation and then, to the morphology and quality of the film. Water is widely used because most metal salts are highly soluble in this solvent. Furthermore, it is safe and minimizes costs. However, organic solvents like ethanol, glycerol or acetic acid are also used. In this study, only water was used as a solvent.

- **Deposition temperature.** The deposition temperature significantly affects the evaporation of the atomized droplets and the decomposition of the precursors. Hence, the deposition temperature is one of the most important parameters to optimize the layer morphology. In particular, thin and dense layers are obtained at high temperature, due to the complete decomposition of the precursors. On the other hand, porous and thick layers are obtained at low temperatures because of the remaining solvent and carbonaceous species in the as-deposited layer, which induce porosity after calcination at higher temperatures (Figure 3.4a,b).

- **Atomization process.** The precursor droplet size and velocity depend on the atomizer. Ultrasonic, pneumatic and electrostatic nebulizers are the most used in spray-pyrolysis deposition. In this PhD thesis, we have employed a pneumatic

UNIVERSIDAD DE MÁLAGA

atomizer, which has several advantages like higher atomization rate and droplet velocity, as well as easier scalability. In a pneumatic atomizer, the precursor solution is atomized by a high-speed air flow, generating the droplets by the Venturi effect (Figure 3.4c). It has to be noted that it is critical to obtain a uniform droplet size distribution and an optimal nozzle-substrate distance to achieve high-quality films.

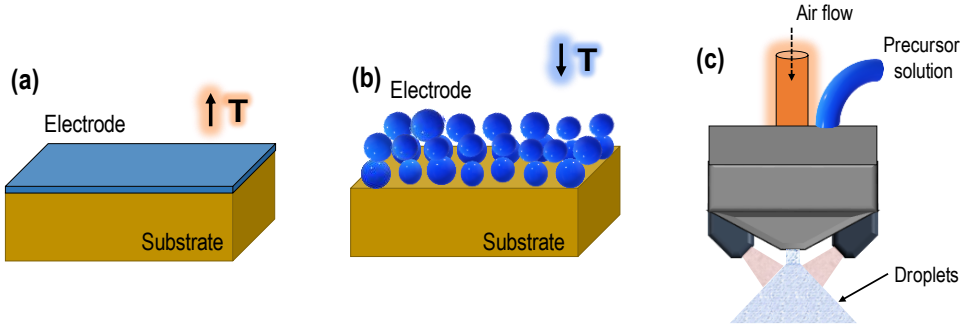

Figure 3.4. Schematic representation of (a) dense and thin film obtained at high deposition temperature, (b) thick and porous film obtained at low temperature and (c) pneumatic atomizer.

In this PhD thesis, a homemade spray-pyrolysis equipment was employed to obtain nanostructured electrodes and active layers with different morphologies and compositions on different electrolyte materials. For the spray-pyrolysis deposition, an aqueous precursor solution containing stoichiometric amounts of the metal nitrates was prepared with a final cation concentration of 0.02 mol L^{-1}. Additionally, EDTA was added as a chelating agent in different ligand:metal molar ratios, between 0.25:1 and 1:1, depending on the electrode composition. Table 3.1 shows the metal salts employed for the preparation of the precursor solutions in Chapters 4-7.

The deposition temperature to obtain homogeneous films with good adhesion to the electrolyte was optimized for the different electrode compositions (250-450 ºC). The nozzle-substrate distance, solution flow rate and air pressure were fixed to 25 cm, 20 mL h^{-1} and 2 bars, respectively. The deposition time for the electrode films and thin active layers was 60 and 30 minutes, respectively. After the deposition, the electrodes were slowly calcined in air at 800 ºC for 1 h to achieve crystallization (2 ºC min^{-1}).

UNIVERSIDAD DE MÁLAGA

Table 3.1. Reagents (supplied by Merck) and EDTA:Metal molar ratio used for the preparation of the different layers by spray-pyrolysis. Purity is indicated in parentheses.

Chapter 4	Chapter 5	Chapter 6	Chapter 7
$La(NO_3)_3 \cdot 6H_2O$(99.99%)	$Sr(NO_3)_2$(99%)	$La(NO_3)_3 \cdot 6H_2O$(99.99%)	$La(NO_3)_3 \cdot 6H_2O$(99.99%)
$Cr(NO_3)_3 \cdot 9H_2O$(100%)	$Pr(NO_3)_3 \cdot 6H_2O$(99.9%)	$Sr(NO_3)_2$(99%)	$Sr(NO_3)_2$(99%)
$Sr(NO_3)_2$ (99%)	$Ti[OCH(CH_3)_2]_4$(97%)	$Fe(NO_3)_2 \cdot 9H_2O$(99.99%)	$Mn(NO_3)_2 \cdot 6H_2O$(98%)
$Ca(NO_3)_2 \cdot 4H_2O$(99%)	$Ce(NO_3)_3 \cdot 6H_2O$(99.99%)	$Ti[OCH(CH_3)_2]_4$(97%)	$Pr(NO_3)_3 \cdot 6H_2O$(99.9%)
$Mn(NO_3)_2 \cdot 6H_2O$(98%)	$Gd(NO_3)_3 \cdot 6H_2O$(99.9%)	$Ni(NO_3)_2 \cdot 6H_2O$(97%)	$Ce(NO_3)_3 \cdot 6H_2O$(99.99%)
$Fe(NO_3)_2 \cdot 9H_2O$(99.99%)		$Ce(NO_3)_3 \cdot 6H_2O$(99.99%)	$Gd(NO_3)_3 \cdot 6H_2O$(99.9%)
$Ti[OCH(CH_3)_2]_4$(97%)		$Gd(NO_3)_3 \cdot 6H_2O$(99.9%)	$Bi(NO_3)_3 \cdot 6H_2O$ (99.99%)
$Cu(NO_3)_2 \cdot 3H_2O$(100%)			$Y(NO_3)_3 \cdot 6H_2O$(99.8%)
$Ce(NO_3)_3 \cdot 6H_2O$(99.99%)			
$Gd(NO_3)_3 \cdot 6H_2O$(99.9%)			
EDTA:Metal (0.25:1)	EDTA:Metal (1:1)	EDTA:Metal (0.25:1)	EDTA:Metal (0.25:1)

3.4. Pulsed laser deposition (PLD)

Pulsed laser deposition (PLD) is a physical technique that ablates a target material with a high-energy pulsed laser in a vacuum chamber. Each pulse of the laser vaporizes and ionizes a part of the target surface, generating a plasma plume composed of ions, atoms and electrons, which condense on the substrate growing a thin film (Figure 3.5).

The most important components of a PLD equipment are the optical system, the excimer laser, the vacuum chamber, the target/substrate holders and the heating system [9–11]. Different parameters, such as pulse repetition frequency, pressure in the chamber and gas employed (*i.e.* O_2, N_2 or Ar), deposition temperature or target-substrate distance are crucial to achieve good quality films with high crystallinity and homogeneity.

UNIVERSIDAD DE MÁLAGA

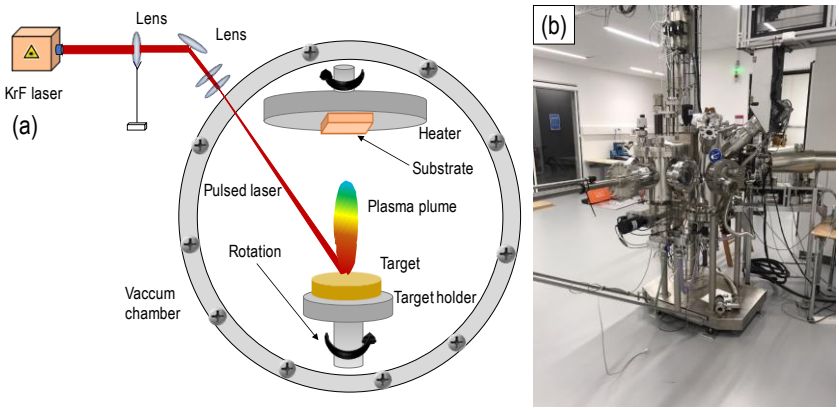

Figure 3.5. (a) Schematic representation of a PLD system and (b) PLD equipment at the Technical University of Denmark (DTU).

The main advantages of PLD to deposit thin films are: (i) high quality and homogenous films with thicknesses ranging from 5 to 200 nm, (ii) the possibility to obtain films with a complex cation stoichiometry and (iii) the growth rate can be tailored because of the pulsed nature of the film deposition. However, the slow deposition rate, the reduced deposition area and the optimization of the parameters to obtain high-quality films are some of its main drawbacks. Interestingly, thin films with different microstructural architectures can be obtained; for instance, single compounds, multilayer materials (composed of two or more alternating layers) or Vertically Aligned Nanostructures (VAN) of two different materials with a columnar microstructure [9].

In this PhD thesis, the PLD technique was employed to deposit VANs of $(La_{0.8}Sr_{0.2})_{0.95}Fe_{0.8}Ti_{0.2}O_{3-\delta}$-CGO, and $(Sr_{0.7}Pr_{0.3})_{0.95}Ti_{0.9}Ni_{0.1}O_{3-\delta}$-CGO on different (001) single crystals of $SrTiO_3$ (STO), YSZ and $(LaAlO_3)_{0.3}(Sr_2TaAlO_6)_{0.7}$ (LSAT). The properties of the VANs were compared to those obtained for the single films.

The targets for the PLD deposition were prepared by solid-state reaction from the corresponding oxides or carbonates, La_2O_3, $SrCO_3$, Fe_2O_3, TiO_2, Pr_6O_{11} and NiO (Merck, purity >99.5%), previously heated at 1000 ºC for 1 h. All the powders were mixed in stoichiometric amounts in an agate mortar for 15 min and then calcined at 1200 ºC for 1 h. After that, the powders were grounded in a planetary ball mill (Pulverisette 7) in absolute ethanol media. The dry powders were uniaxially pressed into disks of 25 cm of diameter and sintered at 1400 and 1500 ºC for 1 h for $LSFT_{0.2}$

UNIVERSIDAD DE MÁLAGA

and SPTNO, respectively, with a heating and cooling rate of 5 ºC min^{-1}. A similar procedure was followed for $LSFT_{0.2}$-CGO and SPTNO-CGO targets (50 wt.%), where the commercial CGO powders were mixed with the $LSFT_{0.2}$ and SPTNO powders (previously calcined at 1200 ºC). Finally, the powders were pressed into disks of 25 cm of diameter and sintered at 1300 and 1400 ºC for 1 h for $LSFT_{0.2}$-CGO and SPTNO-CGO, respectively. In all cases, the relative density was higher than 97%.

The equipment employed for the deposition was a Surface PLD with a KrF laser (Coherent Lambda Physic GmbH) with a target-substrate distance of 18 mm and a vacuum pressure of $6.67 \cdot 10^{-3}$ mbar in O_2 at 650 ºC and repetition rate of 10 Hz for 20 min. This research was carried out during two research stays for a total of 7 months at DTU Energy Conversion and Storage at the Technical University of Denmark (DTU), under the supervision of Profs. Nini Pryds and Vincenzo Esposito.

3.5. X-ray diffraction (XRD)

X-ray diffraction (XRD) is a non-destructive analytical technique to study the crystallographic structure of materials. XRD is based on exposing a crystal to an incident X-ray beam, which has a wavelength similar to the interatomic distance in an ordered crystal structure, producing a scattering by the electrons of the atoms (Figure 3.6a).

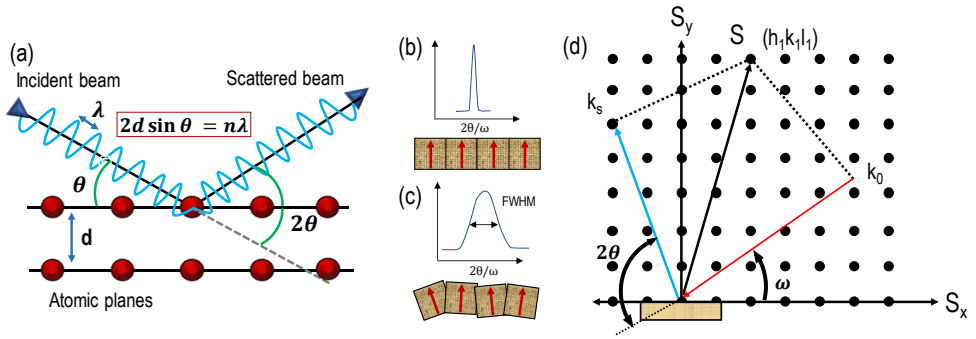

Figure 3.6. Representation of (a) the interaction of the X-ray incident beam with the sample in a θ-2θ XRD measurement, (b,c) rocking curve and (d) reciprocal space map.

Because of the structural periodicity, the interaction between the material and the beam light creates constructive interferences at certain scattering angles, according to the Bragg's law (Eq. 3.1):

UNIVERSIDAD DE MÁLAGA

$$2d_{hkl} \sin\theta = n\lambda \qquad \text{(Eq. 3.1)}$$

where d_{hkl} is the interplanar distance, (h,k,l) are the Miller indexes, θ is the incident angle of X-ray beam, n is a positive integer number and λ is the wavelength of the incident radiation. A complete XRD pattern is obtained by varying the incident angle of the X-ray beam.

In this PhD thesis, XRD with a Bragg-Brentano geometry was employed to determine the crystal structure, lattice parameters, phase identification and quantitative analysis using the Rietveld method. These measurements were performed using a PANalytical X'Pert PRO equipped with a Ge(111) monochromator using $CuK_{\alpha1}$ monochromatic radiation or a PANalytical Empyrean with $CuK_{\alpha1,2}$ radiation between 2θ=10-100º with a step of 0.01º, both located at the "Servicios Centrales de Apoyo a la Investigación (SCAI)'' at the University of Málaga. The crystallise size of the samples was estimated by the Scherrer's equation from the broadening of the peaks in the XRD pattern (Eq. 3.2).

$$D = \frac{0.94\lambda}{\beta\cos\theta} \qquad \text{(Eq. 3.2)}$$

where β is the full width at the half maximum of the peak corrected with the instrument broadening by using a standard LaB_6 material.

Additionally, rocking curve, reciprocal space mapping and phi-scan analysis were performed for the characterization of epitaxial films deposited by PLD. These studies were carried out in a Rigaku Smartlab at DTU. The phase identification was carried out using the X'Pert High Score software.

– *Rocking Curve* analysis (RC)

This technique was used to study the thickness, strain and lattice mismatch on thin layers obtained by PLD. The rocking curve of a specific crystal reflection provides valuable information about the quality of the crystalline lattice. In these measurements, the sample angle (ω) is scanned with the detector angle (2θ) fixed,

UNIVERSIDAD DE MÁLAGA

when the Bragg angle is previously obtained [12]. The resulting plot of ω vs intensity is known as a rocking curve (Figure 3.6b,c).

– *Reciprocal Space Mapping* (RSM)

Reciprocal Space Mapping (RSM) can be employed to determine the structural properties of epitaxial films such as layer tilting, lattice relaxation or crystal quality. This is an extension of the rocking curve technique to study the strain or mismatch in a thin film [13–15]. These measurements are obtained by collecting series of ω-2θ scans at different omega offsets (Figure 3.6d).

3.5.1. Rietveld method

The Rietveld method is used to analyse the X-ray diffraction patterns by fitting different parameters, such as background, scale factor, cell parameter and atomic positions, among others. Previous to the refinement, the crystal structure of the sample has to be identified to further obtain the calculated patterns [16–18]. The Rietveld refinements were carried out using the GSAS program, which takes into account not only the Bragg peaks but also the entire angular region, including the background, the peak width and intensity. The refinement of the X-ray diffraction pattern is based on minimizing a function S_y by the method of least squares (Ec. 3.3):

$$S_Y = \sum_i W_I (Y_I - Y_{calc})^2 \qquad \text{(Ec. 3.3)}$$

where W_I is a weighting factor, Y_I is the experimental intensity and Y_{calc} is the calculated intensity at the i^{th} step. The quality of the fit can be determined by different parameters such as the residual R_F and the weighted residual R_{wp}, disagreement factors that should be lower than 10% to confirm the good fitting of the experimental X-ray diffraction data. The starting structural models for the Rietveld analysis were obtained from the Inorganic Crystal Structure Database (ICSD).

UNIVERSIDAD DE MÁLAGA

3.6. X-ray photoelectron spectroscopy (XPS)

X-ray Photoelectron Spectroscopy (XPS) is used to characterize the chemical composition and oxidation states of the elements presented on the material surface. X-ray radiation is used to induce the photoexcitation of the electrons from the different atoms of the sample (Figure 3.7a). The released electrons have a characteristic kinetic energy that is proportional to the binding energy of the electron of a certain atom (Eq 3.4). After detecting the kinetic energy of the electrons, the binding energy can be calculated just by knowing the wavelength of the incident photoelectrons [19–21].

$$KE=E-(BE+\Phi) \qquad \text{(Eq 3.4)}$$

where *KE* is the measured kinetic energy of the photoelectron; *E*, is the initial energy of the incident photoelectron; *BE*, is the binding energy of the electron and *Φ*, is the energy lost, which depends on the instrument.

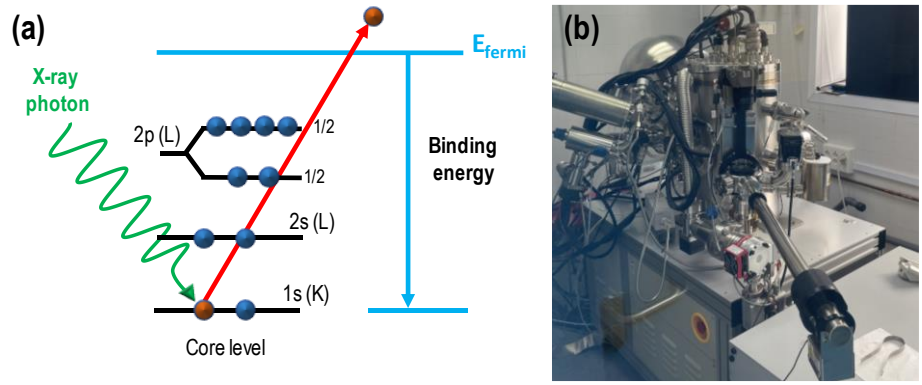

Figure 3.7. (a) Representation of the XPS process and (b) XPS instrument used in this work.

The samples were characterized in a Physical Electronics PHI-VERSAPROBE II using a monochromatic AlK_{α} source (1486.6 eV, 15 kV) (Figure 3.7b). The studied area was fixed to 200 µm and the vacuum in the chamber was maintained below $2.0 \cdot 10^{-7}$ Pa during the spectra acquisition. Before the measurements, the spectrometer was calibrated using the Cu $2p^{3/2}$, Ag $3d^{5/2}$ and Au $4f^{7/2}$ bands with binding energies of 932.7, 368.3 and 84.0 eV, respectively.

UNIVERSIDAD DE MÁLAGA

3.7. Scanning electron microscopy (SEM)

Scanning electron microscopy (SEM) is used to study the microstructure of the materials. In this technique, an electron beam is focused on the sample surface, being possible to obtain images from both backscattered electrons (BE) and secondary electrons (SE), respectively. In the case of the backscattered electrons, areas with higher atomic number (Z) appear "brighter", since the probability of an elastic interaction is higher for large atoms. On the other hand, secondary electron detectors give better information about the surface and microstructure of the sample. This technique was employed to study the morphology, porosity, electrode thickness and grain size of the materials. Previous to the SEM characterization, due to the poor conductive properties of the samples, an iridium layer of ~2 nm thickness was deposited by sputtering.

The samples were analysed in a Dual Beam Field Emission Scanning Electron Microscope with a Focused Ion Beam (FESEM-FIB, Helios Nanolab 650) at the University of Málaga (Figure 3.8a). The electron beam is generated from a tungsten single crystal at a relatively low voltage, achieving higher resolution than a traditional SEM with a thermionic gun. Energy dispersive X-ray spectroscopy (EDS, Oxford instruments) was employed for the chemical characterization of the materials (Figure 3.8b,c). This technique was crucial to confirm the formation of nanocomposite materials, the formation of reaction products at the interface between the different layers of the cell, as well as cation interdiffusion between the cell components. It has to be noted that for quantitative analysis, it is necessary a previous calibration with different standards. In principle, all elements from Beryllium to Uranium can be detected but the accuracy and sensibility of the measurement of light elements with $Z < 10$ is lower due to the adsorption of the heavy atoms present in the sample.

Additionally, this microscope incorporates a focused ion beam (FIB) of Ga^{3+} to prepare ultrathin lamellas of the thin films prepared by PLD, which were further analysed by Transmission Electron Microscopy (TEM).

UNIVERSIDAD DE MÁLAGA

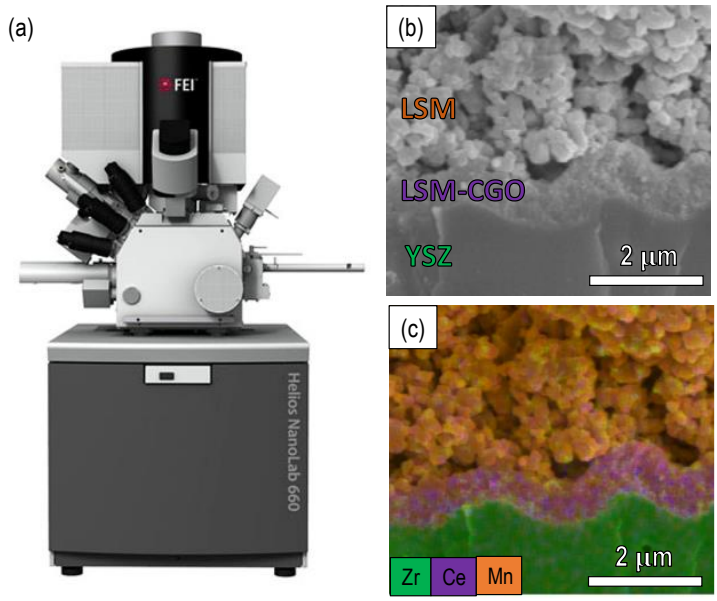

Figure 3.8. (a) FESEM-FIB Helios Nanolab 650 and (b,c) EDS mapping showing the cation distribution.

3.8. Transmission electron microscopy (TEM)

This technique consists in the transmission of a highly focused electron beam through an ultrathin sample at an ultra-high vacuum. The interaction between the electrons and the sample generates an image, which can be focused and monitored by a CCD camera. TEM is widely used to analyse the microstructure at the nanoscale, the lattice defects, grain size or deeply study the crystalline structure. There are different working modes when operating in a transmission electron microscope.

One of the most employed modes is *bright field* imaging, in which the image is produced by the non-diffracted electron beam that passes through a very thin film (Figure 3.9a,b). The thicker particles appear darker than the thin areas, also giving information about the sample thickness. This mode is very useful to identify crystal lattice defects or atomic ordering. In the diffraction mode, the *Selected Area Electron Diffraction* (SAED) patterns are obtained from the diffracted electrons of the sample, where polycrystalline areas produce a ring pattern (Figure 3.9c) meanwhile a single crystal generates a spot pattern (Figure 3.9d). The HRTEM images were analysed

UNIVERSIDAD DE MÁLAGA

with the Digital Micrograph software from Gatan to determine the interplanar distances and the fast Fourier transform (FFT) of the crystalline domains.

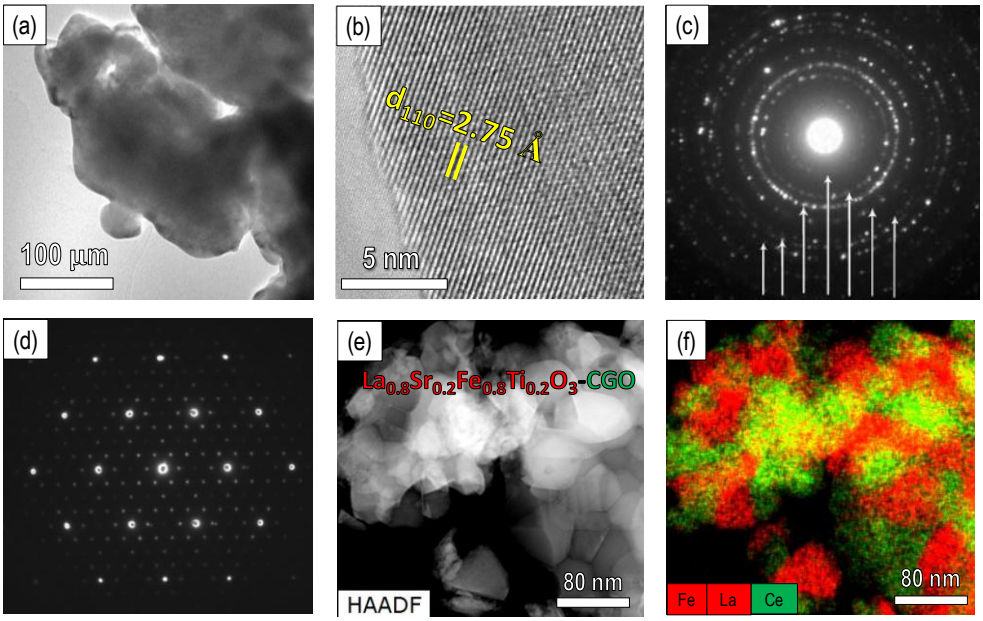

Figure 3.9. (a) Bright field and (b) HRTEM image; (c) ring and (d) SAED pattern obtained by electron diffraction; (e) HAADF-STEM image and (f) EDS analysis.

A Talos F200X was employed for the TEM characterization. This TEM can operate in both bright and dark field modes and also scanning transmission electron microscopy (STEM). STEM scans a very focused electron beam over the sample in a raster pattern. High Angle Annular Dark Field (HAADF)-STEM images provides information about the morphology of the sample, which can be combined with EDS analysis to obtain information about the chemical composition of the sample (Figure 3.9e,f) [22,23].

3.9. Atomic Force Microscopy (AFM)

Atomic Force Microscopy (AFM) was employed for studying the surface topography of the samples prepared by PLD with an extremely sharp tip attached to a small cantilever [24,25]. The two main operating modes are the contact and tapping modes. When the tip contacts the sample surface, the cantilever bends, process that

UNIVERSIDAD DE MÁLAGA

is controlled by a laser and a photodetector generating an image (Figure 3.10a), obtaining information about the sample morphology.

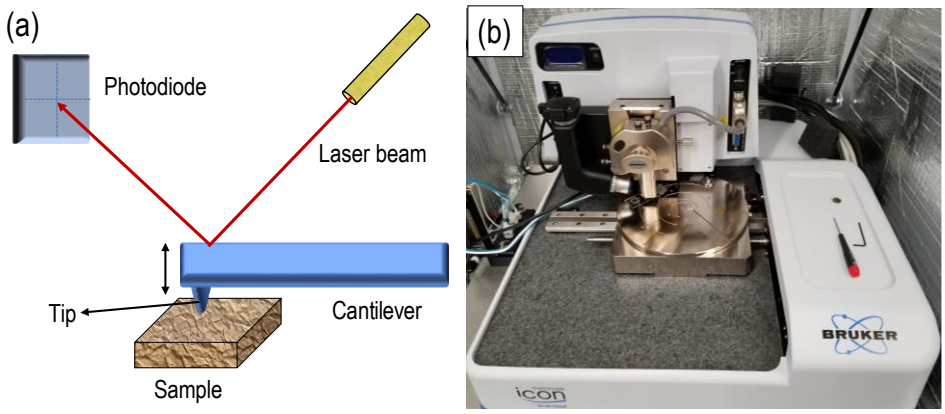

Figure 3.10. (a) Illustration of the AFM technique and (b) image of the Bruker AFM.

In tapping mode, the cantilever vibrates near its resonance frequency, moving the tip up and down close to the sample surface. The resonance frequency of the probe is affected by the irregularities of the sample surface, but a piezoelectric system is employed to maintain the same tip-surface distance. This fact causes a variation of the cantilever height depending on the sample morphology, information that is collected by the photodetector to generate the image.

A Bruker Icon Dimension AFM working in tapping mode with a silicon nitride tip and a typical XYZ scan range of 10 x 10 x 10 μm^3 was employed to characterize the samples prepared by PLD (Figure 3.10b).

3.10. Electrical measurements

3.10.1. Electrochemical impedance spectroscopy (EIS)

The electrochemical properties of the different electrodes for SOFC applications were studied by Electrochemical Impedance Spectroscopy (EIS). This technique has been used to determine the electrolyte resistance, including bulk and grain boundary contributions; the polarization resistance of the electrodes in two and three-electrode configuration at open circuit voltage and different dc-bias, respectively

UNIVERSIDAD DE MÁLAGA

[26–28]. The different electrochemical processes that take place in a single fuel cell were also determined by EIS, such as ohmic resistance, cathode and anode contributions (*i.e.* charge transfer, diffusion limitations, etc.)

EIS is based on applying a sinusoidal voltage with a variable frequency (*w*) to a sample and measuring the transient current generated [29]. The applied voltage can be described as follows (Eq. 3.5):

$$E(t) = E_o \cdot \text{sen}(wt) \qquad \text{(Eq. 3.5)}$$

where $E(t)$ is a voltage as a function of time, E_o is the dc voltage amplitude and w is the angular frequency.

The current generated in the electrochemical system can be described as (Eq. 3.6):

$$I(t) = I_o \cdot \text{sen}(wt+\phi) \qquad \text{(Eq. 3.6)}$$

where $I(t)$ is the current as a function of time and ϕ is the phase shift between the voltage and the current. Similarly to the Ohm's law, the impedance can be described as (Eq. 3.7):

$$Z(t) = \frac{E(t)}{I(t)} = \frac{E_o \cdot \text{sen}(wt+\phi)}{I_o \cdot \text{sen}(wt+\phi)} = |Z|e^{-j\phi} \qquad \text{(Eq. 3.7)}$$

Hence, the impedance can be also written as a function of real and imaginary components (Eq. 3.8):

$$Z(\omega) = |Z|(\cos\phi + j\,\text{sen}\,\phi) = Z'(w) + jZ''(w) \qquad \text{(Eq. 3.8)}$$

The plot of the imaginary component (Z'') and the real component (Z') is known as impedance spectra or Nyquist plots. In polycrystalline materials, the conductive species have to go through both the bulk and the grain boundary region. The resistance of the conduction at the grain boundaries is different and thus the capacity associated with this process is also different. For this reason, two arcs are observed in an ionic-conductor ceramic electrolyte (Figure 3.11).

UNIVERSIDAD DE MÁLAGA

Additional resistance contributions are observed at low frequencies, which are related to electrode processes, such as charge transfer and diffusion or interfacial processes at the electrode surface. The resistance of each process can be obtained from the diameter of each arc. The capacity of each process can be determined from the relaxation frequency (the frequency at the maximum of each contribution) with the following equation (Eq. 3.9):

$$f_{max} = \frac{1}{2\pi RC} \qquad \text{(Eq. 3.9)}$$

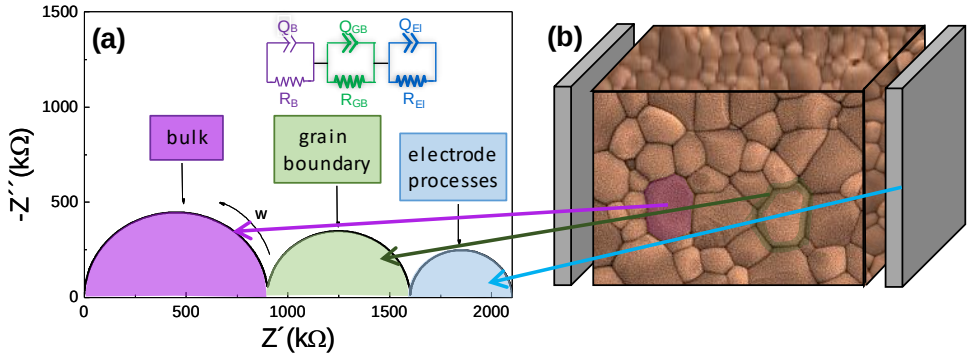

Figure 3.11. (a) Impedance spectra and (b) schematic representation of a ceramic material showing the bulk, grain boundary and electrode contributions to the total resistance.

3.10.2. Equivalent circuit analysis

EIS spectra of a solid oxide cell typically show different contributions attributed to the electrolyte resistance, *i.e.* bulk and grain boundary conduction in the electrolyte and different electrode processes, such as oxygen/hydrogen adsorption/dissociation and oxygen/hydrogen atom reduction/oxidation on the electrode surface, gas diffusion or charge transfer at the electrolyte/electrode interface, etc. All these processes have different resistance and capacitance values (Table 3.2). Each contribution in the impedance spectra can be ideally simulated by an equivalent circuit formed by a resistance in parallel with a capacitor, which is a semicircle with centre in the real Z´ axis. In order to fit all the contributions of a cell, a linear combination of several *RC* elements can be used.

UNIVERSIDAD DE MÁLAGA

Table 3.2. Typical capacity values for different processes in a ceramic fuel cell [27].

Process	Capacitance (F cm^{-1})
Bulk	10^{-12}
Secondary phases	10^{-11}
Grain Boundary	10^{-8}-10^{-11}
Electrode/material interface	10^{-5}-10^{-7}
Electrochemical reaction	10^{-4}

Sometimes, these processes cannot be simulated by using ideal (RC) elements because depressed arcs are observed with the centre below the Z´ axis. This phenomenon can be explained by the fact that the relaxation frequency has not a single value but a discrete distribution due to the presence of inhomogeneities in the materials. In this case, the ideal capacitance (C) is substituted by a constant phase element with a capacitance value (Eq. 3.10):

$$Z_{CPE} = \frac{1}{Q(j\omega)^n} \qquad \text{(Eq. 3.10)}$$

where *Q* is a pseudo-capacitance and *n* ranges between $0 \leq n \leq 1$ [30]. In the particular case of $n=1$, the impedance is equal to an ideal condenser [27,31,32]. In order to fit the impedance spectra, several serial (RQ) elements were employed to simulate the electrode contributions to the overall electrode polarization. In addition, an inductance L and a series resistance R_s are also included to take into account the inductive effects of the electrical connections of the cell and the ohmic contribution of the electrolyte, respectively (inset Figure 3.11a). For each electrode contribution, the resistance R_i, the pseudocapacitance Q_i and the exponential parameter n_i were obtained. These parameters are related to the real capacitance C_i by the following relation (Eq. 3.11):

$$C_i = \frac{(R_i Q_i)^{1/n_i}}{R} \qquad \text{(Eq. 3.11)}$$

The EIS measurements were performed in a Solartron 1260 FRA (frequency response analyzer) with an ac amplitude of 50 mV at high temperatures and 100 mV at low temperatures (T < 350 ºC), in a frequency range from 10^6 to 10^{-2} Hz. The

UNIVERSIDAD DE MÁLAGA

measurements were taken at different temperatures between 800-200 ºC on cooling with a stabilization time of 30 minutes between consecutive measurements under different atmospheres (Air, 5% H_2-Ar and H_2) in a homemade electrochemical cell (Figure 3.12). The impedance spectra were analysed and adjusted with Zview and Zplot software. For the electrochemical measurements, CDT temperature controller software with Eurotherm 808 was employed.

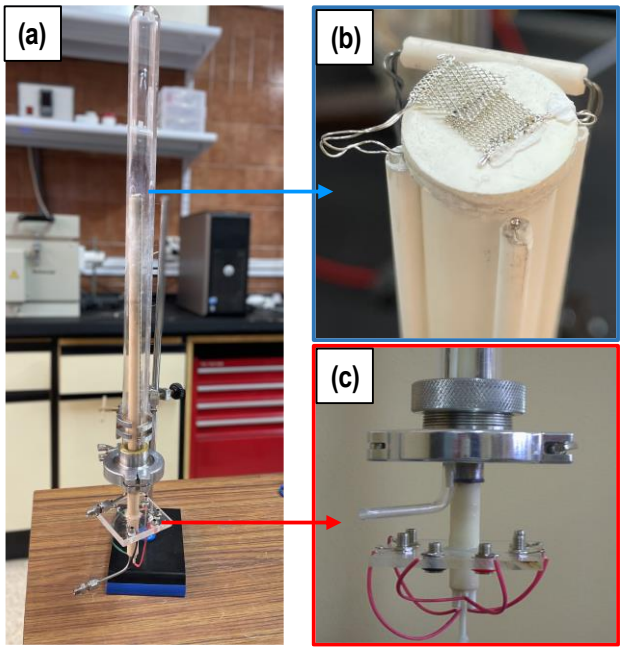

Figure 3.12. (a) Image of the electrochemical cell (b) Pt wires and thermocouple and (c) the cell connections.

3.10.3. Distribution of relaxation times (DRT)

In some cases, the different contributions in the impedance spectra appear overlapped and they cannot be differentiated by equivalent circuit fitting. In this case, distribution of relaxation times (DRT) is an alternative approach to deconvolute EIS spectra [33]. The interpretation of EIS data by equivalent circuit models is sometimes challenging and less accurate because it is necessary to have a hypothesis about how many processes compose the spectra. This step is crucial to correctly identify the

UNIVERSIDAD DE MÁLAGA

number of electrochemical processes, avoiding misattributions and over-fitted data [33–35].

One of the main advantages of the DRT method is that a model or previous knowledge about the electrochemical system is not required (Figure 3.13). In order to elucidate the specific electrochemical processes, the impedance spectra can be modelled as:

$$Z_{DRT}(f)=2i\pi L_o+R_s+R_p\int_{-\infty}^{\infty}\frac{\gamma(\log\tau)}{1+2i\pi f\tau}\,d\log\tau \qquad \text{(Eq. 3.11)}$$

where L_o, R_s, f and $\gamma(\log\tau)$ are attributed to the inductance of the equipment, ohmic resistance of the electrolyte, frequency and DRT, respectively. The $\gamma(\log\tau)$, DRT, determines the time scale distribution. The time constant, τ, can be also expressed as (Eq. 3.12), where ω is the angular frequency:

$$\tau=\frac{1}{2\pi f}=\frac{1}{\omega} \qquad \text{(Eq. 3.12)}$$

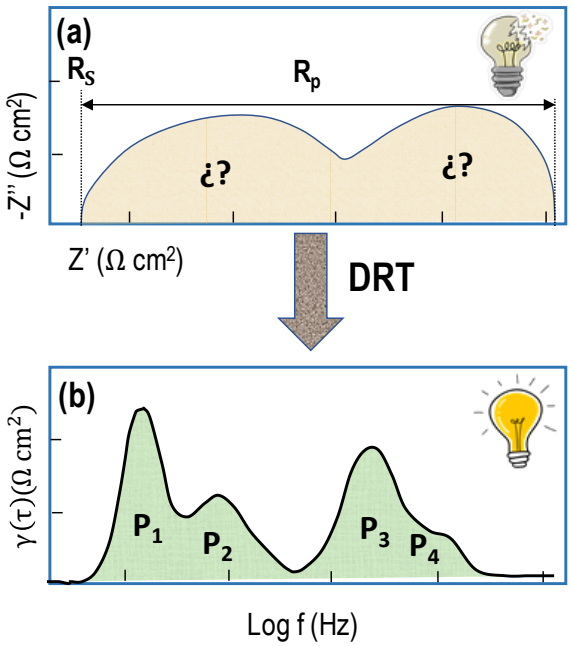

Figure 3.13. (a) Impedance spectra with an unknown number of processes and (b) DRT spectra clearly showing the different electrode contributions.

UNIVERSIDAD DE MÁLAGA

In this PhD thesis, the inversion of the impedance data to DRT was carried out by the DRTtools software developed by Ciucci *et col*. [36], which is based on employing the Tikhonov regularization [37]. This software leads to a plot with different peaks related to relaxation processes of each contribution. Additionally, the area under the peak is proportional to the resistance of each contribution. Thus, the resistance of the different processes of an impedance spectrum can be determined from the deconvolution of the DRT data.

3.10.4. Variation of the polarization resistance under a dc bias

Typically, the electrode polarization resistance (R_p) is studied under Open Circuit Voltage (OCV) in a symmetrical cell configuration (2-probe method). However, the electrode response under OCV cannot be directly extrapolated to a real SOFC due to the electrode overpotential during the fuel cell operation, drastically affecting the electrochemical performance [38].

In order to study the performance of the cell at different overpotentials, the impedance spectra were collected at different external dc-current using a three-probe configuration (Figure 3.14) [38,39]. A circular working (WE) and counter electrodes (CE) were deposited symmetrically onto dense electrolyte pellets of 20 mm of diameter. A Pt-ring surrounding the working electrode was employed as a reference electrode (RE) for the 3-probe configuration. The electrodes were tested by EIS at different temperatures under both cathodic and anodic polarization between 0 and ± 0.4 V using a Zahner XC potentiostat/galvanostat/FRA.

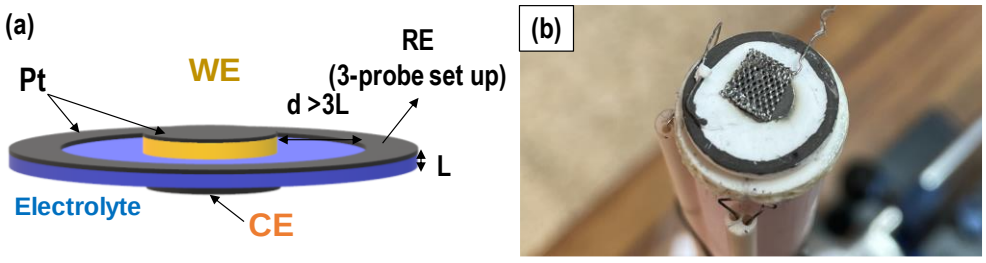

Figure 3.14. (a) Illustration of the 3-probe electrode configuration employed in this PhD thesis and (b) homemade electrochemical cell.

UNIVERSIDAD DE MÁLAGA

3.10.5. Impedance spectra at different oxygen partial pressure (pO_2)

The electrode processes involved in the oxygen reduction reaction (ORR) are not only dependent on the temperature but also depend on the oxygen partial pressure (pO_2). The relationship between the resistance of the rate-limiting steps of the electrode polarization and the oxygen partial pressure can be described as follows (Eq 3.13):

$$R_i = R_i^0 (pO_2)^{-m} \qquad \text{(Eq. 3.13)}$$

where R_i^0 is a constant and the exponent m provides information about the species involved in the ORR. The main electrochemical processes involved in the ORR are identified from the reaction order m. In particular, the process with negligible pO_2 dependence (m = 0) is associated with oxide-ion transport at the electrode/electrolyte interface. The oxygen dissociation and diffusion processes show a stronger dependence on the oxygen partial pressure with m= 1/2 and 1, respectively. Similar elemental rate-limiting steps can be obtained for the hydrogen oxidation reaction (HOR). Further information about the rate-limiting steps and the reactions involved in both ORR and HOR are summarized in Figure 3.15 and Tables 3.3 and 3.4.

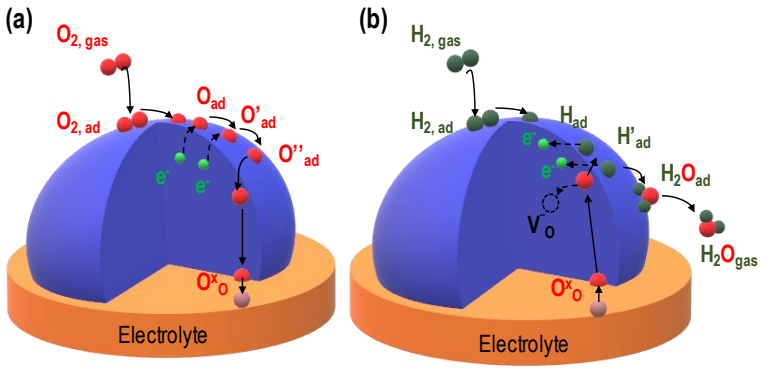

Figure 3.15. Illustration of the different (a) ORR and (b) HOR sub-reactions.

UNIVERSIDAD DE MÁLAGA

Table 3.3. Rate-limiting steps and the corresponding reaction orders *m* for the oxygen reduction reaction.

Reaction	Description	*m*	Ref.
$O^{x}_{o,\ electrode} \rightarrow O^{x}_{o,\ electrolyte}$	O^{2-} incorporation from the TPB to the electrolyte	0	[40,41]
$O_{ad} + e^{-} \rightarrow O'_{ad}$	One electron reduction	3/8	[42]
$O'_{ad} + e^{-} \rightarrow O''_{ad}$	One electron reduction	1/8	[42]
$O_{ad} + 2e^{-} + V^{\cdot\cdot}_{o,} \rightarrow O^{x}_{o}$	Charge transfer	1/4	[43,44]
$O_{2,\ ad} \rightarrow 2O_{ad}$	Oxygen dissociation	1/2	
$O_{2,\ gas} \rightarrow O_{2,\ ad}$	Oxygen adsorption	1	

Table 3.4. Rate-limiting steps and the corresponding reaction orders *m* for the hydrogen oxidation reaction.

Reaction	Description	*m*	Ref.
$O^{x}_{o,\ electrolyte} \rightarrow O^{x}_{o,\ electrode}$	O^{2-} incorporation from electrolyte to the TPB	0	[40,41]
$H_2O_{ad} + e^{-} \rightarrow H_2O_{gas}$	Desorption of the water molecules	0	[45]
$2H_{ad} + O^{x}_{o} \rightarrow V^{\cdot\cdot}_{o} + H_2O_{ad} + 2e^{''}$	Formation of water molecules	1/4	[45,46]
$H_{2,\ ad} \rightarrow 2H_{,\ ad}$	Hydrogen dissociation	1/2	[47]
$H_{2,\ gas} \rightarrow H_{2,\ ad}$	Hydrogen adsorption	1	[45]

EIS measurements as a function of the pO_2 were collected by using an electrochemical cell equipped with an oxygen pump and a YSZ sensor (Figure 3.15c). The pO_2 was changed by varying the applied potential to the oxygen pump to remove/incorporate O_2 into the gas tight cell. The pO_2 was continuously monitored with a YSZ sensor.

3.10.6. Total conductivity by Van der Pauw method

The electrical conductivity of mixed ionic-electronic conductors cannot be determined by impedance spectroscopy in a two-probe configuration due to their low resistance. In this study, the four-probe Van der Pauw method was employed to determine the electrical conductivity of dense pellets and thin film materials [48,49].
The main requirements to obtain accurate results are that the film has to be homogeneous in both composition and thickness and the electrical contacts must be very small compared to the sample size (ideally, point contacts are desirable). One of

UNIVERSIDAD DE MÁLAGA

the most important advantages of the Van der Pauw method is the use of samples with different shapes (Figure 3.16).

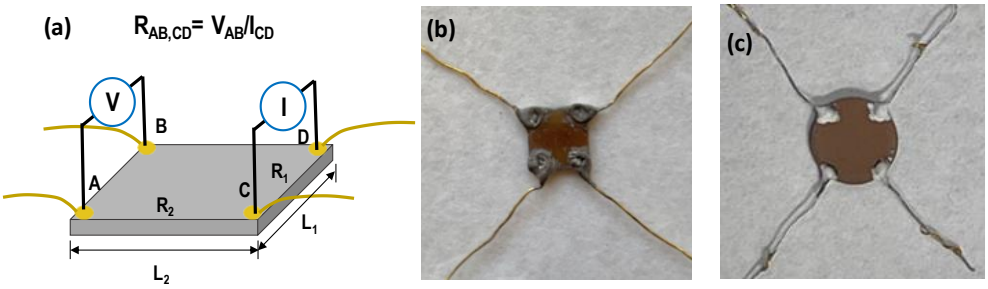

Figure 3.16. (a) Representation of the Van der Pauw method, (b) thin layer deposited by PLD on a single crystal and (c) dense pellet both with the 4-probe connections for the electrical measurement.

Four-point contacts of Pt-ink were symmetrically painted at the edge of the samples (Figure 3.16a). A dc current was applied between C and D (I_{CD}) and the voltage between A and B was measured (V_{AB}). The resistance (R) is then determined from the equation (Eq. 3.14):

$$R=\frac{V_{AB}}{I_{CD}} \qquad \text{(Eq. 3.14)}$$

If the 4-contacts are symmetrically distributed (L_1=L_2) in the sample, $R_{AB,CD}$=$R_{AC,BD}$ and the conductivity is determined from (Eq. 3.15):

$$\sigma_{dc}=\frac{\ln 2}{\pi d R_{AB,CD}} \qquad \text{(Eq. 3.15)}$$

The Van der Pauw method was used to obtain the conductivity of the thin films deposited by PLD (Figure 3.16b) and different polycrystalline dense pellets (Figure 3.16c). In addition, the Van der Pauw method was employed to study the conductivity as a function of the pO_2 in a tight gas cell (Figure 3.17).

UNIVERSIDAD DE MÁLAGA

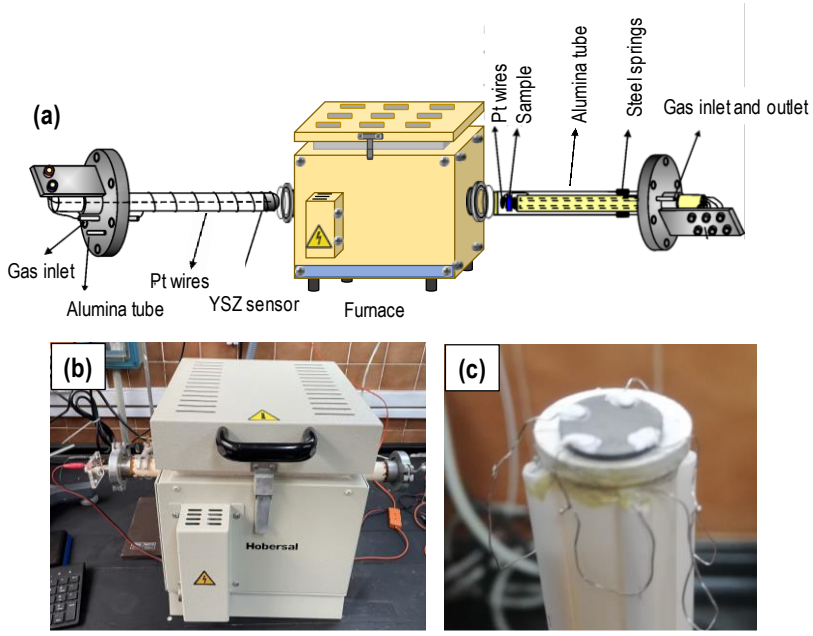

Figure 3.17. (a) Scheme of the equipment employed for the conductivity measurements as a function of the pO_2 by the Van der Pauw method, (b) furnace with the gas-tight system and (c) electrochemical cell.

The samples were reduced in 5% H_2-Ar until no variation in the conductivity was observed. The electrical measurements were acquired during the reoxidation process (24-48 h). A YSZ sensor was employed to constantly monitor the oxygen partial pressure inside the cell. The current and voltage in the sample were measured with a Keithley 2700 multimeter and a Yokogawa 7651 source was employed to apply the voltage.

3.11. Fuel cell tests

The performance of the materials with better electrochemical properties was tested under real operation conditions in a single SOFC. Electrolyte-supported cells with an LSGM electrolyte (300 μm thickness) and a Ni-YSZ/YSZ anode-supported cells (with 5 μm of electrolyte thickness) were investigated (Figure 3.18).

UNIVERSIDAD DE MÁLAGA

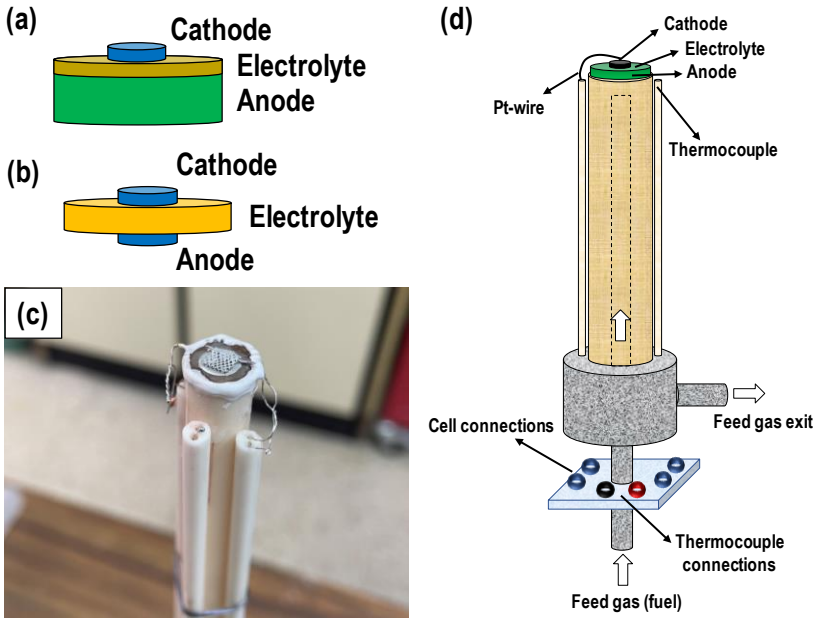

Figure 3.18. Representation of (a) anode-supported cell and (b) electrolyte-supported cell. (c) Photograph and (d) representation of the electrochemical setup employed for fuel cell test.

– *Anode-supported cells*: The Ni-YSZ cermet was prepared from an aqueous mixture of 60 wt.% NiO by dissolving $Ni(NO_3)_2 \cdot 6H_2O$ in distilled water and adding 40 wt.% YSZ powders. The mixture was slowly heated under continuous stirring until dryness. The dried mixture was calcined at 800 ºC for 1 h to obtain the NiO-YSZ composites. The resulting powders were pressed into pellets of 13 mm in diameter and 1 mm in thickness and then pre-sintered at 1200 ºC for 1 h. A thin YSZ electrolyte layer was deposited onto the pre-sintered pellets by airbrushing and then sintered at 1400 ºC for 4 h to reach high densification (Figure 3.18a).

– *Electrolyte-supported cells*: Commercial LSGM powders (Kceracell) were pressed into pellets of 13 mm diameter and pre-sintered at 1100 ºC for 1 h. After the calcination process, the pellets were polished with sandpaper and sintered at 1400 ºC for 4 h to obtain dense pellets of 300 µm thickness (Figure 3.18b).

– *Electrode deposition*: The powders and nanostructured electrodes were deposited by screen-printing or spray-pyrolysis through a 0.2 cm^2 circular shadow mask. Pt-paste was screen-printed to act as a current collector and Pt-wires were employed

UNIVERSIDAD DE MÁLAGA

to connect the samples to the electrochemical cell (Figure 3.18c,d). The single cells were sealed on top of an alumina tube with a ceramic based sealant (Ceramabond 668, Aremco). After that, the sealant was slowly dried at room temperature for 3 h and then heated in a furnace at 180 ºC for 2 h with a heating/cooling ramp of 1 ºC min^{-1}. Finally, a glass (Thinner, Aremco) was applied and then calcined at 600-800 ºC for 2 h with a heating/cooling ramp of 1 ºC min^{-1} to fully seal the cell.

After reaching the desired operating temperature, the fuel gases (wet 5% H_2-Ar and H_2) were constantly fed to the anode, meanwhile static air was used in the cathode side. After reducing the anode material for several hours and checking that the Open Circuit Voltage (OCV) is close to the theoretical one (1.1 V for H_2), I-V curves and EIS data were collected at different temperatures using a Zahner XC potentiostat/galvanostat/FRA. The stability of the cells was also evaluated after long-term operation (100-150 h) at a constant current density.

References

1. Mi, S.; Liu, Z.; Luo, C.; Cai, L.; Zhang, Z.; Li, L. A Review on Preparing New Energy Ultrafine Powder Materials by Freeze-Drying. *Dry Technol.* **2020**, *38*, 1544–1564, doi:10.1080/07373937.2019.1651733.
2. Leng, J.; Wang, Z.; Wang, J.; Wu, H.H.; Yan, G.; Li, X.; Guo, H.; Liu, Y.; Zhang, Q.; Guo, Z. Advances in Nanostructures Fabricated: Via Spray Pyrolysis and Their Applications in Energy Storage and Conversion. *Chem. Soc. Rev.* **2019**, *48*, 3015–3072, doi:10.1039/c8cs00904j.
3. dos Santos-Gómez, L.; Zamudio-García, J.; Porras-Vázquez, J.M.; Losilla, E.R.; Marrero-López, D. Recent Progress in Nanostructured Electrodes for Solid Oxide Fuel Cells Deposited by Spray Pyrolysis. *J. Power Sources* **2021**, *507*, 230277, doi:10.1016/j.jpowsour.2021.230277.
4. Patil, P.S. Versatility of Chemical Spray Pyrolysis Technique. *Mater. Chem. Phys.* **1999**, *59*, 185–198, doi:10.1016/S0254-0584(99)00049-8.
5. Perednis, D.; Gauckler, L.J. Thin Film Deposition Using Spray Pyrolysis. *J. Electroceramics* **2005**, *14*, 103–111, doi:10.1007/s10832-005-0870-x.
6. dos Santos-Gómez, L.; Zamudio-García, J.; Porras-Vázquez, J.M.; Losilla, E.R.; Marrero-López, D. Highly Oriented and Fully Dense CGO Films Prepared by Spray-Pyrolysis and Different Precursor Salts. *J. Eur. Ceram. Soc.* **2020**, *40*, 3080–3088, doi:10.1016/j.jeurceramsoc.2020.03.026.
7. Dos Santos-Gómez, L.; Porras-Vázquez, J.M.; Losilla, E.R.; Marrero-López, D. Ti-Doped $SrFeO_3$ Nanostructured Electrodes for Symmetric Solid Oxide Fuel Cells. *RSC Adv.* **2015**, *5*, 107889–107895, doi:10.1039/c5ra23771h.

UNIVERSIDAD DE MÁLAGA

8. Santos-Gómez, L. Dos; Porras-Vázquez, J.M.; Losilla, E.R.; Marrero-López, D. Improving the Efficiency of Layered Perovskite Cathodes by Microstructural Optimization. *J. Mater. Chem. A* **2017**, *5*, 7896–7904, doi:10.1039/c6ta10946b.
9. Xu, M.; Yu, J.; Song, Y.; Ran, R.; Wang, W.; Shao, Z. Advances in Ceramic Thin Films Fabricated by Pulsed Laser Deposition for Intermediate-Temperature Solid Oxide Fuel Cells. *Energy and Fuels* **2020**, *34*, 10568–10582, doi:10.1021/acs.energyfuels.0c02338.
10. Ashfold, M.N.R.; Claeyssens, F.; Fuge, G.M.; Henley, S.J. Pulsed Laser Ablation and Deposition of Thin Films. *Chem. Soc. Rev.* **2004**, *33*, 23–31, doi:https://doi.org/10.1039/B207644F.
11. Chrisey, D.B.; Hubler, G.K. *Pulsed Laser Deposition of Thin Films*; Wiley-VCH, **2013**; ISBN 0-471-59218-8.
12. Speriosu, V.S.; Vreeland, T. X-Ray Rocking Curve Analysis of Superlattices. *J. Appl. Phys.* **1984**, *56*, 1591–1600, doi:10.1063/1.334169.
13. Fewster, P.F. *Reciprocal Space Mapping*; **1997**; Vol. 22; ISBN 1040843970824.
14. Bauer, G.; Li, J.; Koppensteiner, E. X-Ray Reciprocal Space Mapping of Si $Si_{1-x}Ge_x$ Heterostructures. *J. Cryst. Growth* **1995**, *157*, 61–67, doi:10.1016/0022-0248(95)00372-X.
15. Šimek, D.; Kužel, R.; Rafaja, D. Reciprocal-Space Mapping for Simultaneous Determination of Texture and Stress in Thin Films. *J. Appl. Crystallogr.* **2006**, *39*, 487–501, doi:10.1107/S0021889806015500.
16. Mccusker, L.B.; Von Dreele, R.B.; Cox, D.E.; Louër, D.; Scardi, P. Rietveld Refinement Guidelines. *J. Appl. Crystallogr.* **1999**, *32*, 36–50, doi:10.1107/S0021889898009856.
17. Rietveld, H.M. The Rietveld Method. *Phys. Scr.* **2014**, *89*, doi:10.1088/0031-8949/89/9/098002.
18. Bish, D.L.; Howard, S.A. Quantitative Phase Analysis Using the Rietveld Method. *J. Appl. Crystallogr.* **1988**, *21*, 86–91, doi:10.1107/S0021889887009415.
19. Fadley, C.S. X-Ray Photoelectron Spectroscopy: Progress and Perspectives. *J. Electron Spectros. Relat. Phenomena* **2010**, *178–179*, 2–32, doi:10.1016/j.elspec.2010.01.006.
20. Proctor, A.; Sherwood, P.M.A. Data Analysis Techniques in X-Ray Photoelectron Spectroscopy. *Anal. Chem.* **1982**, *54*, 13–19, doi:10.1021/ac00238a008.
21. Bagus, P.S.; Ilton, E.S.; Nelin, C.J. The Interpretation of XPS Spectra: Insights into Materials Properties. *Surf. Sci. Rep.* **2013**, *68*, 273–304, doi:10.1016/j.surfrep.2013.03.001.
22. Shindo, D.; Oikawa, T. *Analytical Electron Microscopy for Materials Science*; **2002**; ISBN 9784431703365.
23. D'Alfonso, A.J.; Freitag, B.; Klenov, D.; Allen, L.J. Atomic-Resolution Chemical Mapping Using Energy-Dispersive x-Ray Spectroscopy. *Phys. Rev. B - Condens. Matter Mater. Phys.* **2010**, *81*, 2–5, doi:10.1103/PhysRevB.81.100101.
24. Muševič, I. Atomic Force Microscopy. *Inf. MIDEM* **2000**, *30*, 223–227, doi:10.1093/oso/9780198856559.003.0016.
25. Giessibl, F.J. Advances in Atomic Force Microscopy. *Rev. Mod. Phys.* **2003**, *75*, 949–983, doi:10.1103/RevModPhys.75.949.
26. Chang, B.Y.; Park, S.M. Electrochemical Impedance Spectroscopy. *Annu. Rev. Anal. Chem.* **2010**, *3*, 207–229, doi:10.1146/annurev.anchem.012809.102211.
27. Irvine, B.J.T.S.; Sinclair, D.C.; West, A.R. Electroceramics Characterisation by Impedance Sepctroscopy. *Adv. Mater.* **1990**, *2*, 132-138. doi: 10.1002/adma.19900020304
28. Barsoukov, E.; Macdonald, J.R. *Impedance Spectroscopy: Theory, Experiment, and*

UNIVERSIDAD DE MÁLAGA

Applications, Second Edition, John Wiley & Sons, Inc.; **2005**.

29. Vivier, V.; Orazem, M.E. Impedance Analysis of Electrochemical Systems. *Chem. Rev.* **2022**, *122*, 11131–11168, doi:10.1021/acs.chemrev.1c00876.
30. Cole, K.S.; Cole, R.H. Dispersion and Absorption in Dielectrics: II. Direct Current Characteristics. *J. Chem. Phys.* **1942**, *10*, 98–105, doi:10.1063/1.1723677.
31. Harrington, D.A.; Van Den Driessche, P. Mechanism and Equivalent Circuits in Electrochemical Impedance Spectroscopy. *Electrochim. Acta* **2011**, *56*, 8005–8013, doi:10.1016/j.electacta.2011.01.067.
32. Lukács, Z.; Kristóf, T. A Generalized Model of the Equivalent Circuits in the Electrochemical Impedance Spectroscopy. *Electrochim. Acta* **2020**, *363*, 137199. doi:10.1016/j.electacta.2020.137199.
33. Osinkin, D.A. An Approach to the Analysis of the Impedance Spectra of Solid Oxide Fuel Cell Using the DRT Technique. *Electrochim. Acta* **2021**, *372*, 137858, doi:10.1016/j.electacta.2021.137858.
34. Dierickx, S.; Weber, A.; Ivers-Tiffée, E. How the Distribution of Relaxation Times Enhances Complex Equivalent Circuit Models for Fuel Cells. *Electrochim. Acta* **2020**, *355*, 136764, doi:10.1016/j.electacta.2020.136764.
35. Boukamp, B.A.; Rolle, A. Analysis and Application of Distribution of Relaxation Times in Solid State Ionics. *Solid State Ionics* **2017**, *302*, 12–18, doi:10.1016/j.ssi.2016.10.009.
36. Wan, T.H.; Saccoccio, M.; Chen, C.; Ciucci, F. Influence of the Discretization Methods on the Distribution of Relaxation Times Deconvolution: Implementing Radial Basis Functions with DRTtools. *Electrochim. Acta* **2015**, *184*, 483–499, doi:10.1016/j.electacta.2015.09.097.
37. Boukamp, B.A.; Rolle, A. Use of a Distribution Function of Relaxation Times (DFRT) in Impedance Analysis of SOFC Electrodes. *Solid State Ionics* **2018**, *314*, 103–111, doi:10.1016/j.ssi.2017.11.021.
38. Pérez-Coll, D.; Aguadero, A.; Escudero, M.J.; Daza, L. Effect of DC Current Polarization on the Electrochemical Behaviour of $La_2NiO_{4+\delta}$ and $La_3Ni_2O_{7+\delta}$-Based Systems. *J. Power Sources* **2009**, *192*, 2–13, doi:10.1016/j.jpowsour.2008.10.073.
39. Aguadero, A.; Alonso, J.A.; Skinner, S.J.; Kilner, J. A New Family of Mo-Doped $SrCoO_{3-\delta}$ Perovskites for Application in Reversible Solid State Electrochemical Cells. *Chem. Mater.* **2012**, *24*, 2655–2663, doi:10.1021/cm300255r.
40. Chen, X.J.; Khor, K.A.; Chan, S.H. Identification of O_2 Reduction Processes at Yttria Stabilized Zirconia|doped Lanthanum Manganite Interface. *J. Power Sources* **2003**, *123*, 17–25, doi:10.1016/S0378-7753(03)00436-1.
41. Kim, J.D.; Kim, G.D.; Moon, J.W.; Park, Y. il; Lee, W.H.; Kobayashi, K.; Nagai, M.; Kim, C.E. Characterization of LSM-YSZ Composite Electrode by Ac Impedance Spectroscopy. *Solid State Ionics* **2001**, *143*, 379–389, doi:10.1016/S0167-2738(01)00877-3.
42. Kenney, B.; Karan, K. Impact of Nonuniform Potential in SOFC Composite Cathodes on the Determination of Electrochemical Kinetic Parameters. *J. Electrochem. Soc.* **2006**, *153*, A1172, doi:10.1149/1.2191187.
43. Takeda, Y.; Kanno, R.; Noda, M.; Tomida, Y.; Yamamoto, O. Cathodic Polarization Phenomena of Perovskite Oxide Electrodes with Stabilized Zirconia. *J. Electrochem. Soc.* **1987**, *134*, 2656–2661, doi:10.1149/1.2100267.
44. Escudero, M.J.; Aguadero, A.; Alonso, J.A.; Daza, L. A Kinetic Study of Oxygen Reduction Reaction on La_2NiO_4 Cathodes by Means of Impedance Spectroscopy. *J. Electroanal. Chem.*

UNIVERSIDAD DE MÁLAGA

2007, *611*, 107–116, doi:10.1016/j.jelechem.2007.08.006.

45. Zhang, Y.; Zhao, H.; Zhang, M.; Du, Z.; Guan, W.; Singhal, S.C.; Świerczek, K. Boosting the Electrode Reaction Kinetics of SSOFCs by the Synergistic Effect of Nanoparticle Codecoration on Both the Cathode and Anode. *Chem. Mater.* **2022**, doi:10.1021/acs.chemmater.2c02861.
46. Chen, M.; Chen, D.; Chang, M.; Hu, H.; Xu, Q. New Insight into Hydrogen Oxidation Reaction on $La_{0.3}Sr_{0.7}Fe_{0.7}Cr_{0.3}O_{3-\delta}$ Perovskite as a Solid Oxide Fuel Cell Anode . *J. Electrochem. Soc.* **2017**, *164*, F405–F411, doi:10.1149/2.1571704jes.
47. Zhu, T.; Troiani, H.E.; Mogni, L. V.; Han, M.; Barnett, S.A. Ni-Substituted $Sr(Ti,Fe)O_3$ SOFC Anodes: Achieving High Performance via Metal Alloy Nanoparticle Exsolution. *Joule* **2018**, *2*, 478–496, doi:10.1016/j.joule.2018.02.006.
48. Chwang, R.; Smith, B.J.; Crowell, C.R. Contact Size Effects on the van Der Pauw Method for Resistivity and Hall Coefficient Measurement. *Solid State Electron.* **1974**, *17*, 1217–1227, doi:10.1016/0038-1101(74)90001-X.
49. Ramadan, A.A.; Gould, R.D.; Ashour, A. On the Van Der Pauw Method of Resistivity Measurements. *Thin Solid Films* **1994**, *239*, 272–275, doi:10.1016/0040-6090(94)90863-X.

UNIVERSIDAD DE MÁLAGA

Chapter 4

UNIVERSIDAD
DE MÁLAGA

UNIVERSIDAD
DE MÁLAGA

$LaCrO_3$-based electrodes

The electrochemical properties of $LaCrO_3$-based electrodes have been traditionally improved by doping in the A-site of the perovskite with alkaline-earth cations (Ca^{2+}, Sr^{2+} or Ba^{2+}) and the B-site with transition metals (Sc^{3+}, Ti^{4+}, Mn^{3+}, Nb^{5+} or Mo^{6+}). Among all compositions studied, $La_{0.75}Sr_{0.25}Cr_{0.5}Mn_{0.5}O_{3-\delta}$ (LSCM) has rendered the most promising results as a symmetrical electrode [1,2]. In this chapter, A-site and B-site doping strategies in $LaCrO_3$ pristine material were investigated to obtain single-phase electrode layers at low sintering temperatures. Additionally, different microstructural approaches *i.e.* nanostructured, infiltration and nanocomposites were prepared by spray-pyrolysis deposition and tested to improve the performance in both oxidizing and reducing conditions.

UNIVERSIDAD DE MÁLAGA

4.1. A-site doping, $(La_{0.8}A_{0.2})_{0.98}CrO_{3-\delta}$ (A=Ca and Sr), and phase formation

Firstly, an A-site doping strategy with alkaline-earth cations was tested by depositing $(La_{0.8}A_{0.2})_{0.98}CrO_{3-\delta}$ (A= Ca and Sr) electrodes by spray-pyrolysis onto YSZ substrates at 300 ºC for 1 h and then calcined at different temperatures between 650-1200 ºC. It is worth mentioning that the electrodes were prepared with A-site deficiency to minimize the possible segregation of alkaline-earth based compounds on the electrode surface. Further information about this work can be found in the articles A1 and A2.

Figure 4.1a shows XRD patterns of $(La_{0.8}Sr_{0.2})_{0.98}CrO_{3-\delta}$ layers at different sintering temperatures. A monoclinic monazite-type structure (s.g. $P2_1/n$) with $LaCrO_4$ composition was identified as the main crystalline phase after calcination at 650 ºC. Above 800 ºC, Cr^{5+} in $LaCrO_4$ is reduced to lower oxidation states, inducing a phase transformation to a perovskite-type structure.

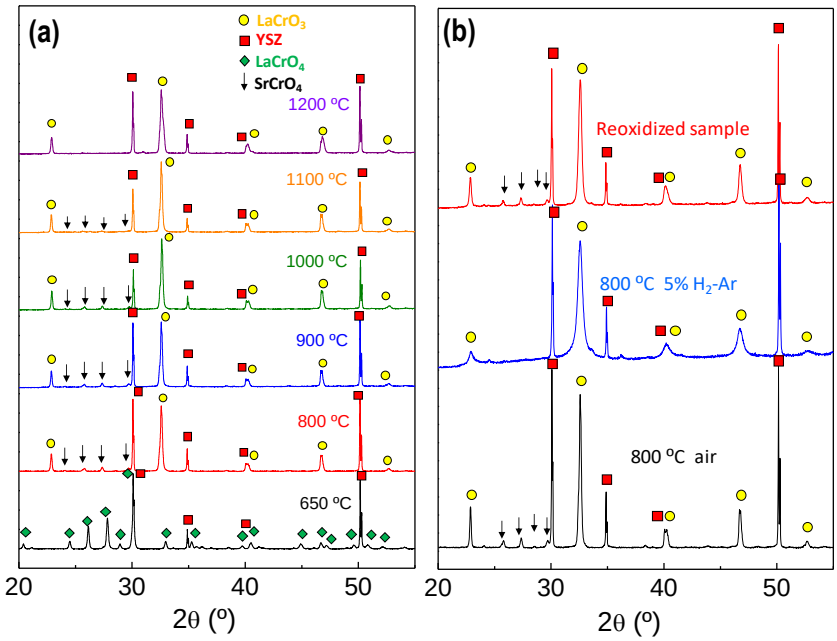

Figure 4.1. (a) XRD patterns of $(La_{0.8}Sr_{0.2})_{0.98}CrO_{3-\delta}$ electrodes deposited onto YSZ pellets and calcined in air at different temperatures. (b) XRD patterns of the reduced and reoxidized layers at 800 ºC.

UNIVERSIDAD DE MÁLAGA

Nevertheless, at temperatures lower than 1100 ºC, a secondary phase of $SrCrO_{4-\delta}$ was identified. Thus, a single $(La_{0.8}Sr_{0.2})_{0.98}CrO_{3-\delta}$ electrode is not obtained after calcination temperatures as high as 1200 ºC. The amount of $SrCrO_{4-\delta}$ estimated by Rietveld quantification decreased from 19 to 8 wt.% at 800 ºC and 1100 ºC, respectively. Similar findings were observed previously for $La_{0.8}Ca_{0.2}CrO_{3-\delta}$ and $La_{0.8}Sr_{0.2}CrO_{3-\delta}$ [3,4]. Such high sintering temperature is undesirable due to a significant grain growth, as well as a loss of electrode porosity, negatively affecting the electrode performance. An alternative approach was used to obtain single-phase electrodes of Sr-doped $LaCrO_3$. The layers were calcined in 5% H_2-Ar at 800 ºC for 24 h to reduce the $Cr^{6+/5+}$ in $SrCrO_{4-\delta}$ to lower oxidation states. Figure 4.1b shows the XRD patterns before and after the reduction treatments. $SrCrO_{4-\delta}$ phase is not observed after reduction; however, it is again visible after reoxidation in air. These findings suggest that $SrCrO_{4-\delta}$ becomes amorphous after the reduction process and it crystallizes again in air atmosphere. Hence, the formation of a solid solution in Sr-doped $LaCrO_3$ is not possible at temperatures lower than 1200 ºC. Further attempts were made for the preparation of Ca-doped $LaCrO_3$ layers, obtaining the same results.

Figure 4.2 displays SEM images of the $(La_{0.8}Sr_{0.2})_{0.98}CrO_{3-\delta}$ electrodes after calcining at 1200 ºC in air for 1 h. The electrode shows a laminated morphology, characteristic of an electrode deposited by spray pyrolysis, but with very low porosity due to the high sintering temperature required to obtain a single-phase electrode; however, the average particle size is still in the nanoscale range ~120 nm.

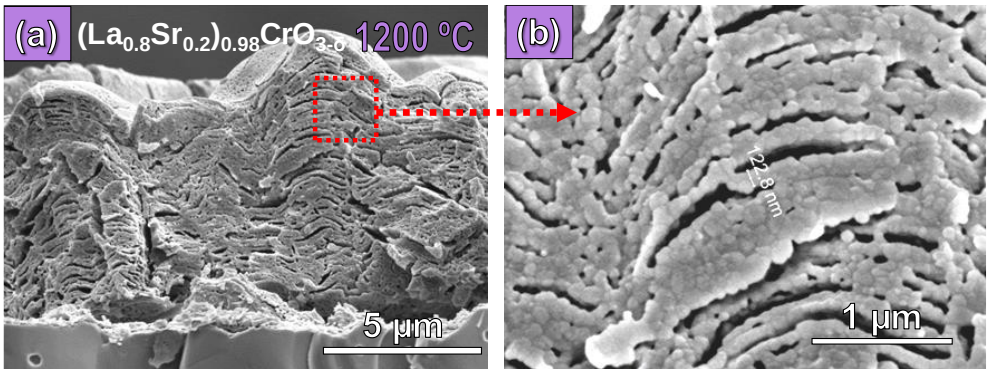

Figure 4.2. (a,b) SEM images at different magnifications of the $(La_{0.8}Sr_{0.2})_{0.98}CrO_{3-\delta}$ layers sintered at 1200 ºC.

UNIVERSIDAD DE MÁLAGA

Nevertheless, the electrochemical characterization of $(La_{0.8}Sr_{0.2})_{0.98}CrO_{3-\delta}$ by impedance spectroscopy reveals polarization resistance values (R_p) of 1.95 Ω cm^2 at 700 ºC in air, which is still lower than those observed for the screen-printed $La_{0.8}Ca_{0.2}CrO_{3-\delta}$ (6.3 Ω cm^2 at 800 ºC) [5].

4.2. B-site doping strategy in $La_{0.98}Cr_{0.75}M_{0.25}O_{3-\delta}$ (M= Mn, Fe, Cu and Ti)

Since high sintering temperatures are needed to obtain single-phase compounds of alkaline-earth doped $LaCrO_3$, an alternative approach of B-site doping was investigated. Chromium was partially substituted with transition metals in $La_{0.98}Cr_{0.75}M_{0.25}O_{3-\delta}$ (M= Mn, Fe, Cu and Ti).

All these electrodes were deposited by spray-pyrolysis onto a porous CGO backbone layer previously fixed on YSZ electrolytes (section 3.2). Additionally, $La_{0.98}Cr_{0.75}M_{0.25}O_{3-\delta}$ (M= Mn and Fe) powders were prepared by a freeze-drying precursor method to compare the results obtained from traditional screen-printing deposition with those obtained by spray-pyrolysis deposition directly on the electrolyte.

The XRD patterns show the formation of single-phase materials for all compositions after calcining at 800 ºC for 1 h in air. The redox stability of the layers was also tested in 5% H_2-Ar at 800 ºC for 24 h (Figure 4.3a). Phase transformation and secondary phases are not observed for Mn, Fe and Ti-doped samples; however, the Cu-doped sample shows a minor secondary phase identified as Cu metal, generated by metal exsolution from the perovskite structure upon reduction, which is explained by the higher reducibility of Cu^{2+} compared to the rest of transition metals investigated [6].

The Rietveld method was employed to determine the lattice parameters and cell volume of the electrodes obtained by freeze-drying and spray-pyrolysis. Three different crystalline phases are observed for the samples deposited by spray-pyrolysis; YSZ and CGO with cubic fluorite structures (s.g. $Fm\bar{3}m$), and doped-$LaCrO_3$ with an orthorhombic perovskite-type structure (s.g. Pbnm) (Figure 4.3b).

UNIVERSIDAD DE MÁLAGA

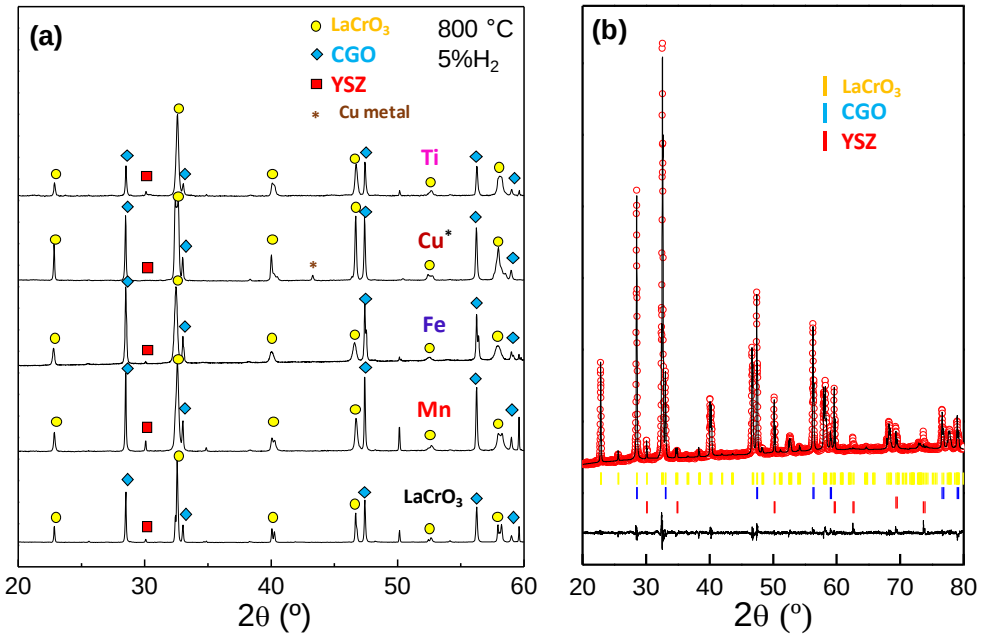

Figure 4.3. (a) XRD patterns of $La_{0.98}Cr_{0.75}M_{0.25}O_{3-\delta}$ (M= Mn, Fe, Cu and Ti) onto YSZ electrolytes with a CGO backbone calcined at 800 ºC in air and then reduced in 5% H_2-Ar at 800 ºC for 24 h. (b) Rietveld analysis of $LaCrO_3$ electrode calcined at 800 ºC in air as a representative example.

The cell volumes and fitting parameters of $La_{0.98}Cr_{0.75}M_{0.25}O_{3-\delta}$ (M= Mn, Fe, Cu and Ti) electrodes prepared by spray-pyrolysis and freeze-drying are summarized in Table 4.1. In general, the unit cell volume of the perovskite structure increases with increasing the ionic radii of the substituted transition metal, from 234.549(2) $Å^3$ for undoped $LaCrO_3$ to 236.678(2) $Å^3$ for Fe-doped $LaCrO_3$. In a reducing atmosphere of 5% H_2-Ar, a slight unit cell expansion is observed due to the partial reduction of the B-site cations to lower oxidation states.

This minor variation of the unit cell volume is consistent with the similar thermal expansion coefficients (TEC) of $LaCrO_3$-based electrodes in both air and hydrogen atmospheres, *i.e.* 8.1-8.6·10^{-6} K^{-1} [7]. These findings reveal that these electrodes would have good mechanical compatibility with the electrolyte, avoiding delaminations or cracks during successive oxidation/reduction cycles in real SOFC operation conditions [8,9]. It is worth mentioning that the cell volume values obtained

UNIVERSIDAD DE MÁLAGA

for the electrodes deposited by spray-pyrolysis are very similar to those obtained for the freeze-dried powders prepared at high temperature.

Table 4.1. Structural parameters of $La_{0.98}Cr_{0.75}M_{0.25}O_{3-\delta}$ (M= Mn, Fe, Cu and Ti) electrodes in air and 5% H_2-Ar atmospheres deposited by spray-pyrolysis onto YSZ substrates (SP) and prepared by the freeze-drying precursor method (FD).

Composition	T (ºC)	Preparation method	Volume (Å^3)		R_{wp} (%)
			Air	5% H_2-Ar	Air/H_2
$La_{0.98}CrO_{3-\delta}$ (LC)	800	SP	234.549(2)	234.679(2)	4.9/5.2
$La_{0.98}Cr_{0.75}Mn_{0.25}O_{3-\delta}$ (LCM)	800	SP	234.912(2)	235.725(2)	5.7/6.6
$La_{0.98}Cr_{0.75}Fe_{0.25}O_{3-\delta}$ (LCF)	800	SP	236.678(2)	236.803(2)	8.6/6.8
$La_{0.98}Cr_{0.75}Cu_{0.25}O_{3-\delta}$	800	SP	235.386(2)	235.130(2)	7.8/9.8
$La_{0.98}Cr_{0.75}Ti_{0.25}O_{3-\delta}$	800	SP	234.800(2)	234.679(2)	8.1/8.9
$La_{0.98}CrO_{3-\delta}$ (LC)	1500	FD	234.641(3)	234.790(3)	3.5/5.2
$La_{0.98}Cr_{0.75}Mn_{0.25}O_{3-\delta}$ (LCM)	1500	FD	235.121(3)	236.425(3)	5.7/6.6
$La_{0.98}Cr_{0.75}Fe_{0.25}O_{3-\delta}$ (LCF)	1500	FD	236.744(3)	237.154(3)	7.2/6.8

The local crystal structure and cation distribution were studied by TEM (Figure 4.4). The HAADF-STEM image and EDS analysis of the Mn-doped sample, obtained by spray-pyrolysis at 800 ºC, show that the electrode is formed by particles with 100-200 nm in diameter with an uniform cation distribution. No visible secondary phases are detected in accordance with the XRD results. HRTEM analysis shows high crystalline particles without the presence of amorphous domains. Furthermore, the orthorhombic crystal structure is confirmed by the analysis of the interatomic distances d_{hkl} along the $[10\bar{1}]$ projection, which matched well with those determined from XRD analyses.

UNIVERSIDAD DE MÁLAGA

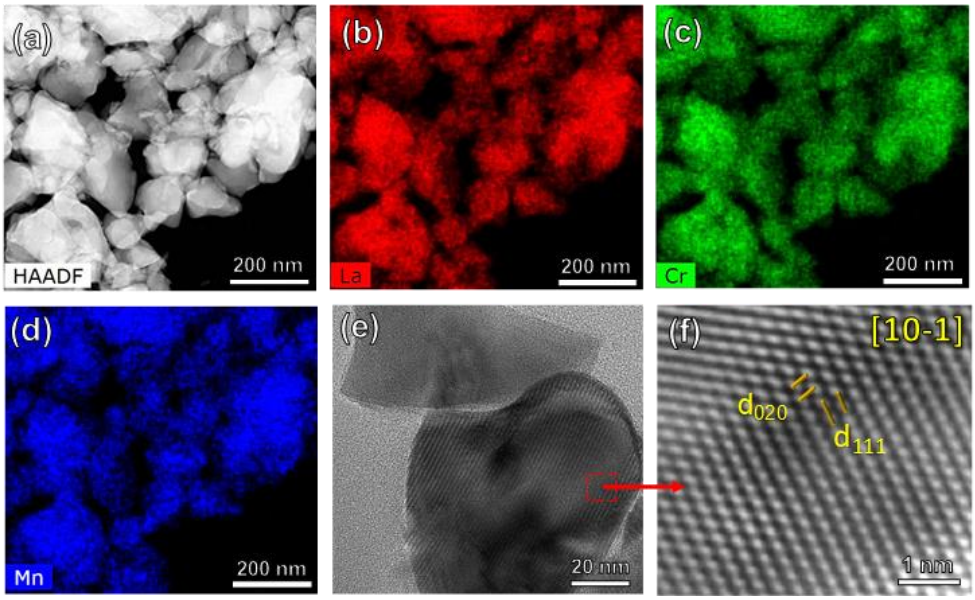

Figure 4.4. (a) HAADF-STEM image and (b-d) EDS analysis of the $La_{0.98}Cr_{0.75}Mn_{0.25}O_{3-\delta}$ electrode obtained by spray-pyrolysis and calcined 800 ºC for 24 h. (e,f) HRTEM image showing a perovskite-type structure.

Further information about the oxidation states of the elements in oxidizing and reducing conditions studied by XPS can be found in Appendix 1.

4.2.1. Influence of the deposition temperature on the electrode performance

The deposition temperature is a crucial parameter to tailor the electrode microstructure and performance of the electrodes obtained by spray-pyrolysis, especially for those deposited into porous CGO backbones. The infiltration strongly depends on the substrate temperature since the solvent evaporation rate and precursor diffusion are seriously influenced by this parameter. In this case, $La_{0.98}Cr_{0.75}Mn_{0.25}O_{3-\delta}$ (LCM) electrode is described as a representative example. It is worth mentioning that the infiltration process was carried out in a single deposition step, contrary to the traditional wet infiltration method where several infiltration/calcination steps are required to reach a minimum amount of loading material. Figure 4.5 clearly shows that the electrode microstructure is influenced by the deposition temperature.

UNIVERSIDAD DE MÁLAGA

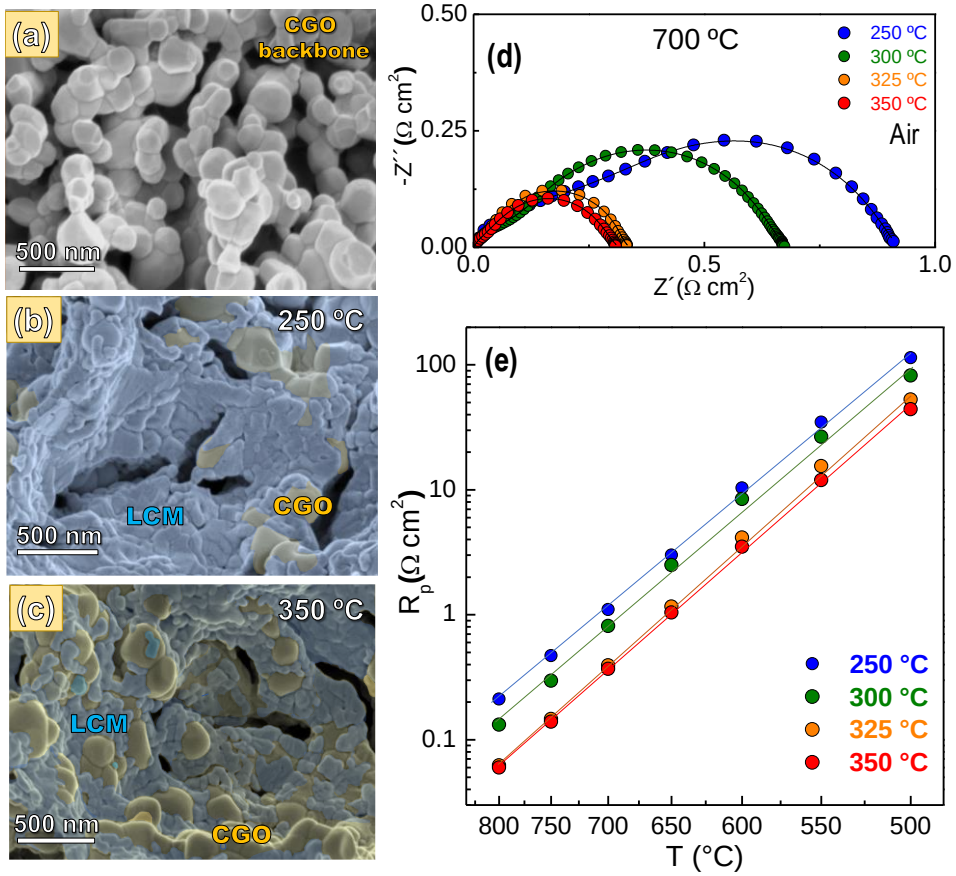

Figure 4.5. SEM images of (a) CGO backbone before infiltration. LCM electrode deposited by spray-pyrolysis onto a CGO backbone (LCM-Inf) at (b) 250 ºC and (c) 350 ºC and then calcined at 800 ºC. (d) Impedance spectra at 700 ºC in air of LCM electrodes deposited between 250 and 350 ºC. (e) Temperature variation of the polarization resistance for the different electrodes.

At low deposition temperatures (250 ºC) (Figure 4.5b), the CGO porous backbone is almost fully coated by LCM particles, whereas a partial coating is observed at higher temperatures (350 ºC) (Figure 4.5c). This is explained by the higher decomposition rate of the precursor droplets during the deposition process, partially limiting the infiltration. The amount of LCM electrode infiltrated into the CGO backbone was estimated by weight difference before and after the deposition process, taking values of 40:60 and 20:80 LCM:CGO wt.% ratios at deposition temperatures of 250 and 350 ºC, respectively.

UNIVERSIDAD DE MÁLAGA

The influence of the microstructure on the electrochemical properties was studied by impedance spectroscopy. Figure 4.5d shows the impedance spectra at 700 ºC of LCM deposited at different temperatures between 250 and 350 ºC for 1 h. At least two different electrode contributions are observed for all samples, where the process at low frequency (LF), usually associated with electrochemical reactions on the electrode surface [10,11], is the main contribution to the overall polarization resistance. In particular, the samples deposited at lower temperatures show a higher LF contribution, which can be related to the lower TPB density in the fully coated electrode because of the predominant electronic conductivity of LCM. However, a partial coating of CGO leads to an enhanced contact and higher surface area between CGO, LCM and the oxygen gas, providing a larger TPB length. The analysis of the electrode polarization resistance (R_p) as a function of the temperature further confirms the greater electrochemical performance of the partially coated electrodes (Figure 4.5e)

4.2.2. Electrochemical characterization of $La_{0.98}Cr_{0.75}M_{0.25}O_{3-\delta}$ (M= Mn, Fe, Cu and Ti) electrodes

Figure 4.6 shows impedance spectra at 700 ºC in different atmospheres of $La_{0.98}Cr_{0.75}M_{0.25}O_{3-\delta}$ (M= Mn, Fe, Cu and Ti) series deposited at 350 ºC onto a YSZ electrolyte with a CGO backbone. Impedance spectra in air revealed two different electrochemical processes for the different electrode compositions. The equivalent circuit (inset Figure 4.6a) was employed for the fitting of the impedance spectra, where L is an inductor associated with the electrochemical cell configuration, R_s is the ohmic resistance of the cell and two RQ elements are employed to simulate the electrode response, in which constant phase elements *Q* are used instead of capacitors to better represent the depressed arcs.

Ti-doped sample shows the highest R_p values in air, (2.08 Ω cm^2 at 700 ºC) (Figure 4.6a,c) which can be linked to not only the lower oxygen vacancy concentration in the structure after Ti^{4+}-doping in B-site but also to the presumably poor electronic conductivity of this phase in air due to the redox stability of Ti^{4+}. The $LaCrO_3$-undoped sample showed polarization resistance values of 0.91 Ω cm^2 at 700 ºC in air, relatively higher than those observed for Cu, Fe and Mn-doped electrodes,

UNIVERSIDAD DE MÁLAGA

0.70, 0.52 and 0.35 Ω cm^2, respectively, at the same temperature. $La_{0.98}Cr_{0.75}Fe_{0.25}O_{3-\delta}$ (LCF) and $La_{0.98}Cr_{0.75}Mn_{0.25}O_{3-\delta}$ (LCM) electrode compositions rendered the most promising electrochemical performance in air and were tested in 5% H_2-Ar and 100% H_2 atmospheres.

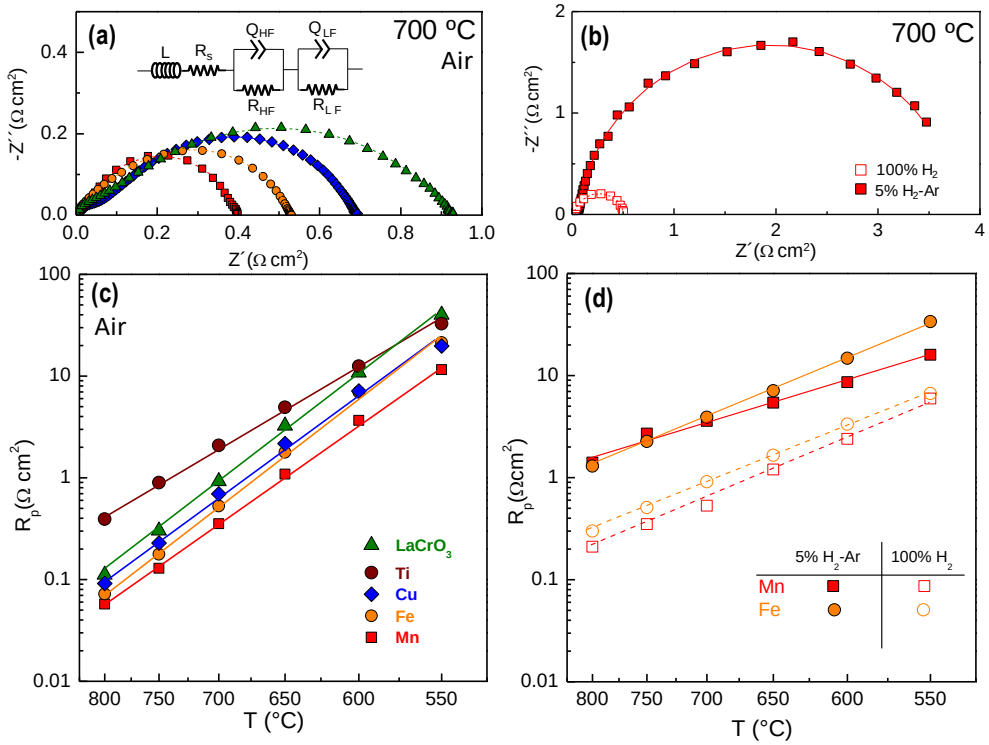

Figure 4.6. Impedance spectra at 700 ºC in (a) air and (b) 5% H_2-Ar and 100% H_2 of $La_{0.98}Cr_{0.75}M_{0.25}O_{3-\delta}$ (M= Mn, Fe, Cu and Ti) samples deposited at 350 ºC by spray-pyrolysis into a CGO backbone. Total polarization resistances as a function of the temperature in (c) air and (d) 5% H_2-Ar and 100% H_2. The inset of (a) displays the equivalent circuit used to fit the impedance spectra.

The impedance spectra in diluted hydrogen show a broad arc at low frequencies between 1.5 and 0.1 Hz with relatively high capacitance values, 0.1-0.16 F cm^{-2} (Figure 4.6b). These findings suggest that this electrode contribution can be related to gas diffusion limitations induced by the use of diluted hydrogen [12]. This hypothesis was further confirmed by the drastic reduction of this contribution when the fed gas was switched from 5% H_2-Ar to 100% H_2, decreasing the polarization resistance of LCM from 3.8 to 0.53 Ω cm^2 at 700 ºC, respectively. The Fe-doped

UNIVERSIDAD DE MÁLAGA

sample showed higher polarization resistance, *i.e.* 0.91 Ω cm^2 at 700 ºC when compared to that observed for LCM (0.53 Ω cm^2) (Figure 4.6b).

The conductivity $La_{0.98}CrO_{3-\delta}$-based electrodes were studied from pellets obtained from freeze-dried powders, which were sintered at 1500 ºC for 4 h. As can be seen in Figure 4.7, the microstructure and relative density of the samples are highly affected by the electrode composition.

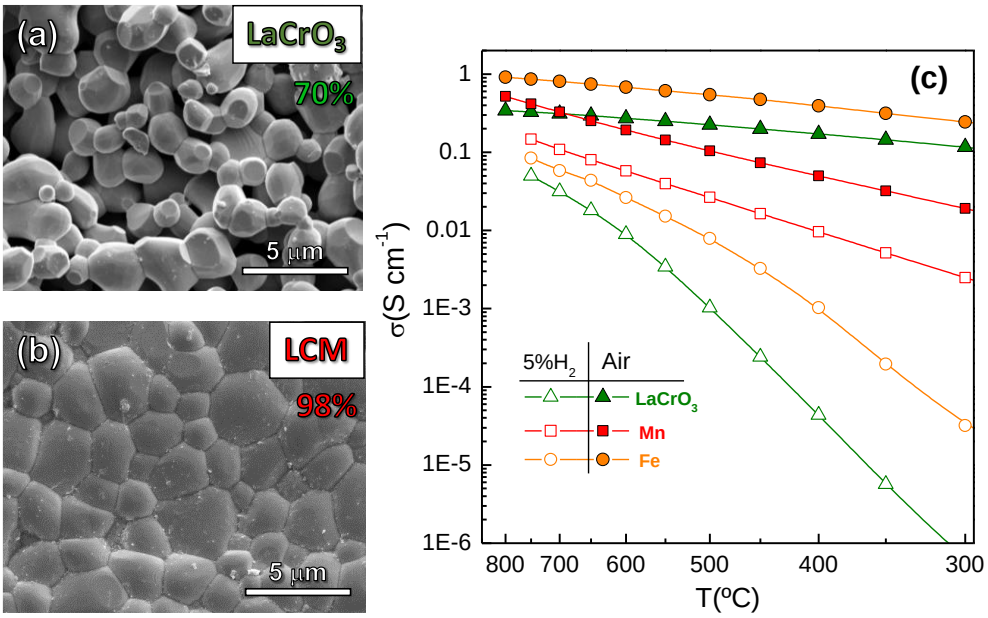

Figure 4.7. SEM images of the pellet surface of the (a) $La_{0.98}CrO_{3-\delta}$ and (b) $La_{0.98}Cr_{0.75}Mn_{0.25}O_{3-\delta}$ samples sintered at 1500 ºC for 4 h in air. The relative density of each sample is indicated in the figures. (c) Total conductivity in air and 5% H_2-Ar for pristine $La_{0.98}CrO_{3-\delta}$ and $La_{0.98}Cr_{0.75}M_{0.25}O_{3-\delta}$ (M= Mn and Fe) samples as a function of the temperature.

Undoped $La_{0.98}CrO_{3-\delta}$ shows very low sinterability with a relative density of only 70% after sintering at 1500 ºC for 4 h (Figure 4.7a). However, such results are not surprising, since previous reports have observed that the densification mechanism of $LaCrO_3$-based materials occurs via evaporation-condensation of chromium oxide species in oxidizing conditions, instead of the typical grain boundary diffusion mechanism. For this reason, sintering temperatures as high as 1700 ºC in a reducing atmosphere are necessary to achieve densification of undoped $LaCrO_3$ [13]. In

UNIVERSIDAD DE MÁLAGA

contrast, the doped samples show high relative density at the same sintering temperature; as can be seen in Figure 4.7b for LCM, as a representative example.

The total conductivity of some selected samples was analysed by the four-probe Van der Pauw method in air and 5% H_2-Ar (Figure 4.7c). The conductivity in air, mainly attributed to electron-hole conduction, varies from 0.81 to 0.33 S cm^{-1} for Fe- and Mn-doped samples at 700 ºC, respectively, values that are slightly higher than that observed for the pure $La_{0.98}CrO_{3-\delta}$, 0.31 S cm^{-1} at the same temperature. However, these conductivity values are considerably lower than those reported for A-site doped $LaCrO_3$ electrodes, which can be explained by the increase of the hole concentration and p-type conductivity, *i.e.* $La_{0.8}Ca_{0.2}CrO_{3-\delta}$ (31 S cm^{-1} at 800 ºC) [14] and $La_{0.75}Sr_{0.25}Cr_{0.5}Mn_{0.5}O_{3-\delta}$ (25.3 S cm^{-1} at 800 ºC) [5].

In a 5% H_2-Ar atmosphere, the total conductivity decreases due to the reduction of B-site cations to lower oxidation states with the consequent decrease of charge carrier concentration. The best conductivity values are found for Mn-doped sample, 0.11 S cm^{-1} at 700 ºC, which are slightly higher than those observed for the Fe-doped sample and the pristine $LaCrO_3$, 0.06 and 0.03 S cm^{-1} at 700 ºC, respectively. The lower conductivity values showed by the Fe-doped sample can be attributed to the easier reduction of Fe cation compared to Mn ions, decreasing the concentration of charge carriers. It is worth mentioning that these conductivity values are comparable to those obtained for $La_{0.75}Sr_{0.25}Cr_{0.5}Mn_{0.5}O_{3-\delta}$ anode in 10% H_2, *i.e.* 0.2 S cm^{-1} at 800 ºC [5].

4.3. $La_{0.98}Cr_{0.75}Mn_{0.25}O_{3-\delta}$-CGO nanocomposite electrodes

The preparation of composite electrodes by combining a perovskite-type electrode with predominant electronic conductivity and an ionic conductor, such as CGO, is one of the main strategies to improve the electrode performance [15–17]. Based on this idea, $La_{0.98}Cr_{0.75}Mn_{0.25}O_{3-\delta}$-$Ce_{0.9}Gd_{0.1}O_{1.95}$ (LCM-CGO) nanocomposite layers were prepared for the first time by spray-pyrolysis deposition directly on the YSZ electrolyte surface by using an aqueous precursor solution containing stoichiometric amounts of the corresponding nitrate salts. It is worth mentioning that quartz substrates were employed for a better analysis of the composition and structure

UNIVERSIDAD DE MÁLAGA

of the nanocomposite electrodes, since polycrystalline YSZ and LSGM substrates show XRD peak overlapping with LCM and CGO phases, hindering a correct phase identification.

Figure 4.8 displays XRD patterns onto quartz substrates at 800 ºC of $La_{0.98}Cr_{0.75}Mn_{0.25}O_{3-\delta}$-$Ce_{0.9}Gd_{0.1}O_{1.95}$ (LCM-CGO) electrodes with different LCM content (40, 50, 60 and 100 wt.%). Hereafter the electrodes are denoted as *x*LCM, where *x* represents the wt. % of LCM. For better comparison, the XRD pattern of the CGO layer obtained under the same conditions is included. Two different phases are identified in the XRD data, assigned to an orthorhombic perovskite (s.g. Pbnm) and a cubic fluorite (s.g. $Fm\bar{3}m$) without additional diffraction peaks assigned to secondary phases.

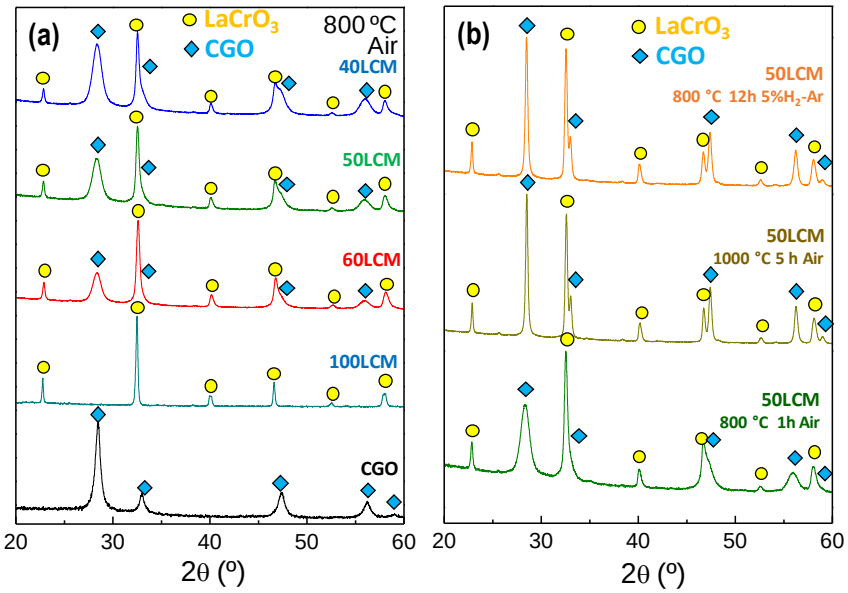

Figure 4.8. (a) XRD patterns of LCM-CGO nanocomposite electrodes deposited by spray-pyrolysis onto quartz substrates and calcined at 800 ºC for 1 h in air. (b) XRD patterns of 50LCM after annealing in air and 5% H_2-Ar at different temperatures.

The thermal stability of the nanocomposite electrodes was confirmed by annealing the layers at 1000 ºC for 5 h in air, not showing any structural transformation or additional phases (Figure 4.8b). In addition, the nanocomposite electrodes are

UNIVERSIDAD DE MÁLAGA

stable in a reducing atmosphere (5% H_2-Ar) at 800 ºC for 12 h, confirming their potential use as symmetrical electrodes (Figure 4.8b).

Rietveld fitting of the samples deposited onto quartz showed that the cell volume at 800 ºC of 100LCM obtained by spray-pyrolysis, 235.050(2) Å^3, is similar to that obtained for the same composition obtained by the freeze-drying method, 235.121(3) Å^3 (Table 4.2 and Figure 4.9). In the case of the nanocomposite electrodes deposited by spray-pyrolysis, the cell volume for the LCM constituent slightly decreases from 235.616(3) Å^3 for 40LCM to 234.934 (3) Å^3 for 60LCM. Regarding the CGO component, the cell volume increases from 159.202(4) Å^3 for the single CGO layer to 162.383(2) Å^3 for 60LCM, suggesting a minor cation exchange between LCM and CGO phases during the co-sintering process.

Table 4.2. Structural and microstructural parameters of LCM-CGO composite electrodes with different LCM contents deposited on amorphous quartz substrates and YSZ and LSGM pellets.

Composition	T (ºC)	Substrate	Volume (Å^3)		LCM (wt.%)	R_{wp} (%)
			LCM	CGO		
100LCM	800	FD	235.121(3)	-	100	3.5
100LCM	1000	FD	234.801(3)	-	100	2.3
100LCM (H_2)	800	FD	235.732(3)	-	100	3.8
100LCM	800	Quartz	235.050(2)	-	100	7.1
60LCM	800	Quartz	234.934(2)	162.383(2)	58	4.1
40LCM	800	Quartz	235.616(2)	161.698(2)	32	4.6
50LCM	800	Quartz	235.171(2)	162.017(2)	47	5.6
50LCM	1000	Quartz	234.389(2)	159.247(2)	54	4.5
50LCM (H_2)	1000	Quartz	234.843(2)	159.428(2)	54	4.7
CGO	800	Quartz	-	159.202(4)	-	2.8
50LCM	1000	YSZ	235.028(2)	160.953(2)	51	1.9
50LCM	1000	LSGM	234.971(2)	161.031(2)	54	3.9

UNIVERSIDAD DE MÁLAGA

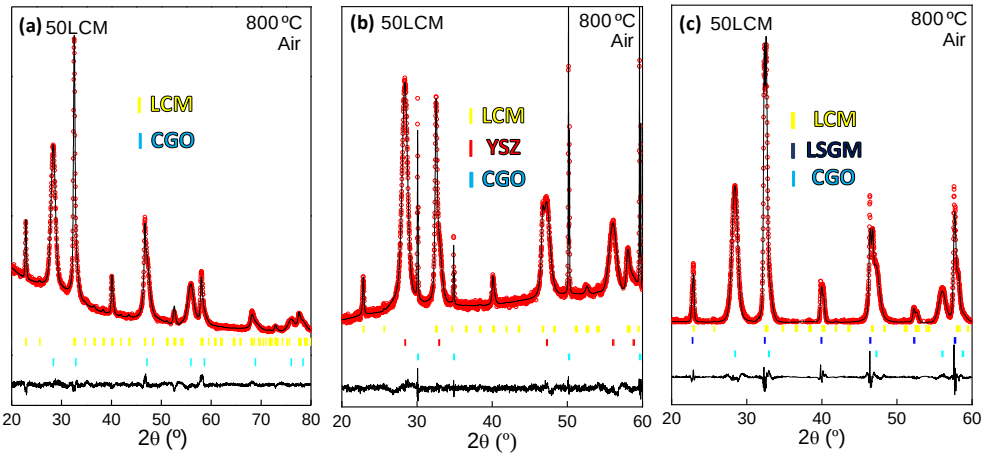

Figure 4.9. Rietveld plots of 50LCM nanocomposite deposited onto (a) quartz (b) YSZ and (c) LSGM at 800 ºC for 1 h in air.

The incorporation of La^{3+} (1.16 Å) into the CGO lattice, with a higher ionic radius than Ce^{4+} (0.97 Å) could explain the increase in the lattice cell volume [18]. This minor cation exchange between LCM and CGO phases is not expected to induce detrimental effects on the electrocatalytic activity of the LCM-CGO electrodes. In fact, Ce-doped $LaCrO_{3-\delta}$ materials showed improved performance for fuel oxidation due to the high catalytic activity of Ce^{4+}/Ce^{3+} redox pair [19]. Additionally, the phase quantification obtained by Rietveld analysis was similar to the nominal one, which further confirms the composition of the *x*LCM nanocomposites. In 5% H_2-Ar, similar trends to that discussed for the infiltrated electrodes are observed.

Figure 4.10a shows the HRTEM images of 50LCM calcined at 800 ºC, which is composed of nanoparticles of 10 nm diameter of both LCM and CGO phases as confirmed by the interplanar distances d_{hkl} of the different crystals. Interestingly, the HAADF-STEM image of 50LCM show that the nanostructure is retained with particle size lower than 50 nm after annealing at 1000 ºC for 5 h, further confirming the improved thermal stability of the nanocomposite electrodes (Figure 4.10b). The composition and homogeneous distribution of LCM and CGO phase in the nanocomposite electrodes are further confirmed by EDS analysis (Figure 4.10c).

UNIVERSIDAD DE MÁLAGA

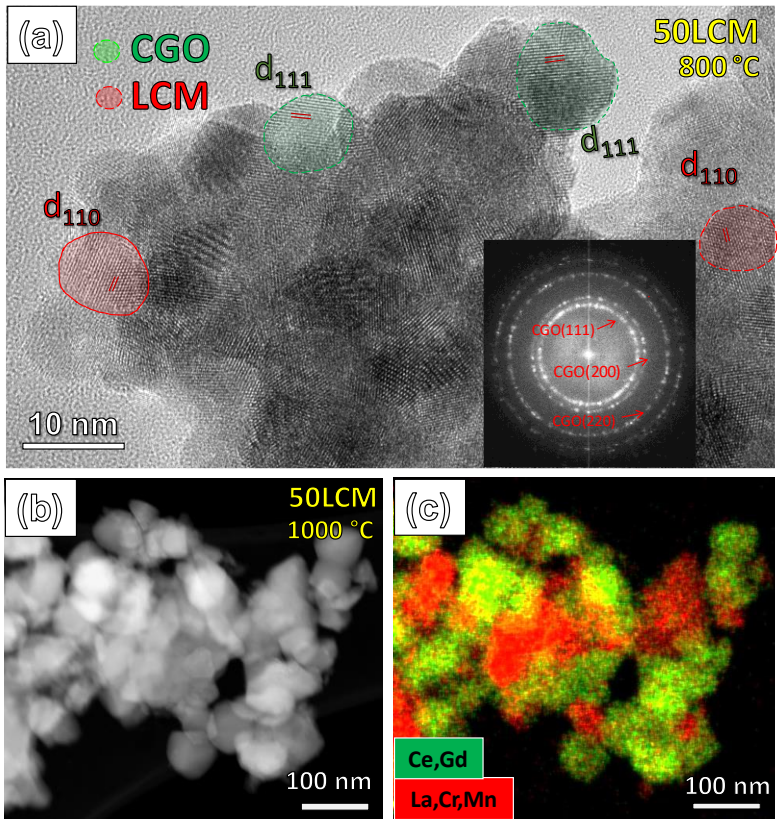

Figure 4.10. (a) HRTEM image of 50LCM nanocomposite calcined at 800 °C for 1 h (b) HAADF-STEM image of 50LCM after calcination at 1000 °C in air and the corresponding (c) EDS elemental mapping distribution. The inset of (a) shows the electron diffraction pattern with the main reflections attributed to a cubic fluorite structure.

The total polarization resistance in air of *x*LCM (x= 40, 50, 60 and 100 wt.%) series decrease considerably for the nanocomposite electrodes compared to 100LCM with R_p values of 5.60, 1.11, 0.77, and 0.92 Ω cm^2 for 100LCM, 60LCM, 50LCM, and 40LCM, respectively, at 700 °C. In 100% H_2, the lowest R_p values were also found for 50LCM, *i.e.* 0.18 Ω cm^2 at 700 ºC compared to 0.54 Ω cm^2 for 60LCM and 3.8 Ω cm^2 for 100LCM, respectively, at the same temperature.

Since the best electrochemical performance of all nanocomposite electrodes was observed for the 50LCM, this composition was further studied for its implementation as a symmetrical electrode (SSOFC).

UNIVERSIDAD DE MÁLAGA

4.4. Electrode architecture optimization for highly boosting the electrochemical properties

In this section, the electrochemical properties of $La_{0.98}Cr_{0.75}Mn_{0.25}O_{3-\delta}$ (LCM) electrodes prepared with different microstructural designs are studied. In particular, four different electrode configurations will be compared and analysed in detail: (i) pure LCM deposited by spray-pyrolysis (100LCM); (ii) 50 wt.% LCM-CGO mixed powder composites deposited by traditional screen-printing (50LCM-P); (iii) LCM electrode infiltrated by spray-pyrolysis into a CGO backbone (LCM-Inf) and (iv) 50 wt.% LCM-CGO nanocomposite deposited by spray-pyrolysis directly on the electrolyte (50LCM). The electrodes deposited by spray-pyrolysis were prepared in the same conditions mentioned in previous sections. The 50LCM-P was prepared by mixing powders of LCM (freeze-drying) and CGO (Rhodia) and then screen-printed onto YSZ electrolytes, followed by a calcination at 1100 ºC for 1 h to ensure adequate adhesion to the electrolyte.

The microstructure of the LCM electrodes obtained by different microstructural strategies is compared in Figure 4.11. The screen-printed 50LCM-P composite electrode shows a particle size lower than 1 μm after sintering at 1100 ºC for 1 h, as well as high porosity that ensures adequate gas diffusion (Figure 4.11a). The 100LCM electrode obtained directly on the electrolyte by spray-pyrolysis is composed of aggregates of particles of 150-200 nm diameter after the calcination at 800 ºC for 1 h (Figure 4.11b). The electrode infiltrated into the CGO backbone, LCM-Inf, shows a partial coating of the CGO surface by LCM particles of ~150 nm diameter (Figure 4.11c,e). Interestingly, in the case of the nanocomposite electrode, 50LCM, the particle size is drastically reduced to 30 nm diameter after annealing at 800 ºC (Figure 4.11d,f). This finding can be attributed to the co-sintering of both LCM and CGO that ensures a nanoscale contact of both phases, limiting the cation diffusion at the grain-boundary region and therefore suppressing the grain growth [20–22].

UNIVERSIDAD DE MÁLAGA

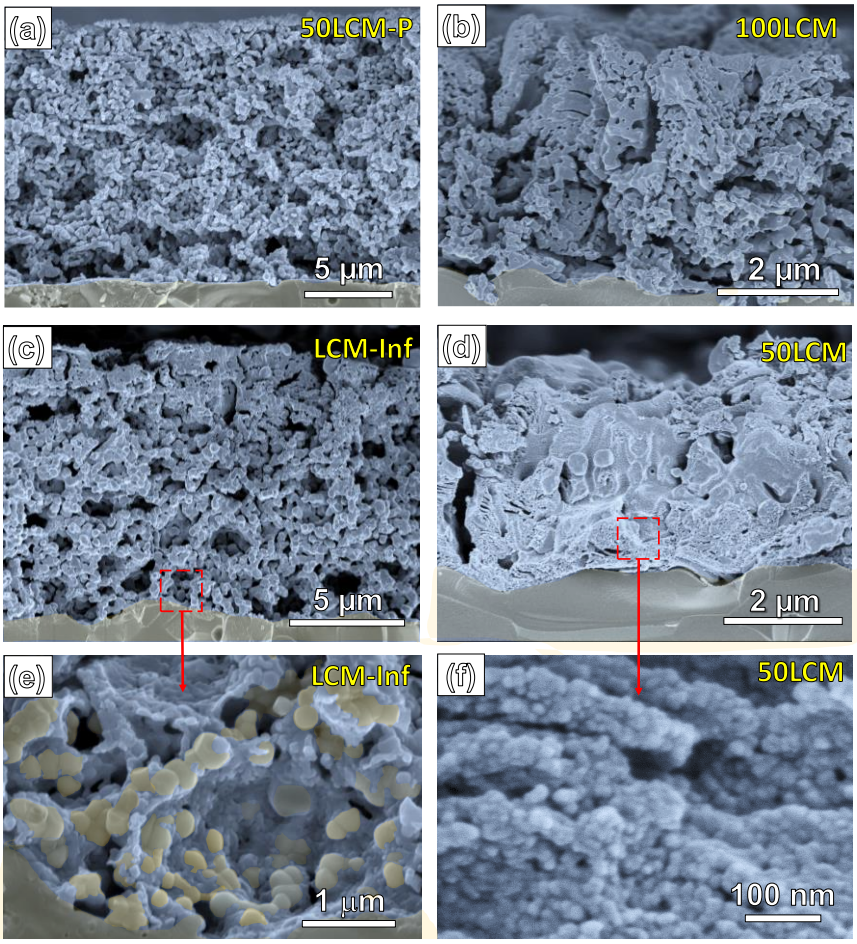

Figure 4.11. SEM images at different magnifications of (a) 50LCM-P electrode deposited by screen-printing, (b) 100LCM obtained directly on the YSZ electrolyte by spray-pyrolysis, (c) LCM-Inf obtained by the infiltration of LCM into CGO backbone by spray-pyrolysis and (d) 50LCM deposited by spray-pyrolysis. (e) and (f) show zoomed images of the LCM-Inf and 50LCM microstructures, respectively.

Figure 4.12 compares the impedance spectra in air at 700 ºC for the different electrode configurations. 50LCM-P and 100LCM show similar and relatively high values of polarization resistance (R_p), 5.60 and 5.10 Ω cm^2, respectively, due to the low mixed ionic-electronic conductivity of pristine 100LCM and the low TPB length of 50LCM-P for ORR (Figure 4.12a). In contrast, the infiltrated (LCM-Inf) and nanocomposite (50LCM) electrodes, exhibit lower R_p at the same temperature, 0.35 and 0.80 Ω cm^2 in air at 700 ºC, respectively. This improvement can be explained by

UNIVERSIDAD DE MÁLAGA

the larger contact area between LCM and CGO phases, which increases significantly the TPB length for the ORR (Figure 4.12b).

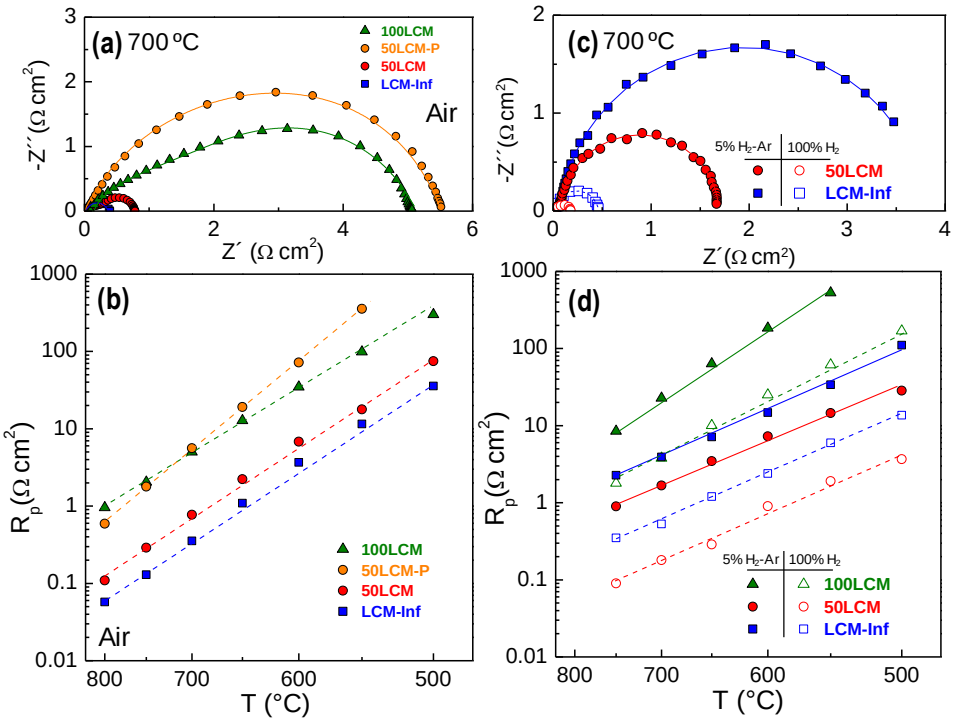

Figure 4.12. (a) Impedance spectra at 700 ºC in air and (b) total polarization resistance as a function of the temperature for the different electrode architectures. (c) Impedance spectra at 700 ºC in 5% H_2-Ar and 100% H_2 and (d) total polarization resistance as a function of the temperature for the different electrode architectures.

In reducing conditions, the total polarization resistance strongly depends on the hydrogen concentration as observed previously in section 4.2.2. Figure 4.12c displays the impedance spectra for some selected electrode configurations in 5% H_2-Ar and 100% H_2. In 5% H_2-Ar, the low-frequency process is the dominant contribution to the overall polarization resistance with a large capacitance of ~ 0.2 F cm^{-2} for all electrodes and the corresponding resistance decreases considerably in 100% H_2 with a pO_2 dependence of $(pH_2)^{\sim 0.9}$, indicating that this process is possibly attributed to gas diffusion limitations due to the use of diluted hydrogen [23,24]. The high frequency (HF) electrode response exhibits a low dependency on the H_2 concentration and it is presumably attributed to oxide-ion transport at the electrode/electrolyte interface [25].

UNIVERSIDAD DE MÁLAGA

In 100% H_2, 50LCM shows a remarkably low R_p of 0.18 Ω cm^2 at 700 ºC, when compared to 3.8 and 0.53 Ω cm^2 for 100LCM and LCM-Inf, respectively. It is worth noting that these values are among the best reported in the literature for $LaCrO_3$-based fuel electrodes in 100% H_2, *i.e.* 0.3 Ω cm^2 at 900 ºC for $La_{0.75}Sr_{0.25}Cr_{0.5}Mn_{0.5}O_{3-\delta}$ [26]; 0.4 Ω cm^2 at 800 ºC for $La_{0.65}Bi_{0.1}Sr_{0.25}Cr_{0.5}Fe_{0.5}O_{3-}$SDC [27]. These values are also comparable to other efficient fuel electrodes such as $Sr_2Fe_{1.5}Mo_{0.5}O_{6-\delta}$ (0.45 Ω cm^2 at 800 ºC) [28] or $Sm_{0.8}Sr_{0.2}Cr_{0.5}Fe_{0.8}Ti_{0.15}Ru_{0.05}O_{3-\delta}$ (0.2 Ω cm^2 at 800 ºC) [29].

Additionally, the activation energy of R_p varies from 1.2 eV for 100LCM to 1.0 eV for 50LCM, which are lower than those values observed in an air atmosphere (1.9 and 1.5 eV, respectively) due to the lower activation energy needed for HOR compared to ORR. The better performance in reducing conditions of 50LCM can be attributed to the synergetic effect of CGO and LCM phases. Interestingly, nanoscale LCM is reported to exhibit improved oxide-ion diffusivity and surface coefficients compared to the bulk material [30]. In particular, the surface exchange kinetics of nanoscale $La_{0.9}Sr_{0.1}CrO_{3-\delta}$ were three orders of magnitude higher through the grain boundary region, fact that would explain the great performance of the 50LCM with nanometric particle size. Furthermore, the presence of CGO nanoparticles with higher reducibility ($Ce^{4+} + e^- \rightarrow Ce^{3+}$) increases both the ionic and n-type electronic conductivity of the nanocomposite electrodes [31].

Since LCM-Inf and 50LCM rendered the best polarization resistance values in a symmetrical configuration in both oxidizing and reducing conditions, they are further characterized to get deeper insights into the nature of the electrochemical processes for ORR and HOR. Firstly, the impedance spectra were acquired as a function of the oxygen partial pressure (pO_2) to elucidate the different processes involved in the ORR. The resistance of each electrochemical process is pO_2-dependent: $R \propto (pO_2)^m$, where the exponent *m* provides information about the nature of the species involved in the ORR sub-reactions, which are discussed in section 3.10.5 [32]. Two main electrode contributions were observed for both LCM-Inf and 50LCM (Figure 4.13a,b). For both electrodes, the process at high frequency (HF) is nearly independent of pO_2, indicating that atomic or molecular oxygen is not involved

UNIVERSIDAD DE MÁLAGA

in this electrode contribution, and therefore, it can be assigned to oxide-ion transport at the electrode/electrolyte interphase ($O^x_{o,\ electrode} \rightarrow O^x_{o,\ electrolyte}$) [33,34].

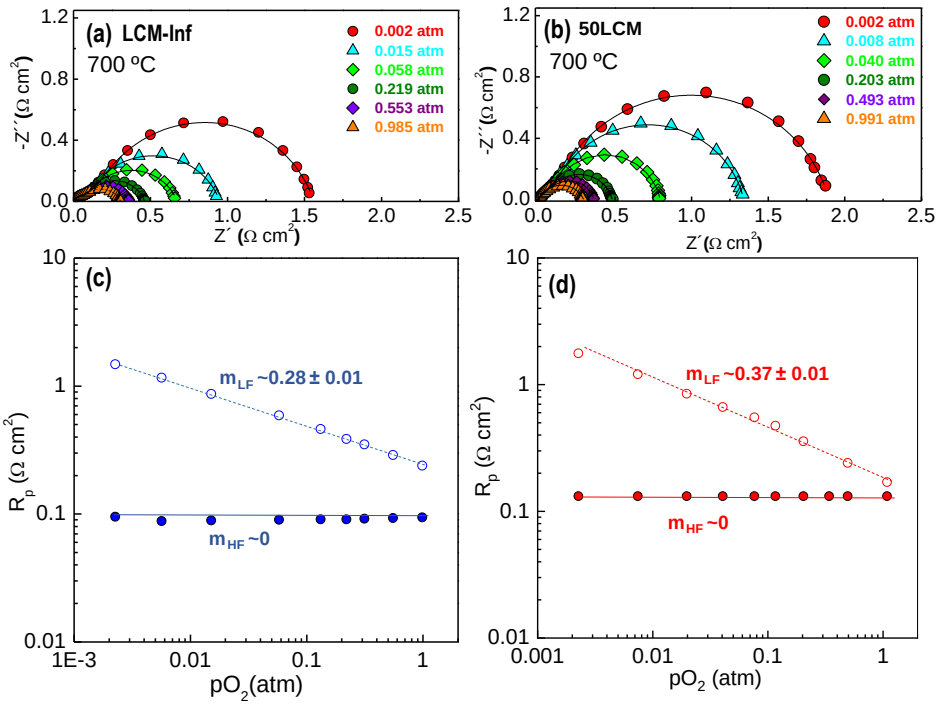

Figure 4.13. Impedance spectra at 700 ºC as a function of the oxygen partial pressure (pO_2) of (a) LCM-Inf and (b) 50LCM. Dependence of the HF and LF resistances as a function of the pO_2 of (c) LCM-Inf and (d) 50LCM.

The low frequency (LF) process is the main contribution to the overall polarization resistance for both electrode configurations but exhibits a different pO_2-dependence. In the case of LCM-Inf, the exponent *m* takes a value of 1/4 and it can be associated with charge transfer on the electrode surface ($O_{ad} + 2e^- + V^{\cdot\cdot}_{o,} \rightarrow O^x_o$) [35] (Figure 4.13c). In contrast, 50LCM shows a different power law dependence with *m* close to 3/8, which is attributed to oxygen dissociative adsorption followed by charge transfer ($O_{ad} + e^- \rightarrow O'_{ad}$) [36] (Figure 4.13d). The different rate-limiting steps for the LF contribution in the infiltrated and nanocomposite electrodes can be associated with the different electrode morphology and porosity. 50LCM shows lower porosity compared to LCM-Inf due to the presence of the thick CGO backbone and consequently, the oxygen adsorption/dissociation on the electrode surface is

UNIVERSIDAD DE MÁLAGA

hindered. However, no evidence of oxygen diffusion limitations (with *m*=1) is observed, confirming that the porosity of this electrode is high enough to act as an efficient cathode material in a wide pO_2 range.

The influence of the dc-current bias on the electrode polarization was also studied by three-probe electrode configuration under both cathodic and anodic polarization as described in section 3.10.4. The corresponding impedance spectra of 50LCM are displayed in Figure 4.14a,b.

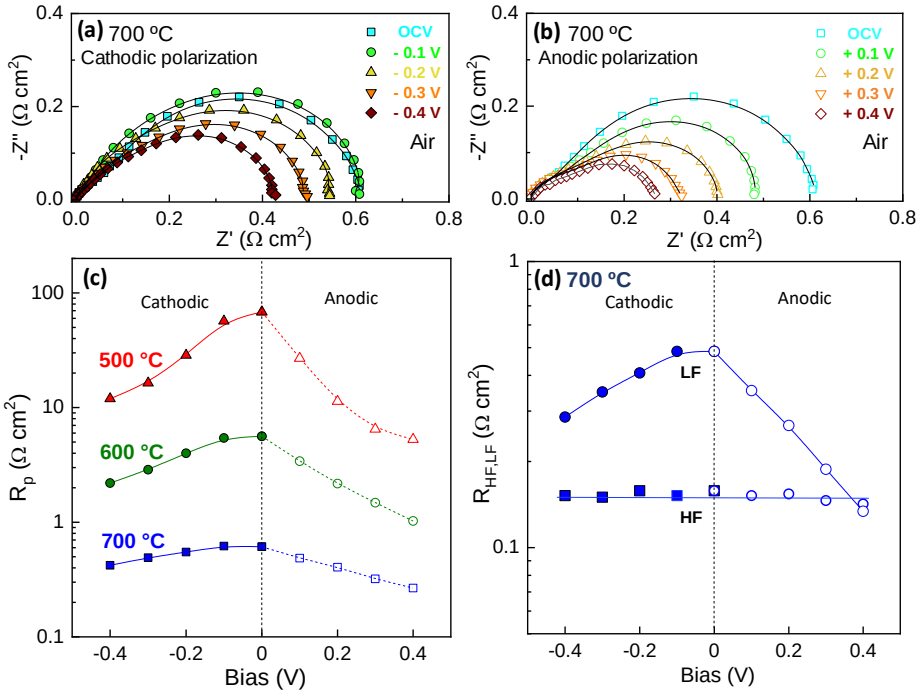

Figure 4.14. Impedance spectra at 700 ºC of 50LCM at different dc bias under (a) cathodic and (b) anodic polarization in a three-probe configuration in air. (c) Total electrode polarization resistance as function of the applied dc-bias at different temperatures. (d) Variation of the R_{HF} and R_{LF} electrode contributions at 700 ºC in air.

Firstly, it is important to remark that the polarization resistance values in three-electrode configuration are similar to those observed in two-electrode configuration (symmetrical cells). After applying a cathodic polarization, the total R_p slightly decreases from 0.60 Ω cm² at open circuit voltage (V=0) to 0.41 Ω cm² at -0.4 V at

UNIVERSIDAD DE MÁLAGA

700 ºC. This improvement of R_p is usually attributed to a reduction of the electrode due to a decrease of pO_2 under cathodic current [37,38]. These findings confirm that the current density accumulates or removes oxygen vacancies at the reaction sites. A higher effect on the electrochemical response is observed after applying a dc bias at lower temperatures, *i.e.* R_p decreases at 500 ºC from 68 to 11 Ω cm^2 under cathodic polarization (Figure 4.14c). A further reduction of the R_p is observed when the dc polarization is reversed to anodic mode, reaching 0.26 and 5.3 Ω cm^2 at 0.4 V at 700 and 500 ºC, respectively (Figure 4.14b). This better performance under anodic polarization has previously been associated with an increase of the pO_2 in the oxygen electrode, improving the electro-hole conductivity [39].

In order to get further information about the influence of the dc bias on each electrode contribution, the impedance spectra are analyzed by equivalent circuits. The R_{HF} contribution, attributed previously to oxide-ion transport at the interface, is not affected by the applied dc current due to the good mixed ionic-electronic conductivity of the nanoengineered electrode and the fast charge transfer process at the interface (Figure 4.14d). Interestingly, the R_{LF} contribution, assigned to electrochemical processes at the electrode surface, is considerably decreased at intermediate temperatures with the dc bias, following a trend similar to that observed with the pO_2. This finding indicates that the variation of the oxygen vacancy concentration at the reaction sites under dc bias has a positive effect on the electrochemical properties, as reported previously for other air electrodes such as $SrCo_{0.9}Ta_{0.1}O_{3-\delta}$, $SrFe_{0.9}Mo_{0.1}O_{3-\delta}$ and $La_2NiO_{4+\delta}$ [37,39,40].

When a dc bias was applied in wet 100% H_2, the R_p under cathodic polarization decreases from 0.29 to 0.15 Ω cm^2 at 700 °C (Figure 4.15a,c). However, this increases when an anodic polarization is applied, *i.e.* 0.55 Ω cm^2 at +0.4 V (Figure 4.15b,c).

UNIVERSIDAD DE MÁLAGA

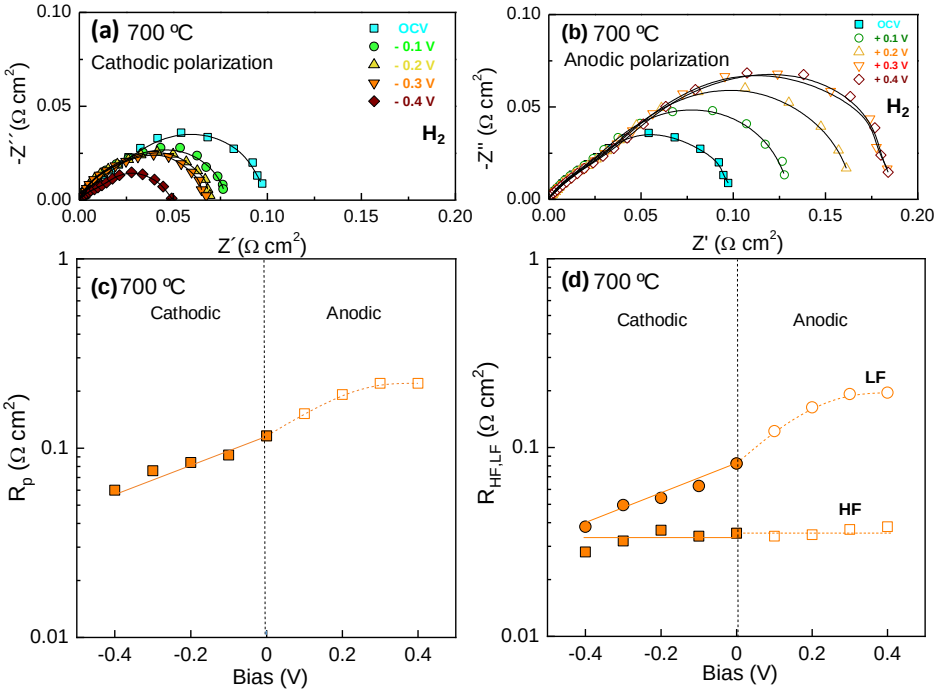

Figure 4.15. Impedance spectra at 700 ºC of 50LCM at different dc bias under (a) cathodic and (b) anodic polarization in a three-probe configuration in 100% H_2. (c) Total electrode polarization resistance as a function of the applied dc bias at 700 ºC. (d) Variation of the R_{HF} and R_{LF} electrode contributions at 700 ºC in 100% H_2.

The charge transfer process (HF contribution) remains constant under both anodic and cathodic polarization, whiles the LF electrode process decreases under cathodic polarization but increases under anodic polarization (Figure 4.15d). A similar trend was observed for $La_{0.3}Sr_{0.7}Fe_{0.7}Cr_{0.3}O_{3-\delta}$ and $Sr_{1.8}Ba_{0.2}Fe_{1.5}Mo_{0.5}O_{6-\delta}$ under anodic polarization [41,42]. Further research at different pH_2O and pH_2 is needed to better identify and understand the different electrode processes involved in the hydrogen oxidation reaction (HOR) and hydrogen evolution reaction (HER).

4.5. Fuel cell tests

The performance of LCM-Inf and 50LCM electrodes was tested in real SOFC operation conditions. LSGM electrolyte-supported cells (300 µm thickness) were prepared and the electrodes were symmetrically deposited onto both faces of the

UNIVERSIDAD DE MÁLAGA

electrolyte by spray-pyrolysis and calcined at 800 ºC for 1 h, as described in previous sections.

Figure 4.16a,b confirmes that the open circuit voltage (OCV) for both cells is close to the theoretical Nernst potential (1.1 V), confirming a good sealing of the cell and no gas leakage across the LSGM electrolyte.

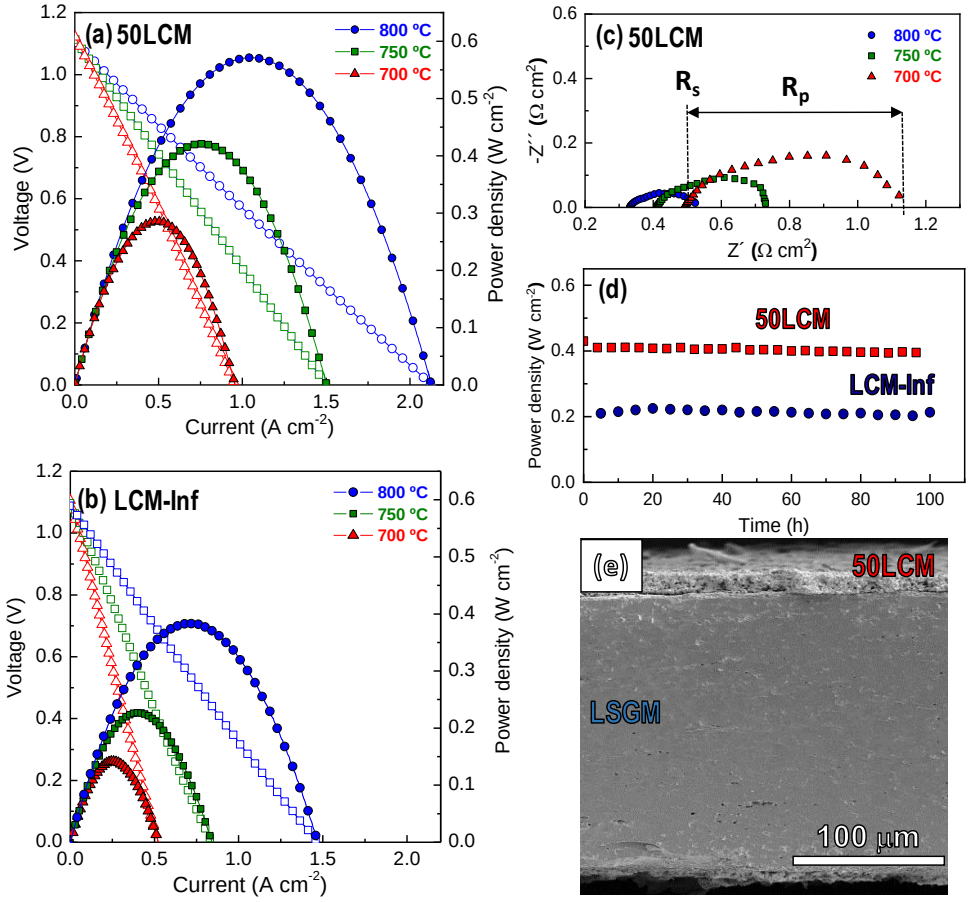

Figure 4.16. I-V-P curves of the LSGM-supported cells with (a) 50LCM and (b) LCM-Inf symmetrical electrodes at different temperatures using wet H_2 as fuel and static air as oxidant. (c) Impedance spectra of the 50LCM symmetrical cell. (d) Stability tests at 750 ºC for 100 h for both cells and (e) cross-sectional SEM image of the 50LCM symmetrical cell after electrochemical characterization.

The 50LCM/LSGM/50LCM cell achieves maximum power density values of 570, 420 and 286 mW cm^{-2} at 800, 750 and 700 ºC, respectively (Figure 4.16a). On

UNIVERSIDAD DE MÁLAGA

the other hand, the LCM-Inf/LSGM/LCM-Inf symmetrical cell with infiltrated electrodes showed maximum power densities slightly lower, 470, 223, 140 mW cm^{-2} at 800, 750 and 700 ºC, respectively (Figure 4.16b). These findings agree with the better performance of 50LCM, determined by impedance spectroscopy in symmetrical cell configuration in reducing conditions.

The ohmic resistance (R_s) of the cells are similar and they increase with decreasing temperature, taking values of ~0.3 and ~0.5 Ω cm^2 at 800 and 700 ºC, respectively for 50LCM (Figure 4.16c). These values agree with those expected for a 300 µm-thick LSGM electrolyte.

It is also worth noting that the maximum power densities obtained in this study were higher than those reported for $LaCrO_3$-based symmetrical electrodes, *i.e.* 175 mW cm^{-2} at 800 ºC for a 300 µm thick LSGM-supported cell with $La_{0.65}Bi_{0.1}Sr_{0.25}Cr_{0.5}Fe_{0.5}O_{3-\delta}$-SDC electrodes [27] or 300 mW cm^{-2} at 900 ºC for a 200 µm thick YSZ supported cell with $La_{0.75}Sr_{0.25}Cr_{0.5}Mn_{0.5}O_3$ electrodes [26]. In addition, the power densities are comparable to $LaCrO_3$-based anodes with exsolved noble metal particles, using highly active cathode materials such as LSCF. For instance, 303 mW cm^{-2} at 800 ºC $La_{0.8}Sr_{0.2}Cr_{0.9}Pd_{0.1}O_{3-\delta}$-CGO/LSGM (400µm)/LSCF [43] or 530 mW cm^{-2} at 800 ºC for $La_{0.8}Sr_{0.2}Cr_{0.82}Ru_{0.18}O_{3-\delta}$-CGO/LSGM(400 µm)/LSCF-CGO [44].

The durability tests at 750 ºC for 100 h confirmed a stable maximum power density for both cell configurations (Figure 4.16d). Cell delamination or cracks were not observed in the single cell by SEM after the electrochemical characterization further confirming the stability of the nanostructured electrodes at intermediate temperatures (Figure 4.16e).

All these results show the great importance of tailoring the electrode microstructure to enhance the electrochemical properties. Among all the microstructural strategies and electrode compositions studied, the infiltrated LCM electrode into a CGO backbone (LCM-Inf) and the nanocomposite electrodes (50LCM), both prepared by spray-pyrolysis, have rendered the best results due to the highly extended TPB for electrochemical reactions. The great results showed by the 50LCM with the intimate mixture of LCM and CGO at the nanoscale open the

UNIVERSIDAD DE MÁLAGA

possibility to improve the electrochemical performance of other symmetrical electrodes by microstructural tailoring.

References

1. Tao, S.; Irvine, J.T.S. A Redox-Stable Efficient Anode for Solid-Oxide Fuel Cells. *Nat. Mater.* **2003**, *2*, 320–323, doi:10.1038/nmat871.
2. Bastidas, D.M.; Tao, S.; Irvine, J.T.S. A Symmetrical Solid Oxide Fuel Cell Demonstrating Redox Stable Perovskite Electrodes. *J. Mater. Chem.* **2006**, *16*, 1603–1605, doi:10.1039/b600532b.
3. Liu, L.; Jiang, M.; Yin, J.; Gui, W.; Jiao, T. Preparation , Sinterability , Electrical Transport and Thermal Expansion of Perovskite-Type $La_{0.8}Ca_{0.2}CrO_3$ Composites. *Appl. Sci.* **2020**, *10*, 4634, doi:https://doi.org/10.3390/app10134634.
4. Mori, M.; Hiei, Y.; Sammes, N.M. Sintering Behavior of Ca- or Sr-Doped $LaCrO_3$ Perovskites Including Second Phase of $AECrO_4$ (AE = Sr, Ca) in Air. *Solid State Ionics* **2000**, *135*, 743–748, doi:10.1016/S0167-2738(00)00372-6.
5. Jiang, S.P.; Liu, L.; Ong, K.P.; Wu, P.; Li, J.; Pu, J. Electrical Conductivity and Performance of Doped $LaCrO_3$ Perovskite Oxides for Solid Oxide Fuel Cells. *J. Power Sources* **2008**, *176*, 82–89, doi:10.1016/j.jpowsour.2007.10.053.
6. Kwon, O.; Joo, S.; Choi, S.; Sengodan, S.; Kim, G. Review on Exsolution and Its Driving Forces in Perovskites. *JPhys Energy* **2020**, *2*, 032001, doi:10.1088/2515-7655/ab8c1f.
7. Tietz, F. Thermal Expansion of SOFC Materials. *Ionics (Kiel).* **1999**, *5*, 129–139, doi:10.1007/BF02375916.
8. La, À.; Cro, M. Dilatometric and High Temperature X-Ray Diffractometric. *Thermochim. Acta* **2002**, *390*, 1–6. doi: 10.1016/S0040-6031(02)00003-5
9. Gupta, S.; Mahapatra, M.K.; Singh, P. Lanthanum Chromite Based Perovskites for Oxygen Transport Membrane. *Mater. Sci. Eng. R Reports* **2015**, *90*, 1–36. doi: 10.1016/j.mser.2015.01.001
10. Osinkin, D.A. An Approach to the Analysis of the Impedance Spectra of Solid Oxide Fuel Cell Using the DRT Technique. *Electrochim. Acta* **2021**, *372*, 137858, doi:10.1016/j.electacta.2021.137858.
11. Zhang, J.; Lei, L.; Li, H.; Chen, F.; Han, M. A Practical Approach for Identifying Various Polarization Behaviors of Redox-Stable Electrodes in Symmetrical Solid Oxide Fuel Cells. *Electrochim. Acta* **2021**, *384*, 138340, doi:10.1016/j.electacta.2021.138340.
12. Dos Santos-Gómez, L.; Porras-Vázquez, J.M.; Losilla, E.R.; Marrero-López, D. Ti-Doped $SrFeO_3$ Nanostructured Electrodes for Symmetric Solid Oxide Fuel Cells. *RSC Adv.* **2015**, *5*, 107889–107895, doi:10.1039/c5ra23771h.
13. La, D.; Groupy, L.; Anderson, H.U. Densification of $La_{1-x}Si_xCrO_3$. *J. Am. Ceram. Soc.* **1976**, *59*, 3–5, doi:10.1111/j.1151-2916.1976.tb09517.x.
14. Ca, L.; Composites, C. Preparation , Sinterability , Electrical Transport and Thermal Expansion of Perovskite-Type. *Appl. Sci.* **2020**, *10*, 4634, doi:10.3390/app10134634.
15. Connor, P.A.; Yue, X.; Savaniu, C.D.; Price, R.; Triantafyllou, G.; Cassidy, M.; Kerherve, G.; Payne, D.J.; Maher, R.C.; Cohen, L.F.; Irvine, J.T.S. Tailoring SOFC Electrode Microstructures for Improved Performance. *Adv. Energy Mater.* **2018**, *8*, 1–20, doi:10.1002/aenm.201800120.
16. Ramadhani, F.; Hussain, M.A.; Mokhlis, H.; Hajimolana, S. Optimization Strategies for Solid Oxide Fuel Cell (SOFC) Application: A Literature Survey. *Renew. Sustain. Energy Rev.* **2017**,

UNIVERSIDAD DE MÁLAGA

76, 460–484, doi:10.1016/j.rser.2017.03.052.
17. Dos Santos-Gómez, L.; Losilla, E.R.; Martín, F.; Ramos-Barrado, J.R.; Marrero-López, D. Novel Microstructural Strategies to Enhance the Electrochemical Performance of $La_{0.8}Sr_{0.2}MnO_{3-\delta}$ Cathodes. *ACS Appl. Mater. Interfaces* **2015**, *7*, 7197–7205, doi:10.1021/acsami.5b00255.
18. Zamudio-García, J.; Porras-Vázquez, J.M.; Canales-Vázquez, J.; Cabeza, A.; Losilla, E.R.; Marrero-López, D. Relationship between the Structure and Transport Properties in the $Ce_{1-x}La_xO_{2-x/2}$ System. *Inorg. Chem.* **2019**, *58*, 9368–9377, doi:10.1021/acs.inorgchem.9b01104.
19. Lay, E.; Benamira, M.; Pirovano, C.; Gauthier, G.; Dessemond, L. Effect of Ce-Doping on the Electrical and Electrocatalytical Behavior of La/Sr Chromo-Manganite Perovskite as New SOFC Anode. *Fuel Cells* **2012**, *12*, 265–274, doi:10.1002/fuce.201100070.
20. Shimada, H.; Yamaguchi, T.; Kishimoto, H.; Sumi, H.; Yamaguchi, Y.; Nomura, K.; Fujishiro, Y. Nanocomposite Electrodes for High Current Density over 3 A cm^{-2} in Solid Oxide Electrolysis Cells. *Nat. Commun.* **2019**, *10*, 1–10, doi:10.1038/s41467-019-13426-5.
21. Fan, L.; Zhu, B.; Su, P.C.; He, C. Nanomaterials and Technologies for Low Temperature Solid Oxide Fuel Cells: Recent Advances, Challenges and Opportunities. *Nano Energy* **2018**, *45*, 148–176, doi:10.1016/j.nanoen.2017.12.044.
22. dos Santos-Gómez, L.; Zamudio-García, J.; Porras-Vázquez, J.M.; Losilla, E.R.; Marrero-López, D. Highly Efficient $La_{0.8}Sr_{0.2}MnO_{3-\delta}$-$Ce_{0.9}Gd_{0.1}O_{1.95}$ Nanocomposite Cathodes for Solid Oxide Fuel Cells. *Ceram. Int.* **2018**, *44*, 4961–4966, doi:10.1016/j.ceramint.2017.12.089.
23. Zhang, J.; Lei, L.; Li, H.; Chen, F.; Han, M. A Practical Approach for Identifying Various Polarization Behaviors of Redox-Stable Electrodes in Symmetrical Solid Oxide Fuel Cells. *Electrochim. Acta* **2021**, *384*, 138340, doi:10.1016/j.electacta.2021.138340.
24. Osinkin, D.A. Hydrogen Oxidation Kinetics on a Redox Stable Electrode for Reversible Solid-State Electrochemical Devices: The Critical Influence of Hydrogen Dissociation on the Electrode Surface. *Electrochim. Acta* **2021**, *389*, 138792, doi:10.1016/j.electacta.2021.138792.
25. Osinkin, D.A. An Approach to the Analysis of the Impedance Spectra of Solid Oxide Fuel Cell Using the DRT Technique. *Electrochim. Acta* **2021**, *372*, 137858, doi:10.1016/j.electacta.2021.137858.
26. Bastidas, D.M.; Tao, S.; Irvine, J.T.S. A Symmetrical Solid Oxide Fuel Cell Demonstrating Redox Stable Perovskite Electrodes. *J. Mater. Chem.* **2006**, *16*, 1603–1605, doi:10.1039/b600532b.
27. Wan, Y.; Xing, Y.; Xu, Z.; Xue, S.; Zhang, S.; Xia, C. A-Site Bismuth Doping, a New Strategy to Improve the Electrocatalytic Performances of Lanthanum Chromate Anodes for Solid Oxide Fuel Cells. *Appl. Catal. B Environ.* **2020**, *269*, 118809, doi:10.1016/j.apcatb.2020.118809.
28. Liu, Q.; Dong, X.; Xiao, G.; Zhao, F.; Chen, F. A Novel Electrode Material for Symmetrical SOFCs. *Adv. Mater.* **2010**, *22*, 5478–5482, doi:10.1002/adma.201001044.
29. Fan, W.; Sun, Z.; Bai, Y.; Wu, K.; Zhou, J.; Cheng, Y. In Situ Growth of Nanoparticles in A-Site Deficient Ferrite Perovskite as an Advanced Electrode for Symmetrical Solid Oxide Fuel Cells. *J. Power Sources* **2020**, *456*, 228000, doi:10.1016/j.jpowsour.2020.228000.
30. Baiutti, F.; Chiabrera, F.; Diercks, D.; Cavallaro, A.; Yedra, L.; López-Conesa, L.; Estradé, S.; Peiró, F.; Morata, A.; Aguadero, A.; Tarancon, A. Direct Measurement of Oxygen Mass Transport at the Nanoscale. *Adv. Mater.* **2021**, doi:10.1002/adma.202105622.
31. Raza, R.; Zhu, B.; Rafique, A.; Naqvi, M.R.; Lund, P. Functional Ceria-Based Nanocomposites for Advanced Low-Temperature (300–600 °C) Solid Oxide Fuel Cell: A Comprehensive Review. *Mater. Today Energy* **2020**, *15*, doi:10.1016/j.mtener.2019.100373.
32. Siebert, E.; Hammouche, A.; Kleitz, M. Impedance Spectroscopy Analysis of La1 -

UNIVERSIDAD DE MÁLAGA

XSritxMnO3-Yttria-Stabilized Zirconia Electrode Kinetics. *Electrochim. Acta* **1995**, *40*, 1741–1753, doi:10.1016/0013-4686(94)00361-4.

33. Marrero-López, D.; Romero, R.; Martín, F.; Ramos-Barrado, J.R. Effect of the Deposition Temperature on the Electrochemical Properties of $La_{0.6}Sr_{0.4}Co_{0.8}Fe_{0.2}O_{3-\delta}$ Cathode Prepared by Conventional Spray-Pyrolysis. *J. Power Sources* **2014**, *255*, 308–317, doi:10.1016/j.jpowsour.2014.01.021.
34. Chen, X.J.; Khor, K.A.; Chan, S.H. Identification of O_2 Reduction Processes at Yttria Stabilized Zirconia|doped Lanthanum Manganite Interface. *J. Power Sources* **2003**, *123*, 17–25, doi:10.1016/S0378-7753(03)00436-1.
35. Chen, J.; Wan, D.; Sun, X.; Li, B.; Lu, M. Electrochemical Impedance Spectroscopic Characterization of Impregnated $La_{0.6}Sr_{0.4}Co_{0.2}Fe_{0.8}O_{3-\delta}$ Cathode for Intermediate-Temperature SOFCs. *Int. J. Hydrogen Energy* **2018**, *43*, 9770–9776, doi:10.1016/j.ijhydene.2018.03.223.
36. Kuai, X.; Yang, G.; Chen, Y.; Sun, H.; Dai, J.; Song, Y.; Ran, R.; Wang, W.; Zhou, W.; Shao, Z. Boosting the Activity of $BaCo_{0.4}Fe_{0.4}Zr_{0.1}Y_{0.1}O_{3-\delta}$ Perovskite for Oxygen Reduction Reactions at Low-to-Intermediate Temperatures through Tuning B-Site Cation Deficiency. *Adv. Energy Mater.* **2019**, *9*, doi:10.1002/aenm.201902384.
37. Pérez-Coll, D.; Aguadero, A.; Escudero, M.J.; Daza, L. Effect of DC Current Polarization on the Electrochemical Behaviour of $La_2NiO_{4+\delta}$ and $La_3Ni_2O_{7+\delta}$-Based Systems. *J. Power Sources* **2009**, *192*, 2–13, doi:10.1016/j.jpowsour.2008.10.073.
38. Chen, X.J.; Khor, K.A.; Chan, S.H. Electrochemical Behavior of La(Sr)MnO_3 Electrode under Cathodic and Anodic Polarization. *Solid State Ionics* **2004**, *167*, 379–387, doi:10.1016/j.ssi.2003.08.049.
39. Wang, J.; Yang, T.; Lei, L.; Huang, K. Ta-Doped $SrCoO_{3-\delta}$ as a Promising Bifunctional Oxygen Electrode for Reversible Solid Oxide Fuel Cells: A Focused Study on Stability. *J. Mater. Chem. A* **2017**, *5*, 8989–9002, doi:10.1039/c7ta02003a.
40. Zapata-Ramírez, V.; Mather, G.C.; Azcondo, M.T.; Amador, U.; Pérez-Coll, D. Electrical and Electrochemical Properties of the $Sr(Fe,Co,Mo)O_{3-\delta}$ System as Air Electrode for Reversible Solid Oxide Cells. *J. Power Sources* **2019**, *437*, doi:10.1016/j.jpowsour.2019.226895.
41. Chen, M.; Chen, D.; Chang, M.; Hu, H.; Xu, Q. New Insight into Hydrogen Oxidation Reaction on $La_{0.3}Sr_{0.7}Fe_{0.7}Cr_{0.3}O_{3-\delta}$ Perovskite as a Solid Oxide Fuel Cell Anode . *J. Electrochem. Soc.* **2017**, *164*, F405–F411, doi:10.1149/2.1571704jes.
42. Kamlungsua, K.; Su, P.C. Moisture-Dependent Electrochemical Characterization of $Ba_{0.2}Sr_{1.8}Fe_{1.5}Mo_{0.5}O_{6-\delta}$ as the Fuel Electrode for Solid Oxide Electrolysis Cells (SOECs). *Electrochim. Acta* **2020**, *355*, 136670, doi:10.1016/j.electacta.2020.136670.
43. Zenou, V.Y.; Fowler, D.E.; Gautier, R.; Barnett, S.A.; Poeppelmeier, K.R.; Marks, L.D. Redox and Phase Behavior of Pd-Substituted $(La,Sr)CrO_3$ Perovskite Solid Oxide Fuel Cell Anodes. *Solid State Ionics* **2016**, *296*, 90–105, doi:10.1016/j.ssi.2016.09.006.
44. Kobsiriphat, W.; Madsen, B.D.; Wang, Y.; Marks, L.D.; Barnett, S.A. $La_{0.8}Sr_{0.2}Cr_{1-x}Ru_xO_{3-\delta}$-$Gd_{0.1}Ce_{0.9}O_{1.95}$ Solid Oxide Fuel Cell Anodes: Ru Precipitation and Electrochemical Performance. *Solid State Ionics* **2009**, *180*, 257–264, doi:10.1016/j.ssi.2008.12.022.

UNIVERSIDAD DE MÁLAGA

UNIVERSIDAD
DE MÁLAGA

Chapter 5

UNIVERSIDAD
DE MÁLAGA

UNIVERSIDAD
DE MÁLAGA

$SrTiO_3$-based electrodes

In order to enhance the electrochemical properties of $SrTiO_3$ electrodes, A-site doping strategies with trivalent elements (La^{3+}, Y^{3+} or Pr^{3+}) or B-site doping with Nb^{5+} have been tested [1–4]. Among all dopant strategies studied, Pr-doped $SrTiO_3$ has attracted great attention due to the enhanced electrochemical properties in both air and H_2 atmospheres by the presence of Pr^{4+}/Pr^{3+} [5].

In this chapter, different strategies were used to obtain $x(Sr_{0.7}Pr_{0.3})_{0.95}TiO_{3\pm\delta}$- (100-$x$)CGO (xSPTO) composite electrodes (x = 40-60 wt.%). The electrodes were deposited by traditional screen-printing or by spray-pyrolysis deposition onto YSZ electrolytes. The influence of the synthetic preparation on the microstructure and the electrochemical properties was studied in detail to achieve highly efficient and stable symmetrical electrodes.

UNIVERSIDAD DE MÁLAGA

5.1. Phase formation of SPTO-CGO nanocomposites

The nanocomposite electrodes with the following nominal composition $x(Sr_{0.7}Pr_{0.3})_{0.95}TiO_{3-\delta}$-(100-$x$)CGO ($x$SPTO) were prepared with different SPTO contents (40, 50 and 60 wt. %) by spray-pyrolysis deposition directly on the YSZ electrolyte. The electrodes were prepared with A-site deficiency to avoid the segregation of Sr-based compounds on electrode surface. The precursor solutions were sprayed onto YSZ and LSGM electrolytes at 450 ºC for 1 h and then calcined at different temperatures between 800 and 1000 ºC in air. It has to be noted that 450 ºC is the optimal deposition temperature to obtain homogeneous films with good adhesion to the electrolyte. Further information about this work can be found in the article A3.

The same electrodes were prepared from the freeze-drying precursor method and screen-printing deposition to compare their properties with those obtained by spray-pyrolysis. In this work, two different approaches were used.

(i) Firstly, SPTO and CGO powders were prepared by the freeze-drying precursor method and then calcined at 800 ºC to achieve crystallization. These powders were physically mixed in a planetary mill in 50 wt.% with Decoflux™ organic binder to obtain an ink.

(ii) In a second approach, the SPTO-CGO composites were prepared by co-sintering in a single step by freeze-drying using a solution containing all cations in stoichiometric amounts. The dried precursors were calcined at 800 ºC and then mixed with Decoflux™ binder.

In both cases, the powders were screen-printed on YSZ electrolytes and sintered at 1100 ºC for 1 h to achieve an adequate adhesion to the electrolyte. Hereafter, the 50 wt.% SPTO electrodes obtained by physically mixing (PM) and the co-synthesized electrodes by freeze-drying (FD) will be labelled as 50SPTO-PM and 50SPTO-FD, respectively. In the case of the blank SPTO, it will be denoted at 100SPTO-FD.

UNIVERSIDAD DE MÁLAGA

Figure 5.1 shows the Rietveld plots of the XRD patterns of SPTO and CGO powders obtained by the freeze-drying precursor method. At 800 ºC, the SPTO with perovskite structure and the CGO with fluorite structure are single phases, which are adequately fitted in the $Pm\bar{3}m$ and $Fm\bar{3}m$ space groups, respectively (Figure 5.1a,b). Interestingly, the composite material is also obtained in one step by co-sintering at 800 ºC, 50SPTO-FD (Figure 5.1c). The main difference between 50SPTO-FD nanocomposite and the single compounds is the average crystallite size estimated by Scherrer's equation, which decreases from 24.1 and 31.7 nm for the SPTO and CGO individual phases, respectively, to 14.6 and 7.4 nm for SPTO and CGO components, respectively, in 50SPTO-FD. This behavior is attributed to the co-sintering process of two immiscible phases as previously observed for nanocomposite layers prepared by spray-pyrolysis in chapter 4.

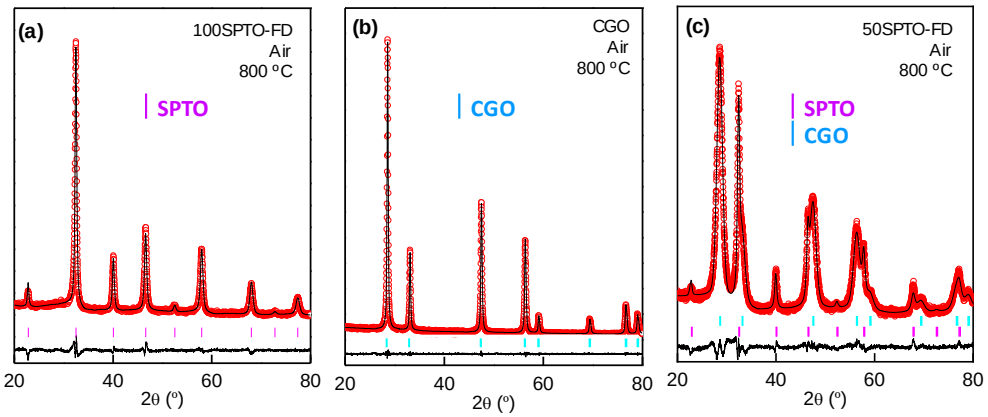

Figure 5.1. Rietveld plots of (a) 100SPTO-FD, (b) CGO and (c) 50SPTO-FD at 800 ºC powders prepared by freeze-drying method and calcined at 800 ºC for 1 h in air.

The cell volumes and fitting parameters of the different electrode compositions obtained by the Rietveld method are summarized in Table 5.1. The Rietveld refinement of 50SPTO-FD revealed minor differences in the cell volumes of SPTO and CGO constituents when compared to the individual phases. At 800 ºC, the cell volumes of SPTO and CGO in 50SPTO-FD are 59.919(2) and 159.749(2) $Å^3$, respectively, slightly different from those observed for the individual phases, 59.128(3) $Å^3$ for SPTO and 159.202(4) $Å^3$ for CGO.

UNIVERSIDAD DE MÁLAGA

Table 5.1. Structural parameters, weight fractions, disagreement factors and particle size of $(Sr_{0.7}Pr_{0.3})_{0.95}TiO_{3\pm\delta}$ (100SPTO-FD) powder, $(Sr_{0.7}Pr_{0.3})_{0.95}TiO_{3\pm\delta}$-CGO (50 wt.%) prepared by powder mixture (50STPO-PM), co-synthesis via freeze-drying (50STPO-FD) and layers directly assembled on the electrolyte by spray-pyrolysis (*x*SPTO).

Composition	T (ºC)	Preparation Method	Volume (Å^3) SPTO	Volume (Å^3) CGO	SPTO (wt.%)	R_{wp} (%)	d_{CGO} (nm)	d_{SPTO} (nm)
100SPTO-FD	800	FD	59.128(3)	-	100	3.8	-	24.1
100SPTO-FD	800(H_2)	FD	59.285(2)	-	100	5.2	-	24.6
100SPTO-FD	1000	FD	59.301(3)	-	100	3.4	-	28.2
100SPTO-FD	1500	FD	59.659(3)	-	100	8.9	-	103.9
100SPTO-FD	800(H_2)	FD	59.710(3)	-	100	9.4	-	104.2
CGO	800	FD	-	159.202(4)	0	7.4	31.7	-
50STPO-FD	800	FD	59.919(2)	159.749(2)	46	4.2	7.4	14.6
50STPO-FD	1400	FD	59.270(2)	159.284(2)	47	5.3	54.2	49.0
50STPO-PM	1400	FD	59.022(2)	158.683(2)	48	6.9	65.4	55.2
40SPTO	800	SP	59.338(2)	157.577(2)	38	3.4	7.3	13.5
50SPTO	800	SP	59.318(2)	157.461(2)	47	3.6	8.2	15.1
60SPTO	800	SP	59.591(2)	157.873(2)	59	3.6	7.7	13.9
40SPTO	1000	SP	58.829(2)	158.636(2)	41	3.4	22.6	24.6
50SPTO	1000	SP	58.954(2)	158.463(2)	52	4.0	19.1	24.2
50SPTO	1000(H_2)	SP	58.963(2)	159.259(2)	53	3.8	19.3	24.5
60SPTO	1000	SP	58.795(2)	158.591(2)	62	4.6	21.0	26.1

These differences in the cell volumes are not surprising due to the different ionic radii in eightfold coordination of rare-earth elements are similar: r(Ce^{4+})=0.97 Å, (Gd^{3+})=1.053 Å, r(Pr^{3+})=1.126 Å and r(Pr^{4+})=0.96 Å [6], and consequently, minor cation exchange between CGO and SPTO cannot be ruled out. However, no major cation exchanges are expected, since previous reports showed very low Gd incorporation in $Sr_{1-x}Gd_xTiO_{3\pm\delta}$ ($x<0.1$) due to the $Gd_2Ti_2O_7$ formation as a secondary phase, explained by the lower ionic radii of Gd^{3+} [7,8]. In addition, very low Ce-doping has been observed previously in $Sr_{1-x}Ce_xTiO_{3\pm\delta}$ with the segregation of CeO_2 for $x>0.03$ [9]. On the contrary, the solubility of Pr into $Sr_{1-x}Pr_xTiO_{3\pm\delta}$ is above $x=0.3$ [5,10].

UNIVERSIDAD DE MÁLAGA

It has to be noted that no secondary phases are observed in the XRD patterns, even at 1400 ºC for 1 h, confirming minor cation exchange between SPTO and CGO phases.

The SPTO-CGO nanocomposites deposited directly on the YSZ electrolyte by spray-pyrolysis also show high crystallinity without the presence of secondary phases (Figure 5.2a). Regardless of the electrode composition, similar lattice parameters and phase fractions were observed. At 800 ºC, the unit cell volume of the SPTO ranges between 59.338(2) to 59.591(2) $Å^3$ for 40SPTO and 60SPTO, respectively, values that are slightly higher than that observed for the 100SPTO-FD powder, 59.128(3) $Å^3$, at the same temperature. Interestingly, the crystallite sizes are relatively small, 14 and 8 nm for the SPTO and CGO, respectively, at 800 ºC. The Rietveld analysis of the nanocomposite layers indicates a good fitting of the experimental data with R_{wp} disagreement factors varying between 3.4 and 9.5% (Table 5.1). In addition, the phase fraction of SPTO and CGO constituents in the nanocomposite electrodes deposited by spray-pyrolysis are similar to the nominal ones.

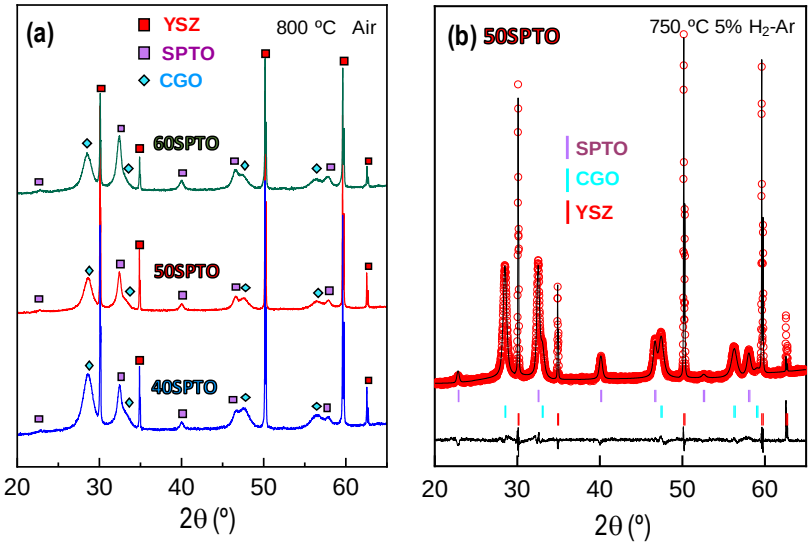

Figure 5.2. (a) XRD patterns of SPTO-CGO nanocomposite layers deposited by spray-pyrolysis on YSZ electrolyte with different SPTO contents (40, 50 and 60 wt.%) and sintered at 800 ºC for 1 h in air. (b) Rietveld plot of 50SPTO after reduction in 5% H_2-Ar at 750 ºC for 12 h.

UNIVERSIDAD DE MÁLAGA

The thermal stability of the nanocomposite electrodes was tested at 1000 ºC for 12 h in air, followed by a reducing treatment at 750 ºC for 12 h in 5% H_2-Ar. A representative Rietveld plot for 50SPTO is displayed in Figure 5.2b.

After calcination at 1000 ºC, the grain size of the nanocomposite layers is still lower than 25 nm due to the nanoscale contact between SPTO and CGO, which suppresses the grain growth rate because of the limited diffusion at the grain boundary. Moreover, the cell volume slightly increases from 58.954(2) to 58.963(2) $Å^3$ for the SPTO constituent after reduction, similar to that reported previously for $Sr_{0.9}Pr_{0.1}TiO_{3\pm\delta}$ and $Sr_{0.7}Pr_{0.3}TiO_{3\pm\delta}$ powders [5,11]. On the other hand, the CGO component showed a cell expansion due to the partial reduction of Ce^{4+} to Ce^{3+} from 158.463(2) to 159.259(2) $Å^3$, as expected.

It is important to highlight that no secondary phases are observed after the calcination process at high temperatures, confirming the good thermal stability of the nanocomposite electrodes in both oxidizing and reducing atmospheres. It is worth mentioning that the cell volume of SPTO is clearly dependent on the calcination temperature and atmosphere, increasing from 59.128(3) to 59.659(3) $Å^3$ from 800 ºC to 1500 ºC for 100SPTO-FD, which can be associated with changes in the Pr^{4+}/Pr^{3+} ratio and different lattice oxygen stoichiometry when the temperature increases [12].

Figure 5.3 shows the HAADF-STEM image and EDS analysis of 100SPTO-FD. A homogeneous cation distribution is observed without the presence of secondary phases. Additionally, the lattice spacing of different crystallographic planes, obtained from the HRTEM images, matches well with those observed in the Rietveld refinement of the experimental XRD data.

UNIVERSIDAD DE MÁLAGA

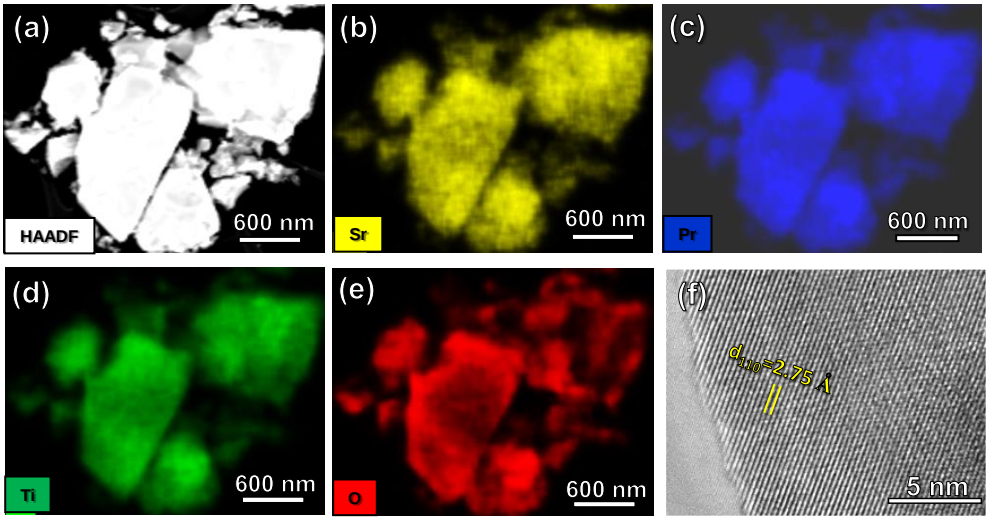

Figure 5.3. (a) HAADF-STEM image and (b-e) EDS mapping of 100SPTO-FD powders obtained by freeze-drying and sintered at 800 ºC. (f) HRTEM image showing the interatomic distances.

Figure 5.4 displays HAADF-STEM-EDS and HRTEM images of 50SPTO nanocomposite electrode prepared by spray-pyrolysis at 800 ºC. EDS analysis confirmed that SPTO and CGO nanoparticles are homogenously distributed, ensuring an intimate contact between both phases and, consequently, an increased TPB length for the electrochemical reactions (Figure 5.4a). HRTEM analysis of 50SPTO shows particle size lower than 10 nm at 800 ºC, with high crystallinity without amorphous domains (Figure 5.4b). Furthermore, the crystallite size and lattice spacing of different crystals are similar to those observed from XRD data analysis.

When the annealing temperature was increased up to 1000 ºC, the nanocomposite electrodes showed a larger grain size, as well as different atomic arrangement in some crystals of SPTO (Figure 5.4c). In particular, layered ordered extended defects are observed due to oxygen non-stoichiometry (δ) increase, which has been reported to be detrimental to the conductive properties in $SrTiO_3$-based materials [13]. Interestingly, the 50SPTO layers calcined at 800 ºC do not present these crystalline defects, which can be attributed to the smaller crystal size of the nanocomposite electrode at low sintering temperatures, hindering their formation.

UNIVERSIDAD DE MÁLAGA

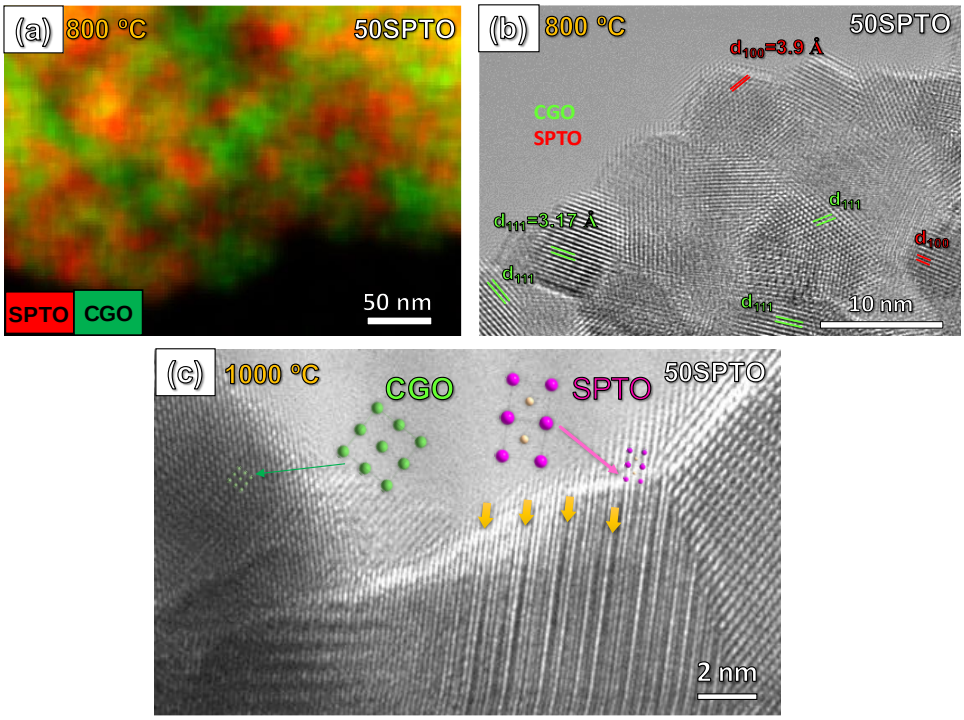

Figure 5.4. (a) HAADF-STEM-EDS images of 50SPTO nanocomposite layers calcined at 800 ºC. HRTEM showing a homogeneous mixture of SPTO and CGO nanoparticles and (c) extended linear defects for the SPTO phase after calcining at 1000 ºC in air.

5.2. Microstructural characterization

The microstructure of the different electrode architectures proposed in this chapter was studied by scanning electron microscopy (SEM) (Figure 5.5). The screen-printed electrodes 50SPTO-PM and 50SPTO-FD have a similar thickness of ~15 µm (Figure 5.5a-d). The most remarkable difference between both electrode architectures is the different average grain size, with values of 450 and 58 nm for 50SPTO-PM and 50SPTO-FD, respectively (Figure 5.5b,d) at the same sintering temperature of 1100 ºC. These findings confirm that the co-synthesis process of two immiscible phases not only leads to a homogeneous mixture of SPTO and CGO phases, but also limits the grain growth during the sintering process [14,15].

UNIVERSIDAD DE MÁLAGA

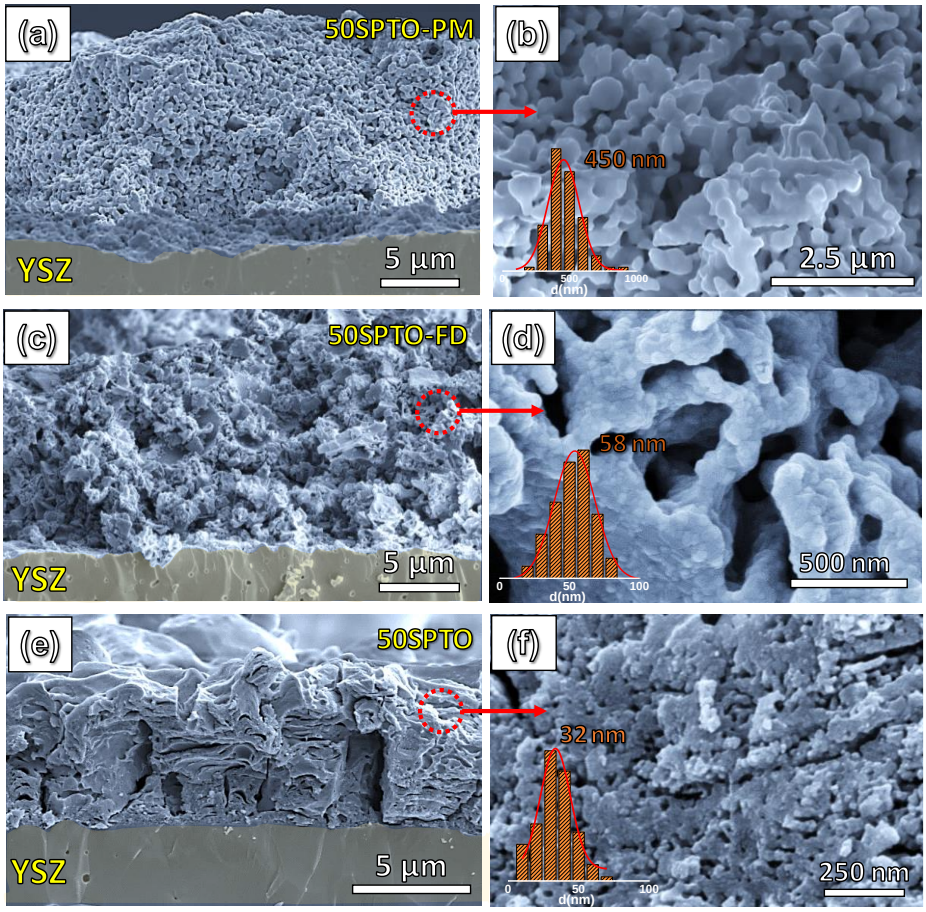

Figure 5.5. SEM images at different magnifications and grain size distribution of the electrodes deposited by screen-printing at 1100 ºC from (a,b) powder mixture and (c,d) co-sintering powders and (e,f) layer deposited by spray-pyrolysis directly on the YSZ electrolyte at 800 ºC.

In the case of the electrodes deposited by spray-pyrolysis on a YSZ electrolyte (50SPTO), a slightly lower electrode thickness is observed (7 µm), showing a laminated morphology typical of this deposition process (Figure 5.5e,f). The most remarkable difference with the electrodes deposited by screen-printing is the smaller particle size of 32 nm at 800 ºC, ensuring an excellent nanoscale contact between both SPTO and CGO phases. The lower particle size of the electrodes prepared by spray-pyrolysis is clearly a consequence of the lower deposition temperature required to ensure an adequate adhesion to the electrolyte.

UNIVERSIDAD DE MÁLAGA

50SPTO-FD electrodes, prepared by co-synthesis, are formed by aggregated nanoparticles, which drastically reduces the active surface area for the electrocatalytic reactions when compared to the analogous electrode deposited by spray-pyrolysis at lower temperatures (50SPTO), which are expected to have improved electrochemical properties and faster reduction kinetics due to the increased gas/solid interface obtained by the nanostructure optimization.

Strong adhesion with the YSZ electrolyte was observed for all electrode architectures after successive redox cycles, not showing delamination or cracks. The good mechanical stability is clearly related to the similar thermal expansion coefficients (TEC) between the different materials: 11.7-12.3·10^{-6} K^{-1} for $Sr_{0.8}Pr_{0.2}TiO_{3\pm\delta}$ in both air and H_2 atmospheres [5], 10.9·10^{-6} K^{-1}, 11.4·10^{-6} K^{-1} and 12.7·10^{-6} K^{-1} for YSZ, CGO and LSGM, respectively [16].

5.3. Electrical conductivity measurements

The total conductivity of the pellet samples was determined by the four-probe Van der Pauw method in both air and 5% H_2-Ar, as well as a function of the oxygen partial pressure (pO_2). In order to obtain dense samples, the precursor powders were pelletized into discs of 13 mm and 1 mm of diameter and thickness, respectively, and then sintered at 1500 ºC for 1 h for 100SPTO-FD and 1400 ºC for 1 h for both 50SPTO-PM and 50SPTO-FD composite powders, reaching in all cases relative densities above 95%. Firstly, the microstructure and phase distribution of the samples was analysed by SEM and EDS, respectively (Figure 5.6).

The 100SPTO-FD shows an average grain size of 1.25 µm and a homogenous cation distribution (Figure 5.6a). The composite electrodes are formed by two different phases without phase segregations as confirmed by XRD. In the case of the electrode obtained from mixed powders, 50SPTO-PM, the grain size distribution is not homogeneous, taking values of approximately of 1 µm in diameter (Figure 5.6b). On the contrary, 50SPTO-FD obtained from the co-synthesis method, shows a considerably lower grain size (0.5 µm) with a more homogeneous phase distribution in comparison to 50SPTO-PM (Figure 5.6c).

UNIVERSIDAD DE MÁLAGA

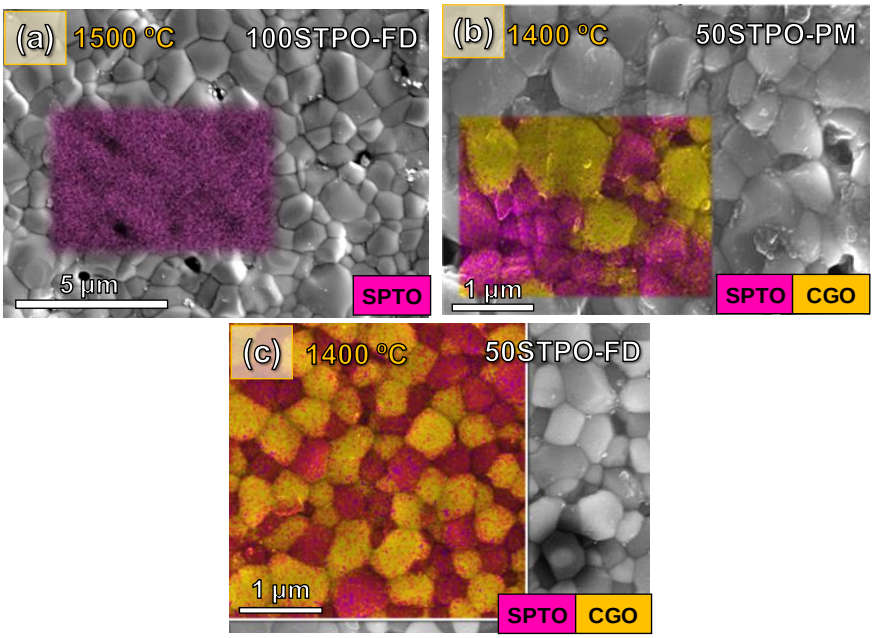

Figure 5.6. SEM images and EDS analysis of (a) 100STPO-FD sintered at 1500 ºC for 1 h, (b) 50STPO-PM (physically mixed powders) at 1400 ºC for 1 h and (c) 50SPTO-FD (co-synthesis method) at 1400 ºC for 1 h.

The electrical conductivity of the samples in different atmospheres as a function of the temperature is displayed in Figure 5.7a. In air, the conductivity of 100SPTO-FD is rather low, *i.e.* $5.9 \cdot 10^{-5}$ S cm^{-1} at 700 ºC due to the low concentration of charge carriers in oxidizing conditions, which is proportional to the Ti^{3+} concentration [5]. Moreover, the presence of the Pr^{4+}/Pr^{3+} redox pair seems to be not significant enough to obtain high electrical conductivity. Previous reports on $Sr_{1-x}Pr_xTiO_{3\pm\delta}$ series revealed that the concentration of charge carriers in air is almost constant and the difference in the conductivity can be associated with the Pr-content [12], reaching a maximum for x=0.1-0.15. Above this concentration the conductivity decreases due to the formation of extended defects. HRTEM studies confirmed that the formation of Ruddlesden-Popper-type defects is possibly responsible for the lower conductivity values in these materials, findings that can be explained by the ability of these linear defect clusters to accommodate the oxygen excess in rare-earth doped $SrTiO_3$ [1,5]. In the literature, the conductivity values in air for similar compositions range widely from $2 \cdot 10^{-5}$ S cm^{-1} for $Sr_{0.7}Pr_{0.3}Ti_{0.93}Co_{0.07}O_{3-\delta}$ to ~10^{-2} S cm^{-1} for

UNIVERSIDAD DE MÁLAGA

$Sr_{0.8}Pr_{0.2}TiO_{3-\delta}$ at 700 ºC [5,12]. The different sintering and preparation conditions (temperature, time and gas atmosphere) can explain these differences.

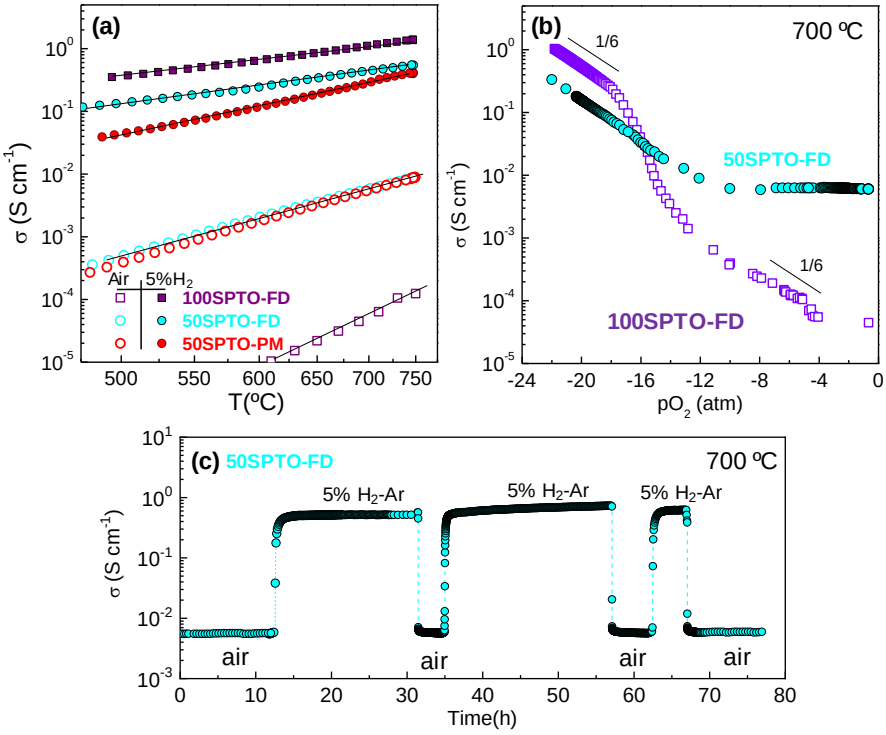

Figure 5.7. (a) Temperature dependence of the total conductivity in air and 5% H_2-Ar of the different electrode compositions. (b) Total conductivity as a function of the oxygen partial pressure (pO_2) of 100SPTO-FD and 50SPTO-FD and (c) variation of the conductivity of the 50SPTO-FD in several oxidation/reduction cycles.

In 5% H_2-Ar, the conductivity of 100STPO-FD significantly increases due to the partial reduction of Ti^{4+} to Ti^{3+}, reaching values of 1.18 S cm^{-1} at 700 ºC (Figure 5.7a); however, this value is lower than that reported previously for the stoichiometric $Sr_{0.7}Pr_{0.3}TiO_{3\pm\delta}$ (~10 S cm^{-1} at 700 ºC) [5]. In this previous study, Yaremchenko *et al.* employed the traditional solid-state reaction method at 1600 ºC in air to prepare the samples, followed by a reduction step at 1500 ºC for 10 h in 10% H_2-N_2. It is well reported that the conductivity of $SrTiO_3$ materials depends on the preparation and thermal treatment history because the defect equilibrium is nearly frozen at temperatures lower than 1200 ºC [17], which could explain the higher conductivity values observed by Yaremchenko *et al.* [5].

UNIVERSIDAD DE MÁLAGA

In the case of the composite electrodes, the conductivity in air is somewhat higher in comparison to 100SPTO, *i.e.* $6 \cdot 10^{-3}$ S cm^{-1} at 700 ºC for both 50SPTO-PM and 50SPTO-FD, due to the presence of CGO with higher ionic conductivity. In reducing conditions, the conductivity reached 0.27 S cm^{-1} at 700 ºC for 50SPTO-FD, values slightly higher than that observed for 50SPTO-PM. As expected, this value is lower than that observed for 100SPTO-FD because the CGO phase has a considerably lower electronic conductivity under reducing conditions when compared to SPTO.

The conductivity was studied as a function of pO_2 to determine the nature of the charge carriers (Figure 5.7b). For 100SPTO-FD increases linearly with decreasing pO_2, indicating a predominant n-type electronic conduction with an almost negligible ionic contribution to the total conductivity. In both oxidizing and reducing atmospheres a $(pO_2)^{-1/6}$ dependence is observed, similar to that predicted in previous studies by the defect chemistry model [5]. A 50SPTO-FD composite pellet is a mixed ionic-electronic conductor due to the combination of the electronic properties of SPTO and ionic conduction of CGO, and the conductivity is almost independent on the pO_2 between 0.1 and 10^{-12} atm, indicating a predominant ionic conduction, while an n-type electronic conductivity with a $(pO_2)^{-1/6}$ dependence appears at lower pO_2, similar to 100SPTO-FD [5]. Furthermore, the redox stability of 50SPTO-FD was tested by measuring the electrical conductivity in consecutive oxidation/reduction cycles at 700 ºC, showing no appreciable degradation and good cyclability (Figure 5.7c). The reduction process in 5% H_2-Ar takes approximately 2 h to be completed while the reoxidation is faster, reaching equilibrium in 20 minutes. It is also worth mentioning that 50SPTO-FD obtained from co-synthesis shows faster reduction/oxidation kinetics than similar compositions despite the higher relative density of the pellets in this study (95%), which is possibly associated with the lower particle size of these samples [5].

5.4. Electrochemical characterization

The electrochemical performance of the different electrode architectures was studied by impedance spectroscopy in symmetrical configuration under oxidizing and reducing conditions. For a better comparison of the electrode response, the ohmic

UNIVERSIDAD DE MÁLAGA

resistance was subtracted from the impedance data. Figure 5.8a,c shows the impedance spectra of some selected electrodes in air and H_2.

It is worth mentioning that the nanocomposite electrodes, deposited directly on the electrolyte, show polarization resistance values considerably lower in both air and H_2 when compared to the screen-printed electrodes, obtaining the best values for 50SPTO.

In order to get further insights into the different electrode processes involved in the ORR and HOR, the impedance spectra were analysed by distribution of relaxation times (DRT) (Figure 5.8b,d) [18,19]. In both air and H_2 atmospheres, three main electrode contributions are observed in the DRT spectra of 50SPTO; however, an additional process, labelled as (HF´), is discernible at a very high frequency of 10^5 Hz in air for the electrode deposited by screen-printing. According to previous studies, the high frequency (HF) response centred at ~10^4 Hz in air is assigned to the oxide ion transfer at the electrode/electrolyte interface [20,21]. The contributions at intermediate (IF) and low frequency (LF) have been typically assigned to electrode surface processes, such as charge transfer or oxygen dissociation [19,20]. The HF' electrode contribution at a very high frequency of 10^5 Hz, observed only for screen-printed 50SPTO-PM, is possibly attributed to the electronic current losses at the current collector/electrode interface in accordance with previous works [22,23]. The poor conductivity of this electrode in air could be the reason for this additional resistance contribution. This hypothesis is further corroborated by the non-presence of this process in a reducing atmosphere due to the enhancement of electronic conductivity. Based on these results, the impedance spectra can be adequately fitted employing an equivalent circuit formed by an inductor (L) due to the electrochemical setup, a resistance (R_s) related to the ohmic resistance of the electrolyte and three/four (RQ) elements in series to simulate each electrode process (inset Figure 5.8a).

UNIVERSIDAD DE MÁLAGA

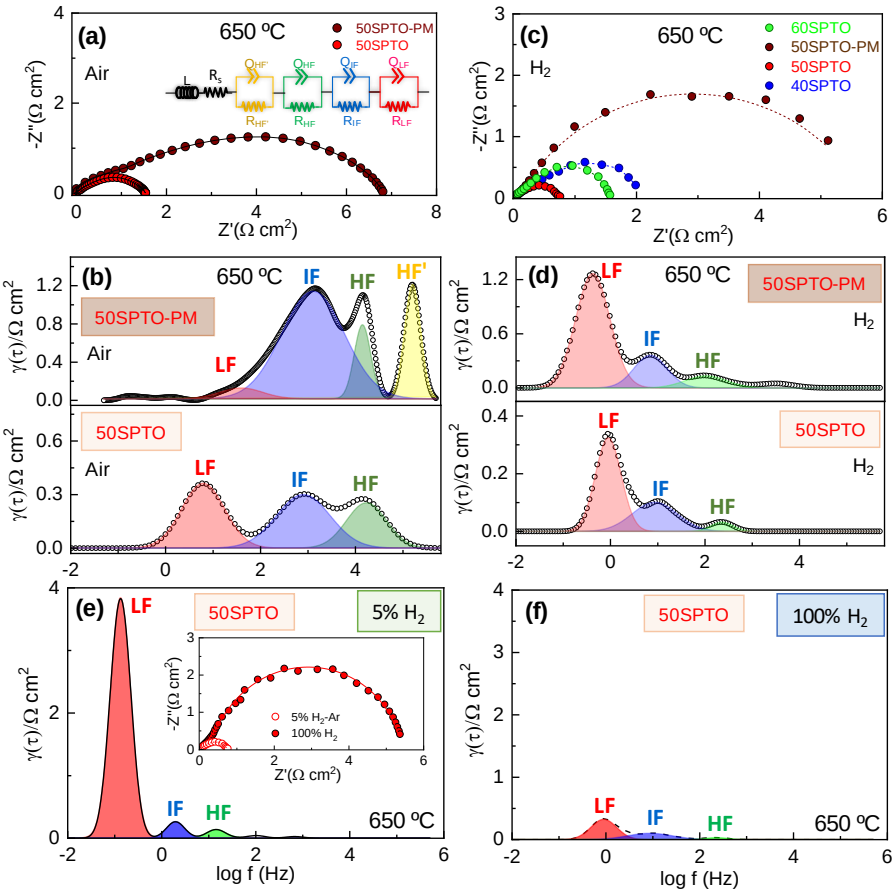

Figure 5.8. (a) Impedance spectra and (b) the corresponding DRT analysis of selected symmetrical cells at 650 ºC in air. The inset figure of (a) shows the equivalent circuit employed to fit the impedance data. (c) Impedance spectra and (d) the corresponding DRT analysis of selected symmetrical cells at 650 ºC in 100% H_2. (e) DRT analysis of 50SPTO in 5% H_2-Ar and (f) 100% H_2 at 650 ºC. The inset of figure (e) shows the impedance spectra of 50SPTO in 5% H_2-Ar and 100% H_2 atmospheres.

In a reducing atmosphere, the LF electrode response is the main contribution to the overall polarization resistance in both 50SPTO-PM and 50SPTO electrodes (Figure 5.8e,f). This electrode contribution significantly decreases when pure hydrogen is employed as feeding gas, showing a hydrogen partial pressure dependence of $\sim(pH_2)^{-0.8}$ and a large capacitance of 0.2 F cm^{-2}, which can be attributed to a gas diffusion process [24]. On the contrary, the IF and HF processes are less dependent on the H_2 concentration and they are possibly assigned

UNIVERSIDAD DE MÁLAGA

to charge transfer and transport processes at the electrode/electrolyte interface, respectively.

In order to elucidate the nature of the electrochemical processes of 50SPTO for ORR, the impedance spectra were acquired at different oxygen partial pressures (Figure 5.9a). Three different electrode contributions are discernible in the DRT spectra in the pO_2 range of 0.001- 0.21 atm (Figure 5.9b).

The pO_2-dependence of each electrode resistance contribution is shown in Figure 5.9c, where the slope *m* provides information about the nature of the species involved in the ORR sub-reactions [25]. The resistance contributions at high, intermediate and low frequencies (HF, IF and LF) to the overall polarization resistance were determined by integration of the DRT curves since the area under the peak is proportional to the resistance of each process.

The electrode process at high frequency (HF) is nearly independent of the pO_2 and can be attributed to the oxide-ion transfer at the electrode/electrolyte interface ($O^x_{o,\,electrode} \rightarrow O^x_{o,\,electrolyte}$) [25], while the IF process with an $m = 1/4$ can be assigned to charge transfer at the electrode surface ($O_{ad} + 2e^- + V_o^{\cdot\cdot} \rightarrow O_o^x$) [26]. Finally, the process at low frequency (LF), which is the dominant step at low oxygen partial pressures, has an $m \sim 1/2$ and it is related to molecular oxygen dissociation on the electrode surface ($O_{2,ad} \rightarrow 2O_{ad}$) [27]. Furthermore, this electrode process is shifted to higher frequency values when the pO_2 is increased, indicating a lower relaxation time, and therefore, faster electrode kinetics. It is worth mentioning that the HF electrode contribution is the rate-limiting step for ORR in air conditions (0.21 atm) due to the rather low ionic conductivity of the SPTO in oxidizing conditions, which hinders the oxide-ion transport from the electrode to the electrolyte.

UNIVERSIDAD DE MÁLAGA

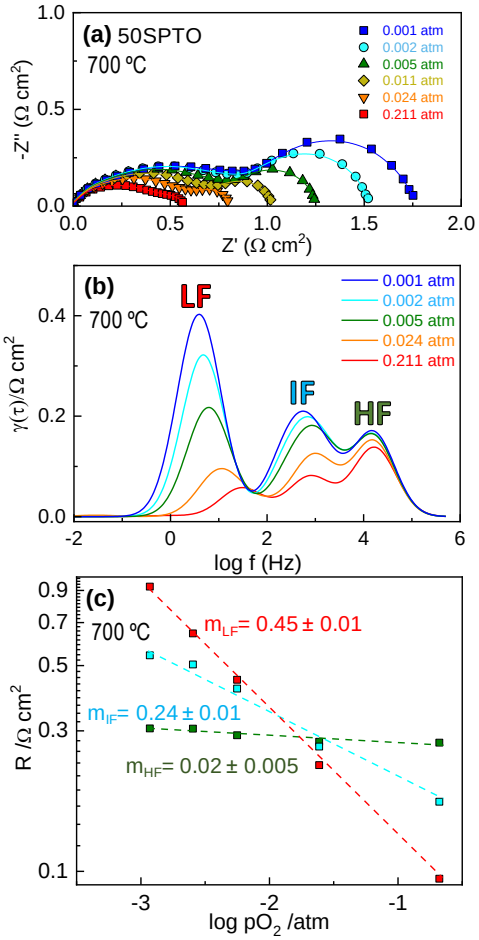

Figure 5.9. (a) Impedance spectra as a function of the oxygen partial pressure (pO_2) at 700 ºC of 50SPTO, (b) the corresponding DRT spectra and (c) electrode resistance contributions as a function of pO_2.

The temperature dependence of total polarization resistance (R_p) in air and H_2 atmosphere for the electrodes deposited on YSZ are displayed in Figure 5.10. In air, 100SPTO-FD, deposited by screen-printing, shows high polarization resistance values (4.81 Ω cm^2 at 700 ºC) due to the low electronic conductivity in oxidizing atmosphere and poor electrochemical activity of $SrTiO_3$-based electrodes for ORR (Figure 5.10a). After the CGO addition, a considerable decrease of R_p is observed due to the incorporation of an ionic conductor, reaching 2.45 and 1.60 Ω cm^2 at 700 ºC for 50SPTO-PM and 50SPTO-FD, respectively.

UNIVERSIDAD DE MÁLAGA

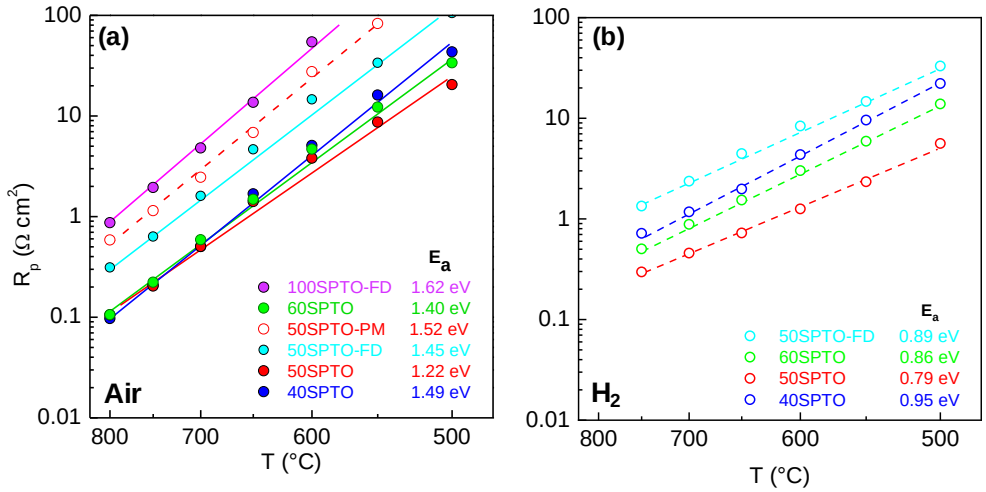

Figure 5.10. Total polarization resistance of the different electrode compositions as a function of the temperature in (a) air and (b) 5% H_2-Ar and 100% H_2.

A further improvement is observed for the nanocomposite electrodes deposited by spray-pyrolysis directly on the electrolyte, reaching approximately 0.53 Ω cm^2 at 700 ºC for all nanocomposite electrodes (40SPTO, 50SPTO and 60SPTO). The optimal composition with the lowest activation energy of 1.22 eV corresponds to 50SPTO, significantly lower than that observed for 100SPTO-FD, 1.62 eV. Interestingly, these values of polarization resistance are one of the lowest reported in the literature for titanate-based air electrodes, such as $La_{0.875}Sr_{0.125}Ti_{0.5}Ni_{0.5}O_{3-\delta}$ (1.1 Ω cm^2 at 800 ºC) [28], $La_{0.43}Ca_{0.37}Ti_{0.94}Rh_{0.06}O_{3-\delta}$ (5.89 Ω cm^2 at 850 ºC) [29] and $La_{1/3}Sr_{2/3}Ti_{0.83}Fe_{0.17}O_{3-\delta}$ (0.5 Ω cm^2 at 900 ºC) [30].

In a 100% H_2 atmosphere, the 50SPTO-FD achieves R_p values of 2.37 Ω cm^2 at 700 ºC, values that are greatly improved by the nanocomposite electrodes deposited by spray-pyrolysis. The best electrochemical performance was achieved for 50SPTO with R_p values as low as 0.46 Ω cm^2 at 700 ºC, which are lower than those observed for 40SPTO and 60SPTO at the same temperature, 1.17 and 0.88 Ω cm^2, respectively. Additionally, 50SPTO has the minimum activation energy of all compositions (0.79 eV) and these values are lower than those observed in air due to the faster HOR kinetics compared to ORR.

UNIVERSIDAD DE MÁLAGA

These R_p values are lower than those reported previously for titanate-based anodes, *i.e.* $La_{0.8}Sr_{0.2}TiO_{3-\delta}$ (9.6 Ω cm^2 at 800 ºC) [31], $La_{0.3}Sr_{0.7}Ti_{0.97}Mo_{0.03}O_{3-\delta}$ (5 Ω cm^2 at 850 ºC) [32] and $La_{0.2}Sr_{0.35}Ca_{0.35}Ti_{0.95}Fe_{0.05}O_{3-\delta}$ (0.21 Ω cm^2 at 850 ºC) [33] or even titanates decorated with exsolved metal nanoparticles in reducing atmosphere, *i.e.* $La_{0.4}Sr_{0.6}Ti_{0.95}Ru_{0.05}O_{3-\delta}$ (2.74 Ω cm^2 at 850 ºC) [34], $La_{0.2}Sr_{0.8}Ti_{0.9}Ni_{0.1}O_{3-\delta}$ (1.66 Ω cm^2 at 800 ºC) [35] and $(Sr_{0.94}Ti_{0.9}Nb_{0.1})_{0.95}Ni_{0.05}O_{3-\delta}$ (7.0 Ω cm^2 at 750 ºC) [36].

In addition, 50SPTO nanocomposite exhibits rather low R_p values in H_2 when compared to traditional symmetrical electrodes, such as $La_{0.75}Sr_{0.25}Cr_{0.5}Mn_{0.5}O_{3-\delta}$ (1.82 Ω cm^2 at 850 ºC) [37], $La_{0.4}Sr_{1.6}MnO_{4\pm\delta}$ (2.07 Ω cm^2 at 800 ºC) [38], $PrBaFe_2O_{5+\delta}$ (0.9 Ω cm^2 at 650 ºC) [39] and $Sr_2Fe_{1.5}Mo_{0.5}O_{6-\delta}$ (0.45 Ω cm^2 at 800 ºC) [40]. It is worth mentioning that the polarization resistance values in 100% H_2 obtained for 50SPTO nanocomposite (0.46 Ω cm^2 at 700 ºC) are slightly higher than that observed for 50LCM-Nano (0.18 Ω cm^2 at 700 ºC) in Chapter 4, while similar R_p values were obtained in air conditions. These findings reveal that lower power density values are expected in real SOFC conditions than those observed in Chapter 4.

5.5. Fuel cell tests

The efficiency of 50SPTO was tested in a SSOFC with configuration: 50SPTO/LSGM(300µm)/50SPTO (Figure 5.11). A symmetrical cell with a screen-printed electrode (50SPTO-PM) was also prepared for comparison purposes. It is worth mentioning that LSGM-supported cells were chosen in order to minimize the ohmic losses of YSZ electrolyte at intermediate temperatures. The electrolyte-supported cell was mounted in the electrochemical cell using a ceramic sealant, as described in detail in the experimental section 3.10.7.

In both cases, the open circuit voltage (OCV) is close to the theoretical Nernst potential, 1.1 V, confirming a good sealing of the cells. The cell with a 50SPTO nanocomposite achieves maximum power densities of 354, 250 and 170 mW cm^{-2} at 800, 750 and 700 ºC, respectively, in wet hydrogen (Figure 5.11a). The performance of 50SPTO symmetrical electrodes clearly outperformed those values observed for the analogous screen-printed electrode 50SPTO-PM, *i.e.* 125, 70 and 40 mW cm^{-2} at 800, 750 and 700 ºC, respectively (Figure 5.11b).

UNIVERSIDAD DE MÁLAGA

It is worth mentioning that the ohmic resistance (R_s) of the cells is slightly higher than that expected for a 300 µm thick LSGM-supported cell (~0.3 Ω cm^2 at 800 ºC), 0.40 and 0.51 Ω cm^2 at 800 ºC for 50SPTO and 50SPTO-PM, respectively (Figure 5.11c), which can be associated with the rather low electrical conductivity in air of these electrodes.

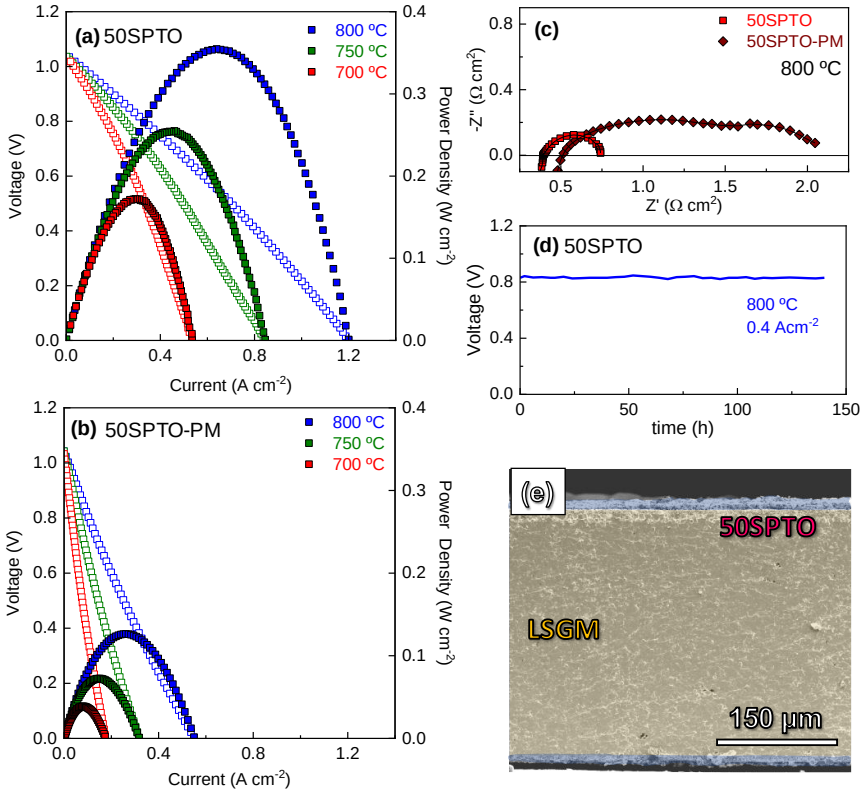

Figure 5.11. I-V-P curves of LSGM symmetrical cells with (a) 50SPTO nanocomposite electrode deposited by spray-pyrolysis and (b) 50SPTO-PM symmetrical electrode deposited by screen-printing using wet H_2 as fuel and static air as oxidant. (c) Impedance spectra of both cells at 800 ºC. (d) Durability test of the cell with 50SPTO at a constant current density of 0.4 A cm^{-2} at 800 ºC and (d) Cross-sectional SEM image of the cell 50SPTO after the durability test.

On the other hand, 50SPTO showed excellent stability for 140 h with a stable maximum power density under continuous operation in H_2 at 800 ºC (Figure 5.11d), not showing any signs of cell delamination or cracks in the post-mortem test of the single cell (Figure 5.11e). The values of power density are among the best reported

UNIVERSIDAD DE MÁLAGA

for $SrTiO_3$-based anodes, *i.e.* 170 mW cm^{-2} at 800 ºC for $La_{0.4}Sr_{0.4}TiO_3$-CGO/LSGM/LSCF-CGO [41], 60 mW cm^{-2} at 800 ºC for $La_{0.3}Sr_{0.7}Ti_{0.97}Mo_{0.03}O_3$/LSGM/BSCF [32] and 200 mW cm^{-2} at 900 ºC for $Sr_{0.89}Y_{0.07}TiO_{3-\delta}$-YSZ/YSZ/LSM-YSZ [42].

However, the poor electrical properties in an air atmosphere of $SrTiO_3$-based electrode induces low power density values. For this reason, *x*SPTO electrodes are most adequate for potential use as anode materials rather than air electrodes. Improved fuel cell performance is expected if these nanocomposite anodes are combined with highly efficient cathodes such as $La_{0.6}Sr_{0.4}Co_{0.8}Fe_{0.2}O_{3-\delta}$, $PrBaCo_2O_{5+\delta}$, or $BaCo_{0.4}Fe_{0.4}Zr_{0.1}Y_{0.1}O_{3-\delta}$ [43,44].

Nevertheless, the results obtained in this chapter demonstrated that the electrochemical activity of electrodes with a modest activity for ORR and HOR but with excellent redox stability can be highly enhanced by microstructural optimization. The nanoscale contact of SPTO and CGO has shown to be crucial to obtain improved performance. On the other hand, the rather low electrochemical activity of Sr-titanates for ORR could be partially solved in future works by incorporating other transition metals in the B-site of the perovskite such as Mn, Fe and Co. Finally, the electrochemical performance in reducing conditions can be further improved by doping with Ni, Pd or Ru to achieve metal nanoparticle exsolution in H_2 atmosphere.

References

1. Yaremchenko, A.A.; Naumovich, E.N.; Patrício, S.G.; Merkulov, O. V.; Patrakeev, M. V.; Frade, J.R. Rare-Earth-Substituted Strontium Titanate: Insight into Local Oxygen-Rich Structures and Redox Kinetics. *Inorg. Chem.* **2016**, *55*, 4836–4849, doi:10.1021/acs.inorgchem.6b00350.
2. Savaniu, C.D.; Irvine, J.T.S. Reduction Studies and Evaluation of Surface Modified A-Site Deficient La-Doped $SrTiO_3$ as Anode Material for IT-SOFCs. *J. Mater. Chem.* **2009**, *19*, 8119–8128, doi:10.1039/b912305a.
3. Drasbæk, D.B.; Welander, M.M.; Traulsen, M.L.; Sudireddy, B.R.; Holtappels, P.; Walker, R.A. Operando Characterization of Metallic and Bimetallic Electrocatalysts for SOFC Fuel Electrodes Operating under Internal Methane Reforming Conditions . *J. Mater. Chem. A* **2022**, *10*, 5550–5560, doi:10.1039/d1ta07299d.
4. Da Rosa Silva, E.; Curi, M.; Nicolini, J. V.; Furtado, J.G.; Secchi, A.R.; Ferraz, H.C. Effect of Doping Concentration and Sintering Atmosphere on the Microstructural and Electrical Characteristics of Y-Doped $SrTiO_3$ Perovskite Anode for SOFC. *Ceram. Int.* **2021**, *47*, 13331–

UNIVERSIDAD DE MÁLAGA

13338, doi:10.1016/j.ceramint.2021.01.189.

5. Yaremchenko, A.A.; Patrício, S.G.; Frade, J.R. Thermochemical Behavior and Transport Properties of Pr-Substituted $SrTiO_3$ as Potential Solid Oxide Fuel Cell Anode. *J. Power Sources* **2014**, *245*, 557–569, doi:10.1016/j.jpowsour.2013.07.019.
6. Shannon, R.D. Revised Effective Ionic Radii and Systematic Studies of Interatomic Distances in Halides and Chalcogenides. *Acta Cryst.* **1976**, *A32*, 751–767, doi:https://doi.org/10.1107/S0567739476001551.
7. Zhou, Y.; Wen, Q.; Ren, Z.; Xie, H.; Tao, S.; Zhou, W. Gadolinium-Doped Strontium Titanate for High-Efficiency Electromagnetic Interference Shielding. *J. Alloys Compd.* **2018**, *733*, 33–39, doi:10.1016/j.jallcom.2017.10.289.
8. Pradhan, J.; Mallick, H.K.; Sahoo, M.P.K.; Pattanaik, A.K. Enhanced Optical and Dielectric Properties of Rare-Earth Co-Doped $SrTiO_3$ Ceramics. *J. Mater. Sci. Mater. Electron.* **2021**, *32*, 13837–13849, doi:10.1007/s10854-021-05959-7.
9. Cumming, D.J.; Kilner, J.A.; Skinner, S. Structural Properties of Ce-Doped Strontium Titanate for Fuel Cell Applications. *J. Mater. Chem.* **2011**, *21*, 5021–5026, doi:10.1039/c0jm03680c.
10. Wang, X.; Hu, Q.; Li, L.; Lu, X. Effect of Pr Substitution on Structural and Dielectric Properties of $SrTiO_3$. *J. Appl. Phys.* **2012**, *112*, doi:10.1063/1.4747937.
11. Yaremchenko, A.A.; Macías, J.; Kovalevsky, A. V.; Arias-Serrano, B.I.; Frade, J.R. Electrical Conductivity and Thermal Expansion of Ln-Substituted $SrTiO_3$ for Solid Oxide Cell Electrodes and Interconnects: The Effect of Rare-Earth Cation Size. *J. Power Sources* **2020**, *474*, 228531, doi:10.1016/j.jpowsour.2020.228531.
12. Kamecki, B.; Miruszewski, T.; Karczewski, J. Structural and Electrical Transport Properties of Pr-Doped $SrTi_{0.93}Co_{0.07}O_{3-\delta}$ a Novel SOEC Fuel Electrode Materials. *J. Electroceramics* **2019**, *42*, 31–40, doi:10.1007/s10832-018-0143-0.
13. Ruiz-Morales, J.C.; Canales-Vázquez, J.; Savaniu, C.; Marrero-López, D.; Zhou, W.; Irvine, J.T.S. Disruption of Extended Defects in Solid Oxide Fuel Cell Anodes for Methane Oxidation. *Nature* **2006**, *439*, 568–571, doi:10.1038/nature04438.
14. Shimada, H.; Yamaguchi, T.; Kishimoto, H.; Sumi, H.; Yamaguchi, Y.; Nomura, K.; Fujishiro, Y. Nanocomposite Electrodes for High Current Density over 3 A cm^{-2} in Solid Oxide Electrolysis Cells. *Nat. Commun.* **2019**, *10*, 1–10, doi:10.1038/s41467-019-13426-5.
15. Shimada, H.; Sumi, H.; Yamaguchi, Y.; Fujishiro, Y. High-Performance $Gd_{0.5}Sr_{0.5}CoO_{3-\delta}$ and $Ce_{0.8}Gd_{0.2}O_{1.9}$ Nanocomposite Cathode for Achieving High Power Density in Solid Oxide Fuel Cells. *Electrochim. Acta* **2021**, *368*, doi:10.1016/j.electacta.2020.137679.
16. Tietz, F. Thermal Expansion of SOFC Materials. *Ionics (Kiel).* **1999**, *5*, 129–139, doi:10.1007/BF02375916.
17. Shi, T.; Chen, Y.; Guo, X. Defect Chemistry of Alkaline Earth Metal (Sr/Ba) Titanates. *Prog. Mater. Sci.* **2016**, *80*, 77–132, doi:10.1016/j.pmatsci.2015.10.002.
18. Xia, J.; Wang, C.; Wang, X.; Bi, L.; Zhang, Y. A Perspective on DRT Applications for the Analysis of Solid Oxide Cell Electrodes. *Electrochim. Acta* **2020**, *349*, 136328, doi:10.1016/j.electacta.2020.136328.
19. Osinkin, D.A. An Approach to the Analysis of the Impedance Spectra of Solid Oxide Fuel Cell Using the DRT Technique. *Electrochim. Acta* **2021**, *372*, 137858, doi:10.1016/j.electacta.2021.137858.
20. Chen, Y.; Bu, Y.; Zhang, Y.; Yan, R.; Ding, D.; Zhao, B.; Yoo, S.; Dang, D.; Hu, R.; Yang, C.; et al. A Highly Efficient and Robust Nanofiber Cathode for Solid Oxide Fuel Cells. *Adv. Energy*

UNIVERSIDAD DE MÁLAGA

Mater. **2017**, *7*, 1–7, doi:10.1002/aenm.201601890.

21. Sumi, H.; Shimada, H.; Yamaguchi, Y.; Yamaguchi, T.; Fujishiro, Y. Degradation Evaluation by Distribution of Relaxation Times Analysis for Microtubular Solid Oxide Fuel Cells. *Electrochim. Acta* **2020**, *339*, 135913, doi:10.1016/j.electacta.2020.135913.
22. Almar, L.; Szász, J.; Weber, A.; Ivers-Tiffée, E. Oxygen Transport Kinetics of Mixed Ionic-Electronic Conductors by Coupling Focused Ion Beam Tomography and Electrochemical Impedance Spectroscopy. *J. Electrochem. Soc.* **2017**, *164*, F289–F297, doi:10.1149/2.0851704jes.
23. Adler, S.B. Mechanism and Kinetics of Oxygen Reduction on Porous $La_{1-x}Sr_xCoO_{3-\delta}$ Electrodes. *Solid State Ionics* **1998**, *111*, 125–134, doi:10.1016/s0167-2738(98)00179-9.
24. Osinkin, D.A. Detailed Analysis of Electrochemical Behavior of High–Performance Solid Oxide Fuel Cell Using DRT Technique. *J. Power Sources* **2022**, *527*, 231120, doi:10.1016/j.jpowsour.2022.231120.
25. Siebert, E.; Hammouche, A.; Kleitz, M. Impedance Spectroscopy Analysis of $La_{1-x}Sr_{itx}MnO_3$-Yttria-Stabilized Zirconia Electrode Kinetics. *Electrochim. Acta* **1995**, *40*, 1741–1753, doi:10.1016/0013-4686(94)00361-4.
26. Chen, X.J.; Khor, K.A.; Chan, S.H. Identification of O_2 Reduction Processes at Yttria Stabilized Zirconia|doped Lanthanum Manganite Interface. *J. Power Sources* **2003**, *123*, 17–25, doi:10.1016/S0378-7753(03)00436-1.
27. Kuai, X.; Yang, G.; Chen, Y.; Sun, H.; Dai, J.; Song, Y.; Ran, R.; Wang, W.; Zhou, W.; Shao, Z. Boosting the Activity of $BaCo_{0.4}Fe_{0.4}Zr_{0.1}Y_{0.1}O_{3-\delta}$ Perovskite for Oxygen Reduction Reactions at Low-to-Intermediate Temperatures through Tuning B-Site Cation Deficiency. *Adv. Energy Mater.* **2019**, *9*, 1–11, doi:10.1002/aenm.201902384.
28. Arrivé, C.; Delahaye, T.; Joubert, O.; Gauthier, G.H. Study of $(La,Sr)(Ti,Ni)O_{3-\delta}$ Materials for Symmetrical Solid Oxide Cell Electrode - Part C: Electrical and Electrochemical Behavior. *Ceram. Int.* **2020**, *46*, 23442–23456, doi:10.1016/j.ceramint.2020.06.114.
29. Kyriakou, V.; Neagu, D.; Zafeiropoulos, G.; Sharma, R.K.; Tang, C.; Kousi, K.; Metcalfe, I.S.; Van De Sanden, M.C.M.; Tsampas, M.N. Symmetrical Exsolution of Rh Nanoparticles in Solid Oxide Cells for Efficient Syngas Production from Greenhouse Gases. *ACS Catal.* **2020**, *10*, 1278–1288, doi:10.1021/acscatal.9b04424.
30. Canales-Vázquez, J.; Ruiz-Morales, J.C.; Marrero-López, D.; Peña-Martínez, J.; Núñez, P.; Gómez-Romero, P. Fe-Substituted $(La,Sr)TiO_3$ as Potential Electrodes for Symmetrical Fuel Cells (SFCs). *J. Power Sources* **2007**, *171*, 552–557, doi:10.1016/j.jpowsour.2007.05.094.
31. Yoo, K. Bin; Choi, G.M. Performance of La-Doped Strontium Titanate (LST) Anode on $LaGaO_3$-Based SOFC. *Solid State Ionics* **2009**, *180*, 867–871, doi:10.1016/j.ssi.2009.02.013.
32. Li, J.; Lv, T.; Hou, N.; Li, P.; Yao, X.; Fan, L.; Gan, T.; Zhao, Y.; Li, Y. Molybdenum Substitution at the B-Site of Lanthanum Strontium Titanate Anodes for Solid Oxide Fuel Cells. *Int. J. Hydrogen Energy* **2017**, *42*, 22294–22301, doi:10.1016/j.ijhydene.2017.03.189.
33. Paydar, S.; Kooser, K.; Möller, P.; Volobujeva, O.; Granroth, S.; Lust, E.; Nurk, G. Optimization of $La_{0.2}Sr_{0.7-x}Ca_xTi_{0.95}Fe_{0.05}O_{3-\delta}$ Fuel Electrode Stoichiometry for Solid Oxide Fuel-Cell Application. *ACS Appl. Energy Mater.* **2022**, *5*, 10119–10129, doi:10.1021/acsaem.2c01808.
34. Yoon, H.; Zou, J.; Sammes, N.M.; Chung, J. Ru-Doped Lanthanum Strontium Titanates for the Anode of Solid Oxide Fuel Cells. *Int. J. Hydrogen Energy* **2015**, *40*, 10985–10993, doi:10.1016/j.ijhydene.2015.05.193.
35. Park, B.H.; Choi, G.M. Ex-Solution of Ni Nanoparticles in a $La_{0.2}Sr_{0.8}Ti_{1-x}Ni_xO_{3-\delta}$ Alternative Anode for Solid Oxide Fuel Cell. *Solid State Ionics* **2014**, *262*, 345–348,

UNIVERSIDAD DE MÁLAGA

doi:10.1016/j.ssi.2013.10.016.

36. Zhang, Y.; Yu, Z.; Tao, Y.; Lu, J.; Liu, Y.; Shao, J. Insight into the Electrochemical Processes of the Titanate Electrode with in Situ Ni Exsolution for Solid Oxide Cells. *ACS Appl. Energy Mater.* **2019**, *2*, 4033–4044, doi:10.1021/acsaem.8b02269.
37. Jung, I.; Lee, D.; Lee, S.O.; Kim, D.; Kim, J.; Hyun, S.H.; Moon, J. LSCM-YSZ Nanocomposites for a High Performance SOFC Anode. *Ceram. Int.* **2013**, *39*, 9753–9758, doi:10.1016/j.ceramint.2013.05.022.
38. Zhou, J.; Chen, G.; Wu, K.; Cheng, Y. The Performance of $La_{0.6}Sr_{1.4}MnO_4$ Layered Perovskite Electrode Material for Intermediate Temperature Symmetrical Solid Oxide Fuel Cells. *J. Power Sources* **2014**, *270*, 418–425, doi:10.1016/j.jpowsour.2014.06.163.
39. Zhang, B.; Wan, Y.; Hua, Z.; Tang, K.; Xia, C. Tungsten-Doped $PrBaFe_2O_{5+\delta}$ Double Perovskite as a High-Performance Electrode Material for Symmetrical Solid Oxide Fuel Cells. *ACS Appl. Energy Mater.* **2021**, *4*, 8401–8409, doi:10.1021/acsaem.1c01618.
40. Liu, Q.; Dong, X.; Xiao, G.; Zhao, F.; Chen, F. A Novel Electrode Material for Symmetrical SOFCs. *Adv. Mater.* **2010**, *22*, 5478–5482, doi:10.1002/adma.201001044.
41. Kim, K.J.; Shin, T.H.; Lee, K.T. A-Site Deficient $La_{0.4}Sr_{0.4}TiO_3$-$Ce_{0.9}Gd_{0.1}O_{1.95}$ Composites as Efficient and Redox Stable Anodes for Solid Oxide Fuel Cells. *J. Alloys Compd.* **2019**, *787*, 1143–1148, doi:10.1016/j.jallcom.2019.02.180.
42. Shao, L.; Si, F.; Fu, X.Z.; Luo, J.L. Archiving High-Performance Solid Oxide Fuel Cells with Titanate Anode in Sulfur- and Carbon-Containing Fuels. *Electrochim. Acta* **2018**, *270*, 9–13, doi:10.1016/j.electacta.2018.03.078.
43. Vinoth Kumar, R.; Khandale, A.P. A Review on Recent Progress and Selection of Cobalt-Based Cathode Materials for Low Temperature-Solid Oxide Fuel Cells. *Renew. Sustain. Energy Rev.* **2022**, *156*, 111985, doi:10.1016/j.rser.2021.111985.
44. Santos-Gómez, L. Dos; Zamudio-García, J.; Porras-Vázquez, J.M.; Losilla, E.R.; Marrero-López, D. Nanostructured $BaCo_{0.4}Fe_{0.4}Zr_{0.1}Y_{0.1}O_{3-\delta}$ Cathodes with Different Microstructural Architectures. *Nanomaterials* **2020**, *10*, doi:10.3390/nano10061055.

UNIVERSIDAD DE MÁLAGA

Chapter 6

UNIVERSIDAD
DE MÁLAGA

UNIVERSIDAD
DE MÁLAGA

(La,Sr)FeO_3-based electrodes

In this chapter, novel nanostructured layers based on Ti-doped (La,Sr)$FeO_{3-\delta}$ were studied to achieve redox stable electrodes with competitive activity for both ORR and HOR. In order to increase the stability of the parent compound in reducing conditions, different electrode compositions $(La_{0.8}Sr_{0.2})_{0.95}Fe_{1-x}Ti_xO_{3-\delta}$-CGO ($LSFT_x$, x=0.2 and 0.4) were prepared. Additionally, several microstructural architectures were designed to boost the electrochemical performance. A Ni-doping strategy in the B-site, $(La_{0.8}Sr_{0.2})_{0.95}(Fe_{0.8}Ti_{0.2})_{0.9}Ni_{0.1}O_{3-\delta,}$ was also tested to improve the electrochemical performance of the fuel electrode. The presence of exsolved Ni nanoparticles was studied by different microstructural techniques, such as SEM and TEM.

UNIVERSIDAD DE MÁLAGA

6.1. Phase formation of LSFT-CGO nanocomposites

The $(La_{0.8}Sr_{0.2})_{0.95}Fe_{1-x}Ti_xO_{3-\delta}$-CGO ($LSFT_x$, x=0.2 and 0.4) composite electrodes were prepared from different synthetic approaches to evaluate the influence of the electrode microstructure on the electrochemical properties. Figure 6.1 displays an illustration of the different electrode microstructures tested in this chapter.

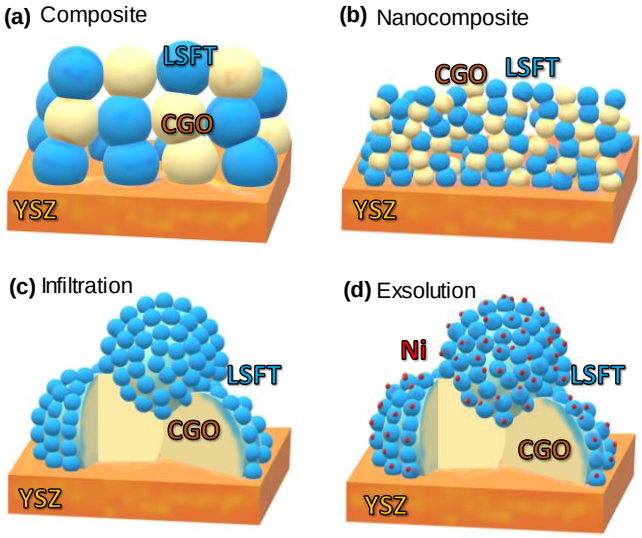

Figure 6.1. Illustration of the different electrode architectures tested to boost the electrochemical performance: (a) composite, (b) nanocomposite, (c) infiltration and (d) exsolution.

(i) Firstly, the freeze-drying precursor method was employed to obtain the single materials, which were calcined at 800 ºC to achieve crystallization: $(La_{0.8}Sr_{0.2})_{0.95}Fe_{0.8}Ti_{0.2}O_{3-\delta}$ ($LSFT_{0.2}$-FD) and $(La_{0.8}Sr_{0.2})_{0.95}Fe_{0.6}Ti_{0.4}O_{3-\delta}$ ($LSFT_{0.4}$-FD). The electrodes were prepared with A-site deficiency to avoid the segregation of Sr-based compounds. Additionally, the $LSFT_{0.2}$-CGO (50:50 wt.%) composite electrode was prepared from two different approaches (Figure 6.1a): (i) by physically mixing both $LSFT_{0.2}$ and CGO powders ($50LSFT_{0.2}$-PM) and (ii) by a single co-sintering step via the freeze-drying method, followed by calcination at 800 ºC ($50LSFT_{0.2}$-FD). After that, the composite powders were

UNIVERSIDAD DE MÁLAGA

screen-printed onto YSZ electrolytes and sintered at 1100 ºC for 1 h to achieve an adequate adhesion to the electrolyte.

(ii) The $LSFT_{0.2}$-CGO (50:50 wt.%) nanocomposite layer ($50LSFT_{0.2}$) was also prepared by spray-pyrolysis deposition directly onto the YSZ electrolyte at 325 ºC and then calcined between 800 and 1000 ºC in air (Figure 6.1b). It is worth mentioning that 325 ºC was the optimum deposition temperature to obtain homogeneous and porous layers with improved adhesion to the electrolyte.

(iii) In an alternative approach, $LSFT_{0.2}$ and $LSFT_{0.4}$ electrodes were infiltrated by spray-pyrolysis process onto porous CGO scaffolds at 325 ºC ($LSFT_{0.2}$-Inf and $LSFT_{0.4}$-Inf, respectively) (Figure 6.1c).

(iv) Finally, a Ni-containing phase, $(La_{0.8}Sr_{0.2})_{0.95}(Fe_{0.8}Ti_{0.2})_{0.9}Ni_{0.1}O_{3-\delta}$, was also prepared to promote the Ni-exsolution in reducing conditions and improve the HOR activity (Figure 6.1d). This composition was prepared as powder the by freeze-drying method ($LSFT_{0.2}$-Ni-FD) and infiltration into a porous CGO backbone by spray-pyrolysis ($LSFT_{0.2}$-Ni) under the same conditions described previously.

Figure 6.2a compares the XRD patterns of $LSFT_{0.2}$ powders after calcination at different temperatures in air and H_2 as a representative example of the series. Independently of the Ti-content, an orthorhombic phase (s.g. Pbnm) and high stability at high calcination temperature and reducing conditions was observed. The cell volume decreases with increasing Ti-content from 241.436(2) to 240.768(2) $Å^3$ for $LSFT_{0.2}$ and $LSFT_{0.4}$, respectively (Table 6.1), due to the lower ionic radii of Ti^{4+} (0.605 Å) when compared to Fe^{3+} (0.645 Å) in an octahedral environment. These results are in accordance with previous reports on $La_{0.6}Sr_{0.4}Fe_{1-x}Ti_xO_{3-\delta}$ (x= 0.1 and 0.3) series [1].

The cell volume obtained by the Rietveld method increases after a calcination at 1400 ºC for 1 h for both compositions, 242.102(3) and 241.915(2) $Å^3$ for $LSFT_{0.2}$ and $LSFT_{0.4}$, respectively, which can be attributed to changes in the oxidation states of iron when the temperature is increased, also leading to changes in the lattice

UNIVERSIDAD DE MÁLAGA

oxygen stoichiometry [1] (Table 6.1). Afterwards, the powders calcined at high temperatures were reduced at 750 ºC for 12 h. The cell volumes of $LSFT_{0.2}$ and $LSFT_{0.4}$ slightly increased up to 242.247(3) and 242.771(2) $Å^3$, respectively.

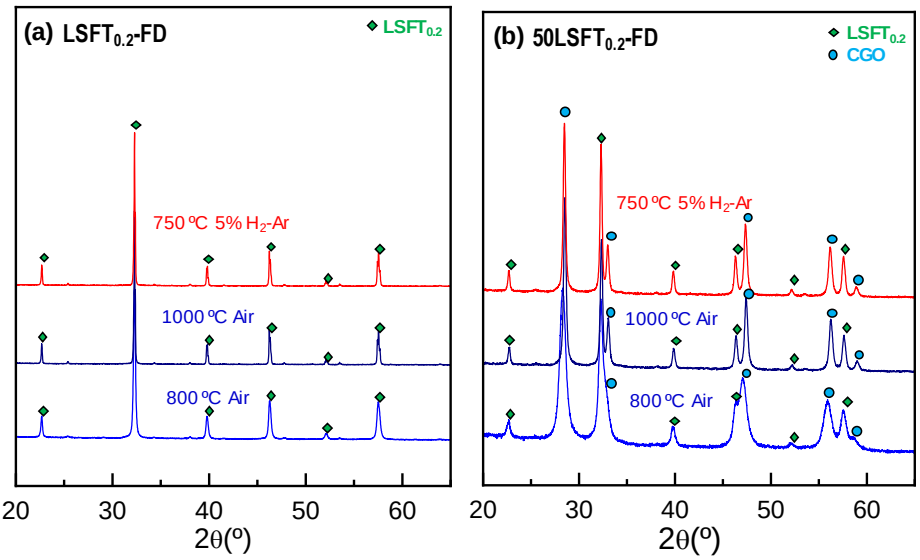

Figure 6.2. XRD patterns of (a) $LSFT_{0.2}$-FD and (b) $50LSFT_{0.2}$-FD electrodes after a calcination in air at different temperatures between 800-1000 ºC for 1 h and 750 ºC in 5% H_2-Ar for 12 h.

The higher cell volume increase in the $LSFT_{0.4}$ can be ascribed to the higher titanium content in this sample, which suffers a reduction from Ti^{4+} to Ti^{3+} in a 5% H_2-Ar atmosphere. Interestingly, the $LSFT_{0.2}$-Ni-FD shows a cell volume very similar to the undoped sample in air and reducing conditions, 240.408 (2) and 241.274(3) $Å^3$, suggesting that Ni^{2+} (0.645 Å) incorporation in B-site does not induce a structural change in the pristine sample (Table 6.1).

Figure 6.2b shows the XRD patterns of the $50LSFT_{0.2}$-FD nanocomposite prepared by freeze-drying. Interestingly, the crystallite size obtained by the Scherrer's equation for the sample calcined at 800 ºC are as low as 19.2 and 11.5 nm for $LSFT_{0.2}$ and CGO phases, respectively, increasing up to 57.5 and 64.2 nm after a calcination at 1300 ºC for 1 h. These findings confirm the grain growth suppression due to the intimate mixture at the nanoscale of two immiscible phases, hindering the cation diffusion at the grain boundary [2,3].

UNIVERSIDAD DE MÁLAGA

Table 6.1. Structural parameters of $(La_{0.8}Sr_{0.2})_{0.95}Fe_{1-x}Ti_xO_3$-$Ce_{0.9}Gd_{0.1}O_{1.95}$ (x=0.2 and 0.4) electrodes with different electrode architectures in air and 5% H_2-Ar. The preparation method is indicated as follows: Freeze-drying (FD), co-synthesis by FD (Co-syn) and spray-pyrolysis (SP).

Composition	T (ºC)	Preparation method	Volume (Å^3)		$LSFT_x$ (wt.%)	R_{wp} (%)	d_{CGO} (nm)	d_{LSFTx} (nm)
			$LSFT_x$	CGO				
$LSFT_{0.2}$-FD	800	FD	241.436(2)	-	100	3.5	-	37.4
$LSFT_{0.2}$-FD	1400	FD	242.102(3)	-	100	3.5	-	95.1
$LSFT_{0.2}$-FD (H_2)	1400	FD	242.247(3)	-	100	4.6	-	94.6
$LSFT_{0.4}$-FD	800	FD	240.768(2)	-	100	5.3	-	25.0
$LSFT_{0.4}$-FD	1400	FD	241.915(2)	-	100	4.2	-	61.8
$LSFT_{0.4}$-FD (H_2)	1400	FD	242.771(2)	-	100	4.7	-	61.2
$LSFT_{0.2}$-Ni-FD	1000	FD	240.408 (2)	-	100	3.2	-	60.0
$LSFT_{0.2}$-Ni-FD (H_2)	1000	FD	241.274 (3)	-	100	4.0	-	62.1
50$LSFT_{0.2}$-FD	800	Co-syn	240.762 (2)	162.067(2)	38	2.6	11.5	19.2
50$LSFT_{0.2}$-FD	1300	Co-syn	241.154 (2)	159.703(2)	48	3.7	57.5	64.2
$LSFT_{0.2}$-Inf	800	SP	241.510 (2)	-	-	2.6	-	24.3
$LSFT_{0.2}$-Inf (H_2)	800	SP	242.408 (2)	-	-	2.8	-	31.7
$LSFT_{0.4}$-Inf	800	SP	240.751 (1)	-	-	2.5	-	21.1
$LSFT_{0.4}$-Inf (H_2)	800	SP	242.878 (1)	-	-	2.4	-	25.0
50$LSFT_{0.2}$	800	SP	240.285 (0)	161.701(1)	44	4.4	9.9	18.6
50$LSFT_{0.2}$	1000	SP	241.026 (2)	159.824 (2)	48	2.9	34.5	40.9
50$LSFT_{0.2}$ (H_2)	750	SP	241.104 (2)	159.958 (3)	48	2.8	34.9	41.2
$LSFT_{0.2}$-Ni-Inf	800	SP	241.440 (2)	-	-	5.5	-	25.6
$LSFT_{0.2}$-Ni-Inf (H_2)	800	SP	242.024 (2)	-	-	4.8	-	30.9

The 50$LSFT_{0.2}$-FD nanocomposite shows cell volumes for the $LSFT_{0.2}$ and CGO phase components of 240.762(2) and 162.067(2) Å^3, which are similar to those obtained for the single materials. The slight changes in the cell volume can be associated with minor cation exchange between $LSFT_{0.2}$ and CGO phases during the co-sintering process. A minor incorporation of La^{3+} (1.16 Å) into the CGO lattice with

UNIVERSIDAD DE MÁLAGA

higher ionic radii, Ce^{4+} (0.97 Å), could explain the observed increase of the lattice cell volume in the CGO component [4]. Similar findings are observed for the 50LCM nanocomposite electrodes in Chapter 4. Additionally, the phase fraction obtained by the Rietveld method is similar to the nominal one. However, it is worth remarking that a minor cation exchange between both phases is not expected to be detrimental to the electrode performance. For instance, Ce-doped (La,Sr)FeO_3 exhibits improved properties for HOR [5].

Figure 6.3 shows the XRD patterns of $LSFT_{0.2}$-Inf, $LSFT_{0.4}$-Inf and $50LSFT_{0.2}$ electrodes prepared by spray-pyrolysis after a calcination in air at 800 ºC for 1 h and 750 ºC in 5% H_2-Ar for 12 h to study the stability in reducing conditions.

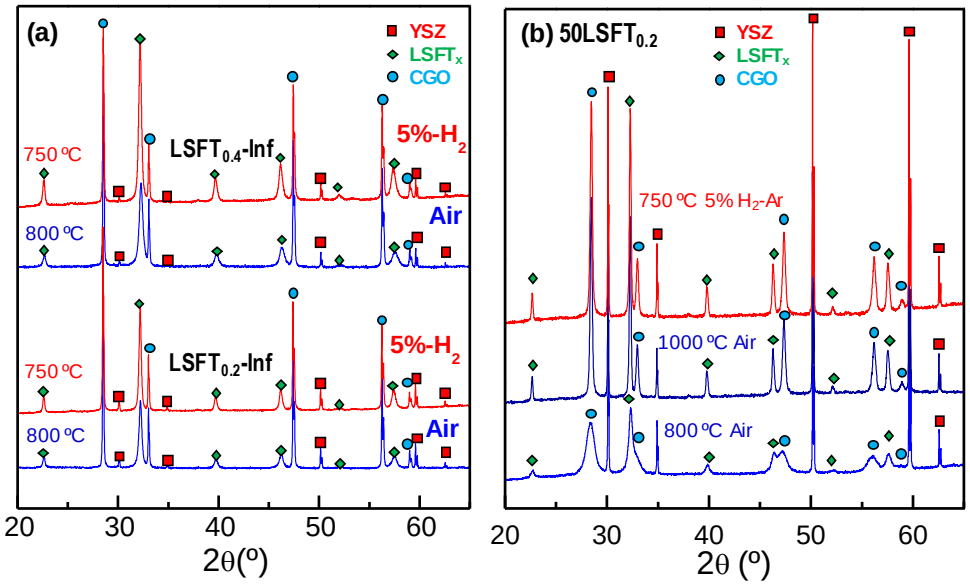

Figure 6.3. XRD patterns of (a) $LSFT_{0.2}$-Inf and $LSFT_{0.4}$-Inf and (b) $50LSFT_{0.2}$ electrodes after a calcination in air at different temperatures between 800-1000 ºC for 1 h and 750 ºC in 5% H_2-Ar for 12 h.

At 800 ºC, both $LSFT_{0.2}$-Inf and $LSFT_{0.4}$-Inf show a perovskite-type structure as observed for the pure compounds prepared by freeze-drying. Additional diffraction peaks attributed to secondary phases are not detected after the stability test in reducing conditions, confirming the redox stability of the samples. The cell volumes of

UNIVERSIDAD DE MÁLAGA

$LSFT_{0.2}$-Inf and $LSFT_{0.4}$-Inf at 800 ºC, 241.510(2) and 240.751(1) $Å^3$, respectively, are similar to those observed for the corresponding powders.

6.2. Microstructural characterization

Figure 6.4a,b shows the HAADF-STEM-EDS and HR-TEM images of the nanocomposite $50LSFT_{0.2}$ layer. The EDS mapping shows that the nanocomposite layer is composed of nanoparticles of 30 nm diameter, confirming the intimate mixture of the $LSFT_{0.2}$ and CGO phases, which ensures a great extension of the TPB length for electrochemical reactions (Figure 6.4b). The crystal structure of both phases was further confirmed by the d_{hkl} interplanar distances in accordance with the XRD data (Figure 6.4c).

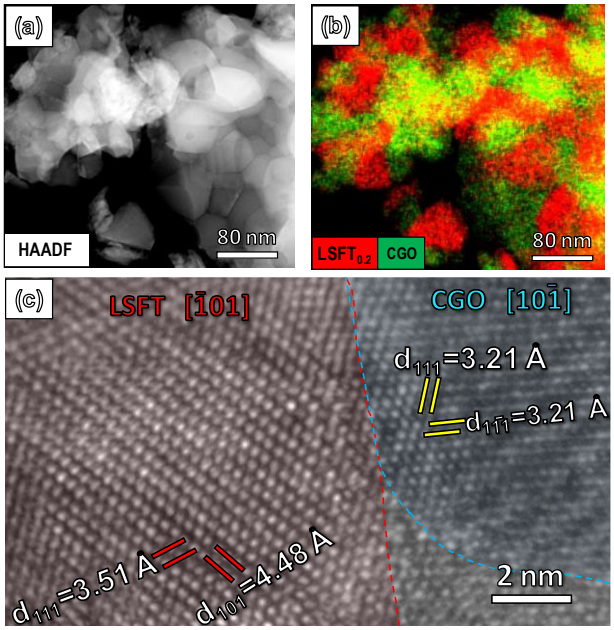

Figure 6.4. (a) HAADF-STEM image of $50LSFT_{0.2}$ after calcination at 800 °C in air and (b) EDS elemental mapping distribution. (c) HRTEM image showing the interatomic distances of the $LSFT_{0.2}$ and CGO phases.

The microstructures of the $LSFT_{0.2}$ electrodes obtained by different microstructural strategies are compared in Figure 6.5. The screen-printed $50LSFT_{0.2}$-

UNIVERSIDAD DE MÁLAGA

PM composite electrode is formed by particles of 250 nm after sintering at 1100 ºC for 1 h (Figure 6.5a,b).

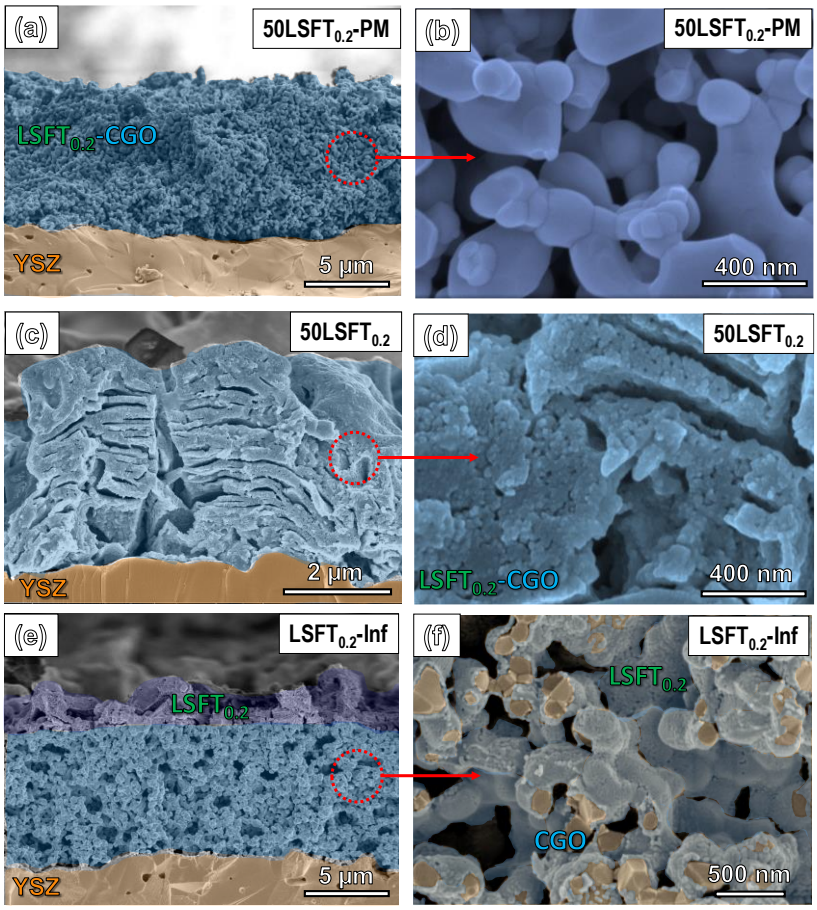

Figure 6.5. SEM images at different magnification of different electrode architectures: (a,b) screen-printed 50LSFT$_{0.2}$-PM; (c,d) 50LSFT$_{0.2}$ nanocomposite and (e,f) LSFT$_{0.2}$-Inf deposited by spray-pyrolysis.

In contrast, the nanocomposite electrode deposited by spray-pyrolysis (50LSFT$_{0.2}$) is composed of nanoparticles of only 30 nm in diameter after annealing at 800 ºC (Figure 6.5c,d). Finally, the infiltrated 50LSFT$_{0.2}$-Inf shows a CGO scaffold completely coated with LSFT$_{0.2}$ particles of ~50 nm diameter (Figure 6.5e,f). Furthermore, a 1 µm thick top layer of LSFT$_{0.2}$ is formed during the spray-pyrolysis deposition from the remaining material that was not infiltrated into the CGO backbone.

UNIVERSIDAD DE MÁLAGA

This layer can induce a better current collection due to the higher conductivity when compared to the inner layer.

The $LSFT_{0.2}$-Ni-FD sample was analysed in detail by SEM and TEM to study the exsolution process of Ni nanoparticles after reduction at 750 ºC for 12 h in 5% H_2-Ar (Figure 6.6). As can be seen in the SEM image, a good homogeneous distribution of Ni nanoparticles of ~15 nm can be observed after reduction on the electrode surface (Figure 6.6a).

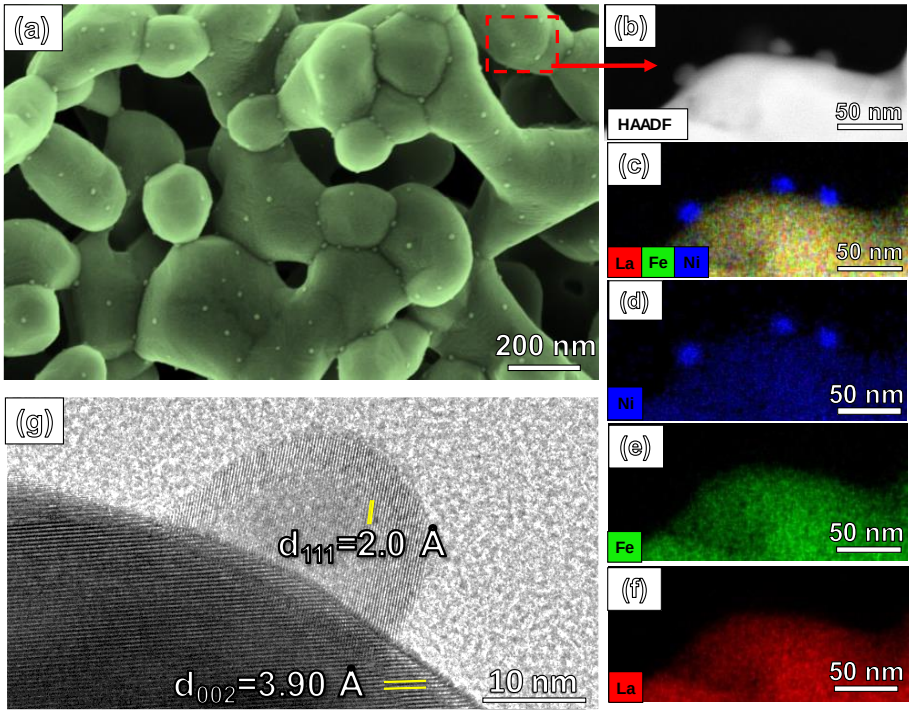

Figure 6.6. (a) SEM image of $LSFT_{0.2}$-Ni-FD electrode after reduction at 750 ºC for 12 h in 5% H_2-Ar. (b) HAADF-STEM image and (c-f) EDS mapping confirming the presence of Ni nanoparticles on the electrode surface. (g) HRTEM image showing the interatomic distances of the perovskite lattice and the Ni nanoparticle.

The HAADF-STEM-EDS characterization of the reduced electrode confirmed the presence of Ni nanoparticles on surface (Figure 6.6b-f). Interestingly, the exsolution of Ni nanoparticles does not induce the segregation of secondary phases, as observed for other ferrite-based electrodes such as $Pr_{0.6}Sr_{0.4}Fe_{0.7}Ni_{0.2}Mo_{0.1}O_{3-\delta}$ [6].

UNIVERSIDAD DE MÁLAGA

The lattice d-spacing in the HRTEM image of the Ni exsolved nanoparticle is similar to that expected for Ni metal.

The Ni exsolution mechanism in 5% H_2-Ar is attributed to nickel oxide migration to the surface, followed by reduction to Ni-metal: $Ni^{2+} + 2e^- \rightarrow Ni^0$, which further grows through particle nucleation [7]. The Ni nanoparticle population is influenced by the H_2 concentration, temperature and strain of the host lattice. In this work, the electrodes were A-site deficient, not only to minimize the possible Sr-compound segregation on surface but also to promote the exsolution of B-site metal nanoparticles [8]. When an A-site deficient perovskite ($A_{1-x}BO_{3-\delta}$) is reduced, additional oxygen vacancies are created in the lattice due to oxygen release. These oxygen vacancies promote the exsolution of certain cations in B-site and re-establishing the oxygen stoichiometry [8,9].

Interestingly, the nanoparticles obtained by exsolution are well anchored on the perovskite surface, avoiding the typical particle agglomeration and inhomogeneities of particles obtained by infiltration of the metal catalysts [10]. It is worth mentioning that the presence of exsolved metal nanoparticles on the electrode surface has demonstrated to considerably boost the performance of the anodes for fuel oxidation, as discussed in detail in the next section.

Figure 6.7 shows HAADF-STEM images and EDS mappings of the $LSFT_{0.2}$-Ni-Inf electrodes deposited by spray-pyrolysis. Ni exsolved nanoparticles are discernible on the surface, similar to the electrode deposited by screen-printing. However, the preliminary studies revealed the presence of Fe in the nanoparticle, suggesting the possible coexsolution of Ni-Fe nanoparticles in the case of the nanostructured electrode. Similar results were observed for $La_{0.6}Sr_{0.4}Fe_{0.8}Ni_{0.2}O_{3-\delta}$ [11] and $Sr_{0.95}(Ti_{0.3}Fe_{0.63}Ni_{0.07})O_{3-\delta}$ [12].

UNIVERSIDAD DE MÁLAGA

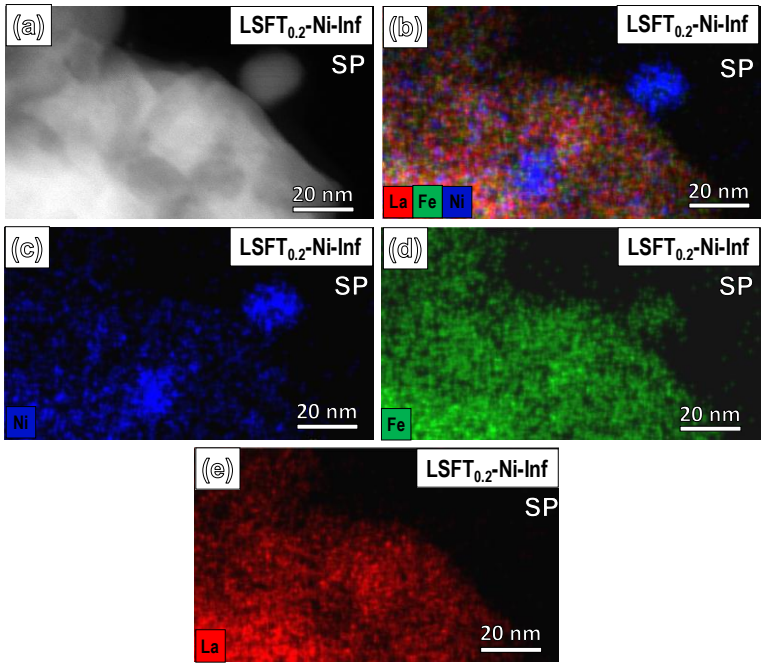

Figure 6.7. (a) HAADF-STEM image and (b-e) EDS mappings confirming the presence of Ni-Fe exsolved nanoparticles in the electrodes deposited by spray-pyrolysis.

6.3. Electrical conductivity measurements

The total conductivity of the samples was determined by the four-probe Van der Pauw method in air and 5% H_2-Ar and as a function of the oxygen partial pressure (pO_2). In order to obtain dense pellets of 13 mm and 1 mm in diameter and thickness, respectively, the precursor powders obtained by the freeze-drying method were pelletized and sintered at 1400 ºC for 1 h for $LSFT_{0.2}$-FD and $LSFT_{0.4}$-FD samples and 1300 ºC for 1 h for $50LSFT_{0.2}$-FD, reaching relative densities of 95% and average grain size of ~1.9 µm for $LSFT_{0.2}$-FD (Figure 6.8a), and 90% and ~0.6 µm for $LSFT_{0.4}$-FD (Figure 6.8b).

Interestingly, the $50LSFT_{0.2}$-FD, obtained from the co-synthesis method, shows an improved densification at 1300 ºC, which also results in smaller grain size (0.5 µm) with an excellent phase distribution homogeneity of both $LSFT_{0.2}$ and CGO phases (Figure 6.8c). It is also worth mentioning that clean grain boundaries are

UNIVERSIDAD DE MÁLAGA

observed without the presence of reaction products or impurities at temperatures as high as 1300 ºC, confirming the great stability of these nanocomposite electrodes.

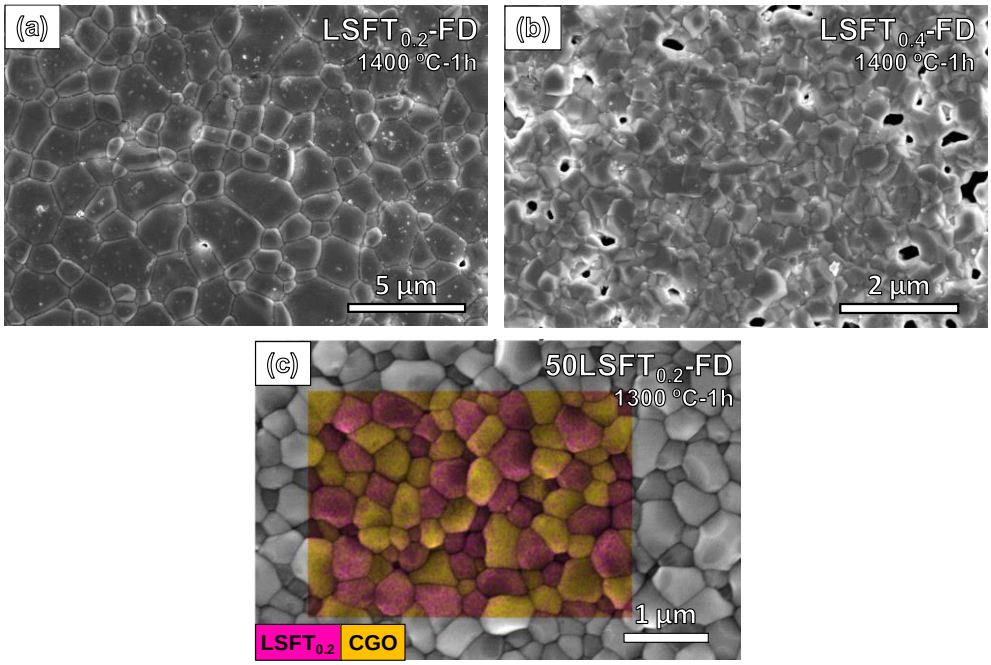

Figure 6.8. SEM images of (a) $LSFT_{0.2}$-FD, (b) $LSFT_{0.4}$-FD and (c) $50LSFT_{0.2}$-FD nanocomposite. The EDS mapping in (c) shows the phase distribution.

The electrical conductivity of the dense pellets measured in air and 5% H_2-Ar as a function of the temperature is displayed in Figure 6.9a. In air, the conductivity decreases with increasing Ti-doping, *i.e.* 0.47 and 0.003 S cm^{-1} at 700 ºC $LSFT_{0.2}$-FD and $LSFT_{0.4}$-FD, respectively, due to the stable oxidation state of Ti^{4+} in air [13]. In the case of the $50LSFT_{0.2}$-FD composite electrode, rather low conductivity values are observed at 700 ºC (0.006 S cm^{-1}) due to the lower ionic conductivity of CGO in an air atmosphere [14]. In 5% H_2-Ar, the conductivity of $LSFT_{0.2}$-FD decreases to 0.08 S cm^{-1} at 700 ºC due to the reduction of Fe cations with the consequent decrease of charge carriers. In contrast, the conductivity of $LSFT_{0.4}$-FD increases up to 3.45 S cm^{-1} at 700 ºC due to partial reduction of Ti^{4+} to Ti^{3+} with the consequent increases of charge carriers [15]. The conductivity of the $50LSFT_{0.2}$-FD composite electrode reached 0.15 S cm^{-1}, which can be assigned to the partial reduction of Ce^{4+} to Ce^{3+}, thus improving the n-type electronic conductivity [16]. Further analysis by XPS is

UNIVERSIDAD DE MÁLAGA

needed to determine the oxidation states of the elements in both oxidizing and reducing conditions.

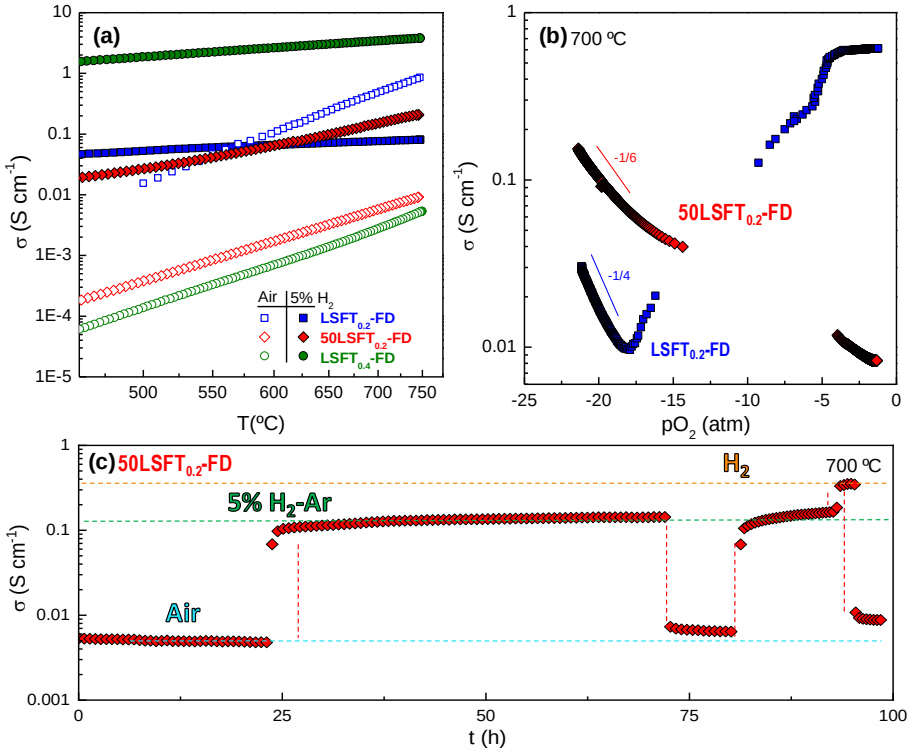

Figure 6.9. (a) Total conductivity in air and 5% H_2-Ar of the different electrode compositions as a function of the temperature, (b) total conductivity as a function of the oxygen partial pressure (pO_2) of $LSFT_{0.2}$-FD and $50LSFT_{0.2}$-FD at 700 ºC. (c) Variation of the conductivity of the $50LSFT_{0.2}$-FD sample in several oxidation/reduction cycles in air, 5% H_2-Ar and H_2 at 700 ºC.

The conductivity was measured as a function of the oxygen partial pressure (pO_2) to elucidate the nature of the charge carriers in both $LSFT_{0.2}$-FD and $50LSFT_{0.2}$-FD samples (Figure 6.9b). The $LSFT_{0.2}$-FD shows a predominant n-type conductivity at very low pO_2 with a $(pO_2)^{-1/4}$ dependence. Additionally, the conductivity saturates to a minimum value at $pO_2 \sim 10^{-17}$ atm due to the n-p transition regime. Above this pO_2, the conductivity increases with a $(pO_2)^{1/4}$ dependence attributed to a p-type contribution with hole-conduction as predicted in the defect chemistry model of $La_{0.9}Sr_{0.1}FeO_{3-\delta}$ and $La_{0.75}Sr_{0.25}FeO_{3-\delta}$ in previous studies [17,18]. In the case of $50LSFT_{0.2}$-FD, a $(pO_2)^{-1/6}$ dependence is observed at low pO_2, presumably attributed

UNIVERSIDAD DE MÁLAGA

to the presence of an important n-type contribution from the CGO phase which suffers a drastic reduction of Ce^{4+} to Ce^{3+}, with the formation of a large concentration of extrinsic vacancies as observed for $Ce_{0.8}Sm_{0.2}O_{1.9}$ [19].

In order to study the redox stability of 50LSFT$_{0.2}$-FD, the electrical conductivity was measured in consecutive oxidation/reduction cycles at 700 ºC, showing good cyclability without the presence of drops in the conductivity (Figure 6.7c). It is worth mentioning that the reduction/oxidation processes took less than 1 h despite the high relative density of the samples (96 %). Interestingly, the conductivity values in reducing conditions increased from 0.15 to 0.35 S cm^{-1} for 5% H_2-Ar and 100% H_2, respectively.

The conductivity values obtained in air in this work are rather low when compared to similar compositions reported previously, *i.e.* $La_{0.5}Sr_{0.5}Fe_{0.9}Ti_{0.1}O_{3-\delta}$ (90 S cm^{-1} at 600 ºC) [20] and $La_{0.7}Sr_{0.3}Fe_{0.6}Ti_{0.1}Ni_{0.3}O_{3-\delta}$ (318 S cm^{-1} at 700 ºC) [21]. These discrepancies can be attributed to the different crystal structures (cubic, $Pm\bar{3}m$), the titanium content in B-site and the La/Sr ratio in A-site, which has shown to have a great influence on the conductivity, achieving the best performance for the compositions with higher Sr-contents [13]. The lower concentration of Fe^{4+} (electronic charge carriers) and the smaller amount of oxygen vacancies at high lanthanum content induce lower conductivity values but higher stability in reducing conditions [13]. On the other hand, the conductivity values in reducing conditions are very similar to those reported previously, *i.e.* $La_{0.4}Sr_{0.6}Fe_{0.6}Ti_{0.4}O_{3-\delta}$ (0.5 S cm^{-1}) [13] and $La_{0.3}Sr_{0.7}Fe_{0.9}Ti_{0.1}O_{3-\delta}$ (0.25 S cm^{-1}) [22] at 600 ºC.

6.4. Electrochemical characterization

Figure 6.10a shows the impedance spectra of some selected electrodes in air at 700 ºC, where the ohmic resistance was subtracted from the impedance data for a better comparison of the electrode contributions.

The screen-printed LSFT$_{0.2}$-FD and LSFT$_{0.4}$-FD electrodes show R_p values of 1.19 and 8.84 Ω cm^2, respectively, at 700 ºC. The phase with higher Ti-content, LSFT$_{0.4}$-FD, exhibits a poorer electrochemical activity in air due to the low electrical

UNIVERSIDAD DE MÁLAGA

conductivity as the Ti-doping increases, similar findings are observed for $SrFe_{1-x}Ti_xO_{3-\delta}$ ($0 < x \leq 0.5$) series [23].

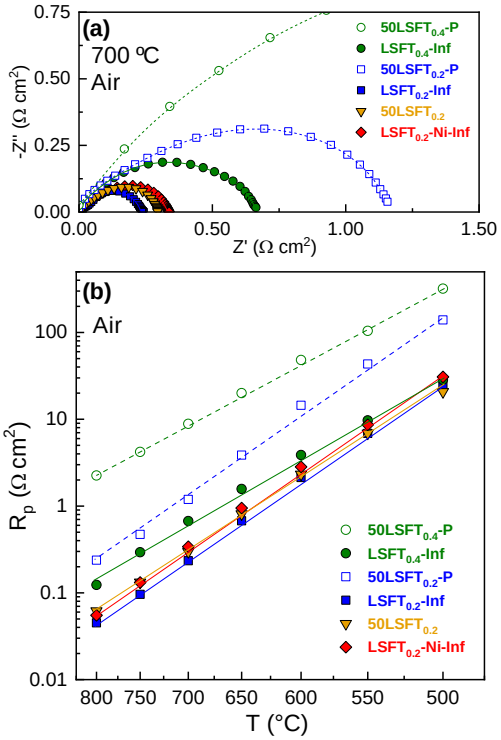

Figure 6.10. (a) Impedance spectra of the different electrode architectures at 700 ºC in air and (b) total polarization resistance as a function of the temperature in air.

The electrochemical properties of $LSFT_{0.2}$ are significantly improved by microstructural engineering, achieving R_p values as low as 0.30 and 0.23 Ω cm² for $50LSFT_{0.2}$ and $LSFT_{0.2}$-Inf at 700 ºC. The R_p values of $LSFT_{0.4}$ (0.67 Ω cm² at 700 ºC) clearly outperformed those obtained for the screen-printed electrodes but they are still high for their consideration as air electrodes (Figure 6.10b). These values are comparable to those observed for $SrFe_{0.9}Ti_{0.1}O_{3-\delta}$ (2.34 Ω cm² at 700 ºC) [24], $SrFe_{0.75}Ti_{0.25}O_{3-\delta}$ (0.25 Ω cm² at 700 ºC) [25] and $La_{0.3}Sr_{0.7}Fe_{0.9}Ti_{0.1}O_{3-\delta}$ (0.08 Ω cm² at 700 ºC) [22] or other compositions with noble metals, such as $Sm_{0.70}Sr_{0.20}Fe_{0.80}Ti_{0.15}Ru_{0.05}O_{3-\delta}$ (0.13 Ω cm² at 800 ºC) [26] and $La_{0.7}Sr_{0.3}Ti_{0.1}Fe_{0.6}Ni_{0.3}O_{3-\delta}$ (0.18 Ω cm² at 700 ºC) [27].

UNIVERSIDAD DE MÁLAGA

The electrochemical processes involved in the ORR of 50LSFT$_{0.2}$ and LSFT$_{0.2}$-Inf were identified by investigating the impedance spectra as a function of the pO_2 (Figure 6.11a,b) [28,29]. Firstly, DRT analysis was performed to determine the main rate-limiting steps involved in the ORR (Figure 6.11c,d). In the pO_2 range studied (0.001- 0.21 atm), only two electrode contributions are discernible in the DRT spectra.

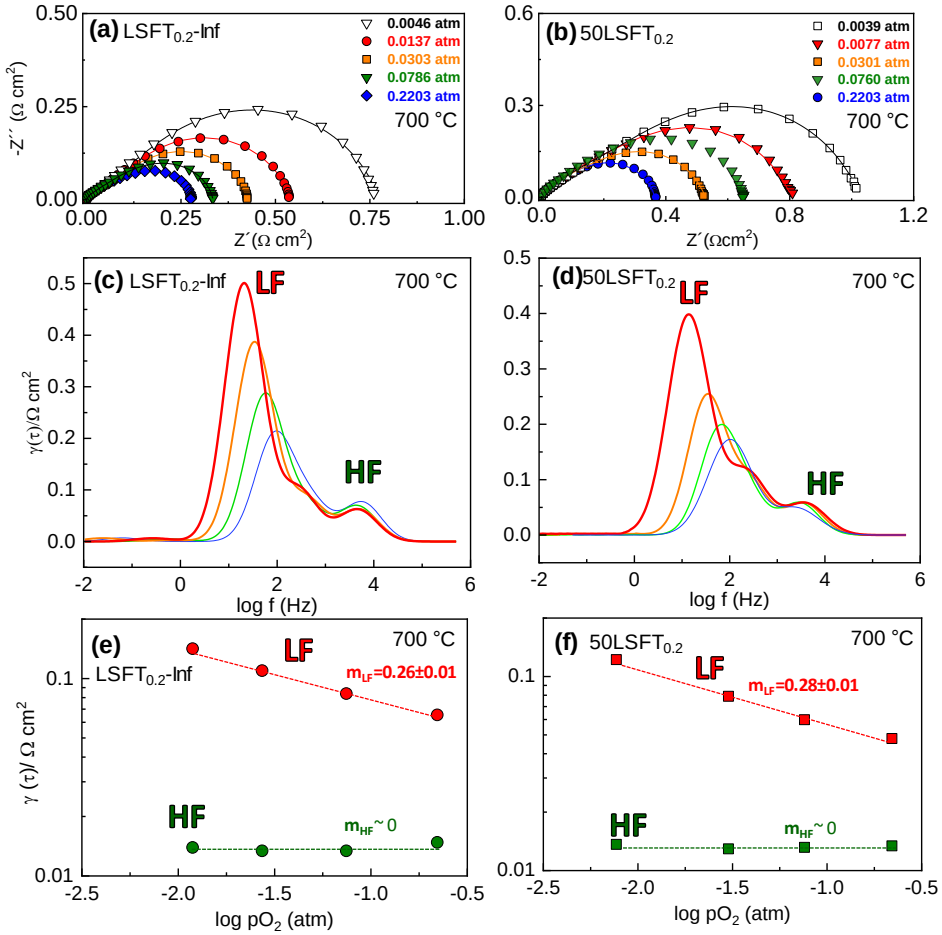

Figure 6.11. Impedance spectra as a function of the oxygen partial pressure (pO_2) for (a) LSFT$_{0.2}$-Inf, and (b) 50LSFT$_{0.2}$ and (c,d) the corresponding DRT spectra. (e-f) pO_2-dependence of the electrodes resistance contributions.

For both 50LSFT$_{0.2}$ and LSFT$_{0.2}$-Inf electrodes, the process at high frequency (HF) is nearly independent of the pO_2 and can be assigned to the oxygen ion transport at the electrode/electrolyte interface ($O^x_{o,\ electrode} \rightarrow O^x_{o,\ electrolyte}$) [30] (Figure 6.11c,d). The resistance at low frequency (LF) with a reaction order of m=1/4 can be attributed

UNIVERSIDAD DE MÁLAGA

to charge transfer at the electrode surface (O_{ad} + 2e^- + $V^{\cdot\cdot}_{o,}$ → O^x_o) [31] (Figure 6.11e,f). Interestingly, both electrodes show the same contributions, revealing that the different architectures do not change the rate-limiting steps for ORR. Similarly, the LF electrode response is shifted to a higher frequency when the pO_2 increases, indicating a lower relaxation time, thus showing faster electrode kinetics. In the pO_2 range studied, the LF contribution is the rate-limiting step for ORR.

In 100% H_2, 50LSF$T_{0.2}$ and LSF$T_{0.2}$-Inf show R_p values of 0.58 and 0.41 Ω cm^2 at 700 ºC, while a lower value of 0.20 Ω cm^2 is obtained for LSF$T_{0.4}$-Inf (Figure 6.12). The better electrochemical performance of LSF$T_{0.4}$-Inf can be linked to its higher electrical conductivity in reducing atmosphere when compared with those electrodes with lower Ti-content. However, the poor performance of LSF$T_{0.4}$-Inf in air limits the potential application of LSF$T_{0.4}$-Inf to work only as a fuel electrode.

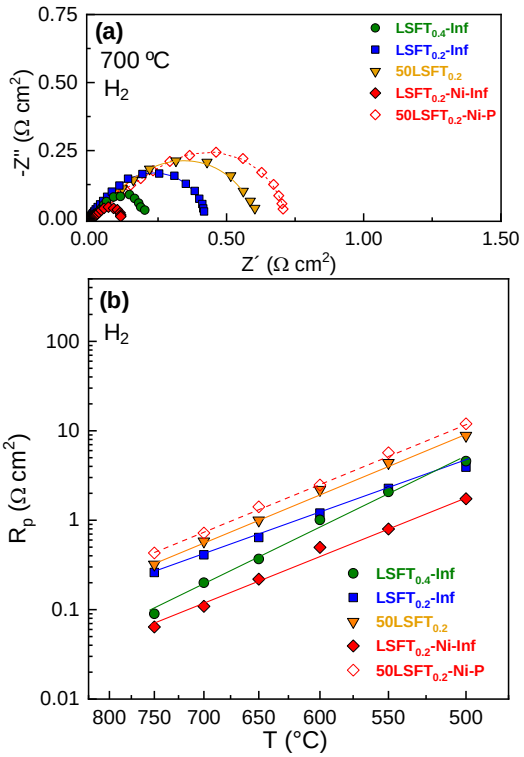

Figure 6.12. (a) Impedance spectra of the different electrode compositions and architectures at 700 ºC in 100% H_2 and (b) temperature dependence of the total polarization resistance.

UNIVERSIDAD DE MÁLAGA

$(La_{0.8}Sr_{0.2})_{0.95}(Fe_{0.8}Ti_{0.2})_{0.9}Ni_{0.1}O_{3-\delta}$ deposited by spray-pyrolysis on a CGO backbone ($LSFT_{0.2}$-Ni-Inf) achieves a polarization resistance of 0.11 Ω cm^2 at 700 ºC in H_2 (Figure 6.12a,b). The greater R_p for this electrode is clearly attributed to the exsolution of Ni nanoparticles under reducing conditions, as observed in section 5.2. Interestingly, $LSFT_{0.2}$-Ni-Inf considerably improves the electrochemical activity for fuel oxidation while similar performance was observed in oxidizing conditions. These R_p values are lower than those reported for related compositions such as $La_{0.3}Sr_{0.7}Ti_{0.3}Fe_{0.7}O_{3-\delta}$ (0.75 Ω cm^2 at 700 ºC) [32] and $La_{0.3}Sr_{0.7}Fe_{0.9}Ti_{0.1}O_{3-\delta}$ (0.58 Ω cm^2 at 700 ºC) [22] or other compositions with exsolved metals particles such as $La_{0.7}Sr_{0.3}Ti_{0.1}Fe_{0.6}Ni_{0.3}O_{3-\delta}$ (0.40 Ω cm^2 at 700 ºC) [27].

6.5. Fuel cell tests

The efficiency in real operation conditions of $50LSFT_{0.2}$-P, $LSFT_{0.2}$-Inf and $LSFT_{0.2}$-Ni-Inf electrodes was tested in symmetrical cells on a 300 μm thick LSGM electrolyte (Figure 6.13).

For all symmetrical cells, the open circuit voltage (OCV) is close to the theoretical Nernst potential, 1.1 V. The single cell with a screen-printed $50LSFT_{0.2}$-P renders maximum power densities of 309, 217, 141 and 86 mW cm^{-2} at 800, 750, 700 and 650 ºC, respectively (Figure 6.13a). These values were improved by the infiltrated electrodes deposited by spray-pyrolysis with maximum power densities for $LSFT_{0.2}$-Inf of 496, 353, 235 and 140 mW cm^{-2} at 800, 750, 700 and 650 ºC, respectively (Figure 6.13b). Since the ohmic resistance is the same for the different cells, it is evident that the improved performance is attributed to the higher TPB density of the nanostructured electrodes. The power output is greatly improved for the analogous Ni-containing electrode ($LSFT_{0.2}$-Ni-Inf) with maximum power densities of 617, 489, 369 and 259 mW cm^{-2} at 800, 750, 700 and 650 ºC, respectively (Figure 6.13c). The incorporation of Ni induces a better performance in reducing conditions due to the formation of highly active Ni nanoparticles.

UNIVERSIDAD DE MÁLAGA

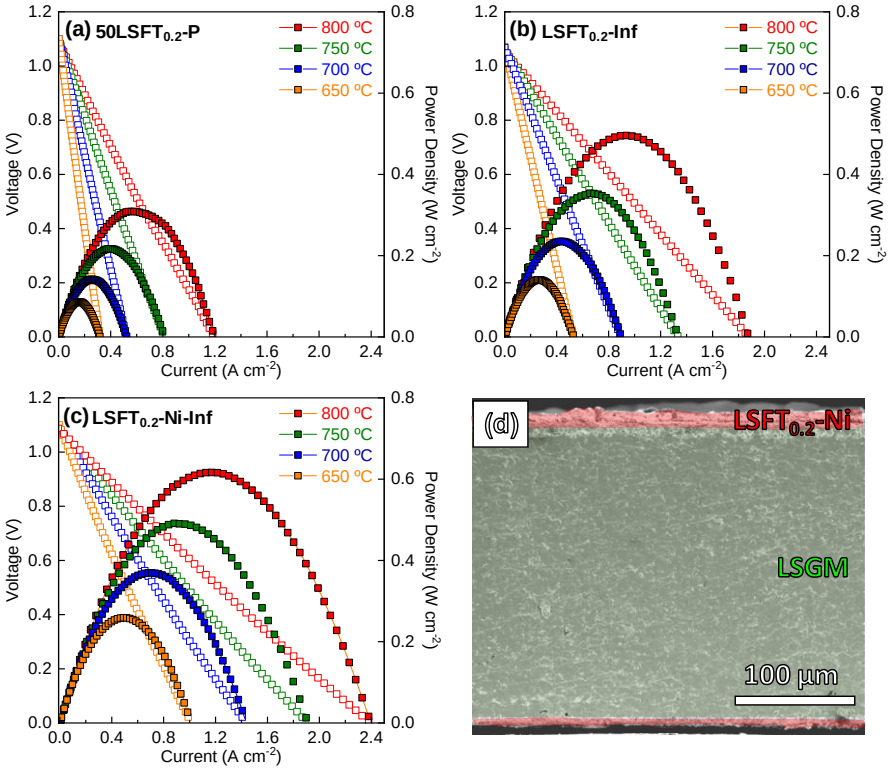

Figure 6.13. I-V-P curves of different LSGM electrolyte supported cell with (a) 50$LSFT_{0.2}$-P, (b) $LSFT_{0.2}$-Inf and (c) $LSFT_{0.2}$-Ni-Inf symmetrical electrodes using wet H_2 as fuel and static air as oxidant. (d) SEM image of the $LSFT_{0.2}$-Ni-Inf symmetrical cell after the electrochemical tests.

Moreover, $LSFT_{0.2}$-Ni-Inf displays excellent stability under continuous operation during 120 h at 800 ºC (Figure 6.14a). The analysis of the cross-section after the electrochemical test further confirmed the cell stability (Figure 6.13d). The power density values of the cell with $LSFT_{0.2}$-Ni-Inf symmetrical electrode are higher than those observed previously for related compositions reported in the literature, such as 200 mW cm^{-2} at 800 ºC for $La_{0.3}Sr_{0.7}Fe_{0.7}Ti_{0.3}O_{3-\delta}$ onto a 400 µm thick YSZ electrolyte [33], 450 mW cm^{-2} at 850 ºC for $La_{0.4}Sr_{0.6}Fe_{0.7}Ti_{0.25}Co_{0.05}O_{3-\delta}$ onto a 300 µm thick LSGM electrolyte [34], 540 mW cm^{-2} at 850 ºC for $La_{0.8}Sr_{0.2}Fe_{0.7}Ni_{0.3}O_{3-\delta}$ onto a 350 µm thick LSGM electrolyte [35] or 300 mW cm^{-2} at 800 ºC for $La_{0.3}Sr_{0.7}Fe_{0.7}Cr_{0.3}O_{3-\delta}$ onto a 500 µm thick LSGM electrolyte [36].

UNIVERSIDAD DE MÁLAGA

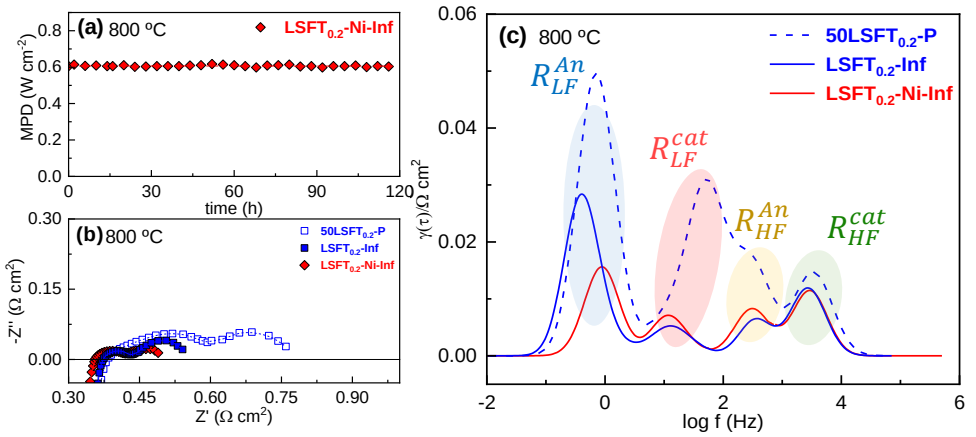

Figure 6.14. (a) Stability test of the $LSFT_{0.2}$-Ni-Inf cell under continuous operation at 800 ºC for 120 h. (b) Impedance spectra and (c) the corresponding DRT analysis of the $50LSFT_{0.2}$-P, $LSFT_{0.2}$-Inf and $LSFT_{0.2}$-Ni-Inf single cells.

The ohmic resistances (R_s) of the cells are comparable and close to that expected for a 300 µm thick LSGM-supported electrolyte (~0.3 Ω cm² at 800 ºC) (Figure 6.14b). It is also remarkable to note that the ohmic resistance of the cells is higher than the polarization resistance, *i.e.,* $LSFT_{0.2}$-Ni-Inf shows ohmic and polarization resistance of 0.35 and 0.14 Ω cm² at 800 ºC, respectively. These findings indicate that the efficiency of the cell is mainly limited by the electrolyte thickness and a higher power output can be achieved by reducing the electrolyte thickness.

Deeper insights about the different electrode processes under SOFC operation conditions were studied by DRT analysis of the impedance data (Figure 6.14c). DRT spectra show that the electrode response is composed of four different contributions assigned to the cathode (Cat) and anode (An). Interestingly, all these processes are reduced for the cell with nanostructured electrodes when compared to the cell with screen-printed electrodes. In particular, the low-frequency processes, R^{Cat}_{LF} and R^{An}_{LF}, attributed to electrochemical processes occurring at the cathode and anode surface, respectively [28,29], are the main contributions to the overall polarization resistance. These findings are in accordance with those obtained in the electrode polarization studies in the previous section. In the case of the $LSFT_{0.2}$-Inf and $LSFT_{0.2}$-Ni-Inf, very similar electrode contributions were observed for the processes at the electrode/electrolyte interface (R^{Cat}_{HF} and R^{An}_{HF}) and the charge

UNIVERSIDAD DE MÁLAGA

transfer at the cathode surface (R^{Cat}_{LF}). However, the R^{An}_{LF} contribution, attributed to hydrogen oxidation processes at the TPB in the fuel electrode [37], decreased considerably for $LSFT_{0.2}$-Ni-Inf, indicating that the formation of Ni exsolved nanoparticles improves the efficiency for fuel oxidation on the electrode surface.

All these findings confirm the great influence of tailoring the electrode microstructure to boost the electrode performance in both oxidizing and reducing conditions. In addition, the Ni-doping strategy has demonstrated to be highly effective to improve the catalytic activity for fuel oxidation. On the other hand, although the microstructural optimization improves the electrochemical processes on the electrode surface, the oxide-ion transfer process at the electrode/electrolyte interface is not significantly enhanced, presumably due to the interfacial nature of this contribution. For this reason, alternative strategies, such as the incorporation of active layers, could be explored to further improve the efficiency of SOFC electrodes.

References

1. Takahashi, Y.; Suzuki, T.; Kawahara, A.; Ando, Y.; Hirano, M.; Shin, W. Dilatometry and High-Temperature X-Ray Diffractometry Study of $La_{0.6}Sr_{0.4}Ti_{0.1}Fe_{0.9}O_{3-\delta}$ and $La_{0.6}Sr_{0.4}Ti_{0.3}Fe_{0.7}O_{3-\delta}$ Oxygen-Permeable Membranes. *Solid State Ionics* **2010**, *181*, 1516–1520, doi:10.1016/j.ssi.2010.08.024.
2. Leng, J.; Wang, Z.; Wang, J.; Wu, H.H.; Yan, G.; Li, X.; Guo, H.; Liu, Y.; Zhang, Q.; Guo, Z. Advances in Nanostructures Fabricated: Via Spray Pyrolysis and Their Applications in Energy Storage and Conversion. *Chem. Soc. Rev.* **2019**, *48*, 3015–3072, doi:10.1039/c8cs00904j.
3. dos Santos-Gómez, L.; Zamudio-García, J.; Porras-Vázquez, J.M.; Losilla, E.R.; Marrero-López, D. Highly Efficient $La_{0.8}Sr_{0.2}MnO_{3-\delta}$-$Ce_{0.9}Gd_{0.1}O_{1.95}$ Nanocomposite Cathodes for Solid Oxide Fuel Cells. *Ceram. Int.* **2018**, *44*, 4961–4966, doi:10.1016/j.ceramint.2017.12.089.
4. Zamudio-García, J.; Porras-Vázquez, J.M.; Canales-Vázquez, J.; Cabeza, A.; Losilla, E.R.; Marrero-López, D. Relationship between the Structure and Transport Properties in the $Ce_{1-x}La_xO_{2-x/2}$ System. *Inorg. Chem.* **2019**, *58*, 9368–9377, doi:10.1021/acs.inorgchem.9b01104.
5. Bian, L.; Duan, C.; Wang, L.; O'Hayre, R.; Cheng, J.; Chou, K.C. Ce-Doped $La_{0.7}Sr_{0.3}Fe_{0.9}Ni_{0.1}O_{3-\delta}$ as Symmetrical Electrodes for High Performance Direct Hydrocarbon Solid Oxide Fuel Cells. *J. Mater. Chem. A* **2017**, *5*, 15253–15259, doi:10.1039/c7ta03001k.
6. Lu, X.; Yang, Y.; Ding, Y.; Chen, Y.; Gu, Q.; Tian, D.; Yu, W.; Lin, B. Mo-Doped $Pr_{0.6}Sr_{0.4}Fe_{0.8}Ni_{0.2}O_{3-\delta}$ as Potential Electrodes for Intermediate-Temperature Symmetrical Solid Oxide Fuel Cells. *Electrochim. Acta* **2017**, *227*, 33–40, doi:10.1016/j.electacta.2016.12.170.
7. Cao, T.; Kwon, O.; Gorte, R.J.; Vohs, J.M. Metal Exsolution to Enhance the Catalytic Activity of Electrodes in Solid Oxide Fuel Cells. *Nanomaterials* **2020**, *10*, 1–23,

UNIVERSIDAD DE MÁLAGA

doi:10.3390/nano10122445.

8. Kwon, O.; Joo, S.; Choi, S.; Sengodan, S.; Kim, G. Review on Exsolution and Its Driving Forces in Perovskites. *JPhys Energy* **2020**, *2*, doi:10.1088/2515-7655/ab8c1f.
9. Yang, Y.; Li, J.; Sun, Y. The Metal/Oxide Heterointerface Delivered by Solid-Based Exsolution Strategy: A Review. *Chem. Eng. J.* **2022**, *440*, 135868, doi:10.1016/j.cej.2022.135868.
10. Kim, S.; Kim, G.; Manthiram, A. A Review on Infiltration Techniques for Energy Conversion and Storage Devices: From Fundamentals to Applications. *Sustain. Energy Fuels* **2021**, *5*, 5024–5037, doi:10.1039/d1se00878a.
11. Tian, Y.; Liu, Y.; Jia, L.; Naden, A.; Chen, J.; Chi, B.; Pu, J.; Irvine, J.T.S.; Li, J. A Novel Electrode with Multifunction and Regeneration for Highly Efficient and Stable Symmetrical Solid Oxide Cell. *J. Power Sources* **2020**, *475*, 228620, doi:10.1016/j.jpowsour.2020.228620.
12. Zhu, T.; Troiani, H.E.; Mogni, L. V.; Han, M.; Barnett, S.A. Ni-Substituted Sr(Ti,Fe)O_3 SOFC Anodes: Achieving High Performance via Metal Alloy Nanoparticle Exsolution. *Joule* **2018**, *2*, 478–496, doi:10.1016/j.joule.2018.02.006.
13. Fagg, D.P.; Kharton, V. V.; Frade, J.R.; Ferreira, A.A.L. Stability and Mixed Ionic-Electronic Conductivity of (Sr,La)(Ti,Fe)$O_{3-\delta}$ Perovskites. *Solid State Ionics* **2003**, *156*, 45–57, doi:10.1016/S0167-2738(02)00257-6.
14. Zhang, Y.; Shen, L.; Wang, Y.; Du, Z.; Zhang, B.; Ciucci, F.; Zhao, H. Enhanced Oxygen Reduction Kinetics of IT-SOFC Cathode with $PrBaCo_2O_{5+\delta}$/$Gd_{0.1}Ce_{0.9}O_{2-\delta}$ coherent Interface. *J. Mater. Chem. A* **2022**, *10*, 3495–3505, doi:10.1039/d1ta09615j.
15. Alvarado Flores, J.J.; Ávalos Rodríguez, M.L.; Andrade Espinosa, G.; Alcaraz Vera, J.V. Advances in the Development of Titanates for Anodes in SOFC. *Int. J. Hydrogen Energy* **2019**, *4*, 12529–12542, doi:10.1016/j.ijhydene.2018.05.171.
16. Schmitt, R.; Nenning, A.; Kraynis, O.; Korobko, R.; Frenkel, A.I.; Lubomirsky, I.; Haile, S.M.; Rupp, J.L.M. A Review of Defect Structure and Chemistry in Ceria and Its Solid Solutions. *Chem. Soc. Rev.* **2020**, *49*, 554–592, doi:10.1039/c9cs00588a.
17. Wærnhus, I.; Grande, T.; Wiik, K. Surface Exchange of Oxygen in $La_{1-x}Sr_xFeO_{3-\delta}$ (x = 0, 0.1). *Top. Catal.* **2011**, *54*, 1009–1015, doi:10.1007/s11244-011-9712-z.
18. Mizusaki, J.; Sasamoto, T.; Cannon, W.R.; Bowen, H.K. Electronic Conductivity, Seebeck Coefficient, and Defect Structure of $La_{1-x}Sr_xFeO_3$ (X=0.l, 0.25). *J. Am. Ceram. Soc.* **1983**, *66*, 247–252, doi:10.1111/j.1151-2916.1983.tb15707.x.
19. Abrantes, J.C.C.; Pérez-Coll, D.; Núñez, P.; Frade, J.R. Electronic Transport in $Ce_{0.8}Sm_{0.2}O_{1.9-\delta}$ Ceramics under Reducing Conditions. *Electrochim. Acta* **2003**, *48*, 2761–2766, doi:10.1016/S0013-4686(03)00395-5.
20. Hou, Y.; Wang, L.; Bian, L.; Zhang, Q.; Chen, L.; Chou, K. chih Effect of High-Valence Elements Doping at B Site of $La_{0.5}Sr_{0.5}FeO_{3-\delta}$. *Ceram. Int.* **2022**, *48*, 4223–4229, doi:10.1016/j.ceramint.2021.10.214.
21. Hanif, M.B.; Gao, J.T.; Shaheen, K.; Wang, Y.P.; Yasir, M.; Zhang, S.L.; Li, C.J.; Li, C.X. Performance Evaluation of Highly Active and Novel $La_{0.7}Sr_{0.3}Ti_{0.1}Fe_{0.6}Ni_{0.3}O_{3-\delta}$ Material Both as Cathode and Anode for Intermediate-Temperature Symmetrical Solid Oxide Fuel Cell. *J. Power Sources* **2020**, *472*, 228498, doi:10.1016/j.jpowsour.2020.228498.
22. Hou, Y.; Wang, L.; Bian, L.; Wang, Y.; Chou, K.C. Excellent Electrochemical Performance of $La_{0.3}Sr_{0.7}Fe_{0.9}Ti_{0.1}O_{3-\delta}$ as a Symmetric Electrode for Solid Oxide Cells. *ACS Appl. Mater. Interfaces* **2021**, *13*, 22381–22390, doi:10.1021/acsami.1c02856.
23. Baharuddin, N.A.; Mohd Nazrul Aman, N.A.; Muchtar, A.; Somalu, M.R.; Abdul Samat, A.;

UNIVERSIDAD DE MÁLAGA

Aznam, M.I. Structural, Morphological, and Electrochemical Behavior of Titanium-Doped $SrFe_{1-x}Ti_xO_{3-\delta}$ (x = 0.1–0.5) Perovskite as a Cobalt-Free Solid Oxide Fuel Cell Cathode. *Ceram. Int.* **2019**, *45*, 12903–12909, doi:10.1016/j.ceramint.2019.03.216.

24. Baharuddin, N.A.; Mohd Nazrul Aman, N.A.; Muchtar, A.; Somalu, M.R.; Abdul Samat, A.; Aznam, M.I. Structural, Morphological, and Electrochemical Behavior of Titanium-Doped $SrFe_{1-x}Ti_xO_{3-\delta}$ (x = 0.1–0.5)Perovskite as a Cobalt-Free Solid Oxide Fuel Cell Cathode. *Ceram. Int.* **2019**, *45*, 12903–12909, doi:10.1016/j.ceramint.2019.03.216.
25. Fernández-Ropero, A.J.; Porras-Vázquez, J.M.; Cabeza, A.; Slater, P.R.; Marrero-López, D.; Losilla, E.R. High Valence Transition Metal Doped Strontium Ferrites for Electrode Materials in Symmetrical SOFCs. *J. Power Sources* **2014**, *249*, 405–413, doi:10.1016/j.jpowsour.2013.10.118.
26. Fan, W.; Sun, Z.; Bai, Y.; Wu, K.; Zhou, J.; Cheng, Y. In Situ Growth of Nanoparticles in A-Site Deficient Ferrite Perovskite as an Advanced Electrode for Symmetrical Solid Oxide Fuel Cells. *J. Power Sources* **2020**, *456*, 228000, doi:10.1016/j.jpowsour.2020.228000.
27. Bilal Hanif, M.; Gao, J.-T.; Shaheen, K.; Wang, Y.-P.; Yasir, M.; Zhang, S.; Li, C.-J.; Li, C.-X. Performance Evaluation of Highly Active and Novel $La_{0.7}Sr_{0.3}Ti_{0.1}Fe_{0.6}Ni_{0.3}O_{3-\delta}$ Material Both as Cathode and Anode for Intermediate-Temperature Symmetrical Solid Oxide Fuel Cell. *J. Power Sources* **2020**, *472*, 228498, doi:10.1016/j.jpowsour.2020.228498.
28. Zhang, J.; Lei, L.; Li, H.; Chen, F.; Han, M. A Practical Approach for Identifying Various Polarization Behaviors of Redox-Stable Electrodes in Symmetrical Solid Oxide Fuel Cells. *Electrochim. Acta* **2021**, *384*, 138340, doi:10.1016/j.electacta.2021.138340.
29. Osinkin, D.A. An Approach to the Analysis of the Impedance Spectra of Solid Oxide Fuel Cell Using the DRT Technique. *Electrochim. Acta* **2021**, *372*, 137858, doi:10.1016/j.electacta.2021.137858.
30. Siebert, E.; Hammouche, A.; Kleitz, M. Impedance Spectroscopy Analysis of $La_{1-x}Sr_{ix}MnO_3$-Yttria-Stabilized Zirconia Electrode Kinetics. *Electrochim. Acta* **1995**, *40*, 1741–1753, doi:10.1016/0013-4686(94)00361-4.
31. Chen, X.J.; Khor, K.A.; Chan, S.H. Identification of O_2 Reduction Processes at Yttria Stabilized Zirconia|doped Lanthanum Manganite Interface. *J. Power Sources* **2003**, *123*, 17–25, doi:10.1016/S0378-7753(03)00436-1.
32. Xu, J.; Zhou, X.; Dong, X.; Pan, L.; Sun, K. Catalytic Activity Improvement for Efficient Hydrogen Oxidation of Infiltrated $La_{0.3}Sr_{0.7}Ti_{0.3}Fe_{0.7}O_{3-\delta}$ Anode for Solid Oxide Fuel Cell. *Ceram. Int.* **2017**, *43*, 10750–10756, doi:10.1016/j.ceramint.2017.05.081.
33. Cao, Z.; Zhang, Y.; Miao, J.; Wang, Z.; Lü, Z.; Sui, Y.; Huang, X.; Jiang, W. Titanium-Substituted Lanthanum Strontium Ferrite as a Novel Electrode Material for Symmetrical Solid Oxide Fuel Cell. *Int. J. Hydrogen Energy* **2015**, *40*, 16572–16577, doi:10.1016/j.ijhydene.2015.10.010.
34. Song, J.; Zhu, T.; Chen, X.; Ni, W.; Zhong, Q. Cobalt and Titanium Substituted $SrFeO_3$ Based Perovskite as Efficient Symmetrical Electrode for Solid Oxide Fuel Cell. *J. Mater.* **2020**, *6*, 377–384, doi:10.1016/j.jmat.2020.02.009.
35. Ben Mya, O.; dos Santos-Gómez, L.; Porras-Vázquez, J.M.; Omari, M.; Ramos-Barrado, J.R.; Marrero-López, D. $La_{1-x}Sr_xFe_{0.7}Ni_{0.3}O_{3-\delta}$ as Both Cathode and Anode Materials for Solid Oxide Fuel Cells. *Int. J. Hydrogen Energy* **2017**, *42*, 23160–23169, doi:10.1016/j.ijhydene.2017.07.150.
36. Chen, M.; Paulson, S.; Thangadurai, V.; Birss, V. Sr-Rich Chromium Ferrites as Symmetrical Solid Oxide Fuel Cell Electrodes. *J. Power Sources* **2013**, *236*, 68–79,

UNIVERSIDAD DE MÁLAGA

doi:10.1016/j.jpowsour.2013.02.024.

37. Osinkin, D.A. Detailed Analysis of Electrochemical Behavior of High–Performance Solid Oxide Fuel Cell Using DRT Technique. *J. Power Sources* **2022**, *527*, 231120, doi:10.1016/j.jpowsour.2022.231120.

UNIVERSIDAD DE MÁLAGA

Chapter 7

UNIVERSIDAD
DE MÁLAGA

UNIVERSIDAD
DE MÁLAGA

Nanocomposite active layers

In this chapter, nanocomposite active layers based on the combination of $La_{0.8}Sr_{0.2}MnO_{3-\delta}$ (LSM) with different oxide-ion conductors, such as $Ce_{0.9}Gd_{0.1}O_{1.95}$ (CGO), Pr_6O_{11} and $Bi_{1.5}Y_{0.5}O_3$ (BYO), were prepared for the first time by spray-pyrolysis. The influence of the incorporation of an active layer at the electrode/electrolyte interface was studied in detail. The microstructural and electrochemical properties of cathodes with biphasic layers were compared to single-phase active layers, taking special attention to their microstructure after calcination at high temperatures and the influence of the nanoscale contact between two immiscible fluorite and perovskite-type phases on the grain growth.

UNIVERSIDAD DE MÁLAGA

7.1. Influence of the ionic conductivity of the electrolyte on the polarization resistance of LSCF cathodes

In order to elucidate the influence of the electrolyte on the electrochemical performance of the cathode, nanostructured $La_{0.6}Sr_{0.4}Co_{0.2}Fe_{0.8}O_{3-\delta}$ (LSCF) was deposited simultaneously by spray-pyrolysis onto different oxide-ion conductor electrolytes: YSZ, CGO, LSGM and BYO [1]. Further information about this work can be found in the Article section, A6.

The electrochemical characterization of the different cells revealed that the polarization resistance (R_p) decreases as the ionic conductivity of the electrolyte increases in the following order: YSZ (0.21 Ω cm^2) > CGO (0.11 Ω cm^2) > LSGM (0.09 Ω cm^2) > BYO (0.058 Ω cm^2) at 700 ºC (Figure 7.1).

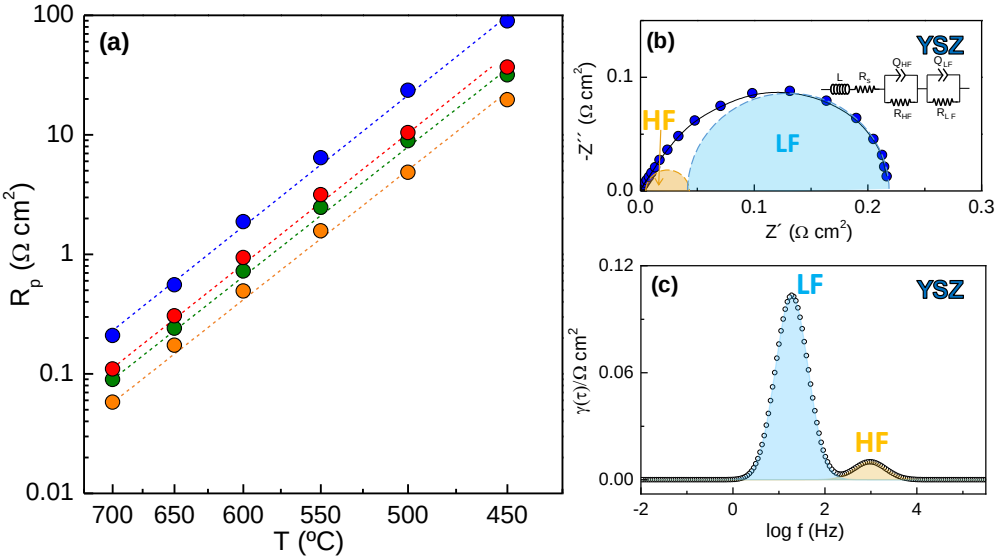

Figure 7.1. (a) Polarization resistance values in air of LSCF deposited onto different electrolytes. (b) Representative impedance spectra and (c) DRT analysis of LSCF deposited onto YSZ.

The analysis of the impedance spectra by equivalent circuits and distribution of relaxation times (DRT) shows two different electrode contributions for all cells. The high-frequency contribution (R_{HF}) is assigned to oxide-ion transfer at the electrode-electrolyte interface [2,3], while the electrode response at low frequency (R_{LF}) is

UNIVERSIDAD DE MÁLAGA

attributed to electrochemical processes on the electrode surface [2]. R_{HF} follows a decreasing trend with increasing the ionic conductivity of the electrolyte, in the order YSZ>CGO>LSGM>BYO, which can be explained by the faster oxide-ion transport at the electrode/electrolyte interface. Moreover, the corresponding activation energy is lower for the BYO sample (1.08 eV) when compared to CGO (1.14 eV), LSGM (1.25 eV) and YSZ (1.33 eV). Interestingly, the R_{LF} contribution is also influenced by the electrolyte, showing lower resistance as the ionic conductivity of the electrolyte increases. This finding suggests that an improvement of the oxide-ion transport at the electrode/electrolyte interface also induces an extension of the surface paths for electrochemical reactions on the electrode surface [4,5].

These results reveal that the limited ionic conductivity of the electrolyte is a bottleneck for the electrode performance. For this reason, the introduction of active layers at the electrode/electrolyte interface could be the key to obtain enhanced electrochemical properties for SOFC electrodes. Moreover, nanocomposite layers, which combine materials with different conducting properties, are expected to exhibit improved polarization resistance values and durability at high temperatures when compared to single-phase layers.

7.2. Nanocomposite active layers for a LSM cathode

Different active layers were evaluated to improve the efficiency of the traditional LSM cathode: LSM, LSM-CGO, LSM-Pr_6O_{11} and LSM-BYO (50 wt.%). The layers were deposited by spray-pyrolysis onto a YSZ electrolyte from aqueous precursor solutions at 450 ºC for 30 min, followed by a calcination at 800 ºC for 1 h for crystallization. Afterwards, commercial LSM (Praxair) was screen-printed onto YSZ electrolytes without and with the active layers and then sintered at 1000 ºC for 1 h. For a better structural characterization, all active layers were also deposited onto amorphous quartz wafers to avoid diffraction peak overlapping with the YSZ electrolyte. Additionally, LSM, CGO and Pr_6O_{11} single layers were prepared for comparison purposes. Further information about this work can be found in the Article section, A7.

Figure 7.2a compares the XRD patterns of the layers deposited onto quartz wafers. All active layers are crystalline at 800 ºC without the presence of additional

UNIVERSIDAD DE MÁLAGA

peaks attributed to secondary phases. LSM crystallizes with a perovskite-type structure, while Pr_6O_{11} and CGO show a cubic fluorite structure with a preferred orientation for the Pr_6O_{11} phase along the (200) plane. BYO layers showed reactivity with quartz at temperatures as low as 600 ºC. The XRD characterization revealed the formation of *α* and *β*- polymorphs and also Bi_2SiO_5 as a secondary phase. On the contrary, the BYO layers deposited on YSZ substrates show a single fluorite structure at 800 ºC [6].

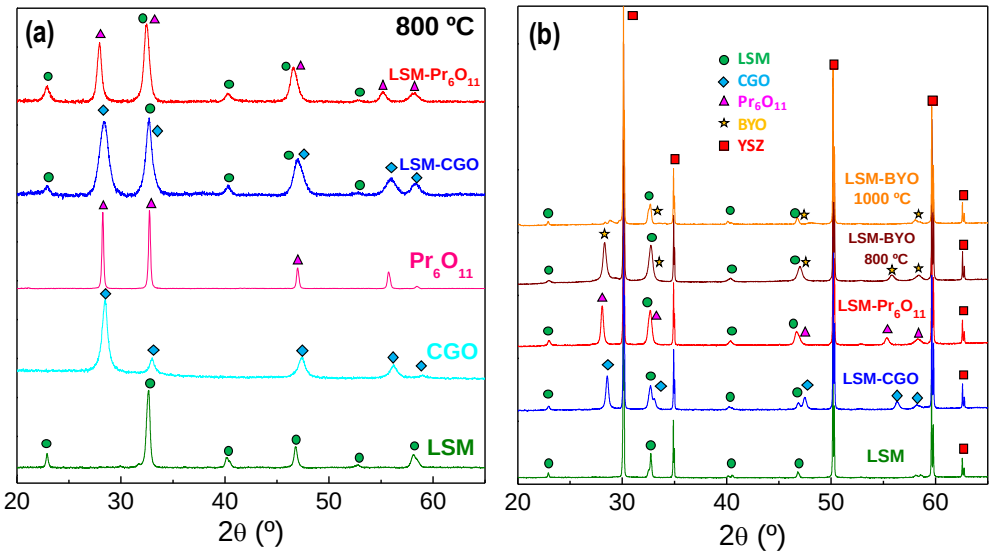

Figure 7.2. (a) XRD patterns of the different active layers deposited by spray-pyrolysis onto quartz wafers and calcined at 800 ºC. (b) XRD patterns of the different active layers deposited by spray-pyrolysis onto YSZ electrolytes and calcined at different temperatures between 800 and 1000 ºC.

The nanocomposite layers are composed of two different crystalline phases, a perovskite structure assigned to LSM and a fluorite structure attributed to Pr_6O_{11} and CGO independently of the substrate employed (Figure 7.2a,b). The co-synthesis of both phases does not promote the formation of secondary phases and, interestingly, the crystallite size estimated by the Scherrer´s equation is substantially lower than that for the single-phase layers. For instance, the LSM layer at 800 ºC shows a crystallite size of 22.3 nm while 14.4 and 12.5 nm are observed for t LSM-Pr_6O_{11} and LSM-CGO nanocomposite layers, respectively (Table 7.1). In addition, more pronounced differences are observed at higher sintering temperatures, *i.e.* 65

UNIVERSIDAD DE MÁLAGA

and 23 nm for the single LSM and the nanocomposite layers, respectively at 1000 ºC. These results confirm that the coexistence of two immiscible phases effectively decreases the grain growth due to the limited grain boundary diffusion during the sintering process [7,8]. In order to get further information about the crystal structure and composition of the different active layers, the XRD data are analyzed by the Rietveld method. LSM was adequately fitted with a rhombohedral perovskite structure (s.g. $R\bar{3}c$) and the Pr_6O_{11}, CGO and BYO with a cubic fluorite structure (s.g. $Fm\bar{3}m$) (Figure 7.3).

Table 7.1. Structural parameters, weight fraction and crystallite size for the different active layers obtained by spray-pyrolysis deposition on different substrates.

Composition	T (ºC)	Substrate	Volume (Å^3)		LSM (wt.%)	R_{wp} (%)	d_{LSM} (nm)	$d_{Fluorite}$ (nm)
			LSM	Fluorite				
LSM	800	Quartz	350.484(2)	-	100	3.3	22.3	-
CGO	800	Quartz	-	159.208(4)	-	2.4	-	16.1
Pr_6O_{11}	800	Quartz	-	163.132(2)	-	3.9	-	35.0
LSM-CGO	800	Quartz	351.483(3)	160.633(1)	52	2.4	12.5	8.2
LSM-Pr_6O_{11}	800	Quartz	350.751(2)	167.287(2)	54	8.7	14.4	17.6
LSM	1000	YSZ	350.358(5)	-	100	5.2	62.5	-
BYO	800	YSZ	-	164.279(2)	-	7.3	-	45.8
LSM-CGO	1000	YSZ	349.871(1)	159.167(3)	50	4.5	22.6	29.6
LSM-Pr_6O_{11}	1000	YSZ	348.453(2)	167.120(2)	51	3.5	23.8	32.9
LSM-BYO	1000	YSZ	351.235(1)	-	-	5.7	24.4	-
LSM-BYO	800	YSZ	350.948(2)	163.516(2)	56	3.6	18.2	25.1

The unit cell volumes of LSM, Pr_6O_{11} and CGO deposited by spray-pyrolysis onto quartz wafers are 350.484(2), 163.132(2) and 159.208(4) Å^3, respectively, values that are close to those reported for the bulk materials [9]. In the case of the nanocomposite layers, slightly different cell volumes are observed when compared to the pure materials (Table 7.1) (Figure 7.3a-c).

UNIVERSIDAD DE MÁLAGA

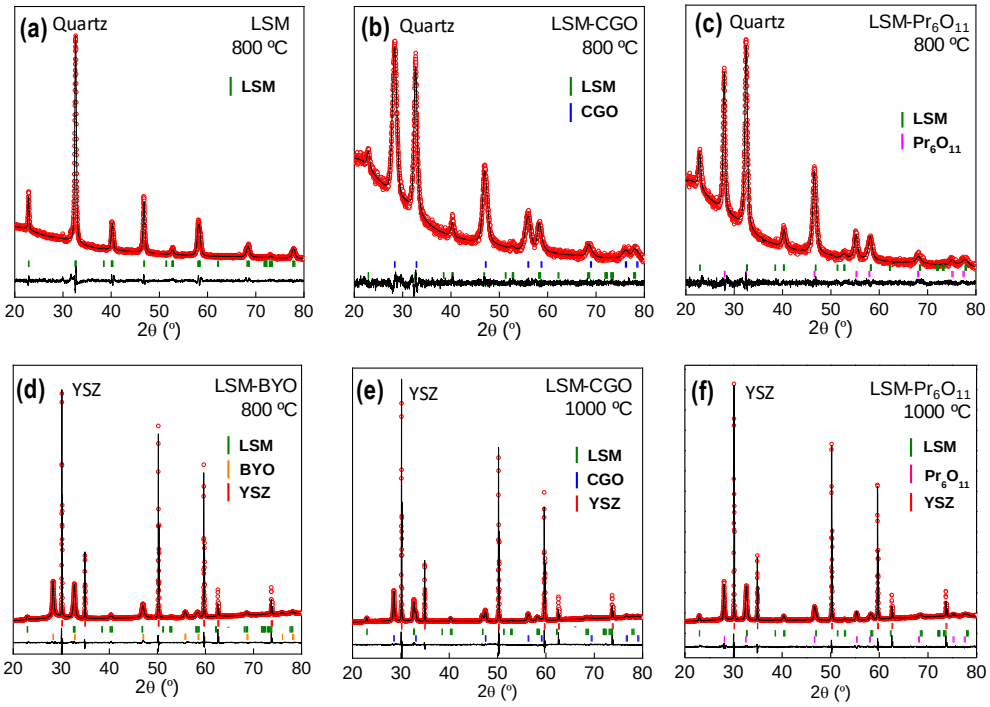

Figure 7.3. Rietveld fitting of (a) LSM, (b) LSM-CGO (c) LSM-Pr_6O_{11} active layers deposited onto quartz and calcined at 800 ºC and (d) LSM-BYO, (e) LSM-CGO and (f) LSM-Pr_6O_{11} deposited onto YSZ electrolytes at different temperatures.

This slightly different cell volumes trend can be explained by a minor cation exchange between LSM and CGO phases since the incorporation of La^{3+} (1.16 Å) in eightfold coordination in the Ce^{4+} (0.97 Å) site of the CGO phase induces a unit cell expansion, and vice versa, for the LSM, as commented in the previous chapter. Additionally, the phase quantification obtained by the Rietveld method is very similar to the nominal one, further confirming that only a minor cation exchange occurs between the perovskite and fluorite phases.

The stability of the active layers was tested after annealing the nanocomposite layers deposited onto YSZ at 1000 ºC, not showing additional peaks attributed to secondary phases or major changes in the unit cell volumes. However, LSM-BYO is not stable above 800 ºC due to Bi-sublimation at high temperature or partial reaction with LSM, giving rise to $(La_{0.8}Sr_{0.2})_{1-x}Bi_xMnO_{3-\delta}$ as reaction product [10].

UNIVERSIDAD DE MÁLAGA

The composition of the nanocomposite layers was further studied by HAADF-STEM and EDS (Figure 7.4a-d).

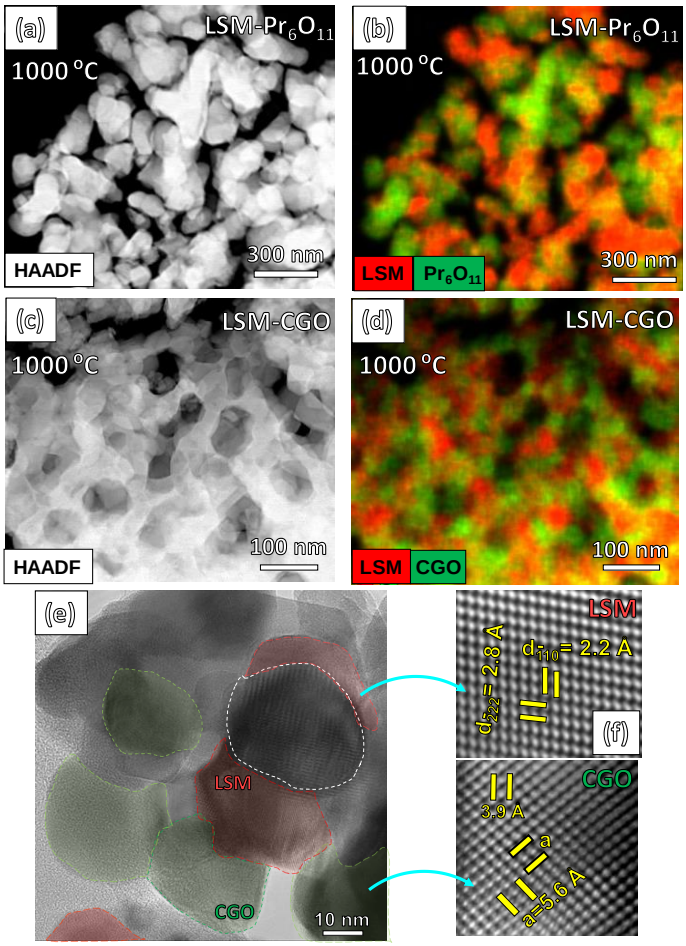

Figure 7.4. HAADF-STEM images and EDS analysis of (a,b) LSM-Pr_6O_{11} and (c,d) LSM-CGO nanocomposites calcined at 1000 ºC, (e,f) HRTEM image of the LSM-CGO nanocomposite, showing the d-spacing for both LSM and CGO crystallographic phases.

LSM-Pr_6O_{11} and LSM-CGO nanocomposite active layers are formed by homogeneously and well-distributed particles of two different phases with a particle size of 20-30 nm after sintering at 1000 ºC, values that are in accordance with XRD data. The intimate mixture between the electronic and ionic conductors ensures a large contact and extended TPB, which is expected to have a positive effect on the electrochemical performance. Furthermore, HRTEM images of the LSM-CGO

UNIVERSIDAD DE MÁLAGA

nanocomposite active layer (Figure 7.4e,f) show that the LSM and CGO particles present a high crystallinity with lattice spacing comparable to those obtained from the XRD characterization.

7.3. Microstructural characterization of nanocomposite active layers

The microstructural characterization of the different cell configurations was studied by SEM after the electrochemical measurements. A low-magnification cross-sectional image of the symmetrical cell with an LSM cathode is displayed in Figure 7.5a as a representative example. The LSM cathode deposited by screen-printing shows a homogenous thickness of 30 µm with a highly porous structure and an average grain size of 500 nm (Figure 7.5a). Additionally, the Pt current collector layer is visible on top of the LSM cathode.

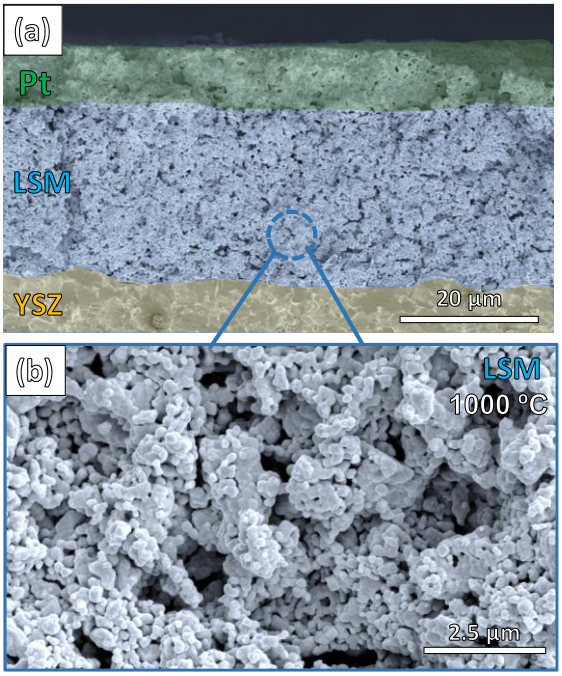

Figure 7.5. (a) Low magnification SEM image of the LSM electrode deposited by screen-printing onto a YSZ electrolyte at 1000 ºC after the electrochemical measurements and (b) SEM image at higher magnification.

UNIVERSIDAD DE MÁLAGA

The electrode/electrolyte interface was studied for each cell by SEM-EDS. Figure 7.6 shows SEM images of the LSM, LSM-CGO, LSM-Pr_6O_{11} and LSM-BYO active layers at different magnifications.

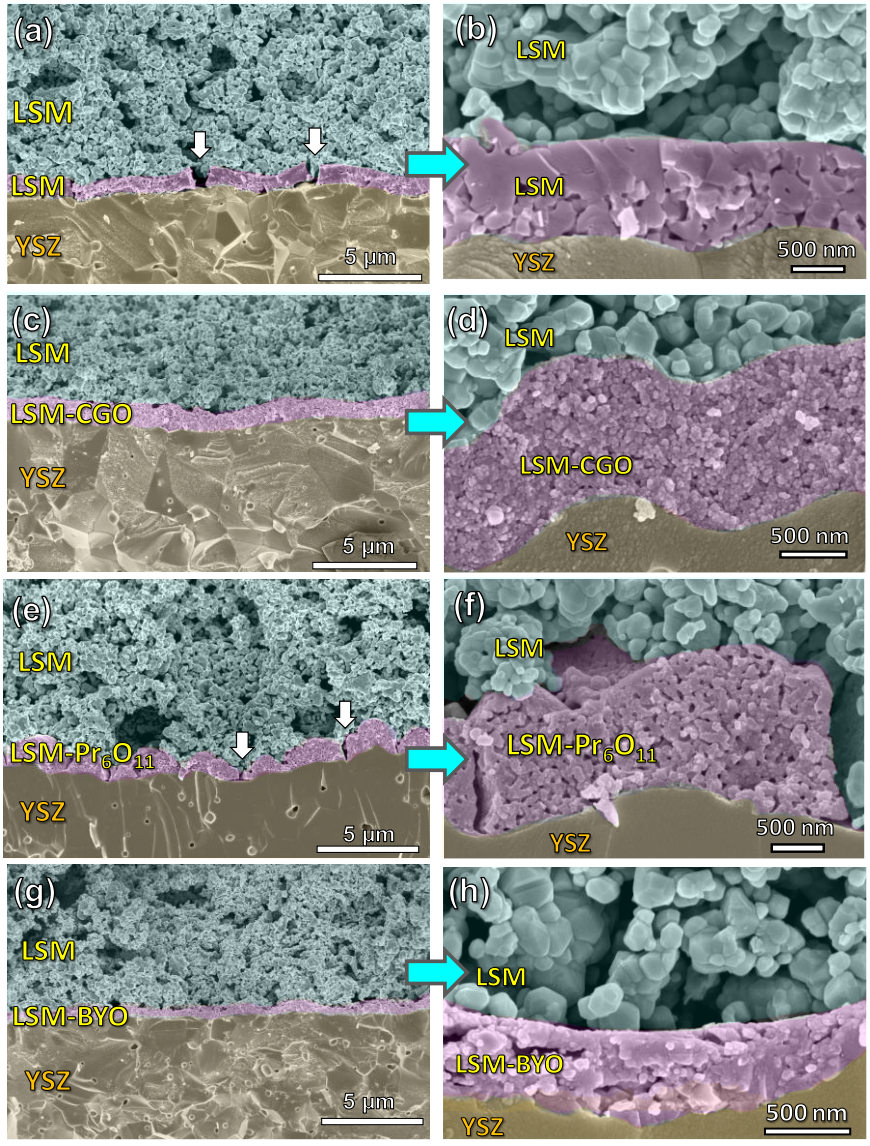

Figure 7.6. SEM images at different magnifications of (a,b) LSM, (c,d) LSM-CGO, (e,f) LSM-Pr_6O_{11} and (g,h) LSM-BYO layers deposited onto YSZ electrolyte after electrochemical characterization.

UNIVERSIDAD DE MÁLAGA

Independently of the composition, the active layers have a rather similar thickness, 0.8 ±0.2 μm, except for the LSM-BYO layer, which is slightly thinner ~0.5 μm. The lower thickness observed for LSM-BYO can be explained by the partial sublimation of bismuth as it was observed previously for other Bi_2O_3-based layers, findings that are in accordance with the low thermal stability observed by XRD after calcination at 1000 ºC (Figure 7.6g,h) [11–13]. In fact, the melting point for undoped and doped-Bi_2O_3 is rather low, 825 and 1100 ºC, respectively, which can be even lower for nanostructured materials [14,15].

Interestingly, the particle size of the nanocomposite active layer is significantly lower than that observed for the LSM single-phase layer (Figure 7.6a,b). For instance, LSM shows an average grain size of ~250 nm after sintering at 1000 ºC compared to ~50 nm for LSM-CGO (Figure 7.6c-d) or ~80 nm for LSM-Pr_6O_{11} (Figure 7.6e-f). Furthermore, LSM-CGO shows improved microstructural characteristics compared to the other active layers, such as good adherence to the electrolyte, lower porosity and absence of delamination after the electrochemical measurements (Figure 7.6c,d). On the other hand, vertical cracks are observed for LSM and LSM-Pr_6O_{11} active layers, presumably attributed to the severe grain growth after the long-term annealing at 1000 ºC, as well as the different thermal expansion mismatch between the cell components, since the thermal expansion coefficient (TEC) of Pr_6O_{11} ($23 \cdot 10^{-6}$ K^{-1}) is relatively high compared to LSM ($13 \cdot 10^{-6}$ K^{-1}), YSZ ($11 \cdot 10^{-6}$ K^{-1}) and CGO ($12 \cdot 10^{-6}$ K^{-1}) [16,17].

In addition, EDS analysis was performed to check the possible reactivity between the cell components (Figure 7.7). No evidence of cation interdiffusion is observed between the cell layers; nevertheless, the bismuth content in the LSM-BYO is inferior to the nominal one, further confirming the Bi evaporation at 1000 ºC.

UNIVERSIDAD DE MÁLAGA

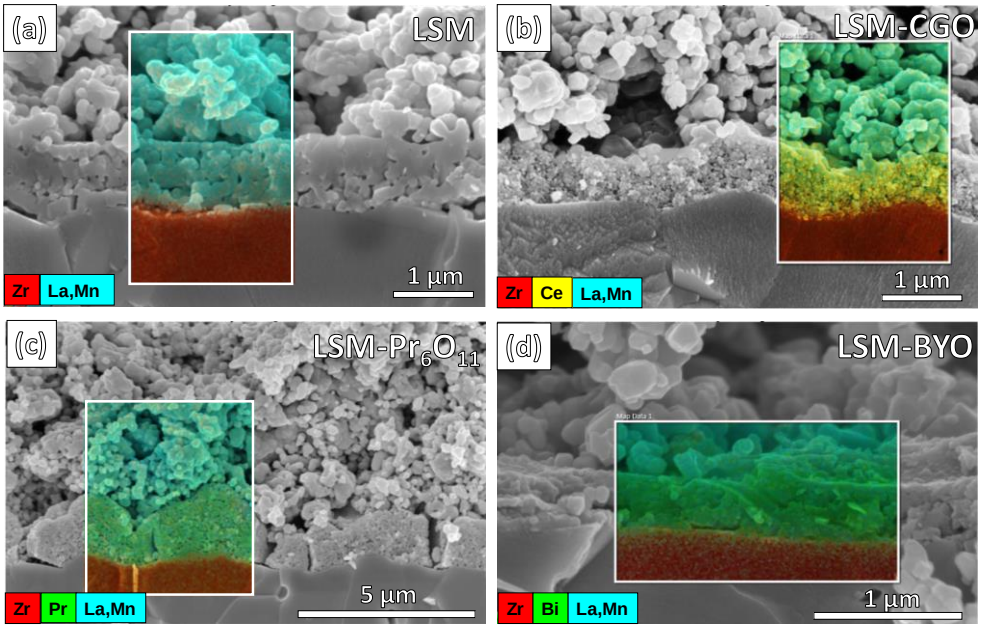

Figure 7.7. Cross-sectional SEM images and EDS analysis of the different cells with (a) LSM, (b) LSM-CGO, (c) LSM-Pr_6O_{11} and (d) LSM-BYO after the electrochemical tests.

7.4. Electrochemical characterization

The influence of the different active layers on the electrochemical properties of LSM was studied by impedance spectroscopy in a symmetrical cell configuration. Figure 7.8a shows the impedance spectra at 700 ºC in air at open circuit voltage (OCV). For comparison purposes, a cell without an active layer, labelled as without A.L., was also studied. Although the ohmic resistance (R_s) was subtracted for a better comparison of the electrode response, the R_s values are similar to a blank YSZ electrolyte, indicating that the incorporation of the active layer does not induce extra ohmic losses to the electrochemical cell in good agreement with the microstructural characterization by SEM. It is worth remarking that the vertical cracks observed for the LSM and LSM-Pr_6O_{11} layers do not affect negatively the ohmic resistance of the cell.

UNIVERSIDAD DE MÁLAGA

Interestingly, the overall polarization resistance is significantly decreased after incorporating the active layers when compared to the blank LSM cathode (without A.L.) (Figure 7.8a).

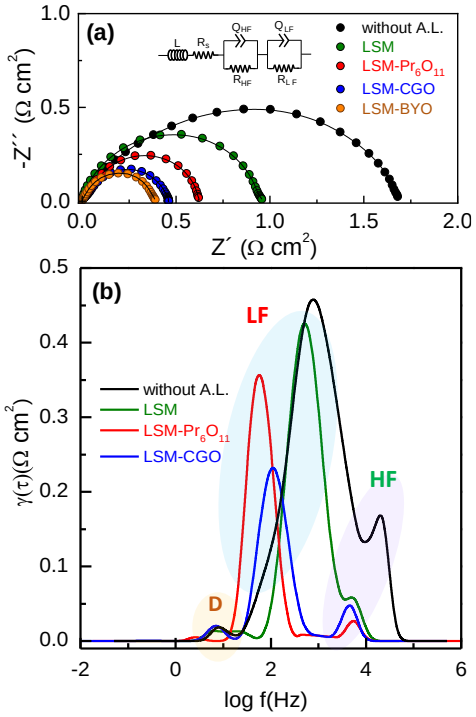

Figure 7.8. (a) Impedance spectra of LSM cathode deposited onto YSZ with different active layers at 700 ºC and (b) the corresponding DRT spectra.

DRT analysis of the impedance data was performed to get further insights into the electrode processes (Figure 7.8b). Two main electrode contributions are observed in the DRT spectra, regardless of the active layer. The high frequency (HF) contribution, centred at ~10^4 Hz, is associated with the oxide-ion transport at the electrode/electrolyte interface [2,3]. Since the area under the peaks is proportional to the resistance of each process, it is evident that the incorporation of an active layer significantly reduces the HF process due to the faster oxide-ion transport at the interface. Furthermore, the low-frequency contribution (LF), which is related to electrochemical processes on the electrode surface, is also decreased in the cells with nanocomposite active layers, suggesting that the introduction of a nanostructured active layer extends the surface paths to the electrolyte surface. In this case, the ORR

UNIVERSIDAD DE MÁLAGA

sub-reactions, such as oxygen diffusion, adsorption or charge transfer processes, can also occur at the surface of the nanocomposite active layer. On the other hand, the electrode processes are slightly shifted to lower frequencies, which has been previously associated with faster oxide-ion conduction at the electrode/electrolyte interface [18,19]. Finally, a minor contribution at a very low frequency, labelled as D, is observed in the DRT spectra, which has been previously attributed to gas diffusion limitations [20]. This minor contribution was not included in the fitting by equivalent circuits due to its very low resistance when compared to HF and LF processes. Based on the results obtained by DRT analysis, an equivalent circuit including two serial (RQ) elements was used to fit the impedance spectra (inset Figure 7.8a).

The overall polarization resistance of the different cells without and with active layers as a function of the temperature is shown in Figure 7.9. The incorporation of the active layers significantly reduces the R_p values in the whole temperature range studied. For instance, the polarization resistance is decreased at 700 ºC from 1.71 Ω cm^2 for LSM without active layer to 0.95, 0.62, 0.46 and 0.29 Ω cm^2 for LSM, LSM-Pr_6O_{11}, LSM-CGO and LSM-BYO cells with active layers, respectively.

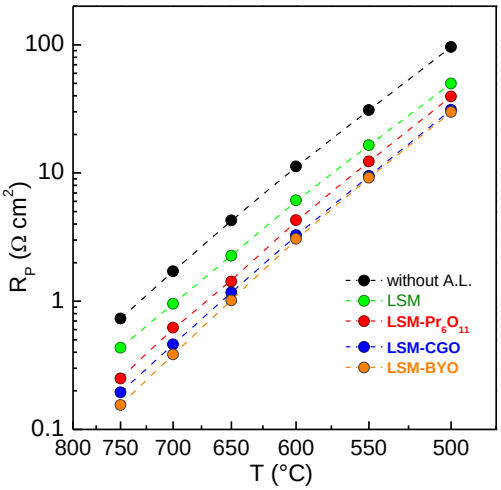

Figure 7.9. Overall polarization resistance of the symmetrical LSM/YSZ/LSM cells with different active layers as a function of the temperature.

It is worth mentioning that these values are better than those reported previously for LSM-YSZ, LSM-CGO or LSM-BYO composite electrodes deposited by

UNIVERSIDAD DE MÁLAGA

screen-printing onto YSZ electrolyte at 700 ºC, 1.20, 1.06 and 0.50 Ω cm^2, respectively [21–23]. It has to be also considered that the R_p values of LSM-BYO are slightly lower than that observed for LSM-CGO; however, the partial sublimation of Bi could negatively affect cell integrity under long-term operation and for this reason, this layer is not further characterized.

The resistance and capacitance values of each electrode process as a function of the temperature are displayed in Figure 7.10. The nature of the active layer clearly affects the resistance of each electrode response, showing the cell without active layers higher R_{HF} and R_{LF} values in the whole temperature range studied.

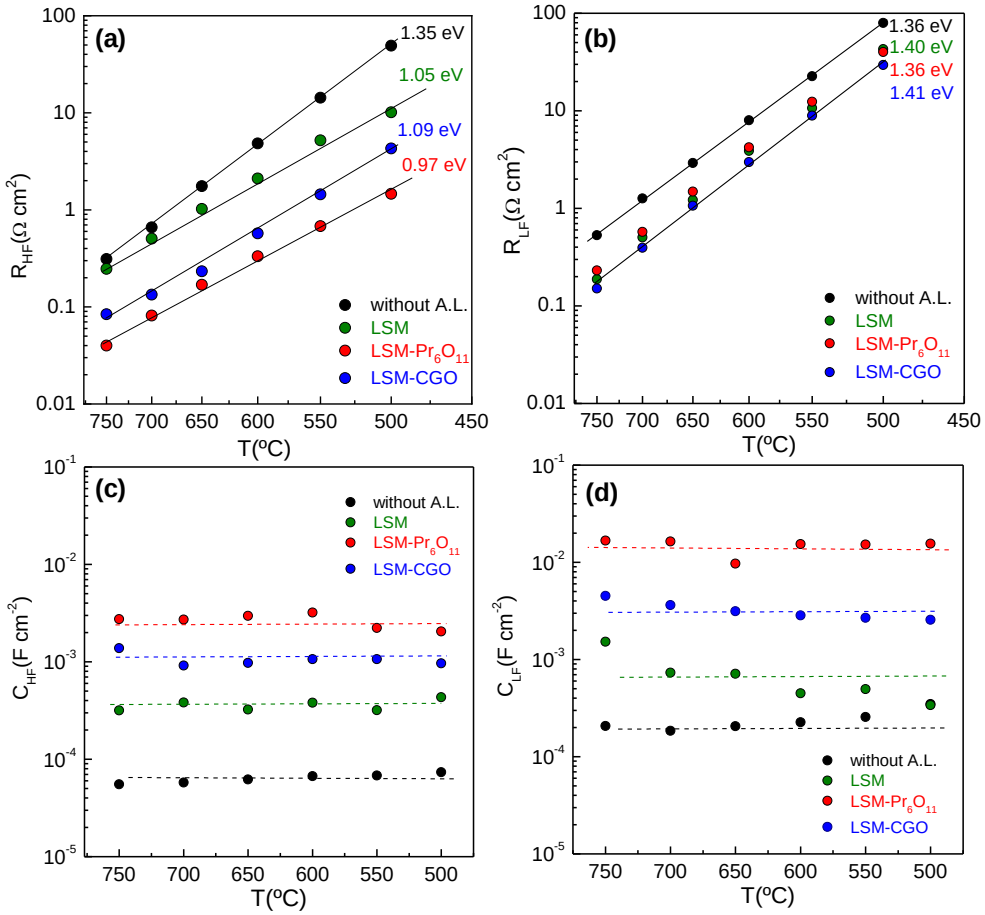

Figure 7.10. (a,b) Resistance contributions and (c,d) capacitance values of the HF and LF electrode responses as a function of the temperature.

UNIVERSIDAD DE MÁLAGA

In the case of R_{HF}, the incorporation of an active layer reduces this contribution up to one order of magnitude, especially at low temperatures, where the blank LSM cathode has poor electrochemical activity (Figure 7.10a,b). R_{HF} decreases in the order: LSM > LSM-CGO > LSM-Pr_6O_{11}, a trend that can be associated with the higher ionic and electronic conductivity of Pr_6O_{11} when compared to CGO, improving the oxide-ion transfer at the electrode/electrolyte interface [24,25]. The faster kinetics of this electrode process is further evidenced by the reduction of the activation energy from 1.35 eV to 0.97 eV after the incorporation of the active layers.

The R_{LF} contribution is also substantially reduced, suggesting that the presence of the active layer not only promotes a faster oxide-ion transfer at the electrolyte interface but also induces an extension of the reaction sites for the ORR. In this case, the LSM-CGO sample shows lower R_{LF} values, which can be attributed to the improved microstructure, *i.e.* lower grain size and good adherence to the electrolyte without crack formation. The corresponding activation energy values are similar for all cells, ranging between 1.42 and 1.36 eV.

The capacitance values of HF and LF are also strongly dependent on the active layer used (Figure 7.10c,d). Previously, an increase in the capacitance values in nanostructured electrodes was related to higher active site density for the electrochemical reactions [26,27]. C_{HF} increased from $7 \cdot 10^{-5}$ F cm^{-2} for the LSM cathode without active layers to $2 \cdot 10^{-3}$ F cm^{-2} for LSM-Pr_6O_{11}, similar to that observed for the R_{HF} resistance. Additionally, the rather low capacitance values of this process confirm that this is associated with oxide-ion transport at the LSM/electrolyte interface. Similar results are observed for C_{LF}, which also increases two orders of magnitude for LSM-Pr_6O_{11} ($2 \cdot 10^{-2}$ F cm^{-2}) when compared to the LSM cathode without active layer ($2 \cdot 10^{-4}$ F cm^{-2}), confirming that the active sites at the electrode surface also increase.

Figure 7.11 shows a schematic diagram of the electrochemical reactions occurring in the different cells to better understand the influence of the active layers in the ORR. As reported previously, the blank LSM cathode shows very low oxide ion conductivity at intermediate temperatures, limiting the active sites for electrochemical reaction to the TPB region close to the electrode/electrolyte interface (Figure 7.11a).

UNIVERSIDAD DE MÁLAGA

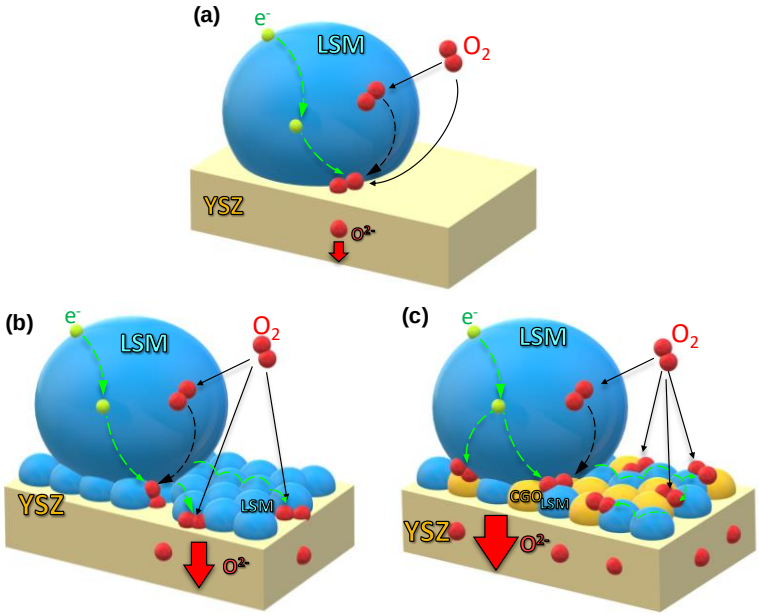

Figure 7.11. Illustration of the different electrochemical processes involved in the LSM cathode for ORR at low temperature: (a) without active layer, (b) with LSM active layer, and (c) with a nanocomposite active layer.

After the introduction of an LSM nanostructured layer, the TPB is extended to the whole electrolyte surface (Figure 7.11b). On the other hand, when a nanocomposite layer formed by the mixture of an electronic and ionic conductor is implemented, both electronic and ionic conducting paths are available, further increasing the active sites at the electrolyte interface (Figure 7.11c). Additionally, the lower particle size in the nanocomposite layer further explains the better electrochemical performance of this configuration.

The impedance spectra for the most promising active layer (LSM-CGO) were collected as a function of the oxygen partial pressure (pO_2) to identify the electrode processes involved in the ORR and the results were compared to those obtained for blank LSM cathode [28].

The impedance spectra are comprised of an asymmetric and depressed arc in the whole pO_2 range studied for LSM without and with LSM-CGO active layer (Figure 7.12a). The same equivalent circuit proposed for the measurements at OCV

UNIVERSIDAD DE MÁLAGA

is used to adequately fit the impedance data. The representation of R_{HF} and R_{LF} vs. pO_2, both in logarithmic scale, gives a linear curve, where the slope *m* provides information about the nature of the species involved in the ORR sub-reaction.

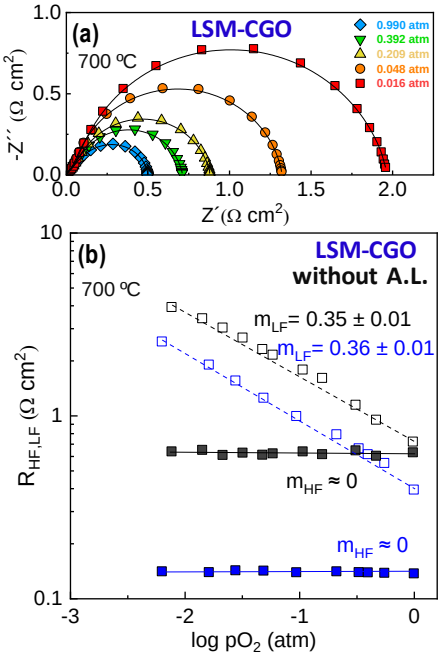

Figure 7.12. (a) Impedance spectra of the cell with LSM-CGO active layer and (b) polarization resistance contributions for LSM cathode without and with LSM-CGO layer as a function of the pO_2 at 700 ºC.

As can be observed, the same rate-limiting steps are identified for the cells without and with LSM-CGO active layer (Figure 7.12b). Firstly, the R_{HF} contribution is one order of magnitude lower in the cell with LSM-CGO active layer, while the R_{LF} electrode response is around two times lower in this cell. The R_{HF} contribution is almost independent on the pO_2, indicating that this process is associated with the oxide-ion transport at the electrode/electrolyte interface ($O^x_{o,\ electrode} \rightarrow O^x_{o,\ electrolyte}$) [28]. The R_{LF} process with a *m* ~ 3/8 can be attributed to the reduction of oxygen atoms at the electrode surface $O_{ad} + e^- \rightarrow O'_{ad}$ [29,30]. Hence, the incorporation of the active layer does not alter the nature of the rate-limiting steps but substantially decreases the polarization resistance of both electrode processes.

UNIVERSIDAD DE MÁLAGA

The electrochemical performance of these cells was also studied by a 3-probe electrode configuration, applying a dc-bias under cathodic and anodic polarization (Figure 7.13). The impedance spectra of the LSM cathode without and with LSM-CGO layer under cathodic polarization from 0 to -0.30 V at 700 ºC are shown in Figure 7.13a and b, respectively.

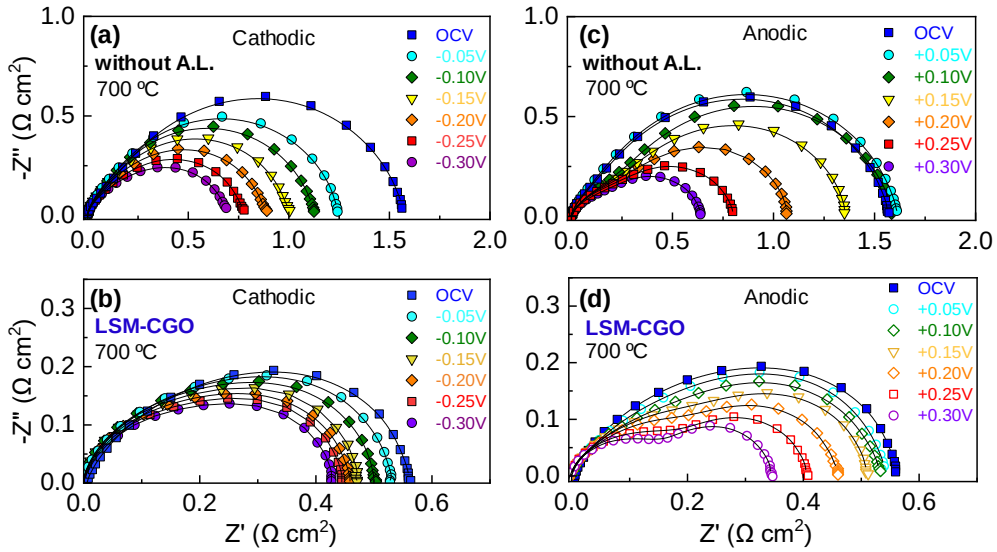

Figure 7.13. Impedance spectra in 3-probe configuration under cathodic polarization of (a) LSM cathode without active layer and (b) and with LSM-CGO active layer. Impedance spectra in 3-probe configuration under anodic polarization of (c) LSM cathode without active layer and (d) and with LSM-CGO active layer.

The blank LSM electrode shows a stronger influence on the applied dc-bias, decreasing the R_p values from 1.56 Ω cm^2 at OCV to 0.69 Ω cm^2 at -0.30 V at 700 ºC, while the R_p values for the cell with LSM-CGO active layer decreased from 0.55 Ω cm^2 to 0.42 Ω cm^2 under the same conditions. At higher temperatures (T = 800 ºC), the influence of the dc bias is lower due to the better ionic conductivity of the LSM cathode and a faster bulk path at the LSM surface for the electrochemical reactions. For instance, in the case of a blank LSM, the R_p slightly decreases at 800 ºC from 0.36 Ω cm^2 at OCV to 0.23 Ω cm^2 at -0.3 V (Figure 7.14a). The total polarization resistance for both cells under cathodic and anodic polarization at 700 and 600 ºC is displayed in Figure 7.13a,b.

UNIVERSIDAD DE MÁLAGA

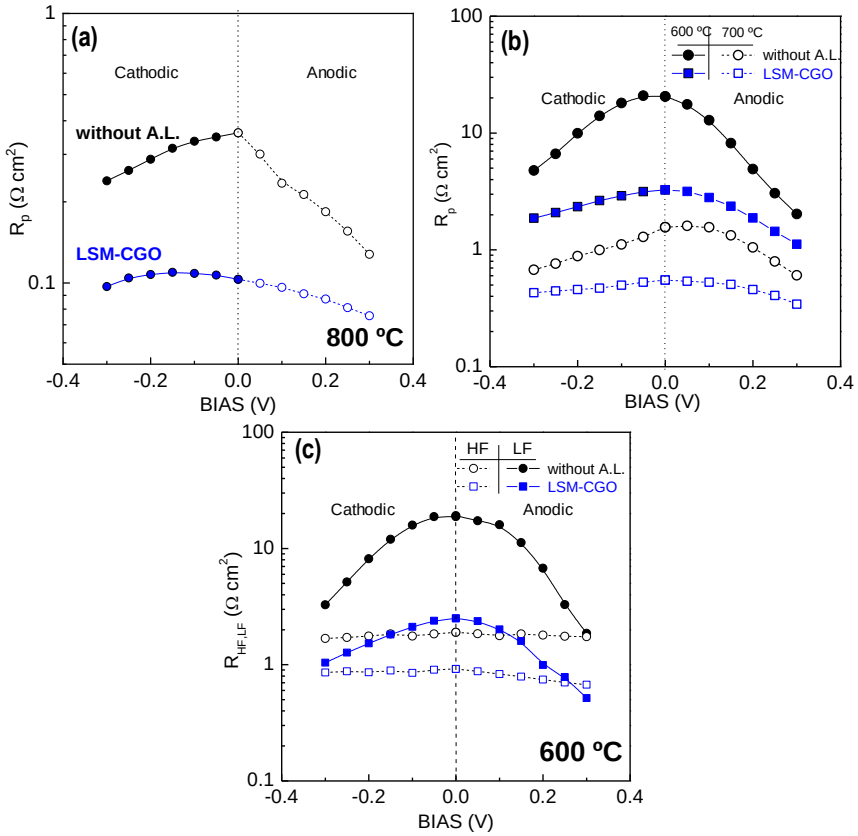

Figure 7.14. Overall polarization resistance of LSM without and with LSM-CGO layers acquired under different dc-bias at (a) 800 ºC and (b) 700-600 ºC. (c) Variation of the high and low-frequency contributions at 600 ºC as a function of the dc bias.

The improvement of the electrochemical properties at intermediate temperatures can be explained by the formation of oxygen vacancies in the lattice under cathodic polarization due to the partial reduction of Mn^{4+} to Mn^{3+}, which promotes a better electrochemical performance [31,32]. In the case of the sample with a LSM-CGO interlayer, the electrochemical reactions mainly occur close to the electrode/electrolyte interface. Under cathodic polarization, a new reaction path involving the bulk of the LSM particles is created, becoming the extension contact between LSM and the electrolyte the rate-determining step for ORR, which is highly enhanced after the incorporation of the active layers, explaining the lower R_p reduction in the sample with LSM-CGO active layer [33,34] (Figure 7.14b).

UNIVERSIDAD DE MÁLAGA

The R_p values showed a further decrease under anodic polarization in both cells when compared to cathodic polarization (Figure 7.13c,d and Figure 7.14a,b), findings that can be explained by the increase of the local oxygen content in the electrode. This behavior is similar to that produced when the oxygen partial pressure is increased, improving the electron-hole conduction in LSM, and consequently, lowering the R_p values. Similar behavior has been observed previously for other cathode materials such as $SrCo_{0.9}Ta_{0.1}O_{3-\delta}$ or $SrFe_{0.9}Mo_{0.1}O_{3-\delta}$ [35,36].

The impedance spectra are also analysed by equivalent circuits to obtain further insights into the effect of the dc bias on the individual electrode processes (Figure 7.14c). Interestingly, the HF contribution is not affected by the applied dc-bias [37]. However, the LF process, which has been attributed to electrochemical reactions at the electrode surface, has a strong dependence on the dc-bias for the sample without and with the LSM-CGO active layer. This trend is in accordance with the oxygen vacancy concentration changes at the active sites induced by the dc-current [38].

7.5. Fuel cell tests

The performance in real SOFC conditions of the cell with the LSM-CGO active layer was tested in an anode-supported cell: Ni-YSZ/YSZ/LSM-CGO/LSM and compared with an analogous cell without an active layer (Figure 7.15).

The OCV in both cells is close to the theoretical Nernst value (1.1 V) when wet hydrogen (3 vol% H_2O) is used as fuel and static air as oxidant, confirming a good sealing of the electrochemical cell. The I-V and power density curves of the cell with the LSM-CGO active layer clearly show a remarkable performance improvement when compared to the blank cell (Figure 7.15). The maximum power densities of the cell with a LSM-CGO active layer are 1.20 and 0.85 W cm^{-2} at 800 and 700 ºC, respectively, outperforming the values obtained for the cell without active layer under the same operation conditions, 0.79 and 0.46 W cm^{-2} at 800 and 700 ºC, respectively. Interestingly, the cell with LSM-CGO active layer exhibits superior power density values than those previously reported for anode-supported cells based on LSM cathodes, *i.e.* LSM (0.34 W cm^{-2} at 800 ºC) [39], LSM-CGO (0.75 W cm^{-2} at 800 ºC) [7] and LSM-BYO (0.78 W cm^{-2} at 700 ºC) [21]. Since the Ni-YSZ/YSZ anode-

UNIVERSIDAD DE MÁLAGA

supported cells were prepared in the same batch and they have the same cathode (LSM), the different maximum power densities between both cells are clearly associated with the incorporation of the LSM-CGO active layer.

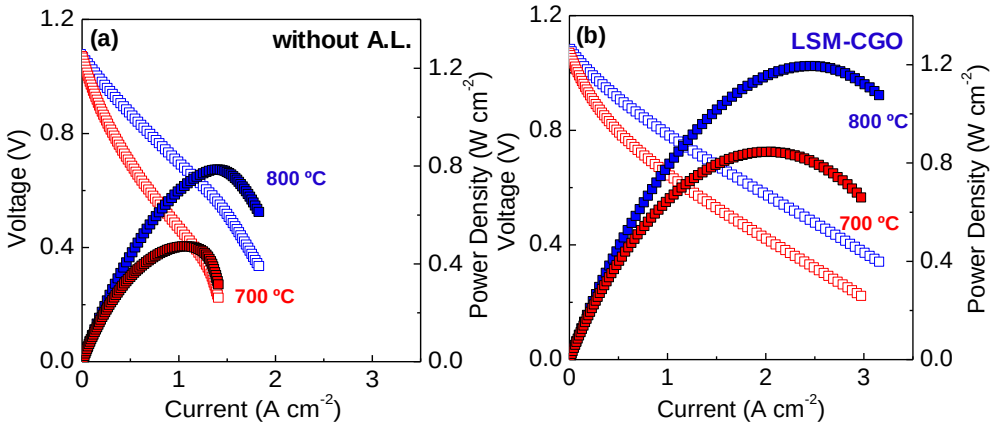

Figure 7.15. I-V and power density curves of the Ni-YSZ/YSZ/LSM single cell (a) without and (b) with LSM-CGO active layer.

Impedance spectra of both cells collected at OCV show that the incorporation of the LSM-CGO active layer decreases significantly the R_p of the cell from 0.58 to 0.31 Ω cm^2 at 700 ºC, while the ohmic resistance of the cell remains almost unaltered by the presence of the active layer with R_s ~ 0.06 Ω cm^2 for both cells (Figure 7.16a).

DRT spectra reveal that the electrode response is composed of at least three electrode contributions (Figure 7.16b). Interestingly, the electrode processes assigned to the oxide-ion transfer at the electrode/electrolyte interface (R^{Cat}_{HF}) and the charge transfer at the LSM cathode surface (R^{Cat}_{LF}) are reduced after the incorporation of the active layer, findings that are in accordance with the results observed for the symmetrical cell tests in the previous section [2,3,18,19].

On the contrary, the electrode process centered at 1 Hz, which is typically associated with hydrogen oxidation processes at the TPB in the fuel electrode (R^{An}), is similar for both cells, further confirming that the presence of the LSM-CGO active layer is the responsible of boosting the cell performance [40]. In addition, a minor

UNIVERSIDAD DE MÁLAGA

electrode contribution at a very low frequency is identified, which can be attributed to gas diffusion limitations at the anode and cathode, according to previous reports [20].

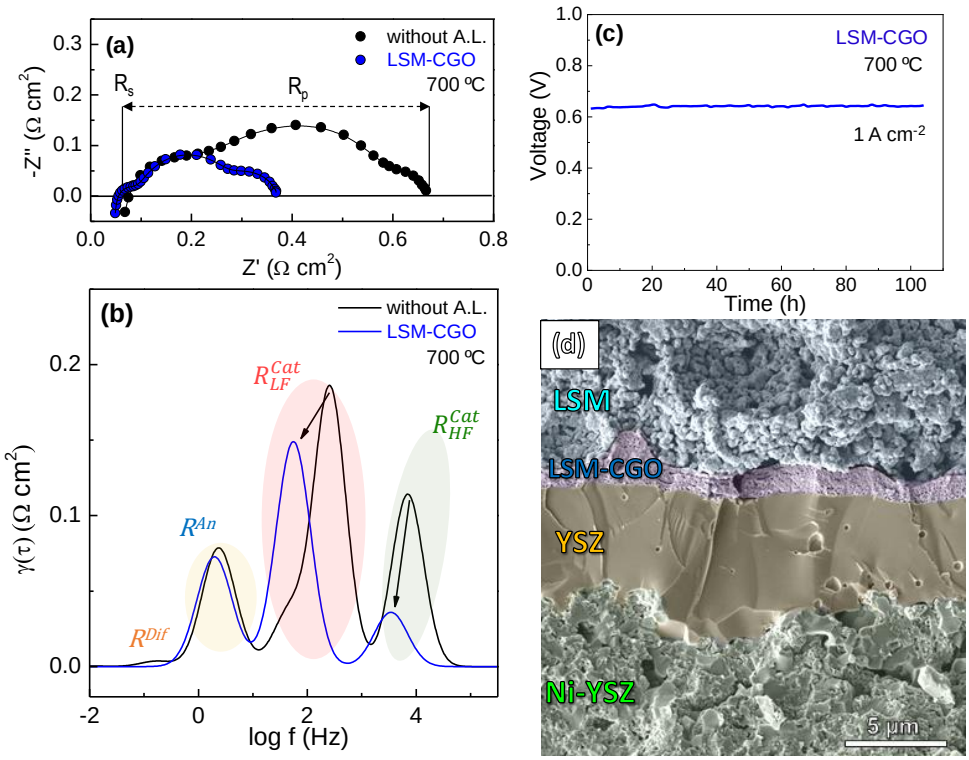

Figure 7.16. (a) Impedance spectra of the anode-supported cells without and with LSM-CGO active layer at 700 ºC and (b) the corresponding DRT analysis. (c) Short stability test of the cell with a LSM-CGO active layer at a current density of 1 A cm^{-2} at 700 ºC and (d) Cross-sectional SEM image of the cell after the electrochemical test.

The stability of the cell with the LSM-CGO active layer was tested under continuous operation for 100 h at 700 ºC, showing a constant cell voltage over time at 1 A cm^{-2} (Figure 7.16c). The negligible degradation in the short stability test confirms the good stability of the cell with nanocomposite LSM-CGO active layer at intermediate temperatures. Moreover, the microstructure of the single cell after the electrochemical tests reveals no visible delamination or cracks of the different cell layers (Figure 7.16d). In addition, the nanoscale microstructure of the LSM-CGO interlayer with ~1 µm thickness is retained and the YSZ electrolyte with a ~5 µm thickness shows high relative density without the presence of cracks.

UNIVERSIDAD DE MÁLAGA

All these results confirm the great influence of the nanocomposite active layers on the electrochemical properties of the state-of-the-art LSM cathode by tailoring the electrode/electrolyte interface. This new approach could be extended to other nanocomposite active layers to operate simultaneously in both oxidizing and reducing conditions, in order to implement this promising approach to symmetrical solid oxide fuel cells. Additionally, other deposition methods, such as pulsed laser deposition (PLD), can be explored to obtain different electrode architectures and properties.

References

1. Zamudio-García, J.; Caizán-Juanarena, L.; Porras-Vázquez, J.M.; R. Losilla, E.; Marrero-López, D. Unraveling the Influence of the Electrolyte on the Polarization Resistance of Nanostructured $La_{0.6}Sr_{0.4}Co_{0.2}Fe_{0.8}O_{3-\delta}$ Cathodes. *Nanomaterials* **2022**, *12*, 3936, doi:10.3390/nano12223936.
2. Osinkin, D.A. An Approach to the Analysis of the Impedance Spectra of Solid Oxide Fuel Cell Using the DRT Technique. *Electrochim. Acta* **2021**, *372*, 137858, doi:10.1016/j.electacta.2021.137858.
3. Zhang, J.; Lei, L.; Li, H.; Chen, F.; Han, M. A Practical Approach for Identifying Various Polarization Behaviors of Redox-Stable Electrodes in Symmetrical Solid Oxide Fuel Cells. *Electrochim. Acta* **2021**, *384*, 138340, doi:10.1016/j.electacta.2021.138340.
4. Araújo, A.J.M.; Loureiro, F.J.A.; Holz, L.I.V.; Graça, V.C.D.; Grilo, J.P.F.; Macedo, D.A.; Paskocimas, C.A.; Fagg, D.P. Creating New Surface-Exchange Pathways on the Misfit Ca-Cobaltite Electrode by the Addition of an Active Interlayer. *J. Power Sources* **2021**, *510*, doi:10.1016/j.jpowsour.2021.230417.
5. Zapata-Ramírez, V.; Dos Santos-Gómez, L.; Mather, G.C.; Marrero-López, D.; Pérez-Coll, D. Enhanced Intermediate-Temperature Electrochemical Performance of Air Electrodes for Solid Oxide Cells with Spray-Pyrolyzed Active Layers. *ACS Appl. Mater. Interfaces* **2020**, *12*, 10571–10578, doi:10.1021/acsami.9b22966.
6. Zamudio-García, J.; Albarrán-Aroca, N.; Porras-Vázquez, J.M.; Losilla, E.R.; Marrero-López, D. Influence of $Bi_{1.5}Y_{0.5}O_3$ Active Layer on the Performance of Nanostructured $La_{0.8}Sr_{0.2}MnO_3$ Cathode. *Appl. Nano* **2020**, *1*, 14–24.
7. dos Santos-Gómez, L.; Zamudio-García, J.; Porras-Vázquez, J.M.; Losilla, E.R.; Marrero-López, D. Highly Efficient $La_{0.8}Sr_{0.2}MnO_{3-\delta}$-$Ce_{0.9}Gd_{0.1}O_{1.95}$ Nanocomposite Cathodes for Solid Oxide Fuel Cells. *Ceram. Int.* **2018**, *44*, 4961–4966, doi:10.1016/j.ceramint.2017.12.089.
8. Shimada, H.; Yamaguchi, T.; Kishimoto, H.; Sumi, H.; Yamaguchi, Y.; Nomura, K.; Fujishiro, Y. Nanocomposite Electrodes for High Current Density over 3 A cm^{-2} in Solid Oxide Electrolysis Cells. *Nat. Commun.* **2019**, *10*, 1–10, doi:10.1038/s41467-019-13426-5.
9. *NIST Inorganic Crystal Structure Database, NIST Standard Reference Database Number 3, National Institute of Standards and Technology, Gaithersburg MD, 20899*;
10. Lalitha, G.; Reddy, P.V. Low Temperature Resistivity Anomalies in Bismuth Doped Manganites. *J. Alloys Compd.* **2010**, *494*, 476–482, doi:10.1016/j.jallcom.2010.01.089.

UNIVERSIDAD DE MÁLAGA

11. Joh, D.W.; Park, J.H.; Kim, D.; Wachsman, E.D.; Lee, K.T. Functionally Graded Bismuth Oxide/Zirconia Bilayer Electrolytes for High-Performance Intermediate-Temperature Solid Oxide Fuel Cells (IT-SOFCs). *ACS Appl. Mater. Interfaces* **2017**, *9*, 8443–8449, doi:10.1021/acsami.6b16660.
12. Lee, K.T.; Jung, D.W.; Camaratta, M.A.; Yoon, H.S.; Ahn, J.S.; Wachsman, E.D. $Gd_{0.1}Ce_{0.9}O_{1.95}$/$Er_{0.4}Bi_{1.6}O_3$ Bilayered Electrolytes Fabricated by a Simple Colloidal Route Using Nano-Sized $Er_{0.4}Bi_{1.6}O_3$ Powders for High Performance Low Temperature Solid Oxide Fuel Cells. *J. Power Sources* **2012**, *205*, 122–128, doi:10.1016/j.jpowsour.2012.01.040.
13. Guo, W.; Liu, J.; Jin, C. Anode-Supported $LaGaO_3$-Based Electrolyte SOFCs with Y_2O_3-Doped Bi_2O_3 and La-Doped CeO_2 Buffer Layers. *J. Alloys Compd.* **2010**, *504*, 21–24, doi:10.1016/j.jallcom.2010.05.117.
14. Jiang, N.; Wachsman, E.D. Structural Stability and Conductivity of Phase-Stabilized Cubic Bismuth Oxides. *J. Am. Ceram. Soc.* **1999**, *82*, 3057–3064, doi:10.1111/j.1151-2916.1999.tb02202.x.
15. Takahashi, T.; Esaka, T.; Iwahara, H. Electrical Conduction in the Sintered Oxides of the System Bi_2O_3BaO. *J. Solid State Chem.* **1976**, *16*, 317–323, doi:10.1016/0022-4596(76)90047-5.
16. Tietz, F. Thermal Expansion of SOFC Materials. *Ionics (Kiel).* **1999**, *5*, 129–139, doi:10.1007/BF02375916.
17. Chen, T.; Pang, S.; Shen, X.; Jiang, X.; Wang, W. Evaluation of Ba-Deficient $PrBa_{1-x}Fe_2O_{5+\delta}$ Oxides as Cathode Materials for Intermediateerature Solid Oxide Fuel Cells. *RSC Adv.* **2016**, *6*, 13829–13836, doi:10.1039/c5ra19555a.
18. He, Z.; Ai, N.; He, S.; Jiang, S.P.; Zhang, L.; Rickard, W.D.A.; Tang, D.; Chen, K. Positive Effect of Incorporating $Er_{0.4}Bi_{1.6}O_3$ on the Performance and Stability of $La_2NiO_{4+\delta}$ Cathode . *J. Electrochem. Soc.* **2019**, *166*, F796–F804, doi:10.1149/2.0841912jes.
19. Kamecki, B.; Karczewski, J.; Jasiński, P.; Molin, S. Improvement of Oxygen Electrode Performance of Intermediate Temperature Solid Oxide Cells by Spray Pyrolysis Deposited Active Layers. *Adv. Mater. Interfaces* **2021**, *8*, doi:10.1002/admi.202002227.
20. Osinkin, D.A. Detailed Analysis of Electrochemical Behavior of High–Performance Solid Oxide Fuel Cell Using DRT Technique. *J. Power Sources* **2022**, *527*, 231120, doi:10.1016/j.jpowsour.2022.231120.
21. Jiang, Z.; Lei, Z.; Ding, B.; Xia, C.; Zhao, F.; Chen, F. Electrochemical Characteristics of Solid Oxide Fuel Cell Cathodes Prepared by Infiltrating (La,Sr)MnO_3 Nanoparticles into Yttria-Stabilized Bismuth Oxide Backbones. *Int. J. Hydrogen Energy* **2010**, *35*, 8322–8330, doi:10.1016/j.ijhydene.2009.12.008.
22. Yang, T.; Kollasch, S.L.; Grimes, J.; Xue, A.; Barnett, S.A. $(La_{0.8}Sr_{0.2})_{0.98}MnO_{3-\delta}$-$Zr_{0.92}Y_{0.16}O_{2-\delta}$:$PrO_x$ for Oxygen Electrode Supported Solid Oxide Cells. *Appl. Catal. B Environ.* **2022**, *306*, 121114, doi:10.1016/j.apcatb.2022.121114.
23. Perry Murray, E.; Barnett, S.A. (La,Sr)MnO_3-(Ce,Gd)O_{2-x} Composite Cathodes for Solid Oxide Fuel Cells. *Solid State Ionics* **2001**, *143*, 265–273, doi:10.1016/S0167-2738(01)00871-2.
24. Nicollet, C.; Flura, A.; Vibhu, V.; Rougier, A.; Bassat, J.M.; Grenier, J.C. An Innovative Efficient Oxygen Electrode for SOFC: Pr_6O_{11} Infiltrated into Gd-Doped Ceria Backbone. *Int. J. Hydrogen Energy* **2016**, *41*, 15538–15544, doi:10.1016/j.ijhydene.2016.04.024.
25. Kharton, V. V.; Figueiredo, F.M.; Navarro, L.; Naumovich, E.N.; Kovalevsky, A. V.; Yaremchenko, A.A.; Viskup, A.P.; Carneiro, A.; Marques, F.M.B.; Frade, J.R. Ceria-Based Materials for Solid Oxide Fuel Cells. *J. Mater. Sci.* **2001**, *36*, 1105–1117,

UNIVERSIDAD DE MÁLAGA

doi:10.1023/A:1004817506146.

26. Wu, L.; Jiang, Z.; Wang, S.; Xia, C. (La,Sr)MnO_3-$(Y,Bi)_2O_3$ Composite Cathodes for Intermediate-Temperature Solid Oxide Fuel Cells. *Int. J. Hydrogen Energy* **2013**, *38*, 2398–2406, doi:10.1016/j.ijhydene.2012.11.111.
27. Santos-Gómez, L. Dos; Porras-Vázquez, J.M.; Losilla, E.R.; Marrero-López, D. Improving the Efficiency of Layered Perovskite Cathodes by Microstructural Optimization. *J. Mater. Chem. A* **2017**, *5*, 7896–7904, doi:10.1039/c6ta10946b.
28. Siebert, E.; Hammouche, A.; Kleitz, M. Impedance Spectroscopy Analysis of $La_{1-x}Sr_{itx}MnO_3$-Yttria-Stabilized Zirconia Electrode Kinetics. *Electrochim. Acta* **1995**, *40*, 1741–1753, doi:10.1016/0013-4686(94)00361-4.
29. Escudero, M.J.; Aguadero, A.; Alonso, J.A.; Daza, L. A Kinetic Study of Oxygen Reduction Reaction on La_2NiO_4 Cathodes by Means of Impedance Spectroscopy. *J. Electroanal. Chem.* **2007**, *611*, 107–116, doi:10.1016/j.jelechem.2007.08.006.
30. Mroziński, A.; Molin, S.; Jasiński, P. Study of Oxygen Electrode Reactions on Symmetrical Porous $SrTi_{0.30}Fe_{0.70}O_{3-\delta}$ Electrodes on $Ce_{0.8}Gd_{0.2}O_{1.9}$ Electrolyte at 800 °C–500 °C. *Electrochim. Acta* **2020**, *346*, doi:10.1016/j.electacta.2020.136285.
31. Liu, J.; Yu, Y.; Yang, T.; Ozmen, O.; Finklea, H.; Sabolsky, E.M.; Abernathy, H.; Ohodnicki, P.R.; Hackett, G.A. The Electrochemical Performance of LSM with A-Site Non-Stoichiometry under Cathodic Polarization. *ECS Meet. Abstr.* **2017**, *MA2017-03*, 46–46, doi:10.1149/ma2017-03/1/46.
32. Chen, X.J.; Khor, K.A.; Chan, S.H. Electrochemical Behavior of La(Sr)MnO_3 Electrode under Cathodic and Anodic Polarization. *Solid State Ionics* **2004**, *167*, 379–387, doi:10.1016/j.ssi.2003.08.049.
33. Carpanese, M.P.; Clematis, D.; Bertei, A.; Giuliano, A.; Sanson, A.; Mercadelli, E.; Nicolella, C.; Barbucci, A. Understanding the Electrochemical Behaviour of LSM-Based SOFC Cathodes. Part I — Experimental and Electrochemical. *Solid State Ionics* **2017**, *301*, 106–115, doi:10.1016/j.ssi.2017.01.007.
34. Gong, M.; Gemmen, R.S.; Mebane, D.S.; Gerdes, K.; Liu, X. Simulation of Surface-Potential Driven ORR Kinetics on SOFC Cathode with Parallel Reaction Pathways. *J. Electrochem. Soc.* **2014**, *161*, F344–F353, doi:10.1149/2.104403jes.
35. Wang, J.; Yang, T.; Lei, L.; Huang, K. Ta-Doped $SrCoO_{3-\delta}$ as a Promising Bifunctional Oxygen Electrode for Reversible Solid Oxide Fuel Cells: A Focused Study on Stability. *J. Mater. Chem. A* **2017**, *5*, 8989–9002, doi:10.1039/c7ta02003a.
36. Zapata-Ramírez, V.; Mather, G.C.; Azcondo, M.T.; Amador, U.; Pérez-Coll, D. Electrical and Electrochemical Properties of the Sr(Fe,Co,Mo)$O_{3-\delta}$ System as Air Electrode for Reversible Solid Oxide Cells. *J. Power Sources* **2019**, *437*, doi:10.1016/j.jpowsour.2019.226895.
37. Bertei, A.; Carpanese, M.P.; Clematis, D.; Barbucci, A.; Bazant, M.Z.; Nicolella, C. Understanding the Electrochemical Behaviour of LSM-Based SOFC Cathodes. Part II - Mechanistic Modelling and Physically-Based Interpretation. *Solid State Ionics* **2017**, *303*, 181–190, doi:10.1016/j.ssi.2016.09.028.
38. Pérez-Coll, D.; Aguadero, A.; Escudero, M.J.; Daza, L. Effect of DC Current Polarization on the Electrochemical Behaviour of $La_2NiO_{4+\delta}$ and $La_3Ni_2O_{7+\delta}$-Based Systems. *J. Power Sources* **2009**, *192*, 2–13, doi:10.1016/j.jpowsour.2008.10.073.
39. Zhang, X.; Wu, W.; Zhao, Z.; Tu, B.; Ou, D.; Cui, D.; Cheng, M. Insight into the Oxygen Reduction Reaction on the LSM|GDC Interface of Solid Oxide Fuel Cells through Impedance Spectroscopy Analysis. *Catal. Sci. Technol.* **2016**, *6*, 4945–4952, doi:10.1039/c5cy02232k.

UNIVERSIDAD DE MÁLAGA

40. Zheng, Z.; Jing, J.; Lei, Z.; Wang, Z.; Yang, Z.; Jin, C.; Peng, S. Performance and DRT Analysis of Infiltrated Functional Cathode Based on the Anode Supported SOFCs with Long-Term Stability. *Int. J. Hydrogen Energy* **2022**, *47*, 18139–18147, doi:10.1016/j.ijhydene.2022.03.289.

UNIVERSIDAD DE MÁLAGA

Chapter 8

UNIVERSIDAD
DE MÁLAGA

UNIVERSIDAD
DE MÁLAGA

Vertically Aligned Nanostructures

In this chapter, Vertically Aligned Nanostructures (VANs) films based on $(La_{0.8}Sr_{0.2})_{0.98}Fe_{0.8}Ti_{0.2}O_{3-\delta}$-$Ce_{0.9}Gd_{0.1}O_{1.95}$ ($LSFT_{0.2}$-CGO) were deposited by PLD onto different substrates for their implementation as functional layers in SSOFCs. The influence of the substrate on the crystal structure and the epitaxial ordering was deeply studied by XRD and different microstructural techniques, such as AFM, SEM and TEM. A complete electrical characterization was performed to test the performance in both air and H_2 atmospheres. The sample preparation and the structural characterization were carried out during an external stay for 3 months at the Technical University of Denmark (DTU) under the supervision of Profs. Nini Pryds and Vincenzo Esposito.

UNIVERSIDAD DE MÁLAGA

8.1. Preparation and structural characterization of $LSFT_{0.2}$ and $LSFT_{0.2}$-CGO films

$LSFT_{0.2}$ and $LSFT_{0.2}$-CGO targets (50 wt.%) for the deposition by pulsed laser deposition (PLD) were prepared by solid-state reaction from the corresponding oxides and carbonates, La_2O_3, $SrCO_3$, Fe_2O_3 and TiO_2, as described in detail in section 3.4. The single $LSFT_{0.2}$ and $LSFT_{0.2}$-CGO thin films were deposited onto $SrTiO_3$ (STO), $Zr_{0.84}Y_{0.16}O_{1.92}$ (YSZ) and $(LaAlO_3)_{0.3}(Sr_2TaAlO_6)_{0.7}$ (LSAT) (001) single crystals at 650 ºC by PLD at $6.67 \cdot 10^{-3}$ mbar in O_2 at 10 Hz for 20 minutes. Further experimental details can be found in section 3.4. The samples were deposited onto insulating LSAT (001) substrates for the electrical conductivity analysis, onto STO (001) substrates for the structural and microstructural characterization and onto YSZ (001) for electrode polarization measurements as discussed later. Hereafter, the $LSFT_{0.2}$-CGO thin film with columnar microstructure will be labelled as "$LSFT_{0.2}$-CGO VAN".

Figure 8.1 shows the θ-2θ XRD diffraction patterns of $LSFT_{0.2}$ and $LSFT_{0.2}$-CGO VAN deposited onto STO (001). $LSFT_{0.2}$ film shows a perovskite structure with a fully epitaxial growth along the (001) orientation without the presence of other crystallographic orientations (Figure 8.1a,c). Similar results were obtained for other ferrite-based perovskites deposited onto STO (001) single crystals such as $SrFeO_3$ and $La_{0.8}Sr_{0.2}FeO_{3-\delta}$ [1,2]. The similar out-of-plane lattice parameter of the $LSFT_{0.2}$ film (3.973 Å) with the STO substrate (3.905 Å) leads to a cube-on-cube growth with a (00*l*) preferred orientation (Figure 8.2a). The rather low lattice mismatch *f* ($[a_{substrate}-a_{film}]/a_{substrate}$) of 1.4 % between the unstrained $LSFT_{0.2}$ (3.919 Å) and the film leads to a fully epitaxial film growth with a coherent interface [3]. Additionally, the thickness fringes close to the $LSFT_{0.2}$ (002) reflection in Figure 8.1b confirm the high quality of the film.

In the case of the $LSFT_{0.2}$-CGO VAN deposited onto STO (001), the $LSFT_{0.2}$ perovskite component also shows an epitaxial growth along the (001) orientation (Figure 8.1b). However, the out-of-plane lattice parameter is slightly higher, 4.062 Å, increasing the lattice mismatch *f* up to 3.5 %, which is still lower than the maximum reported value (~ 7%) to obtain high-quality epitaxial films [3].

UNIVERSIDAD DE MÁLAGA

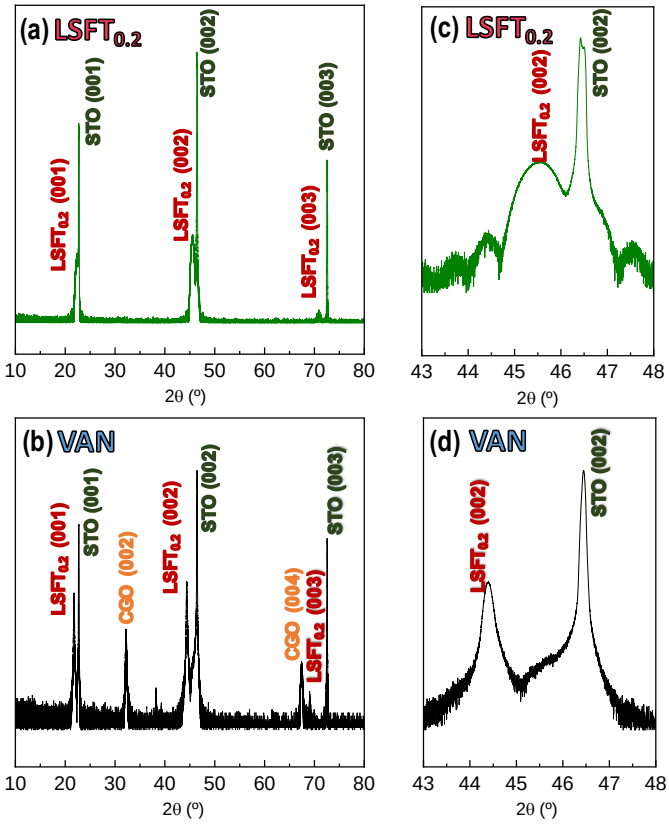

Figure 8.1. θ-2θ XRD patterns of (a) $LSFT_{0.2}$ and (b) $LSFT_{0.2}$-CGO VAN deposited onto STO (001) and (c,d) the corresponding HR-XRD patterns near the STO (002) reflection, showing the epitaxial growth of $LSFT_{0.2}$ in the (00*l*) direction. The thickness fringes close to the $LSFT_{0.2}$ (002) in (c) confirm the high quality of the film.

In the case of the CGO phase, previous works have shown that materials with a fluorite-type structure can be accommodated onto cubic perovskite substrates by a 45º in-plane rotation of the cell during the deposition to minimize the lattice mismatch (5.54 Å · $\frac{\sqrt{2}}{2}$=3.92 Å) (Figure 8.2b). The lattice mismatch for the CGO phase is also rather low, 1.8%, ensuring a good epitaxial growth. The XRD diffraction pattern further confirms this hypothesis for the CGO component, showing an epitaxial growth along the (002) orientation (Figure 8.1b). Figure 8.2 shows schematic representations of the crystal growth of the films on the different substrates to clarify the discussion of the results.

UNIVERSIDAD DE MÁLAGA

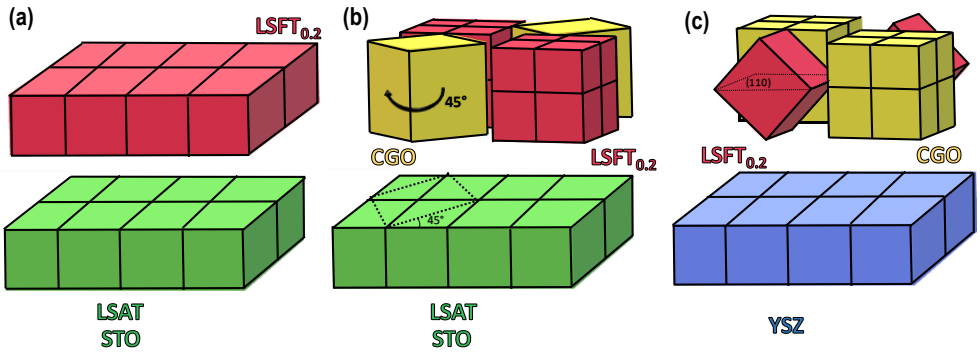

Figure 8.2. Illustration of the thin film growth of (a) epitaxial $LSFT_{0.2}$ on LSAT/STO, (b) $LSFT_{0.2}$-CGO VAN on LSAT/STO and (c) $LSFT_{0.2}$-CGO VAN on YSZ showing the microstructure ordering.

The θ-2θ XRD diffraction patterns of $LSFT_{0.2}$-CGO VAN onto LSAT (001), STO (001) and YSZ (001) clearly show a different column ordering depending on the substrate employed (Figure 8.3). The similar lattice parameter of STO (3.905 Å) and LSAT (3.868 Å) with $LSFT_{0.2}$ leads to accommodate the perovskite component with a (00*l*) preferred orientation as described previously (Figure 8.3a). These results suggest that the same growth mechanism is obtained for (001) oriented single crystals with perovskite-type structure and similar lattice parameters, regardless of the cation composition of the substrate.

In the case of the $LSFT_{0.2}$-CGO VAN deposited onto YSZ (001), with a cubic fluorite structure (5.143 Å), a cube-on-cube growth is observed for the CGO component with a (002) preferred orientation, showing an out-of-plane lattice parameter of 5.476 Å; however, a minor (111) reflection is also detected (Figure 8.2c and 8.3b). In the case of the $LSFT_{0.2}$ phase, a perfect vertical orientation growth along the (110) direction is discernible, which is parallel to the CGO (002). The very close lattice spacing between $LSFT_{0.2}$ (110) (d=5.52 Å) with CGO (002) (d=5.44 Å) induces a great out-of-plane coherence of both structures. The same behavior was previously observed for an LSM-SDC VAN deposited onto YSZ (001) [4]. These results reveal the great influence of the lattice cell parameters of the substrate on the nanostructure ordering, which makes possible to tailor the functional properties of the film by changing the substrate type.

UNIVERSIDAD DE MÁLAGA

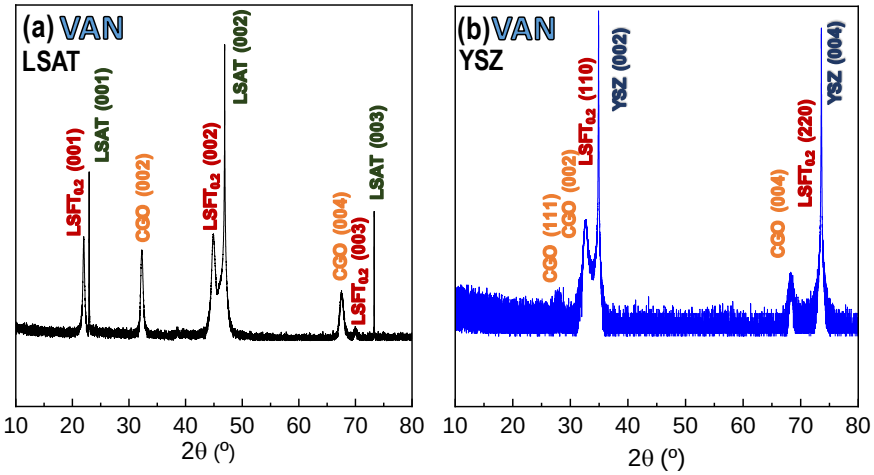

Figure 8.3. θ-2θ XRD patterns of $LSFT_{0.2}$-CGO VAN deposited onto (a) LSAT (001) and (b) YSZ (001).

In order to get further information about the crystal structure of the $LSFT_{0.2}$-CGO VAN samples, ϕ-scans, 2θ-ω rocking curves and reciprocal space mapping were carried out (Figure 8.4). The in-plane arrangement was elucidated by performing ϕ-scans on asymmetric reflections of the different components. The ϕ-scan of LSAT (111) shows four narrow peaks 90º apart in ϕ that corresponds to a cubic perovskite structure with a [001]/[010] in-plane crystallographic growth direction. The ϕ-scan of $LSFT_{0.2}$ (111) also shows 4 reflections at the same ϕ, which is consistent with a cube-on-cube growth as suggested previously. Interestingly, the ϕ-scan of CGO (111) presents 4 reflections that are shifted by 45º from LSAT (111), indicating a CGO[110]/LSAT[010] in-plane relationship. These results confirm the necessity of a 45º cell rotation of the CGO structure onto both LSAT and STO substrates to minimize the lattice mismatch (Figure 8.4a).

UNIVERSIDAD DE MÁLAGA

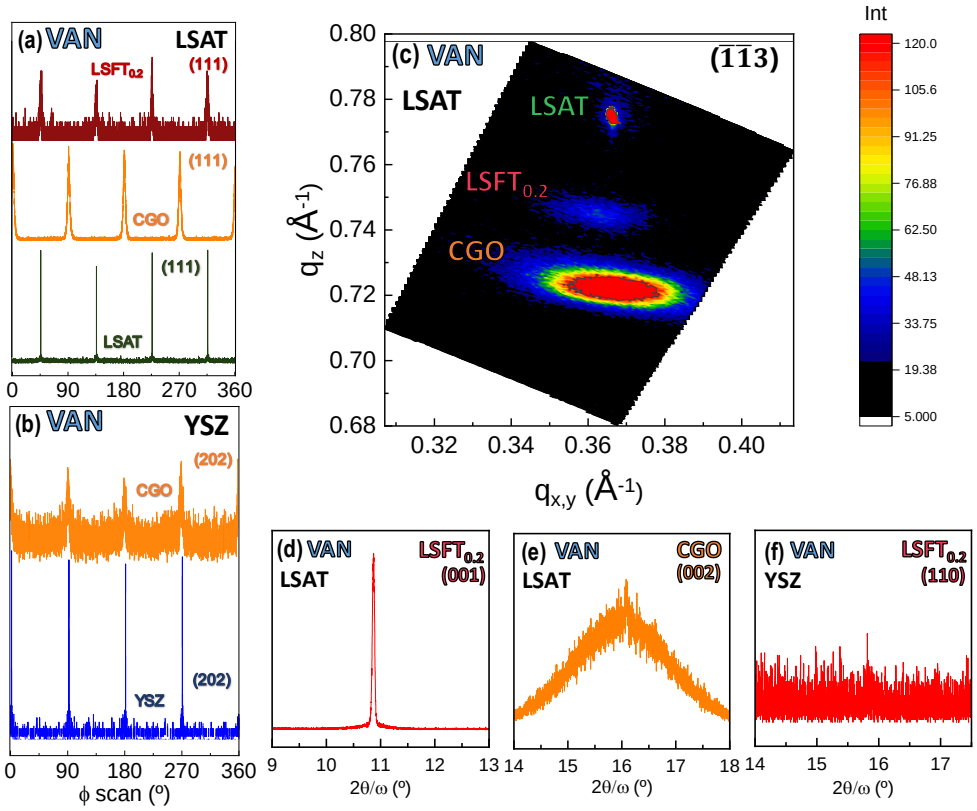

Figure 8.4. ϕ-scan analysis of (a) VAN deposited on LSAT around the (111) direction and (b) VAN deposited on YSZ around the (202) direction. (c) Reciprocal space map of the ($\bar{1}\bar{1}3$) asymmetric reflection of the VAN deposited on LSAT. 2θ-ω rocking curve measurements of the VAN film deposited on (d,e) LSAT and (f) YSZ.

In the case of the $LSFT_{0.2}$-CGO VAN deposited onto YSZ, the (202) ϕ-scan for both the YSZ substrate and CGO phase show four peaks with the same ϕ displacement (Figure 8.4b), confirming the cube-on-cube growth of CGO on YSZ. However, additional reflections are not detected after the (202) ϕ-scan of the $LSFT_{0.2}$ phase. In order to explain these results, 2θ-ω rocking curve (RC) analysis were performed. In the case of the RC of $LSFT_{0.2}$ (001) in the $LSFT_{0.2}$-CGO VAN on LSAT (Figure 8.4d), a sharp and narrow peak is observed, indicating the good quality of the epitaxial growth, while a wide peak is visible in the RC of CGO (002) (Figure 8.4e), revealing the presence of dislocations in the film that affects to the parallelism of atomic planes. This fact is very common in CeO_2-based films deposited onto single crystals with perovskite structure [5,6]. In the case of the RC of $LSFT_{0.2}$ (110) in the

UNIVERSIDAD DE MÁLAGA

$LSFT_{0.2}$-CGO VAN on YSZ, no extra peaks are detected, revealing the very low quality of the phase ordering, presumably attributed to a high concentration of crystalline defects (Figure 8.4f). This result explains the non-presence of signals in the 202 ϕ-scan of the $LSFT_{0.2}$ phase on YSZ.

The reciprocal space map (RMS) of the $LSFT_{0.2}$-CGO VAN deposited onto LSAT in the asymmetric reflection $(\bar{1}\bar{1}3)$ is displayed in Figure 8.4c. Three bands are clearly identified, attributed to the substrate (LSAT), the perovskite ($LSFT_{0.2}$) and the fluorite (CGO) components. The widespread of in-plane lattice parameters for the CGO phase is responsible for the broad band observed for this phase. The in-plane ($a_{x,y}$) and out-of-plane (a_z) lattice parameters can be obtained from the RSM by the following equations (Eqs. 8.1 and 8.2) [7]:

$$a_z = \frac{\sqrt{l^2}}{q_z} \qquad \text{(Eq. 8.1)}$$

$$a_{x,y} = \frac{\sqrt{h^2+k^2}}{q_{x,y}} \qquad \text{(Eq. 8.2)}$$

where q_z and $q_{x,y}$ are associated with the out-of-plane and in-plane parameters of the diffracted vector in the RMS.

In the case of the LSAT substrate, the in-plane and out-of-plane lattice parameters show very similar values, 3.863 and 3.872 Å, respectively, as expected due to its cubic structure. Interestingly, the in-plane lattice parameter of the $LSFT_{0.2}$ phase (3.889 Å) is very close to that observed for the LSAT substrate, revealing that the film is strained. Since the lattice parameter of the unstrained $LSFT_{0.2}$ (3.919 Å) is somewhat higher, the LSAT (001) induces an in-plane strain compression of the $LSFT_{0.2}$ phase, leading to an expansion of the out-of-plane lattice parameter (4.062 Å), as observed previously on the θ-2θ XRD analysis. In the case of the CGO component, a widespread of in-plane lattice parameters are obtained, which ranged from 5.349 to 5.571 Å, while similar out-of-plane lattice parameter to that observed in the θ-2θ XRD was obtained. These findings indicate the difficulty of perfectly accommodating the CGO phase with a 45 º rotation while simultaneously growing the $LSFT_{0.2}$ columns. Similar results have been observed for other VAN structures [3,8,9].

UNIVERSIDAD DE MÁLAGA

It is worth mentioning that the in-plane periodic arrangement of the nanocolumns of both phases was previously related to the presence of dislocations, in order to relax the strain induced by the lattice mismatching [10,11]. Similarly, the out-of-plane spontaneous ordering is highly influenced by the strain energy and anisotropic in-plane strain. This in-plane strain anisotropy induces the atoms adsorbed on the crystal surface to diffuse to sites with lower energy, partially releasing the strain energy and leading to achieve out-of-plane spontaneous ordering. Additionally, the substrate orientation modifies the surface energy, leading to a change in the atomic arrangement. On the other hand, a different crystallographic orientation of the substrate could induce a completely different microstructure, including the size and shape of the nanodomains [10,12]. For this reason, the $LSFT_{0.2}$-CGO VAN deposited onto STO single crystals with (110) and (111) orientations could lead to a completely different crystal arrangement and thus different electrical properties [13].

In order to study the stability in reducing atmosphere, the $LSFT_{0.2}$-CGO VAN on STO (001) was annealed at 650 ºC for 5 h in 5% H_2-Ar and then analyzed by XRD (Figure 8.5). The θ-2θ XRD patterns show that the $LSFT_{0.2}$-CGO VAN is stable in reducing conditions without the formation of secondary phases or other crystallographic orientations (Figure 8.5a). The out-of-plane lattice parameter for the $LSFT_{0.2}$ phases slightly decreased from 4.062 to 4.045 Å, suggesting an out-of-plane cell relaxation after the reduction (Figure 8.5b).

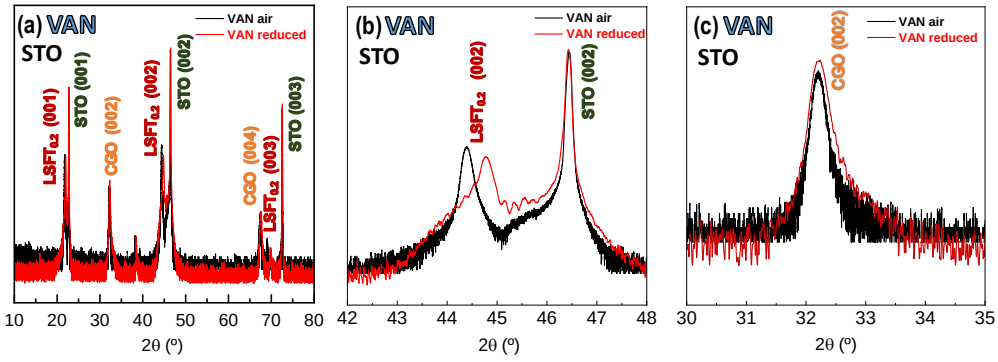

Figure 8.5. θ-2θ XRD patterns after reduction in 5% H_2-Ar of (a) $LSFT_{0.2}$-CGO VAN and the corresponding high resolution XRD patterns near the (b) STO (002) and (c) CGO (002).

UNIVERSIDAD DE MÁLAGA

In the case of the CGO component, a similar out-of-plain lattice parameter was observed (Figure 8.5c). Although the out-of-plane lattice parameter is expected to increase due to the partial reduction of Fe^{3+}, Ti^{4+} and Ce^{4+} to lower oxidation states, the dense and rigid microstructure and vertical strain seem to avoid significant changes in the out-of-plane lattice parameters.

It is worth mentioning that these findings are different to those observed for porous $LSFT_{0.2}$-CGO nanocomposite electrodes in Chapter 6. In particular, the lattice cell parameter of $LSFT_{0.2}$ remained almost constant after reduction while the CGO component showed a slight expansion. Hence, the different behavior of strained films when compared to polycrystalline materials could induce different electrical performances in both air and H_2 atmospheres.

8.2. Microstructural characterization

The microstructure of the $LSFT_{0.2}$-CGO VAN sample on STO (001) was studied by preparing an electron transparent cross-sectional lamella that was characterized by HAADF-STEM (Figure 8.6a). It has to be mentioned that Ir and Pt coatings were needed for the preparation of the lamella.

A low magnification HAADF-STEM image shows a long-range ordered columnar microstructure with a column width of about 5 nm and 100 nm length perpendicular to the STO substrate in the entire film thickness. Interestingly, the $LSFT_{0.2}$-CGO VAN presents a dense structure without visible porosity or delamination. The EDS map confirms the formation of homogeneously distributed $LSFT_{0.2}$ and CGO columns (Figure 8.6b,c). The Lanthanum mapping is not included because it does not show a clear difference between the columns, suggesting a certain incorporation of this element into the CGO matrix [4]. The phase separation, with clearly defined interfaces, suggests that the spontaneous ordering of nanodomains is induced by strain energy minimization. The unique microstructure of the VAN films enables vertical strain engineering with numerous interfaces, partially solving the limitations of critical thickness due to cell relaxation [14].

UNIVERSIDAD DE MÁLAGA

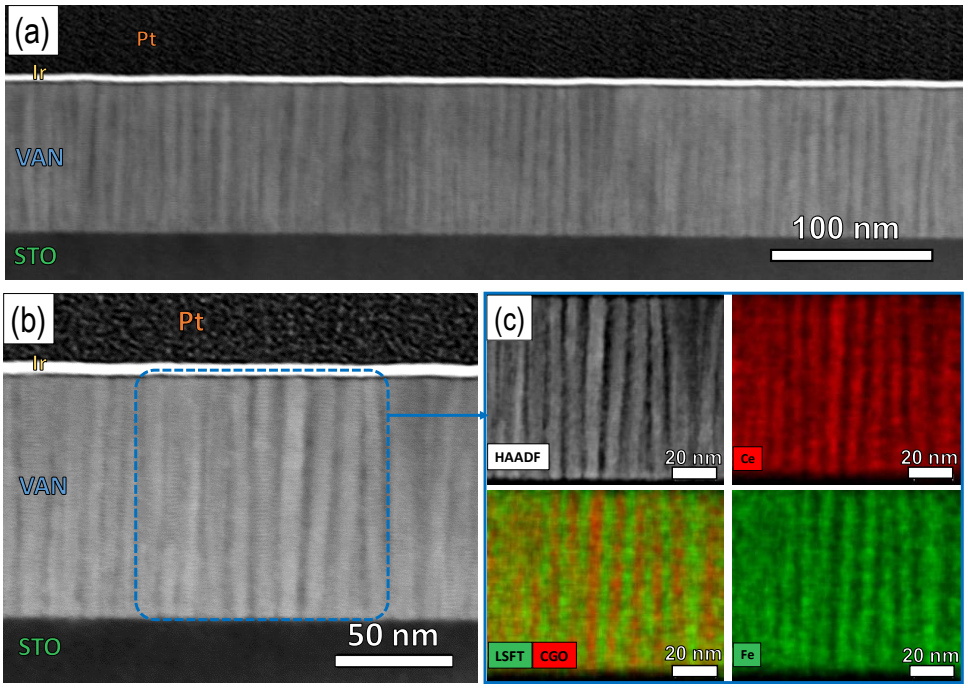

Figure 8.6. (a) Low magnification cross-sectional HAADF-STEM image of the $LSFT_{0.2}$-CGO VAN film deposited onto STO (001) substrate at 650 ºC and (b) zoomed image, showing the columnar microstructure. (c) HAADF-STEM image and EDS of a selected area of the film, revealing the presence of alternating columns of both $LSFT_{0.2}$ and CGO phases.

HRTEM images show high crystalline nanocolumns of both $LSFT_{0.2}$ and CGO phases. The CGO columns in dark are homogeneously distributed in the $LSFT_{0.2}$ bright matrix (Figure 8.7). A higher magnification HRTEM shows the vertical interfaces between both phases (Figure 8.7b). Both $LSFT_{0.2}$ and CGO phases show an atomic arrangement in the (001) direction leading to an epitaxial growth on STO (001). In the case of the CGO, the 45º in-plane rotation is observed to minimize the lattice mismatch. The d-spacing obtained for both phases is in accordance with the XRD results.

UNIVERSIDAD DE MÁLAGA

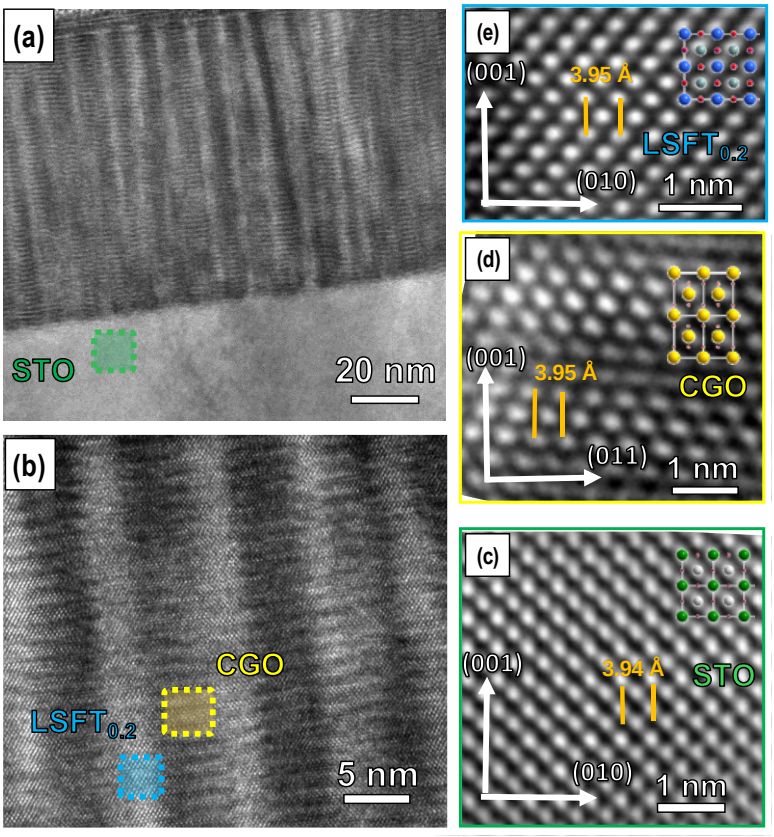

Figure 8.7. (a,b) HRTEM images of the $LSFT_{0.2}$-CGO VAN with a columnar microstructure at different magnifications. Atomic arrangement of (c) STO substrate, (d) CGO and (e) $LSFT_{0.2}$ phases.

The microstructure ordering, in this case, is similar to other VANs reported in the literature, such as LSM-SDC or STO-SDC, with a nanocheckerboard microstructure (Figure 8.8a) [4,5]. On the contrary, an ordered pillar-in-matrix arrangement was also observed for other VAN films, such as $BiFeO_3$-$CoFe_2O_4$ (Figure 8.8b). The VAN films with nanocheckerboard ordering with higher number of interfaces have demonstrated a great influence on magnetic and ionic properties [5,15].

UNIVERSIDAD DE MÁLAGA

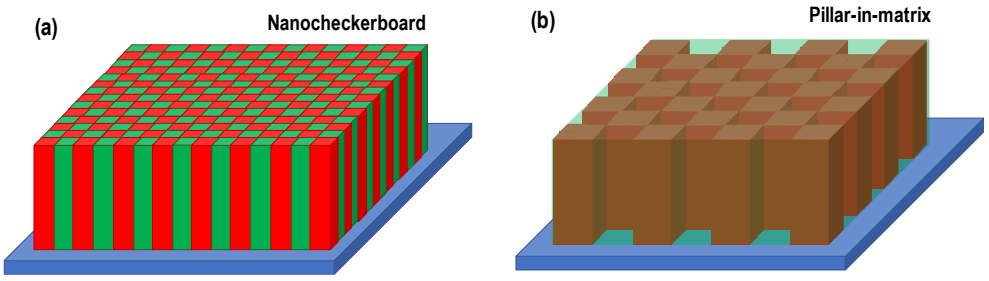

Figure 8.8. Illustration of (a) VAN with a nanocheckerboard microstructure with the homogenous ordering of nanocolumns of both phases and (b) VAN with a pillar-in-matrix microstructure with pillars embedded in a matrix.

AFM images of the $LSFT_{0.2}$-CGO VAN deposited onto LSAT and YSZ are displayed in Figure 8.9. Both films show a dense microstructure but different grain sizes and roughnesses. In the case of the $LSFT_{0.2}$-CGO VAN on LSAT, a lower roughness is observed ~ 2.1 nm when compared with the same film deposited onto YSZ ~ 9.6 nm, respectively, indicating that the VAN deposited on YSZ has a more disordered microstructure, as observed in the rocking curve patterns.

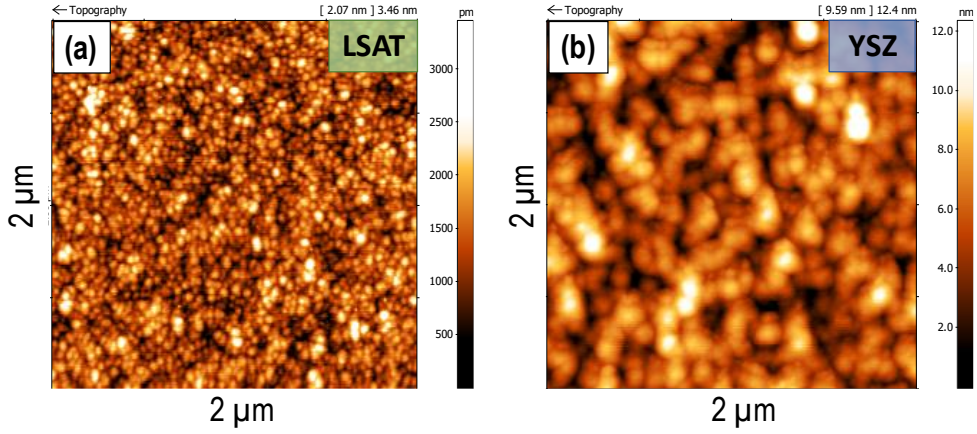

Figure 8.9. AFM top-view micrographs of the $LSFT_{0.2}$-CGO VAN deposited onto (a) LSAT (001) and (b) YSZ (001) substrates.

8.3. XPS characterization

The composition of the as-deposited films and after a reduction treatment at 750 ºC 12 h in 5% H_2-Ar was characterized by XPS (Figure 8.10). The O1s core level

UNIVERSIDAD DE MÁLAGA

shows two different bands (Figure 8.10a), centered at 529 and 531.3 eV, which can be assigned to lattice oxygen and other species adsorbed on surface (such as carbonates or hydroxides), respectively [16]. It is not possible to differentiate the lattice oxygen from the perovskite and the fluorite phases since their binding energy are very similar.

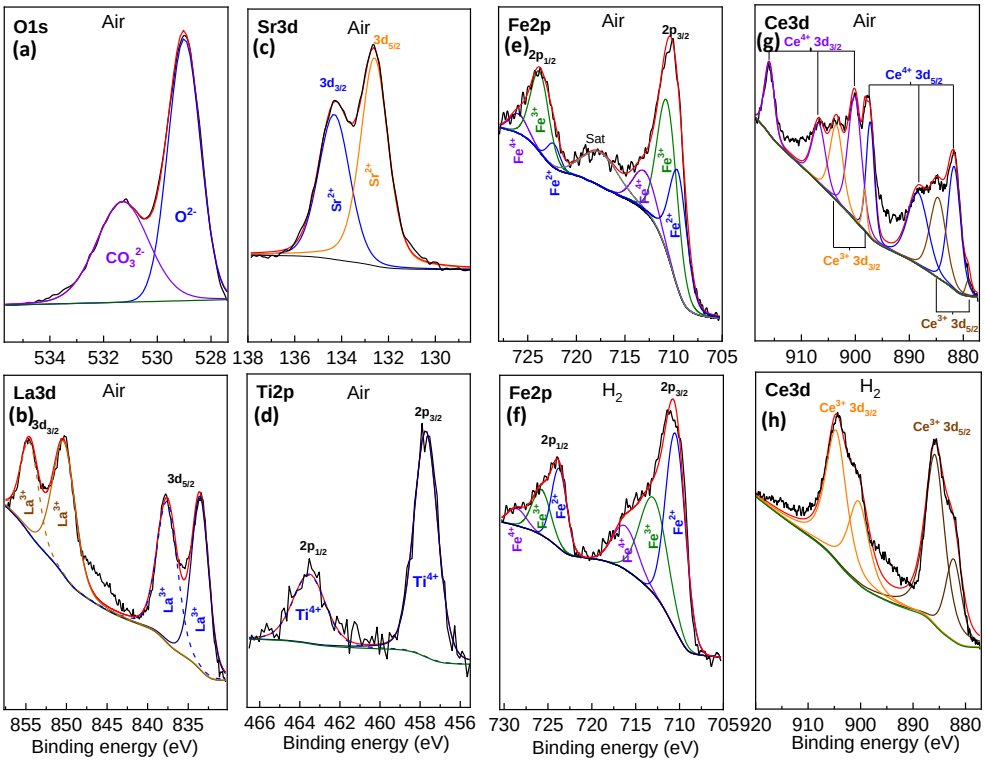

Figure 8.10. XPS spectra of the surface of $LSFT_{0.2}$-CGO VAN in air and 5% H_2-Ar (a) O1s, (b) La3d, (c) Sr 3d, (d) Ti 2p, (e,f) Fe 2p and (g,h) Ce 3d.

The $La3d_{5/2}$ region shows two peaks, in which the signal at higher binding energy is a satellite produced by an electron transfer from the filled O_{2p} band to the La_{4f} level (Figure 8.10b). The band centred at 833.4 eV is assigned to lattice La^{3+} in $LSFT_{0.2}$ [17]. The Sr3d core shows a characteristic doublet with a binding energy of 132.5 eV for Sr $3d_{5/2}$, which is consistent with Sr^{2+} (Figure 8.10c), as observed in previous reports of $SrFeO_3$ [18]. It is also remarkable that similar XPS spectra were observed for these three elements after reducing the samples in 5% H_2-Ar.

UNIVERSIDAD DE MÁLAGA

The Ti2$p_{3/2}$ spectra in both air and 5% H_2-Ar show a band at 457.7 eV characteristic of Ti^{4+} [19] (Figure 8.10d). Additional shoulders at lower binding energy attributed to Ti^{3+} are not identified, suggesting that the Ti^{3+} concentration is below the XPS detection limit.

The Fe 2$p_{3/2}$ signal in air can be deconvoluted into three different contributions (Fe^{2+}, Fe^{3+} and Fe^{4+}) with binding energies of 709.8, 710.8 and 713.2 eV (Figure 8.10e), respectively, similar to that previously reported for $LaFeO_3$ [20], $La_{0.6}Sr_{0.4}Fe_{0.95}Pd_{0.05}O_{3-\delta}$ [21] or $Sm_{0.9}Sr_{0.1}Fe_{0.8}Cr_{0.2}O_{3-\delta}$ [22]. Additionally, a shake-up satellite peak (centered at 717.6 eV) from Fe 2$p_{3/2}$ region is also observed [21]. The correct quantitative interpretation of Fe 2p is difficult due to the low chemical shift between the bands. For these reasons, only the presence of the different oxidation states of iron is studied and a quantification was not performed. A better interpretation of the oxidation states of Fe could be obtained by alternative techniques, such as Mössbauer spectroscopy of ^{57}Fe. After reducing the films in 5% H_2-Ar at 750 ºC for 12 h, the Fe^{4+} band is slightly reduced, while Fe^{2+} amount increases, confirming only a partial reduction of the iron, as observed previously for $Sm_{0.9}Sr_{0.1}FeO_{3-\delta}$ [22].

The Ce 3d core level shows numerous contributions for the Ce 3$d_{5/2}$ and Ce 3$d_{3/2}$ levels. Ce^{4+} is the main valence state in the sample but also a certain amount of Ce^{3+} is present on the surface of the VAN film (Figure 8.10g). The same behaviour was previously observed for $Ce_{0.9}Gd_{0.1}O_{1.95}$ and $Ce_{0.9}Sm_{0.1}O_{1.9}$ films prepared by the Pechini and precipitation method, respectively [23,24]. The peaks at binding energies of 884.8 and 879.1 eV are associated with Ce^{3+} 3$d_{5/2}$, findings that have been previously associated with the formation of oxygen vacancies in CeO_2-doped compounds [24]. After reduction, the Ce^{4+} on the surface of the films is almost completely reduced to Ce^{3+} (Figure 8.10h) [25]. This is clearly confirmed by the absence of the peak centred at 916.2 eV, characteristic of the Ce^{4+}3$d_{5/2}$.

However, the better electrical properties in reducing conditions for the $LSFT_{0.2}$-CGO VAN sample, as discussed in the following paragraphs, suggest the presence of Ce^{4+}/Ce^{3+} redox couple due to the important electronic component to the total conductivity.

UNIVERSIDAD DE MÁLAGA

8.4. Electrical characterization

The in-plain conductivity of $LSFT_{0.2}$ and $LSFT_{0.2}$-CGO VAN films deposited onto LSAT (001) was determined by the four-probe Van der Pauw method under air and 5% H_2-Ar atmospheres (Figure 8.11). In these measurements, LSAT substrates are employed due to its negligible conductivity in both oxidizing and reducing atmospheres. The samples deposited onto $SrTiO_3$ (STO) are not suitable for electrical characterization due to the partial reduction of Ti^{4+} to Ti^{3+} in a hydrogen atmosphere, leading to an overestimation of the film conductivity.

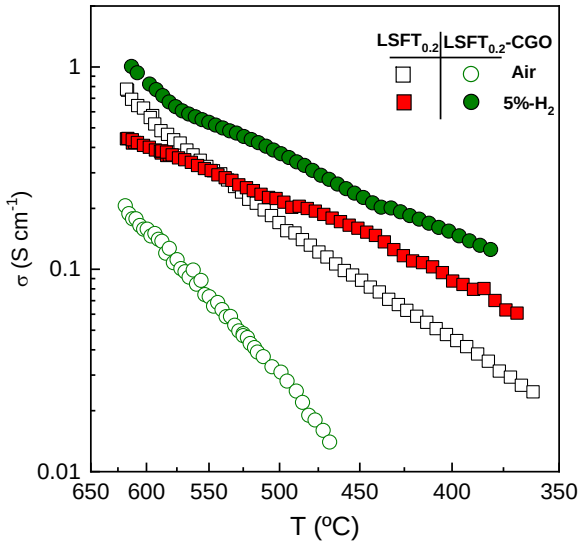

Figure 8.11. In-plane conductivity of the different films deposited onto LSAT in air and 5%-H_2 as a function of the temperature.

The in-plain conductivity of the epitaxial $LSFT_{0.2}$ (001) reaches 0.57 S cm^{-1} in air at 600 ºC, which is higher than that found for the corresponding $LSFT_{0.2}$ polycrystalline pellets (0.11 S cm^{-1}) at the same temperature in Chapter 6. In reducing conditions, the conductivity slightly decreases to 0.40 S cm^{-1} at 600 ºC due to the partial reduction of iron in the lattice. As observed previously, the amount of titanium in this sample is enough to stabilize the perovskite structure in reducing atmosphere but not sufficient to promote high conductivity values.

UNIVERSIDAD DE MÁLAGA

The $LSFT_{0.2}$-CGO VAN films show a decrease of the total conductivity in air, *i.e.* 0.16 S cm^{-1} at 600 ºC, when compared to the pure $LSFT_{0.2}$, which is attributed to the lower conductivity of CGO in oxidizing conditions. However, the conductivity in 5% H_2-Ar increases up to 0.82 S cm^{-1} at 600 ºC, which can be linked to the partial reduction of Ce^{4+} to Ce^{3+} and the enhancement of the electronic conductivity.

Interestingly, the conductivity values of the $LSFT_{0.2}$-CGO VAN at 600 ºC are higher than those observed for the polycrystalline $LSFT_{0.2}$-CGO pellets in Chapter 6 (*i.e.* 0.0017 and 0.06 S cm^{-1}, in air and 5%H_2-Ar, respectively, at 600 ºC). These results are in agreement with previous reports about the better conductivity of the VAN films with columnar microstructures due to the numerous vertical interfaces, leading to tailor not only the in-plain strain but also promoting vertical strain engineering, thus improving the electrical properties.

Although better conductivity values are obtained for the $LSFT_{0.2}$-CGO VAN when compared to the polycrystalline sample, the real conductivity through the columns is not determined (Figure 8.12a). It is worth to be commented that the in-plain conductivity is determined by Van der Pauw method in this work. However, using Scanning Probe Microscopy (SPM) technique, which employs a conductive tip, it is possible to obtain further information about the conductivity in the direction of the columns (Figure 8.12b) [5].

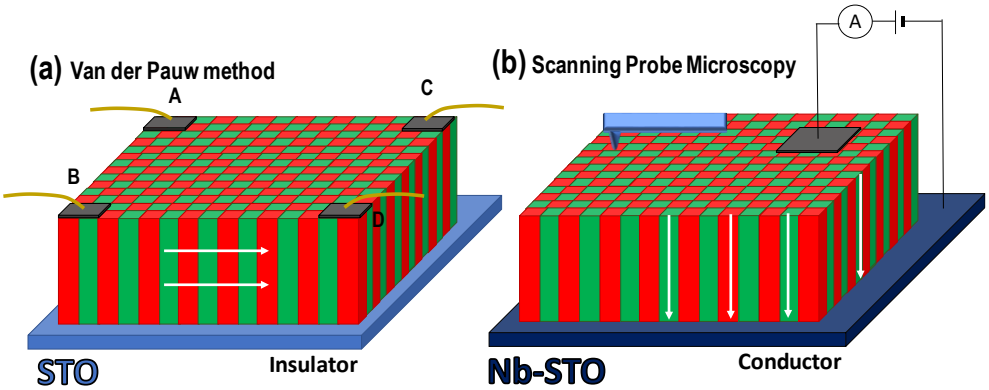

Figure 8.12. Illustration of the electrical characterization of the VAN film by (a) four probe Van der Pauw method and (b) Scanning Probe Microscopy.

UNIVERSIDAD DE MÁLAGA

Nevertheless, a substrate with high conductivity, such as Nb-doped STO single crystal, is needed to correctly perform this technique. In our study, STO (001) substrate (insulator) was employed for the deposition of the films, leading to a very bad signal-to-noise ratio, which impedes the use of SPM. Future work is needed to study the conductivity of the columns in the VAN structure.

The conductivity was also determined as a function of the pO_2 to evaluate the different contributions to the total conductivity (Figure 8.13). The curves for both $LSFT_{0.2}$ and $LSFT_{0.2}$-CGO VAN films are typical of a mixed ionic electronic conductor with a pO_2-dependence of $\pm 1/4$.

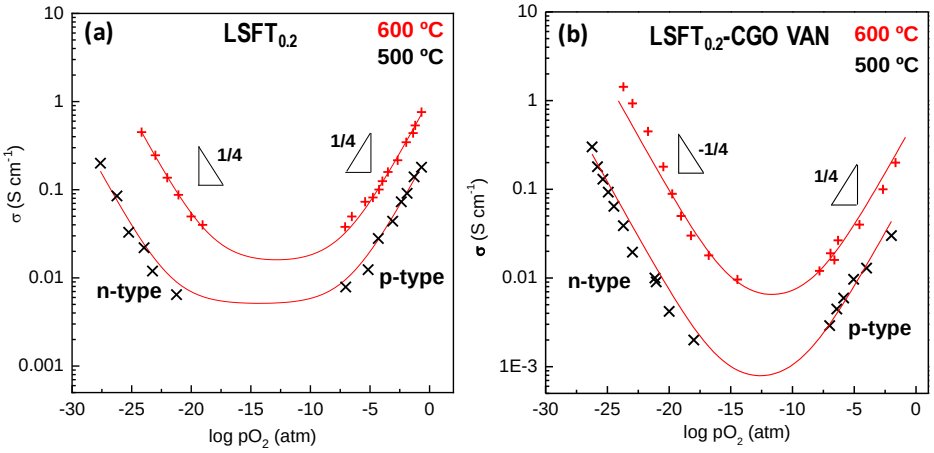

Figure 8.13. Conductivity as a function of the oxygen partial pressure for (a) single $LSFT_{0.2}$ and (b) $LSFT_{0.2}$-CGO VAN at different temperatures.

The pO_2 curves of the $LSFT_{0.2}$ show a similar trend to that observed for the bulk $LSFT_{0.2}$ in Chapter 6, in which both n-type and p-type conductivity contributions are clearly discernible. The greater electronic conductivity of the $LSFT_{0.2}$-CGO VAN compared to $LSFT_{0.2}$-CGO pellets can be associated with the easier reducibility of the CGO component.

8.5. Electrochemical characterization

The electrode polarization resistance of $LSFT_{0.2}$ and $LSFT_{0.2}$-CGO VAN on YSZ (001) was studied by impedance spectroscopy on symmetrical cell configuration using Au ink as a current collector. Figure 8.14a shows the impedance spectra in air

UNIVERSIDAD DE MÁLAGA

at 650 ºC. The ohmic resistance of the electrolyte, which was very similar in both cases, was subtracted for a better comparison of the electrode response. The impedance spectra were fitted with the equivalent circuit displayed in the inset of Figure 8.14a, in which two RQ elements were necessary to adequately fit the impedance data.

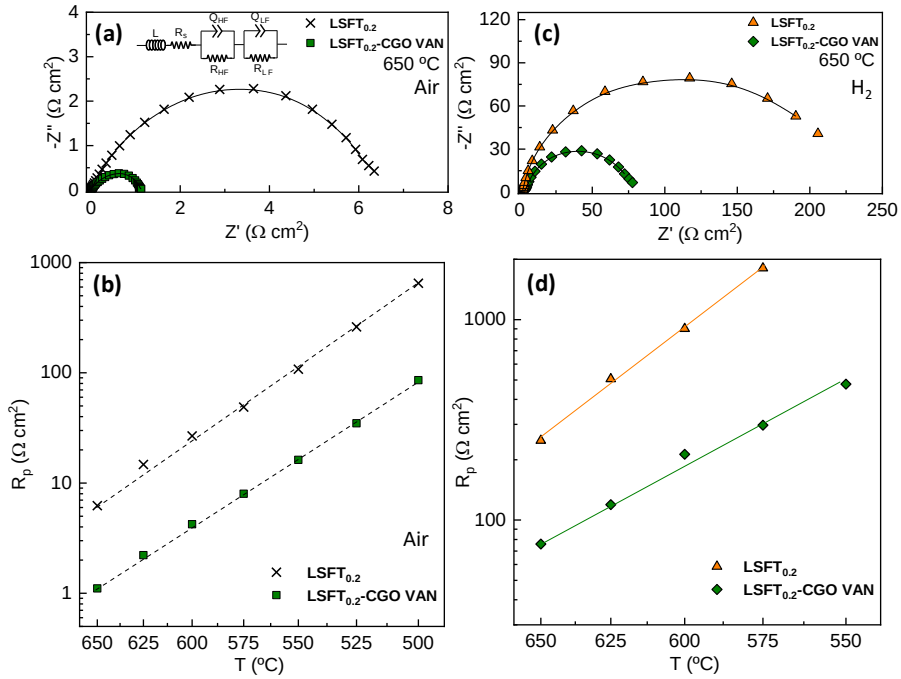

Figure 8.14. Impedance spectra of $LSFT_{0.2}$ and $LSFT_{0.2}$-CGO VAN in (a) air and (b) 100% H_2 at 650 ºC. Temperature dependence of the polarization resistance in (c) air and (d) 100% H_2.

The $LSFT_{0.2}$-CGO VAN shows a polarization resistance of 1.1 Ω cm^2 at 650 ºC in air, which is considerably lower than that observed for the $LSFT_{0.2}$ film at the same temperature ~ 6.2 Ω cm^2. Figure 8.14b shows the polarization resistance in air as a function of the temperature, where $LSFT_{0.2}$-CGO VAN exhibits lower R_p values compared to $LSFT_{0.2}$ film in all temperature range studied. The columnar microstructure with vertical strain enlarges the active sites for ORR when compared to the epitaxial $LSFT_{0.2}$, in which the ionic pathway provided by the CGO is not available. Interestingly, these R_p values are lower than those observed for other VANs recently reported in the literature, such as $La_{0.75}Sr_{0.25}Cr_{0.5}Mn_{0.5}O_{3-\delta}$-SDC (27.8 Ω cm^2

UNIVERSIDAD DE MÁLAGA

at 750 ºC) [26] and $La_{0.8}Sr_{0.2}MnO_{3-\delta}$-SDC (7 Ω cm^2 at 700 ºC) [4], and similar to highly efficient air electrodes deposited by PLD such as $PrBaCo_2O_{5+\delta}$ (0.71 Ω cm^2 at 600 ºC) [27].

In a wet H_2 atmosphere, the R_p values of the VAN are significantly lower than that of $LSFT_{0.2}$ film, 75.9 and 225.4 Ω cm^2, respectively, at 650 ºC. Even though these values are considerably higher than those observed in air conditions, they are similar to those reported for the $La_{0.75}Sr_{0.25}Cr_{0.5}Mn_{0.5}O_{3-\delta}$-SDC VAN (~ 80 Ω cm^2 at 630 ºC) or single film of $La_{0.75}Sr_{0.25}Cr_{0.5}Mn_{0.5}O_{3-\delta}$ (~ 300 Ω cm^2 at 630 ºC) [26].

The electrochemical performance of the $LSFT_{0.2}$-CGO VAN in air is similar to that observed in Chapter 6 for the $LSFT_{0.2}$ infiltrated onto CGO scaffold (0.67 Ω cm^2) and $LSFT_{0.2}$-CGO nanocomposite (0.82 Ω cm^2) deposited by spray-pyrolysis at 650 ºC, and even better than that observed for screen-printed $LSFT_{0.2}$-CGO composite (3.86 Ω cm^2) at the same temperature. However, the polarization resistance values in H_2 are very high when compared to those observed for $LSFT_{0.2}$ infiltrated onto a CGO scaffold (0.64 Ω cm^2) and $LSFT_{0.2}$-CGO nanocomposite (0.99 Ω cm^2) deposited by spray-pyrolysis at the same temperature.

It is also worth mentioning that the aforementioned electrodes show a highly porous microstructure, with extended TPB sites for the electrochemical reactions in comparison to the dense $LSFT_{0.2}$-CGO VAN. This fact impedes the accurate comparison between the performance of the electrode with similar chemical composition. The application of VANs in reducing conditions is relatively new and only the LSCM-SDC VAN reported in 2022 by Sirvient *et al.* is available in the literature [26]. Although the R_p values are relatively high for application in SOFC, the better electrochemical properties of the VAN compared to the single $LSFT_{0.2}$ suggest that they can be used as active layers between the electrolyte and a porous electrode deposited by low deposition techniques such as spray-pyrolysis.

In order to elucidate the different electrode contributions to the overall electrode polarization for the ORR in the $LSFT_{0.2}$-CGO VAN sample, the impedance spectra were collected as a function of pO_2 at 650 ºC (Figure 8.15).

UNIVERSIDAD DE MÁLAGA

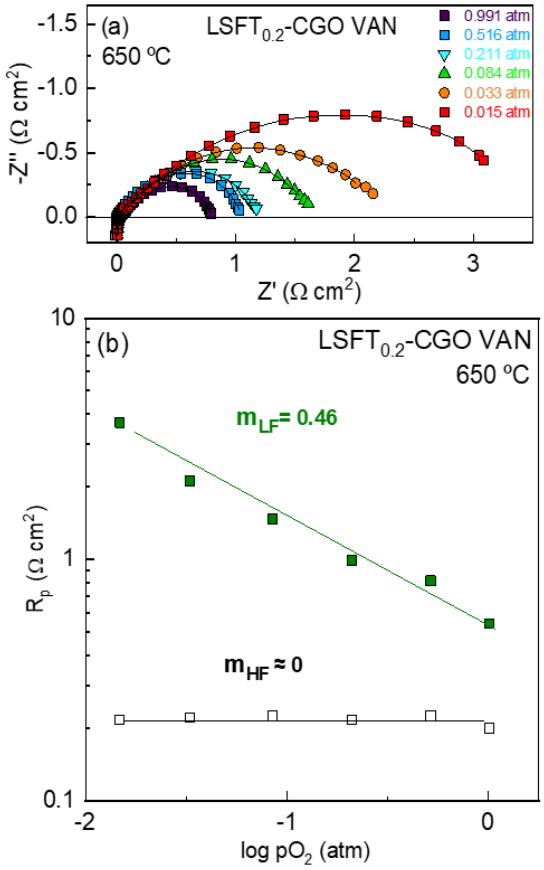

Figure 8.15. (a) Nyquist spectra of the $LSFT_{0.2}$-CGO VAN on YSZ (001) at 650 ºC as a function of the pO_2 and (b) dependence of the HF and LF electrode resistances as function of the pO_2.

The impedance spectra at different pO_2 show two different contributions (Figure 8.15a). The process located at high frequency (HF) shows a negligible dependency on the oxygen partial pressure and can be attributed to oxide-ion transport at the electrode/electrolyte interphase ($O^x_{o,\ electrode} \rightarrow O^x_{o,\ electrolyte}$) [28,29]. The low frequency (LF) process is the main contribution to the overall polarization resistance and shows a pO_2 dependence with a reaction order of m ~ 0.5 which can be assigned to oxygen dissociation at the electrode surface ($O_{2,\ ad} \rightarrow 2O_{ad}$) (Figure 8.15b). Similar rate-limiting steps were found for related compositions, such as $La_{0.9}Sr_{0.1}FeO_{3-\delta}$ [30] and $Sr_{0.1}Fe_{0.8}Ti_{0.2}O_{3-\delta}$ [31]. However, a different rate-limiting step was observed for the $LSFT_{0.2}$ infiltrated into a CGO scaffold and $LSFT_{0.2}$-CGO

UNIVERSIDAD DE MÁLAGA

deposited by spray-pyrolysis (m ~ 0.25). These differences are possibly attributed to the different electrode microstructure, since highly porous microstructures are obtained by spray-pyrolysis deposition and dense films by PLD. Thus, the different electrode porosity directly is expected to affects both the electrode performance and the rate-limiting steps involved in the ORR [32,33].

These promising results suggest the possibility to implement VANs based on Ti-doped (La,Sr)$FeO_{3-\delta}$ as functional layers for SSOFCs, working efficiently in both oxidizing and reducing conditions. The deposition conditions of the VAN were fixed at 650 ºC and $6.67 \cdot 10^{-6}$ bar in O_2. Since a lower column size in VAN films has demonstrated to lower the polarization resistance in a LSM-YSZ VAN, deposition rates higher than 10 Hz could be explored to further reduce the column size [34]. Interestingly, another report also showed that higher deposition temperatures increased the lateral width of the nanocolumns on different oriented substrates, becoming crucial to explore new VANs at different synthetic conditions [35,36]. The electrode performance in reducing conditions can be improved by depositing a porous structure on top of the active layers or incorporating active metals (Ni, Ru or Pd) to promote metal nanoparticle exsolution in reducing conditions, which have demonstrated to highly enhance the activity for HOR.

References

1. Wang, L.; Du, Y.; Sushko, P. V.; Bowden, M.E.; Stoerzinger, K.A.; Heald, S.M.; Scafetta, M.D.; Kaspar, T.C.; Chambers, S.A. Hole-Induced Electronic and Optical Transitions in $La_{1-x}Sr_xFeO_3$ Epitaxial Thin Films. *Phys. Rev. Mater.* **2019**, *3*, doi:10.1103/PhysRevMaterials.3.025401.
2. Wang, L.; Yang, Z.; Wu, J.; Bowden, M.E.; Yang, W.; Qiao, A.; Du, Y. Time- and Strain-Dependent Nanoscale Structural Degradation in Phase Change Epitaxial Strontium Ferrite Films. *npj Mater. Degrad.* **2020**, *4*, 3–8, doi:10.1038/s41529-020-0120-3.
3. Chen, A.; Su, Q.; Han, H.; Enriquez, E.; Jia, Q. Metal Oxide Nanocomposites: A Perspective from Strain, Defect, and Interface. *Adv. Mater.* **2019**, *31*, 1–30, doi:10.1002/adma.201803241.
4. Baiutti, F.; Chiabrera, F.; Acosta, M.; Diercks, D.; Parfitt, D.; Santiso, J.; Wang, X.; Cavallaro, A.; Morata, A.; Wang, H.; Taracón, A. A High-Entropy Manganite in an Ordered Nanocomposite for Long-Term Application in Solid Oxide Cells. *Nat. Commun.* **2021**, *12*, 1–11, doi:10.1038/s41467-021-22916-4.
5. Yang, S.M.; Lee, S.; Jian, J.; Zhang, W.; Lu, P.; Jia, Q.; Wang, H.; Won Noh, T.; Kalinin, S. V.; MacManus-Driscoll, J.L. Strongly Enhanced Oxygen Ion Transport through Samarium-Doped CeO_2 Nanopillars in Nanocomposite Films. *Nat. Commun.* **2015**, *6*, 1–8, doi:10.1038/ncomms9588.

UNIVERSIDAD DE MÁLAGA

6. Cho, S.; Yun, C.; Tappertzhofen, S.; Kursumovic, A.; Lee, S.; Lu, P.; Jia, Q.; Fan, M.; Jian, J.; Wang, H.; MacManus-Driscoll, J.L. Self-Assembled Oxide Films with Tailored Nanoscale Ionic and Electronic Channels for Controlled Resistive Switching. *Nat. Commun.* **2016**, *7*, doi:10.1038/ncomms12373.
7. Šimek, D.; Kužel, R.; Rafaja, D. Reciprocal-Space Mapping for Simultaneous Determination of Texture and Stress in Thin Films. *J. Appl. Crystallogr.* **2006**, *39*, 487–501, doi:10.1107/S0021889806015500.
8. Sun, X.; MacManus-Driscoll, J.L.; Wang, H. Spontaneous Ordering of Oxide-Oxide Epitaxial Vertically Aligned Nanocomposite Thin Films. *Annu. Rev. Mater. Res.* **2020**, *50*, 229–253, doi:10.1146/annurev-matsci-091719-112806.
9. Misra, S.; Wang, H. Review on the Growth, Properties and Applications of Self-Assembled Oxide-Metal Vertically Aligned Nanocomposite Thin Films-Current and Future Perspectives. *Mater. Horizons* **2021**, *8*, 869–884, doi:10.1039/d0mh01111h.
10. Zheng, H.; Zhan, Q.; Zavaliche, F.; Sherburne, M.; Straub, F.; Cruz, M.P.; Chen, L.; Dahmen, U.; Ramesh, R. Controlling Self-Assembled Perovskite − Spinel Nanostructures. **2006**, 1–7.
11. Brune, H.; Giovannini, M.; Bromann, K.; Kern, K. Self-Organized Growth of Nanostructure Arrays on Strain-Relief Patterns. *Nature* **1998**, *394*, 451–453, doi:10.1038/28804.
12. Biswas, A.; Rossen, P.B.; Yang, C.H.; Siemons, W.; Jung, M.H.; Yang, I.K.; Ramesh, R.; Jeong, Y.H. Universal Ti-Rich Termination of Atomically Flat $SrTiO_3$ (001), (110), and (111) Surfaces. *Appl. Phys. Lett.* **2011**, *98*, doi:10.1063/1.3549860.
13. Kim, K.J.; Han, H.; Defferriere, T.; Yoon, D.; Na, S.; Kim, S.J.; Dayaghi, A.M.; Son, J.; Oh, T.S.; Jang, H.M.; et al. Facet-Dependent in Situ Growth of Nanoparticles in Epitaxial Thin Films: The Role of Interfacial Energy. *J. Am. Chem. Soc.* **2019**, *141*, 7509–7517, doi:10.1021/jacs.9b02283.
14. MacManus-Driscoll, J.; Suwardi, A.; Kursumovic, A.; Bi, Z.; Tsai, C.F.; Wang, H.; Jia, Q.; Lee, O.J. New Strain States and Radical Property Tuning of Metal Oxides Using a Nanocomposite Thin Film Approach. *APL Mater.* **2015**, *3*, doi:10.1063/1.4919059.
15. Zhang, K.; Dai, J.; Zhu, X.; Zhu, S.; Yin, L.; Tang, X.; Sun, Y. Vertically Aligned Nanostructure Control and Tunable Low-Field Magnetoresistance in $La_{0.5}Ca_{0.5}MnO_3$ Single-Phase Thin Films Manipulated by a High Magnetic Field. *Appl. Phys. Lett.* **2020**, *116*, 0–5, doi:10.1063/1.5141389.
16. Thirumalairajan, S.; Girija, K.; Hebalkar, N.Y.; Mangalaraj, D.; Viswanathan, C.; Ponpandian, N. Shape Evolution of Perovskite $LaFeO_3$ Nanostructures: A Systematic Investigation of Growth Mechanism, Properties and Morphology Dependent Photocatalytic Activities. *RSC Adv.* **2013**, *3*, 7549–7561, doi:10.1039/c3ra00006k.
17. Li, J.P.H.; Zhou, X.; Pang, Y.; Zhu, L.; Vovk, E.I.; Cong, L.; Van Bavel, A.P.; Li, S.; Yang, Y. Understanding of Binding Energy Calibration in XPS of Lanthanum Oxide by: In Situ Treatment. *Phys. Chem. Chem. Phys.* **2019**, *21*, 22351–22358, doi:10.1039/c9cp04187g.
18. Abd El-Naser, A.; Abdel-Khalek, E.K.; Nabhan, E.; Rayan, D.A.; Gaafar, M.S.; Abd El-Aal, N.S. Study the Influence of Oxygen-Deficient (δ = 0.135) in $SrFeO_{3-\delta}$ Nanoparticles Perovskite on Structural, Electrical and Magnetic Properties. *Philos. Mag.* **2021**, *101*, 710–728, doi:10.1080/14786435.2020.1862427.
19. Yaremchenko, A.A.; Patrício, S.G.; Frade, J.R. Thermochemical Behavior and Transport Properties of Pr-Substituted $SrTiO_3$ as Potential Solid Oxide Fuel Cell Anode. *J. Power Sources* **2014**, *245*, 557–569, doi:10.1016/j.jpowsour.2013.07.019.
20. Hu, S.; Zhang, L.; Liu, H.; Cao, Z.; Yu, W.; Zhu, X.; Yang, W. Alkaline-Earth Elements (Ca, Sr

UNIVERSIDAD DE MÁLAGA

and Ba) Doped $LaFeO_{3-\delta}$ Cathodes for CO_2 Electroreduction. *J. Power Sources* **2019**, *443*, 227268, doi:10.1016/j.jpowsour.2019.227268.

21. Marcucci, A.; Zurlo, F.; Sora, I.N.; Placidi, E.; Casciardi, S.; Licoccia, S.; Di Bartolomeo, E. A Redox Stable Pd-Doped Perovskite for SOFC Applications. *J. Mater. Chem. A* **2019**, *7*, 5344–5352, doi:10.1039/c8ta10645b.
22. Bu, Y.; Zhong, Q.; Xu, D.; Tan, W. Redox Stability and Sulfur Resistance of $Sm_{0.9}Sr_{0.1}Cr_xFe_{1-x}O_{3-\delta}$ Perovskite Materials. *J. Alloys Compd.* **2013**, *578*, 60–66, doi:10.1016/j.jallcom.2013.05.020.
23. Borchert, H.; Borchert, Y.; Kaichev, V. V.; Prosvirin, I.P.; Alikina, G.M.; Lukashevich, A.I.; Zaikovskii, V.I.; Moroz, E.M.; Paukshtis, E.A.; Bukhtiyarov, V.I.; et al. Nanostructured, Gd-Doped Ceria Promoted by Pt or Pd: Investigation of the Electronic and Surface Structures and Relations to Chemical Properties. *J. Phys. Chem. B* **2005**, *109*, 20077–20086, doi:10.1021/jp051525m.
24. Liu, Y.; Fan, L.; Cai, Y.; Zhang, W.; Wang, B.; Zhu, B. Superionic Conductivity of Sm^{3+}, Pr^{3+}, and Nd^{3+} Triple-Doped Ceria through Bulk and Surface Two-Step Doping Approach. *ACS Appl. Mater. Interfaces* **2017**, *9*, 23614–23623, doi:10.1021/acsami.7b02224.
25. Romeo, M.; Bak, K.; El Fallah, J.; Le Normand, F.; Hilaire, L. XPS Study of the Reduction of Cerium Dioxide. *Surf. Interface Anal.* **1993**, *20*, 508–512, doi:10.1002/sia.740200604.
26. Sirvent, J. de D.; Carmona, A.; Rapenne, L.; Chiabrera, F.; Morata, A.; Burriel, M.; Baiutti, F.; Tarancón, A. Nanostructured $La_{0.75}Sr_{0.25}Cr_{0.5}Mn_{0.5}O_3$-$Ce_{0.8}Sm_{0.2}O_2$ Heterointerfaces as All-Ceramic Functional Layers for Solid Oxide Fuel Cell Applications. *ACS Appl. Mater. Interfaces* **2022**, *14*, 42178–42187, doi:10.1021/acsami.2c14044.
27. Gao, Y.; Chen, D.; Chen, C.; Shao, Z.; Ciucci, F. Oriented $PrBaCo_2O_{5+\delta}$ Thin Films for Solid Oxide Fuel Cells. *J. Power Sources* **2015**, *278*, 623–629, doi:10.1016/j.jpowsour.2014.12.110.
28. Osinkin, D.A. An Approach to the Analysis of the Impedance Spectra of Solid Oxide Fuel Cell Using the DRT Technique. *Electrochim. Acta* **2021**, *372*, 137858, doi:10.1016/j.electacta.2021.137858.
29. Osinkin, D.A. Detailed Analysis of Electrochemical Behavior of High–Performance Solid Oxide Fuel Cell Using DRT Technique. *J. Power Sources* **2022**, *527*, doi:10.1016/j.jpowsour.2022.231120.
30. Bocquet, A.E.; Fujimori, A.; Mizokawa, T.; Saitoh, T.; Namatame, H.; Suga, S.; Kimizuka, N.; Takeda, Y.; Takano, M. Electronic Structure of $SrFe^{4+}O_3$ and Related Fe Perovskite Oxides. *Phys. Rev. B* **1992**, *45*, 1561–1570, doi:10.1103/PhysRevB.45.1561.
31. Dos Santos-Gómez, L.; Porras-Vázquez, J.M.; Losilla, E.R.; Marrero-López, D. Ti-Doped $SrFeO_3$ Nanostructured Electrodes for Symmetric Solid Oxide Fuel Cells. *RSC Adv.* **2015**, *5*, 107889–107895, doi:10.1039/c5ra23771h.
32. Connor, P.A.; Yue, X.; Savaniu, C.D.; Price, R.; Triantafyllou, G.; Cassidy, M.; Kerherve, G.; Payne, D.J.; Maher, R.C.; Cohen, L.F.; Irvine, J.T.S. Tailoring SOFC Electrode Microstructures for Improved Performance. *Adv. Energy Mater.* **2018**, *8*, 1–20, doi:10.1002/aenm.201800120.
33. dos Santos-Gómez, L.; Zamudio-García, J.; Porras-Vázquez, J.M.; Losilla, E.R.; Marrero-López, D. Recent Progress in Nanostructured Electrodes for Solid Oxide Fuel Cells Deposited by Spray Pyrolysis. *J. Power Sources* **2021**, *507*, doi:10.1016/j.jpowsour.2021.230277.
34. Su, Q.; Yoon, D.; Sisman, Z.; Khatkhatay, F.; Jia, Q.; Manthiram, A.; Wang, H. Vertically Aligned Nanocomposite $La_{0.8}Sr_{0.2}MnO_{3-\delta}$/$Zr_{0.92}Y_{0.08}O_{1.96}$ Thin Films as Electrode/Electrolyte Interfacial Layer for Solid Oxide Reversible Fuel Cells. *Int. J. Hydrogen Energy* **2013**, *38*,

UNIVERSIDAD DE MÁLAGA

16320–16327, doi:10.1016/j.ijhydene.2013.09.128.

35. Dix, N.; Muralidharan, R.; Warot-Fonrose, B.; Varela, M.; Sánchez, F.; Fontcuberta, J. Critical Limitations in the Fabrication of Biferroic $BiFeO_3$-$CoFe_2O_4$ Columnar Nanocomposites Due to Bismuth Loss. *Chem. Mater.* **2009**, *21*, 1375–1380, doi:10.1021/cm803480q.

36. Jiang, J.; Yang, Q.; Zhang, Y.; Li, X.Y.; Shao, P.W.; Hsieh, Y.H.; Liu, H.J.; Peng, Q.X.; Zhong, G.K.; Pan, X.Q. Self-Assembled Ferroelectric Nanoarray. *ACS Appl. Mater. Interfaces* **2019**, *11*, 2205–2210, doi:10.1021/acsami.8b14775.

UNIVERSIDAD DE MÁLAGA

Chapter 9

UNIVERSIDAD
DE MÁLAGA

UNIVERSIDAD
DE MÁLAGA

VAN with exsolved Ni nanoparticles

In this Chapter, Vertically Aligned Nanostructures (VAN) derived from the titanate-based electrodes studied in Chapter 5, $(Sr_{0.9}Pr_{0.1})_{0.9}Ti_{0.9}Ni_{0.1}O_{3-\delta}$-$Ce_{0.9}Gd_{0.1}O_{1.95}$ (SPTNO-CGO), were prepared by PLD. To the best of my knowledge, the exsolution of Ni metal nanoparticles in a VAN is studied for the first time in this work. The influence of the columnar microstructure on the nanoparticle shape and population density was investigated. Different reduction times were tested in order to study the nanoparticle growth process in a VAN. The sample preparation and the structural characterization were carried out during an external stay for 4 months at the Technical University of Denmark (DTU) under the supervision of Profs. Nini Pryds and Vincenzo Esposito.

UNIVERSIDAD DE MÁLAGA

9.1. Synthesis and structural characterization of SPTNO-CGO VAN

The SPTNO and SPTNO-CGO targets were prepared from the corresponding oxides and carbonates $SrCO_3$, Pr_6O_{11}, TiO_2, NiO and CGO by conventional solid-state reaction. It is worth mentioning that the targets for the film deposition by PLD were prepared with A-site deficiency to promote the exsolution of Ni nanoparticles in reducing conditions [1,2]. Further details about the target preparation can be found in section 3.4. SPTNO and SPTNO-CGO thin films were deposited by PLD onto $SrTiO_3$ (STO) and $(LaAlO_3)_{0.3}(Sr_2TaAlO_6)_{0.7}$ (LSAT) (001) single crystals at 650 ºC at 10 Hz for 20 min. The films were deposited onto highly insulating LSAT (001) substrates to study the electrical conductivity, while STO (001) was employed for the structural and microstructural analysis. Hereafter, the SPTNO-CGO thin film will be labelled as "SPTNO-CGO VAN".

Figure 9.1 shows the θ-2θ XRD diffraction patterns of SPTNO film and SPTNO-CGO VAN deposited onto STO (001) at 650 ºC in O_2 and then reduced in 5% H_2-Ar. In the case of the SPTNO film, a cubic structure with a fully epitaxial growth along the (001) orientation is observed without the presence of other crystallographic orientations (Figure 9.1a,c).

The similar out-of-plane lattice parameter of the SPTNO film (3.962 Å) with the STO substrate (3.905 Å) leads to a cube-on-cube growth with a (00*l*) preferred orientation. In this case, the very low lattice mismatch $f \sim 1.4\%$ between the unstrained polycrystalline SPTNO (3.919 Å) and the SPTNO film (3.962 Å) leads to an epitaxial strained film with a coherent interface [2].

After reduction at 650 ºC for 6 h (Figure 9.1a,c), the out-of-plane lattice parameter of SPTNO decreases from 3.962 to 3.930 Å, a behaviour that is similar to that observed previously for other Ni-doped $SrTiO_3$-based epitaxial films [3–5]. Although the partial reduction of Ti^{4+} to Ti^{3+} induces a lattice cell expansion, the concomitant reduction of NiO from the lattice to form Ni^0 nanoparticles on the electrode surface results in a larger cell contraction. This fact would explain the counterintuitive out-of-plain lattice expansion in reducing conditions.

UNIVERSIDAD DE MÁLAGA

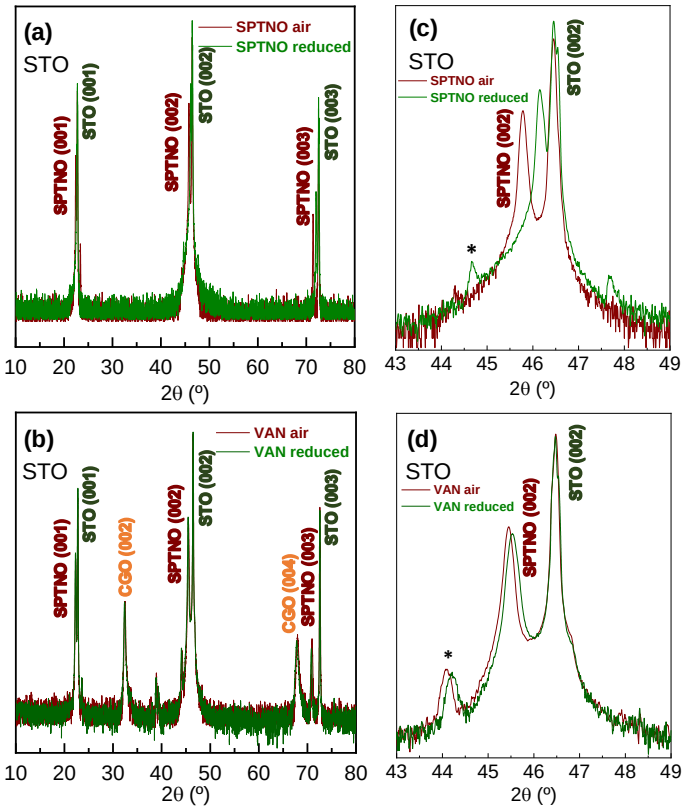

Figure 9.1. θ-2θ XRD patterns of (a) SPTNO and (b) SPTNO-CGO VAN deposited onto STO (001) at 650 ºC; and the corresponding high-resolution XRD patterns near the (c,d) STO (002) showing the epitaxial growth of SPTNO phase in the (00*l*) direction.

In the case of the SPTNO-CGO VAN, the SPTNO phase also shows a perovskite structure with a cube-on-cube epitaxial growth along the (001) orientation with a lattice parameter of 3.988 Å, which is slightly higher to that observed for the SPTNO film (3.962 Å), indicating a certain vertical strain, as expected (Figure 9.1c,d). Additionally, a certain cation intermixing of praseodymium from SPTNO into CGO lattice is plausible, but a negative influence is not expected as observed in previous nanocomposite materials [6,7]. In the case of the CGO phase, a similar behavior to that observed in Chapter 8 for $LSFT_{0.2}$-CGO VAN phase is observed, in which the CGO fluorite phase is successfully accommodated onto STO (001) by a 45º in-plane rotation of the cell. This hypothesis was confirmed by the presence of only (002) and (004) reflections, which indicates an epitaxial growth of the CGO component. The

UNIVERSIDAD DE MÁLAGA

lattice mismatch *f* for both phases was 3.5 and 1.6 % for SPTNO and CGO, respectively, leading to high quality epitaxial films due to the low lattice misfit [2].

When the SPTNO-CGO VAN was reduced 650 ºC for 6 h, only a minor decrease of the out-of-plane lattice parameter for the SPTNO phase is observed, from 3.988 to 3.981 Å, while the CGO phase remained practically unchanged, as observed previously for the $LSFT_{0.2}$-CGO VAN in the previous chapter. This behavior is presumably attributed to the unique microstructure of the VAN film, in which both in-plane and vertical strain are present due to the coexistence of columns of two different materials, impeding large changes in the cell volume. It is worth mentioning that a minor reflection at 2θ=39º in the VAN film is observed due to the presence of a (111) orientation for the SPTNO phase. In addition, the extra peak centered at 2θ=44º highlighted with an asterisk (*), can be assigned to the out-of-plane relaxation of the SPTNO cell.

In this work, the SPTNO phase crystallizes in a perovskite structure as previously observed for polycrystalline SPTO powders (s.g. $Pm\bar{3}m$) in Chapter 5. This finding indicates that Ni-doping into SPTO does not modify the crystal structure of the parent compound and more interestingly, the crystal structure is retained after Ni-exsolution under a reducing atmosphere, confirming the good redox stability of the $SrTiO_3$-based nanomaterials [8].

Further information about the nanostructure ordering and strain was obtained from the reciprocal space maps (RMS) in air of the SPTNO on LSAT (001) and SPTNO-CGO VAN on STO (001) in the asymmetric reflection ($\bar{1}\bar{1}3$) (Figure 9.2). The SPTNO film is strained, showing almost identical in-plain lattice parameter ($a_{x,y}$=3.886 Å) to the LSAT substrate but different out-of-plain lattice parameter (a_z=3.955 Å), as previously observed in the θ-2θ XRD patterns. In the case of the SPTNO-CGO VAN, an additional and relatively strained broad band associated with the CGO phase is observed. The widespread of in-plain lattice parameters is responsible for the broad shape of this band, as observed previously for other CeO_2-based films deposited onto perovskite single crystals [2,9,10]. As observed for the single film, the SPTNO phase in the SPTNO-CGO VAN deposited onto STO is strained with an in-plain lattice parameter of $a_{x,y}$=3.991 Å and out-of-plain lattice parameter of a_z=3.954 Å, which are

UNIVERSIDAD DE MÁLAGA

similar to those observed for SPTNO film. In the case of the CGO component, the in-plane lattice parameters range from 5.415 to 5.624 Å, while a similar out-of-plane lattice parameter to that observed in the θ-2θ XRD is obtained. It is also worth mentioning that the in-plane lattice parameter for the polycrystalline CGO is slightly higher than that reported in the literature (~5.41 Å), which is attributed to the in-plane strain induced by the substrate and a possible minor cation exchange between SPTNO and CGO.

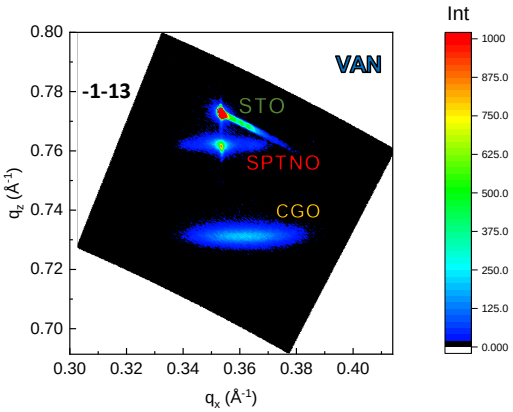

Figure 9.2. Reciprocal space map in the ($\bar{1}\bar{1}3$) asymmetric reflection of SPTNO-CGO VAN deposited on STO (001).

9.2. Microstructural characterization

The microstructure of the SPTNO-CGO VAN film was studied in detail by HAADF-STEM (Figure 9.3). The low-magnification STEM image shows a general overview of the film thickness and the long-range columnar architecture (Figure 9.3a). The SPTNO-CGO VAN film has a dense microstructure with a homogeneous thickness of about 200 nm, as well as columns of approximately 5 nm width.

It is worth mentioning that the film thickness of this VAN is one of the highest reported in the literature [2,10–12], in which well-defined columns with 200 nm length are clearly discernible without losing the strain induced by the substrate, which is attributed to the influence of the vertical interfacial strain. Typically, epitaxial films with more than 100 nm thick suffer from structure relaxation, changing their properties away from the substrate [2]. In contrast, the VAN heterostructures in this study retain their columnar morphology even with a 200 nm thickness, opening the possibility to

UNIVERSIDAD DE MÁLAGA

explore thicker VANs in the future with controlled microstructure for their application in energy conversion devices.

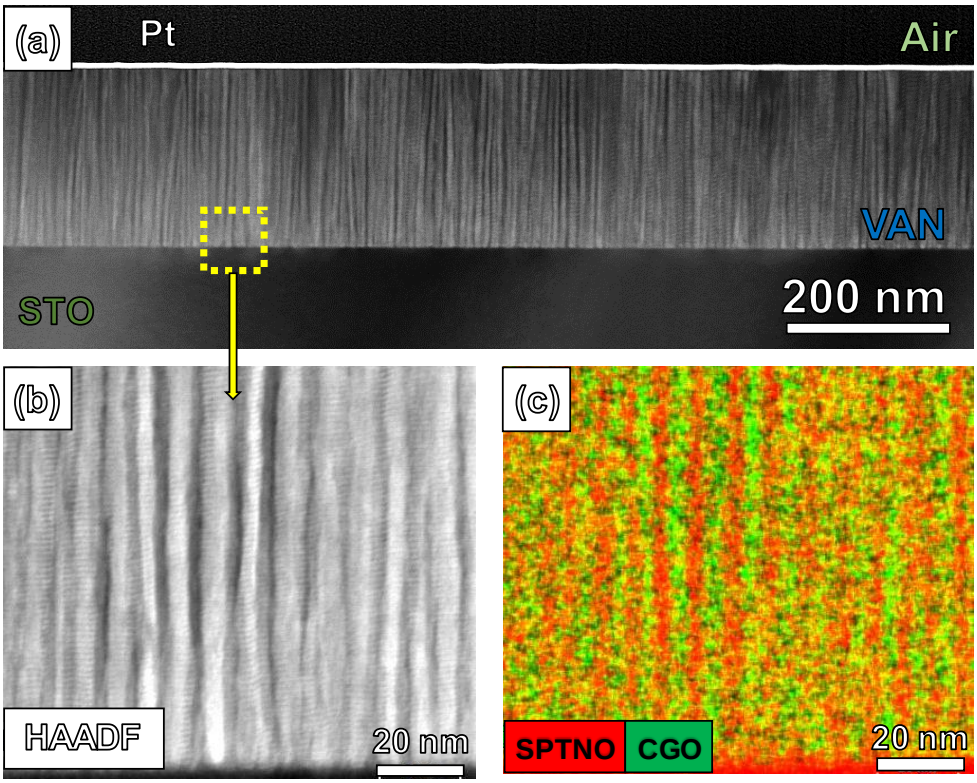

Figure 9.3. (a) Low magnification cross-sectional HAADF-STEM image of the SPTNO-CGO VAN film deposited onto STO (001) substrate at 650 ºC. (b) HAADF-STEM image at high magnification and (c) EDS of a selected area of the VAN film close to the substrate surface, showing the presence of alternating 5 nm width columns of both SPTNO and CGO phases.

EDS analysis further confirms the formation of alternating columns of SPTNO and CGO in the VANs (Figure 9.3b,c). More interestingly, the composition of the columns is maintained in the whole film thickness, despite that a minor cation exchange is plausible as commented previously.

HRTEM images of the SPTNO-CGO VAN confirm the formation of highly crystalline nanopillars of both SPTNO and CGO phases (Figure 9.4a). A higher magnification image clearly shows that the CGO width columns (in dark) are homogeneously distributed in the SPTNO bright matrix (Figure 9.4b). These results

UNIVERSIDAD DE MÁLAGA

confirm the spontaneous ordering of both phases on STO (001) substrate. Both SPTNO and CGO show an epitaxial growth in the (001) orientation. Interestingly, the 45º in-plane rotation is observed for the CGO component to minimize the lattice mismatch. The d-spacing obtained for both phases is in accordance with the XRD results.

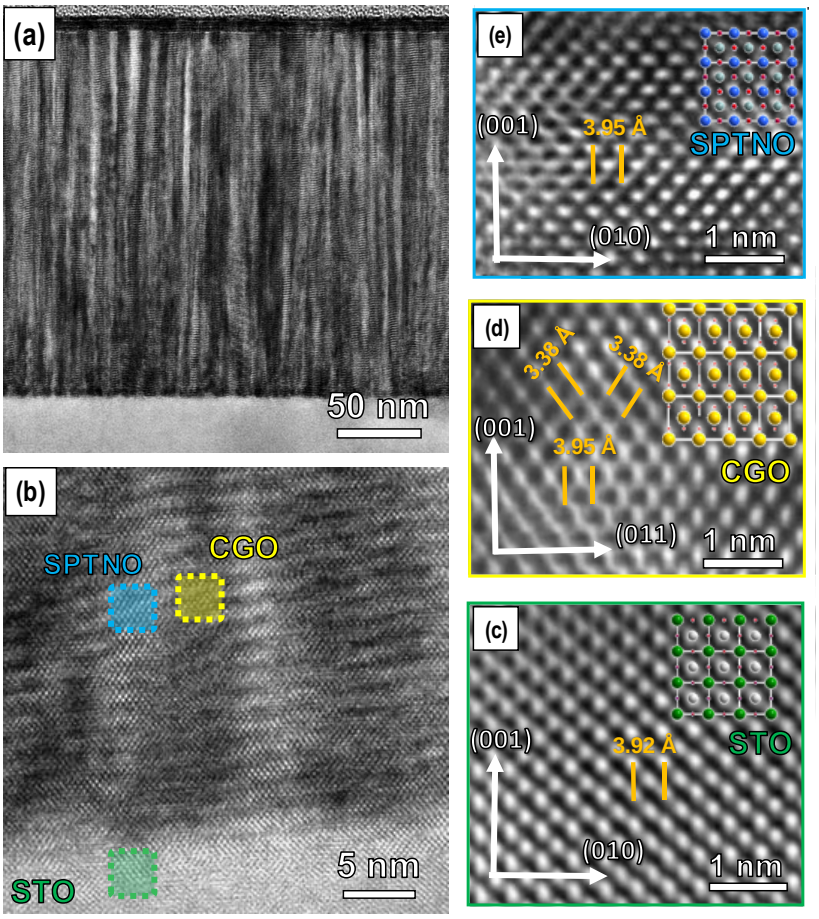

Figure 9.4. (a,b) HRTEM images of the SPTNO-CGO VAN at different magnifications. Atomic arrangement of (c) STO substrate, (d) CGO and (e) SPTNO phases.

The films were reduced in 5% H_2-Ar at 650 ºC for 12 h in order to promote the exsolution of Ni nanoparticles on the surface. Figure 9.5a,b compare low-magnification SEM images of the surface of SPTNO and SPTNO-CGO VAN films with

UNIVERSIDAD DE MÁLAGA

the presence of Ni metal nanoparticles, as confirmed later by EDS analysis (Figure 9.6).

As can be observed, the particle size, shape and population density are different in both samples. The average particle size of the Ni nanoparticles in the SPTNO film is ~ 120 nm (Figure 9.5a,b), considerably higher than that for the VAN ~ 67 nm (Figure 9.5c,d). In addition, the population density of Ni nanoparticles in the VAN is higher than that observed for the SPTNO. These results reveal that the columnar VAN film morphology could suppress the Ni growth due to NiO diffusion limitations through the CGO columns and the stronger interaction with the substrate. The higher population density in the VAN is desirable for energy applications because of the higher active sites for the electrochemical reactions, thus improving the performance.

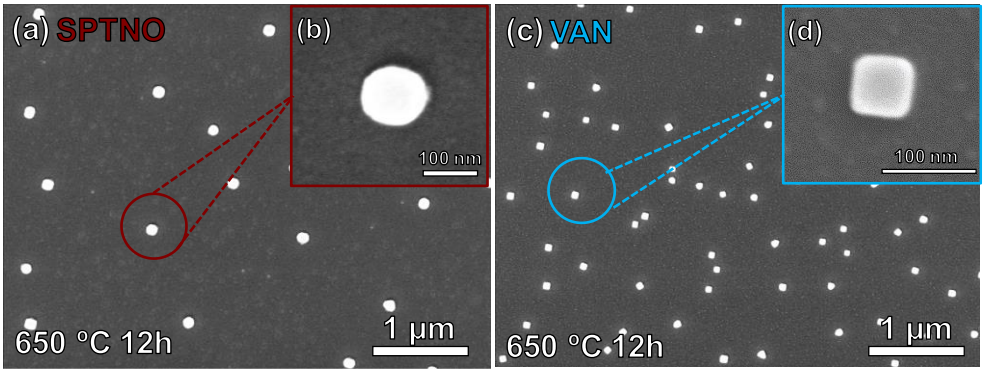

Figure 9.5. Top-view SEM images of (a) SPTNO and (c) SPTNO-CGO VAN samples after the reduction treatment at 650 ºC for 12 h in 5% H_2-Ar and (b,d) the corresponding high magnification SEM images showing the shape of the Ni-exsolved nanoparticles.

The shape of the Ni nanoparticles is also different for SPTNO film and SPTNO-CGO VAN (Figure 9.5b,d). SPTNO film shows spherical nanoparticles (isotropic growth) while a square-shape (anisotropic growth) is observed in the case of the VAN. This finding indicates that the microstructure of the VAN film promotes the formation of oriented Ni nanoparticles, presumably in the (001) orientation, which has the lower energy interface orientation due to the STO (001) substrate. On the other hand, no preferred orientation growth is observed on the SPTNO film, suggesting that either oriented Ni nanoparticles are not formed on this substrate or more time is

UNIVERSIDAD DE MÁLAGA

needed to achieve the lower energy interface orientation. The different findings for both films are not surprising, since the surface diffusivity of Ni is reported to be anisotropic on different metal oxide supports [13,14]. Since the microstructure and composition of the SPTNO (coherent epitaxial film) and VAN (columnar microstructure with vertical interfaces) are different, the NiO diffusion paths could be also different, affecting both the mobility and the growth mechanism of Ni nanoparticles [13]. The high concentration of interfaces in the VAN is expected to have a positive effect on the exsolution of metal nanoparticles because they can provide fast diffusion pathways for NiO towards the surface. In addition, the grain-boundary interfaces and defects are also preferred sites for the nucleation of metallic nanoparticles [15].

The composition of the exsolved particles was confirmed by EDS analysis (Figure 9.6). As can be seen, the EDS mapping confirms the composition of the Ni nanoparticles on surface without the presence of secondary phases induced by the exsolution of Ni from the lattice (Figure 9.6b). The Ti and Sr EDS mappings show a homogeneous cation distribution in the film (Figure 9.6c,d).

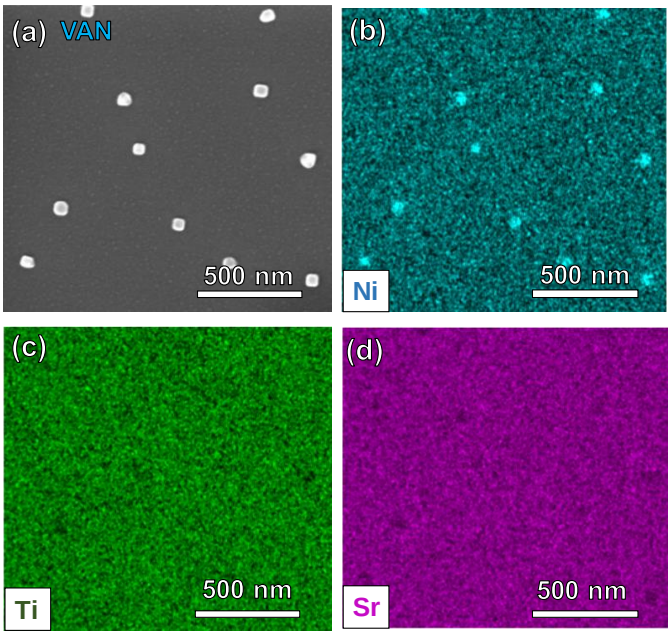

Figure 9.6. SEM image and EDS analysis of the SPTNO-CGO VAN after the reduction treatment at 650 ºC for 12 h in 5% H_2-Ar, confirming the presence of Ni-nanoparticles.

UNIVERSIDAD DE MÁLAGA

AFM images of the SPTNO and VAN before and after reduction are displayed in Figure 9.7. Both films show a dense microstructure with a similar roughness and lower than 1 nm (Figure 9.7a,b). After reduction, Ni nanoparticles are discernible in both films, showing the VAN a higher particle density and lower size (Figure 9.7c,d). It is worth mentioning that the height of the particles for the SPTNO and VAN is around 84 and 58 nm, respectively, which are somewhat lower than the corresponding particle diameter determined from SEM images, suggesting that the Ni nanoparticles are not perfectly spherical, since they are presumably socketed to the parent perovskite [3].

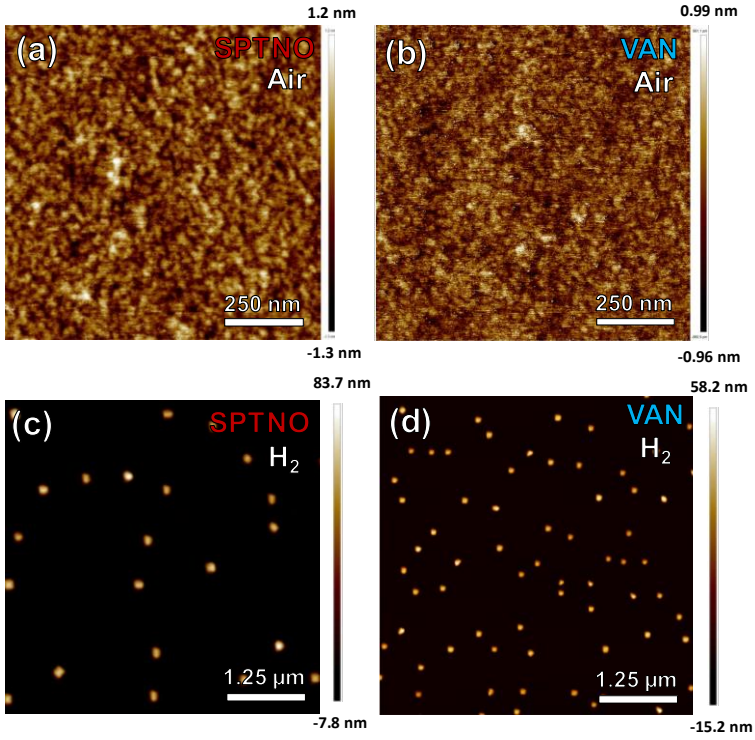

Figure 9.7. Top-view AFM images of (a) SPTNO and (b) SPTNO-CGO VAN in air and (c,d) the corresponding images after the reduction treatment at 650 ºC for 12 h in 5% H_2-Ar.

The cross-section of the SPTNO-CGO VAN film was studied by HAADF-STEM after reduction at 650 ºC for 12 h to evaluate the effect of the exsolution process on the columnar microstructure (Figure 9.8). Figure 9.8a,b confirms that the long-range columnar ordering remains unaltered after the Ni-exsolution process and the

UNIVERSIDAD DE MÁLAGA

columns of both phases are clearly discernible in the HAADF-STEM image. EDS analysis further confirms the presence of nickel on the surface of the VAN structure (Figure 9.8c-e).

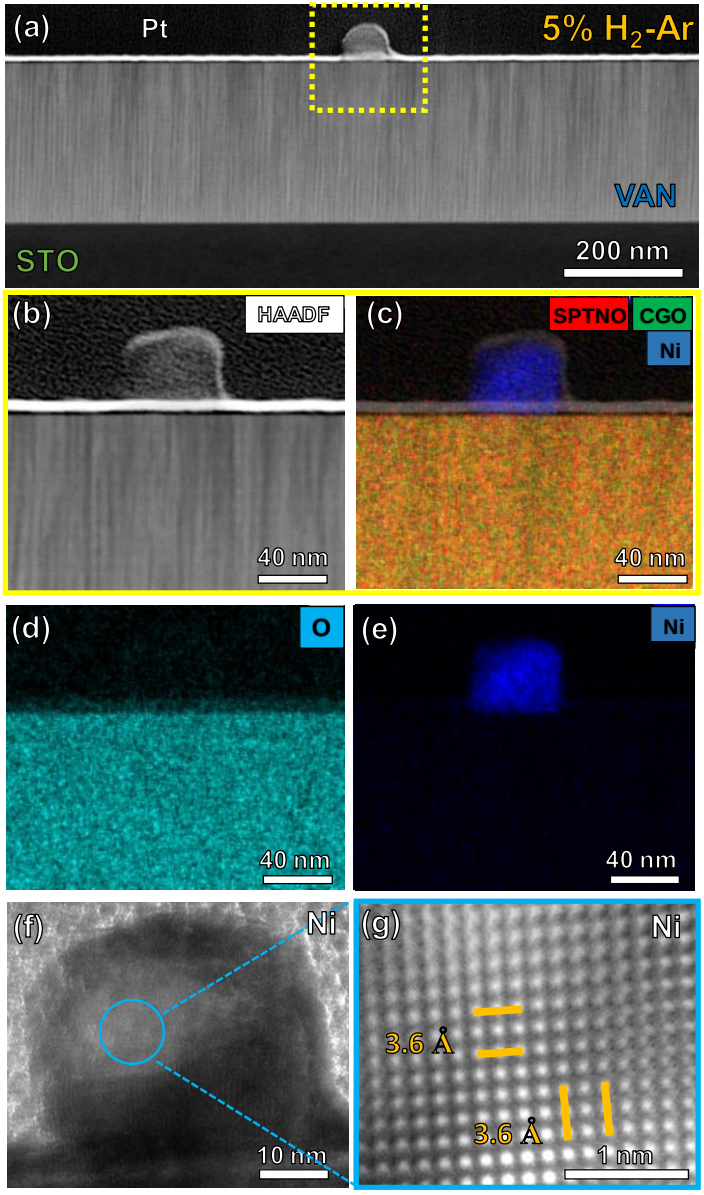

Figure 9.8. (a) Cross-sectional HAADF-STEM image of the SPTNO-CGO VAN film after reduction at 650 ºC in 5% H_2-Ar for 12 h. (b) HAADF-STEM image and (c,e) EDS mappings. (f,g) HRTEM images of the Ni exsolved nanoparticle showing the atomic ordering.

UNIVERSIDAD DE MÁLAGA

Interestingly, the film is still fully dense without the presence of visible porosity or film degradation after the Ni-exsolution process. In contrast, previous reports about $La_{0.2}Sr_{0.7}Ti_{0.9}Ni_{0.1}O_{3-\delta}$ film deposited onto STO (001) have shown that the Ni-exsolution induces a partial degradation of the film with the formation of porosity and phase inhomogeneities [4,16]. Similar findings were found for the Ni exsolution from other perovskite-based materials deposited by PLD onto STO (001), such as $La_{0.2}Ba_{0.7}Sn_{0.9}Ni_{0.1}O_{3-\delta}$ [17] or $BaZr_{0.9}Y_{0.1}O_{3-\delta}$ with 1 wt. % Ni [13]. The HRTEM image of the Ni nanoparticle shows a d-spacing of 3.6 Å, which is in accordance with the one expected for the Ni-metal (Figure 9.8f,g).

9.3. Influence of the reduction time on the Ni-nanoparticle growth

The SPTNO-CGO VAN samples were reduced at 650 ºC in 5% H_2-Ar at different times in order to investigate the influence of the reduction time on the Ni nanoparticle growth, as well as the nucleation mechanism (Figure 9.9).

The sample reduced at 650 ºC for only 1 minute and then fast cooled down to room temperature (quenching) shows a very low Ni-nanoparticle size of ~ 17 nm and a high population density (~ 100 particles μm^{-2}) (Figure 9.9a). This particle size and population density are desirable for different catalytic and energy applications due to the good distribution of the Ni. After the reduction at 650 ºC for 1 h with a cooling ramp of 3 ºC min^{-1}, the population density significantly decreases to 5 particles per μm^{-2} while the particle size increases up to ~46 nm (Figure 9.9b). In this case, the Ni migration and coalescence induce the particle growth. The Ni metal nanoparticles show an irregular shape and they are surrounded by a secondary phase, presumably nickel oxide. The nature of this second phase is still unclear but a similar particle shape was found in other reports of Ni-exsolved nanoparticles in thin films, such as $La_{0.8}Ce_{0.1}Ni_{0.4}Ti_{0.6}O_{3-\delta}$ [18] and $La_{0.2}Sr_{0.7}Ti_{0.9}Ni_{0.1}O_{3-\delta}$ [19] and also in the Fe-Co bimetallic exsolution in $La_{0.3}Sr_{0.7}Cr_{0.3}Fe_{0.6}Co_{0.1}O_{3-\delta}$ [20]. Further research is needed to elucidate the nature of this intermediate stage in the nucleation of Ni nanoparticles in a VAN.

UNIVERSIDAD DE MÁLAGA

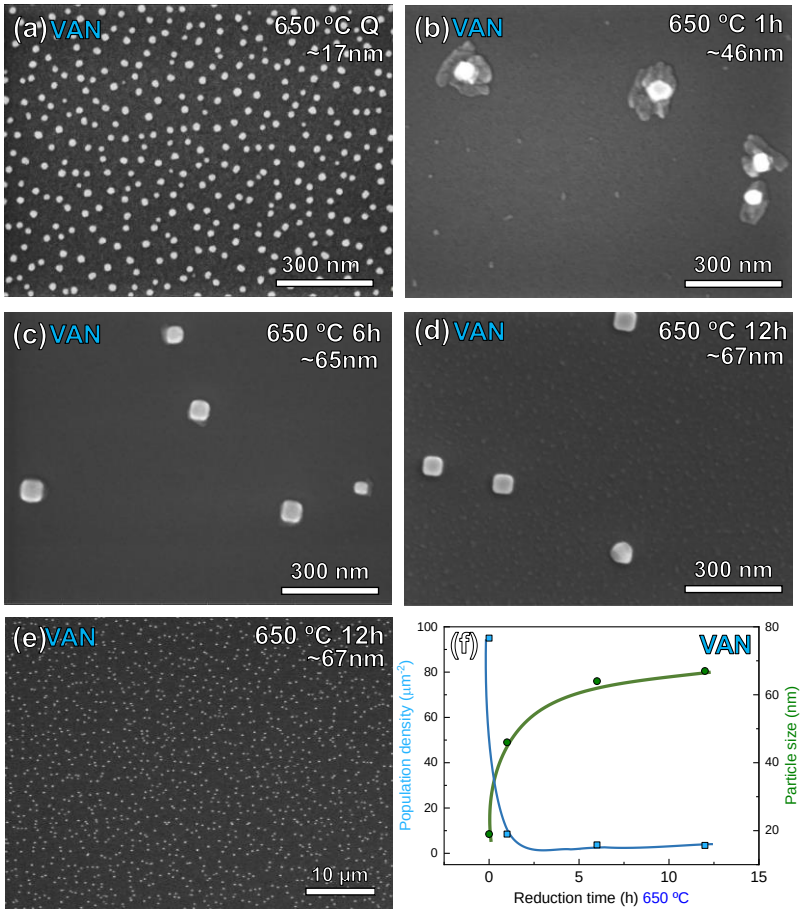

Figure 9.9. SEM images of the SPTNO-CGO VAN at different reduction times at 650 ºC in 5% H_2-Ar: (a) quenching, (b) 1 h, (c) 6 h and (d) 12 h. (e) Low magnification SEM image of the sample reduced for 12 h and (f) population density and particle size distribution as a function of the reduction time at 650 ºC

Increasing up to 6 h the reduction time leads to nanoparticles with a cubic shape, suggesting that the intermediate material is nucleating to form the Ni nanoparticles with an average size of ~ 65 nm (Figure 9.9c). After reduction for 12 h, the average particle size is very similar, ~ 67 nm, showing the particles a faceted shape, as commented previously. Interestingly, there is no presence of the intermediate phase, indicating that the nucleation process is completed (Figure 9.9d). A low-magnification SEM image shows that the Ni nanoparticles are homogeneously

UNIVERSIDAD DE MÁLAGA

distributed on the VAN surface without the presence of Ni agglomeration (Figure 9.9e). Figure 9.9f shows the population density and particle size distribution as a function of the reduction time. As expected, the Ni-nanoparticle grows up to 67 nm and the population density decreases. It is worth mentioning that other reduction temperatures could be explored to have a better overview of the Ni-exsolution process.

In order to establish a plausible mechanism for the particle growth, the different chemical processes in the lattice during the reduction process have to be studied in detail (Figure 9.10a,b). Firstly, the NiO has to diffuse through the film to the surface and then reduced to Ni-metal: $Ni^{2+} + 2e^- \rightarrow Ni^0$. The numerous vertical interfaces in the SPTNO-CGO VAN film provide a good diffusion path for NiO to the surface (Figure 9.10c), becoming the most probable diffusion mechanism [15,21]. However, the diffusion of nickel oxide inside the SPTNO columns cannot be excluded and need to be further studied by in-situ STEM and DFT calculations.

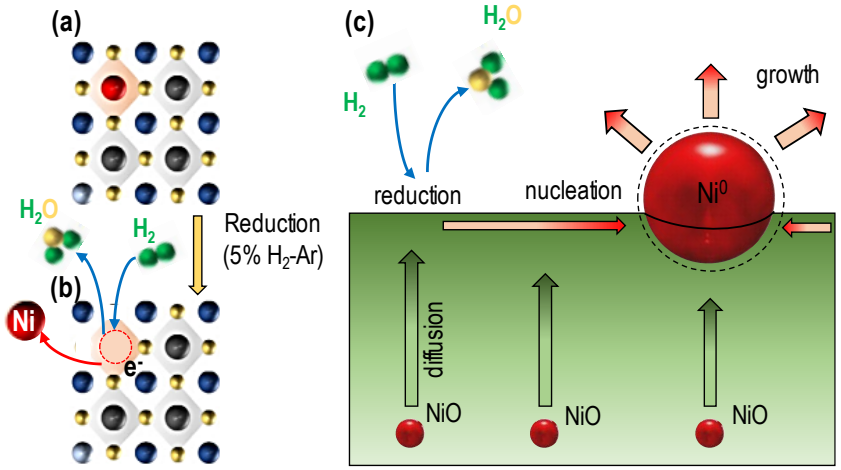

Figure 9.10. Illustration of the SPTNO perovskite lattice (a) in air and (b) after reduction showing the Ni-exsolution and (c) scheme of the Ni-exsolution process.

After the Ni^0 nanoparticle formation, the nucleation process induces the particle growth. In the literature, different mechanisms for the nanoparticle growth have been proposed, such as coalescence, Oswald ripening and evaporation-condensation growth, which are thermally activated [20]. It is worth remarking that

UNIVERSIDAD DE MÁLAGA

further analyses are needed to elucidate the particle growth mechanism and only preliminary insights based on previous reports are discussed in this work. In this study, the reduction temperature was fixed to 650 ºC due to this is the temperature employed for the preparation of the SPTNO-CGO VAN.

At this temperature, the evaporation-condensation growth is not favorable because very high temperatures are required (close to the melting point of the nickel nanoparticles). However, a decrease of the particle size below 10 nm induces a lower melting temperature, making possible this process at intermediate temperatures (~700 ºC) [20,22]. In this case, the particle migration and coalescence are feasible mechanisms when the nanoparticles are close to each other, as observed in Figure 9.9a. However, the strong interaction of the nanoparticles with the VAN matrix impedes this mechanism at large stages. Interestingly, the shape of the nanoparticles on a perovskite film has demonstrated to be highly influenced by the interfacial interaction between the nanoparticle and the perovskite support. In general, a weak particle-support interaction induces a spherical shape with a lower surface-area-to-volume ratio in order to decrease the surface energy, similar to traditional nanoparticles prepared by infiltration [23]. On the contrary, when the interaction between the metal and the oxide support is strong, the nanoparticle shape becomes hemispherical or faceted nanoparticles, as observed for SPTNO film and SPTNO-CGO VAN, respectively.

Another plausible particle growth mechanism is the Ostwald ripening, in which a large nanoparticle grows by incorporation of a neighboring smaller particle. The adjacent atoms migrate through the oxide support from the smaller particle to finally merge into a large particle [33]. Systems with strong metal-oxide interaction often show the Ostwald ripening as the main mechanism of particle growth, since the sluggish coalescence process. In this work, both coalescence and Ostwald ripening are possible mechanisms for the growth of Ni nanoparticles due to the low reduction temperature. Further research should be carried out towards to better understand the exsolution in order to control the Ni-nanoparticle growth and population density.

In order to study the redox stability of the Ni nanoparticles, the VAN film previously reduced at 650 ºC for 1 min was calcined in air at different times

UNIVERSIDAD DE MÁLAGA

(Figure 9.11). The reduced VAN exhibits a high population of Ni nanoparticles with spherical morphology as discussed previously (Figure 9.11a).

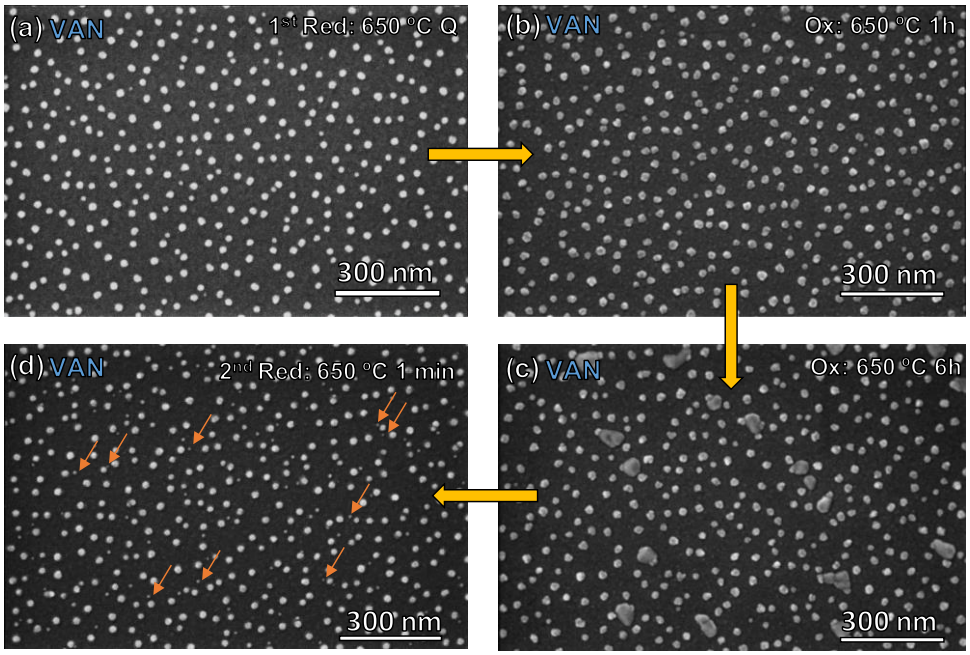

Figure 9.11 SEM images of the SPTNO-CGO VAN after (a) reduction at 650 ºC for 1 min in 5% H_2-Ar; reoxidation at 650 ºC in air for (b) 1 h and (c) 6 h and (d) second reduction at 650 ºC for 1 min.

After a thermal treatment in air at 650 ºC for 1 h (Figure 9.11b), the Ni exsolved nanoparticles remain stable and they are not redissolved into the SPTNO perovskite lattice; however, they become flatter, suggesting a partial oxidation to NiO. A prolonged oxidation treatment in air at 650 ºC for 6 h reveals the formation of a flat material close to the Ni nanoparticles, similar to that previously observed during the Ni nanoparticle formation under reducing atmosphere. Hence, this intermediate phase is possibly attributed to the formation of NiO. Interestingly, the particle size and population are stable without severe signs of decomposition or drift across the surface in contrast to other systems [22]. Finally, a second reduction treatment at 650 ºC for 1 min was performed, showing additional Ni nanoparticles with lower grain size (~5 nm, indicated with orange arrows), presumably coming from the intermediate material that is no longer present on the VAN surface. These particles can also come from the

UNIVERSIDAD DE MÁLAGA

SPTNO bulk that has a lower concentration of Ni due to the previous exsolution, leading to the formation of smaller nanoparticles. Interestingly, a reincorporation of the NiO into the VAN was not observed, presumably attributed to the columnar microstructure.

The good stability of the Ni-nanoparticles upon oxidation is very important for the implementation of the SPTNO-CGO VAN as an active layer for symmetrical SOFCs, since good cell reversibility has demonstrated to be crucial to avoid stability drawbacks, such as Sulphur poisoning and carbon deposition just by switching between fuel and oxidant feeds.

9.4. XPS characterization

The surface composition of the VAN film was studied by XPS after reduction/oxidation treatments (Figure 9.12). The O1s core level shows two different bands, centred at 529.1 and 531.4 eV, that can be attributed to lattice oxygen and carbonates adsorbed on surface, respectively [24] (Figure 9.12a). It is worth mentioning that it is not possible to differentiate the lattice oxygen from the SPTNO perovskite and the CGO fluorite phases since the binding energies are very similar, as observed for the $LSFT_{0.2}$-CGO VAN.

The Sr 3d presents a characteristic doublet, showing the Sr $3d_{5/2}$ band a binding energy of 132.6 eV, which is consistent with Sr^{2+}, as observed for $SrTiO_3$ [24] (Figure 9.12b). Similar XPS spectra were observed in the O1s and Sr3d core level after reduction in 5% H_2-Ar. The Pr $3d_{5/2}$ region shows two bands centered at 932.5 and 935.6 eV assigned to Pr^{4+} and Pr^{3+} (Figure 9.12c), respectively, similar to that reported for $Sr_{0.7}Pr_{0.3}Ti_{0.93}Co_{0.07}O_{3-\delta}$ [25] and $Sr_{0.8}Pr_{0.2}TiO_{3-\delta}$ [26]. The relatively low Pr-content in the sample impedes the correct identification of the Pr^{4+}/Pr^{3+} ratio (approximately 3:1), nevertheless, the main oxidation state for praseodymium in this sample is 3+. A similar Pr^{4+}/Pr^{3+} ratio and binding energies were observed after reduction. The Ti $2p_{3/2}$ core level in air shows a band at 457.9 eV characteristic of Ti^{4+}, similar to undoped $SrTiO_3$ [24] and Pr-doped $SrTiO_3$ compositions [25,26] (Figure 9.12d). It is worth mentioning that the presence of Ti^{3+} could not be identified at lower

UNIVERSIDAD DE MÁLAGA

binding energy, suggesting that the Ti^{3+} concentration is below the XPS detection limits [26].

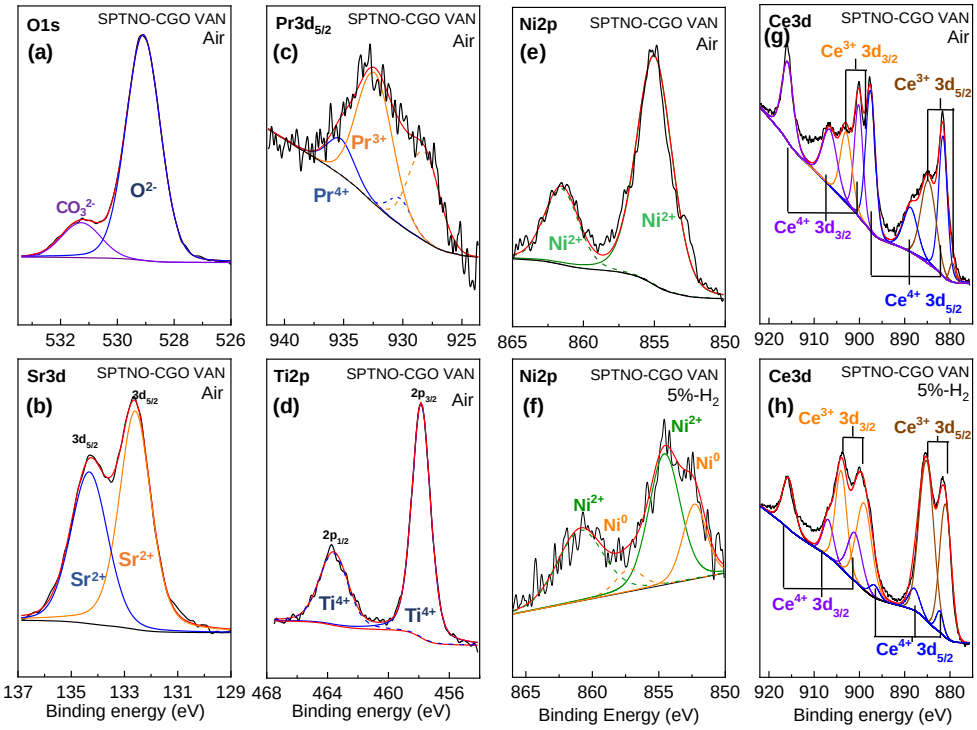

Figure 9.12. XPS spectra of the surface of SPTNO-CGO VAN in air and 5% H_2-Ar (a) O1s, (b) Sr3d, (c) Ti 2p, (d) Pr $3d_{5/2}$, (e,f) Ni 2p and (g,h) Ce 3d.

The Ni 2p region in air shows the presence of a band centered at 854.8 eV corresponding to the presence of Ni^{2+} in the perovskite lattice, as observed previously for Ni-doped titanates electrodes, such as $La_{0.45}Sr_{0.45}Ti_{0.9}Ni_{0.1}O_{3-\delta}$ [27] and $La_{0.25}Sr_{0.25}Ca_{0.4}Ti_{0.95}Ni_{0.05}O_{3-\delta}$ [28] (Figure 9.12e). Interestingly, the presence of Ni^0 with a peak centered at 852.4 eV is clearly discernible after the reduction treatment (Figure 9.12f).

The Ce 3d core level shows the characteristic Ce $3d_{5/2}$ and Ce $3d_{3/2}$ splitting. Ce^{4+} is the main valence state in air but also a certain amount of Ce^{3+} is present on the surface of the VAN film [29,30] (Figure 9.12g). The peaks at binding energies of 879.6, 881.6, 884.9, 888.8 and 897.6 eV are assigned to the Ce $3d_{5/2}$, in which a

UNIVERSIDAD DE MÁLAGA

mixture of Ce^{3+} and Ce^{4+} is observed, findings that have been previously associated with the formation of oxygen vacancies in CeO_2-doped compounds [30]. In reducing conditions, the Ce^{4+} is partially reduced to Ce^{3+} (Figure 9.12h). Such results are different to that observed for $LSFT_{0.2}$-CGO VAN film in Chapter 8, presumably attributed to the higher reduction temperature and time employed in the previous work (750 ºC for 12 h).

9.5. Electrical characterization

The in-plain conductivity of the SPTNO and SPTNO-CGO VAN films deposited onto LSAT (001) was determined by the four-probe Van der Pauw method under air and 5% H_2-Ar atmospheres (Figure 9.13). It is worth mentioning that a LSAT substrate was employed due to its negligible electrical conductivity in both oxidizing and reducing conditions. SPTNO exhibits a conductivity in air of 0.077 S cm^{-1} at 650 ºC, values that are considerably higher than those observed for polycrystalline pellets of SPTO ~$5 \cdot 10^{-5}$ S cm^{-1} at 650 ºC in Chapter 5.

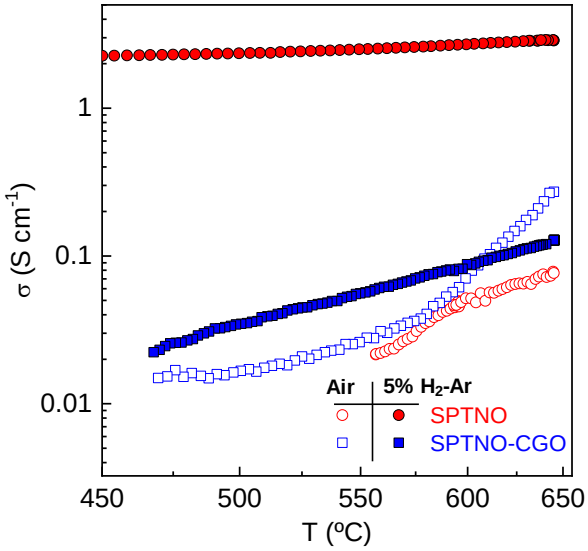

Figure 9.13. In-plane conductivity measured by the Van der Pauw method of SPTNO and SPTNO-CGO VAN samples in air and 5% H_2-Ar as a function of the temperature.

In a 5% H_2-Ar atmosphere, the conductivity significantly increases up to 2.87 S cm^{-1} at 650 ºC due to the partial reduction of Ti^{4+} to Ti^{3+}, which increases the charge

UNIVERSIDAD DE MÁLAGA

carrier concentration. The conductivity values in a reducing atmosphere are slightly higher than those observed for the SPTO pellets, 0.84 S cm^{-1} at the same temperature. Interestingly, the conductivity values obtained in this work are still comparable to those observed for polycrystalline $Sr_{0.7}Pr_{0.3}TiO_{3-\delta}$ (~10 S cm^{-1}) or $Sr_{0.92}Y_{0.08}TiO_{3-\delta}$ (0.4 S cm^{-1}) [26,31].

In the case of the VAN sample, the conductivity in air is slightly superior to the blank SPTNO, ~ 0.27 S cm^{-1} at 650 ºC, despite the lower ionic conductivity of the CGO bulk (0.02 S cm^{-1} at 650 ºC). In reducing conditions, the conductivity of the VAN slightly decreases at high temperatures to 0.1 S cm^{-1} at 650 ºC. It has to be noted that very fast reduction kinetics was observed in the case of the SPTNO-CGO VAN sample, obtaining stable conductivity values in only 30 minutes after feeding with 5% H_2-Ar. Since the conductivity in reducing conditions for the SPTNO and CGO phases increases significantly, the rather low increase of conductivity values in reducing conditions for SPTNO-CGO VAN could be attributed to the particular nickel exsolution process in the VAN. As observed previously, the presence of vertical interfaces promotes an easier Ni exsolution, thus inducing a B-site deficiency that seems to decrease the conductivity. The high number of interfaces could also negatively affect to the total resistance of the cell. Further studies are necessary to clarify this issue.

The conductivity values in air of this work are better than those observed previously for other related compositions at 650 ºC such as $SrTi_{0.9}Fe_{0.1}O_{3-\delta}$ (~10^{-5} S cm^{-1}) or $SrTi_{0.996}Ni_{0.004}O_{3-\delta}$ (~10^{-6} S cm^{-1}) deposited by PLD [32,33]. Recently, Morgenbesser *et al.* have studied the reason for the low conductivity values observed in the literature for $SrTiO_3$-based epitaxial films [32,33]. The authors observed a severe A-site non-stoichiometry with Sr vacancies in thin films prepared by PLD. Only targets with 7% Sr-excess led to obtain near-stoichiometric films, which rendered conductivity values close to the ones for the bulk material [32,33]. Since targets with A-site deficiency were employed to promote Ni-exsolution in reducing conditions, a further A-site deficiency was presumably created, negatively affecting the conducting properties.

In order to study the surface exchange kinetics in reducing conditions, electrical conductivity relaxation (ECR) measurements were performed by switching from wet to dry 5% H_2-Ar at a constant temperature of 650 ºC. In this technique, the

UNIVERSIDAD DE MÁLAGA

transient conductivity is measured after changing the oxygen partial pressure abruptly to obtain the chemical surface exchange coefficient (k_{chem}) [34–36]. The relaxation profile is described by the Fick's second law (Ec. 9.1):

$$\frac{\sigma(t)-\sigma(0)}{\sigma(\infty)-\sigma(0)} = 1-\exp\left(\frac{k_{chem}t}{l}\right) \qquad \text{(Ec. 9.1)}$$

where σ(0) is the initial conductivity and σ(∞) the steady state conductivity after the pO_2 change and *l* is the film thickness. Typically, the normalized conductivity (term *y* in the equation) is expressed as g(t).

Figure 9.14 shows the conductivity relaxation profiles of SPTNO and SPTNO-CGO VAN after switching from wet to dry 5% H_2 at 650 ºC. As can be seen, the relaxation time at 650 ºC for the SPTNO (~140 s) is higher than that observed for the SPTNO-CGO VAN (~80 s), with k_{chem} values of $7.53 \cdot 10^{-7}$ and $1.27 \cdot 10^{-6}$ cm s^{-1} for the SPTNO and SPTNO-CGO VAN, respectively.

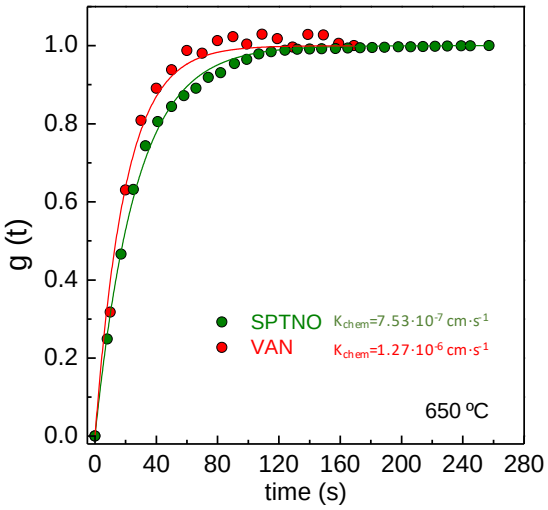

Figure 9.14. Conductivity relaxation profiles of SPTNO film and SPTNO-CGO VAN after switching from wet to dry 5% H_2-Ar at 650 ºC and the corresponding surface exchange properties (k_{chem}). The solid red and green lines are the fitting curves using Eq. 9.1.

The improvement of the surface exchange properties after the incorporation of an ionic conductor, such as CGO, was also observed in previous reports [9,37]. On the other hand, Ni-doped perovskite electrodes such as

UNIVERSIDAD DE MÁLAGA

$Ba(Co_{0.4}Fe_{0.4}Zr_{0.1}Y_{0.1})_{0.95}Ni_{0.05}O_{3-\delta}$ [38] and $(PrBa)_{0.95}Fe_{1.6}Ni_{0.3}Mo_{0.1}O_{6-\delta}$ [39] have demonstrated improved surface kinetics when compared to the pristine compounds. It is worth mentioning that the presence of Ni nanoparticles on the electrode surface is expected to promote faster kinetics due to their great activity for fuel oxidation [40]. However, due to the novelty of this work, more research is needed to confirm this hypothesis and elucidate the influence of the Ni particle size and population density on the surface kinetics in reducing conditions.

The k_{chem} for the SPTNO-CGO VAN observed in this work is lower than that found for polycrystalline $La_{0.5}Sr_{1.5}Fe_{1.5}Mo_{0.5}O_{6-\delta}$ ($1 \cdot 10^{-3}$ cm s^{-1} at 800 ºC in pure H_2) [36] or polycrystalline $Ce_{0.85}Sm_{0.15}O_{1.925}$ ($1.8 \cdot 10^{-5}$ cm s^{-1} at 800 ºC in pure H_2) pellets [34]. However, the considerably higher temperature employed in the ECR measurements, which has demonstrated to highly improve the surface kinetics [34,35], and the use of diluted hydrogen (5% H_2-Ar), could explain these discrepancies. Interestingly, the k_{chem} values obtained are comparable to oxygen exchange coefficients observed for highly efficient cathodes for ORR deposited by PLD such as, $La_{0.6}Sr_{0.4}Co_{0.2}Fe_{0.8}O_{3-\delta}$ ($2 \cdot 10^{-8}$ cm s^{-1} at 600 ºC) [41] and $La_{0.8}Sr_{0.2}CoO_{3-\delta}$ ($3 \cdot 10^{-9}$ cm s^{-1} at 550 ºC) [42].

Finally, a microstructural characterization of the samples was carried out after the electrochemical measurements in order to check the stability of the films after successive oxidation/reduction cycles (Figure 9.15). As can be seen, the Ni-exsolved nanoparticles remain stable after several oxidation/reduction cycles. In the particular case of the SPTNO film (Figure 9.15a), the particle size is higher and the population density is lower when compared to the SPTNO-CGO VAN (Figure 9.15b). Additionally, small cracks and degradation of the sample surface can be observed for the SPTNO film while no signs of degradation are detected for the SPTNO-CGO VAN. In addition, the VAN sample shows the presence of the flat intermediate material surrounding some Ni nanoparticles, which is presumably attributed to the partial oxidation of the nanoparticles to NiO.

UNIVERSIDAD DE MÁLAGA

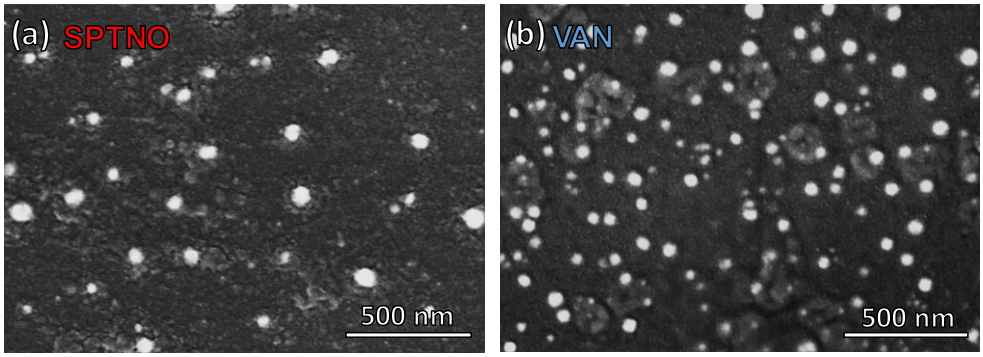

Figure 9.15. SEM images of (a) SPTNO and (b) SPTNO-CGO VAN after the electrochemical characterization.

Future work about understanding the NiO diffusion mechanism from the VAN film to the surface during the exsolution process is needed. In order to achieve this goal, a comprehensive characterization by in-situ STEM combined with DFT calculations could help to elucidate the diffusion pathways and growth mechanisms in this complex system. Furthermore, the incorporation of noble metals, such as Ru or Pd in the lattice of the perovskite of the VAN, could be the key to extend the application of this system to hydrocarbon fuelled SOFCs.

References

1. Kwon, O.; Joo, S.; Choi, S.; Sengodan, S.; Kim, G. Review on Exsolution and Its Driving Forces in Perovskites. *JPhys Energy* **2020**, *2*, doi:10.1088/2515-7655/ab8c1f.
2. Chen, A.; Su, Q.; Han, H.; Enriquez, E.; Jia, Q. Metal Oxide Nanocomposites: A Perspective from Strain, Defect, and Interface. *Adv. Mater.* **2019**, *31*, 1–30, doi:10.1002/adma.201803241.
3. Neagu, D.; Oh, T.S.; Miller, D.N.; Ménard, H.; Bukhari, S.M.; Gamble, S.R.; Gorte, R.J.; Vohs, J.M.; Irvine, J.T.S. Nano-Socketed Nickel Particles with Enhanced Coking Resistance Grown in Situ by Redox Exsolution. *Nat. Commun.* **2015**, *6*, doi:10.1038/ncomms9120.
4. Kim, K.J.; Han, H.; Defferriere, T.; Yoon, D.; Na, S.; Kim, S.J.; Dayaghi, A.M.; Son, J.; Oh, T.S.; Jang, H.M. Facet-Dependent in Situ Growth of Nanoparticles in Epitaxial Thin Films: The Role of Interfacial Energy. *J. Am. Chem. Soc.* **2019**, *141*, 7509–7517, doi:10.1021/jacs.9b02283.
5. Han, H.; Xing, Y.; Park, B.; Bazhanov, D.I.; Jin, Y.; Irvine, J.T.S.; Lee, J.; Oh S.H. Anti-Phase Boundary Accelerated Exsolution of Nanoparticles in Non-Stoichiometric Perovskite Thin Films. *Nat. Commun.* **2022**, 1–10, doi:10.1038/s41467-022-34289-3.
6. Teng, J.; Xia, T.; Sun, L.; Huo, L.; Li, Q.; Zhao, H. Designing One-Step Co-Assembled $Pr_{1.95}Ce_{0.05}CuO_4$-$Ce_{0.8}Pr_{0.2}O_{1.9}$ Composite Cathode with Extraordinary Oxygen Reduction

UNIVERSIDAD DE MÁLAGA

Activity for Solid Oxide Fuel Cells. *J. Alloys Compd.* **2022**, *929*, 167311, doi:10.1016/j.jallcom.2022.167311.

7. Raza, R.; Zhu, B.; Rafique, A.; Naqvi, M.R.; Lund, P. Functional Ceria-Based Nanocomposites for Advanced Low-Temperature (300–600 °C) Solid Oxide Fuel Cell: A Comprehensive Review. *Mater. Today Energy* **2020**, *15*, doi:10.1016/j.mtener.2019.100373.
8. Alvarado Flores, J.J.; Ávalos Rodríguez, M.L.; Andrade Espinosa, G.; Alcaraz Vera, J.V. Advances in the Development of Titanates for Anodes in SOFC. *Int. J. Hydrogen Energy* **2019**, *4*, 12529–12542, doi:10.1016/j.ijhydene.2018.05.171.
9. Baiutti, F.; Chiabrera, F.; Acosta, M.; Diercks, D.; Parfitt, D.; Santiso, J.; Wang, X.; Cavallaro, A.; Morata, A.; Wang, H.; Tarancón, A. A High-Entropy Manganite in an Ordered Nanocomposite for Long-Term Application in Solid Oxide Cells. *Nat. Commun.* **2021**, *12*, 1–11, doi:10.1038/s41467-021-22916-4.
10. Yang, S.M.; Lee, S.; Jian, J.; Zhang, W.; Lu, P.; Jia, Q.; Wang, H.; Won Noh, T.; Kalinin, S. V.; MacManus-Driscoll, J.L. Strongly Enhanced Oxygen Ion Transport through Samarium-Doped CeO_2 Nanopillars in Nanocomposite Films. *Nat. Commun.* **2015**, *6*, 1–8, doi:10.1038/ncomms9588.
11. Sun, X.; MacManus-Driscoll, J.L.; Wang, H. Spontaneous Ordering of Oxide-Oxide Epitaxial Vertically Aligned Nanocomposite Thin Films. *Annu. Rev. Mater. Res.* **2020**, *50*, 229–253, doi:10.1146/annurev-matsci-091719-112806.
12. Misra, S.; Wang, H. Review on the Growth, Properties and Applications of Self-Assembled Oxide-Metal Vertically Aligned Nanocomposite Thin Films-Current and Future Perspectives. *Mater. Horizons* **2021**, *8*, 869–884, doi:10.1039/d0mh01111h.
13. Jennings, D.; Ricote, S.; Santiso, J.; Caicedo, J.; Reimanis, I. Effects of Exsolution on the Stability and Morphology of Ni Nanoparticles on BZY Thin Films. *Acta Mater.* **2022**, *228*, 117752, doi:10.1016/j.actamat.2022.117752.
14. Bonzel, H.P.; Latta, E.E. Surface Self-Diffusion on Ni(110): Temperature Dependence and Directional Anisotropy. *Surf. Sci.* **1978**, *76*, 275–295, doi:10.1016/0039-6028(78)90098-5.
15. Kwak, N.W.; Jeong, S.J.; Seo, H.G.; Lee, S.; Kim, Y.J.; Kim, J.K.; Byeon, P.; Chung, S.Y.; Jung, W.C. In Situ Synthesis of Supported Metal Nanocatalysts through Heterogeneous Doping. *Nat. Commun.* **2018**, *9*, 1–8, doi:10.1038/s41467-018-07050-y.
16. Han, H.; Park, J.; Nam, S.Y.; Kim, K.J.; Choi, G.M.; Parkin, S.S.P.; Jang, H.M.; Irvine, J.T.S. Lattice Strain-Enhanced Exsolution of Nanoparticles in Thin Films. *Nat. Commun.* **2019**, *10*, 1–8, doi:10.1038/s41467-019-09395-4.
17. Yu, S.; Yoon, D.; Lee, Y.; Yoon, H.; Han, H.; Kim, N.; Kim, C.J.; Ihm, K.; Oh, T.S.; Son, J. Metal Nanoparticle Exsolution on a Perovskite Stannate Support with High Electrical Conductivity. *Nano Lett.* **2020**, *20*, 3538–3544, doi:10.1021/acs.nanolett.0c00488.
18. Neagu, D.; Papaioannou, E.I.; Ramli, W.K.W.; Miller, D.N.; Murdoch, B.J.; Ménard, H.; Umar, A.; Barlow, A.J.; Cumpson, P.J.; Irvine, J.T.S.; et al. Demonstration of Chemistry at a Point through Restructuring and Catalytic Activation at Anchored Nanoparticles. *Nat. Commun.* **2017**, *8*, doi:10.1038/s41467-017-01880-y.
19. Spring, J.; Sediva, E.; Hood, Z.D.; Gonzalez-Rosillo, J.C.; O'Leary, W.; Kim, K.J.; Carrillo, A.J.; Rupp, J.L.M. Toward Controlling Filament Size and Location for Resistive Switches via Nanoparticle Exsolution at Oxide Interfaces. *Small* **2020**, *16*, 1–11, doi:10.1002/smll.202003224.
20. Lai, K.Y.; Manthiram, A. Evolution of Exsolved Nanoparticles on a Perovskite Oxide Surface during a Redox Process. *Chem. Mater.* **2018**, *30*, 2838–2847,

UNIVERSIDAD DE MÁLAGA

doi:10.1021/acs.chemmater.8b01029.

21. Kolobov, Y.R.; Grabovetskaya, G.P.; Ivanov, M.B.; Zhilyaev, A.P.; Valiev, R.Z. Grain Boundary Diffusion Characteristics of Nanostructured Nickel. *Scr. Mater.* **2001**, *44*, 873–878, doi:10.1016/S1359-6462(00)00699-0.
22. Yang, Y.; Li, J.; Sun, Y. The Metal/Oxide Heterointerface Delivered by Solid-Based Exsolution Strategy: A Review. *Chem. Eng. J.* **2022**, *440*, 135868, doi:10.1016/j.cej.2022.135868.
23. Lu, Y.; Gasper, P.; Nikiforov, A.Y.; Pal, U.B.; Gopalan, S.; Basu, S.N. Co-Infiltration of Nickel and Mixed Conducting $Gd_{0.1}Ce_{0.9}O_{2-\delta}$ and $La_{0.6}Sr_{0.3}Ni_{0.15}Cr_{0.85}O_{3-\delta}$ Phases in Ni-YSZ Anodes for Improved Stability and Performance. *Jom* **2019**, *71*, 3835–3847, doi:10.1007/s11837-019-03723-1.
24. Thirumalairajan, S.; Girija, K.; Hebalkar, N.Y.; Mangalaraj, D.; Viswanathan, C.; Ponpandian, N. Shape Evolution of Perovskite $LaFeO_3$ Nanostructures: A Systematic Investigation of Growth Mechanism, Properties and Morphology Dependent Photocatalytic Activities. *RSC Adv.* **2013**, *3*, 7549–7561, doi:10.1039/c3ra00006k.
25. Kamecki, B.; Miruszewski, T.; Karczewski, J. Structural and Electrical Transport Properties of Pr-Doped $SrTi_{0.93}Co_{0.07}O_{3-\delta}$ a Novel SOEC Fuel Electrode Materials. *J. Electroceramics* **2019**, *42*, 31–40, doi:10.1007/s10832-018-0143-0.
26. Yaremchenko, A.A.; Patrício, S.G.; Frade, J.R. Thermochemical Behavior and Transport Properties of Pr-Substituted $SrTiO_3$ as Potential Solid Oxide Fuel Cell Anode. *J. Power Sources* **2014**, *245*, 557–569, doi:10.1016/j.jpowsour.2013.07.019.
27. Cavazzani, J.; Squizzato, E.; Brusamarello, E.; Glisenti, A. Exsolution in Ni-Doped Lanthanum Strontium Titanate: A Perovskite-Based Material for Anode Application in Ammonia-Fed Solid Oxide Fuel Cell. *Int. J. Hydrogen Energy* **2022**, *47*, 13921–13932, doi:10.1016/j.ijhydene.2022.02.133.
28. Korjus, O.; Möller, P.; Kooser, K.; Käämbre, T.; Volobujeva, O.; Nerut, J.; Kotkas, S.; Lust, E.; Nurk, G. Influence of Ni Concentration on Electrochemical and Crystallographic Properties of $La_{0.25}Sr_{0.25}Ca_{0.4}Ti_{1-x}Ni_xO_{3-\delta}$ Solid Oxide Fuel Cell Anode. *J. Power Sources* **2021**, *494*, doi:10.1016/j.jpowsour.2021.229739.
29. Borchert, H.; Borchert, Y.; Kaichev, V. V.; Prosvirin, I.P.; Alikina, G.M.; Lukashevich, A.I.; Zaikovskii, V.I.; Moroz, E.M.; Paukshtis, E.A.; Bukhtiyarov, V.I.; et al. Nanostructured, Gd-Doped Ceria Promoted by Pt or Pd: Investigation of the Electronic and Surface Structures and Relations to Chemical Properties. *J. Phys. Chem. B* **2005**, *109*, 20077–20086, doi:10.1021/jp051525m.
30. Liu, Y.; Fan, L.; Cai, Y.; Zhang, W.; Wang, B.; Zhu, B. Superionic Conductivity of Sm^{3+}, Pr^{3+}, and Nd^{3+} Triple-Doped Ceria through Bulk and Surface Two-Step Doping Approach. *ACS Appl. Mater. Interfaces* **2017**, *9*, 23614–23623, doi:10.1021/acsami.7b02224.
31. Kim, H.S.; Yoon, S.P.; Yun, J.W.; Song, S.A.; Jang, S.C.; Nam, S.W.; Shul, Y.G. $Sr_{0.92}Y_{0.08}TiO_{3-\delta}$/Sm $_{0.2}Ce_{0.8}O_{2-\delta}$ Anode for Solid Oxide Fuel Cells Running on Methane. *Int. J. Hydrogen Energy* **2012**, *37*, 16130–16139, doi:10.1016/j.ijhydene.2012.08.030.
32. Morgenbesser, M.; Taibl, S.; Kubicek, M.; Schmid, A.; Viernstein, A.; Bodenmüller, N.; Herzig, C.; Baiutti, F.; De Dios Sirvent, J.; Liedke, M.O.; Tarancón, A.; Fleig, J. Cation Non-Stoichiometry in Fe:$SrTiO_3$ thin Films and Its Effect on the Electrical Conductivity. *Nanoscale Adv.* **2021**, *3*, 6114–6127, doi:10.1039/d1na00358e.
33. Morgenbesser, M.; Viernstein, A.; Schmid, A.; Herzig, C.; Kubicek, M.; Taibl, S.; Bimashofer, G.; Stahn, J.; Vaz, C.A.F.; Döbeli, M.; Fleig, J. Unravelling the Origin of Ultra-Low Conductivity in SrTiO3 Thin Films: Sr Vacancies and Ti on A-Sites Cause Fermi Level Pinning. *Adv. Funct.*

UNIVERSIDAD DE MÁLAGA

Mater. **2022**, *32*, doi:10.1002/adfm.202202226.

34. Gopal, C.B.; Haile, S.M. An Electrical Conductivity Relaxation Study of Oxygen Transport in Samarium Doped Ceria. *J. Mater. Chem. A* **2014**, *2*, 2405–2417, doi:10.1039/c3ta13404k.
35. Lane, J.A.; Kilner, J.A. Measuring Oxygen Diffusion and Oxygen Surface Exchange by Conductivity Relaxation. *Solid State Ionics* **2000**, *136–137*, 997–1001, doi:10.1016/S0167-2738(00)00554-3.
36. Qi, H.; Xia, F.; Yang, T.; Li, W.; Li, W.; Ma, L.; Collins, G.; Shi, W.; Tian, H.; Hu, S.; et al. In Situ Exsolved Nanoparticles on $La_{0.5}Sr_{1.5}Fe_{1.5}Mo_{0.5}O_{6-\delta}$ Anode Enhance the Hydrogen Oxidation Reaction in SOFCs . *J. Electrochem. Soc.* **2020**, *167*, 024510, doi:10.1149/1945-7111/ab6a82.
37. Zhang, Y.; Shen, L.; Wang, Y.; Du, Z.; Zhang, B.; Ciucci, F.; Zhao, H. Enhanced Oxygen Reduction Kinetics of IT-SOFC Cathode with $PrBaCo_2O_{5+\delta}/Gd_{0.1}Ce_{1.9}O_{2-\delta}$ coherent Interface. *J. Mater. Chem. A* **2022**, *10*, 3495–3505, doi:10.1039/d1ta09615j.
38. Liang, M.; He, F.; Zhou, C.; Chen, Y.; Ran, R.; Yang, G.; Zhou, W.; Shao, Z. Nickel-Doped $BaCo_{0.4}Fe_{0.4}Zr_{0.1}Y_{0.1}O3_{-\delta}$ as a New High-Performance Cathode for Both Oxygen-Ion and Proton Conducting Fuel Cells. *Chem. Eng. J.* **2021**, *420*, 127717, doi:10.1016/j.cej.2020.127717.
39. Xue, S.; Shi, N.; Wan, Y.; Xu, Z.; Huan, D.; Zhang, S.; Xia, C.; Peng, R.; Lu, Y. Novel Carbon and Sulfur-Tolerant Anode Material $FeNi_3$ $PrBa(Fe,Ni)_{1.9}Mo_{0.1}O_{5+\delta}$ for Intermediate Temperature Solid Oxide Fuel Cells. *J. Mater. Chem. A* **2019**, *7*, 21783–21793, doi:10.1039/c9ta07027c.
40. Kousi, K.; Tang, C.; Metcalfe, I.S.; Neagu, D. Emergence and Future of Exsolved Materials. *Small* **2021**, *17*, doi:10.1002/smll.202006479.
41. Chen, H.; Guo, Z.; Zhang, L.A.; Li, Y.; Li, F.; Zhang, Y.; Chen, Y.; Wang, X.; Yu, B.; Shi, J.M.; Improving the Electrocatalytic Activity and Durability of the $La_{0.6}Sr_{0.4}Co_{0.2}Fe_{0.8}O_{3-\delta}$ Cathode by Surface Modification. *ACS Appl. Mater. Interfaces* **2018**, *10*, 39785–39793, doi:10.1021/acsami.8b14693.
42. Lee, D.; Lee, Y.-L.; Grimaud, A.; Hong, W.T.; Biegalski, M.D.; Morgan, D.; Shao-Horn, Y. Enhanced Oxygen Surface Exchange Kinetics and Stability on Epitaxial $La_{0.8}Sr_{0.2}CoO_{3-\delta}$ Thin Films by $La_{0.8}Sr_{0.2}MnO_{3-\delta}$ Decoration. **2014**.

UNIVERSIDAD DE MÁLAGA

Chapter 10

UNIVERSIDAD
DE MÁLAGA

UNIVERSIDAD
DE MÁLAGA

Conclusions and future prospects

In this work, new nanocomposite materials have been investigated for their implementation in symmetrical SOFCs. The most remarkable results are summarized below:

- Spray-pyrolysis deposition is a suitable method to assemble nanocomposite electrodes directly on the electrolyte surface without excessive sintering temperatures to limit the grain growth.

- The great versatility of spray-pyrolysis deposition allowed obtaining electrodes with different microstructural architectures, including layers of single compounds, nanocomposites or infiltrated electrodes for application as air, fuel electrodes or active layers in SOFCs.

UNIVERSIDAD DE MÁLAGA

- The nanocomposite layers, obtained by combining two immiscible phases with different crystal structures, exhibit improved thermal stability at high temperatures due to the nanoscale contact between both phases, which hinders the grain growth at high temperatures due to cation diffusion limitations at the grain boundary. Moreover, the intimate contact between an ionic and mainly electronic conductor extends the TPB sites for both ORR and HOR.

- The nanocomposite electrodes exhibit an improved electrochemical performance when compared to the same electrodes obtained by traditional screen-printing deposition.

- $La_{0.98}Cr_{0.75}Mn_{0.25}O_{3-\delta}$-CGO and $(La_{0.8}Sr_{0.2})_{0.95}Fe_{0.8}Ti_{0.2}O_{3-\delta}$-CGO are promising electrodes for SSOFCs with good electrochemical properties and durability in both oxidizing and reducing atmospheres. In particular, $La_{0.98}Cr_{0.75}Mn_{0.25}O_{3-\delta}$-CGO exhibits polarization resistance of 0.09 Ω cm^2 at 700 ºC in H_2, comparable to the state-of-the-art Ni-YSZ anode.

- The exsolution of Ni particles in $(La_{0.8}Sr_{0.2})_{0.95}(Fe_{0.8}Ti_{0.2})_{0.9}Ni_{0.1}O_{3-\delta}$ decreases significantly the polarization resistance in H_2 with values as low as 0.11 Ω cm^2 at 700 ºC and a maximum output of 617 mW cm^{-2} at 800 ºC in symmetrical cell configuration.

- Nanocomposite active layers were also prepared by spray-pyrolysis deposition to improve the ORR activity of a LSM cathode. Among the different compositions, LSM-CGO layers showed improved adherence and electrical properties. The incorporation of this active layer enhances the ion transfer at the cathode/electrode interface and also extended the ionic/electronic conducting paths for electrochemical reactions. A Ni-YSZ/YSZ/LSM-CGO/LSM anode-supported cell showed a maximum power density of 1200 mW cm^{-2} at 800 ºC compared to 790 mW cm^{-2} for the same cell without an active layer.

- Vertically Aligned Nanostructures (VANs) of $(La_{0.8}Sr_{0.2})_{0.98}Fe_{0.8}Ti_{0.2}O_{3-\delta}$-CGO and $(Sr_{0.7}Pr_{0.3})_{0.95}Ti_{0.9}Ni_{0.1}O_{3-\delta}$-CGO were prepared by PLD for their

UNIVERSIDAD DE MÁLAGA

implementation as redox stable active layers for SOFCs. The heteroepitaxial films exhibited long-range columnar architecture of 5 nm width. The VAN films showed higher conductivity than that observed for the polycrystalline samples.

- The exsolution of Ni-metal nanoparticles in a VAN film of $(Sr_{0.7}Pr_{0.3})_{0.95}Ti_{0.9}Ni_{0.1}O_{3-\delta}$-CGO was studied for the first time. The reduction process at 650 ºC in 5% H_2-Ar and the subsequent exsolution of Ni-metal do not negatively affect the VAN microstructure, retaining the columnar architecture. The Ni nanoparticle size is lower and the population density is higher for the SPTNO-CGO VAN when compared to SPTNO film. Good redox stability was observed for the Ni nanoparticles after several oxidation/reduction cycles.

Future prospects

Since the implementation of nanocomposite electrodes by combining single perovskite mixed conductors and CGO fluorite is a promising approach to design highly efficient and durable electrodes for SOFCs, this study could be extended to layered perovskites, such as $Sr_2Fe_{1.5}Mo_{0.5}O_{6-\delta}$ and $PrBa(Fe,Mn)_2O_{5+\delta}$. Alternatively, the perovskite-type electrodes could be combined with MIECs with different crystal structures, *i.e.* $CuBi_2O_4$ spinel. In addition, the improved performance observed for LSM cathode by incorporating nanocomposite active layers could be extended to symmetrical SOFCs.

Further research about the performance of these nanocomposite electrodes with hydrocarbon fuels, such as CH_4, C_3H_8 or syngas, and their application in electrolysis mode for simultaneous H_2O and CO_2 electroreduction could also be investigated.

UNIVERSIDAD DE MÁLAGA

UNIVERSIDAD
DE MÁLAGA

Appendixes

UNIVERSIDAD
DE MÁLAGA

UNIVERSIDAD
DE MÁLAGA

Appendix 1

UNIVERSIDAD DE MÁLAGA

UNIVERSIDAD
DE MÁLAGA

XPS characterization of $La_{0.98}Cr_{0.75}Mn_{0.25}O_{3-\delta}$

In order to get further information on the oxidation states in oxidizing and reducing conditions of the different elements of $La_{0.98}Cr_{0.75}Mn_{0.25}O_{3-\delta}$ (LCM), a careful XPS characterization was performed (Figure A.1). The O_{1s} signal is composed by two bands, centred at 529 and 531 eV, which are associated to lattice oxygen and superficial adsorbed materials (such as carbonates or hydroxides), respectively (Figure A.1a) [1]. The $La3d_{5/2}$ region is composed by two peaks, in which the peak at higher binding energy (BE) is a satellite attributed to an electron transfer from the filled O_{2p} band to the La_{4f} level. The band at lower binding energy centred at 834.4 eV is attributed to La^{3+} in a perovskite structure [2] (Figure A.1b). It is worth mentioning that no significant changes were observed for these two elements after the reduction treatment, showing no changes in the oxidation states, as expected.

UNIVERSIDAD DE MÁLAGA

In the $Cr2p_{3/2}$ level in air, three different bands located at 576.0, 577.2 and 579.3 eV are clearly identified, which are linked to Cr^{3+}, Cr^{5+} and Cr^{6+} oxidation states, respectively (Figure A.1c). A similar behaviour has been observed previously for other compositions such as $LaCr_{0.8}Ru_{0.2}O_{3-\delta}$ and $La_{0.7}Sr_{0.2}Cr_{0.9}Ni_{0.1}O_{3-\delta}$ [3,4]. After the reduction treatment, in the spectra, only the two peaks centred at 575.9 and 577.1 eV appear and the band assigned Cr^{6+} is not present (Figure A.1d). Furthermore, the area of the Cr^{5+} band is considerably decreased, also showing the partial reduction to lower oxidation states.

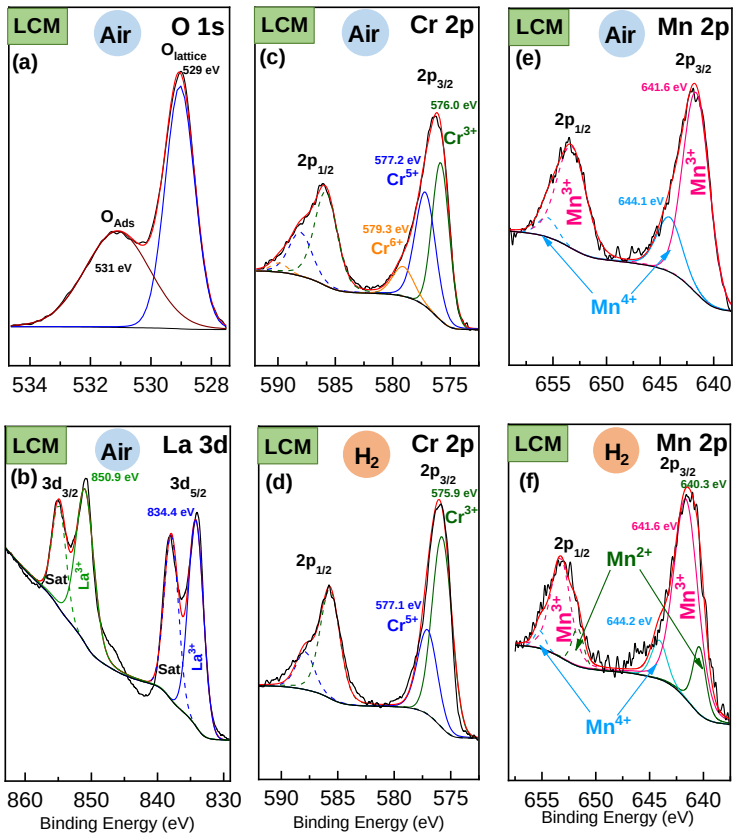

Figure A.1. XPS spectra of the surface of $La_{0.98}Cr_{0.75}Mn_{0.25}O_{3-\delta}$ in air and 5% H_2-Ar (a) O1s, (b) La3d, (c,d) Cr 2p and (e,f) Mn 2p.

The $Mn2p_{3/2}$ level in air shows two different contributions centred at 641.6 and 644.1 eV, which can be associated to Mn^{3+} and Mn^{4+} oxidation states, respectively (Figure A.1e). It is worth noting that the experimental Mn^{3+}/Mn^{4+} ratio in this sample,

UNIVERSIDAD DE MÁLAGA

~1:0.33, is close to that observed previously for $LaMnO_3$ in air [5]. In reducing conditions, a new band at lower binding energy attributed to Mn^{2+} species is observed (Figure A.1f), which is in agreement with previous results [6]. Furthermore, the Cr/Mn ratio (1:0.35) obtained from the XPS analysis is very similar to the nominal one in $La_{0.98}Cr_{0.75}Mn_{0.25}O_{3-\delta}$ (1:0.33).

References

1. Coşkun, M.; Polat, A.O.; Coşkun, F.M.; Durmuş, Z.; Caglar, C.M.; Türüt, A. The Electrical Modulus and Other Dielectric Properties by the Impedance Spectroscopy of $LaCrO_3$ and $LaCr_{0.90}Ir_{0.10}O_3$ Perovskites. *RSC Adv.* **2018**, *8*, 4634–4648, doi:10.1039/c7ra13261a.
2. Li, J.P.H.; Zhou, X.; Pang, Y.; Zhu, L.; Vovk, E.I.; Cong, L.; Van Bavel, A.P.; Li, S.; Yang, Y. Understanding of Binding Energy Calibration in XPS of Lanthanum Oxide by: In Situ Treatment. *Phys. Chem. Chem. Phys.* **2019**, *21*, 22351–22358, doi:10.1039/c9cp04187g.
3. Nenning, A.; Fleig, J. Electrochemical XPS Investigation of Metal Exsolution on SOFC Electrodes: Controlling the Electrode Oxygen Partial Pressure in Ultra-High-Vacuum. *Surf. Sci.* **2019**, *680*, 43–51, doi:10.1016/j.susc.2018.10.006.
4. Jeon, Y.; Park, D.H.; Park, J. Il; Yoon, S.H.; Mochida, I.; Choy, J.H.; Shul, Y.G. Hollow Fibers Networked with Perovskite Nanoparticles for H_2 Production from Heavy Oil. *Sci. Rep.* **2013**, *3*, 1–8, doi:10.1038/srep02902.
5. Karuppiah, C.; Thirumalraj, B.; Alagar, S.; Piraman, S.; Li, Y.J.J.; Yang, C.C. Solid-State Ball-Milling of Co_3O_4 Nano/Microspheres and Carbon Black Endorsed $LaMnO_3$ Perovskite Catalyst for Bifunctional Oxygen Electrocatalysis. *Catalysts* **2021**, *11*, 1–17, doi:10.3390/catal11010076.
6. Chung, Y.S.; Kim, T.; Shin, T.H.; Yoon, H.; Park, S.; Sammes, N.M.; Kim, W.B.; Chung, J.S. In Situ Preparation of a $La_{1.2}Sr_{0.8}Mn_{0.4}Fe_{0.6}O_4$ Ruddlesden-Popper Phase with Exsolved Fe Nanoparticles as an Anode for SOFCs. *J. Mater. Chem. A* **2017**, *5*, 6437–6446, doi:10.1039/c6ta09692a.

UNIVERSIDAD DE MÁLAGA

UNIVERSIDAD
DE MÁLAGA

Appendix 2

UNIVERSIDAD
DE MÁLAGA

UNIVERSIDAD
DE MÁLAGA

Article section

Articles included in this thesis

1. Javier Zamudio-García, José M. Porras-Vázquez, Enrique R. Losilla, David Marrero-López, Efficient symmetrical electrodes based on $LaCrO_3$ via microstructural engineering. *J. Eur. Ceram. Soc.* **2022**, *42*, 181-192. doi: 10.1016/j.jeurceramsoc.2021.09.059

2. Javier Zamudio-García, José M. Porras-Vázquez, Enrique R. Losilla, David Marrero-López, $LaCrO_3$-CeO_2-Based Nanocomposite Electrodes for Efficient Symmetrical Solid Oxide Fuel Cells. *ACS Applied Energy Mater.* **2022**, *5*, 4536-4546. doi: 10.1021/acsaem.1c04116

3. Javier Zamudio-García, Lucía dos Santos-Gómez, José M. Porras-Vázquez, Enrique R. Losilla, David Marrero-López, Symmetrical Solid Oxide Fuel Cells based on titanate nanocomposite electrodes, *J. Eur. Ceram. Soc.* **2023**, *43*, 1548-1558. doi: 10.1016/j.jeurceramsoc.2022.11.059

4. Javier Zamudio-García*, José M. Porras-Vázquez, Enrique R. Losilla, David Marrero-López, Tunable electrode architectures for $La_{0.8}Sr_{0.2}Fe_{1-x}Ti_xO_{3-\delta}$. *ECS Transations* **2021**, *103*, 1601-1606. doi: 10.1149/10301.1601ecst

UNIVERSIDAD DE MÁLAGA

5. Javier Zamudio-García*, Leire Caizán-Juanarena, José M. Porras-Vázquez, Enrique R. Losilla, David Marrero-López, A review on recent advances and trends in symmetrical electrodes for solid oxide cells. *J. Power Sources* **2022**, *520*, 230852. doi: 10.1016/j.jpowsour.2021.230852 (Review paper)

6. Javier Zamudio-García*, Leire Caizán-Juanarena, José M. Porras-Vázquez, Enrique R. Losilla, David Marrero-López, Unraveling the influence of the electrolyte on the polarization resistance of Nanostructured $La_{0.6}Sr_{0.4}Co_{0.2}Fe_{0.8}O_{3-\delta}$ cathodes. *Nanomaterials* **2022**, *12*, 3936. doi: 10.3390/nano12223936

7. Javier Zamudio-García, Leire Caizán-Juanarena, José M. Porras-Vázquez, Enrique R. Losilla, David Marrero-López, Boosting the performance of $La_{0.8}Sr_{0.2}MnO_{3-\delta}$ electrodes by the incorporation of nanocomposite active layers. *Adv. Mat. Interfaces.* **2022**, *9*, 2200702. doi: 10.1002/admi.202200702

Other Articles not included in the PhD thesis

8. Javier Zamudio-García, José M. Porras-Vázquez, Lucía dos Santos-Gómez, Enrique R. Losilla, David Marrero-López. Effect of Zn addition on the structure and electrochemical properties of co-doped $BaCe_{0.6}Zr_{0.2}Ln_{0.2}O_{3-\delta}$ (Ln=Y, Gd, Yb) proton conductors. *Ceram. Int.* **2018,** *44*, 14113-14121. doi: 10.1016/j.ceramint.2018.05.010

9. Lucía dos Santos-Gómez, Javier Zamudio-García, José M. Porras-Vázquez, Enrique R. Losilla, David Marrero-López. Highly efficient $La_{0.8}Sr_{0.2}MnO_{3-\delta}$-$Ce_{0.9}Gd_{0.1}O_{1.95}$ nanocomposite cathodes for solid oxide fuel cells. *Ceram. Int.* **2018**, *44*, 4961-4966. doi: 10.1016/j.ceramint.2017.12.089

10. Javier Zamudio-García, José M. Porras-Vázquez, Jesús Canales-Vázquez, Aurelio Cabeza, Enrique R. Losilla, David Marrero-López, Relationship between the Structure and Transport Properties in the $Ce_{1-x}La_xO_{2-x}$ System. *Inorg. Chem.* **2019**, *58*, 9368-9377. doi: 10.1021/acs.inorgchem.9b01104

11. Javier Zamudio-García, Lucía dos Santos-Gómez, José M. Porras-Vázquez, Enrique R. Losilla, David Marrero-López. Doping effects on the structure and electrical properties of $La_2Ce_2O_7$ proton conductors. *J. Alloys Comp.* **2020**, *816*, 152600. doi: 10.1016/j.jallcom.2019.152600

12. Adrián López-Vergara, Marta Bergillos-Ruiz, Javier Zamudio-García, José M. Porras-Vázquez, Jesús Canales-Vázquez, David Marrero-López, Enrique R. Losilla, Synergic Effect of Metal and Fluorine Doping on the Structural and Electrical Properties of $La_{5.4}MoO_{11.1}$-Based Materials. *Inorg. Chem.* **2020**, *59*, 2, 1444-1452. doi: 10.1021/acs.inorgchem.9b03194

UNIVERSIDAD DE MÁLAGA

13. Lucía Santos-Gómez, Javier Zamudio-García, José M. Porras-Vázquez, Enrique R. Losilla, David Marrero-López, Nanostructured $BaCo_{0.4}Fe_{0.4}Zr_{0.1}Y_{0.1}O_{3-\delta}$ cathodes with different microstructural architectures. *Nanomaterials* **2020**, *10*, 6, 1055. doi: 10.3390/nano10061055

14. Lucía dos Santos-Gómez, Javier Zamudio-García, José M. Porras-Vázquez, Enrique R. Losilla, David Marrero-López, Highly oriented and fully dense CGO films prepared by spray-pyrolysis and different precursor salts. *J. Eur. Ceram. Soc.* **2020**, *40*, 8, 3080-3088. doi: 10.1016/j.jeurceramsoc.2020.03.026

15. Javier Zamudio-García*, Nerea Albarrán-Aroca, José M. Porras-Vázquez, Enrique R. Losilla, David Marrero-López, Influence of $Bi_{1.5}Y_{0.5}O_3$ active layer on the performance of nanostructured $La_{0.8}Sr_{0.2}MnO_3$ cathode. *Applied Nano* **2020**, *1*, 1, 14-24. doi: 10.3390/applnano1010003

16. Lucía dos Santos-Gómez, Javier Zamudio-García, José M. Porras-Vázquez, Enrique R. Losilla, David Marrero-López, Recent progress in nanostructured electrodes for solid oxide fuel cells deposited by spray pyrolysis. *J. Power Sources* **2021**, *507*, 230277. doi: 10.1016/j.jpowsour.2021.230277 (Review paper)

17. G.C. Mather, Daniel Muñoz-Gil, Javier Zamudio-García, José M. Porras-Vázquez, David Marrero-López, Domingo Pérez-Coll, Perspectives on cathodes for protonic ceramic fuel cells. *Applied Sciences* **2021**, *11*, 12, 5363. doi: 10.3390/app11125363 (Review paper)

18. Lucía Santos-Gómez, Javier Zamudio-García, José M. Porras-Vázquez, Enrique R. Losilla, David Marrero-López, Modification of the Microstructure and Transport Properties of $La_2CuO_{4+\delta}$ electrodes via halogenation Routes. *Processes* **2022**, *10*, 1206. doi: 10.3390/pr10061206

19. Rafael Rubio-Vives, José M. Porras-Vázquez, Lucía dos Santos-Gómez, Javier Zamudio-García, Antonia Infantes-Molina, Jesús Canales-Vazquez, David Marrero-López, Enrique R. Losilla. Impact of the lanthanide size on the polymorphism and electrical properties of $Ln_{5.4}MoO_{11.1}$ (Ln = Nd, Sm and Gd). *Ceram. Int.* **(2022)**, Accepted manuscript. doi: 10.1016/j.ceramint.2022.12.146

UNIVERSIDAD DE MÁLAGA

UNIVERSIDAD
DE MÁLAGA

Journal of the European Ceramic Society 42 (2022) 181–192

Contents lists available at ScienceDirect

Journal of the European Ceramic Society

journal homepage: www.elsevier.com/locate/jeurceramsoc

Original Article

Efficient symmetrical electrodes based on $LaCrO_3$ via microstructural engineering

Javier Zamudio-García [a], José M. Porras-Vázquez [a], Enrique R. Losilla [a], David Marrero-López [b,*]

[a] Universidad de Málaga, Dpto. de Química Inorgánica, Cristalografía y Mineralogía, 29071, Málaga, Spain
[b] Universidad de Málaga, Dpto. de Física Aplicada I, 29071, Málaga, Spain

ARTICLE INFO

Keywords:
$LaCrO_3$
Symmetrical solid oxide fuel cell
Nanomaterials
Spray-pyrolysis

ABSTRACT

Novel nanostructured electrodes, $La_{0.98}Cr_{0.75}B_{0.25}O_{3\delta}$ (B = Mn, Fe, Ti and Cu), are prepared by a single spray-pyrolysis deposition method directly on the electrolyte and a porous $Ce_{0.9}Gd_{0.1}O_{1.95}$ (CGO) scaffold. These perovskite-type electrodes without alkaline-earth metals exhibit low ionic/electronic conductivity; however, the polarization resistance is greatly enhanced by microstructural design. The best results are obtained for $La_{0.98}Cr_{0.75}Mn_{0.25}O_{3-\delta}$ deposited into a porous CGO-scaffold due to the synergetic effect of CGO, with high ionic conductivity, and doped-$LaCrO_3$ with a predominantly electronic conductivity. The materials are investigated as both air and fuel electrodes for solid oxide fuel cells (SOFCs) by different structural, microstructural and electrochemical techniques. Low values of polarization resistance are achieved for nanostructured $La_{0.98}Cr_{0.75}Mn_{0.25}O_{3-\delta}$-CGO electrodes, *i.e.* 0.057 Ω cm^2 in air at 800 °C, compared to 0.96 Ω cm^2 for the same powder electrode obtained by screen-printing deposition. An electrolyte-supported symmetrical cell generates a stable maximum power output of 475 mW cm^{-2} at 800 °C.

1. Introduction

Solid oxide fuel cells (SOFCs) are considered to be a promising technology for efficient energy production and storage, and in contrast to other fuel cells, they have the potential to produce electrical energy not only from hydrogen but also from hydrocarbon fuels [1,2]. Furthermore, SOFCs can operate in reverse mode as a Solid Oxide Electrolyzer to produce H_2 by water electrolysis from renewable sources [3]. Nevertheless, the development of this technology requires to overcome several challenges before becoming commercially viable. In particular, the operating temperature needs to be reduced to the intermediate temperature range (500–800 °C) to provide an adequate lifetime of the cell components [4]. A reduction of the fabrication costs is also crucial to be competitive with other fuel cell technologies.

The traditional SOFC configuration is comprised of two porous ceramic electrodes separated by an ionic conductor electrolyte. The anode and cathode materials usually have different compositions to fulfill the required properties for the fuel oxidation and oxygen reduction reactions, respectively. However, in the last few years, symmetrical solid oxide fuel cells (SSOFC), where the same material is employed as both air and fuel electrode, are attracting attention because they offer important advantages compared to the traditional anode-supported SOFCs [5,6]. In particular, the manufacturing costs are reduced since the electrodes are deposited on the electrolyte and sintered in only one sintering step, minimizing chemical and physical incompatibility issues. Moreover, the possible performance degradation of the anode, caused by sulfur poisoning and carbon deposition in the electroactive sites, may be reverted by switching the gas flow to oxidize the polluting species [7,8]. However, the requirements of the symmetrical electrodes are very strict, including structural stability, physical and chemical compatibility with the electrolyte, sufficient ionic and electronic conductivity, simultaneous electrocatalytic activity toward fuel oxidation and oxygen reduction reactions in both reducing and oxidizing atmospheres, respectively.

The first symmetrical electrodes reported in the literature were those based on lanthanum chromite perovskites, typically used as interconnector material in SOFCs, because of their superior thermomechanical stability in a broad range of oxygen partial pressures and temperatures. This is associated with the high-chemical stability of Cr^{3+} at the B-site of the perovskite among the first row of the transition metals ($Cr^{3+} > Fe^{3-} > Mn^{3+} > Co^{3+}$) [9]. The transport properties of $LaCrO_3$ are tailored by modifying the crystal structure through doping in the A-

* Corresponding author. Present address: Dpto. de Física Aplicada I, Facultad de Ciencias, Campus de Teatinos, Universidad de Málaga, 29071, Málaga, Spain.
E-mail address: marrero@uma.es (D. Marrero-López).

https://doi.org/10.1016/j.jeurceramsoc.2021.09.059
Received 29 August 2021; Received in revised form 27 September 2021; Accepted 28 September 2021
Available online 30 September 2021
0955-2219/© 2021 Elsevier Ltd. All rights reserved.

UNIVERSIDAD DE MÁLAGA

Appendix 2

fuel cells, J. Power Sources 270 (2014) 418–425, https://doi.org/10.1016/j.jpowsour.2014.06.163.
[60] L. Dos Santos-Gómez, J.M. Compana, S. Bruque, E.R. Losilla, D. Marrero-López, Symmetric electrodes for solid oxide fuel cells based on Zr-doped SrFeO3-δ, J. Power Sources 279 (2015) 419–427, https://doi.org/10.1016/j.jpowsour.2015.01.043.
[61] J. Zhang, L. Lei, H. Li, F. Chen, M. Han, A practical approach for identifying various polarization behaviors of redox-stable electrodes in symmetrical solid oxide fuel cells, Electrochim. Acta 384 (2021) 138340, https://doi.org/10.1016/j.electacta.2021.138340.
[62] D.A. Osinkin, An approach to the analysis of the impedance spectra of solid oxide fuel cell using the DRT technique, Electrochim. Acta 372 (2021) 137858, https://doi.org/10.1016/j.electacta.2021.137858.
[63] D.A. Osinkin, Hydrogen oxidation kinetics on a redox stable electrode for reversible solid-state electrochemical devices: the critical influence of hydrogen dissociation on the electrode surface, Electrochim. Acta 389 (2021) 138792, https://doi.org/10.1016/j.electacta.2021.138792.
[64] J. Xia, C. Wang, X. Wang, L. Bi, Y. Zhang, A perspective on DRT applications for the analysis of solid oxide cell electrodes, Electrochim. Acta 349 (2020) 136328, https://doi.org/10.1016/j.electacta.2020.136328.

UNIVERSIDAD DE MÁLAGA

ACS APPLIED ENERGY MATERIALS

www.acsaem.org Article

$LaCrO_3$–CeO_2-Based Nanocomposite Electrodes for Efficient Symmetrical Solid Oxide Fuel Cells

Javier Zamudio-García, José M. Porras-Vázquez, Enrique R. Losilla, and David Marrero-López*

Cite This: *ACS Appl. Energy Mater.* 2022, 5, 4536–4546 Read Online

ACCESS | Metrics & More | Article Recommendations | Supporting Information

ABSTRACT: $La_{0.98}Cr_{0.75}Mn_{0.25}O_{3-\delta}$–$Ce_{0.9}Gd_{0.1}O_{1.95}$ (LCM-CGO) nanocomposite layers with different LCM contents, between 40 and 60 wt %, are prepared in a single step by a spray-pyrolysis deposition method and evaluated as both air and fuel electrodes for solid oxide fuel cells (SOFCs). The formation of fluorite (CGO) and perovskite (LCM) phases in the nanocomposite electrode is confirmed by different structural and microstructural techniques. The intimate mixture of LCM and CGO phases inhibits the grain growth, retaining the nanoscale microstructure even after annealing at 1000 °C with a grain size lower than 50 nm for LCM-CGO compared to 200 nm for pure LCM. The synergetic effect of nanosized LCM and CGO by combining their high electronic and ionic conductivity, respectively, leads to efficient and durable symmetrical electrodes. The best electrochemical properties are found for 50 wt % LCM-CGO, showing polarization resistance values of 0.29 and 0.09 Ω cm^2 at 750 °C in air and H_2, respectively, compared to 2.05 and 1.9 Ω cm^2 for a screen-printed electrode with the same composition. This outstanding performance is mainly ascribed to the nanoscale electrode microstructure formed directly on the electrolyte at a relatively low temperature. These results reveal that the combination of different immiscible phases with different crystal structures and electrochemical properties could be a promising strategy to design highly efficient and durable air and fuel electrodes for SOFCs.

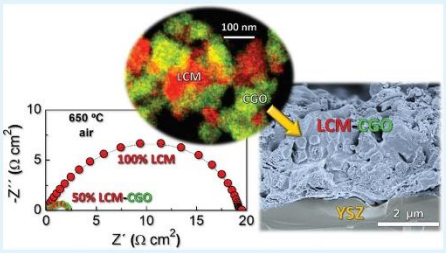

KEYWORDS: *$LaCrO_3$, CeO_2, nanocomposite electrode, symmetrical solid oxide fuel cell, spray pyrolysis*

INTRODUCTION

The high demand for electrical energy and the need for the protection of the natural environment make the development of an effective infrastructure to produce energy from renewable sources, such as solar and wind, necessary. However, the electrical production from these sources is discontinuous and intermittent to meet the immediate demand;[1,2] consequently, alternative methods for electrical production and storage are required. In this context, solid oxide cells (SOCs) are of great interest for electrical generation as they can convert the chemical energy of a wide variety of fuels, i.e., H_2 and hydrocarbons, into electrical energy.[3] Such devices can also operate reversibly in electrolysis mode to convert the excess of electricity generated by renewable sources into hydrogen, offering numerous advantages compared to rechargeable batteries, such as higher energy density, longer duration, and more flexibility.[4]

A conventional SOC is composed of a dense ceramic ion conductor electrolyte that separates two porous ceramic electrodes with different compositions, typically a mixed ionic–electronic conductor for the air electrode and a Ni-cermet for the fuel electrode.[5] However, Ni-based anodes present mechanical stability issues upon redox cycling as well as carbon deposition and sulfur poisoning when hydrocarbon fuels are employed.[6] An alternative cell configuration, known as symmetrical solid oxide cells (SSOCs), where the same electrode material is used as both air and fuel electrodes, has gained great attention in the last few years because of its simpler fabrication process and improved chemical and thermomechanical stability to operate in fuel cell and electrolysis modes.[7] Nevertheless, the major challenge for the development of SSOCs is to find a suitable electrode with high electrocatalytic activity and adequate long-term stability in both oxidizing and reducing environments.[8,9]

Different symmetrical electrodes have been reported in the literature, including doped $LaCrO_3$, $SrFeO_3$, $PrBa(Fe,Mn)_2O_{5+\delta}$, and $La_{0.4}Sr_{1.6}MnO_{4+\delta}$.[10−13] Among them, doped $LaCrO_3$ is one of the most widely studied due to its high redox stability, resistance to sulfur poisoning, and carbon

Received: December 30, 2021
Accepted: March 25, 2022
Published: April 5, 2022

ACS Publications © 2022 American Chemical Society

https://doi.org/10.1021/acsaem.1c04116
ACS Appl. Energy Mater. 2022, 5, 4536–4546

UNIVERSIDAD DE MÁLAGA

(49) Song, Y.; Zhong, Q.; Tan, W. Synthesis and Electrochemical Behaviour of Ceria-Substitution LSCM as a Possible Symmetric Solid Oxide Fuel Cell Electrode Material Exposed to H_2 Fuel Containing H2S. *Int. J. Hydrogen Energy* **2014**, *39*, 13694−13700.
(50) Osinkin, D. A.; Kolchugin, A. A.; Bogdanovich, N. M.; Beresnev, S. M. Performance and Redox Stability of a Double−Layer $Sr_2Fe_{1.5}Mo_{0.5}O_{6-\delta}$—Based Electrode for Solid State Electrochemical Application. *Electrochim. Acta* **2020**, *361*, No. 137058.
(51) Hou, Y.; Wang, L.; Bian, L.; Wang, Y.; Chou, K. C. Excellent Electrochemical Performance of $La_{0.3}Sr_{0.7}Fe_{0.9}Ti_{0.1}O_{3-\delta}$ as a Symmetric Electrode for Solid Oxide Cells. *ACS Appl. Mater. Interfaces* **2021**, *13*, 22381−22390.
(52) Marcucci, A.; Zurlo, F.; Sora, I. N.; Placidi, E.; Casciardi, S.; Licoccia, S.; Di Bartolomeo, E. A Redox Stable Pd-Doped Perovskite for SOFC Applications. *J. Mater. Chem. A* **2019**, *7*, 5344−5352.
(53) Dong, X.; Ma, S.; Huang, K.; Chen, F. $La_{0.9-X}Ca_XCe_{0.1}CrO_{3-\delta}$ as Potential Anode Materials for Solid Oxide Fuel Cells. *Int. J. Hydrogen Energy* **2012**, *37*, 10866−10873.
(54) Wei, T.; Zhou, X.; Hu, Q.; Gao, Q.; Han, D.; Lv, X.; Wang, S. A High Power Density Solid Oxide Fuel Cell Based on Nano-Structured $La_{0.8}Sr_{0.2}Cr_{0.5}Fe_{0.5}O_{3-\delta}$ Anode. *Electrochim. Acta* **2014**, *148*, 33−38.
(55) Fowler, D. E.; Haag, J. M.; Boland, C.; Bierschenk, D. M.; Barnett, S. A.; Poeppelmeier, K. R. Stable, Low Polarization Resistance Solid Oxide Fuel Cell Anodes: $La_{1-x}Sr_xCr_{1-x}Fe_xO_{3-\delta}$ (x = 0.2-0.67). *Chem. Mater.* **2014**, *26*, 3113−3120.
(56) Zenou, V. Y.; Fowler, D. E.; Gautier, R.; Barnett, S. A.; Poeppelmeier, K. R.; Marks, L. D. Redox and Phase Behavior of Pd-Substituted (La,Sr)CrO_3 Perovskite Solid Oxide Fuel Cell Anodes. *Solid State Ionics* **2016**, *296*, 90−105.
(57) Kobsiriphat, W.; Madsen, B. D.; Wang, Y.; Marks, L. D.; Barnett, S. A. $La_{0.8}Sr_{0.2}Cr_{1-X}Ru_xO_{3-\delta}$-$Gd_{0.1}Ce_{0.9}O_{1.95}$ Solid Oxide Fuel Cell Anodes: Ru Precipitation and Electrochemical Performance. *Solid State Ionics* **2009**, *180*, 257−264.
(58) Siebert, E.; Hammouche, A.; Kleitz, M. Impedance Spectroscopy Analysis of $La_{1-X}Sr_{ltx}MnO_{3-\delta}$Yttria-Stabilized Zirconia Electrode Kinetics. *Electrochim. Acta* **1995**, *40*, 1741−1753.
(59) Kuai, X.; Yang, G.; Chen, Y.; Sun, H.; Dai, J.; Song, Y.; Ran, R.; Wang, W.; Zhou, W.; Shao, Z. Boosting the Activity of $BaCo_{0.4}Fe_{0.4}Zr_{0.1}Y_{0.1}O_{3-\delta}$ Perovskite for Oxygen Reduction Reactions at Low-to-Intermediate Temperatures through Tuning B-Site Cation Deficiency. *Adv. Energy Mater.* **2019**, *9*, No. 1902384.
(60) Chen, X. J.; Khor, K. A.; Chan, S. H. Identification of O_2 Reduction Processes at Yttria Stabilized Zirconiadoped Lanthanum Manganite Interface. *J. Power Sources* **2003**, *123*, 17−25.
(61) Marrero-López, D.; Dos Santos-Gómez, L.; Canales-Vázquez, J.; Martín, F.; Ramos-Barrado, J. R. Stability and Performance of Nanostructured $La_{0.8}Sr_{0.2}MnO_3$ Cathodes Deposited by Spray-Pyrolysis. *Electrochim. Acta* **2014**, *134*, 159−166.
(62) Santos-Gómez, L. d.; Dos; Porras-Vázquez, J. M.; Losilla, E. R.; Marrero-López, D. Improving the Efficiency of Layered Perovskite Cathodes by Microstructural Optimization. *J. Mater. Chem. A* **2017**, *5*, 7896−7904.
(63) Chen, X. J.; Khor, K. A.; Chan, S. H. Electrochemical Behavior of La(Sr)MnO_3 Electrode under Cathodic and Anodic Polarization. *Solid State Ionics* **2004**, *167*, 379−387.
(64) Zapata-Ramírez, V.; Mather, G. C.; Azcondo, M. T.; Amador, U.; Pérez-Coll, D. Electrical and Electrochemical Properties of the Sr(Fe,Co,Mo)$O_{3-\delta}$ System as Air Electrode for Reversible Solid Oxide Cells. *J. Power Sources* **2019**, *437*, No. 226895.
(65) Wang, J.; Yang, T.; Lei, L.; Huang, K. Ta-Doped $SrCoO_{3-\delta}$ as a Promising Bifunctional Oxygen Electrode for Reversible Solid Oxide Fuel Cells: A Focused Study on Stability. *J. Mater. Chem. A* **2017**, *5*, 8989−9002.
(66) Kamlungsua, K.; Su, P. C. Moisture-Dependent Electrochemical Characterization of $Ba_{0.2}Sr_{1.8}Fe_{1.5}Mo_{0.5}O_{6-\delta}$ as the Fuel Electrode for Solid Oxide Electrolysis Cells (SOECs). *Electrochim. Acta* **2020**, *355*, No. 136670.
(67) Chen, M.; Chen, D.; Chang, M.; Hu, H.; Xu, Q. New Insight into Hydrogen Oxidation Reaction on $La_{0.3}Sr_{0.7}Fe_{0.7}Cr_{0.3}O_{3-\delta}$ Perovskite as a Solid Oxide Fuel Cell Anode. *J. Electrochem. Soc.* **2017**, *164*, F405−F411.
(68) Marrero-López, D.; Ruiz-Morales, J. C.; Peña-Martínez, J.; Martín-Sedeño, M. C.; Ramos-Barrado, J. R. Influence of Phase Segregation on the Bulk and Grain Boundary Conductivity of LSGM Electrolytes. *Solid State Ionics* **2011**, *186*, 44−52.
(69) Raza, R.; Zhu, B.; Rafique, A.; Naqvi, M. R.; Lund, P. Functional Ceria-Based Nanocomposites for Advanced Low-Temperature (300−600 °C) Solid Oxide Fuel Cell: A Comprehensive Review. *Mater. Today Energy* **2020**, *15*, No. 100373.
(70) Li, Y.; Zhang, W.; Zheng, Y.; Chen, J.; Yu, B.; Chen, Y.; Liu, M. Controlling cation segregation in perovskite-based electrodes for high electro-catalytic activity and durability. *Chem. Soc. Rev.* **2017**, *46*, 6345−6378.
(71) Baiutti, F.; Chiabrera, F.; Diercks, D.; Cavallaro, A.; Yedra, L.; López-Conesa, L.; Estradé, S.; Peiró, F.; Morata, A.; Aguadero, A.; Tarancón, A. Direct Measurement of Oxygen Mass Transport at the Nanoscale. *Adv. Mater.* **2021**, *33*, No. 2105622.

Recommended by ACS

Enhanced Intermediate-Temperature Electrochemical Performance of Air Electrodes for Solid Oxide Cells with Spray-Pyrolyzed Active Layers
Víctor Zapata-Ramírez, Domingo Pérez-Coll, *et al.*
FEBRUARY 14, 2020
ACS APPLIED MATERIALS & INTERFACES
READ

Enhanced Ionic Conductivity and Durability of Novel Solid Oxide Fuel Cells by Constructing a Heterojunction Based on Transition and Rare Earth Metal Co-doped Ceria
Jingjing Liu, Xinlei Yang, *et al.*
NOVEMBER 16, 2021
ACS APPLIED ENERGY MATERIALS
READ

Achieving Robust Redox Stability of SOFC through Ni-YSZ Anode Layer Thinning and Inert Support Mechanical Compensation
Zongying Han, Zhibin Yang, *et al.*
APRIL 27, 2022
ACS APPLIED ENERGY MATERIALS
READ

Anion Fluorine-Doped $La_{0.6}Sr_{0.4}Fe_{0.8}Ni_{0.2}O_{3-\delta}$ Perovskite Cathodes with Enhanced Electrocatalytic Activity for Solid Oxide Electrolysis Cell Direct CO_2 Electrolysis
Caichen Yang, Bo Chi, *et al.*
JANUARY 03, 2022
ACS SUSTAINABLE CHEMISTRY & ENGINEERING
READ

Get More Suggestions >

https://doi.org/10.1021/acsaem.1c04116
ACS Appl. Energy Mater. 2022, 5, 4536−4546

UNIVERSIDAD DE MÁLAGA

Journal of the European Ceramic Society 43 (2023) 1548–1558

Contents lists available at ScienceDirect

Journal of the European Ceramic Society

journal homepage: www.elsevier.com/locate/jeurceramsoc

Symmetrical solid oxide fuel cells based on titanate nanocomposite electrodes

Javier Zamudio-García [a], Lucía dos Santos-Gómez [a], José Manuel Porras-Vázquez [a], Enrique R. Losilla [a], David Marrero-López [b,*,1]

[a] Universidad de Málaga, Departamento de Química Inorgánica, 29071 Málaga, Spain
[b] Universidad de Málaga, Departamento de Física Aplicada I, 29071 Málaga, Spain

ARTICLE INFO

Keywords:
SOFC
$SrTiO_3$
CeO_2
Symmetrical electrode
Nanocomposite

ABSTRACT

Nanocomposite electrodes of $(Sr_{0.7}Pr_{0.3})_{0.95}TiO_{3\pm\delta}$–$Ce_{0.9}Gd_{0.1}O_{1.95}$ are directly prepared by spray-pyrolysis deposition on $Zr_{0.82}Y_{0.16}O_{1.92}$ electrolytes and their properties are compared with those obtained by the traditional screen-printing powder method. The structural, microstructural and electrical characteristics are investigated for their potential use as both cathode and anode in Solid Oxide Fuel Cells. The nanocomposite electrodes with reduced particle size ~30 nm achieved a polarization resistance at 700 °C of 0.50 and 0.46 Ω cm^2 in air and pure H_2, respectively, outperforming those obtained for the analogous screen-printed electrodes with particle size of 450 nm, i.e. 4.8 and 3.9 Ω cm^2, respectively. An electrolyte-supported cell with symmetrical electrodes reached a maximum and stable power density of 354 mW cm^{-2} at 800 °C. These results demonstrate that the performance of electrode materials with modest electrochemical properties but high phase stability, such as doped-$SrTiO_3$, can be highly improved by preparing nanocomposite electrodes directly on the electrolyte surface.

1. Introduction

Nowadays, Solid Oxide Fuel Cells (SOFCs) are considered as one of the most promising and efficient technologies for electricity generation from a wide variety of fuel gases, such as hydrogen or hydrocarbons [1,2]. However, their commercialization is still hindered by several issues, such as high manufacturing and maintenance costs, as well as short durability of the cell components at high operation temperature.

In particular, the traditional Ni-based cermet anodes, suffer from thermomechanical stability upon redox cycles due to Ni agglomeration and they are prone to coking and sulphur poisoning, leading to degradation of the microstructure and loss of performance under long-term operation [3,4]. Several mixed oxide anodes with perovskite-type structure have been investigated to overcome these issues, such as $La_{0.75}Sr_{0.25}Cr_{0.5}Mn_{0.5}O_{3-\delta}$ [5], $Sr_2MgMoO_{6-\delta}$ [6,7], $Sr_2Fe_{1.5}Mo_{0.5}O_{6-\delta}$ [8] or $PrBa(Fe,Mn)_2O_{5+\delta}$ [9]. Moreover, these electrodes have been also tested in symmetrical solid oxide fuel cells (SSOFCs), in which the same electrode material is employed simultaneously as both air and fuel electrode [10].

Among the different anode materials, doped-$SrTiO_3$ are highly attractive because of their exceptional stability under both oxidizing and reducing conditions, moderate thermal expansion, as well as high tolerance to sulphur and carbon deposition [11,12]. Furthermore, strontium titanates are chemically compatible with the most widely used solid electrolytes up to 1400 °C, such as $Zr_{0.82}Y_{0.16}O_{1.92}$ (YSZ), $La_{0.9}Sr_{0.1}Ga_{0.8}Mg_{0.2}O_{3-\delta}$ (LSGM) and $Ce_{0.9}Gd_{0.1}O_{1.95}$ (CGO) [13]. However, the performance of strontium titanates is rather modest compared to the state-of-the-art anode materials due to their poor ionic conductivity and electrocatalytic activity.

The electrochemical properties of $SrTiO_{3\pm\delta}$ are usually improved by doping with higher valence cations, such as rare-earth elements (La^{3+}, Pr^{3+}, Nd^{3+} and Y^{3+}) in the Sr-site [14–16] or Nb^{5+} in the Ti-site [17]. These materials exhibit high electronic conductivity in reducing atmospheres due to the Ti^{4+}/Ti^{3+} redox couple but the conductivity is relatively low in oxidizing conditions. The oxygen non-stoichiometry, δ, also plays a critical role in both structural and electrochemical properties. In particular, layered perovskite related phases with poor electrochemical properties have been observed by increasing the lattice oxygen content [18,19]. Furthermore, significant differences in the conductivity values are reported in the literature, suggesting that the electronic conductivity

* Corresponding author.
E mail address: marrero@uma.es (D. Marrero-López).
[1] Present address: Dpto. de Física Aplicada I, Facultad de Ciencias, Campus de Teatinos, Universidad de Málaga, 29071-Málaga, Spain.

https://doi.org/10.1016/j.jeurceramsoc.2022.11.059
Received 3 October 2022; Received in revised form 22 November 2022; Accepted 25 November 2022
Available online 26 November 2022
0955-2219/© 2022 The Author(s). Published by Elsevier Ltd. This is an open access article under the CC BY-NC-ND license (http://creativecommons.org/licenses/by-nc-nd/4.0/).

UNIVERSIDAD DE MÁLAGA

Appendix 2

[42] R.D. Shannon, Revised effective ionic radii and systematic studies of interatomic distances in halides and chalcogenides, Acta Cryst. A32 (1976) 751–767, https://doi.org/10.1107/S0567739476001551.

[43] J. Pradhan, H.K. Mallick, M.P.K. Sahoo, A.K. Pattanaik, Enhanced optical and dielectric properties of rare-earth co-doped $SrTiO_3$ ceramics, J. Mater. Sci. Mater. Electron 32 (2021) 13837–13849, https://doi.org/10.1007/s10854-021-05959-7.

[44] Y. Zhou, Q. Wen, Z. Ren, H. Xie, S. Tao, W. Zhou, Gadolinium-doped strontium titanate for high-efficiency electromagnetic interference shielding, J. Alloy. Compd. 733 (2018) 33–39, https://doi.org/10.1016/j.jallcom.2017.10.289.

[45] D.J. Cumming, J.A. Kilner, S. Skinner, Structural properties of Ce-doped strontium titanate for fuel cell applications, J. Mater. Chem. 21 (2011) 5021–5026, https://doi.org/10.1039/c0jm03680e.

[46] B. Kamecki, T. Miruszewski, J. Karczewski, Structural and electrical transport properties of Pr-doped $SrTi_{0.93}Co_{0.07}O_{3-\delta}$ a novel SOEC fuel electrode materials, J. Electroceram. 42 (2019) 31–40, https://doi.org/10.1007/s10832-018-0143-0.

[47] F. Tietz, Thermal expansion of SOFC materials, Ion. (Kiel.) 5 (1999) 129–139, https://doi.org/10.1007/BF02375916.

[48] H. Shimada, Y. Fujimaki, Y. Fujishiro, Highly active and durable $La_{0.4}Sr_{0.6}MnO_{3-\delta}$ and $Ce_{0.8}Gd_{0.2}O_{1.9}$ nanocomposite electrode for high-temperature reversible solid oxide electrochemical cells, Ceram. Int 46 (2020) 19617–19623, https://doi.org/10.1016/j.ceramint.2020.05.030.

[49] A.A. Yaremchenko, E.N. Naumovich, S.G. Patrício, O.V. Merkulov, M.V. Patrakeev, J.R. Frade, Rare-earth-substituted strontium titanate: insight into local oxygen-rich structures and redox kinetics, Inorg. Chem. 55 (2016) 4836–4849, https://doi.org/10.1021/acs.inorgchem.6b00350.

[50] T. Shi, Y. Chen, X. Guo, Defect chemistry of alkaline earth metal (Sr/Ba) titanates, Prog. Mater. Sci. 80 (2016) 77–132, https://doi.org/10.1016/j.pmatsci.2015.10.002.

[51] D.A. Osinkin, An approach to the analysis of the impedance spectra of solid oxide fuel cell using the DRT technique, Electrochim. Acta 372 (2021), 137858, https://doi.org/10.1016/j.electacta.2021.137858.

[52] J. Xia, C. Wang, X. Wang, L. Bi, Y. Zhang, A perspective on DRT applications for the analysis of solid oxide cell electrodes, Electrochim. Acta 349 (2020), 136328, https://doi.org/10.1016/j.electacta.2020.136328.

[53] D.A. Osinkin, Detailed analysis of electrochemical behavior of high–performance solid oxide fuel cell using DRT technique, J. Power Sources 527 (2022), 231120, https://doi.org/10.1016/j.jpowsour.2022.231120.

[54] Y. Chen, Y. Bu, Y. Zhang, R. Yan, D. Ding, B. Zhao, S. Yoo, D. Dang, R. Hu, C. Yang, M. Liu, A highly efficient and robust nanofiber cathode for solid oxide fuel cells, Adv. Energy Mater. 7 (2017) 1–7, https://doi.org/10.1002/aenm.201601890.

[55] H. Sumi, H. Shimada, Y. Yamaguchi, T. Yamaguchi, Y. Fujishiro, Degradation evaluation by distribution of relaxation times analysis for microtubular solid oxide fuel cells, Electrochim. Acta 339 (2020), 135913, https://doi.org/10.1016/j.electacta.2020.135913.

[56] J. Zamudio-García, L. Caizán-Juanarena, J.M. Porras-Vázquez, E.R. Losilla, D. Marrero-López, Boosting the performance of $La_{0.8}Sr_{0.2}MnO_{3-d}$ electrodes by the incorporation of nanocomposite active layers, Adv. Mat. Interfaces 9 (2022) 2200702, https://doi.org/10.1002/admi.202200702.

[57] Z. He, N. Ai, S. He, S.P. Jiang, L. Zhang, W.D.A. Rickard, D. Tang, K. Chen, Positive effect of incorporating $Er_{0.4}Bi_{1.6}O_3$ on the performance and stability of $La_2NiO_{4+\delta}$ cathode, J. Electrochem. Soc. 166 (2019) F796–F804, https://doi.org/10.1149/2.0841912jes.

[58] L. Almar, J. Szász, A. Weber, E. Ivers-Tiffée, Oxygen transport kinetics of mixed ionic-electronic conductors by coupling focused ion beam tomography and electrochemical impedance spectroscopy, J. Electrochem. Soc. 164 (2017) F289–F297, https://doi.org/10.1149/2.0851704jes.

[59] S.B. Adler, Mechanism and kinetics of oxygen reduction on porous $La_{1-x}Sr_xCoO_{3-\delta}$ electrodes, Solid State Ion. 111 (1998) 125–134, https://doi.org/10.1016/s0167-2738(98)00179-9.

[60] E. Siebert, A. Hammouche, M. Kleitz, Impedance spectroscopy analysis of $La_{1-x}Sr_{1+x}MnO_3$-yttria-stabilized zirconia electrode kinetics, Electrochim. Acta 40 (1995) 1741–1753, https://doi.org/10.1016/0013-4686(94)00361-4.

[61] Y. Zhang, L. Shen, Y. Wang, Z. Du, B. Zhang, F. Ciucci, H. Zhao, Enhanced oxygen reduction kinetics of IT-SOFC cathode with $PrBaCo_2O_{5+\delta}/Gd_{0.1}Ce_{1.9}O_{2-\delta}$ coherent interface, J. Mater. Chem. A 10 (2022) 3495–3505, https://doi.org/10.1039/d1ta09615j.

[62] X. Kuai, G. Yang, Y. Chen, H. Sun, J. Dai, Y. Song, R. Ran, W. Wang, W. Zhou, Z. Shao, Boosting the activity of $BaCo_{0.4}Fe_{0.4}Zr_{0.1}Y_{0.1}O_{3-\delta}$ perovskite for oxygen reduction reactions at low-to-intermediate temperatures through tuning B-site cation deficiency, Adv. Energy Mater. 9 (2019) 1–11, https://doi.org/10.1002/aenm.201902384.

[63] X.J. Chen, K.A. Khor, S.H. Chan, Identification of O_2 reduction processes at yttria stabilized zirconia=doped lanthanum manganite interface, J. Power Sources 123 (2003) 17–25, https://doi.org/10.1016/S0378-7753(03)00436-1.

[64] J. Zhang, L. Lei, H. Li, F. Chen, M. Han, A practical approach for identifying various polarization behaviors of redox-stable electrodes in symmetrical solid oxide fuel cells, Electrochim. Acta 384 (2021), 138340, https://doi.org/10.1016/j.electacta.2021.138340.

[65] D. Marrero-López, L. Dos Santos-Gómez, J. Canales-Vázquez, F. Martín, J. R. Ramos-Barrado, Stability and performance of nanostructured $La_{0.8}Sr_{0.2}MnO_3$ cathodes deposited by spray-pyrolysis, Electrochim. Acta 134 (2014) 159–166, https://doi.org/10.1016/j.electacta.2014.04.154.

[66] V. Kyriakou, D. Neagu, G. Zafeiropoulos, R.K. Sharma, C. Tang, K. Kousi, I. S. Metcalfe, M.C.M. Van De Sanden, M.N. Tsampas, Symmetrical exsolution of Rh nanoparticles in solid oxide cells for efficient syngas production from greenhouse gases, ACS Catal. 10 (2020) 1278–1288, https://doi.org/10.1021/acscatal.9b04424.

[67] W. Fan, Z. Sun, Y. Bai, K. Wu, J. Zhou, Y. Cheng, In situ growth of nanoparticles in A-site deficient ferrite perovskite as an advanced electrode for symmetrical solid oxide fuel cells, J. Power Sources 456 (2020), 228000, https://doi.org/10.1016/j.jpowsour.2020.228000.

[68] I. Jung, D. Lee, S.O. Lee, D. Kim, J. Kim, S.H. Hyun, J. Moon, LSCM-YSZ nanocomposites for a high performance SOFC anode, Ceram. Int. 39 (2013) 9753–9758, https://doi.org/10.1016/j.ceramint.2013.05.022.

[69] B.H. Park, G.M. Choi, Ex-solution of Ni nanoparticles in a $La_{0.2}Sr_{0.8}Ti_{1-x}Ni_xO_{3-\delta}$ alternative anode for solid oxide fuel cell, Solid State Ion. 262 (2014) 345–348, https://doi.org/10.1016/j.ssi.2013.10.016.

[70] H. Yoon, J. Zou, N.M. Sammes, J. Chung, Ru-doped lanthanum strontium titanates for the anode of solid oxide fuel cells, Int. J. Hydrog. Energy 40 (2015) 10985–10993, https://doi.org/10.1016/j.ijhydene.2015.05.193.

[71] L. Shao, F. Si, X.Z. Fu, J.L. Luo, Archiving high-performance solid oxide fuel cells with titanate anode in sulfur- and carbon-containing fuels, Electrochim. Acta 270 (2018) 9–13, https://doi.org/10.1016/j.electacta.2018.03.078.

[72] O. Korjus, P. Möller, K. Kooser, T. Käämbre, O. Volobujeva, J. Nerut, S. Kotkas, E. Lust, G. Nurk, Influence of Ni concentration on electrochemical and crystallographic properties of $La_{0.25}Sr_{0.25}Ca_{0.4}Ti_{1-x}Ni_xO_{3-\delta}$ solid oxide fuel cell anode, J. Power Sources 494 (2021), https://doi.org/10.1016/j.jpowsour.2021.229739.

[73] J. Cheng, J. Gong, S. Yue, Y. Jiang, X. Hou, J. Ma, Y. Yao, C. Jiang, Electrochemical investigation of $La_{0.4}Sr_{0.6}TiO_3$ synthesized in air for SOFC application, J. Appl. Electrochem 51 (2021) 1175–1188, https://doi.org/10.1007/s10800-021-01568-8.

[74] K. Bin Yoo, G.M. Choi, Performance of La-doped strontium titanate (LST) anode on $LaGaO_3$-based SOFC, Solid State Ion. 180 (2009) 867–871, https://doi.org/10.1016/j.ssi.2009.02.013.

[75] K. Bin Yoo, G.M. Choi, LST-GDC composite anode on $LaGaO_3$-based solid oxide fuel cell, Solid State Ion. 192 (2011) 515–518, https://doi.org/10.1016/j.ssi.2010.06.048.

[76] M.C. Verbraeken, B. Iwanschitz, A. Mai, J.T.S. Irvine, Evaluation of Ca Doped $La_{0.2}Sr_{0.7}TiO_3$ as an Alternative Material for Use in SOFC Anodes, J. Electrochem. Soc. 159 (2012) F757–F762, https://doi.org/10.1149/2.001212jes.

[77] J. Li, T. Lv, N. Hou, P. Li, X. Yao, L. Fan, T. Gan, Y. Zhao, Y. Li, Molybdenum substitution at the B-site of lanthanum strontium titanate anodes for solid oxide fuel cells, Int. J. Hydrog. Energy 42 (2017) 22294–22301, https://doi.org/10.1016/j.ijhydene.2017.03.189.

[78] X.C. Lu, J.H. Zhu, Z. Yang, G. Xia, J.W. Stevenson, Pd-impregnated SYT/LDC composite as sulfur-tolerant anode for solid oxide fuel cells, J. Power Sources 192 (2009) 381–384, https://doi.org/10.1016/j.jpowsour.2009.03.009.

[79] B.H. Park, G.M. Choi, Electrochemical performance and stability of $La_{0.2}Sr_{0.8}Ti_{0.9}Ni_{0.1}O_{3-\delta}$ and $La_{0.2}Sr_{0.8}Ti_{0.9}Ni_{0.1}O_{3-\delta}$ - $Gd_{0.2}Ce_{0.8}O_{2-\delta}$ anode with anode interlayer in H_2 and CH_4, Electrochim. Acta 182 (2015) 39–46, https://doi.org/10.1016/j.electacta.2015.09.017.

[80] R. Martínez-Coronado, A. Aguadero, D. Pérez-Coll, L. Troncoso, J.A. Alonso, M. T. Fernández-Díaz, Characterization of $La_{0.2}Sr_{0.5}Co_{0.5}Ti_{0.5}O_{3-\delta}$ as symmetrical electrode material for intermediate-temperature solid-oxide fuel cells, Int. J. Hydrog. Energy 37 (2012) 18310–18318, https://doi.org/10.1016/j.ijhydene.2012.09.033.

UNIVERSIDAD DE MÁLAGA

Tunable Electrode Architectures for $La_{0.8}Sr_{0.2}Fe_{1-x}Ti_xO_{3-\delta}$ Based Symmetrical Solid Oxide Fuel Cells

J. Zamudio-García[a], J.M. Porras-Vázquez[a], E.R. Losilla[a], and D. Marrero-López[b]

[a]Universidad de Málaga, Departamento de Química Inorgánica, 29071-Málaga, Spain.
[b]Universidad de Málaga, Departamento de Física Aplicada I, 29071-Málaga, Spain.

New strategies are necessary to enhance the efficiency of the electrodes for solid oxide fuel cells (SOFC) applications. Most of the preparation techniques require high sintering temperatures that drastically increases the grain size, leading to a very poor electrochemical activity. On this way, titanium doped ferrites have demonstrated to be promising electrodes, showing high redox stability and acceptable performance. In this study, spray-pyrolysis has been used to prepare nanostructured electrodes of $La_{0.8}Sr_{0.2}Fe_{1-x}Ti_xO_{3-\delta}$ (x= 0.2 and 0.4) in a single deposition step. An infiltrated electrode architecture was obtained by depositing the electrodes directly on a porous $Ce_{0.9}Gd_{0.1}O_{1.95}$ (CGO) backbone previously screen-printed onto a $Zr_{0.84}Y_{0.16}O_{1.92}$ (YSZ) electrolyte. The properties of this electrode, in comparison with the traditional electrode, are investigated in both oxidizing and reducing conditions for the implementation of these electrodes in Symmetrical Solid Oxide Fuel Cells (SSOFC).

Introduction

Solid Oxide Fuel Cells (SOFCs) have been proposed as one of the best candidates for energy conversion, producing electricity from different fuels at high temperatures (600-1000 ºC). Lowering the operating temperature of SOFCs is crucial to mitigate the reaction between the cell components and reduce the operation and production costs (1, 2). Nowadays, symmetrical Solid Oxide Fuel Cells (SSOFC), with the same material as cathode and anode, have attracted great attention due to their several advantages compared to the traditional cell configuration (3, 4). In SSOFC, only a single step is required to assemble the electrodes to the electrolyte, resulting in a beneficial effect on the mechanical and chemical compatibility between the cell components, as well as lowering the fabrication time and cost. These advantages play a key role in the implementation and commercialization of SSOFC devices.

The traditional synthetic methods to prepare electrodes require high sintering temperature during long times or multiple infiltration/calcination processes, having a negative impact on the electrochemical properties. In this context, spray-pyrolysis deposition is an efficient and cost-effective method to prepare electrodes with different architectures at low temperatures, such as single phases, nanocomposites, infiltrated electrodes into porous backbones as well as the preparation of active interlayers (5, 6, 7).

UNIVERSIDAD DE MÁLAGA

References

1. E. D. Wachsman, and K. T. Lee, *Science,* **334**(6058), 935 (2011).
2. Z. Zakaria, Z. A. Mat, S. H. A. Hassan, and Y. B. Kar, *Int. J. Energy Res.,* **44**(2), 594 (2020).
3. J. C. Ruíz-Morales, D. Marrero-López, J. Canales-Vázquez, and J. T. S. Irvine, *RSC Adv,*. **1**(8), 1403 (2011).
4. C. Su, W. Wei, M. Liu, M. O. Tadé, and Z. Shao, *Adv. Energy Mater.,* **5**(14), 1500188 (2015).
5. L. dos-Santos-Gómez, J. Zamudio-García, J.M. Porras-Vázquez, E.R. Losilla, and D. Marrero-López, *Ceram. Int.,* **44**(5), 4961 (2018).
6. L. dos-Santos-Gómez, J. Zamudio-García, J.M. Porras-Vázquez, E.R. Losilla, and D. Marrero-López, *Nanomaterials*, **10**(6), 1055 (2020).
7. S. S. Shin, J. H. Kim, G. Li, S. Y. Lee, J.-W. Son, H. Kim, and M. Choi, *Int. J. Hydrog. Energy*, **44**(9), 4476 (2019).
8. J. Zamudio-García, J. M. Porras-Vázquez, L. dos Santos-Gómez, E. R. Losilla, and D. Marrero-López, *Ceram. Int.*, **44**(12), 14113 (2018).
9. D. Ding, X. Li, S. Y. Lai, K. Gerdes, and M. Liu, *Energy Environ. Sci.*, **7**(2), 552 (2014).
10. L. dos-Santos-Gómez, J.M. Porras-Vázquez, E.R. Losilla, and D. Marrero-López, *J. Mater. Chem A,* **5**(17), 7896 (2017).
11. Z. Cao, L. Fan, G. Zhang, K. Shao, C. He, Q. Zhang, Z. Lv, and B. Zhu, Catal. Today, **330,** 217 (2019).
12. Z. Cao, Y. Zhang, J. Miao, Z. Wang, Z. Lü, Y. Sui, X. Huang, and W. Jiang, *Int. J. Hydrog. Energy*, **40**(46), 16572 (2015).
13. N. A. Baharuddin, N. A. M. N. Aman, A. Muchtar, M. R. Somalu, A. A. Samat, and M. I. Aznam, *Ceram. Int.*, **45**(10), 12903 (2019).
14. P. A. Connor, X. Yue, C. D. Savaniu, R. Price, G. Triantafyllou, M. Cassidy, G. Kerherve, D. J. Payne, R. C. Maher, L. F. Cohen, R. I. Tomov, B. A. Glowacki, R. V. Kumar, and J. T. S. Irvine, *Adv. Energy Mater.*, **8**(23), 1800120 (2018).

UNIVERSIDAD DE MÁLAGA

Journal of Power Sources 520 (2022) 230852

Contents lists available at ScienceDirect

Journal of Power Sources

journal homepage: www.elsevier.com/locate/jpowsour

Review article

A review on recent advances and trends in symmetrical electrodes for solid oxide cells

Javier Zamudio-García [a,**,1], Leire Caizán-Juanarena [b], José M. Porras-Vázquez [a], Enrique R. Losilla [a], David Marrero-López [b,*,1]

[a] Universidad de Málaga, Dpto. de Química Inorgánica, Cristalografía y Mineralogía, 29071, Málaga, Spain
[b] Universidad de Málaga, Dpto. de Física Aplicada I, 29071, Málaga, Spain

HIGHLIGHTS

- Symmetrical solid oxide fuel cells with identical air and fuel electrodes are reviewed.
- The state-of-the-art and future perspectives of SSOFCs and SSOECs are provided.
- Doping strategies, structure, microstructure and electrochemical properties of electrodes are discussed.
- This review will be helpful for the development of new symmetrical electrodes.

GRAPHICAL ABSTRACT

ARTICLE INFO

Keywords:
Solid oxide cells
Symmetrical electrodes
Perovskite
Exsolution
CO_2 electroreduction
Electrolysis cell

ABSTRACT

Symmetrical solid oxide cells (SSOCs) with identical air and fuel electrodes have gained significant scientific interest in the last decade because they offer several advantages over conventional cell configurations. Among other features, simpler fabrication, better chemical and thermo-mechanical compatibility between cell layers, and electrode reversibility, make them attractive for electricity generation, H_2 production and CO_2 electroreduction. This review offers an overview of the most recent advances in the field of SSOCs, paying special attention to the relationship between electrode composition, crystal structure and properties. With that aim, symmetrical electrodes are classified in four groups according to their redox stability, i.e. single phases, composites, electrodes with exsolved metal particles and those that suffer a drastic phase transformation under reducing conditions, known in the literature as quasi-symmetrical electrodes. Furthermore, an outlook of other cell configurations with increased scientific interest are also discussed, i.e. symmetrical protonic fuel cells (H-SSOCs) and solid oxide electrolyzers for CO_2 electroreduction. With this overview in mind, the authors would like to highlight the challenge ahead of finding electrode materials that optimally work under both oxidizing and reducing conditions in terms of redox stability and electrochemical properties, and further conclude on the future development of SSOCs.

* Corresponding author.
** Corresponding author.
E-mail addresses: zamudio@uma.es (J. Zamudio-García), marrero@uma.es (D. Marrero-López).
[1] Current address: Dpto. de Física Aplicada I, Facultad de Ciencias, Campus de Teatinos, Universidad de Málaga, 29071-Málaga, Spain.

https://doi.org/10.1016/j.jpowsour.2021.230852
Received 18 October 2021; Received in revised form 22 November 2021; Accepted 27 November 2021
Available online 4 December 2021
0378-7753/© 2021 Elsevier B.V. All rights reserved.

UNIVERSIDAD DE MÁLAGA

Appendix 2

electrode, J. Electrochem. Soc. 165 (2018) F17–F23, https://doi.org/10.1149/2.0351802jes.

[268] Y. Tian, L. Zhang, L. Jia, X. Wang, J. Yang, B. Chi, J. Pu, J. Li, Novel quasi-symmetrical solid oxide electrolysis cells with in-situ exsolved cathode for CO_2 electrolysis, J. CO2 Util. 31 (2019) 43–50, https://doi.org/10.1016/j.jcou.2019.02.017.

[269] L. Bian, C. Duan, L. Wang, Y. Hou, L. Zhu, R. O'Hayre, K.-C. Chou, Highly efficient, redox-stable, $La_{0.5}Sr_{0.5}Fe_{0.9}Nb_{0.1}O_{3-\delta}$ symmetric electrode for both solid-oxide fuel cell and H_2O/CO_2 Co-electrolysis operation, J. Electrochem. Soc. 165 (2018) F981–F985, https://doi.org/10.1149/2.0961811jes.

[270] Z. Yang, C. Ma, N. Wang, X. Jin, C. Jin, S. Peng, Electrochemical reduction of CO_2 in a symmetrical solid oxide electrolysis cell with $La_{0.4}Sr_{0.6}Co_{0.2}Fe_{0.7}Nb_{0.1}O_{3-\delta}$ electrode, J. CO2 Util. 33 (2019) 445–451, https://doi.org/10.1016/j.jcou.2019.07.021.

[271] H. Lv, T. Liu, X. Zhang, Y. Song, H. Matsumoto, N. Ta, C. Zeng, G. Wang, X. Bao, Atomic-Scale insight into exsolution of CoFe alloy nanoparticles in $La_{0.4}Sr_{0.6}Co_{0.2}Fe_{0.7}Mo_{0.1}O_{3-\delta}$ with efficient CO_2 electrolysis, Angew. Chem. Int. Ed. 59 (2020), https://doi.org/10.1002/anie.202006536, 15968–15973.

[272] Z. Yang, N. Wang, C. Ma, X. Jin, Z. Lei, X. Xiong, S. Peng, Co-electrolysis of H_2O-CO_2 in a solid oxide electrolysis cell with symmetrical $La_{0.4}Sr_{0.6}Co_{0.2}Fe_{0.7}Nb_{0.1}O_{3-\delta}$ electrode, J. Electroanal. Chem. 836 (2019) 107–111, https://doi.org/10.1016/j.jelechem.2019.01.064.

[273] Z. Huang, H. Qi, Z. Zhao, L. Shang, B. Tu, M. Cheng, Efficient CO_2 electroreduction on a solid oxide electrolysis cell with $La_{0.6}Sr_{0.4}Co_{0.2}Fe_{0.8}O_{3-\Delta}$-$Gd_{0.2}Ce_{0.8}O_{2-\Delta}$ infiltrated electrode, J. Power Sources 434 (2019) 226730, https://doi.org/10.1016/j.jpowsour.2019.226730.

[274] X. Peng, Y. Tian, Y. Liu, W. Wang, L. Jia, J. Pu, B. Chi, J. Li, An efficient symmetrical solid oxide electrolysis cell with LSFM-based electrodes for direct electrolysis of pure CO_2, J. CO2 Util. 36 (2020) 18–24, https://doi.org/10.1016/j.jcou.2019.10.017.

[275] Z. Cao, B. Wei, J. Miao, Z. Wang, Z. Lü, W. Li, Y. Zhang, X. Huang, X. Zhu, Q. Feng, Y. Sui, Efficient electrolysis of CO_2 in symmetrical solid oxide electrolysis cell with highly active $La_{0.5}Sr_{0.7}Fe_{0.7}Ti_{0.3}O_3$ electrode material, Electrochem. Commun. 69 (2016) 80–83, https://doi.org/10.1016/j.elecom.2016.06.008.

[276] Y. Li, S. Zou, J. Ju, C. Xia, Characteristics of nano-structured SFM infiltrated onto YSZ backbone for symmetrical and reversible solid oxide cells, Solid State Ionics 319 (2018) 98–104, https://doi.org/10.1016/j.ssi.2018.02.003.

[277] Y. Wang, T. Liu, S. Fang, F. Chen, Syngas production on a symmetrical solid oxide H_2O/CO_2 co-electrolysis cell with $Sr_2Fe_{1.5}Mo_{0.5}O_6$-$Sm_{0.2}Ce_{0.8}O_{1.9}$ electrodes, J. Power Sources 305 (2016) 240–248, https://doi.org/10.1016/j.jpowsour.2015.11.097.

[278] S. Hou, K. Xie, Enhancing the performance of high-temperature H_2O/CO_2 co-electrolysis process on the solid oxide $Sr_2Fe_{1.6}Mo_{0.5}O_{6-\delta}$-SDC/LSGM/$Sr_2Fe_{1.5}Mo_{0.5}O_{6-\delta}$-SDC, Electrochim. Acta 301 (2019) 63–68, https://doi.org/10.1016/j.electacta.2019.01.164.

[279] Y. Li, Z. Zhan, C. Xia, Highly efficient electrolysis of pure CO_2 with symmetrical nanostructured perovskite electrodes, Catal. Sci. Technol. 8 (2018) 980–984, https://doi.org/10.1039/c7cy02324c.

[280] D. Huan, L. Zhang, S. Zhang, N. Shi, X. Li, K. Zhu, C. Xia, R. Peng, Y. Lu, Ruddlesden-Popper oxide $SrEu_2Fe_2O_7$as a promising symmetrical electrode for pure CO_2 electrolysis, J. Mater. Chem. A. 9 (2021) 2706–2713, https://doi.org/10.1039/d0ta09585k.

[281] L. Zhang, Y. Tian, Y. Liu, L. Jia, J. Yang, B. Chi, J. Pu, J. Li, Direct electrolysis of CO_2 in a symmetrical solid oxide electrolysis cell with spinel $MnCo_2O_4$ as electrode, ChemElectroChem 6 (2019) 1359–1364, https://doi.org/10.1002/celc.201801831.

UNIVERSIDAD DE MÁLAGA

nanomaterials

MDPI

Article

Unraveling the Influence of the Electrolyte on the Polarization Resistance of Nanostructured $La_{0.6}Sr_{0.4}Co_{0.2}Fe_{0.8}O_{3-\delta}$ Cathodes

Javier Zamudio-García [1,*], Leire Caizán-Juanarena [2], José M. Porras-Vázquez [1], Enrique R. Losilla [1] and David Marrero-López [2,*]

[1] Departamento de Química Inorgánica, Universidad de Málaga, 29071 Málaga, Spain
[2] Departamento de Física Aplicada I, Universidad de Málaga, 29071 Málaga, Spain
* Correspondence: zamudio@uma.es (J.Z.-G.); marrero@uma.es (D.M.-L.)

Abstract: Large variations in the polarization resistance of $La_{0.6}Sr_{0.4}Co_{0.2}Fe_{0.8}O_{3-\delta}$ (LSCF) cathodes are reported in the literature, which are usually related to different preparation methods, sintering temperatures, and resulting microstructures. However, the influence of the electrolyte on the electrochemical activity and the rate-limiting steps of LSCF remains unclear. In this work, LSCF nanostructured electrodes with identical microstructure are prepared by spray-pyrolysis deposition onto different electrolytes: $Zr_{0.84}Y_{0.16}O_{1.92}$ (YSZ), $Ce_{0.9}Gd_{0.1}O_{1.95}$ (CGO), $La_{0.9}Sr_{0.1}Ga_{0.8}Mg_{0.2}O_{2.85}$ (LSGM), and $Bi_{1.5}Y_{0.5}O_{3-\delta}$ (BYO). The ionic conductivity of the electrolyte has a great influence on the electrochemical performance of LSCF due to the improved oxide ion transport at the electrode/electrolyte interface, as well as the extended ionic conduction paths for the electrochemical reactions on the electrode surface. In this way, the polarization resistance of LSCF decreases as the ionic conductivity of the electrolyte increases in the following order: YSZ > LSGM > CGO > BYO, with values ranging from 0.21 Ω cm^2 for YSZ to 0.058 Ω cm^2 for BYO at 700 °C. In addition, we demonstrate by distribution of relaxation times and equivalent circuit models that the same rate-limiting steps for the ORR occur regardless of the electrolyte. Furthermore, the influence of the current collector material on the electrochemical performance of LSCF electrodes is also analyzed.

Keywords: nanostructured materials; SOFC; cathode; electrolyte; spray-pyrolysis

check for updates

Citation: Zamudio-García, J.; Caizán-Juanarena, L.; Porras-Vázquez, J.M.; Losilla, E.R.; Marrero-López, D. Unraveling the Influence of the Electrolyte on the Polarization Resistance of Nanostructured $La_{0.6}Sr_{0.4}Co_{0.2}Fe_{0.8}O_{3-\delta}$ Cathodes. *Nanomaterials* **2022**, *12*, 3936. https://doi.org/10.3390/nano12223936

Received: 17 October 2022
Accepted: 4 November 2022
Published: 8 November 2022

Publisher's Note: MDPI stays neutral with regard to jurisdictional claims in published maps and institutional affiliations.

Copyright: © 2022 by the authors. Licensee MDPI, Basel, Switzerland. This article is an open access article distributed under the terms and conditions of the Creative Commons Attribution (CC BY) license (https://creativecommons.org/licenses/by/4.0/).

1. Introduction

Solid oxide fuel cells (SOFCs) are one of the most promising technologies for efficient power generation and hydrogen production [1]. The main challenges regarding the commercialization of these devices are the reduction of the operating temperature and the development and optimization of alternative cell components (electrolyte, electrodes and interconnectors) with the aim of reducing their production costs [2,3].

One of the most limiting factors to achieve highly efficient SOFC devices at intermediate temperatures (600–800 °C) is the high polarization resistances of the cathode due to the sluggish oxygen reduction reaction (ORR) compared to the hydrogen oxidation reaction (HOR). In order to overcome this drawback, new cathode materials have been investigated, such as $Sm_{0.5}Sr_{0.5}CoO_{3-\delta}$, $La_{0.6}Sr_{0.4}CoO_{3-\delta}$, (Pr,Gd)$BaCo_2O_{5+\delta}$, or $Ca_3Co_4O_{9+\delta}$, achieving remarkable results at 600 °C compared to the traditional $La_{0.8}Sr_{0.2}MnO_{3-\delta}$ (LSM) cathode [4,5]. However, these cobalt-based electrodes suffer from several disadvantages, including high thermal expansion coefficients, chemical reactivity with the electrolyte and low phase stability after long-term operation [6–8]. In contrast, iron-cobalt based perovskites, such as $La_{0.6}Sr_{0.4}Co_{0.2}Fe_{0.8}O_{3-\delta}$ (LSCF), exhibit moderate thermal expansion while having a good electrocatalytic activity for ORR, which makes it one of the most promising cathodes for SOFCs [9,10].

It is evident that the performance of SOFC electrodes depends on their intrinsic bulk properties, which are related to the composition and crystal structure, since they affect

UNIVERSIDAD DE MÁLAGA

51. Hong, J.; Bhardwaj, A.; Bae, H.; Kim, I.; Song, S.-J. Electrochemical Impedance Analysis of SOFC with Transmission Line Model Using Distribution of Relaxation Times (DRT). *J. Electrochem. Soc.* **2020**, *167*, 114504. [CrossRef]
52. Chen, Y.; Bu, Y.; Zhang, Y.; Yan, R.; Ding, D.; Zhao, B.; Yoo, S.; Dang, D.; Hu, R.; Yang, C.; et al. A Highly Efficient and Robust Nanofiber Cathode for Solid Oxide Fuel Cells. *Adv. Energy Mater.* **2017**, *7*, 1–7. [CrossRef]
53. Zapata-Ramírez, V.; Dos Santos-Gómez, L.; Mather, G.C.; Marrero-López, D.; Pérez-Coll, D. Enhanced Intermediate-Temperature Electrochemical Performance of Air Electrodes for Solid Oxide Cells with Spray-Pyrolyzed Active Layers. *ACS Appl. Mater. Interfaces* **2020**, *12*, 10571–10578. [CrossRef]
54. Araújo, A.J.M.; Loureiro, F.J.A.; Holz, L.I.V.; Graça, V.C.D.; Grilo, J.P.F.; Macedo, D.A.; Paskocimas, C.A.; Fagg, D.P. Creating New Surface-Exchange Pathways on the Misfit Ca-Cobaltite Electrode by the Addition of an Active Interlayer. *J. Power Sources* **2021**, *510*. [CrossRef]
55. Dos Santos-Gómez, L.; Zamudio-García, J.; Porras-Vázquez, J.M.; Losilla, E.R.; Marrero-López, D. Nanostructured $BaCo_{0.4}Fe_{0.4}Zr_{0.1}Y_{0.1}O_{3-\delta}$ Cathodes with Different Microstructural Architectures. *Nanomaterials* **2020**, *10*, 1055. [CrossRef] [PubMed]
56. Jiang, Z.; Lei, Z.; Ding, B.; Xia, C.; Zhao, F.; Chen, F. Electrochemical Characteristics of Solid Oxide Fuel Cell Cathodes Prepared by Infiltrating (La,Sr)MnO_3 Nanoparticles into Yttria-Stabilized Bismuth Oxide Backbones. *Int. J. Hydrogen Energy* **2010**, *35*, 8322–8330. [CrossRef]
57. Peng, R.; Wu, T.; Liu, W.; Liu, X.; Meng, G. Cathode Processes and Materials for Solid Oxide Fuel Cells with Proton Conductors as Electrolytes. *J. Mater. Chem.* **2010**, *20*, 6218–6225. [CrossRef]
58. Wang, Y.; Wang, D.; Li, Y. A Fundamental Comprehension and Recent Progress in Advanced Pt-based ORR Nanocatalysts. *SmartMat* **2021**, *2*, 56–75. [CrossRef]
59. Simner, S.P.; Electrochem, J.; Soc, A.; Simner, S.P.; Anderson, M.D.; Pederson, L.R.; Stevenson, J.W. Performance Variability of La(Sr)FeO_3 SOFC Cathode with Pt, Ag, and Au Current Collectors. *J. Electrochem. Soc.* **2005**, *152*, A1851. [CrossRef]

UNIVERSIDAD DE MÁLAGA

Check for updates

RESEARCH ARTICLE

ADVANCED MATERIALS INTERFACES
www.advmatinterfaces.de

Boosting the Performance of $La_{0.8}Sr_{0.2}MnO_{3-\delta}$ Electrodes by The Incorporation of Nanocomposite Active Layers

*Javier Zamudio-García, Leire Caizán-Juanarena, José M. Porras-Vázquez, Enrique R. Losilla, and David Marrero-López**

The use of active layers is a promising strategy to improve the properties of air electrodes for solid oxide fuel cells (SOFCs). In this work, $La_{0.8}Sr_{0.2}MnO_{3-\delta}$ is combined with different oxide ion conductors $Ce_{0.9}Gd_{0.1}O_{1.95}$, $Bi_{1.5}Y_{0.5}O_3$ and Pr_6O_{11} to form highly efficient nanocomposite active layers in a single step by spray-pyrolysis deposition. One of the main advantages of these nanocomposite layers is that the nanoscale microstructure is retained at relatively high sintering temperatures. As a consequence, the interfacial area between the electrode and the electrolyte increases significantly, leading to fast oxide ion transport at the interface, as well as more active sites for the electrochemical reactions. An exhaustive structural, microstructural, and electrochemical characterization of the layers are performed to evaluate their potential use in SOFCs. The incorporation of a $La_{0.8}Sr_{0.2}MnO_{3-\delta}$-$Ce_{0.9}Gd_{0.1}O_{1.95}$ (LSM-CGO) interlayer decreases the polarization resistance of LSM cathode from 1.71 to 0.46 Ω cm^2 at 700 °C. Moreover, a single cell with LSM-CGO interlayer generates a peak power density of 1.20 W cm^{-2} at 800 °C compared to 0.79 W cm^{-2} for the same cell without active layer. These results demonstrate the great benefits of using nanocomposite layers to improve the properties of air electrodes.

1. Introduction

Within the current energy scenario, there is a strong willingness to transit toward a sustainable energy production, involving renewable sources and clean conversion processes with no harmful emissions for the environment. Technologies such as fuel cells efficiently convert the chemical energy into electricity, thus becoming suitable candidates to achieve such transition.[1,2] In particular, solid oxide fuel cells (SOFCs) are of great interest for energy conversion due to their robustness, entirely solid structure and flexibility to use a wide variety of fuels, such as hydrogen, natural gas, and other gasified renewable biofuels.[3,4] In addition, they can also operate in reverse mode as solid oxide electrolysis cells (SOECs) to convert electricity back into chemical energy when needed.[5]

Nowadays, the main applications of SOFCs are related to medium and large stationary power generation plants, while their presence in portable devices and transportation is still limited.[6,7] One of the main reasons for that is their high operating temperatures (>800 °C) which, despite allowing high fuel conversion efficiencies, lead to accelerated material degradation and thereby shortening the cell lifetime. For that reason, an increasing research interest has grown around intermediate temperature SOFCs (IT-SOFCs), operating between 600 and 800 °C.[8] In this temperature range, the cell performance is mainly limited by the air electrode due its low kinetics toward the oxygen reduction reaction (ORR).[9] This is the case for the conventional air electrode material $La_{0.8}Sr_{0.2}MnO_{3-\delta}$ (LSM), which exhibits poor electrocatalytic activity for ORR below 800 °C.[10] Since the ionic conductivity of LSM is extremely low (4×10^{-8} S cm^{-1} at 900 °C),[11] the electrochemical reaction sites for ORR are limited to the triple phase boundary (TPB) region close to the electrode/electrolyte interface.

In this context, mixed ionic-electronic conductors (MIECs) with better electrochemical properties have been developed as air electrodes in the last few years, e.g. $La_{0.8}Sr_{0.2}Co_{0.2}Fe_{0.8}O_{3-\delta}$ (LSCF), $Ba_{0.5}Sr_{0.5}Co_{0.8}Fe_{0.2}O_{3-\delta}$ (BSCF), or $PrBaCo_2O_{5+\delta}$.[12] However, they suffer from several drawbacks, such as high thermal expansion coefficients, phase instability or phase segregation on the electrode surface.[13] For this reason, LSM is still considered an appropriate cathode for SOFC construction, despite its poorer performance at intermediate temperatures.

Numerous strategies have been proposed to improve the performance of LSM by increasing the TPB region for ORR: i) the use of composite electrodes by combining LSM with different oxide ion conductors, such as $Zr_{0.84}Y_{0.16}O_{1.92}$ (YSZ) and

J. Zamudio-García, J. M. Porras-Vázquez, E. R. Losilla
University of Málaga
Deparment of Inorganic Chemistry
Málaga 29071, Spain
L. Caizán-Juanarena, D. Marrero-López
University of Málaga
Department of Applied Physics I
Málaga 29071, Spain
E-mail: damarre@uma.es
The ORCID identification number(s) for the author(s) of this article can be found under https://doi.org/10.1002/admi.202200702.

© 2022 The Authors. Advanced Materials Interfaces published by Wiley-VCH GmbH. This is an open access article under the terms of the Creative Commons Attribution-NonCommercial-NoDerivs License, which permits use and distribution in any medium, provided the original work is properly cited, the use is non-commercial and no modifications or adaptations are made.

DOI: 10.1002/admi.202200702

© 2022 The Authors. Advanced Materials Interfaces published by Wiley-VCH GmbH

21967350, 2022, 22, Downloaded from https://onlinelibrary.wiley.com/doi/10.1002/admi.202200702 by Rbua - Consorcio De Bibliotecas, Wiley Online Library on [22/12/2022]. See the Terms and Conditions (https://onlinelibrary.wiley.com/terms-and-conditions) on Wiley Online Library for rules of use; OA articles are governed by the applicable Creative Commons License

UNIVERSIDAD DE MÁLAGA

Appendix 2

R. Schlögl, A. Knop-Gericke, C. Scheurer, T. Lunkenbein, *Adv. Mater. Interfaces* **2021**, *8*, https://doi.org/10.1002/admi.202100967.
[22] H. Fan, M. Keane, P. Singh, M. Han, *J. Power Sources* **2014**, *268*, 634.
[23] M. Morales, V. Miguel-Pérez, A. Tarancón, A. Slodczyk, M. Torrell, B. Ballesteros, J. P. Ouweltjes, J. M. Bassat, D. Montinaro, A. Morata, *J. Power Sources* **2017**, *344*, 141.
[24] S. Molin, J. Karczewski, B. Kamecki, A. Mroziński, S. F. Wang, P. Jasiński, *J. Eur. Ceram. Soc.* **2020**, *40*, 5626.
[25] L. dos Santos-Gómez, J. Zamudio-García, J. M. Porras-Vázquez, E. R. Losilla, D. Marrero-López, *J. Power Sources* **2021**, *507*, 230277.
[26] M. Xu, J. Yu, Y. Song, R. Ran, W. Wang, Z. Shao, *Energy Fuels* **2020**, *34*, 10568.
[27] L. Bouleau, N. Coton, P. Coquoz, R. Ihringer, A. Billard, P. Briois, *Crystals* **2020**, *10*, https://doi.org/10.3390/cryst10090759.
[28] R. K. Sharma, N. I. Kharnidy, L. Rapenne, F. Charlot, H. Moussaoui, J. Laurencin, E. Djurado, *J. Power Sources* **2019**, *419*, 171.
[29] J. Zamudio-García, N. Albarrán-Aroca, J. M. Porras-Vázquez, E. R. Losilla, D. Marrero-López, *Appl. Nano* **2020**, *1*, 14.
[30] V. Zapata-Ramírez, L. dos Santos-Gómez, G. C. Mather, D. Marrero-López, D. Pérez-Coll, *ACS Appl. Mater. Interfaces* **2020**, *12*, 10571.
[31] S. Molin, P. Z. Jasinski, *Mater. Lett.* **2017**, *189*, 252.
[32] R. K. Sharma, M. Burriel, L. Dessemond, J. M. Bassat, E. Djurado, *J. Mater. Chem. A* **2016**, *4*, 12451.
[33] B. Kamecki, J. Karczewski, P. Jasiński, S. Molin, *Adv. Mater. Interfaces* **2021**, *8*, 2002227.
[34] L. dos Santos-Gómez, J. Zamudio-García, J. M. Porras-Vázquez, E. R. Losilla, D. Marrero-López, *Ceram. Int.* **2018**, *44*, 4961.
[35] L. Fan, B. Zhu, P. C. Su, C. He, *Nano Energy* **2018**, *45*, 148.
[36] NIST Inorganic Crystal Structure Database, *NIST Standard Reference Database Number 3*, National Institute of Standards and Technology, Gaithersburg MD, 20899.
[37] N. Jiang, E. D. Wachsman, *J. Am. Ceram. Soc.* **1999**, *82*, 3057.
[38] G. Lalitha, P. V. Reddy, *J. Alloys Compd.* **2010**, *494*, 476.
[39] D. W. Joh, J. H. Park, D. Kim, E. D. Wachsman, K. T. Lee, *ACS Appl. Mater. Interfaces* **2017**, *9*, 8443.
[40] K. T. Lee, D. W. Jung, M. A. Camaratta, H. S. Yoon, J. S. Ahn, E. D. Wachsman, *J. Power Sources* **2012**, *205*, 122.
[41] Y. J. Leng, S. H. Chan, *Electrochem. Solid-State Lett.* **2006**, *9*, A56.
[42] W. Guo, J. Liu, C. Jin, *J. Alloys Compd.* **2010**, *504*, L21.
[43] T. Takahashi, T. Esaka, H. Iwahara, *J. Solid State Chem.* **1976**, *16*, 317.
[44] F. Tietz, *Ionics* **1999**, *5*, 129.
[45] T. Chen, S. Pang, X. Shen, X. Jiang, W. Wang, *RSC Adv.* **2016**, *6*, 13829.
[46] J. Zhang, L. Lei, H. Li, F. Chen, M. Han, *Electrochim. Acta* **2021**, *384*, 138340.
[47] D. A. Osinkin, *Electrochim. Acta* **2021**, *372*, 137858.
[48] Z. He, N. Ai, S. He, S. P. Jiang, L. Zhang, W. D. A. Rickard, D. Tang, K. Chen, *J. Electrochem. Soc.* **2019**, *166*, F796.
[49] V. V. Kharton, F. M. Figueiredo, L. Navarro, E. N. Naumovich, A. V. Kovalevsky, A. A. Yaremchenko, A. P. Viskup, A. Carneiro, F. M. B. Marques, J. R. Frade, *J. Mater. Sci.* **2001**, *36*, 1105.
[50] C. Nicollet, A. Flura, V. Vibhu, A. Rougier, J. M. Bassat, J. C. Grenier, *Int. J. Hydrogen Energy* **2016**, *41*, 15538.
[51] L. Dos Santos-Gómez, J. M. Porras-Vázquez, E. R. Losilla, D. Marrero-López, *J. Mater. Chem. A* **2017**, *5*, 7896.
[52] L. Wu, Z. Jiang, S. Wang, C. Xia, *Int. J. Hydrogen Energy* **2013**, *38*, 2398.
[53] B. J. T. S. Irvine, D. C. Sinclair, A. R. West, *Adv. Mater.* **1990**, *2*, 132.
[54] T. Yang, S. L. Kollasch, J. Grimes, A. Xue, S. A. Barnett, *Appl. Catal. B Environ.* **2022**, *306*, 121114.
[55] E. P. Murray, S. A. Barnett, *Solid State Ionics* **2001**, *143*, 265.
[56] Z. Jiang, Z. Lei, B. Ding, C. Xia, F. Zhao, F. Chen, *Int. J. Hydrogen Energy* **2010**, *35*, 8322.
[57] Y. Zhang, L. Shen, Y. Wang, Z. Du, B. Zhang, F. Ciucci, H. Zhao, *J. Mater. Chem. A* **2022**, *10*, 3495.
[58] J. D. Kim, G. D. Kim, J. W. Moon, Y. il Park, W. H. Lee, K. Kobayashi, M. Nagai, C. E. Kim, *Solid State Ionics* **2001**, *143*, 379.
[59] A. Mroziński, S. Molin, P. Jasiński, *Electrochim. Acta* **2020**, *346*, 136285.
[60] M. J. Escudero, A. Aguadero, J. A. Alonso, L. Daza, *J. Electroanal. Chem.* **2007**, *611*, 107.
[61] L. Dos Santos-Gómez, J. Zamudio-García, J. M. Porras-Vázquez, E. R. Losilla, D. Marrero-López, *Nanomaterials* **2020**, *10*, 1055.
[62] J. Wang, F. Meng, T. Xia, Z. Shi, J. Lian, C. Xu, H. Zhao, J. M. Bassat, J. C. Grenier, *Int. J. Hydrogen Energy* **2014**, *39*, 18392.
[63] M. P. Carpanese, D. Clematis, A. Bertei, A. Giuliano, A. Sanson, E. Mercadelli, C. Nicolella, A. Barbucci, *Solid State Ionics* **2017**, *301*, 106.
[64] M. Gong, R. S. Gemmen, D. S. Mebane, K. Gerdes, X. Liu, *J. Electrochem. Soc.* **2014**, *161*, F344.
[65] B. Kenney, K. Karan, *J. Electrochem. Soc.* **2010**, *157*, B1126.
[66] X. J. Chen, K. A. Khor, S. H. Chan, *Solid State Ionics* **2004**, *167*, 379.
[67] J. Liu, Y. Yu, T. Yang, O. Ozmen, H. Finklea, E. M. Sabolsky, H. Abernathy, P. R. Ohodnicki, G. A. Hackett, *ECS Trans.* **2017**, *78*, 689.
[68] J. Wang, T. Yang, L. Lei, K. Huang, *J. Mater. Chem. A* **2017**, *5*, 8989.
[69] V. Zapata-Ramírez, G. C. Mather, M. T. Azcondo, U. Amador, D. Pérez-Coll, *J. Power Sources* **2019**, *437*, 226895.
[70] A. Bertei, M. P. Carpanese, D. Clematis, A. Barbucci, M. Z. Bazant, C. Nicolella, *Solid State Ionics* **2017**, *303*, 181.
[71] D. Pérez-Coll, A. Aguadero, M. J. Escudero, L. Daza, *J. Power Sources* **2009**, *192*, 2.
[72] J. Zamudio-García, J. M. Porras-Vázquez, E. R. Losilla, D. Marrero-López, *J. Eur. Ceram. Soc.* **2021**, *42*, 181.
[73] Z. Zheng, J. Jing, Z. Lei, Z. Wang, Z. Yang, C. Jin, S. Peng, *Int. J. Hydrogen Energy* **2022**, *47*, 18139.
[74] P. Caliandro, A. Nakajo, S. Diethelm, J. Van herle, *J. Power Sources* **2019**, *436*, 226838.
[75] D. A. Osinkin, *J. Power Sources* **2022**, *527*, 231120.
[76] D. Marrero-López, R. Romero, F. Martín, J. R. Ramos-Barrado, *J. Power Sources* **2014**, *255*, 308.
[77] X'Pert *HighScore Plus Software, v3.0e, PANalytical B. V*, Amelo, The Netherlands **2012**.
[78] A. C. Larson, R. B. V. Dreele, *General Structure Analysis System (GSAS) Software*, LosAlamos National Lab, Rep. No.LA-UR-86748.
[79] D. Johnson, Z. View, *A Software Program for IES Analysis, Version 2.8*, Scribner Associates, Inc., Southern Pines, NC **2002**.
[80] T. H. Wan, M. Saccoccio, C. Chen, F. Ciucci, *Electrochim. Acta* **2015**, *184*, 483.

© 2022 The Authors. Advanced Materials Interfaces published by Wiley-VCH GmbH

21967350, 2022, 22, Downloaded from https://onlinelibrary.wiley.com/doi/10.1002/admi.202200702 by Otaa - Consorcio De Bibliotecas, Wiley Online Library on [23/12/2022]. See the Terms and Conditions (https://onlinelibrary.wiley.com/terms-and-conditions) on Wiley Online Library for rules of use; OA articles are governed by the applicable Creative Commons License

UNIVERSIDAD DE MÁLAGA

Appendix 3, permissions

UNIVERSIDAD
DE MÁLAGA

UNIVERSIDAD
DE MÁLAGA

Article 1

16/2/23, 11:20 Rightslink® by Copyright Clearance Center

CCC RightsLink

Home | Help | Live Chat | Javier Zamudio-Garcia

Efficient symmetrical electrodes based on LaCrO3 via microstructural engineering

Author: Javier Zamudio-García,José M. Porras-Vázquez,Enrique R. Losilla,David Marrero-López
Publication: Journal of the European Ceramic Society
Publisher: Elsevier
Date: January 2022

© 2021 Elsevier Ltd. All rights reserved.

Journal Author Rights

Please note that, as the author of this Elsevier article, you retain the right to include it in a thesis or dissertation, provided it is not published commercially. Permission is not required, but please ensure that you reference the journal as the original source. For more information on this and on your other retained rights, please visit: https://www.elsevier.com/about/our-business/policies/copyright#Author-rights

BACK CLOSE WINDOW

© 2023 Copyright - All Rights Reserved | Copyright Clearance Center, Inc. | Privacy statement | Data Security and Privacy | For California Residents | Terms and ConditionsComments? We would like to hear from you. E-mail us at customercare@copyright.com

UNIVERSIDAD DE MÁLAGA

Article 3

16/2/23, 11:23 Rightslink® by Copyright Clearance Center

RightsLink

Home | Help | Live Chat | Javier Zamudio-Garcia

Symmetrical solid oxide fuel cells based on titanate nanocomposite electrodes

Author:
Javier Zamudio-García,Lucía dos Santos-Gómez,José Manuel Porras-Vázquez,Enrique R. Losilla,David Marrero-López

Publication: Journal of the European Ceramic Society

Publisher: Elsevier

Date: April 2023

© 2022 The Author(s). Published by Elsevier Ltd.

Journal Author Rights

Please note that, as the author of this Elsevier article, you retain the right to include it in a thesis or dissertation, provided it is not published commercially. Permission is not required, but please ensure that you reference the journal as the original source. For more information on this and on your other retained rights, please visit: https://www.elsevier.com/about/our-business/policies/copyright#Author-rights

BACK CLOSE WINDOW

© 2023 Copyright - All Rights Reserved | Copyright Clearance Center, Inc. | Privacy statement | Data Security and Privacy | For California Residents | Terms and ConditionsComments? We would like to hear from you. E-mail us at customercare@copyright.com

UNIVERSIDAD DE MÁLAGA

Article 4

CCC Marketplace

This is a License Agreement between Javier Zamudio Garcia ("User") and Copyright Clearance Center, Inc. ("CCC") on behalf of the Rightsholder identified in the order details below. The license consists of the order details, the Marketplace Permissions General Terms and Conditions below, and any Rightsholder Terms and Conditions which are included below.

All payments must be made in full to CCC in accordance with the Marketplace Permissions General Terms and Conditions below.

Order Date	20-Feb-2023	Type of Use	Republish in a thesis/dissertation
Order License ID	1325731-1		
ISSN	1938-5862	Publisher	IOP Publishing
		Portion	Page

LICENSED CONTENT

Publication Title	ECS transactions	Country	United States of America
Author/Editor	Electrochemical Society.	Rightsholder	IOP Publishing, Ltd
Date	01/01/2005	Publication Type	Monographic Series
Language	English		

REQUEST DETAILS

Portion Type	Page	Rights Requested	Main product
Page Range(s)	2	Distribution	Worldwide
Total Number of Pages	2	Translation	Original language of publication
Format (select all that apply)	Print, Electronic	Copies for the Disabled?	No
Who Will Republish the Content?	Academic institution	Minor Editing Privileges?	No
Duration of Use	Current edition and up to 5 years	Incidental Promotional Use?	No
		Currency	USD
Lifetime Unit Quantity	Up to 499		

NEW WORK DETAILS

Title	Microstructural tailoring of nanocomposite electrodes for solid oxide fuel cells	Institution Name	Universidad de Málaga
		Expected Presentation Date	2023-04-14
Instructor Name	Enrique Ramírez Losilla		

ADDITIONAL DETAILS

Order Reference Number	N/A	The Requesting Person/Organization to Appear on the License	Javier Zamudio Garcia

REQUESTED CONTENT DETAILS

Title, Description or Numeric Reference of the Portion(s)	Tunable Electrode Architectures for La0.8Sr0.2Fe1-XTixO3-δ Based Symmetrical Solid Oxide Fuel Cells	Title of the Article/Chapter the Portion Is From	N/A
		Author of Portion(s)	Electrochemical Society.
Editor of Portion(s)	N/A		

UNIVERSIDAD DE MÁLAGA

Article 5

16/2/23, 11:28 Rightslink® by Copyright Clearance Center

RightsLink

Home | Help | Live Chat | Javier Zamudio-Garcia

A review on recent advances and trends in symmetrical electrodes for solid oxide cells

Author:
Javier Zamudio-García,Leire Caizán-Juanarena,José M. Porras-Vázquez,Enrique R. Losilla,David Marrero-López

Publication: Journal of Power Sources

Publisher: Elsevier

Date: 1 February 2022

© 2021 Elsevier B.V. All rights reserved.

Journal Author Rights

Please note that, as the author of this Elsevier article, you retain the right to include it in a thesis or dissertation, provided it is not published commercially. Permission is not required, but please ensure that you reference the journal as the original source. For more information on this and on your other retained rights, please visit: https://www.elsevier.com/about/our-business/policies/copyright#Author-rights

BACK CLOSE WINDOW

© 2023 Copyright - All Rights Reserved | Copyright Clearance Center, Inc. | Privacy statement | Data Security and Privacy | For California Residents | Terms and ConditionsComments? We would like to hear from you. E-mail us at customercare@copyright.com

UNIVERSIDAD DE MÁLAGA

Article 7

CCC RightsLink

Home | Help | Live Chat | Javier Zamudio-Garcia

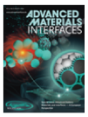

Boosting the Performance of La0.8Sr0.2MnO3-δ Electrodes by The Incorporation of Nanocomposite Active Layers

Author: David Marrero-López, Enrique R. Losilla, José M. Porras-Vázquez, et al
Publication: Advanced Materials Interfaces
Publisher: John Wiley and Sons
Date: Jul 7, 2022

© 2022 The Authors. Advanced Materials Interfaces published by Wiley-VCH GmbH

Order Completed

Thank you for your order.

This Agreement between University of Málaga -- Javier Zamudio-Garcia ("You") and John Wiley and Sons ("John Wiley and Sons") consists of your license details and the terms and conditions provided by John Wiley and Sons and Copyright Clearance Center.

Your confirmation email will contain your order number for future reference.

Printable Details

License Number	5490700507467
License date	Feb 16, 2023

Licensed Content

Licensed Content Publisher	John Wiley and Sons
Licensed Content Publication	Advanced Materials Interfaces
Licensed Content Title	Boosting the Performance of La0.8Sr0.2MnO3-δ Electrodes by The Incorporation of Nanocomposite Active Layers
Licensed Content Author	David Marrero-López, Enrique R. Losilla, José M. Porras-Vázquez, et al
Licensed Content Date	Jul 7, 2022
Licensed Content Volume	9
Licensed Content Issue	22
Licensed Content Pages	11

Order Details

Type of use	Dissertation/Thesis
Requestor type	Author of this Wiley article
Format	Print and electronic
Portion	Full article
Will you be translating?	No

About Your Work

Title	Microstructural tailoring of nanocomposite electrodes for solid oxide fuel cells
Institution name	Universidad de Málaga
Expected presentation date	Apr 2023

Additional Data

Order reference number	12

UNIVERSIDAD DE MÁLAGA

Figure 1.3

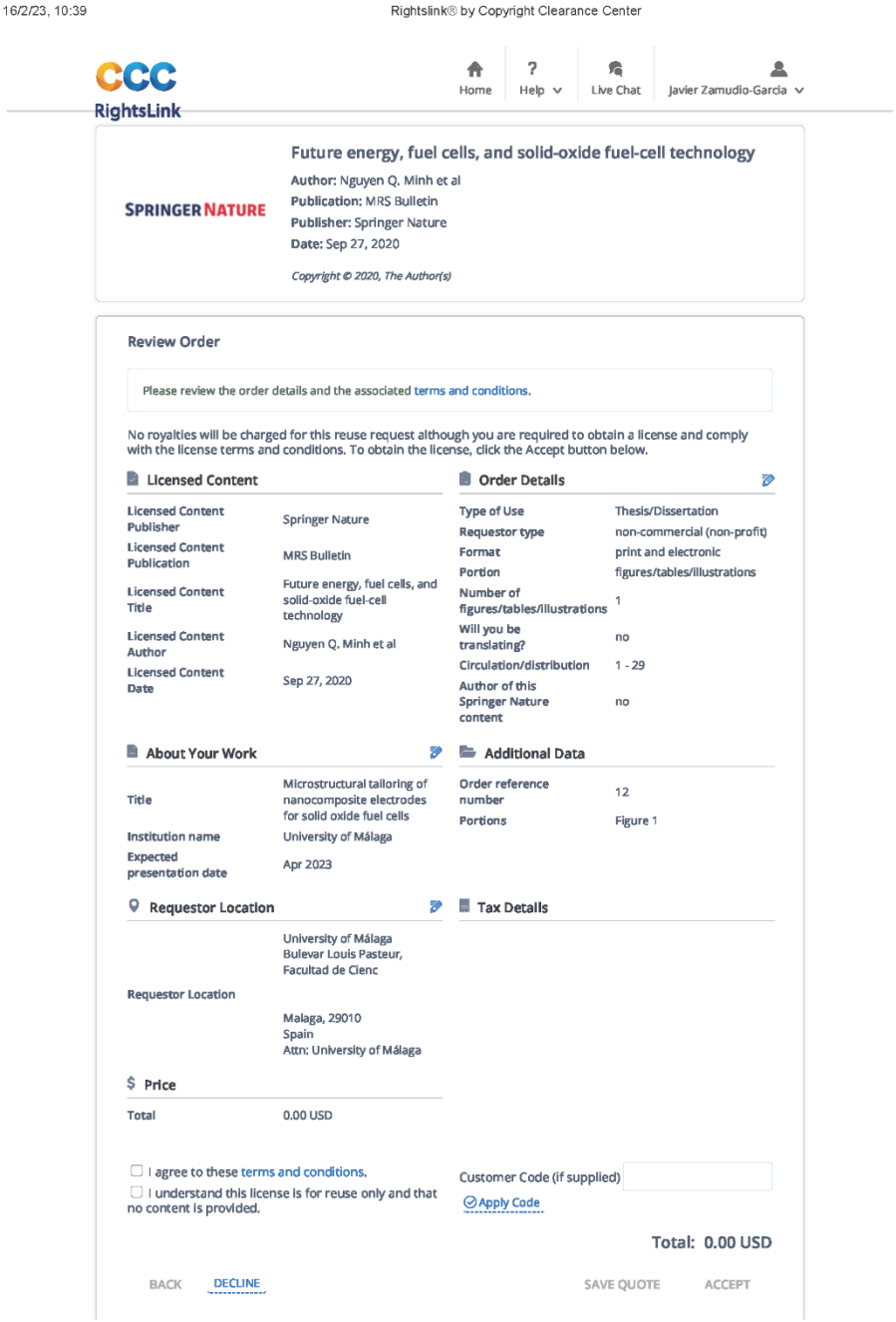

16/2/23, 10:39 Rightslink® by Copyright Clearance Center

RightsLink

Home | Help | Live Chat | Javier Zamudio-Garcia

SPRINGER NATURE

Future energy, fuel cells, and solid-oxide fuel-cell technology

Author: Nguyen Q. Minh et al
Publication: MRS Bulletin
Publisher: Springer Nature
Date: Sep 27, 2020

Copyright © 2020, The Author(s)

Review Order

Please review the order details and the associated terms and conditions.

No royalties will be charged for this reuse request although you are required to obtain a license and comply with the license terms and conditions. To obtain the license, click the Accept button below.

Licensed Content

Licensed Content Publisher	Springer Nature
Licensed Content Publication	MRS Bulletin
Licensed Content Title	Future energy, fuel cells, and solid-oxide fuel-cell technology
Licensed Content Author	Nguyen Q. Minh et al
Licensed Content Date	Sep 27, 2020

Order Details

Type of Use	Thesis/Dissertation
Requestor type	non-commercial (non-profit)
Format	print and electronic
Portion	figures/tables/illustrations
Number of figures/tables/illustrations	1
Will you be translating?	no
Circulation/distribution	1 - 29
Author of this Springer Nature content	no

About Your Work

Title	Microstructural tailoring of nanocomposite electrodes for solid oxide fuel cells
Institution name	University of Málaga
Expected presentation date	Apr 2023

Additional Data

Order reference number	12
Portions	Figure 1

Requestor Location

Requestor Location	University of Málaga Bulevar Louis Pasteur, Facultad de Cienc Malaga, 29010 Spain Attn: University of Málaga

Tax Details

Price

Total	0.00 USD

☐ I agree to these terms and conditions.
☐ I understand this license is for reuse only and that no content is provided.

Customer Code (if supplied)
Apply Code

Total: 0.00 USD

BACK DECLINE SAVE QUOTE ACCEPT

UNIVERSIDAD DE MÁLAGA

Figure 1.4

UNIVERSIDAD DE MÁLAGA

Figure 1.6

20/2/23, 15:06 https://marketplace.copyright.com/rs-ui-web/mp/license/57276a4d-48d4-4970-8034-ac1b55c85094/7b34d962-0ce9-419e-bc23-...

CCC Marketplace

This is a License Agreement between Javier Zamudio García ("User") and Copyright Clearance Center, Inc. ("CCC") on behalf of the Rightsholder identified in the order details below. The license consists of the order details, the Marketplace Permissions General Terms and Conditions below, and any Rightsholder Terms and Conditions which are included below.

All payments must be made in full to CCC in accordance with the Marketplace Permissions General Terms and Conditions below.

Order Date	20-Feb-2023	Type of Use	Republish in a thesis/dissertation
Order License ID	1325748-1		
ISSN	1754-5706	Publisher	RSC Publishing
		Portion	Chart/graph/table/figure

LICENSED CONTENT

Publication Title	Energy & environmental science	Publication Type	e-Journal
		Start Page	1602
Article Title	A perspective on low-temperature solid oxide fuel cells	End Page	1644
		Issue	5
Author/Editor	Royal Society of Chemistry (Great Britain)	Volume	9
		URL	http://www.rsc.org/Publishing/Journals/EE/Index.asp
Date	01/01/2008		
Language	English		
Country	United Kingdom of Great Britain and Northern Ireland		
Rightsholder	Royal Society of Chemistry		

REQUEST DETAILS

Portion Type	Chart/graph/table/figure	Distribution	Worldwide
Number of Charts / Graphs / Tables / Figures Requested	1	Translation	Original language of publication
		Copies for the Disabled?	No
Format (select all that apply)	Print, Electronic	Minor Editing Privileges?	No
Who Will Republish the Content?	Academic institution	Incidental Promotional Use?	No
Duration of Use	Current edition and up to 5 years	Currency	USD
Lifetime Unit Quantity	Up to 499		
Rights Requested	Main product		

NEW WORK DETAILS

Title	Microstructural tailoring of nanocomposite electrodes for solid oxide fuel cells	Institution Name	Universidad de Málaga
		Expected Presentation Date	2023-04-14
Instructor Name	Enrique Ramírez Losilla		

ADDITIONAL DETAILS

Order Reference Number	N/A

UNIVERSIDAD DE MÁLAGA

Figure 1.8

16/2/23, 10:48 Rightslink® by Copyright Clearance Center

CCC RightsLink

Home | Help | Live Chat | Javier Zamudio-Garcia

Morphology and performance evolution of anode microstructure in solid oxide fuel cell: A model-based quantitative analysis

Author: Yang Wang,Chengru Wu,Qing Du,Meng Ni,Kui Jiao,Bingfeng Zu

Publication: Applications in Energy and Combustion Science

Publisher: Elsevier

Date: March 2021

© 2020 The Authors. Published by Elsevier Ltd.

Creative Commons Attribution-NonCommercial-No Derivatives License (CC BY NC ND)

This article is published under the terms of the Creative Commons Attribution-NonCommercial-No Derivatives License (CC BY NC ND).
For non-commercial purposes you may copy and distribute the article, use portions or extracts from the article in other works, and text or data mine the article, provided you do not alter or modify the article without permission from Elsevier. You may also create adaptations of the article for your own personal use only, but not distribute these to others. You must give appropriate credit to the original work, together with a link to the formal publication through the relevant DOI, and a link to the Creative Commons user license above. If changes are permitted, you must indicate if any changes are made but not in any way that suggests the licensor endorses you or your use of the work.

Permission is not required for this non-commercial use. For commercial use please continue to request permission via RightsLink.

BACK CLOSE WINDOW

© 2023 Copyright - All Rights Reserved | Copyright Clearance Center, Inc. | Privacy statement | Data Security and Privacy | For California Residents | Terms and ConditionsComments? We would like to hear from you. E-mail us at customercare@copyright.com

UNIVERSIDAD DE MÁLAGA

Figure 1.10

16/2/23, 10:53 Rightslink® by Copyright Clearance Center

RightsLink

Home Help Live Chat Javier Zamudio-Garcia

A-site bismuth doping, a new strategy to improve the electrocatalytic performances of lanthanum chromate anodes for solid oxide fuel cells

Author:
Yanhong Wan,Yulin Xing,Zheqiang Xu,Shuangshuang Xue,Shaowei Zhang,Changrong Xia

Publication: Applied Catalysis B: Environmental

Publisher: Elsevier

Date: 15 July 2020

© 2020 Elsevier B.V. All rights reserved.

Review Order

Please review the order details and the associated terms and conditions.

No royalties will be charged for this reuse request although you are required to obtain a license and comply with the license terms and conditions. To obtain the license, click the Accept button below.

Licensed Content

Licensed Content Publisher	Elsevier
Licensed Content Publication	Applied Catalysis B: Environmental
Licensed Content Title	A-site bismuth doping, a new strategy to improve the electrocatalytic performances of lanthanum chromate anodes for solid oxide fuel cells
Licensed Content Author	Yanhong Wan,Yulin Xing,Zheqiang Xu,Shuangshuang Xue,Shaowei Zhang,Changrong Xia
Licensed Content Date	15 July 2020
Licensed Content Volume	269
Licensed Content Issue	n/a
Licensed Content Pages	1

Order Details

Type of Use	reuse in a thesis/dissertation
Portion	figures/tables/illustrations
Number of figures/tables/illustrations	3
Format	both print and electronic
Are you the author of this Elsevier article?	No
Will you be translating?	No

About Your Work

Title	Microstructural tailoring of nanocomposite electrodes for solid oxide fuel cells
Institution name	University of Málaga
Expected presentation date	Apr 2023

Additional Data

Order reference number	92
Portions	3 Figures

UNIVERSIDAD DE MÁLAGA

Figure 1.11

16/2/23, 10:54 Rightslink® by Copyright Clearance Center

CCC RightsLink

Home | Help | Live Chat | Javier Zamudio-Garcia

ACS Publications
Most Trusted. Most Cited. Most Read.

A Ce/Ru Codoped SrFeO3−δ Perovskite for a Coke-Resistant Anode of a Symmetrical Solid Oxide Fuel Cell

Author: Bangxin Li, Shuai He, Jibiao Li, et al
Publication: ACS Catalysis
Publisher: American Chemical Society
Date: Dec 1, 2020

Copyright © 2020, American Chemical Society

PERMISSION/LICENSE IS GRANTED FOR YOUR ORDER AT NO CHARGE

This type of permission/license, instead of the standard Terms and Conditions, is sent to you because no fee is being charged for your order. Please note the following:

- Permission is granted for your request in both print and electronic formats, and translations.
- If figures and/or tables were requested, they may be adapted or used in part.
- Please print this page for your records and send a copy of it to your publisher/graduate school.
- Appropriate credit for the requested material should be given as follows: "Reprinted (adapted) with permission from {COMPLETE REFERENCE CITATION}. Copyright {YEAR} American Chemical Society." Insert appropriate information in place of the capitalized words.
- One-time permission is granted only for the use specified in your RightsLink request. No additional uses are granted (such as derivative works or other editions). For any uses, please submit a new request.

If credit is given to another source for the material you requested from RightsLink, permission must be obtained from that source.

BACK CLOSE WINDOW

© 2023 Copyright - All Rights Reserved | Copyright Clearance Center, Inc. | Privacy statement | Data Security and Privacy | For California Residents | Terms and ConditionsComments? We would like to hear from you. E-mail us at customercare@copyright.com

UNIVERSIDAD DE MÁLAGA

Figure 1.12

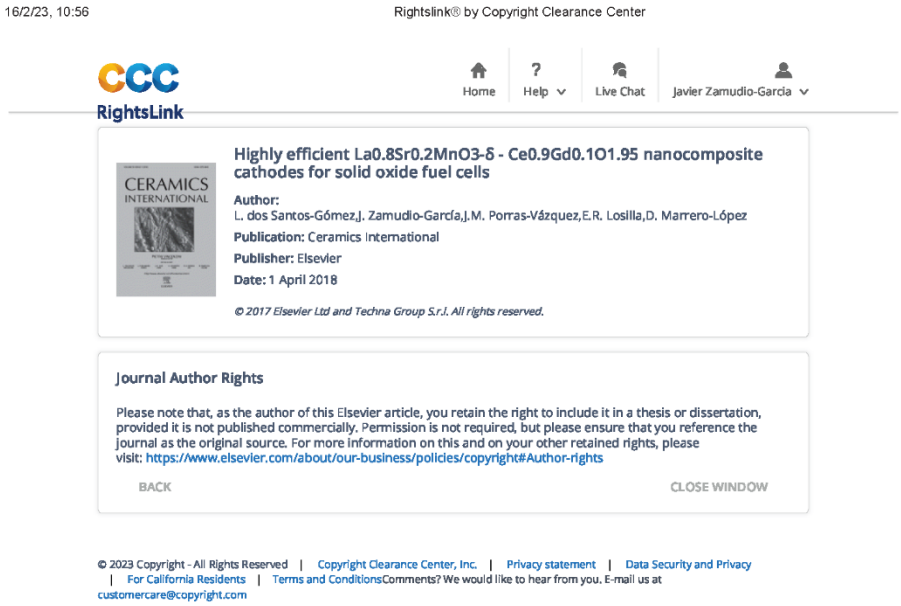

16/2/23, 10:56 Rightslink® by Copyright Clearance Center

CCC RightsLink

Home | Help | Live Chat | Javier Zamudio-Garcia

Highly efficient La0.8Sr0.2MnO3-δ - Ce0.9Gd0.1O1.95 nanocomposite cathodes for solid oxide fuel cells

Author:
L. dos Santos-Gómez,J. Zamudio-García,J.M. Porras-Vázquez,E.R. Losilla,D. Marrero-López

Publication: Ceramics International

Publisher: Elsevier

Date: 1 April 2018

© 2017 Elsevier Ltd and Techna Group S.r.l. All rights reserved.

Journal Author Rights

Please note that, as the author of this Elsevier article, you retain the right to include it in a thesis or dissertation, provided it is not published commercially. Permission is not required, but please ensure that you reference the journal as the original source. For more information on this and on your other retained rights, please visit: https://www.elsevier.com/about/our-business/policies/copyright#Author-rights

BACK CLOSE WINDOW

© 2023 Copyright - All Rights Reserved | Copyright Clearance Center, Inc. | Privacy statement | Data Security and Privacy | For California Residents | Terms and ConditionsComments? We would like to hear from you. E-mail us at customercare@copyright.com

UNIVERSIDAD DE MÁLAGA

Figure 1.13a

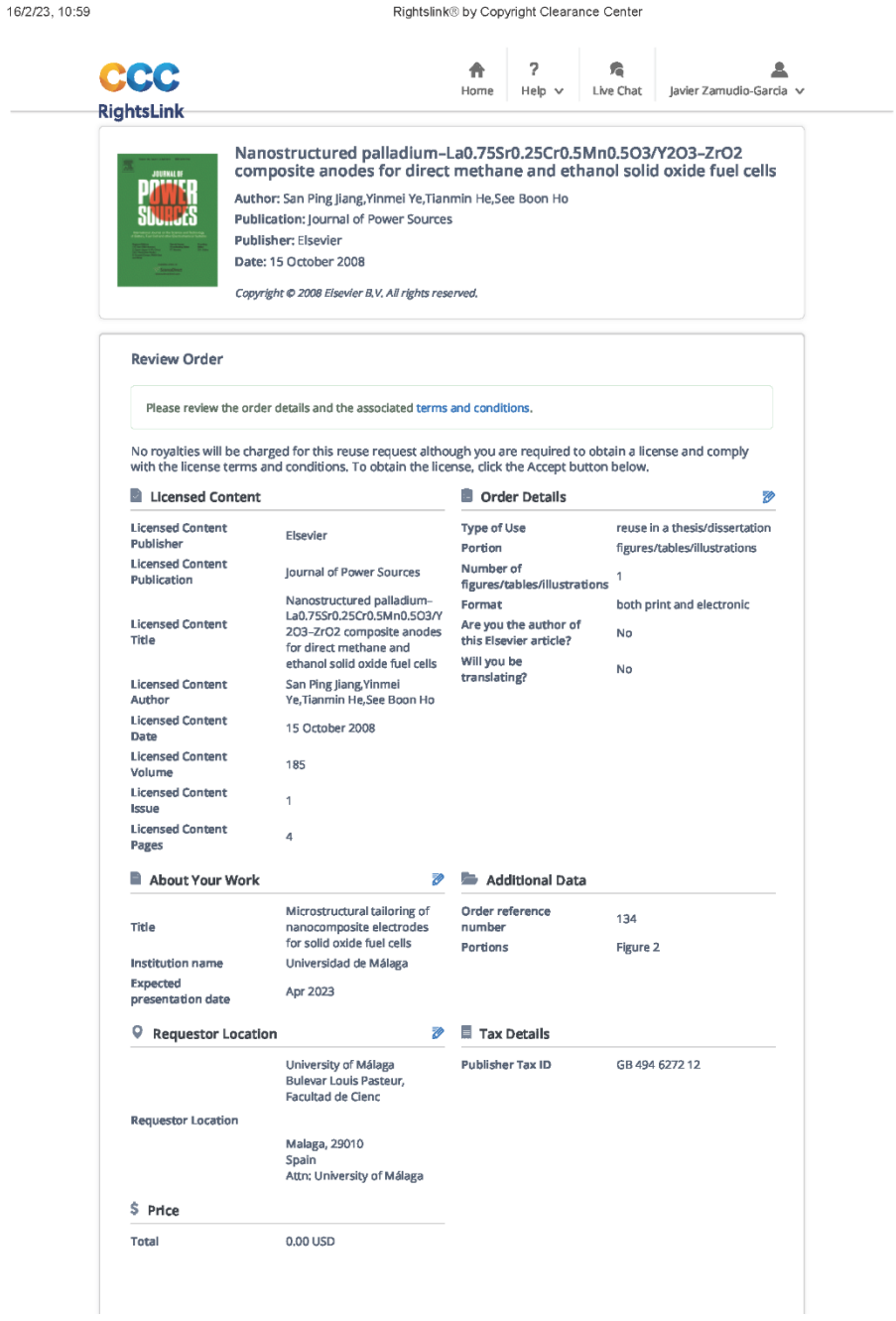

16/2/23, 10:59 Rightslink® by Copyright Clearance Center

RightsLink

Home | Help | Live Chat | Javier Zamudio-Garcia

Nanostructured palladium–La0.75Sr0.25Cr0.5Mn0.5O3/Y2O3–ZrO2 composite anodes for direct methane and ethanol solid oxide fuel cells

Author: San Ping Jiang,Yinmei Ye,Tianmin He,See Boon Ho
Publication: Journal of Power Sources
Publisher: Elsevier
Date: 15 October 2008

Copyright © 2008 Elsevier B.V. All rights reserved.

Review Order

Please review the order details and the associated terms and conditions.

No royalties will be charged for this reuse request although you are required to obtain a license and comply with the license terms and conditions. To obtain the license, click the Accept button below.

Licensed Content

Licensed Content Publisher	Elsevier
Licensed Content Publication	Journal of Power Sources
Licensed Content Title	Nanostructured palladium–La0.75Sr0.25Cr0.5Mn0.5O3/Y2O3–ZrO2 composite anodes for direct methane and ethanol solid oxide fuel cells
Licensed Content Author	San Ping Jiang,Yinmei Ye,Tianmin He,See Boon Ho
Licensed Content Date	15 October 2008
Licensed Content Volume	185
Licensed Content Issue	1
Licensed Content Pages	4

Order Details

Type of Use	reuse in a thesis/dissertation
Portion	figures/tables/illustrations
Number of figures/tables/illustrations	1
Format	both print and electronic
Are you the author of this Elsevier article?	No
Will you be translating?	No

About Your Work

Title	Microstructural tailoring of nanocomposite electrodes for solid oxide fuel cells
Institution name	Universidad de Málaga
Expected presentation date	Apr 2023

Additional Data

Order reference number	134
Portions	Figure 2

Requestor Location

Requestor Location	University of Málaga Bulevar Louis Pasteur, Facultad de Cienc Malaga, 29010 Spain Attn: University of Málaga

Tax Details

Publisher Tax ID	GB 494 6272 12

Price

Total	0.00 USD

UNIVERSIDAD DE MÁLAGA

Figure 1.13b

CCC Marketplace

This is a License Agreement between Javier Zamudio García ("User") and Copyright Clearance Center, Inc. ("CCC") on behalf of the Rightsholder identified in the order details below. The license consists of the order details, the Marketplace Permissions General Terms and Conditions below, and any Rightsholder Terms and Conditions which are included below.

All payments must be made in full to CCC in accordance with the Marketplace Permissions General Terms and Conditions below.

Order Date	16-Feb-2023	Type of Use	Republish in a thesis/dissertation
Order License ID	1324653-1		
ISSN	1944-8775	Publisher	IOP Publishing
		Portion	Chart/graph/table/figure

LICENSED CONTENT

Publication Title	Electrochemical and solid-state letters	Country	United States of America
		Rightsholder	IOP Publishing, Ltd
Author/Editor	Electrochemical Society, Institute of Electrical and Electronics Engineers.	Publication Type	e-Journal
		URL	http://ojps.aip.org/ESL
Date	01/01/1998		
Language	English		

REQUEST DETAILS

Portion Type	Chart/graph/table/figure	Distribution	Worldwide
Number of Charts / Graphs / Tables / Figures Requested	1	Translation	Original language of publication
		Copies for the Disabled?	No
Format (select all that apply)	Print, Electronic	Minor Editing Privileges?	No
Who Will Republish the Content?	Academic institution	Incidental Promotional Use?	No
		Currency	USD
Duration of Use	Current edition and up to 5 years		
Lifetime Unit Quantity	Up to 499		
Rights Requested	Main product		

NEW WORK DETAILS

Title	Microstructural tailoring of nanocomposite electrodes for solid oxide fuel cells	Institution Name	Universidad de Málaga
		Expected Presentation Date	2023-04-14
Instructor Name	Enrique Ramírez Losilla		

ADDITIONAL DETAILS

Order Reference Number	132	The Requesting Person/Organization to Appear on the License	Javier Zamudio García

REQUESTED CONTENT DETAILS

Title, Description or Numeric Reference of the Portion(s)	Figure	Title of the Article/Chapter the Portion Is From	LSM-Infiltrated Solid Oxide Fuel Cell Cathodes
Editor of Portion(s)	N/A	Author of Portion(s)	Electrochemical Society; Institute of Electrical and Electronics Engineers.
Volume of Serial or Monograph	N/A		
Page or Page Range of Portion	A376	Issue, if Republishing an Article From a Serial	N/A
		Publication Date of Portion	1998-01-01

UNIVERSIDAD DE MÁLAGA

Figure 1.14

20/2/23, 10:30 https://marketplace.copyright.com/rs-ui-web/mp/license/8dc33e7f-3eb2-48b8-8a99-7f0aa57445d5/25c5f0c9-4979-433c-bc74-52...

CCC Marketplace

This is a License Agreement between Javier Zamudio Garcia ("User") and Copyright Clearance Center, Inc. ("CCC") on behalf of the Rightsholder identified in the order details below. The license consists of the order details, the Marketplace Permissions General Terms and Conditions below, and any Rightsholder Terms and Conditions which are included below.

All payments must be made in full to CCC in accordance with the Marketplace Permissions General Terms and Conditions below.

Order Date	16-Feb-2023	Type of Use	Republish in a thesis/dissertation
Order License ID	1324654-1		
ISSN	2050-7496	Publisher	Royal Society of Chemistry
		Portion	Chart/graph/table/figure

LICENSED CONTENT

Publication Title	Journal of materials chemistry. A, Materials for energy and sustainability	Publication Type	e-Journal
		Start Page	7896
Article Title	Improving the efficiency of layered perovskite cathodes by microstructural optimization	End Page	7904
		Issue	17
		Volume	5
		URL	http://pubs.rsc.org/en/journals/journalissues/ta
Author/Editor	Royal Society of Chemistry (Great Britain)		
Date	01/01/2013		
Language	English		
Country	United Kingdom of Great Britain and Northern Ireland		
Rightsholder	Royal Society of Chemistry		

REQUEST DETAILS

Portion Type	Chart/graph/table/figure	Distribution	Worldwide
Number of Charts / Graphs / Tables / Figures Requested	4	Translation	Original language of publication
		Copies for the Disabled?	No
Format (select all that apply)	Print, Electronic	Minor Editing Privileges?	No
Who Will Republish the Content?	Academic institution	Incidental Promotional Use?	No
		Currency	USD
Duration of Use	Current edition and up to 5 years		
Lifetime Unit Quantity	Up to 499		
Rights Requested	Main product		

NEW WORK DETAILS

Title	Microstructural tailoring of nanocomposite electrodes for solid oxide fuel cells	Institution Name	Universidad de Málaga
		Expected Presentation Date	2023-04-14
Instructor Name	Enrique Ramírez Losilla		

UNIVERSIDAD DE MÁLAGA

Figure 1.15

16/2/23, 11:12 Rightslink® by Copyright Clearance Center

RightsLink

Home Help Live Chat Javier Zamudio-Garcia

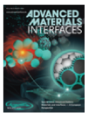

Improvement of Oxygen Electrode Performance of Intermediate Temperature Solid Oxide Cells by Spray Pyrolysis Deposited Active Layers

Author: Sebastian Molin, Piotr Jasiński, Jakub Karczewski, et al
Publication: Advanced Materials Interfaces
Publisher: John Wiley and Sons
Date: Mar 15, 2021

© 2021 Wiley-VCH GmbH

Order Completed

Thank you for your order.

This Agreement between University of Málaga -- Javier Zamudio-Garcia ("You") and John Wiley and Sons ("John Wiley and Sons") consists of your license details and the terms and conditions provided by John Wiley and Sons and Copyright Clearance Center.

Your confirmation email will contain your order number for future reference.

Printable Details

License Number	5490690837112
License date	Feb 16, 2023

Licensed Content

Licensed Content Publisher	John Wiley and Sons
Licensed Content Publication	Advanced Materials Interfaces
Licensed Content Title	Improvement of Oxygen Electrode Performance of Intermediate Temperature Solid Oxide Cells by Spray Pyrolysis Deposited Active Layers
Licensed Content Author	Sebastian Molin, Piotr Jasiński, Jakub Karczewski, et al
Licensed Content Date	Mar 15, 2021
Licensed Content Volume	8
Licensed Content Issue	9
Licensed Content Pages	11

Order Details

Type of use	Dissertation/Thesis
Requestor type	University/Academic
Format	Print and electronic
Portion	Figure/table
Number of figures/tables	3
Will you be translating?	No

About Your Work

Title	Microstructural tailoring of nanocomposite electrodes for solid oxide fuel cells
Institution name	Universidad de Málaga
Expected presentation date	Apr 2023

Additional Data

Order reference number	153
Portions	3 Figures

UNIVERSIDAD DE MÁLAGA

Figure 1.16

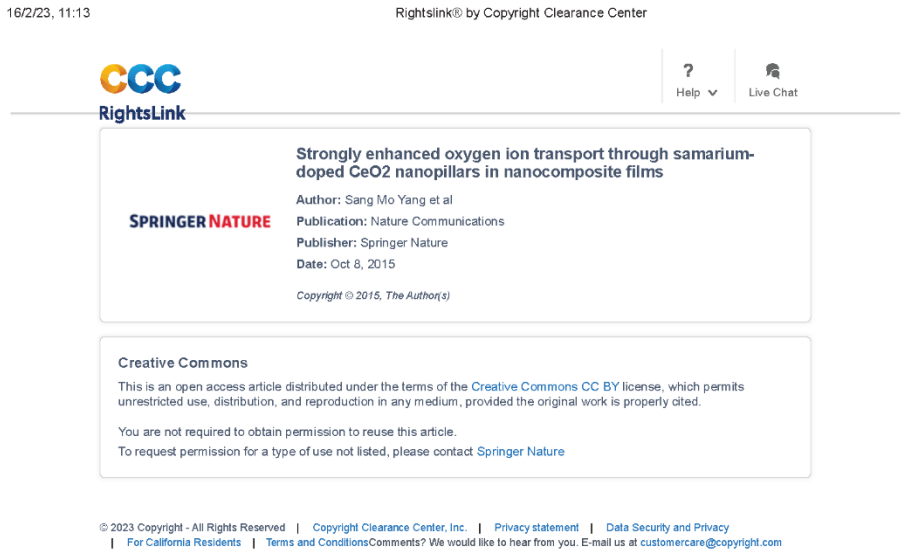

16/2/23, 11:13 Rightslink® by Copyright Clearance Center

RightsLink

Help Live Chat

SPRINGER NATURE

Strongly enhanced oxygen ion transport through samarium-doped CeO2 nanopillars in nanocomposite films

Author: Sang Mo Yang et al
Publication: Nature Communications
Publisher: Springer Nature
Date: Oct 8, 2015

Copyright © 2015, The Author(s)

Creative Commons

This is an open access article distributed under the terms of the Creative Commons CC BY license, which permits unrestricted use, distribution, and reproduction in any medium, provided the original work is properly cited.

You are not required to obtain permission to reuse this article.
To request permission for a type of use not listed, please contact Springer Nature

© 2023 Copyright - All Rights Reserved | Copyright Clearance Center, Inc. | Privacy statement | Data Security and Privacy | For California Residents | Terms and ConditionsComments? We would like to hear from you. E-mail us at customercare@copyright.com

UNIVERSIDAD DE MÁLAGA

Figure 1.17

16/2/23, 11:14 Rightslink® by Copyright Clearance Center

RightsLink

Help Live Chat

SPRINGER NATURE

Nanoengineering of cathode layers for solid oxide fuel cells to achieve superior power densities

Author: Katherine Develos-Bagarinao et al

Publication: Nature Communications

Publisher: Springer Nature

Date: Jun 25, 2021

Copyright © 2021, The Author(s)

Creative Commons

This is an open access article distributed under the terms of the Creative Commons CC BY license, which permits unrestricted use, distribution, and reproduction in any medium, provided the original work is properly cited.

You are not required to obtain permission to reuse this article.

To request permission for a type of use not listed, please contact Springer Nature

© 2023 Copyright - All Rights Reserved | Copyright Clearance Center, Inc. | Privacy statement | Data Security and Privacy | For California Residents | Terms and ConditionsComments? We would like to hear from you. E-mail us at customercare@copyright.com

UNIVERSIDAD DE MÁLAGA

Figure 1.18

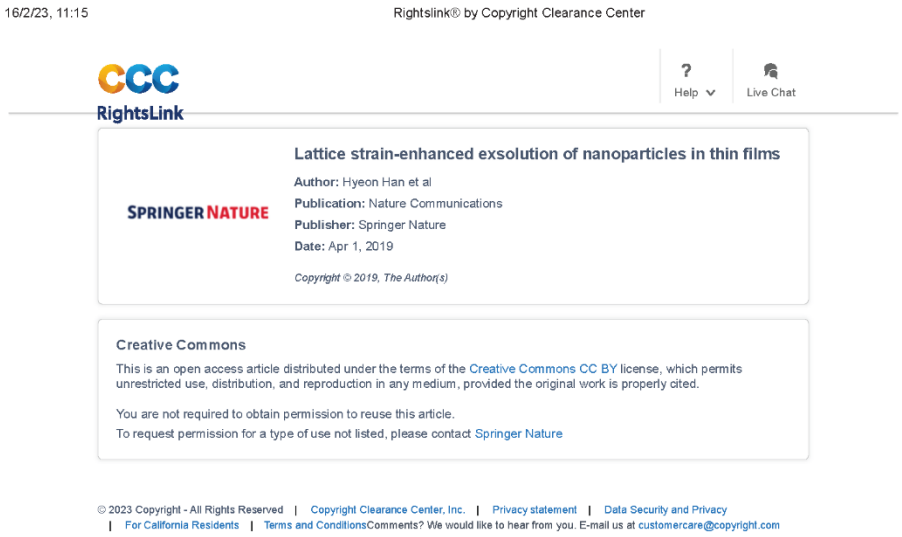

UNIVERSIDAD DE MÁLAGA

UNIVERSIDAD
DE MÁLAGA